Amazon Forest Response to Changes in Rainfall Regime: Results from an Individual-Based Dynamic Vegetation Model

a dissertation presented

by

Marcos Longo

to

Department of Earth and Planetary Sciences

in partial fulfillment of the requirements

for the degree of

Doctor of Philosophy

in the subject of

Earth and Planetary Sciences

Harvard University

Cambridge, Massachusetts
December, 2013

Amazon Forest Response to Changes in Rainfall Regime: Results from an Individual-Based Dynamic Vegetation Model

Abstract

The Amazon is the largest tropical rainforest in the world, and thus plays a major role on global water, energy, and carbon cycles. However, it is still unknown how the Amazon forest will respond to the ongoing changes in climate, especially droughts, which are expected to become more frequent. To help answering this question, in this thesis I developed and improved the representation of biophysical processes and photosynthesis in the Ecosystem Demography model (ED-2.2), an individual-based land ecosystem model. I also evaluated the model biophysics against multiple data sets for multiple forest and savannah sites in tropical South America. Results of this comparison showed that ED-2.2 is able to represent the radiation and water cycles, but exaggerates heterotrophic respiration seasonality. Also, the model generally predicted correct distribution of biomass across different areas, although it overestimated biomass in subtropical savannahs.

To evaluate the forest resilience to droughts, I used ED-2.2 to simulate the plant community dynamics at two sites in Eastern Amazonia, and developed scenarios by resampling observed annual rainfall but increasing the probability of selecting dry years. While the model predicted little response at French Guiana, results at the mid-Eastern Amazonia site indicated substantial biomass loss at modest rainfall reductions. Also, the response to drier climate varied within the plant community, with evergreen, early-successional, and larger trees being the most susceptible. The model also suggests that competition for water during prolonged periods of drought caused the largest impact on larger trees, when insufficient wet season rainfall did not recharge deeper soil layers.

Finally, results suggested that a decrease in return period of long-lasting droughts could prevent ecosystem recovery. Using different rainfall datasets, I defined vulnerability based on the change in climate needed to reduce the return period of long droughts. The most vulnerable areas would be near Southeastern edge, a large band in mid-Eastern Amazonia, Western and Northern Bolivia and areas in Eastern Peru, whereas areas in mid-Southern Amazonia could be surprisingly resilient.

Contents

Acknowledgements

The work I present in this dissertation was only possible because of the help, advice, and support I received from so many people. First, I would like to thank my advisors Steve Wofsy and Paul Moorcroft for always sharing their enthusiasm and knowledge along the way, helping me to think about the scientific questions I wanted to answer, guiding me and keeping me on track on how to answer the questions, and at the same time giving me the freedom and independence to explore how I would approach these questions.

Developing and improving a complex numerical model is always a very challenging task, but it was much more manageable thanks to the great collaborations, discussions I had along the way. I would like to thank Ryan Knox, Naomi Levine and David Medvigy for friendship and for sharing the task to translate our discussions and ideas from teleconferences, blackboards, scratch papers, and napkins into computer language. I would also like to thank Lu Alves, Matt Hayek, Natalia Restrepo-Coupe, and Kenia Wiedemann for helping me out in the data analysis and processing and discussions, friendship, and for always being available to help me.

I am indebted to Maria Assunção Silva Dias, who first introduced me to science and scientific thinking during my undergraduate and master years, encouraged me to participate on several field campaigns in the Amazon, and to apply to graduate school abroad. I am also grateful to Zhiming Kuang for giving me the opportunity to be a teaching fellow in two different courses, which not only was fun but also a great opportunity for learning new skills. Also, many thanks to Damien Bonal, Rafael Bras, Saulo Freitas, Robinson Juaréz, and Karla Longo for their very thoughtful insights and discussions.

Being part of two groups means twice the opportunity to work in a friendly and collaborative environment. I would like to thank Ben Lee, V.Y. Chow, Bin Xiang, Rick Wehr, Eric Kort, Greg Santoni, Alex Antonarakis, Abby Swann, Yeonjoo Kim, Archana Dayalu, Ke Zhang, Tom Powell, Eunjee Lee, Janice Chan, and to all current and former members of the Moorcroft and Wofsy groups and the EPS and OEB departments for making the graduate school experience fun and exciting. I would also Carla Barger, Erin Sullivan, Erin Ciccone, Brenda Mathieu, Arlene Pippin, Sarah Colgan, Paul Kelley, Cindy Marsh and Maryorie Grande for their great and prompt work on keeping the groups and the department running smoothly. Also, my special thanks to the Harvard Research Computing team for maintaing and supporting my huge computational needs. Last but not the least, I counted with truly great friends from both here and across the Equator, and in particular I would to thank Talee, Jeronimo, Andrea, Elizabeth, Aline, Rachel, Inês, Ana Claudia, Fabricio, Giovanni, and Enzo.

My sincere thanks to Regina Alvalá, Alessandro Araújo, Alessandro Baccini, Damien Bonal, Plínio de Camargo, Jeffrey Chambers, Bradley Christoffersen, Bruce Daube, David Fitzjarrald, Helber Freitas, Elaine Gottlieb, Lucy Hutyra, Antonio Manzi, Bill Munger, Celso von Randow, Humberto da Rocha, Sassan Saatchi, Scott Saleska, Scott Stark, Rodrigo da Silva, and Raphael Tapajós, who have been willing to overcome the challenges and make relevant measurements and compiling enormous datasets, and were likewise willing to share the results of their efforts with me. Also, I would also like to acknowledge the Conselho Nacional de Pesquisas e Desenvolvimento Científico (CNPq), NASA, and the Amazon-PIRE projects for supporting my studies throughout these years.

Finally, I would like to thank my family, in special my parents Silvana D. Paião Longo and Admar Longo, my brother and sister-in-law Admar Longo Jr. and Patrícia Akeda, and my cousins Silvana Biazeto and Bruno Biazeto for all their support, kindness, and for always encouraging me to pursue my endeavours.

Chapter 1

Introduction

1.1 Motivation

Global climate is undergoing significant and widespread changes due to anthropogenic emissions of greenhouse gases, most notably carbon dioxide (CO_2). The recently released Fifth Assessment Report of Intergovernmental Panel for Climate Change (IPCC, 2013) reinforces the previous reports in which widespread warming is certain, and that further warming throughout the remaining of the century is *virtually certain* according to the assessment. Of particular interest is the impact of such changes in climate to land ecosystems, in particular tropical rainforests, which store a significant amount of carbon: for instance recent assessments of carbon stocks suggest that tropical forests may store between 159 and 193 Pg of carbon in above-ground biomass (Baccini et al., 2012; Saatchi et al., 2011). In addition, terrestrial ecosystems contribute as active sinks of anthropogenic CO_2 emissions, with and a recent study by Ciais et al. (2013) suggests that between $25-30\%$ of fossil fuel emissions to the atmosphere are eventually sequestered by land, and roughly an equal amount being removed through ocean uptake.

Despite storing large amounts of carbon and working as a sink, it remains unknown how how terrestrial ecosystems will respond to further changes in climate throughout the 21^{st} century. While the most extreme scenarios using an earlier version of integrated atmosphere-ocean-biosphere

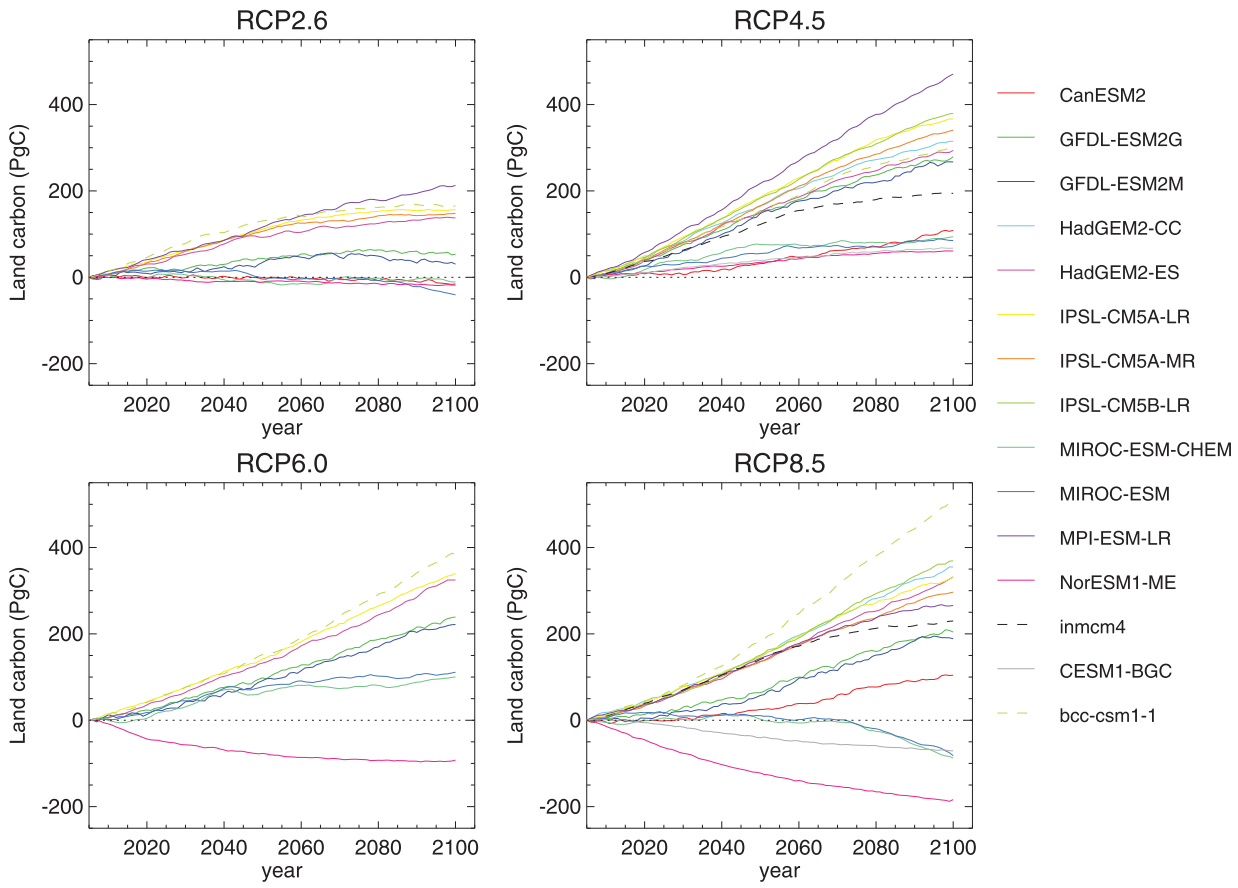

Figure 1.1: Predicted changes of total land carbon by the multiple CMIP-5 models for all tested scenarios using 2005 as the reference (figure taken from Jones et al. (2013)). Colors indicate different models, and dashed lines correspond to models without land use change. According to Jones et al. (2013), all scenarios but RCP-4.5 include a net loss of natural vegetation due to land use.

models suggested that land could turn into a carbon source after drier and warmer conditions collapsed the Amazon forest (Cox et al., 2004; Jones et al., 2009), recent evaluations constraining the results with observed variability and sensitive analysis of separate forcing (temperature, rainfall, and CO_2) indicated that such collapse is unlikely due to the positive effect of CO_2 fertilization (Cox et al., 2013; Huntingford et al., 2013). Nevertheless, the new generation of Earth system Jones et al. (2013) compared the predictions from the new generation of Earth system models (CMIP-5, also see Fig. 1.1), and large range of potential changes still exist, although simulations with the least land use change (RCP-4.5) generally shows increase in land carbon stores.

While these predictions suggest that CO_2 fertilization effect could significantly enhance forest resilience by increasing water use efficiency, and thus mitigate impacts from warmer and drier climates, there is still great uncertainty on the actual contribution of the atmopsheric CO_2 enrichment to biomass accumulation. The impact of CO_2 on photosynthesis at the leaf level has been extensively studied and has been relatively well characterized for decades (c.f. Farquhar et al., 1980; Collatz et al., 1991; Leuning, 1995; von Caemmerer, 2000; Lambers et al., 2008) and such knowledge has been used as the basis for most dynamic global vegetation models (DGVMs) (e.g. Sellers et al., 1996; Foley et al., 1996; Oleson et al., 2010; Clark et al., 2011), but the scaling from leaf to ecosystem level, and from the typical time scale of photosynthesis controls to long term dynamics at tropical forests is far from trivial (Körner, 2009, and references therein). In addition, changes in CO_2 and climate are unlikely to be the same across all species: for instance, several studies have suggested that lianas are becoming more abundant in tropical forests and their high leaf area relative to total mass ay be a reason for their faster growth (Schnitzer and Bongers, 2011); if this increase has been caused by the ongoing CO_2 increase, then the net effect of CO_2 enhancement can be significantly reduced. Recently, Clark et al. (2013) assessed the long term measurements of above-ground net primary productivity (ANPP) at La Selva, a tropical rainforest site in Costa Rica, and did not find any evidence of CO_2 fertilization effect over the past decade, and were unable to identify an increase in ANPP due to increasing CO_2; instead, wood production was more (negatively) correlated with nighttime temperature and vapour pressure deficit. Likewise, Zhao and Running (2010) used the MODIS net primary productivity algorithm to estimate the NPP variability and trends over the past decade, and their estimates suggested that global NPP may have marginally decreased, and that the decrease was mostly due to droughts in the Southern Hemisphere, in particular in 2005, which coincided with a major drought in the Southwestern Amazon (Marengo et al., 2008).

The Amazon is the largest contiguous tropical rainforest, with the area within the Amazon Basin extending over 5.8 million km^2 (Keller et al., 2004b) and storing nearly 100 Pg of carbon (Baccini et al., 2012, see Fig. 1.2 for estimated distribution of biomass across the region from

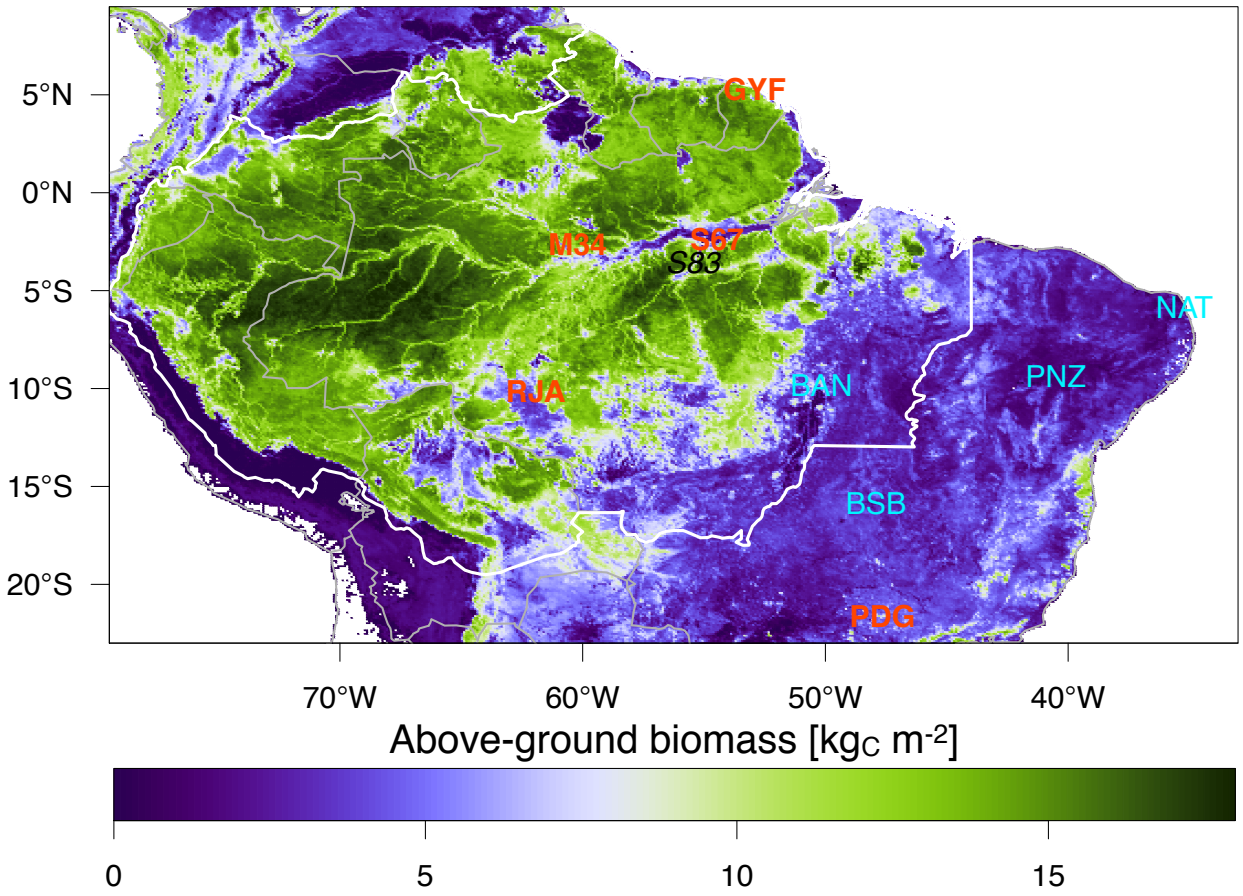

Figure 1.2: Above-ground biomass distribution across tropical South America, using the dataset from Baccini et al. (2012). Grey lines are political boundaries and the white line corresponds to Amazonia (Amazon Basin plus the Guiana Shield). The position of several sites that will be used throughout this dissertation are shown for reference.

dataset), and it has been the focus of a large scientific efforts under the Large-Scale Biosphere Experiment in Amazonia (LBA Keller et al., 2004b; Davidson et al., 2012). The LBA project aggregated a wide range of multi-disciplinary studies involving researchers from numerous institutions, areas of knowledge, and countries, towards better understanding how the Amazon region would respond to future changes in climate and land use. In spite of the significant progress in knowledge brought by LBA, many questions remain open to date. One such question is exactly on how resilient to droughts the Amazonian forests will be should the frequency of droughts increase, and whether the forest is approaching a *tipping point* in which large areas of the forest could be lost and replaced by a lower biomass, more open canopy ecosystem akin to savannahs (Nobre and

Borma, 2009; Marengo et al., 2011a). The Amazon has experienced at least four major droughts over the past 25 years, most notably 1991-1992 and 1997-1998 in the North and East, and 2004-2005 and 2010 in the Southwestern part, (Davidson et al., 2012)), and some areas of the Amazon, particularly the Southern part, may be experiencing a drying trend (Fu et al., 2013). Controlled field experiments simulating reduction of 50% of rainfall at two locations in the Amazon showed significant increase in mortality after 3 years of the experiment, with large trees being particularly susceptible (Nepstad et al., 2007; da Costa et al., 2010). In addition, Phillips et al. (2009) found significant decrease in net biomass accumulation over large areas of the Amazon following the 2005 drought, and later Phillips et al. (2010) using pantropical data also found higher mortality amongst larger trees following droughts. While observed mortality cannot be directly attributed to droughts and confounding effects such as windthrow due to squall lines (Negrón-Juárez et al., 2010), results from remote sensing suggest that significant changes in the forest structure occurred after the drought and these changes persisted for several years (Saatchi et al., 2013).

Several numerical modelling studies have been carried out testing the possibility of savannization in the Amazon, and generally found that large areas of the Amazon may be vulnerable to become either savannahs or dry forests, particularly in Southern Amazonia, and when the CO_2 fertilization effect is not included (e.g. Lapola et al., 2009; Senna et al., 2009; Rammig et al., 2010). While such studies provide important insights on vulnerable areas and contain sophisticated and realistic representation of ecosystem processes, their representation of the vegetation is often simplistic and biome-based as opposed to individual-based. The relevance of individual-based becomes evident from studies showing the response of plant community to climate extremes. For example, mortality in plant communities following a climate extreme is strongly dependent on abiotic and biotic variability in the micro-environment, and rates are also strongly dependent on different tolerances between species (Allen et al., 2010, and references therein); moreover, as mentioned before, both the controlled experiments and observations from tropical forests have indication mortality rates amongst larger trees, and also varied across different genera (Nepstad et al., 2007; da Costa et al., 2010). Different responses within the plant community are not restricted

to the Amazon: for example, Carnicer et al. (2011) found that while Mediterranean species responded to increasing drought and warming with increased defoliation and mortality, the response varied significantly amongst different species. Furthermore, plant community significantly alters the local environment, and results from such modifications may further affect the dynamics of the plant community as well as the establishment and maintenance of populations at longer term. For instance, recently De Frenne et al. (2013) used plant presence data from forest inventories in Europe and North America, and found that increase in presence of warm adapted understory species over the past decades was lower at denser forests. Finally, disturbances are also important drivers of the plant community dynamics, and vegetation structure and floristic composition is often significantly different depending on the disturbance history: for example, Chambers et al. (2009) compared the forest structure and floristic composition of two areas near Manaus (M34 Fig. 1.2), one undisturbed region and another that had been affected by a large blowdown event, and found significantly lower average wood density, basal area, and above-ground biomass in the disturbed area, with significantly higher abundance of typical pioneer genera such as *Pouroma*, *Cecropia*, adn *Vismia* at the area affected by blowdowns. Likewise, Xaud et al. (2013) found that areas affected by multiple fires in transitional forests in Roraima had significantly lower stature and basal area, and higher abundance of *Cecropia*.

Given the relevance of distribution of individuals and micro-environments within the ecosystems, many authors have advocated that the next generation of predictive ecosystem models must be based on individuals as opposed to average properties of the biomes (e.g. Moorcroft, 2006; Purves and Pacala, 2008; van der Molen et al., 2011; Evans, 2012). Amongst individual based models, the Ecosystem Demography Model (Moorcroft et al., 2001) solves the dynamics of the ecosystem by accounting for individuals of different sizes and life strategy groups, and different patches characterized by the type of disturbance that last occurred and the time since last disturbance. More importantly, the basic equations that describe the ecosystem do not require solving every individual and every single patch; instead, it solves the probability distribution function of patch ages for each disturbance type, and for any given patch, it solves the demographic density of

each plant functional group by size. This model has previously applied to a wide range of applications and biomes (e.g. Moorcroft et al., 2001; Albani et al., 2006; Desai et al., 2007; Medvigy et al., 2009; Ise and Moorcroft, 2010; Fisher et al., 2010; Antonarakis et al., 2011; Kim et al., 2012). Recently, Powell et al. (2013) compared the ability of a suite of dynamic vegetation models to represent the results from the throughfall exclusion experiments in the Amazon, and found that the Ecosystem Demography model had a better prediction of the timing of biomass loss, presumably due to a more realistic representation of the processes and interactions and competition between individuals.

How the model represents the structure of the population and landscape at a variety of biomes is illustrated in Fig. 1.3, for typical tropical rainforest and a woody savannah sites. It can be observed that in ED-2.2 biomes are also emerging properties that come with the distribution of size and age: for example, Paracou (GYF) has a low disturbance regime, which allows a high density of stems to develop (Fig. 1.3c) whereas in Brasília (BSB) a high disturbance regime (Fig. 1.3d) generated a low density of trees of generally lower stature. Moreover, the population community is structurally different between the sites (Fig. 1.3e,f), with absence of tall trees at recently disturbed sites and high abundance of early successional trees, as opposed to old patches, where mid or late successional trees become more common, and in general the population of small trees is greater amongst small trees living in old cohorts. In addition, the differences in the plant community emerge from different probability density functions of patches (Fig. 1.3g), being several times higher for recently disturbed patches, and an absence of very old patches (older than 100 yr) in Brasília.

1.2 Thesis overview

Because of the relevance of the Amazon forest in the global context of changes in climate, carbon stocks, and biodiversity, it is fundamental to understand how resilient the ecosystem is to changes in climate that may push it outside the optimal conditions. In this context, the main goal of this dis-

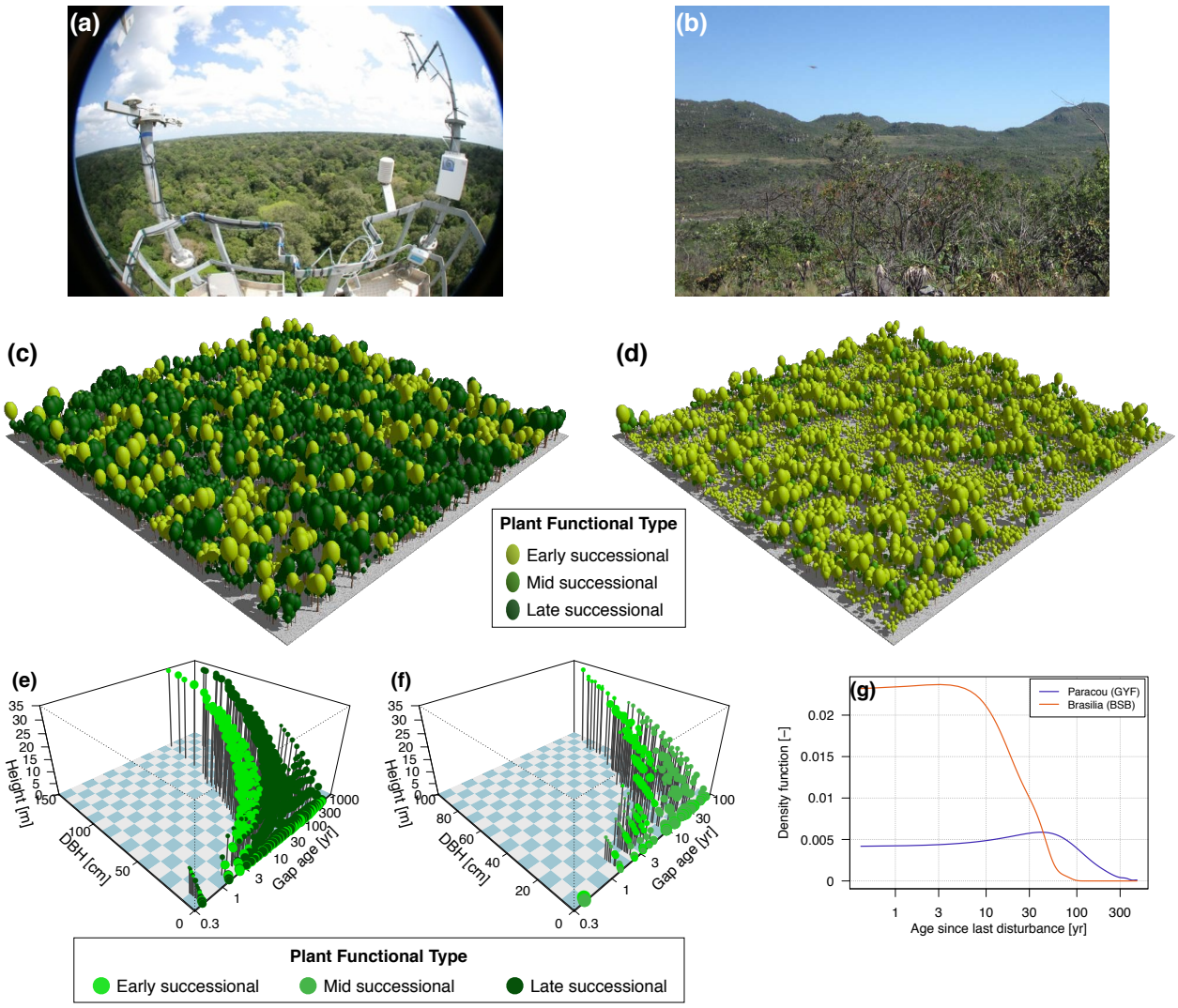

Figure 1.3: Overview on how the size and age structure represents different biomes, (a) Paracou (GYF), a tropical rainforest site in French Guiana, and (b) Brasília (BSB), a woody savannah site at the Cerrado region in Brazil. Model representation of (c) GYF and (d) BSB at near equilibrium stage (Sec. 3.4.1). Distribution of cohorts within (e) GYF and (f) BSB(), by size (diameter at the breast height and DBH and height), age since last disturbance (gap age) and functional group (colors). Dot size is proportional to the logarithm of population of individuals within each patch. (g) Distribution of ages since last disturbance at both locations. Photograph credits: (a) `http://www.ecofog.gf/spip.php?article365`, and (b) Enzo Todesco. See Fig. 1.2 for location of both sites in South America.

sertation is to estimate how much shift in the rainfall regime at different areas of the Amazon forest could stand before they experienced major significant losses. In addition, I aimed at identifying how the plant community structure and composition could change should the Amazon responded

to drier climates. To answer this question, I used the Ecosystem Demography Model, which has the unique way of representing the structure of the biome in terms of individuals, and their ability to access and compete for resources that are needed for plants to maintain their living tissues, grow and reproduce, and represent their death in case they fail to access such resources or are affected by some other disturbance. Model development and improvement was a major part of this dissertation, and this effort was largely done in collaboration with Ryan G. Knox. The first version of the Ecosystem Demography model (Moorcroft et al., 2001) had a very simplistic representation of biophysical processes, which limited its use for understanding the impact of changes that strongly depend on processes that occur in high frequency. A major improvement in the biophysics had been carried out by Medvigy (2006), and the work presented here is largely built on top of his development; nevertheless, many issues had to be addressed before I could effectively use the model for this work. First, the model had been previously tested only for forest sites, and several original assumptions and phenomenological formulations would cause instabilities over non-forested regions. This eventually lead us to develop a much improved biophysical model, which is now derived from formal derivations from thermodynamic laws, and the system of prognostic equations is based on enthalpy and internal energy as opposed to temperature.

In Chap. 2, I present the development of the version 2.2 of the Ecosystem Demography Model (ED-2.2), with particular emphasis on the new thermodynamic closure, and all modules necessary to close the enthalpy, water, and carbon dioxide cycles. In addition, I present detailed description of all modules that directly contribute to the aforementioned cycles, including hydrology and energy exchange between soil layers; the updated two-stream model for resolving the distribution of irradiance throughout the canopy; the surface layer model, which simulates the eddy covariance fluxes leaving the canopy, and the exchange of heat and water between the different surfaces and the canopy air space; the updated leaf physiology model, which controls photosynthetic activity and transpiration loss; and the autotrophic and heterotrophic respiration model. While this chapter is heavily mathematical, it constitutes an important reference for future model developments. The work in this chapter is in preparation for submission to a journal with focus on model development

(e.g. Geoscientific Model Development).

In Chap. 3, I present an extensive model evaluation of the current model against multiple data sets to determine the main strengths and areas where further development of the model are needed. First I evaluate the model with imposed plant community structure from forest censuses, and drive the model using site-level measurements at several locations in tropical South America, mostly but not exclusively at the Amazon forest, and compare results with eddy covariance towers, additional auxiliary measurements, and values reported from publications, in order to determine the main source of uncertainties, and identify potentially confounding effects. In addition, I compare equilibrium vegetation simulations starting from near bare ground conditions for the same locations plus additional sites located either at the transition or outside the Amazon, in order to evaluate whether the model can reproduce the variability between sites and across the region. Finally I evaluate the differences in the model dynamics towards equilibrium by using the ED-2.2 compared with simplified versions in which size, age, or functional diversity are averaged. This extensive evaluation will be also prepared as a companion publication for Chap. 2 on the same journal.

In Chap. 4, I present the results on the estimates of the vulnerability of Amazonian forests to a drier climate. Here I focus on two sites with the most data on biophysical and long term dynamics available, that also have a significant seasonality and interannual variability of rainfall — Paracou (GYF) and Santarém km 67 (S67), and develop multiple rainfall regime scenarios that are based on long-term rainfall observations at both locations. I start by presenting the comparison between the observed and modelled dynamics, and explore the predicted response to increasingly drier scenarios, first looking into the effects on the community as a whole, where I observed that while Paracou showed very little response to increasingly drier conditions due to the excessive average rainfall, in Santarém km 67 the forest could start losing significant biomass at relatively modest shifts in climate, with the actual magnitude being dependent on soil conditions and plant drought adaptations. In addition, I analyse the structural changes in plant community for the simulations that showed the most response, and found that while all plants could experience higher mortality,

evergreen, early successional, and larger trees had most losses and least recovery, whereas in some cases losses of the most vulnerable trees was compensated by the increase of population of trees with lower demand. Finally, I also identified the return period of extreme of sufficiently long droughts, defined as a consecutive period of 12 months with water deficit, could be used to predict areas most vulnerable to droughts, and calculated the return period from multiple rainfall data sets to estimate which regions would be the most vulnerable to drying climate. While the extreme South and Eastern Amazonia were also predicted to be as vulnerable as previous works, a large band crossing the northern and central areas of the Amazon, along with drier areas in Bolivia and Peru, could also be less resilient particularly if the average rainfall decreased. The main findings in this chapter is being prepared for submission to *Ecological Applications*.

In Chap. 5 I present a summary of the main findings, along with suggestions for future work that could improve our understanding of the response and resilience of tropical forests to future changes in climate and land use.

Finally, a significant amount of work also done in collaboration with Ryan Knox was to couple the Brazilian Regional Atmospheric Modelling System (BRAMS, K. Longo et al., 2013) to the Ecosystem Demography model. This coupling also required extensive model development of the atmospheric component, from ensuring that the thermodynamic laws between the two models were consistent to improvements on cumulus parameterizations, planetary boundary layer turbulence, and the feedbacks of parameterized clouds on radiation profile. The coupled model system is currently being used to evaluate the feedbacks between the ecosystem and the atmosphere under predicted changes in land use in South America, in particular how future change in land use from realistic scenarios (e.g. SimAmazonia Soares-Filho et al., 2006; Merry et al., 2009) could affect the distribution of heat and rainfall within the Amazon, and how this could further affect the dynamics of the remaining forests. This is an ongoing project, thus it has not been included in this dissertation. Nevertheless, the resulting coupled model has been also actively used for research led by other researchers, and the first results of this collaborative development have been submitted for publication (Knox et al., 2013a,b).

Chapter 2

Enthalpy, water, and carbon-dioxide cycles in the Ecosystem Demography Model, version 2.2

The developments and improvements to the biophysical and biogeochemical parameterizations of ED-2.2 were done in collaboration with Ryan Knox, David Medvigy, and Naomi Levine.

2.1 Introduction

Modelling the interactions between vegetation and the atmosphere has evolved considerably over the past decades (Levis, 2010). In one of the first studies analysing the interaction between biosphere and atmosphere, Charney et al. (1975) obtained a significant increase in rainfall over the Sahara by only lowering the Saharan albedo to values typical of plant-covered landscape; a few years later, Deardorff (1978) demonstrated that predictions of near surface temperature for a wheat field in England could be substantially improved by including a bulky parameterization of vegetation that became the first generation of "big leaf" models, later extended and modified to provide global surface boundary conditions (e.g., NCAR/BATS, Dickinson et al., 1986). The next genera-

tions of biosphere models increased in complexity by including more mechanistic representation of radiation transfer, roughness and transpiration (e.g. SiB, Sellers et al., 1986), and some representation of photosynthesis and respiration for prescribed biomes (e.g. TEM, LSM, and SiB2, Raich et al., 1991; Bonan, 1995; Sellers et al., 1996, respectively). Meanwhile, several biogeographic models were being developed to predict the global distribution of potential equilibrium biomes based on mean climate conditions (e.g. BIOME and MAPSS, Prentice et al., 1992; Neilson, 1995, respectively), although processes such as establishment, competition, and mortality were still incipient and were largely independent of the biophysical processes. In 1996, Haxeltine and Prentice and Foley et al. presented a new approach in which competition and dominance of different plant functional types (PFTs) was directly related to the productivity, linking processes occurring at high temporal frequency such as net primary productivity to long-term dynamics. By also including climate variability, Foley et al. introduced the concept of dynamic global vegetation model (DGVM), by which changes in climate could also shift the ecosystem out of equilibrium. Later developments of DGVMs, such as LPJ (Sitch et al., 2003), CLM-DGVM (Levis et al., 2004) and TRIFFID/JULES (Hughes et al., 2004; Clark et al., 2011) among others, also included mechanisms such as disturbance through fires and multiple types of mortality due to the various constraints on biome.

Although DGVMs are capable of reproducing the main patterns of the current biome distribution (e.g. Sitch et al., 2003; Blyth et al., 2011), there is still a significant uncertainty on how the ecosystems may respond to climate change, in part because of the uncertainties on the impact in regional climate, but also because of the uncertainty of how the ecosystems may respond to any given change, as discussed by Sitch et al. (2008). In particular, transitions between closed-canopy forests and treeless biomes are much sharper in these models when compared with observations (Good et al., 2011). One reason for such result is that the classic definition of PFT is blurred between individual and biome characteristics: Purves and Pacala (2008) mentioned that PFTs are defined from a combination of biogeographic range, and some very simple morphological aspects; however, they lack variation in height (or rooting depth) and function in the ecosystem. As a result,

plant communities are often represented as a single vegetation type, preventing a proper representation of complex interactions between individuals that form this biome (Moorcroft, 2006; Evans, 2012). Both the traits and developmental stage of a plant are fundamental explaining its ability to compete for resources. For example, in forest ecosystems, tree size determines how much water and light an individual can access, and its physiological and life history traits determine how much resources are needed, and how efficiently the individual can obtain such resources compared to other individuals that are also accessing the same resources. Experimental studies indicate that biodiversity can enhance the ecosystem function, especially if they are carried out for longer periods (e.g., Tilman and Downing, 1994; Naeem and Li, 1997; Cardinale et al., 2007), while some studies carried out on dry lands suggest that biodiversity could contribute to enhanced ecosystem functionality in highly stressed environments (Jucker and Coomes, 2012).

An alternative approach to most big-leaf based DGVMs are the individual based vegetation models, also know as gap models (c.f. Bugmann, 2001). These models simulate the birth, growth, and death of individual plants, hence incorporating the heterogeneity of the plant community. Since birth and death are stochastic processes, multiple realisations are required to determine the long-term, large-scale dynamics of these models, which limits its applicability over large regions or global scale.

The Ecosystem Demography Model (ED), developed by Moorcroft et al. (2001), specifically addresses the need to incorporate heterogeneity in the plant community while remaining deterministic. The equations that describe the plant community are derived from the individual properties, but properly scaled in order to obtain the dynamics of the distribution of demographic density as a function of the individual size and PFT, and the age since the last disturbance, later extended to by Albani et al. (2006) to account for the type of disturbance; this approach was originally named the size- and age-structured model (Moorcroft et al., 2001), and along this text will be referred to as the size-, strategy-, and age-structured model (SSAS), Strategy has been included in the name to stress that unlike most DGVMs, PFTs in ED are defined not only based on biogeographic range, but, as pointed out by van der Molen et al. (2011), they also represent plant strategical properties, or dif-

ferent functional groups within the same community, which is often considered more descriptive of ecosystem functioning than strict taxonomic classes (Hooper et al., 2002; Reiss et al., 2009). These functional groups represent a suite of physiological, morphological, and life history traits, thereby mechanistically representing the different ways plants utilise resources, although this also requires knowing how such traits vary in the plant community of interest (Fisher et al., 2010).

The original formulation of the ED model had a very simple representation of the biogeophysical processes that drive the energy, water, and carbon dioxide (CO_2) cycles. Since the inception of version 2, there has been an ongoing effort towards a more comprehensive and mechanistic representation of the biogeophysical and biogeochemical cycles (Medvigy, 2006; Medvigy et al., 2009; Knox, 2012). In this chapter I describe the state of the improved biogeophysical and biogeochemical module in the most recent version of the model (ED-2.2), with a special focus on processes that occur in sub-daily scale. While one will notice that many parameterizations and sub-models in ED-2.2 are based on other DVGMs, one fundamental difference, is that in ED-2.2 all biogeophysical properties are those of a horizontally and vertically heterogeneous plant community and define the resource availability and micro-environment of the different individuals within the plant canopy.

In Sec. 2.2, I present a general overview of the model, including the multiple hierarchical levels associated with the SSAS approach, the different time scales associated with the model, and the input data required to drive the model. In Sec. 2.3, I present an overview of the fundamental prognostic and diagnostic equations used to determine the enthalpy, water and carbon dioxide cycles. In Sec. 2.4, I present the main sub-models used to determine the enthalpy, water, and CO_2 fluxes.

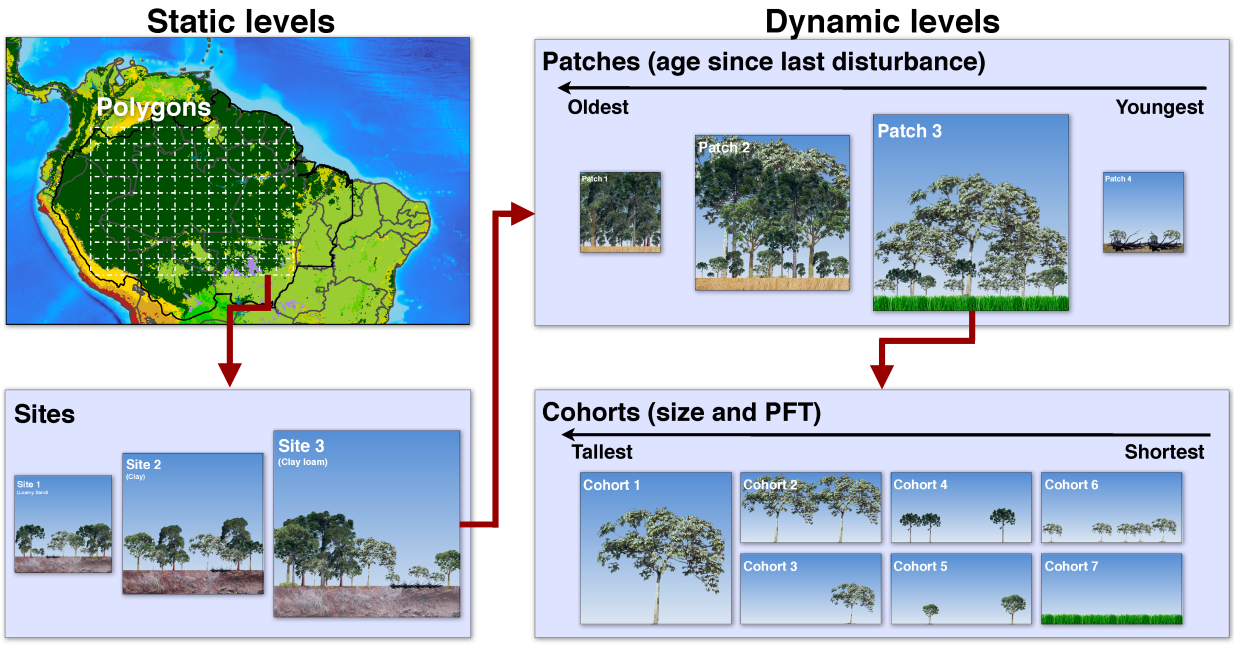

Figure 2.1: Schematic of the multiple hierarchical levels in ED-2.2. Red arrows represent the nesting, showing how each parent level is split into the child groups. The definition of polygons and sites (static levels) and patches and cohorts (dynamic levels) is given in the main text.

2.2 Structure of the ED-2.2 model

2.2.1 Hierarchical levels

The solution of the plant community dynamics in ED is determined through hierarchical structures within the domain of interest and time span, as shown in the schematic in Fig. 2.1. The domain of interest is geographically divided into polygons (y): within any polygon, we assume all that time-dependent abiotic conditions such as meteorological conditions above the plant community are uniform, therefore, a polygon can be thought as a site of interest near an eddy flux tower, or the lower boundary condition for one grid column in an atmospheric model. The polygon may be subdivided into S sites; each site with fractional area A_s shares the same time-independent abiotic conditions such as soil texture. Both polygons and sites are defined at the beginning of the simulation and are fixed in time, and no geographic information is assumed for sites and further

sub-divisions. In addition, let $a[\,\mathrm{s}]$[1] be the age since the last disturbance of any patch of plant community within the site; $i \in \{1,2,\ldots,I\}$ be the index of the disturbance types that can generate a new patch; and $\alpha \equiv \alpha(a,t)$ be the age- and time-dependent matrix of probability distribution of age since last disturbance, where each element $\alpha_{i,s,y}$ corresponds to one disturbance type i within a site of area A_s that satisfies

$$\sum_{s=1}^{S} A_s = 1, \tag{2.1a}$$

$$\sum_{i=1}^{I} \left[\int_0^{\infty} \alpha_{i,s,y}(a,t)\,\mathrm{d}a \right] = 1. \tag{2.1b}$$

From Eqn. (2.1b), the probability can be also thought as the patch relative area within a site. Finally, let $\mathbf{N} \equiv \mathbf{N}(\mathbf{c},a,t)$ be the array where each element $n_{m,i,s,y}$ corresponds to the distribution of cohorts of same size $\mathbf{c}$ living in a patch of age a at time t, for each PFT m, and disturbance type i within site s of polygon y; and $\mathbf{c} = \left(C_\lambda; C_\rho; C_\sigma; C_\delta; C_\tau\right)[\,\mathrm{kg_C\,plant^{-1}}]$ is the vector that determines the size of any individual plant, and whose components are the biomass of leaves, fine roots, sapwood, structural tissues, and storage (starch and sugars), respectively.

Following Moorcroft et al. (2001), Albani et al. (2006), and Medvigy and Moorcroft (2012), the fundamental partial differential equations that describe the dynamics of demographic density and probability distribution within each site in the SSAS model are defined as (dependencies omitted for clarity):

$$\underbrace{\frac{\partial n_{m,i,s,y}}{\partial t}}_{\substack{\text{Change in}\\ \text{demographic}\\ \text{density}}} = \underbrace{-\frac{\partial n_{m,i,s,y}}{\partial a}}_{\substack{\text{Ageing}\\ \text{of plant}\\ \text{community}}} \underbrace{-\nabla_{\mathbf{c}} \cdot \left(\dot{\mathbf{g}}_m \cdot n_{m,i,s,y}\right)}_{\text{Growth}} \underbrace{-\dot{\mu}_m \cdot n_{m,i,s,y}}_{\text{Mortality}}, \tag{2.2a}$$

$$\underbrace{\frac{\partial \alpha_{i,s,y}}{\partial t}}_{\substack{\text{Change in}\\ \text{age structure}}} = \underbrace{-\frac{\partial \alpha_{i,s,y}}{\partial a}}_{\substack{\text{Ageing}\\ \text{of plant}\\ \text{community}}} \underbrace{-\sum_{i'=1}^{I} \dot{\lambda}_{i,i'}\,\alpha_{i,s,y}}_{\text{Disturbance}}, \tag{2.2b}$$

[1] Throughout this text, units of variables will be shown between square brackets.

where $\dot{\mu}_m[\,\mathrm{s}^{-1}]$ is the mortality rate for each PFT; $\dot{\mathbf{g}}_m[\,\mathrm{kg_C\,plant^{-1}\,s^{-1}}]$ is the growth rate for each size component, and $\nabla_{\mathbf{c}}\cdot$ is the divergent operator for the size vector; $\dot{\lambda}_{i,i'}[\,\mathrm{s}^{-1}]$ is the disturbance rate from a patch of type i to a patch of type i'. The boundary conditions for Eqn. (2.2) are:

$$n_{m,i,s,y}(\mathbf{c}_{0_m},a,t) = \frac{1}{\dot{\mathbf{g}}_{0_m}\cdot\mathbf{1}}\left\{\underbrace{\iiint_{\mathbf{c}_0}^{\infty}(1-\acute{d}_m)\,\dot{r}_m\,n_{m,i}\alpha_i\,\mathrm{d}\mathbf{c}}_{\text{Local recruitment}}\right. \\ \left. + \underbrace{\sum_{s=1}^{S}\sum_{i=1}^{I}\left[\int_0^{\infty}\iiint_{\mathbf{c}_0}^{\infty}\acute{d}_m\,\dot{r}_m\,n_{m,i,s,y}\alpha_{i,s,y}\,\mathrm{d}\mathbf{c}\,\mathrm{d}a\right]}_{\text{Recruitment from random dispersal}}\right\}, \tag{2.3a}$$

$$n_{m,i,s,y}(\mathbf{c},0,t) = \underbrace{\sum_{i'=1}^{I}\left[\int_0^{\infty}\dot{\sigma}_{m,i'}\,n_{m,i',s,y}\alpha_{i',s,y}\,\mathrm{d}a\right]}_{\text{Plant community following disturbance}}, \tag{2.3b}$$

$$\alpha_{i,s,y}(0,t) = \underbrace{\sum_{i'=1}^{I}\left[\int_0^{\infty}\dot{\lambda}_{i',i}\,\alpha_{i',s,y}\,\mathrm{d}a\right]}_{\text{Probability of recently disturbed patch}}, \tag{2.3c}$$

where $\mathbf{c}_{0_m}$ is the size of the smallest individual; $\dot{\mathbf{g}}_{0_m}$ is the growth rate for individuals with size $\mathbf{c}_{0_m}$; $\mathbf{1}$ is the unity vector for size; $\dot{r}_m[\,\mathrm{s}^{-1}]$ is the recruitment rate; $\acute{d}_m$ is the fraction of recruits that are randomly dispersed instead of locally recruited, which depends on the PFT; and $\dot{\sigma}_{m,i} \equiv \dot{\sigma}_{m,i}(\mathbf{c})$ is the survivorship probability for a PFT m following a disturbance of type i. The model initial conditions are discussed in the next section.

In addition, let $C_{\mathrm{B}} \equiv C_{\mathrm{B}}(\mathbf{e})$ be the individual carbon balance. This property plays a direct role on controlling the plant community dynamics, which is represented by the functional form of mortality ($\dot{\mu}_m \equiv \dot{\mu}_m(\mathbf{c}, C_{\mathrm{B}}(\mathbf{e}))$), growth ($\dot{\mathbf{g}}_m \equiv \dot{\mathbf{g}}_m(\mathbf{c}, C_{\mathrm{B}}(\mathbf{e}))$), and recruitment rates ($\dot{r}_m \equiv \dot{r}_m(\mathbf{c}, C_{\mathrm{B}}(\mathbf{e}))$). Carbon balance is a function of the environment perceived by the individual, here represented by the vector $\mathbf{e} \equiv \mathbf{e}(m,\mathbf{c},s,y,t,\mathbf{n}_i)$ where each component represents a different environmental variable. The perceived environment ultimately determines the resource availability for the individual, therefore it depends on the individual characteristics $(m,\mathbf{c})$, abiotic factors (s,y,t), and biotic factors due to the plant community where the individual lives (represented by $\mathbf{n}_i$, the population vector

within any patch). Finally, let $\mathbf{E} = \mathbf{E}(s, y, t, \mathbf{n}_i)$ be the vector of environmental conditions associated with the plant community as a whole; this vector is also a function of abiotic factors (s, y, t) and biotic factors associated with the local community ($\mathbf{n}_i$), and ultimately controls the disturbance rates ($\dot{\lambda}_{i,i'} = \dot{\lambda}_{i,i'}(\mathbf{E})$). Because the microenvironment and plant community structure vary within the same large-scale conditions, in ED-2.2 we must solve the biogeophysical and biogeochemical cycles for each patch separately.

Because Eqn. (2.2) cannot be solved analytically, the distribution of cohorts and patches is approximated by discrete classes. In principle I new patches could be created every time step taken to solve Eqn. (2.2b) and M cohorts could be created within each patch for every Eqn. (2.2a) time step, whereas older patches and older cohorts would lose area through disturbance and population through mortality. Since the number of patches and cohorts would rapidly become too large for viable simulations, it is necessary to aggregate them. Because the SSAS approach accounts for heterogeneities in the plant community environment, we aggregate patches and cohorts based on the similarity of the environmental conditions; in ED-2.2, the default method to aggregate patches of the same disturbance history is by comparing the cumulative leaf area index at multiple height levels, using the methodology illustrated in Fig. 2.2. For simplicity in this example I assume only one type of disturbance (e.g. natural disturbance), and the environment to be defined by the cumulative leaf area index (ΣLAI) at two height levels (in this example referred to as mid-canopy and understorey). Each environment characteristic is sub-divided into environmental levels (six levels in this example). Patches are grouped together only if their age classes are contiguous and the environmental level for each environment property. In Fig. 2.2, the widest boundary between patches is shown as vertical dot-dashed lines, and there are as many lines as times that either mid-canopy or understorey ΣLAI changes the environmental level. The only exception for age contiguity is when a patch is empty (i.e. no size class amongst all PFTs contain any vegetation), in which case they are all merged into a single patch. Importantly, patches are not evenly distributed in area or age, only environmental conditions.

Likewise, cohorts of the same PFT that have similar DBH and leaf phenological conditions

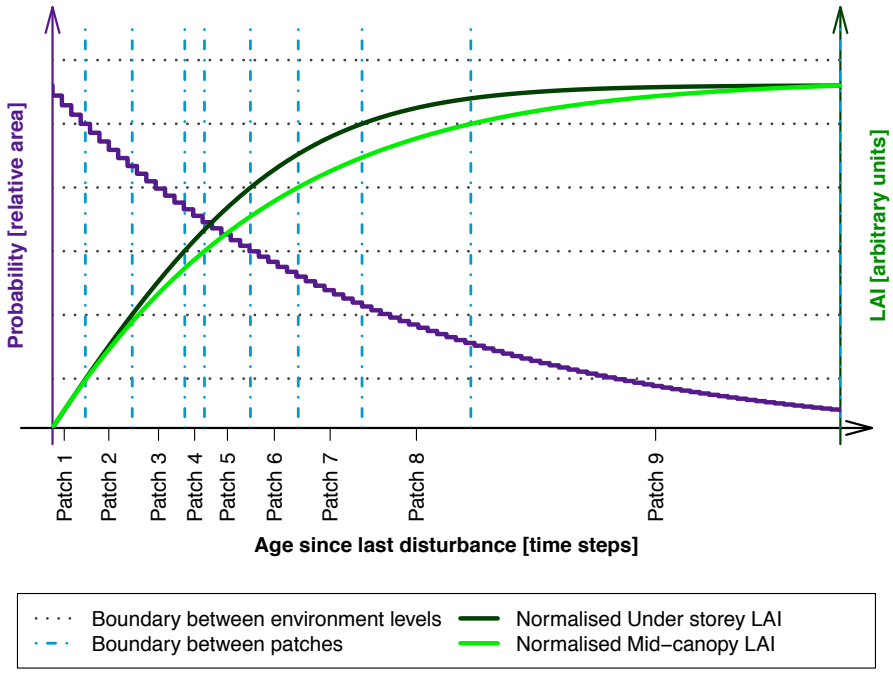

Figure 2.2: Schematic of the grouping of patches for one particular land use type using environmental conditions to group different age classes. Green curves correspond to the ΣLAI of each height level, here shown as the relative value to the maximum ΣLAI of each height level, so the environmental boundaries of both classes overlap; horizontal dotted lines are the boundaries between environmental levels, and vertical dot-dashed lines are the edges between two patches. Purple line corresponds to the probability of each age class, but notice that this value is not used to define patches.

may be merged. While the user may define the ideal number of patches and cohorts per patch, the actual number may be higher or lower depending on the similarities.

Since ED-2.2 represents a multitude of processes that inherently have different time scales, the model also integrates different processes using a variety of nested time steps that are appropriate for each process; Tab. 2.1 contains the list with the group of processes solved by each time step. It must be noted that the biogeophysical and biogeochemical processes are dynamic: these processes are solved using a fourth-order Runge-Kutta integration scheme, which is dynamically adjusted according to error estimates.

Table 2.1: Time step associated with processes resolved by ED-2.2. The thermodynamic sub-step is dynamic and it depends on the error evaluation of the integrator, but it cannot be longer than the biophysics step, which is defined by the user. Other steps are fixed as of ED-2.2.

Step	**Symbol**	**Time scale**	**Processes**
Thermodynamic sub-step	Δt_{thermo}	$1\text{ s} - \Delta t_{\text{biophys}}$	Energy and water fluxes
			Eddy fluxes (including CO_2 flux)
			Most thermodynamic state functions
Biophysics step	$\Delta t_{\text{biophys}}$	$2 - 15$ min	Canopy air space pressure
			Evaluation of energy, water, and CO_2 budgets
			Radiation model
			Photosynthesis model
			Root respiration
			Heterotrophic respiration
			Update of the above-canopy environment
Phenology step	Δt_{live}	1 day	Maintenance of active tissues
			Update of the storage pool
			Leaf phenology
			Plant carbon balance
			Integration of mortality rate due to cold
			Soil litter pools
Cohort dynamics step	Δt_{cohort}	1 mo	Growth of structural tissues
			Cohort height update
			Mortality rate
			Reproduction – Cohort creation
			Integration of fire disturbance rate
			Cohort fusion, fission, and extinction
Patch (gap) dynamics step	Δt_{patch}	1 yr	Patch creation due to natural disturbance
			Patch creation due to land use change
			Patch fusion and termination

2.2.2 Model requirements

ED-2.2 source code is mostly written in Fortran 90, with a few file management routines written in C, with output files in HDF-5 format, and the option of running regional-level simulations in parallel mode, hence requiring HDF-5 and MPI libraries. The code uses dynamic allocation of variables and extensive use of pointers to efficiently reduce the amount of data transferred between routines. Polygon-, site-, patch-, and cohort-dependent variables are always written as long vectors that contain information from all polygons, sites, patches, and cohorts in the simulation and mapped using

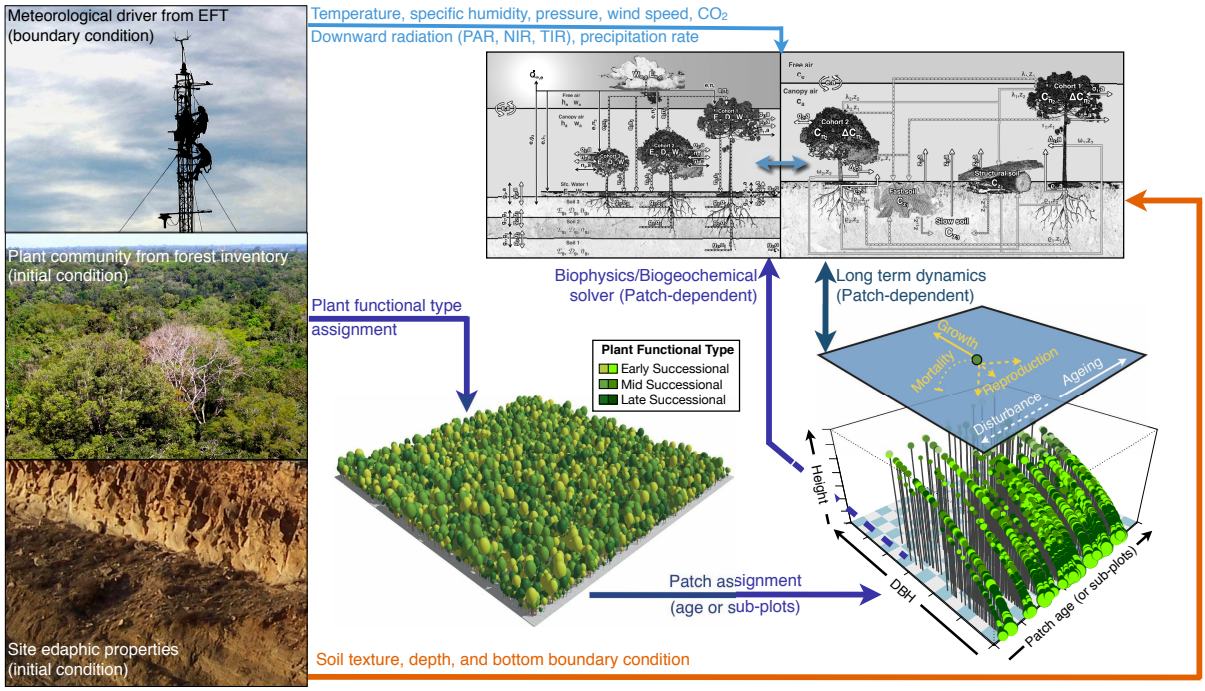

Figure 2.3: Schematic of the integration between forest inventory data, meteorological conditions, and the different modules in ED-2.2. Further description on biophysical and biogeochemical solvers is described in Sec. 2.3, and long-term dynamics description is available at Moorcroft et al. (2001); Medvigy et al. (2009).

auxiliary vectors with size and count information. This approach reduces the amount of memory required and output file size, which is fundamental for long-term simulations. In addition, to ensure readability and consistency throughout the code, and allow efficient future developments, any procedure that is carried out by multiple modules is always written into functions or subroutines.

In Fig. 2.3, I present an schematic of which initial and boundary conditions are necessary for running ED-2.2, and where these conditions are used. Input data falls into three main categories: demographic (initial condition), edaphic (fixed boundary condition), and meteorological (initial condition and time-dependent boundary condition).

Five types of initial demographic conditions are possible in ED-2.2. To initialize a plant community from tree inventory, one must ideally have a full list of all individuals with size greater than $\mathbf{c}_0$, identified to the species level, along with the coordinates or some sort of geographic information such as quadrants within the plot. If quadrants are not provided, the user may split the plot into

quadrants that should roughly represent the crown area of the largest trees (Moorcroft et al., 2001, e.g., 15 m $\times$ 15 m in a tropical forest); the age since last disturbance and the type of disturbance may be included if they are known, otherwise they are assumed to be old age and natural disturbance. Alternatively, initial conditions can be derived from airborne measurements, following the methodology described by Antonarakis et al. (2011). In addition, a prescribed near bare ground condition may be used: in this case a small population of cohorts $n_{m,1}(\mathbf{c}_0, 0, 0) = 0.1\,\text{plant}\,\text{m}^{-2}$ for all PFTs is assigned to natural disturbance type, with the entire polygon being at age $a = 0$ and natural disturbance. For theoretical applications, it is also possible to run the model assuming no vegetation (true bare ground). Finally, plant community from previous simulations can be used to provide the initial conditions.

Edaphic conditions include the predominant soil texture class or the sand, silt, and clay fraction (App. B), and the type of bottom soil boundary condition (bedrock, reduced drainage, or free drainage). Soils in ED-2.2 are generally assumed inorganic; although there is an option to assign peat, the hydraulic parameters must be manually adjusted for the site.

Meteorological conditions are typical measurements of eddy flux towers and include temperature, specific humidity, CO_2 mixing ratio, and pressure of the air above canopy, precipitation rate, incoming solar (shortwave) radiation and incoming thermal (longwave). Although ED-2.2 can read different variables with different time resolutions, it is highly recommended to use at least hourly resolution, or at the very least four values a day, and any gap filling on time series must be done prior to the simulation. In case of solar radiation, ideally photosynthetically active radiation (PAR) and near infrared (NIR), both split into direct and diffuse radiation, may be provided; otherwise, the total incoming shortwave radiation is split amongst these components using the Weiss and Norman (1985) model.

2.3 Overview of enthalpy, water, and carbon dioxide cycles

Here I present the fundamental equations that describe the biogeophysical and biogeochemical cycles. Since the environmental conditions are function of the local plant community, and resources are shared by the individuals, these cycles must be described at the patch level, and the aggregated response of the plant community can be aggregated to the polygon level once the cycles are resolved for each patch. One important assumption in ED-2.2 is that patches do not exchange enthalpy, water, and carbon dioxide with other patches, thus patches are treated as independent systems. From this point I will only refer to the patch- and cohort-levels, and indices associated with patches, sites and polygons will be omitted for clarity.

2.3.1 Definition of the thermodynamic state

Consider that each patch is a *thermodynamic envelope* comprised of multiple thermodynamic systems: the soil layers, temporary surface water or snow, cohorts[2], and the canopy air space. Although patches do not exchange heat and mass with other patches, they are allowed to exchange heat and mass with the air aloft and lose water and associated internal energy through surface and sub-surface runoff. We also assume that each thermodynamic system within the patch instantaneously reaches thermal equilibrium, and that intensive variables such as pressure and temperature are uniform within each thermodynamic system. The fundamental equations that describe the system thermodynamics are the first law of thermodynamics in terms of enthalpy H $[\,\mathrm{J\,m^{-2}}]$, and mass continuity for incompressible fluids for total water mass $W[\,\mathrm{kg_W\,m^{-2}}]$:

$$\underbrace{\frac{\mathrm{d}H}{\mathrm{d}t}}_{\substack{\text{Change in}\\ \text{enthalpy}}} = \underbrace{\dot{Q}}_{\text{Net heat flux}} + \underbrace{\dot{H}}_{\substack{\text{Net enthalpy flux}\\ \text{due to mass flux}}} - \underbrace{\mathcal{V}\frac{\mathrm{d}p}{\mathrm{d}t}}_{\text{Pressure correction}} \quad , \tag{2.4a}$$

[2]In this section, I assume that only the above-ground part of the cohort is an independent thermodynamic system; roots are assumed to be in thermal equilibrium with the soil layers, and having negligible heat capacity compared to the soil layers.

$$\underbrace{\frac{\mathrm{d}W}{\mathrm{d}t}}_{\substack{\text{Change in}\\ \text{water mass}}} = \underbrace{\dot{W}}_{\text{Net mass flux}} \tag{2.4b}$$

where $\mathcal{V}$ is the volume of the thermodynamic system and p is the ambient pressure, and enthalpy and internal energy . The merit of solving the changes in enthalpy over internal energy (E) is that pressure is always included in atmospheric measurements. Nonetheless, the only thermodynamic system where this distinction matters is the canopy air space: work associated with thermal expansion of solids and liquids is several orders of magnitude smaller than heat (c.f. Dufour and van Mieghem, 1975), and changes in pressure contribute significantly less to enthalpy because the specific volume is small. Hence, for all systems except the canopy air space, changes in enthalpy are roughly equivalent to changes in internal energy, and for these systems I use internal energy and enthalpy interchangeably.

Variations in internal energy and enthalpy are more important than their actual values. Therefore, enthalpy is defined as the difference between the current state and an arbitrary but predetermined and fixed reference state where we assume enthalpy to be zero. First, let $Y\,[\,\mathrm{kg_Y\,m^{-2}}]$ be the mass of the material and h_y be the specific enthalpy of any material $y\,[\,\mathrm{J\,kg_Y^{-1}}]$; because enthalpy is an extensive thermodynamic variable, the total enthalpy is the sum of enthalpies ($H = \sum_y Y_y h_y$). For any material other than water (d), h_d is defined as zero when the material temperature is 0 K; for water, the zero level is also at 0 K, with the additional condition that water is completely frozen. The specific enthalpy for all materials other than water (h_d), ice (h_i), liquid water (h_ℓ) or vapor (h_v) are defined as:

$$h_\mathrm{d}(T) = \underbrace{q_\mathrm{d}\,T}_{\text{Heating material}}\quad , \tag{2.5a}$$

$$h_i(T) = \underbrace{q_i T}_{\text{Heating ice}}\quad , \tag{2.5b}$$

$$h_\ell(T) = \underbrace{q_i T_{i\ell}}_{\text{Heating ice}} + \underbrace{l_{i\ell}(T_{i\ell})}_{\text{Melting ice}} + \underbrace{q_\ell\,(T - T_{i\ell})}_{\text{Heating liquid}}, \tag{2.5c}$$

$$h_v(T) = \underbrace{q_i T_{i\ell}}_{\text{Heating ice}} + \underbrace{l_{i\ell}(T_{i\ell})}_{\text{Melting ice}} + \underbrace{q_\ell\,(T_{\ell v} - T_{i\ell})}_{\text{Heating liquid}} + \underbrace{l_{\ell v}(T_{i\ell})}_{\text{Vaporization}} + \underbrace{q_{pv}\,(T - T_{\ell v})}_{\text{Heating vapor}}, \tag{2.5d}$$

where q_i and q_ℓ are the specific heats for ice and liquid water; q_{pv} is the specific heat at constant pressure for water vapor; $T_{i\ell}$ and $T_{\ell v}$ are the temperatures where ice melted and liquid water vaporised; and $l_{i\ell}$ and $l_{\ell v}$ are the latent heat of melting and vaporization, respectively. In case ice sublimates, Eqn. (2.5d) is still valid, since $l_{iv}(T) = l_{\ell v}(T) + l_{i\ell}(T)$ for any temperature T. By definition (e.g. Dufour and van Mieghem, 1975), the latent heat associated with phase change is the difference in enthalpy between the two phases at the temperature in which the phase change happens, therefore, we can determine the dependency of latent heat on temperature:

$$\left(\frac{\partial l_{\ell v}}{\partial T}\right)_p = \left(\frac{\partial h_v}{\partial T}\right)_p - \left(\frac{\partial h_\ell}{\partial T}\right)_p = q_{pv} - q_\ell \tag{2.6a}$$

$$\left(\frac{\partial l_{i\ell}}{\partial T}\right)_p = \left(\frac{\partial h_\ell}{\partial T}\right)_p - \left(\frac{\partial h_i}{\partial T}\right)_p = q_\ell - q_i \tag{2.6b}$$

If we further assume that the transition between ice and liquid phases can only occur at the water triple point (T_3), and that the latent heat of fusion $l_{i\ell 3} \overset{\text{def}}{=} l_{i\ell}(T_3)$ and vaporization $l_{\ell v 3} \overset{\text{def}}{=} l_{\ell v}(T_3)$ are known, we can combine Eqn. (2.5) to obtain a generic state function for h:

$$h = \frac{H}{D+W} = \underbrace{\frac{D}{D+W}}_{\text{d}}\, q_{\text{d}} T + \underbrace{\frac{W}{D+W}}_{\text{w}} \left[i\, q_i\, T + \ell\, q_\ell\, (T - T_{sc\ell}) + v\, q_{pv}\, (T - T_{scv})\right], \tag{2.7a}$$

$$T_{sc\ell} = T_3 - \frac{q_i T_3 + l_{i\ell 3}}{q_\ell}, \tag{2.7b}$$

$$T_{scv} = T_3 - \frac{q_i T_3 + l_{i\ell 3} + l_{\ell v 3}}{q_{pv}}, \tag{2.7c}$$

where d and w are the specific mass of other materials and water, respectively, and i, ℓ, and v are fraction of ice, liquid water, and vapor, respectively. Importantly, Eqn. (2.7a) does not contain any information about the temperature at which the phase changes had occurred, which is necessary since enthalpy must be a state function (path-independent). Hereafter, we will refer to the enthalpy as internal energy for all pools other than the canopy air space, since they are assumed equivalent,

Table 2.2: Independent state functions for each pool solved by ED-2.2 that are not universal constants. Each soil layer k, temporary surface water layer j and cohort n are considered independent pools.

Thermodyn. system	State function	Time step	Symbol	Units
Vegetation (cohort m)	Internal energy	Δt_{thermo}	E_{π_m}	$\text{J}\,\text{m}^{-2}$
	Intercepted water mass	Δt_{thermo}	W_{π_m}	$\text{kg}_{\text{W}}\,\text{m}^{-2}$
	Mass of vegetation tissues	Δt_{live}	D_{π_m}	$\text{kg}_{\text{Dry}}\,\text{m}^{-2}$
Surface water (layer j)	Internal energy	Δt_{thermo}	E_{s_j}	$\text{J}\,\text{m}^{-2}$
	Water mass	Δt_{thermo}	W_{s_j}	$\text{kg}_{\text{W}}\,\text{m}^{-2}$
Soil (layer k)	Bulk internal energy	Δt_{thermo}	$\mathcal{E}_k$	$\text{J}\,\text{m}^{-3}$
	Volumetric soil moisture	Δt_{thermo}	ϑ_k	$\text{m}^3_{\text{W}}\,\text{m}^{-3}$
	Mass (bulk density) of dry soil	Constant	$\mathcal{D}_k$	$\text{kg}_{\text{Dry}}\,\text{m}^{-3}$
Canopy air space	Specific enthalpy	Δt_{thermo}	h_a	$\text{J}\,\text{kg}_{\text{A}}^{-1}$
	Specific humidity	Δt_{thermo}	w_a	$\text{kg}_{\text{C}}\,\text{kg}_{\text{A}}^{-1}$
	Pressure	$\Delta t_{\text{biophys}}$	p_a	Pa
	Equivalent canopy depth	Δt_{cohort}	$\bar{z}_a$	m

whereas enthalpy will be used only when a gas phase is present. In Tab. 2.2, I present the list of independent thermodynamic variables needed to determine the thermodynamic state.

2.3.2 Heat, mass flux, and enthalpy fluxes

The enthalpy and water cycles for each patch in ED-2.2 is summarized in Fig. 2.4, and these cycles are solved every thermodynamic sub-step Δt_{thermo}, using a fourth-order Runge-Kutta integrator with dynamic time step to maintain the error within prescribed tolerance. For all fluxes and variables, the following subscripts correspond to the different thermodynamic systems: canopy air space (CAS, a); cohort ($\pi_m, m \in \{1,2,\ldots,M\}$); temporary surface water layers (TSW, $s_j, j \in \{1,2,\ldots,J\}$); and soil (ground) layers ($g_k, k \in \{1,2,\ldots,K\}$). For cohorts, we also use the additional subscripts to refer to specific plant components: leaf and leaf surface (λ_m), leaf boundary layer (β_m) and leaf intercellular space χ_m; and branch wood, wood surface, and wood boundary layer (ω_m). The system surroundings are also represented by subscripts: environment above the canopy air space (e), and runoff/drainage sink (o). Flux variables are denoted by a dot and two indices, and fluxes are positive when they go from the system represented by the first subscript

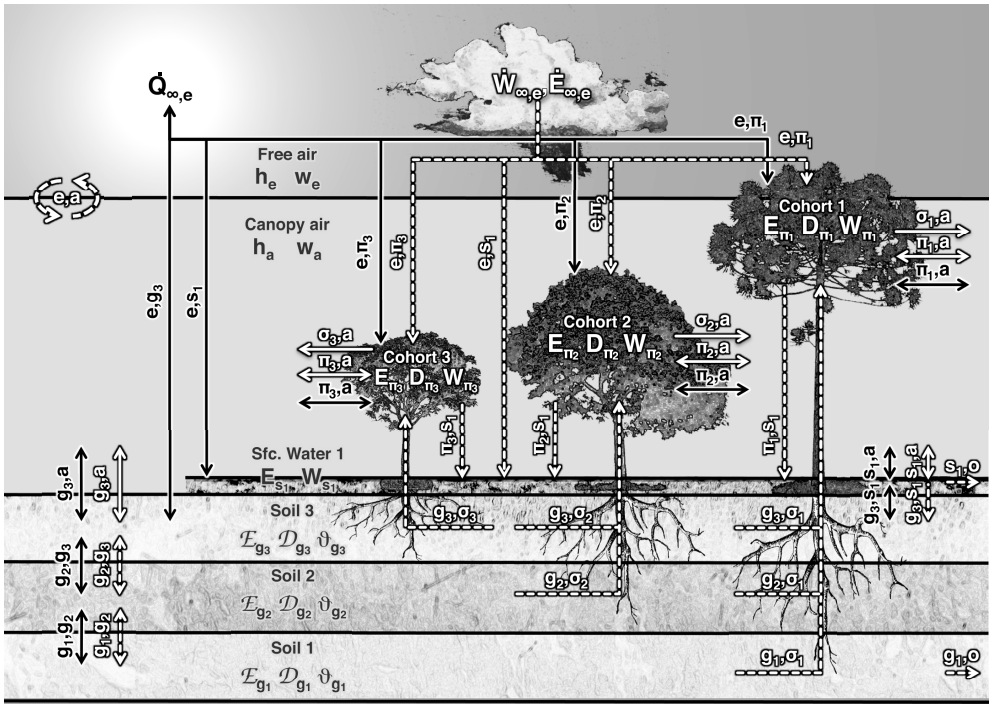

Figure 2.4: Schematic of the enthalpy fluxes (all arrows) and water fluxes (all but solid black arrows) that are solved in ED-2.2; The schematic is based on Walko et al. (2000); Medvigy et al. (2009). In this example, the patch has three cohorts, a single surface water layer, and three soil layers. Letters near the arrows are the subscripts associated with fluxes, although the flux variable has been omitted here for clarity. Black arrows represent heat flux with no exchange of mass, and white arrows represent exchange of mass and associated enthalpy (solid for processes involving phase change, dashed otherwise).

towards the second subscript; arrows in Fig. 2.4 represent allowed directions.

Soil

Every soil layer is assumed fixed; and let Δz_{g_k} be the thickness of any given layer. The thermodynamic state is defined in terms of the soil volume: the bulk specific internal energy $\mathcal{E}_k, [\mathrm{J\,m^{-3}}]$ and volumetric soil water content $\vartheta_k, [\mathrm{m^3_W\,m^{-3}}]$, which can be related to Eqn. (2.4) by defining $E_{g_k} \stackrel{\text{def}}{=} \mathcal{E}_k \Delta z_{g_k}$ and $W_{g_k} \stackrel{\text{def}}{=} \rho_\ell \cdot \vartheta_k \cdot \Delta z_{g_k}$, where ρ_ℓ is the density of liquid water. Soil net fluxes for any layer k are defined as:

$$\dot{Q}_{g_k} = \underbrace{\delta_{k1}\cdot\dot{Q}_{g_{k-1},g_k} - \delta_{kK}\cdot\dot{Q}_{g_k,g_{k+1}}}_{\text{Heat diffusion between layers}} - \delta_{kK}\cdot\Big(\underbrace{\dot{Q}_{g_K,s_1}}_{\substack{\text{Heat diffusion}\\ \text{Ground to TSW}}} + \underbrace{\dot{Q}_{g_K,a}}_{\substack{\text{Heat flux}\\ \text{Ground to CAS}}} - \underbrace{\dot{Q}_{e,g_K}}_{\text{Net radiation}}\Big), \tag{2.8a}$$

$$\dot{H}_{g_k} = \underbrace{\delta_{k1}\cdot\dot{E}_{g_{k-1},g_k} - \delta_{kK}\cdot\dot{E}_{g_k,g_{k+1}}}_{\text{Water flux between layers}} - \delta_{kK}\cdot\Big(\underbrace{\dot{E}_{g_K,s_1}}_{\substack{\text{Percolation}\\ \text{from TSW}}} + \underbrace{\dot{H}_{g_K,c}}_{\substack{\text{Ground}\\ \text{evaporation}}}\Big)$$

$$- \underbrace{\delta_{k1}\cdot\dot{E}_{g_1,o}}_{\substack{\text{Sub-surface}\\ \text{Runoff}}} - \underbrace{\sum_{\substack{n=1\\ k_{\rho_m}\geq k}}^{M}\left(\dot{E}_{g_k,\chi_m}\right)}_{\text{Plant water uptake}}, \tag{2.8b}$$

$$\dot{W}_{g_k} = \underbrace{\delta_{k1}\cdot\dot{W}_{g_{k-1},g_k} - \delta_{kK}\cdot\dot{W}_{g_k,g_{k+1}}}_{\text{Water flux between layers}} - \delta_{kK}\cdot\Big(\underbrace{\dot{W}_{g_K,s_1}}_{\substack{\text{Percolation}\\ \text{from TSW}}} + \underbrace{\dot{W}_{g_K,a}}_{\substack{\text{Ground}\\ \text{evaporation}}}\Big)$$

$$- \underbrace{\delta_{k1}\cdot\dot{W}_{g_1,o}}_{\substack{\text{Sub-surface}\\ \text{Runoff}}} - \underbrace{\sum_{\substack{n=1\\ k_{\rho_m}\geq k}}^{M}\dot{W}_{g_k,\chi_m}}_{\text{Plant water uptake}}, \tag{2.8c}$$

where δ_{xy} is the Kronecker's delta function (1 if $x = y$, 0 otherwise) and $\not\delta_{xy} \stackrel{\text{def}}{=} 1 - \delta_{xy}$, and k_{ρ_m} is the deepest layer that cohort m can access water, and is a function of the cohort size and functional type (c.f. App. C).

To convert internal energy into temperature, we must also know the mass and specific heats. Soil water is normally expressed in terms of liquid-equivalent volumetric fraction (ϑ_k), thus the bulk density of water in the layer is simply $\mathcal{W}_k^l = \rho_\ell \vartheta_k$. Dry soil is a combination of sand, silt, clay, and air filling any pore space not filled by water, and its bulk density $\mathcal{D}$ for each layer is based on Monteith and Unsworth (2008) (Section 15.3):

$$\mathcal{D} = \left(\sum_{t=0}^{3}\rho_t \mathcal{V}_t^l\right), \tag{2.9a}$$

$$\mathcal{V}_t^l = \begin{cases} \vartheta_{\text{Po}} - \vartheta_k \approx \dfrac{\vartheta_{\text{Re}} + \vartheta_{\text{Po}}}{2} & t = 0 \\ v_t\left(1 - \vartheta_{\text{Po}}\right) & t \neq 0 \end{cases}, \tag{2.9b}$$

where t indices 0, 1, 2, 3 correspond to air, sand, silt, and clay, respectively; ρ_t and $\mathcal{V}_t^l$ are the spe-

cific gravity and the volumetric fraction of each component. The volumetric soil content depends on the following texture-dependent variables (App. B): v_t, the soil texture-dependent, volumetric fraction of each soil component excluding water and air; ϑ_{Po}, the total porosity or maximum soil moisture; and ϑ_{Re} is the residual water content. In reality, the volumetric fraction of air is not constant and depends on soil moisture; nevertheless, the total air mass is three orders of magnitude less than the solid materials, thus the contribution of varying air in the pore space is negligible. To reduce the maximum error associated with this assumption, we use the volumetric fraction corresponding to halfway between the minimum and maximum soil moisture.

Specific heat of dry soil is also determined following Monteith and Unsworth (2008), as the weighted average of the specific heats of the four components:

$$c_{dg} = \frac{\sum_{t=0}^{3} (\rho_t \mathcal{V}_t c_t)}{\sum_{t=0}^{3} (\rho_t \mathcal{V}_t)}. \tag{2.10}$$

Temporary surface water

Temporary surface water exists whenever water falls to the ground, or dew or frost develops on the ground. The layer will be maintained only if the top soil layer cannot hold all water that reaches the ground, or when precipitation falls as snow. If a snowpack develops, the temporary surface water can be divided into several layers (subscript j), and the thickness of each layer is defined using the same algorithm as LEAF-2 (Walko et al., 2000). Net fluxes are defined as:

$$\dot{Q}_{s_j} = \underbrace{\delta_{j1} \cdot \dot{Q}_{s_{j-1},s_j} - \delta_{jJ} \cdot \dot{Q}_{s_j,s_{j+1}}}_{\text{Heat diffusion between layers}} + \underbrace{\delta_{j1} \cdot \dot{Q}_{g_K,s_1}}_{\substack{\text{Heat diffusion} \\ \text{Ground to TSW}}} + \underbrace{\dot{Q}_{e,s_j}}_{\text{Net radiation}} - \underbrace{\delta_{jJ} \dot{Q}_{s_J,a}}_{\substack{\text{Heat flux} \\ \text{TSW to CAS}}}, \tag{2.11a}$$

$$\dot{H}_{s_j} = \underbrace{\delta_{j1} \cdot \dot{E}_{s_{j-1},s_j} - \delta_{jJ} \cdot \dot{E}_{s_j,s_{j+1}}}_{\substack{\text{Percolation between} \\ \text{TSW layers}}} + \underbrace{\delta_{j1} \cdot \dot{E}_{g_K,s_1}}_{\substack{\text{Percolation} \\ \text{to ground}}} + \delta_{jJ} \cdot \Big[\underbrace{\sum_{m=1}^{M} (\dot{E}_{\pi_m,s_J})}_{\text{Canopy dripping}} - \underbrace{\dot{E}_{s_J,o}}_{\substack{\text{Surface} \\ \text{Runoff}}} - \underbrace{\dot{H}_{s_J,a}}_{\substack{\text{TSW} \\ \text{evaporation}}} \Big], \tag{2.11b}$$

$$\dot{W}_{s_j} = \underbrace{\delta_{j1}\cdot\dot{W}_{s_{j-1},s_j} - \delta_{jJ}\cdot\dot{W}_{s_k,s_{k+1}}}_{\substack{\text{Percolation between}\\ \text{TSW layer}}} + \underbrace{\delta_{j1}\cdot\dot{W}_{s_K,s_1}}_{\substack{\text{Percolation}\\ \text{to ground}}} + \delta_{jJ}\cdot\Big[\underbrace{\sum_{m=1}^{M}(\dot{W}_{\pi_m,s_J})}_{\text{Canopy dripping}} - \underbrace{\dot{W}_{s_J,o}}_{\substack{\text{Surface}\\ \text{Runoff}}} - \underbrace{\dot{W}_{s_J,a}}_{\substack{\text{TSW}\\ \text{evaporation}}}\Big]. \quad (2.11c)$$

Vegetation

Vegetation is solved as an independent thermodynamic system only if the cohort is sufficiently large. In ED-2.2 the minimum mass is defined as the mass of a cohort of minimum allowed size and population density of $1.67\cdot10^{-2}\,\mathrm{plant\,m^{-2}}$ (one sixth of the initial population). Although the actual number varies for each PFT, the typical minimum heat capacity solved by ED-2.2 is of the order of $10\,\mathrm{J\,m^{-2}\,K^{-1}}$ and leaf area index of $0.005\,\mathrm{m^2_{leaf}\,m^{-2}}$. In case a cohort is smaller than this threshold, it is neglected from all energy and water cycle calculations. The net fluxes for cohorts included in the analysis are:

$$\dot{Q}_{\pi_m} = \underbrace{\dot{Q}_{e,\pi_m}}_{\text{Net radiation}} - \underbrace{\dot{Q}_{\pi_m,a}}_{\substack{\text{Heat flux}\\ \text{Plant to CAS}}} \quad (2.12a)$$

$$\dot{H}_{\pi_m} = \underbrace{\dot{E}_{e,\pi_m}}_{\substack{\text{Precipitation}\\ \text{Interception}}} - \underbrace{\dot{E}_{\pi_m,s_J}}_{\substack{\text{Canopy}\\ \text{dripping}}} + \underbrace{\sum_{k=k_{\rho m}}^{K}(\dot{E}_{g_k,\lambda_m})}_{\substack{\text{Water uptake}\\ \text{from soil}}} - \underbrace{\dot{H}_{\chi_m,c}}_{\text{Transpiration}} - \underbrace{\dot{H}_{\pi_m,c}}_{\substack{\text{Evaporation of}\\ \text{intercepted water}}} \quad (2.12b)$$

$$\dot{W}_{\pi_m} = \underbrace{\dot{W}_{e,\pi_m}}_{\substack{\text{Precipitation}\\ \text{Interception}}} - \underbrace{\dot{W}_{\pi_m,s_J}}_{\substack{\text{Canopy}\\ \text{dripping}}} + \underbrace{\sum_{k=k_{\rho m}}^{K}(\dot{W}_{g_k,\lambda_m})}_{\substack{\text{Water uptake}\\ \text{from soil}}} - \underbrace{\dot{W}_{\chi_m,a}}_{\text{Transpiration}} - \underbrace{\dot{W}_{\pi_m,a}}_{\substack{\text{Evaporation of}\\ \text{intercepted water}}} \quad (2.12c)$$

In ED-2.2, vegetation biomass of the different pools is usually expressed in $[\mathrm{kg_C\,plant^{-1}}]$, which we call intensive biomass from analogy with thermodynamic definition. For the energy budget, however, we must account for the total extensive internal mass $[\mathrm{kg\,m^{-2}}]$ since internal energy is also stored in non-carbon material, including the interstitial and intracellular water of leaves and above ground wood. Internal water is considered a plant functional trait that remains constant throughout the simulation, although it can be different for different plant functional types.

Therefore the extensive mass of the vegetation tissue (D_{π_m}) for any cohort m is given by

$$D_{\pi_m} = D_{\lambda_m} + D_{\omega_m}, \tag{2.13a}$$

$$D_{\lambda_m} = n_{\pi_m} \mathrm{M}^{C:Bio} C_{\lambda_m} \left(1 + \mathrm{M}_{\lambda_m}^{WD}\right), \text{ and} \tag{2.13b}$$

$$D_{\omega_m} = n_{\pi_m} \mathrm{M}^{C:Bio} f_{\mathrm{AG}_m} C_{\omega} \left(1 + \mathrm{M}_{\omega_m}^{WD}\right), \tag{2.13c}$$

where $\mathrm{M}^{C:Bio}$ is the conversion from carbon to oven dry biomass; n_{π_m} is the demographic density $[\,\mathrm{plant\,m^{-2}}]$; C_{λ_m} and C_{ω_m} are the intensive carbon biomass of leaves and wood (App. C), respectively; D_{λ_m} and D_{ω_m} are the extensive internal mass leaves and wood, respectively; f_{AG_m} is the fraction of woody biomass that is above ground; and $\mathrm{M}_{\lambda_m}^{WD}$ and $\mathrm{M}_{\omega_m}^{WD}$ are the PFT-dependent water to oven dry mass ratios for leaves and wood.

The vegetation specific heat ($q_{d\pi_m}$) is based on Gu et al. (2007) parameterization, and it is determined by the weighted average of leaves and wood specific heats, which in turn are weighted averages of the specific heat of the oven-dry materials and water:

$$q_{d\pi_m} = \frac{1}{D_{\pi_m}} \left[D_{\lambda_m} \frac{q_{\lambda}^{\mathrm{OD}} + \mathrm{M}_{\lambda_m}^{WD} q_{\ell}}{1 + \mathrm{M}_{\lambda_m}^{WD}} + D_{\omega_m} \left(\frac{q_{\omega}^{\mathrm{OD}} + \mathrm{M}_{\omega_m}^{WD} q_{\ell}}{1 + \mathrm{M}_{\omega_m}^{WD}} + \Delta q_{\omega}^{\mathrm{Bond}} \right) \right], \tag{2.14}$$

where $q_{\lambda}^{\mathrm{OD}}$ and q_{ω}^{OD} are the specific heats of oven-dry leaves and wood, respectively; and $\Delta q_{\omega}^{\mathrm{Bond}}$ is a term included by Gu et al. (2007) and Forest Products Laboratory (2010) to represent the additional heat capacity associated with the bonding between wood and water. Although q_{ω}^{OD} and $\Delta q_{\omega}^{\mathrm{Bond}}$ are both functions of temperature in Gu et al., we further simplified them to constants in ED-2.2. In addition, using q_{ℓ} as the specific heat for water is equivalent to assume that internal water does not freeze.

Canopy air space (CAS)

Since the canopy air space is a gas, extensive properties are not well constrained because the total mass cannot be directly compared to observations, therefore, all prognostic and diagnostic variables are solved in the intensive form. Total enthalpy and total water mass at the canopy air

space can be written in terms of air density ρ_a and the equivalent depth of the canopy air space $\bar{z}_a$ as:

$$H_a = \rho_a \bar{z}_a h_a, \tag{2.15a}$$

$$W_a = \rho_a \bar{z}_a w_a, \tag{2.15b}$$

$$\bar{z}_a = \max \left[5.0, \frac{\sum_{m=1}^{M_{\text{closed}}} z_{\pi_m} \text{BA}_{\pi_m}}{\sum_{m=1}^{M_{\text{closed}}} \text{BA}_{\pi_m}} \right], \tag{2.15c}$$

where $\text{BA}_{\pi_m}[\,\text{cm}^2\,\text{m}^{-2}]$ and $z_{\pi_m}[\,\text{m}]$ are the basal area and the height of cohort m, respectively; and M_{closed} is the cohort below which the fraction of open canopy is zero, and we assume that cohorts are ordered from tallest to shortest. In case the canopy is open, M_{closed} is the total number of cohorts, and a minimum value of 5 m is imposed when vegetation is absent or too short, to prevent numerical instabilities. Because the equivalent canopy depth depends only on the cohort size, $\bar{z}_a$ is updated at the cohort dynamics step (Δt_{cohort}). If we substitute Eqn. (2.15a) and (2.15b) into Eqn. (2.4a) and (2.4b), respectively, and assume that changes in density over short time steps are much smaller than changes in enthalpy or humidity, we obtain the following equations for the canopy air space budget:

$$\frac{\mathrm{d}h_a}{\mathrm{d}t} = \frac{1}{\rho_a \bar{z}_a} \cdot \left(\dot{Q}_a + \dot{H}_a - \bar{z}_a \frac{\mathrm{d}p_a}{\mathrm{d}t} \right), \tag{2.16a}$$

$$\frac{\mathrm{d}w_a}{\mathrm{d}t} = \frac{\dot{W}_a}{\rho_a \bar{z}_a}, \tag{2.16b}$$

where

$$\dot{Q}_a = \underbrace{\sum_{m=1}^{M} \dot{Q}_{\pi_m,a}}_{\substack{\text{Heat flux} \\ \text{Plant to CAS}}} + \underbrace{\dot{Q}_{s_J,a}}_{\substack{\text{Heat flux} \\ \text{TSW to CAS}}} + \underbrace{\dot{Q}_{g_K,a}}_{\substack{\text{Heat flux} \\ \text{Ground to CAS}}}, \tag{2.16c}$$

$$\dot{H}_a = \underbrace{\dot{H}_{e,a}}_{\text{Eddy flux}} + \sum_{m=1}^{M} \left(\underbrace{\dot{H}_{\pi_m,a}}_{\substack{\text{Evaporation of} \\ \text{intercepted water}}} + \underbrace{\dot{H}_{\chi_m,a}}_{\text{Transpiration}} \right) + \underbrace{\dot{H}_{s_J,a}}_{\text{TSW evaporation}} + \underbrace{\dot{H}_{g_K,a}}_{\text{Ground evaporation}} , \tag{2.16d}$$

$$\dot{W}_a = \underbrace{\dot{W}_{e,a}}_{\text{Eddy flux}} + \sum_{m=1}^{M} \left(\underbrace{\dot{W}_{\pi_m,a}}_{\substack{\text{Evaporation of} \\ \text{intercepted water}}} + \underbrace{\dot{W}_{\chi_m,a}}_{\text{Transpiration}} \right) + \underbrace{\dot{W}_{s_J,a}}_{\text{TSW evaporation}} + \underbrace{\dot{W}_{g_K,a}}_{\text{Ground evaporation}} . \tag{2.16e}$$

Canopy air pressure p_a is assumed to remain constant throughout the integration time step (Δt_{thermo}). At the end of the time step, the air pressure above canopy p_e is updated using the meteorological forcing, at which time p_a and h_a are also updated. To determine p_a we combine three assumptions:

1. Both canopy air space and the air above are a mix of two perfect gases, dry air and water vapor (Dufour and van Mieghem, 1975):

$$p = \rho \mathcal{R}^\star \left[\frac{1}{\mathcal{M}_d} (1-w) + \frac{1}{\mathcal{M}_w} w \right] T = \rho \frac{\mathcal{R}^\star}{\mathcal{M}_d} T_V, \tag{2.17}$$

   where $\mathcal{R}^\star$ is the universal gas constant, and $\mathcal{M}_d$ and $\mathcal{M}_w$ are the molar masses of dry air and water, and T_V is the virtual temperature, which is the temperature that pure dry air would be at if pressure and density were the same as the observed air.

2. p_a instantaneously changes when p_e is updated, and this update does not involve any exchange of mass or energy. This is equivalent to assume that potential temperature of the canopy air space θ_a and air aloft θ_e do not change when pressure is updated, even if enthalpy and temperature are not conserved. Potential temperature, approximated to the potential temperature of dry air, is defined as:

$$\theta = T \left(\frac{p_0}{p} \right)^{\frac{\mathcal{R}^\star}{\mathcal{M}_d q_{p\mathrm{d}}}}, \tag{2.18}$$

   where $p_0 \stackrel{\text{def}}{=} 10^5 Pa$.

3. The layer between canopy air space depth $\bar{z}_a$ and reference height of the air aloft z_e is in hydrostatic equilibrium:

$$\frac{\partial p}{\partial z} = -\rho\, g_{\oplus}, \tag{2.19}$$

where $g_{\oplus}$ is the gravity acceleration.

Combining Eqn. (2.17), (2.18), and (2.19), and assuming that $\theta_V \overset{\text{def}}{=} \theta(T_V)$ yields to

$$p_a = \left[p_e^{\frac{\mathcal{R}^\star}{\mathcal{M}_d q_{p\mathrm{d}}}} + \frac{g_{\oplus}\,(z_e - \bar{z}_a)}{q_{p\mathrm{d}}\overline{\theta_V}} p_0^{\frac{\mathcal{R}^\star}{\mathcal{M}_d q_{p\mathrm{d}}}} \right]^{\frac{\mathcal{M}_d q_{p\mathrm{d}}}{\mathcal{R}^\star}}, \tag{2.20}$$

where $\overline{\theta_V}$ is the virtual potential temperature averaged between z_e and $\bar{z}_a$. Once pressure is updated at the biophysics time step, temperature and enthalpy are also updated using Eqn. (2.18) and (2.7), respectively. Since canopy air pressure is known at all times, canopy air density ρ_a is determined using Eqn. (2.17).

The specific heat at constant pressure of the canopy air space (q_{p_a}) is determined similarly to the vegetation and soils, as the weighted average between dry air and water vapor:

$$q_{p_a} = (1 - w_a)\, q_{p\mathrm{d}} + w_a q_{pv}. \tag{2.21}$$

2.3.3 ED-2.2 Carbon dioxide cycle

In ED-2.2, the carbon dioxide cycle is a subset of the full carbon cycle, and is shown in Fig. 2.5, and the canopy air space is the only thermodynamic system solved by ED-2.2 with CO_2 storage; nonetheless, we assume that the contribution of CO_2 to density and heat capacity of the canopy air space is negligible, hence only the molar CO_2 mixing ratio $c_a[\,\mathrm{mol_C\,mol_{Air}^{-1}}]$ is traced.

The change in CO_2 storage is determined by the following differential equation:

$$\rho_a \bar{z}_a \frac{\mathrm{d}c_a}{\mathrm{d}t} = \dot{C}_{e,a} - \sum_{m=1}^{M} \left(\dot{C}_{\chi_m,a} + \dot{C}_{\rho_m,a} + \dot{C}_{\tau_m,a} + \dot{C}_{\Delta_m,a} \right) - \sum_{i=1}^{3} \left(\dot{C}_{z_i,a} \right), \tag{2.22}$$

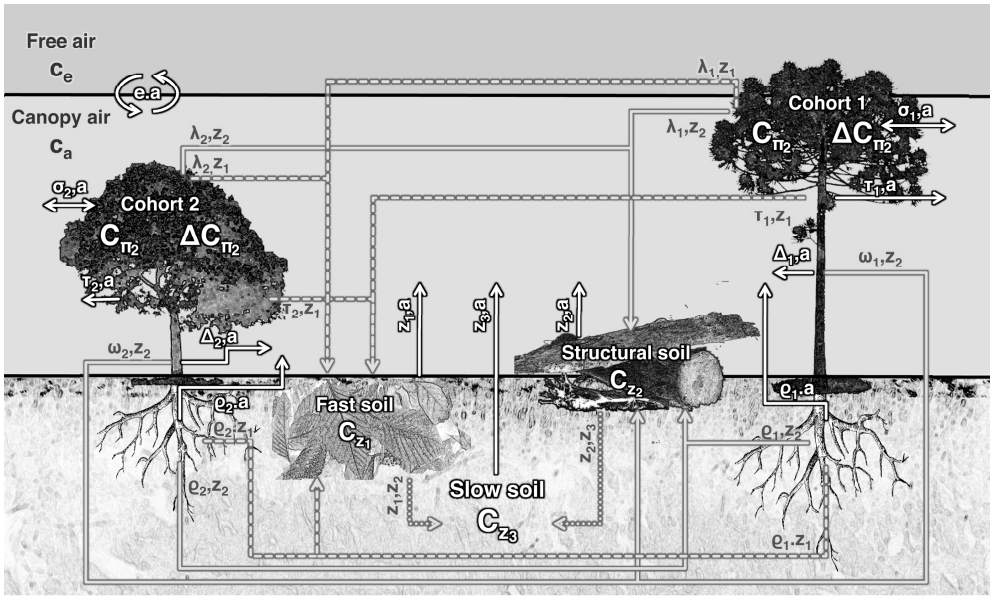

Figure 2.5: Schematic of the patch-level carbon cycle solved in ED-2.2; for a patch containing two cohorts. Like in Fig. 2.4, letter near the arrows are the subscripts associated with fluxes. Fluxes shown in white are part of the CO_2 cycle discussed in this manuscript.

where $\dot{C}_{\chi m,a}$ is the net flux of CO_2 between leaf and canopy air space (positive when leaf respiration exceeds photosynthetic assimilation); $\dot{C}_{\rho m,a}$ is the root respiration; $\dot{C}_{\tau_m,a}$ and $\dot{C}_{\Delta_m,a}$ are the respiration terms associated with the storage pool, the first related to the turnover, and the second with the maintenance of the existing tissues and growth of new tissues; and the $\dot{C}_{z_i}$ terms are the heterotrophic respiration associated with the soil carbon, which is divided in three pools according to their characteristic life time: fast z_1, intermediate (structural) z_2, and slow z_3.

In addition to canopy air space, we also define a virtual cohort pool of carbon biomass (ΔC_{π_m} $[\,\mathrm{kg_C\,plant^{-1}}]$) which contains the net uptake of CO_2:

$$n_m \frac{\mathrm{d}\Delta C_{\pi_m}}{\mathrm{d}t} = -\mathcal{M}_\mathrm{C}\left(\dot{C}_{\chi_m,a} + \dot{C}_{\rho_m,a} + \dot{C}_{\Delta_m,a}\right) \tag{2.23}$$

This virtual pool is used at the phenology step to perform maintenance of live tissues and to update the storage pool. The update of living tissue biomass from ΔC_{π_m} is summarized in App. F.2, and the transfer of carbon from plants to the soil carbon pools and between the soil carbon pools have been discussed in previous ED publications (c.f. Moorcroft et al., 2001; Albani et al., 2006; Medvigy,

2006) thus not discussed here.

2.4 Sub-models and parameterizations

In this section I present the sub-model and parameterizations used to determine each of the flux terms presented in Sec. 2.3.2 and Sec. 2.3.3.

2.4.1 Precipitation and vegetation dripping

Total incoming precipitation $\dot{W}_{\infty,e}$ is split into through fall $\dot{W}_{e,s_J}$ and the interception by each cohort $\dot{W}_{e,\pi_m}$, based on the fraction of open canopy o_a, and the total plant area index:

$$\dot{W}_{e,s_J} = o_a \dot{W}_{\infty,e}, \tag{2.24}$$

$$\dot{W}_{e,\pi_m} = (1 - o_a)\, \dot{W}_{\infty,e} \left[\frac{\Pi_m}{\sum_{m=1}^{M} \Pi_m} \right], \tag{2.25}$$

$$o_a = \prod_{m=1}^{M} (1 - X_{\pi_m}), \tag{2.26}$$

where $\Pi_m = \Lambda_m + \Omega_m$ is the total plant area index, Λ_m and Ω_m being the leaf and wood area indices, both defined from PFT-dependent allometric relations (App. C); X_{π_m} is the crown area index of each cohort m, defined in App. C. Through fall precipitation is always placed on the topmost temporary surface water layer ($j = J$). In case no temporary surface water layer exists, a new layer is created, although it may be extinct in case all water is able to percolate down to the top soil layer (c.f. Appendix 2.4.2).

Precipitation is assumed to be either rain, snow, or a mix of both. Rain is only allowed when T_e is above freezing, and rain temperature is always assumed to be at T_e; snow is usually at T_e as well, except when T_e is slightly above freezing, in which case snow temperature is assumed to be at T_3:

$$\dot{E}_{\infty,e} = \dot{W}_{\infty,e} \left[(1 - \ell_e)\, q_i \min(T_3, T_e) + \ell_e\, q_\ell\, (T_e - T_{sc\ell}) \right], \tag{2.27}$$

where ℓ_e is the rainfall fraction, from Jin et al. (1999) parameterization, slightly modified to make the function continuous:

$$\ell_e = \begin{cases} 1.0 & \text{, if } T_e > 275.66\,K \\ 0.4 + 1.2\,(T_e - T_3 - 2.0) & \text{, if } 275.16\,K < T_e \leq 275.66\,K \\ 0.2\,(T_e - T_3) & \text{, if } T_3 < T_e \leq 275.16\,K \\ 0.0 & \text{, if } T_e \leq T_3 \end{cases} . \tag{2.28}$$

The internal energy flux due to precipitation is then partitioned using the same scaling as in Eqn. (2.24) and (2.25).

Water is only allowed to accumulate on top of leaves and branches until it reaches the local cohort holding capacity $w_{\max}$, which can be set by the user, and is typically of the order of $0.05 - 0.40\,\mathrm{kg_W\,m^{-2}_{leaf+wood}}$ (Wohlfahrt et al., 2006). Water and the associated internal energy in excess of the holding capacity is immediately lost to the top temporary surface water layer due to vegetation dripping:

$$\dot{W}_{\pi_m,s_J} = -\frac{1}{\Delta t_{\text{thermo}}} \max\left[0, W_{\pi_m} - w_{\max}\left(\Lambda_m + \Omega_m\right)\right], \tag{2.29a}$$

$$\dot{E}_{\pi_m,s_J} = \dot{W}_{\pi_m,s_J}\left[\left(1-\ell_{\pi_m}\right) q_i T_{\pi_m} + \ell_{\pi_m}\left(T_{\pi_m} - T_{sc\ell}\right)\right], \tag{2.29b}$$

where ℓ_{π_m} is the liquid fraction of surface water on top of cohort m. Vegetation dripping does not distinguish water and ice that had been accumulated due to precipitation and due to dew or frost formation.

2.4.2 Hydrology sub-model and ground energy exchange

The ground model encompasses energy and water fluxes between adjacent layers of soil and temporary surface water, as well as losses of water and internal energy due to surface runoff and drainage. In this section fluxes between adjacent layers are positive when they are upwards, whereas runoff and drainage fluxes are non-negative.

In ED-2.2, the total number of soil layers K and the thickness of each layer Δz_{g_k} are defined by the user. Typically, the top layer is set to 0.02 m, which is a compromise between computational

efficiency and ability to represent the stronger gradients near the surface, and layers with increasing depth are added for the entire rooting zone. The maximum number of temporary surface water layers $J_{\max}$ is also defined by the user; however, the actual number of layers J and equivalent thickness of each layer ($\Delta\overline{z}_{s_j}$) is dynamic, and it depends on the total mass and the water phase. Both J and $\Delta\overline{z}_{s_j}$ are updated every Δt_{thermo} using the same methodology as LEAF-2 (Walko et al., 2000).

Sensible heat flux between two adjacent soil (temporary surface water) layers $k-1$ and k ($j-1$ and j) are determined based on thermal conductivity Υ_H and temperature gradient (Bonan, 2008), with an additional term for temporary surface water to scale the flux when the temporary surface water covers only a fraction f_{tsw} of the ground:

$$\dot{Q}_{g_{k-1},g_k} = -\left\langle \Upsilon_H \right\rangle_{g_{k-1},g_k} \left(\frac{\partial T_g}{\partial z}\right)_{g_{k-1},g_k}, \tag{2.30a}$$

$$\dot{Q}_{s_{j-1},s_j} = -f_{\text{tsw}} \left\langle \Upsilon_H \right\rangle_{s_{j-1},s_k} \left(\frac{\partial T_s}{\partial z}\right)_{s_{j-1},s_j}, \tag{2.30b}$$

where the operator $\langle\ \rangle$ is the log-linear interpolation from the mid-point height of layers $k-1(j-1)$ and $k(j)$ to the height at the interface. The bottom boundary condition of Eqn. (2.30a) is $\left(\partial T_g/\partial z\right)_{g_0,g_1} \stackrel{\text{def}}{=} 0$. The interface between the top soil layer and the first temporary surface water $\dot{Q}_{g_K,s_1}$ is found by applying Eqn. (2.30b) with $(T;\Upsilon_H;\Delta z)_{s_0} = (T;\Upsilon_H;\Delta z)_{g_K}$.

The fraction of ground covered by the temporary surface water is determined using the same formulation proposed by (Niu and Yang, 2007), with the same coefficients used in the Community Land Model (NCAR-CLM Oleson et al., 2010):

$$f_{\text{tsw}} = \begin{cases} 0 & \text{if } J = 0 \\ \tanh\left[\dfrac{\sum_{j=1}^{J} z_{g_j}}{2.5 z_{0_{\text{soil}}}} \left(\dfrac{\overline{\rho}_s}{\rho^{\circledast}}\right)^{-1.0}\right] & \text{if } J > 0 \end{cases}, \tag{2.31a}$$

where

$$\overline{\rho}_s = \left(\sum_{j=1}^{J} W_{s_j}\right) \cdot \left(\sum_{j=1}^{J} \overline{z}_{s_j}\right)^{-1} \tag{2.31b}$$

Soil thermal conductivity at layer (Υ_{Hg_k}) is a function of the soil texture and soil moisture, and is determined using the de Vries weighted average of conductivities of each constituent of the soil (e.g. Parlange et al., 1998):

$$\Upsilon_{Hg_k} = \frac{\sum_{t=0}^{3} \left[\left(\frac{3\Upsilon_{H\ell}}{2\Upsilon_{H\ell} + \Upsilon_{Ht}} \right) \mathcal{V}_{t,k} \Upsilon_{Ht} \right] + \vartheta_{g_k} \Upsilon_{H\ell}}{\sum_{t=0}^{3} \left[\left(\frac{3\Upsilon_{H\ell}}{2\Upsilon_{H\ell} + \Upsilon_{Ht}} \right) \mathcal{V}_{t,k} \right] + \vartheta_{g_k}}, \tag{2.32a}$$

$$\mathcal{V}_{t,k} = \begin{cases} \vartheta_{\mathrm{Po}} - \vartheta_k & t = 0 \\ \mathcal{V}_t^{\mathrm{Dry}} (1 - \vartheta_{\mathrm{Po}}) & t \neq 0 \end{cases}, \tag{2.32b}$$

where subscript $\mathcal{V}_{t,k}$ are the volumetric fraction for soil components air, sand, silt, and clay ($t = 0,1,2,3$, respectively); $\Upsilon_{Ht} = (0.025; 8.80; 5.87; 2.92)\ \mathrm{W\,m^{-1}\,K^{-1}}$ are the thermal conductivities for air, sand, silt, and clay, respectively; $\Upsilon_{H\ell} = 0.57\ \mathrm{W\,m^{-1}\,K^{-1}}$ is the thermal conductivity of water; $\mathcal{V}_t^{\mathrm{Dry}}$ is the dry matter volumetric fraction; and ϑ_{Po} is the soil porosity. In Eqn. (2.32a), the weights are the product between the volumetric fraction and a function that represents both the ratio of the thermal gradient of the soil constituents and the thermal gradient of water and the shape of each soil constituent (Camillo and Schmugge, 1981); in ED-2.2 we assume all particles to be spherical. The thermal conductivity of each temporary surface water layer (Υ_{Hs_j}) is a function of the layer temperature T_{s_j} and bulk layer density $\rho_{s_j} \overset{\mathrm{def}}{=} W_{s_j}/\Delta\overline{z}_{s_j}$, and is found using the same parameterization as LEAF-2 (Walko et al., 2000):

$$\begin{aligned} \Upsilon_{Hs_j} = {} & 1.093 \cdot 10^{-3} \exp\left(0.028\, T_{s_j}\right) \\ & \times \left(0.03 + 3.03 \cdot 10^{-4} \rho_{s_j} - 1.77 \cdot 10^{-7} \rho_{s_j}^2 + 2.25 \cdot 10^{-9} \rho_{s_j}^3\right). \end{aligned} \tag{2.33}$$

Ground water exchange between layers occurs only if water is in liquid phase. The water flux between soil layers g_{k-1} and $g_k, k \in \{2,3,\ldots,K-1\}$ is determined from Darcy's law (Bonan,

2008):

$$\dot{W}_{g_{k-1},g_k} = -\rho_\ell \left\langle G_\Psi \right\rangle_{g_{k-1},g_k} \left[\frac{\partial \Psi}{\partial z} + \frac{\mathrm{d}z_g}{\mathrm{d}z} \right]_{g_{k-1},g_k}, \tag{2.34}$$

where $\Psi[\,\mathrm{m}]$ is the soil matric potential and $G_\Psi[\,\mathrm{kg_W\,m^{-2}\,s^{-1}}]$ is the hydraulic conductivity, both defined after Brooks and Corey (1964), with an additional correction term applied to hydraulic conductivity to reduce conductivity in case the soil is partially or completely frozen:

$$\Psi_k = \Psi_{\mathrm{Po}} \left(\frac{\vartheta_{\mathrm{Po}}}{\vartheta_k} \right)^{\acute{b}}, \tag{2.35a}$$

$$G_{\Psi_k} = \left[10^{-7\left(1-\ell_{g_k}\right)} \right] G_{\Psi,\mathrm{Po}} \left(\frac{\vartheta_{\mathrm{Po}}}{\vartheta_k} \right)^{2\acute{b}+3}, \tag{2.35b}$$

where Ψ_{Po} and $G_{\Psi,\mathrm{Po}}$ are the soil-texture dependent, matric potential and hydraulic conductivity at bubbling pressure (assumed to be when $\vartheta = \vartheta_{\mathrm{Po}}$); $\acute{b}$ is the slope of the retention curve in logarithm scale (Cosby et al., 1984) and ℓ_{g_k} is the fraction of liquid water of soil moisture at layer g_k. The definition of Ψ_{Po}, $G_{\Psi,\mathrm{Po}}$, and $\acute{b}$ follows Cosby et al. (1984) and is available in App. B.

The term $\mathrm{d}z_g/\mathrm{d}z$ in Eqn. (2.34) is the flux due to gravity, and it is 1 for all layers except the bottom boundary condition, which depends on the sub-surface drainage. Sub-surface drainage at the bottom boundary depends on the type of drainage, and is determined using a slight modification of Eqn. (2.34). Let a_o be the angle between the impeding layer beneath the lowest level and the horizontal. By assuming zero gradient in soil moisture between the lowest layer and the boundary condition, the sub-surface drainage flux $\dot{W}_{g_1,o}$ becomes:

$$\dot{W}_{g_1,o} = -\dot{W}_{g_0,g_1} = \rho_\ell G_{\Psi_{g_1}} \sin a_o. \tag{2.36}$$

Special cases of Eqn. (2.36) are the zero-flow conditions ($a_o = 0$) and free drainage ($a_o = \pi/2$).

For the temporary surface water, water flux between layers through percolation is calculated similarly to LEAF-2 (Walko et al., 2000). Liquid water in excess of 10 % is in principle free to percolate to the layer below, although the maximum percolation of the first surface water layer is

limited by the amount of pore space available at the top ground layer:

$$\dot{W}_{g_K,s_1} = -\frac{1}{\Delta t_{\text{thermo}}} \max\left[0, W_{s_1}\left(\frac{\ell_{s_1}-0.1}{0.9}\right), \rho_\ell\left(\vartheta_{\text{Po}}-\vartheta_K\right)\Delta z_{g_K}\right] \quad , \tag{2.37a}$$

$$\dot{W}_{s_{j-1},s_j} = -\frac{W_{s_j}}{\Delta t_{\text{thermo}}} \max\left(0, \frac{\ell_{s_j}-0.1}{0.9}\right) \quad , \text{if } j>1. \tag{2.37b}$$

Surface runoff of liquid water is simulated using a simple extinction function, applied only at the top most temporary surface water layer:

$$\dot{W}_{s_J,o} = \ell_{s_J} W_{s_J} \exp\left(-\frac{\Delta t_{\text{thermo}}}{t_{\text{Runoff}}}\right) \tag{2.38}$$

where t_{Runoff} is a user-defined decay time, usually of the order of a few minutes to a few hours.

Because water fluxes exchange mass, they also exchange internal energy. Runoff and sub-surface drainage fluxes are functions of the layer temperature:

$$\dot{E}_{g_1,o} = \dot{W}_{g_1,o}\, q_\ell\left(T_{g_1}-T_{sc\ell}\right), \tag{2.39a}$$

$$\dot{E}_{g_J,o} = \dot{W}_{s_J,o}\, q_\ell\left(T_{s_J}-T_{sc\ell}\right), \tag{2.39b}$$

whereas the internal energy flux between two adjacent layers depends on the sign of the flux in order to determine the donor layer:

$$\dot{E}_{f_{l-1}f_l} = \begin{cases} \dot{W}_{f_{l-1}f_l} q_\ell\left(T_{f_l}-T_{sc\ell}\right) & \text{, if } \dot{W}_{f_{l-1}f_l}<0 \\ 0 & \text{, if } \dot{W}_{f_{l-1}f_l}=0 \\ \dot{W}_{f_{l-1}f_l} q_\ell\left(T_{f_{l-1}}-T_{sc\ell}\right) & \text{, if } \dot{W}_{f_{l-1}f_l}>0 \end{cases}, \tag{2.40}$$

where the subscript f_l represents either soil (g_k) or temporary surface water (s_j).

2.4.3 Radiation model

The radiation budget is solved for three independent bands (subscript b), the photosynthetically active radiation (PAR, $b=1$), near infra-red radiation (NIR, $b=2$) and the thermal infra-red radiation (TIR, $b=3$). For each band, the canopy radiation solver assumes that each cohort corresponds

to one layer, and within each layer the optical and thermal properties are constant. For all bands, the top boundary condition is provived by the meteorological forcing; in case of PAR and NIR, the downward radiation is comprised of a beam (direct) and isotropic (diffuse) components, whereas TIR radiation is assumed to be all diffuse. Direct radiation that is intercepted then reflected or transmitted by the cohorts or reflected by the ground becomes all diffuse.

Canopy radiation

Two solvers for canopy radiation exist in ED-2.2: a multi-layer version of the two-stream model Sellers (1985); Liou (2002); Medvigy (2006); and a multiple scattering model based on Zhao and Qualls (2005, 2006). Since the algorithm for solving the multiple scattering model is the same as presented by Zhao and Qualls (2005, 2006), in this section I only present the derivation of the two-stream model. The layer optical properties described here, however, are used by both models.

Below I present the general equations that describe the extinction of downward direct radiation (Eqn. 2.41a) and the two-stream model for hemispheric diffuse radiation (Eqn. 2.41b, and Eqn. 2.41c) for each band b and each cohort m, where $m = 1$ and $m = M$ correspond to the shortest and tallest cohort, respectively, based on Sellers (1985):

$$\mu_m^{\odot} \frac{\mathrm{d}\dot{Q}_{b,m}^{\odot}}{\mathrm{d}\tilde{\Pi}} = -\dot{Q}_{b,m}^{\odot}, \tag{2.41a}$$

$$\begin{aligned} \overline{\mu}_m \frac{\mathrm{d}\dot{Q}_{b,m}^{\Downarrow}}{\mathrm{d}\tilde{\Pi}} = & -\dot{Q}_{b,m}^{\Downarrow} + \left(1-\beta_{b,m}\right)\varsigma_{b,m}\dot{Q}_{b,m}^{\Downarrow} + \varsigma_{b,m}\beta_{b,m}\dot{Q}_{b,m}^{\Uparrow} \\ & + \frac{\overline{\mu}_m}{\mu_m^{\odot}}\varsigma_{b,m}\left(1-\beta_{b,m}^{\odot}\right)\dot{Q}_{b,m}^{\odot} + \left(1-\varsigma_{b,m}\right)\dot{Q}_{b,m}^{\blacklozenge}, \end{aligned} \tag{2.41b}$$

$$\begin{aligned} -\overline{\mu}_m \frac{\mathrm{d}\dot{Q}_{b,m}^{\Uparrow}}{\mathrm{d}\tilde{\Pi}} = & -\dot{Q}_{b,m}^{\Uparrow} + \left(1-\beta_{b,m}\right)\varsigma_{b,m}\dot{Q}_{b,m}^{\Uparrow} + \varsigma_{b,m}\beta_{b,m}\dot{Q}_{b,m}^{\Downarrow} \\ & + \beta_{b,m}^{\odot}\frac{\overline{\mu}_m}{\mu_m^{\odot}}\varsigma_{b,m}\dot{Q}_{b,m}^{\odot} + \left(1-\varsigma_{b,m}\right)\dot{Q}_{b,m}^{\blacklozenge}, \end{aligned} \tag{2.41c}$$

where

$$\dot{\mathbf{Q}}_b^{\odot} = \left(\dot{Q}_{b,1}^{\odot}, \dot{Q}_{b,2}^{\odot}, \ldots, \dot{Q}_{b,M}^{\odot}\right) \quad , \tag{2.42a}$$

$$\dot{\mathbf{Q}}_b^{\Downarrow} = \left(\dot{Q}_{b,1}^{\Downarrow}, \dot{Q}_{b,2}^{\Downarrow}, \ldots, \dot{Q}_{b,M}^{\Downarrow}\right) \quad , \tag{2.42b}$$

$$\dot{\mathbf{Q}}_b^{\Uparrow} = \left(\dot{Q}_{b,1}^{\Uparrow}, \dot{Q}_{b,2}^{\Uparrow}, \ldots, \dot{Q}_{b,M}^{\Uparrow}\right) \quad , \tag{2.42c}$$

$$\dot{\mathbf{Q}}_b^{\blacklozenge} = \left(\dot{Q}_{b,1}^{\blacklozenge}, \dot{Q}_{b,2}^{\blacklozenge}, \ldots, \dot{Q}_{b,M}^{\blacklozenge}\right) = \delta_{b3}\, \sigma_{\mathrm{B}} \left(T_{v_1}^4, T_{v_2}^4, \ldots, T_{v_M}^4\right), \tag{2.42d}$$

are the profiles of downward direct, downward (hemispheric) diffuse, upward (hemispheric) diffuse irradiances and irradiance emitted by a black body at the same temperature as the cohort (T_{v_m}), respectively (Fig. 2.6); and σ_{B} is the Stefan-Boltzmann constant; $\varsigma_{b,m}$ is the scattering coefficient ($1-\varsigma_{b,m}$ is the absorptivity); $\beta_{b,m}$ and $\beta_{b,m}^{\odot}$ are the backscattered fraction of scattered direct and diffuse irradiance, respectively; $\tilde{\Pi}$ is the effective cumulative plant area index, assumed zero at the top of each layer and increasing downwards ($\tilde{\Pi}_m$ is the total for layer m); and $\mu_m^{\odot}$ and $\overline{\mu}_m$ are the inverse of the optical depth per unit of P for direct and diffuse radiation, respectively.

The first term on the right-hand side of Eqn. (2.41a), (2.41b), and (2.41c) represent the light extinction due to interception by leaves and branches. The remaining terms of Eqn. (2.41b) and (2.41c) represent the contribution from the following interactions, respectively: (2) forward scattering of intercepted diffuse irradiance from the same hemisphere; (3) backscattering of intercepted irradiance from the opposite hemisphere; (4) scattering of intercepted direct radiation (forward scattering for $\dot{Q}_{b,m}^{\Downarrow}$, and backscattering for $\dot{Q}_{b,m}^{\Uparrow}$); and (5) thermal emission of radiation, where it is assumed that absorptivity equals to emissivity, hence the $1-\varsigma$ term. The system present in Eqn. (2.41) is never solved with all terms: $\dot{\mathbf{Q}}_1^{\blacklozenge} = \dot{\mathbf{Q}}_2^{\blacklozenge} = \mathbf{0}$, because thermal emission is negligible in the PAR-NIR range; and $\dot{\mathbf{Q}}_3^{\odot} = \mathbf{0}$, because we assume that all incoming irradiance is diffuse in the TIR band.

The effective plant area index $\tilde{\Pi}$ is the total area (leaves and branches) that is corrected to account for that leaves are not uniformly distributed in the layer, and it is defined as $\tilde{\Pi}_m = \Omega_m + \not{p}_m \Lambda_m$, where $\not{p}_m$ is the PFT-dependent clumping index (Chen and Black, 1992). $\tilde{\Pi}$ is assumed zero at the top of the layer, increasing downwards.

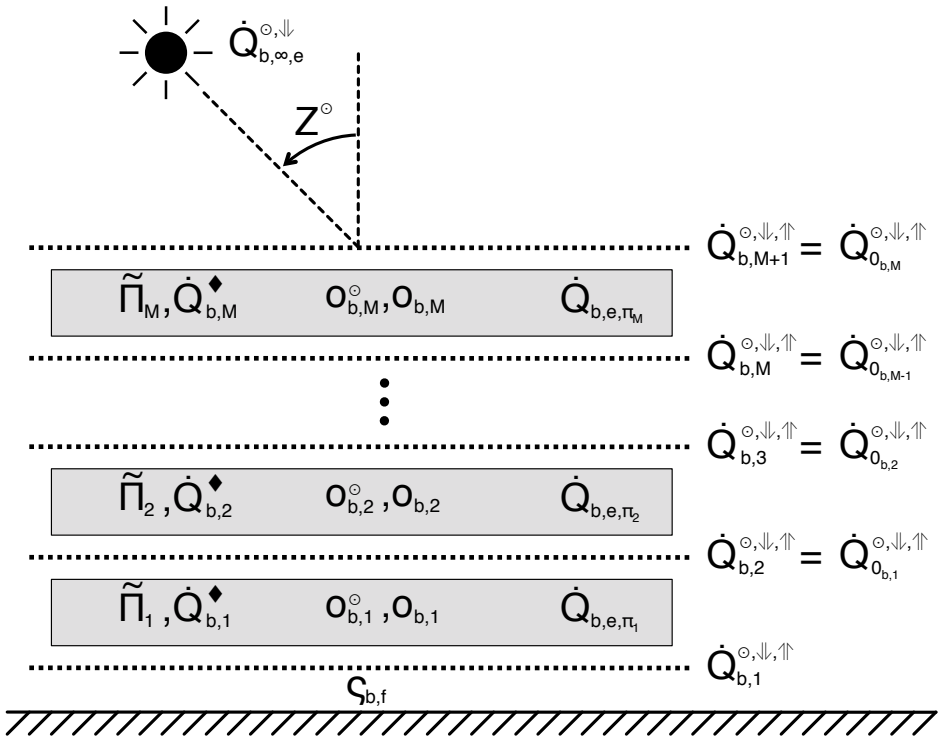

Figure 2.6: Schematic of the radiation layers for a patch with M layers, showing the grid arrangement of the irradiance profiles relative to the cohort positions. Symbols $o^{\odot}_{b,m}$ and $o_{b,m}$ represent the various optical properties of direct and diffuse irradiance, respectively; other symbols are described in the main text.

The inverse of the optical depth per unit of plant area index (μ) for a radiation beam coming from any given angle of incidence Z is determined from the same parameterization described by Sellers (1985) and Oleson et al. (2010):

$$\mu\left(Z,\chi_v\right) = \frac{\cos Z}{\mathcal{G}\left(Z,\chi_v\right)} \tag{2.43}$$

where $\mathcal{G}\left(Z,\chi_v\right)$ is the average projection of all leaves and branches onto the horizontal, defined after Goudriaan (1977):

$$\begin{aligned} \mathcal{G}\left(Z,\chi_v\right) &= F_1 + F_2 \cos Z, \\ F_1 &= 0.5 - 0.633\chi_v - 0.33\chi_v^2, \\ F_2 &= 0.877\left(1 - 2F_1\right); \end{aligned} \tag{2.44}$$

where Z is 0 when the beam is coming from the zenith and π when coming from the nadir (Fig. 2.6); and χ_v is the mean orientation of leaves and branches, a PFT-dependent parameter that ranges from -1 (vertical leaves) to +1 (horizontal leaves), with 0 corresponding to spherically distributed leaves. Equation (2.44) is valid only when $-0.4 \leq \chi_v \leq 0.6$, which is the case for most plants in the wild (Goudriaan, 1977), and also all plant functional types in ED-2.2.

For direct radiation, $\mu_m^{\odot} = \mu\left(Z^{\odot}, \chi_{v_m}\right)$, where $Z^{\odot}$ is the solar zenith angle, whereas for hemispheric radiation, all angles between 0 and $\pi/2$ contribute equally[3], and therefore $\overline{\mu}_m$ is the average across all possible values (Sellers, 1985):

$$\overline{\mu}_m = \int_0^{\pi/2} \frac{\cos(Z)}{\mathcal{G}\left(Z, \chi_{v_m}\right)} \sin(Z)\, \mathrm{d}Z = \frac{1}{F_{2_m}} \left[1 + \frac{F_{1_m}}{F_{2_m}} \log\left(\frac{F_{1_m}}{F_{1_m} + F_{2_m}}\right)\right]. \tag{2.45}$$

The scattering parameters $\varsigma_{b,m}$, $\beta_{b,m}$ and $\beta_{b,m}^{\odot}$ for each cohort m are found using the same formulation as the Community Land Model (CLM, Oleson et al., 2010), which is mostly derived from Goudriaan (1977) and Sellers (1985). The scattering coefficient is $\varsigma_{b,m} = \varsigma_{R_{b,m}} + \varsigma_{T_{b,m}}$, where $\varsigma_{R_{b,m}}$ and $\varsigma_{T_{b,m}}$ are the PFT- and band-dependent reflectance and transmittance, respectively. The cohort parameters are found by scaling the PFT-dependent, leaf ($\varsigma_{R_{b,\lambda}}$; $\varsigma_{T_{b,\lambda}}$) and wood ($\varsigma_{R_{b,\omega}}$; $\varsigma_{T_{b,\omega}}$) properties with their effective area:

$$\varsigma_{R_{b,m}} = \frac{1}{\tilde{\Pi}_m} \left(\Omega_m\, \varsigma_{R_{b,\omega}} + b_m \Lambda_m\, \varsigma_{R_{b,\lambda}}\right), \tag{2.46a}$$

$$\varsigma_{T_{b,m}} = \frac{1}{\tilde{\Pi}_m} \left(\Omega_m \varsigma_{T_{b,\omega}} + b_m \Lambda_m\, \varsigma_{T_{b,\lambda}}\right), \tag{2.46b}$$

Both the bulk diffuse backscattering $\beta_{b,m}$ and forwarding scattering $1 - \beta_{b,m}$ contain contribution from reflectance and transmittance because leaves and branches are not perfectly horizontal; therefore the fraction depends on the mean leaf and branch inclination relative to the horizontal plane ($\overline{a}_m$), which is related to the leaf orientation by the same approximation used by Oleson et al. (2010):

[3]For upward radiation, the actual values are between $\pi/2$ and π. The value, however, is equivalent to the downward hemisphere except for the sign, hence the negative sign at the left-hand side of Eqn. (2.41c).

$$\beta_{b,m} = \frac{1}{2\varsigma_{b,m}} \left[\varsigma_{R_{b,m}} + \varsigma_{T_{b,m}} + \left(\varsigma_{R_{b,m}} - \varsigma_{T_{b,m}}\right) \cos^2\left(\overline{a}_m\right)\right], \tag{2.47a}$$

$$\cos \overline{a}_m \approx \frac{1+\chi_{v_m}}{2}. \tag{2.47b}$$

For direct radiation, backscattering $\beta^{\odot}_{b,m}$ and single-scattering albedo $\varsigma^{\odot}_{b,m}$ are the same as Sellers (1985); Oleson et al. (2010) and are determined by taking the limit $\varsigma_{b,m} \to 0$ of Eqn. (2.41b) and (2.41c), assuming isotropic scattering of leaves and branches, and the projected area from Eqn. (2.44):

$$\beta^{\odot}_{b,m} = \frac{\overline{\mu}_m + \mu^{\odot}_m}{\overline{\mu}_m} \frac{\varsigma^{\odot}_{b,m}}{\varsigma_{b,m}}, \tag{2.48a}$$

$$\begin{aligned} \frac{\varsigma^{\odot}_{b,m}}{\varsigma_{b,m}} &= \frac{1}{2} \int_0^{\pi/2} \frac{\mathcal{G}\left(Z^{\odot}, \chi_{v_m}\right) \cos Z}{\mathcal{G}\left(Z^{\odot}, \chi_{v_m}\right) \cos Z + \mathcal{G}\left(Z, \chi_{v_m}\right) \cos Z^{\odot}} \sin Z \, \mathrm{d}Z \\ &= \frac{1}{2\left(1 + F_{2_m} \mu^{\odot}_m\right)} \left\{1 - \frac{F_{1_m} \mu^{\odot}_m}{1 + F_{2_m} \mu^{\odot}_m} \ln\left[\frac{1 + \left(F_{1_m} + F_{2_m}\right) \mu^{\odot}_m}{F_{1_m} \mu^{\odot}_m}\right]\right\}. \end{aligned} \tag{2.48b}$$

Because we assume that the optical properties are constant within each layer, it is possible to find an analytical solution for the full profile of direct and diffuse radiation. First, let $\dot{Q}^{\odot}_{b,m}$, $\dot{Q}^{\Downarrow}_{b,m}$, and $\dot{Q}^{\Uparrow}_{b,m}$ be the solution for band b and layer m immediately beneath the cohort ($\tilde{\Pi} = \tilde{\Pi}_m$), and $\dot{Q}^{\odot}_{0_{b,m}}$, $\dot{Q}^{\Downarrow}_{0_{b,m}}$, and $\dot{Q}^{\Uparrow}_{0_{b,m}}$ be the solution for band b and layer m immediately above the cohort ($\tilde{\Pi} = 0$), as shown in Fig. 2.6. The direct radiation profile within each layer is simply given by

$$\dot{Q}^{\odot}_{b,m} = \dot{Q}^{\odot}_{0_{b,m}} \exp\left(-\frac{\tilde{\Pi}}{\mu^{\odot}_m}\right), \tag{2.49a}$$

$$\dot{Q}^{\odot}_{0_{b,m}} = \dot{Q}^{\odot}_{b,m+1}, \tag{2.49b}$$

$$\dot{Q}^{\odot}_{b,N+1} = \dot{Q}^{\odot}_{b,\infty,e}, \tag{2.49c}$$

where $\dot{Q}^{\odot}_{b,\infty,e}$ is the above-canopy, incoming direct radiation for band b and serves as the top boundary condition. Because the value at level $M+1$ is known, it is possible to determine all levels $m \in (1,2,\ldots,M)$ by integrating the layers from top to bottom.

For the diffuse components, an analytic solution can be found by defining two auxiliary vari-

ables $\dot{Q}_m^+ \stackrel{\text{def}}{=} \dot{Q}_m^{\Downarrow} + \dot{Q}_m^{\Uparrow}$ and $\dot{Q}_m^- = \dot{Q}_m^{\Downarrow} - \dot{Q}_m^{\Uparrow}$. By subtracting (adding) Eqn. (2.41b) to (2.41c), and using Eqn. (2.49) we obtain

$$\frac{\mathrm{d}\dot{Q}_{b,m}^+}{\mathrm{d}\tilde{\Pi}} = -\frac{1-\left(1-2\beta_{b,m}\right)\varsigma_{b,m}}{\overline{\mu}_m}\dot{Q}_{b,m}^- + \frac{\left(1-2\beta_{b,m}^{\odot}\right)\varsigma_{b,m}\dot{Q}_{b,m+1}^{\odot}}{\mu_m^{\odot}}, \tag{2.50a}$$

$$\frac{\mathrm{d}\dot{Q}_{b,m}^-}{\mathrm{d}\tilde{\Pi}} = -\frac{1-\varsigma_{b,m}}{\overline{\mu}_m}\dot{Q}_{b,m}^+ + \frac{\varsigma_{b,m}\dot{Q}_{b,m+1}^{\odot}}{\mu_m^{\odot}} + \frac{2\left(1-\varsigma_{b,m}\right)\dot{Q}_{b,m}^{\blacklozenge}}{\mu_m}. \tag{2.50b}$$

By differentiating Eqn. (2.50a) and (2.50b) and substituting the first derivatives by Eqn. (2.50b) and (2.50a), we obtain two independent, second-order ordinary differential equations:

$$\frac{\mathrm{d}^2\dot{Q}_{b,m}^+}{\mathrm{d}\tilde{\Pi}^2} = \varkappa_{b,m}^2\dot{Q}_{b,m}^+ + \kappa_{b,m}^+\exp\left(-\frac{\tilde{\Pi}}{\mu_m^{\odot}}\right) - 2\varkappa_{b,m}^2\dot{Q}_{b,m}^{\blacklozenge}, \tag{2.51a}$$

$$\frac{\mathrm{d}^2\dot{Q}_{b,m}^-}{\mathrm{d}\tilde{\Pi}^2} = -\varkappa_{b,m}^2\dot{Q}_{b,m}^- + \kappa_{b,m}^-\exp\left(-\frac{\tilde{\Pi}}{\mu_m^{\odot}}\right), \tag{2.51b}$$

$$\varkappa_{b,m} = \frac{1}{\overline{\mu}_m}\sqrt{\left[1-\left(1-2\beta_{b,m}\right)\varsigma_{b,m}\right]\left(1-\varsigma_{b,m}\right)}, \tag{2.51c}$$

$$\kappa_{b,m}^+ = -\left[\frac{1-\left(1-2\beta_{b,m}\right)\varsigma_{b,m}}{\overline{\mu}_m} + \frac{1-2\beta_{b,m}^{\odot}}{\mu_m^{\odot}}\right]\frac{\varsigma_{b,m}\dot{Q}_{b,m+1}^{\odot}}{\mu_m^{\odot}}, \tag{2.51d}$$

$$\kappa_{b,m}^- = -\left[\frac{\left(1-\varsigma_{b,m}\right)\left(1-2\beta_{b,m}^{\odot}\right)}{\overline{\mu}_m} + \frac{1}{\mu_m^{\odot}}\right]\frac{\varsigma_{b,m}\dot{Q}_{b,m+1}^{\odot}}{\mu_m^{\odot}}. \tag{2.51e}$$

The solution of Eqn. (2.51a) and Eqn. (2.51b) is a combination of homogeneous and particular solution, and can be determined analytically to be:

$$\begin{aligned}\dot{Q}_{b,m}^+(\tilde{\Pi}) = {} & x_{1,b,m}^-\exp\left(-\varkappa_{b,m}\tilde{\Pi}\right) + x_{2,b,m}^-\exp\left(+\varkappa_{b,m}\tilde{\Pi}\right) \\ & + \frac{\kappa_{b,m}^+\,{\mu_m^{\odot}}^2}{1-\varkappa_{b,m}^2\,{\mu_m^{\odot}}^2}\exp\left(-\frac{\tilde{\Pi}}{\mu_m^{\odot}}\right) + 2\,\dot{Q}_{b,m}^{\blacklozenge}\end{aligned}, \tag{2.52a}$$

$$\begin{aligned}\dot{Q}_{b,m}^-(\tilde{\Pi}) = {} & x_{1,b,m}^+\exp\left(-\varkappa_{b,m}\tilde{\Pi}\right) + x_{2,b,m}^+\exp\left(+\varkappa_{b,m}\tilde{\Pi}\right) \\ & + \frac{\kappa_{b,m}^-\,{\mu_m^{\odot}}^2}{1-\varkappa_{b,m}^2\,{\mu_m^{\odot}}^2}\exp\left(-\frac{\tilde{\Pi}}{\mu_m^{\odot}}\right)\end{aligned}, \tag{2.52b}$$

where $x^{-}_{1,b,m}$, $x^{-}_{2,b,m}$, $x^{+}_{1,b,m}$, and $x^{+}_{2,b,m}$ are coefficients to be determined. By differentiating Eqn. (2.52) and comparing with Eqn. (2.50), and using that they must be equal for any $\tilde{\Pi}$, $\mu^{\odot}_{m}$, $\varkappa_{b,m}$, and $\dot{Q}^{\blacklozenge}_{b,m}$, it can be shown that the number of parameters is reduced to two, which I will call $\left(x_{b,2m-1}, x_{b,2m}\right); m \in \{1,2,\ldots,M,M+1\}$. In addition, by recalling the definition of $\dot{Q}^{+}_{m}$ and $\dot{Q}^{-}_{m}$, one obtain the profile of downward and upward diffuse irradiances:

$$\begin{aligned}\dot{Q}^{\Downarrow}_{b,m}(\tilde{\Pi}) = {} & x_{b,2m-1}\,\upsilon^{+}_{b,m}\exp\left(-\varkappa_{b,m}\tilde{\Pi}\right) + x_{b,2m}\,\upsilon^{-}_{b,m}\exp\left(+\varkappa_{b,m}\tilde{\Pi}\right) \\ & + \Upsilon^{+}_{b,m}\exp\left(-\frac{\tilde{\Pi}}{\mu^{\odot}_{m}}\right) + \dot{Q}^{\blacklozenge}_{b,m},\end{aligned} \tag{2.53a}$$

$$\begin{aligned}\dot{Q}^{\Uparrow}_{b,m}(\tilde{\Pi}) = {} & x_{b,2m-1}\,\upsilon^{-}_{b,m}\exp\left(-\varkappa_{b,m}\tilde{\Pi}\right) + x_{b,2m}\,\upsilon^{+}_{b,m}\exp\left(+\varkappa_{b,m}\tilde{\Pi}\right) \\ & + \Upsilon^{-}_{b,m}\exp\left(-\frac{\tilde{\Pi}}{\mu^{\odot}_{m}}\right) + \dot{Q}^{\blacklozenge}_{b,m},\end{aligned} \tag{2.53b}$$

$$\upsilon^{\pm}_{b,m} = \frac{1}{2}\left[1 \pm \sqrt{\frac{1-\varsigma_{b,m}}{1-\left(1-2\beta_{b,m}\right)\varsigma_{b,m}}}\right], \tag{2.53c}$$

$$\Upsilon^{\pm}_{b,m} = \frac{\left(\kappa^{+}_{b,m} \pm \kappa^{-}_{b,m}\right)\mu^{\odot\,2}_{m}}{2\left(1-\varkappa^{2}_{b,m}\,\mu^{\odot\,2}_{m}\right)}. \tag{2.53d}$$

To determine $\left(x_{b,2m-1}, x_{b,2m}\right); m \in \{1,2,\ldots,M,M+1\}$ we need three independent systems of $2M+2$ equations (one system of equations for each band). For $m \in \{1,2,\ldots,M\}$, the solution must be such that meets boundary conditions for all middle layers (Fig. 2.6), with one additional boundary condition for upward radiation coming out of the ground (Line 1), and another for incoming downward radiation from above the canopy (Line $2M+2$):

$$\begin{aligned}
\text{Line } 1: \quad & \dot{Q}^{\Uparrow}_{b,1} - \varsigma_{b,f}\left(\dot{Q}^{\Downarrow}_{b,1} + \dot{Q}^{\odot}_{b,1}\right) - \left(1-\varsigma_{b,f}\right)\dot{Q}^{\blacklozenge}_{b,f} = 0 & & \\
\text{Line } 2m: \quad & \dot{Q}^{\Downarrow}_{0_{b,m}} - \dot{Q}^{\Downarrow}_{b,m+1} = 0 & & , \; m \in \{1,2,\ldots,M\} \\
\text{Line } 2m+1: \quad & \dot{Q}^{\Uparrow}_{0_{b,m}} - \dot{Q}^{\Uparrow}_{b,m+1} = 0 & & , \; m \in \{1,2,\ldots,M\} \\
\text{Line } 2M+2: \quad & \dot{Q}^{\Downarrow}_{0_{b,M+1}} - \dot{Q}^{\Downarrow}_{b,\infty,e} = 0 & &
\end{aligned} \tag{2.54}$$

where $\varsigma_{b,f}$ is the ground (soil and temporary surface water) scattering coefficient (Sec. 2.4.3), $\dot{Q}^{\blacklozenge}_{b,f}$ is the ground black body emission, and $\dot{Q}^{\Downarrow}_{b,e\infty}$ is the above-canopy, downward diffuse radiation

for the band. For the top boundary condition, it is also assumed that $\tilde{\Pi}_{M+1} = 0$; $\overline{\mu}_{M+1} = 1$; $\dot{Q}^{\blacklozenge}_{b,M+1} = 0$; $\varsigma_{b,M+1} = 1$ (no absorption or emission); and $\beta_{b,M+1} = \beta^{\odot}_{b,M+1} = 0$ (all irradiance is transmitted). Because $\varsigma_{b,M+1} = 1$ creates singularities for $\upsilon^{\pm}_{b,M+1}$, we use the limit $\varsigma_{b,M+1} \to 0$, so that $\upsilon^{+}_{b,M+1} = 1$ and $\upsilon^{-}_{b,M+1} = 0$. Substituting Eqn. (2.49) and (2.53) into (2.54) yields to

$$\mathbf{S}_b \cdot \mathbf{x}_b = \mathbf{y}_b, \tag{2.55}$$

where $\mathbf{x}_b = \left(x_{b,1}, x_{b,2}, \ldots, x_{b,2M+1}, x_{b,2M+2}\right)$ are the constants from Eqn. (2.53a) and (2.53b); $\mathbf{S}_b$ is a $(2M+2) \times (2M+2)$ sparse matrix with following non-zero elements:

$$\begin{aligned}
s_{b_{1,1}} &= \left(\upsilon^{-}_{b,1} - \varsigma_{b,f}\upsilon^{+}_{b,1}\right)\exp\left(-\varkappa_{b,1}\tilde{\Pi}_1\right) \\
s_{b_{1,2}} &= \left(\upsilon^{+}_{b,1} - \varsigma_{b,f}\upsilon^{-}_{b,1}\right)\exp\left(\varkappa_{b,1}\tilde{\Pi}_1\right) \\
s_{b_{2m,2m-1}} &= \upsilon^{+}_{b,m} && , m \in (1,2,\ldots,M+1) \\
s_{b_{2m,2m}} &= \upsilon^{-}_{b,m} && , m \in (1,2,\ldots,M+1) \\
s_{b_{2m,2m+1}} &= -\upsilon^{+}_{b,m+1}\exp\left(-\varkappa_{b,m+1}\tilde{\Pi}_{b,m+1}\right) && , m \in (1,2,\ldots,M) \\
s_{b_{2m,2m+2}} &= -\upsilon^{-}_{b,m+1}\exp\left(+\varkappa_{b,m+1}\tilde{\Pi}_{b,m+1}\right) && , m \in (1,2,\ldots,M) \\
s_{b_{2m+1,2m-1}} &= \upsilon^{-}_{b,m} && , m \in (1,2,\ldots,M) \\
s_{b_{2m+1,2m}} &= \upsilon^{+}_{b,m} && , m \in (1,2,\ldots,M) \\
s_{b_{2m+1,2m+1}} &= -\upsilon^{-}_{b,m+1}\exp\left(-\varkappa_{b,m+1}\tilde{\Pi}_{m+1}\right) && , m \in (1,2,\ldots,M) \\
s_{b_{2m+1,2m+2}} &= -\upsilon^{+}_{b,m+1}\exp\left(+\varkappa_{b,m+1}\tilde{\Pi}_{m+1}\right) && , m \in (1,2,\ldots,M)
\end{aligned}, \tag{2.56}$$

and $\mathbf{y}_b = \left(y_{b,1}, y_{b,2}, \ldots, y_{b,2M+1}, y_{b,2M+2}\right)$, where

$$\begin{aligned}
y_{b,1} &= \varsigma_{b,f}\dot{Q}^{\odot}_{b,1} + \left(1-\varsigma_{b,f}\right)\left(\dot{Q}^{\blacklozenge}_{b,f} - \dot{Q}^{\blacklozenge}_{b,1}\right) - \left(\Upsilon^{-}_{b,1} - \varsigma_{b,f}\Upsilon^{+}_{b,1}\right)\mathrm{e}^{\left(-\frac{P_1}{\mu^{\odot}_1}\right)} \\
y_{b,2m} &= \Upsilon^{+}_{b,m+1}\exp\left(-\frac{P_{m+1}}{\mu^{\odot}_{m+1}}\right) - \Upsilon^{+}_{b,m} + \dot{Q}^{\blacklozenge}_{b,m+1} - \dot{Q}^{\blacklozenge}_{b,m} && , m \in (1,2,\ldots,M) \\
y_{b,2m+1} &= \Upsilon^{-}_{b,m+1}\exp\left(-\frac{P_{m+1}}{\mu^{\odot}_{m+1}}\right) - \Upsilon^{-}_{b,m} + \dot{Q}^{\blacklozenge}_{b,m+1} - \dot{Q}^{\blacklozenge}_{b,m} && , m \in (1,2,\ldots,M) \\
y_{b,2M+2} &= \dot{Q}^{\Downarrow}_{b,\infty,e} - \Upsilon^{+}_{b,M+1} - \dot{Q}^{\blacklozenge}_{b,M+1}
\end{aligned} \tag{2.57}$$

Once all $\mathbf{x}_b$ are resolved and $\dot{\mathbf{Q}}^{\Downarrow}_b$ and $\dot{\mathbf{Q}}^{\Uparrow}_b$ profiles are fully determined, we find the irradiance that

is absorbed by each cohort $\dot{Q}_{ev_m}, m \in \{1, 2, \ldots, M\}$:

$$\dot{Q}_{e,\pi_m} = \sum_{b=1}^{3} \dot{Q}_{b,e,\pi_m}, \tag{2.58a}$$

where $\dot{Q}_{b,e,\pi_m}$ is the difference between incoming and outgoing irradiance for each band:

$$\dot{Q}_{b,e,\pi_m} = \left(\dot{Q}^{\odot}_{b,m+1} + \dot{Q}^{\Downarrow}_{b,m+1} + \dot{Q}^{\Uparrow}_{b,m}\right) - \left(\dot{Q}^{\odot}_{b,m} + \dot{Q}^{\Downarrow}_{b,m} + \dot{Q}^{\Uparrow}_{b,m+1}\right). \tag{2.58b}$$

Ground radiation

The ground radiation sub-model determines the irradiance emitted by the ground surface, and the profile of irradiance through the temporary surface water layers and top soil layer. In reality, the ground radiation and the canopy radiation model are interdependent, since the incoming radiation at the top ground layer is determined from the canopy radiation model, and the ground scattering coefficient (ς_g) is needed for the bottom boundary condition (Eqn. (2.54) and Eqn. (2.57)). Nonetheless, the scattering coefficient does not depend on the total incoming radiation, therefore we can solve the irradiance profile for a standardized incoming radiation, and once we determine the downward radiation at the bottom of the canopy, we can scale the absorbed irradiance for each layer.

The effective ground scattering coefficient ς_g is the weighted average of the exposed soil scattering ς_s, the combined backscattering of temporary surface water and soil scattering of irradiance transmitted through the temporary surface water:

$$\varsigma_{b,f} = (1 - f_{\text{tsw}})\,\varsigma_{b,g} + f_{\text{tsw}}\varsigma_{b,s}\left(1 + \tau_{b,s}\,\varsigma_{b,g}\right), \tag{2.59}$$

where $\varsigma_{b,g}$ is the reflectance of the top soil layer; and $\varsigma_{b,s}$ and $\tau_{b,s}$ are the reflectance and transmittance of the temporary surface water, respectively. Soil reflectance is a function of the soil color and volumetric soil moisture at the topmost layer, determined from the same parameterization and soil color classes as in Oleson et al. (2010):

$$\varsigma_{b,g} = \min\left[\varsigma^{\mathrm{Po}}_{b,g_K} + 0.11 - 0.40\vartheta_{g_K}, \varsigma^{\mathrm{Re}}_{b,gK}\right], \tag{2.60}$$

where $\varsigma^{\mathrm{Re}}_{b,g_K}$ and $\varsigma^{\mathrm{Po}}_{b,g_K}$ are the soil color-dependent reflectance for dry and saturated soils, respectively. In reality, the temporary surface water reflectance $\varsigma_{b,s}$ depends on the liquid fraction, snow grain size and age, impurities, and the direction of incoming radiation, but here we simply assume a linear interpolation of soil reflectance at saturation and pure snow reflectance ($\varsigma^{\circledast}_b$), assumed constant for each band:

$$\varsigma_{b,s} = \varsigma^{\circledast}_b + \ell_{s_J}\left(\varsigma^{\mathrm{Po}}_{b,g_K} - \varsigma^{\circledast}_b\right). \tag{2.61}$$

Following Verseghy (1991) and Walko et al. (2000), the transmissivity of intercepted irradiance for PAR and NIR is solved following Beer's law, with a direction-independent extinction coefficient:

$$\tau_{b,s} = (1-\delta_{b3})\exp\left(-\frac{\sum_{j=1}^{J}\Delta\bar{z}_{s_j}}{f_{\mathrm{tsw}}\overline{\mu}_s}\right), \tag{2.62}$$

where $\overline{\mu}_s \stackrel{\mathrm{def}}{=} 0.05\,m$ is the same coefficient used by Verseghy (1991) and Walko et al. (2000), and the additional $1/f_{\mathrm{tsw}}$ term accounts for the temporary surface water clumping when it does not cover all ground. Temporary surface water is assumed to be opaque for the TIR band.

Black body emission from the ground ($\dot{Q}^{\blacklozenge}_{b,f}$) is determined from the weighted average of exposed soil and temporary surface water, with the weights being the product between the area and the emissivities ($1-\varsigma$):

$$\dot{Q}^{\blacklozenge}_{b,s} = \delta_{b3}\frac{(1-f_{\mathrm{tsw}})\left(1-\varsigma_{b,g}\right)\left(\sigma_B T^4_{g_K}\right) + f_{\mathrm{tsw}}\left(1-\varsigma_{b,s}\right)\left(\sigma_B T^4_{s_J}\right)}{(1-f_{\mathrm{tsw}})\left(1-\varsigma_{b,g}\right) + f_{\mathrm{tsw}}\left(1-\varsigma_{b,s}\right)}. \tag{2.63}$$

Once the irradiance profile is determined for the canopy, we obtain irradiance absorbed by each temporary surface water layer by integrating the transmissivity profile for each layer, starting from the top layer:

$$\dot{Q}_{e,s_j} = \begin{cases} \sum_{b=1}^{2} \left\{ f_{\text{tsw}} \left(\dot{Q}_{b,1}^{\Downarrow} + \dot{Q}_{b,1}^{\odot} \right) \left[1 - \mathrm{e}^{\left(-\frac{\Delta \bar{z}_{s_J}}{\bar{\mu}_s} \right)} \right] \right\} & \\ \quad + f_{\text{tsw}} \left(1 - \varsigma_{3,s} \right) \left(\dot{Q}_{3,1}^{\Downarrow} - \sigma_B T_{s_J}^4 \right) & \text{, if } j = J \\ \sum_{b=1}^{2} \left\{ f_{\text{tsw}} \left(\dot{Q}_{b,1}^{\Downarrow} + \dot{Q}_{b,1}^{\odot} \right) \left[\mathrm{e}^{\left(-\frac{\sum_{j'=j+1}^{J} \Delta \bar{z}_{s_{j'}}}{\bar{\mu}_s} \right)} - \mathrm{e}^{\left(-\frac{\Delta \bar{z}_{s_J}}{\bar{\mu}_s} \right)} \right] \right\} & \text{, otherwise} \end{cases} \tag{2.64}$$

2.4.4 Surface layer model and eddy fluxes

The surface layer model determines the fluxes of enthalpy, water, and carbon dioxide between the canopy air space and the air aloft, and is based on the Monin-Obukhov similarity theory (Monin and Obukhov, 1954; Foken, 2006). This theory has been widely used by biosphere-atmosphere models representing a variety of biomes (e.g. Walko et al., 2000; Oleson et al., 2010; Best et al., 2011), although this is often an extrapolation of the original theory that may not be applicable to heterogeneous vegetation, or tall vegetation, as pointed out by Foken (2006).

The first step is to find the characteristic displacement height z_d and vegetation roughness length z_0 of the patch. When the patch contains cohorts, we determine z_d and z_0 by adapting the momentum transfer model proposed by Massman (1997). This model is convenient for use in ED-2.2 because it does not assume fixed vegetation structures, therefore it can be determined and updated based on the demography of each patch. In ED-2.2, we use the discrete form of the original formulation. The canopy environment is split in a fixed vertical grid with F_∞ layers spanning from the ground to the maximum possible vegetation height $z_{a_\infty} = 35\,\text{m}$. Layers are thinner near the ground to capture the higher density of the small size plants in more detail. The height of the top of each canopy layer (z_{a_f}), and the top layer with vegetation (F) are defined as:

$$z_{a_f} = z_{a_1} f^{\left(\frac{\ln z_{a_\infty} - \ln z_{a_1}}{\ln F_\infty} \right)} \qquad f \in \{0, 1, \ldots, F\}\,, \tag{2.65a}$$

$$F = \left\lceil (F_\infty)^{\left(\frac{\ln z_{\pi_1} - \ln z_{a_1}}{\ln z_{\pi_\infty} - \ln z_{a_1}} \right)} \right\rceil \qquad , \tag{2.65b}$$

where $z_{a_1} = 0.05\,\mathrm{m}$, z_{π_1} is the height of the tallest cohort, and $\lceil\ \rceil$ is the ceiling operator.

The displacement height is defined according to Shaw and Pereira (1982) and represents the effective height of the mean drag from all cohorts and soil surface. The roughness height is defined after Raupach (1994, 1995) and represents the limit above the displacement height below which the typical logarithmic-based, surface layer wind profile is no longer valid. In the original formulation the displacement height is normalized by the height of the tallest cohort; in ED-2.2 we apply a correction to scale the height with the effective canopy depth $\bar{z}_a$ while using the contribution from all cohorts:

$$z_d = \bar{z}_a \left\{ 1 - \frac{1}{z_{v_1}} \sum_{f=1}^{F} \left[\mathrm{e}^{-\frac{2\left(\Xi_F - \Xi_f\right)}{\xi_{\mathrm{sfc}}}} \Delta z_{a_f} \right] \right\}, \tag{2.66}$$

$$z_0 = (\bar{z}_a - z_d) \exp\left(-\kappa \sqrt{\frac{2}{\xi_{\mathrm{sfc}}}} + \tilde{\psi}_0 \right), \tag{2.67}$$

where κ is the von Kármán constant; $\Delta z_{a_f} = z_{a_f} - z_{a_{f-1}}$ is the layer thickness; ξ_{sfc} is the surface drag coefficient, which is related to the ratio of the wind speed at the top cohort and the surface (c.f. Albini, 1981); Ξ_f is the cumulative cohort drag area per unit of ground area at layer f; and $\tilde{\psi}_0$ is the flux profile function of momentum at the roughness height (see Eqn. 2.79 below), here approximated to 0.190 as in Raupach (1995). Both ξ_{sfc} and Ξ_f are defined after Massman (1997):

$$\xi_{\mathrm{sfc}} = 2\left[y_{s1} + y_{s2} \mathrm{e}^{y_{s3}\Xi_F} \right]^2, \tag{2.68}$$

$$\Xi_f = \sum_{f'=1}^{f} \frac{\xi_{D_{f'}} a_{f'}}{\mathcal{P}_{f'}} \Delta z_{a_{f'}}, \tag{2.69}$$

where ξ_{D_f} is the drag coefficient due to cohorts at layer f; $(y_{s1}, y_{s2}, y_{s3}) = (0.320, 0.264, 15.1)$ are constants (Massman, 1997); $\mathcal{P}$ is the sheltering factor for momentum associated with the cohorts; and ϖ_f is the plant (leaves and wood) area density function at layer f:

$$\varpi_f = \sum_{m=1}^{M} \frac{\Lambda_m + \Omega_m}{z_{\pi_m} - \hat{z}_{\pi_m}} \mathrm{v}_{f,m}, \tag{2.70a}$$

$$\mathrm{v}\varpi_{f,m} = \begin{cases} 0 & \text{if } z_{\pi_m} \leq z_{a_{f-1}} \text{ or } \hat{z}_{\pi_m} \geq z_{a_f} \\ \dfrac{\min\left(z_{\pi_m}, z_{a_f}\right) - \max\left(\hat{z}_{\pi_m}, z_{a_{f-1}}\right)}{\Delta z_{a_f}} & \text{otherwise} \end{cases}, \tag{2.70b}$$

where $\hat{z}_{\pi_m}$ and z_{π_m} are the height at the bottom and top of the crown of cohort m, as described in App. C. Wohlfahrt and Cernusca (2002) pointed out that the drag coefficient and the shelter factor are not completely separable, and provided an alternative functional form of the $\xi_D/_{\mathcal{P}}$ ratio. The function used in ED-2.2 is derived from Wohlfahrt and Cernusca fit for plant density function, although we re-wrote the original parameterization using logistic function to reduce the number of parameters:

$$\frac{\xi_{D_f}}{\mathcal{P}_f} = x_1 + \frac{x_2}{1 + \mathrm{e}^{x_3 \varpi_f}}, \tag{2.71}$$

where $\mathbf{x} = (0.086, 1.192, 0.480)$ are adjustable parameters.

In case the patch has no cohorts, we assume that the roughness height $z_{0\varnothing}$ depends only on the bare soil roughness z_{0g} plus any snow or water standing on top of the ground z_{0s}:

$$z_{0\varnothing} = z_{0g}\left(1 - f_{\mathrm{tsw}}\right) + z_{0s} f_{\mathrm{tsw}}. \tag{2.72}$$

The momentum ($\dot{U}_{e,a}$) and buoyancy ($\dot{\Theta}_{e,a}$) fluxes between the free atmosphere and the canopy air space at the top of the canopy air space can be represented either by the gradient or the eddy flux form (Monteith and Unsworth, 2008):

$$\dot{U}_{e,a} = \rho_a K_U \frac{\partial u}{\partial z} = \rho_a \overline{u_z' u_x'}, \qquad \text{(Momentum)} \tag{2.73}$$

$$\dot{\Theta}_{e,a} = -\rho_a K_\Theta q_{p_a} \frac{\partial \theta_V}{\partial z} = -\rho_a q_{p_a} \overline{u_z' \theta_V'}, \qquad \text{(Buoyancy)} \tag{2.74}$$

where K_U and K_Θ are the eddy diffusivities of momentum and buoyancy [4], respectively; u_x is the horizontal wind speed, u_z is the vertical velocity; θ_V is the virtual potential temperature; and q_{p_a} is the specific heat of the canopy air space (Eqn. 2.21).

[4] Eddy diffusivities of enthalpy, moisture and CO_2 are assumed to be the same as the buoyancy, a common assumption based on observations, according to Stull (1988).

The Monin-Obukhov similarity theory is based on the Buckingham Π-theory (Stull, 1988), which requires as many fundamental scales as fundamental dimensions. Let the fundamental dimensions be the canopy air density (ρ_a) and three characteristic scales, namely the friction velocity ($u^\star$), characteristic virtual temperature gradient ($\theta_V^\star$), and the diffusivity-corrected Obukhov length LO (Panofsky, 1963):

$$u^\star = \sqrt{\frac{\dot{U}_{e,a}}{\rho}} \qquad = \sqrt{\left|\overline{u_x' u_z'}\right|}, \tag{2.75a}$$

$$\theta_V^\star = -\frac{1}{\kappa u^\star}\frac{\dot{\Theta}_{e,a}}{\rho q_{p_a}} \quad = -\frac{\overline{u_z' \theta_V'}}{u^\star}, \tag{2.75b}$$

$$\mathrm{LO} = \frac{1}{\mathrm{Pr}}\frac{\dot{U}_{e,a}}{\dot{\Theta}_{e,a}}\frac{\theta_{V_0}}{g_\oplus}\frac{u^\star}{\kappa} \approx \frac{(\theta_{V_e} + \theta_{V_a})\, u^{\star 2}}{2\kappa g_\oplus \theta_V^\star}, \tag{2.75c}$$

where κ is the von Kármán constant, $g_\oplus$ is the gravity acceleration, and $\mathrm{Pr} \overset{\text{def}}{=} K_U / K_\Theta$ is the turbulent Prandtl number. Another important dimensionless quantity is the bulk Richardson number Ri_B, defined as:

$$\mathrm{Ri}_B = \frac{2 g_\oplus (z^\star - z_0)(\theta_{V_e} - \theta_{V_a})}{(\theta_{V_e} + \theta_{V_a})\, u_e^2}, \tag{2.76}$$

where $z^\star \overset{\text{def}}{=} z_e - z_d$. The bulk Richardson number depends only on variables that are already determined and it is informative on whether the layer between the canopy air space and the reference height z_e is unstable, neutral, or unstable. By combining Eqn. (2.76) and (2.75c), we determine a dimensionless height scale ζ:

$$\zeta(z) = \frac{z - z_d}{\mathrm{LO}}, \tag{2.77a}$$

and the particular cases

$$\zeta^\star = \frac{z^\star}{\mathrm{LO}} = \zeta_0 + \kappa \mathrm{Ri}_B \left(\frac{u_e}{u^\star}\right)^2 \frac{\theta_V^\star}{\theta_{V_e} - \theta_{V_a}}, \tag{2.77b}$$

$$\zeta_0 = \frac{z_0}{\mathrm{LO}} = \frac{z_0}{z^\star}\zeta^\star. \tag{2.77c}$$

By choosing an appropriate combination of factors, Monin and Obukhov (1954) have shown that the dimensionless gradients of wind and temperature (here based on virtual potential temperature and the accounting for the Prandtl number) can be written as a function of the characteristic scales and dimensionless stability functions φ_U and φ_Θ, which can be thought as correction factors from the logarithmic wind profile under neutral conditions (Monteith and Unsworth, 2008):

$$\frac{\partial}{\partial \zeta}\left(\frac{u_x}{u^\star}\right) = \frac{1}{\kappa\zeta}\varphi_U(\zeta), \tag{2.78a}$$

$$\frac{\partial}{\partial \zeta}\left(\frac{\theta_V}{\theta_V^\star}\right) = \frac{\mathrm{Pr}}{\kappa\zeta}\varphi_\Theta(\zeta). \tag{2.78b}$$

Following Panofsky (1963), if we define the flux profile functions:

$$\psi_U(\zeta) = \int_0^\zeta \frac{1-\varphi_U(\zeta')}{\zeta'}\,\mathrm{d}\zeta' \tag{2.79}$$

$$\psi_\Theta(\zeta) = \int_0^\zeta \frac{1-\varphi_\Theta(\zeta')}{\zeta'}\,\mathrm{d}\zeta' \tag{2.80}$$

and integrate Eqn. (2.78a) and (2.78b) between ζ_0, where wind is assumed to be zero, and any reference level ζ using the Leibniz integration rule, we obtain the horizontal wind and virtual potential temperature profile functions:

$$u_x(\zeta) = \frac{u^\star}{\kappa}\left[\ln\left(\frac{\zeta}{\zeta_0}\right) - \psi_U(\zeta) + \psi_U(\zeta_0)\right] \tag{2.81}$$

$$\theta_V(\zeta) = \theta_{V_a} + \frac{\mathrm{Pr}\,\theta_V^\star}{\kappa}\left[\ln\left(\frac{\zeta}{\zeta_0}\right) - \psi_\Theta(\zeta) + \psi_\Theta(\zeta_0)\right] \tag{2.82}$$

If we substitute Eqn. (2.81) and (2.82) for $\zeta = \zeta^\star$ into Eqn. (2.77b), we obtain an equation where the only unknown is $\zeta^\star$:

$$\zeta^\star = \frac{\mathrm{Ri}_B}{\mathrm{Pr}} \left(\frac{z^\star}{z^\star - z_0} \right) \frac{\left[\ln\left(\frac{\zeta^\star}{\zeta_0} \right) - \psi_U(\zeta^\star) + \psi_U(\zeta_0) \right]^2}{\ln\left(\frac{\zeta^\star}{\zeta_0} \right) - \psi_\Theta(\zeta^\star) + \psi_\Theta(\zeta_0)} \tag{2.83}$$

The flux profile functions used here are the same as described by Beljaars and Holtslag (1991). These functions are the Businger-Dyer flux profile equations for the unstable case (Businger et al., 1971), but they are modified for the stable case to avoid the underestimated flux between the canopy air space and the air aloft under stable conditions:

$$\psi_U(\zeta) = \begin{cases} 2\ln\left[\frac{1+y(\zeta)}{2}\right] + \ln\left[\frac{1+y^2(\zeta)}{2}\right] - 2\arctan[y(\zeta)] + \frac{\pi}{2} & \text{, if } \mathrm{Ri}_B < 0 \\ x_1\zeta + x_2\left(\zeta - \frac{x_3}{x_4}\right)\mathrm{e}^{-x_4\zeta} + \frac{x_2 x_3}{x_4} & \text{, if } \mathrm{Ri}_B \geq 0 \end{cases}, \tag{2.84a}$$

$$\psi_\Theta(\zeta) = \begin{cases} 2\ln\left[\frac{1+y^2(\zeta)}{2}\right] & \text{, if } \mathrm{Ri}_B < 0 \\ 1 - \left(1 - \frac{x_1}{x_5}\zeta\right)^{x_5} + x_2\left(\zeta - \frac{x_3}{x_4}\right)\mathrm{e}^{-x_4\zeta} + \frac{x_2 x_3}{x_4} & \text{, if } \mathrm{Ri}_B \geq 0 \end{cases}, \tag{2.84b}$$

$$y(\zeta) = \sqrt[4]{1 - x_6\zeta} \tag{2.84c}$$

where $\mathbf{x} = (-1; -\frac{2}{3}; 5; 0.35; \frac{3}{2}; 13)$ are empirical and adjustable parameters.

Equation (2.83) is transcendental, therefore $\zeta^\star$ is calculated using a root-finding technique. Once $\zeta^\star$ is determined, we can find $u^\star$ using Eqn. (2.81), and define the canopy conductance $g_a\,[m\,s^{-1}]$ using Eqn. (2.82) as the starting point, similarly to Oleson et al. (2010):

$$g_a = \frac{u^\star\,\theta_V^\star}{\theta_{V_e} - \theta_{V_a}} = \frac{\kappa\,u^\star}{\mathrm{Pr}\left[\ln\left(\frac{\zeta^\star}{\zeta_0}\right) - \psi_\Theta(\zeta^\star) + \psi_\Theta(\zeta_0)\right]}. \tag{2.85}$$

If we assume that the diffusitivity K_Θ is the same for water vapor and enthalpy and CO_2, we obtain the following equations for fluxes between canopy air space and the free atmosphere:

$$\dot{W}_{e,a} = \rho_a \underbrace{g_a\,(w_e - w_a)}_{\stackrel{\mathrm{def}}{=} u^\star\,w^\star}, \tag{2.86a}$$

$$\dot{H}_{e,a} = \rho_a \underbrace{g_a \left(\tilde{h}_e - h_a\right)}_{\stackrel{\text{def}}{=} u^\star \tilde{h}^\star}, \tag{2.86b}$$

$$\dot{C}_{e,a} = \rho_a \underbrace{g_a \left(c_e - c_a\right)}_{\stackrel{\text{def}}{=} u^\star c^\star}, \tag{2.86c}$$

where θ_a and θ_e are $\tilde{h}_e$ is the equivalent enthalpy of air at reference height z_e when the air is adiabatically moved to the top of the canopy air space, using the definition of potential temperature:

$$\tilde{h}_e = h\left(\tilde{T}_e = \theta_e \left(\frac{p_a}{p_0}\right)^{\frac{\mathcal{R}^\star}{\mathcal{M}_d q_{p\mathrm{d}}}}, w_e\right) \qquad \text{, from Eqn. (2.7).} \tag{2.87}$$

Sensible heat flux between the free atmosphere and canopy air space ($Q_{e,a}$) can be derived from the definition of enthalpy and enthalpy flux (Eqn. 2.7 and Eqn. 2.86b):

$$\begin{aligned}
\dot{H}_{e,a} &= \rho_a g_a \left[(1-w_e)\, q_{p\mathrm{d}} \tilde{T}_e + w_e q_{pv}\left(\tilde{T}_e - T_{scv}\right) - (1-w_a)\, q_{p\mathrm{d}} T_a + w_a q_{pv}\left(T_a - T_{scv}\right)\right] \\
&= \underbrace{\rho_a g_a \left(q_{p_e} \tilde{T}_e - q_{p_a} T_a\right)}_{\stackrel{\text{def}}{=} \dot{Q}_{e,a}} - \rho_a g_a \left(w_e - w_a\right) q_{pv} T_{scv}, \\
\dot{Q}_{e,a} &= \dot{H}_{e,a} + \dot{W}_{e,a}\, q_{pv}\, T_{scv}.
\end{aligned} \tag{2.88}$$

2.4.5 Heat and water exchange between surfaces and canopy air space

Leaves and branches

Fluxes of sensible heat ($\dot{Q}_{\pi_m,a}$) and water vapor ($\dot{W}_{\pi_m,a}$) between the leaf and wood surface and the canopy air space follow the same principle of conductance and gradient that define the eddy fluxes between the free atmosphere and canopy air space (Eqn. 2.86); let $g_{H\beta_m}[\mathrm{m\,s^{-1}}]$ and $g_{W\beta_m}[\mathrm{m\,s^{-1}}]$ be the conductances of heat and water between the leaf surface and the canopy air space, and $g_{H\omega_m}$ and $g_{W\omega_m}$ be the wood boundary layer counterparts, the sensible heat and water vapor fluxes are:

$$\dot{Q}_{\pi_m,a} = \dot{Q}_{\lambda_m,a} + \dot{Q}_{\omega_m,a} = 2\,\Lambda_m\, g_{H\beta_m}\, \rho_a\, q_{p_a}\left(T_{\lambda_m} - T_a\right) + \pi\,\Omega_m\, g_{H\omega_m}\, \rho_a\, q_{p_a}\left(T_{\omega_m} - T_a\right), \tag{2.89a}$$

$$\dot{W}_{\pi_m,a} = \dot{W}_{\lambda_m,a} + \dot{W}_{\omega_m,a} = \quad \Lambda_m\, g_{W\beta_m}\, \rho_a \left(w_{\lambda_m} - w_a\right) \quad + \quad \Omega_m\, g_{W\omega_m}\, \rho_a \left(w_{\omega_m} - w_a\right), \tag{2.89b}$$

where the factors 2 and π in Eqn. (2.89a) means that sensible heat is exchanged on both sides of the leaves, and on the longitudinal area of the branches, which are assumed cylindrical. Intercepted water and dew and frost formation is allowed only on one side of the leaves, and an area equivalent to a one-sided flat plate for branches, and therefore only the leaf and wood area indices are used in Eqn. (2.89b). Canopy air space temperature, specific humidity, density, and specific heat, leaf temperature, and wood temperature are determined diagnostically. Specific humidity at the leaf surface $w_{\lambda_m} \overset{\text{def}}{=} w^{\equiv}\left(T_{\lambda_m}, p_a\right)$ and branch surface $w_{\omega_m} \overset{\text{def}}{=} w^{\equiv}\left(T_{\omega_m}, p_a\right)$ are assumed to be the saturation specific humidity $w^{\equiv}$ at the surface temperature and canopy air space pressure:

$$w^{\equiv}(T,p) = \frac{1}{1+\dfrac{\mathcal{M}_d}{\mathcal{M}_w}\left[\dfrac{p}{p^{\equiv}(T)}-1\right]}, \tag{2.90}$$

where $p^{\equiv}(T) = \min\left[p_{vi}^{\equiv}(T), p_{v\ell}^{\equiv}(T)\right]$ [Pa] is the partial pressure of water vapor at phase equilibrium (saturation) with the most favorable condensed phase, ice ($p_{vi}^{\equiv}$) or liquid ($p_{v\ell}^{\equiv}$), both defined after Murphy and Koop (2005):

$$\ln\left[p_{vi}^{\equiv}(T)\right] = 9.550426 - \frac{5723.265}{T} + 3.53068\ln(T) - 0.00728332\,T, \tag{2.91a}$$

$$\begin{aligned}\ln\left[p_{v\ell}^{\equiv}(T)\right] = {} & \left[54.842763 - \frac{6763.22}{T} - 4.210\ln(T) + 0.000367\,T\right] \\ & + \left[0.0415\,(T-218.8)\right] \\ & \times \left[53.878 - \frac{1331.22}{T} - 9.44523\ln(T) + 0.014025\,T\right].\end{aligned} \tag{2.91b}$$

Eqn. (2.91a) and Eqn. (2.91b) converge to the same vapor pressure when $T = T_3$, within an accuracy of $\approx 5\cdot 10^{-8}$.

Heat conductance for leaves and branches are based on the convective heat transfer overview by Monteith and Unsworth (2008, Section 10.1), where further description of the theory can be found. Following Monteith and Unsworth, convection can be of two types: forced convection, which depends on mechanic turbulence associated with the fluid velocity; and free convection, which is due to buoyancy of the boundary layer fluid. Although convection is often dominated by

either forced or free convection, in ED-2.2 we always assume that the total conductance is a simple combination of forced and free convection resistances as if they were parallel and independent:

$$g_H = g_H^{\text{Free}} + g_H^{\text{Forced}}, \tag{2.92}$$

For each convective regime, we define the conductance in terms of the Nusselt number Nu, a dimensionless number that corresponds to the ratio between heat exchange through convection and conduction:

$$g_H = \frac{\eta_a \,\text{Nu}}{\beta}. \tag{2.93}$$

where η_a is the thermal diffusivity of canopy air space and β is the characteristic size of the obstacle. For leaves, the characteristic size β_{λ_m} is a PFT-dependent constant corresponding to the typical leaf width, whereas for branch wood the typical size β_{ω_m} is a function of the cohort volume (App. C).

Free convection is a result of the thermal gradient between the obstacle surface and the fluid, and this is normally expressed in terms of the Grashof number Gr[5], a dimensionless index that relates buoyancy and viscous forces. In ED-2.2 we use the same empirical functions as Monteith and Unsworth (2008), using flat plate geometry for leaves and horizontal cylinder geometry for branch wood:

$$\text{Nu}_{\lambda_m}^{\text{Free}} = \max\left[\underbrace{0.50\,\text{Gr}_{\lambda_m}^{\frac{1}{2}}}_{\text{Laminar flow}},\ \underbrace{0.13\,\text{Gr}_{\lambda_m}^{\frac{1}{3}}}_{\text{Turbulent flow}}\right], \tag{2.94a}$$

$$\text{Nu}_{\omega_m}^{\text{Free}} = \max\left[\underbrace{0.48\,\text{Gr}_{\omega_m}^{\frac{1}{2}}}_{\text{Laminar flow}},\ \underbrace{0.09\,\text{Gr}_{\omega_m}^{\frac{1}{3}}}_{\text{Turbulent flow}}\right], \tag{2.94b}$$

$$\text{Gr}_{?_m} = \frac{\varepsilon_a\, g_{\oplus} \beta_{?_m}^3}{\nu_a^2} \left|T_{?_m} - T_a\right|, \tag{2.94c}$$

where ε_a is the thermal dilatation coefficient for the canopy air space and ν_a is the kinematic vis-

[5]For both forced and free convection, the Nusselt number is also a function of the Prandtl number Pr; however, for any given gas, the Prandtl number is independent of temperature, thus it is incorporated to the empirical coefficients.

cosity of the canopy air space, and ?$_m$ represents either the leaf or wood surface. Like in Monteith and Unsworth, thermal diffusivity and dynamic viscosity are assumed to be linear functions of the canopy air space temperature:

$$\eta_a = 1.89 \cdot 10^{-5} \left[1 + 0.007 \left(T_a - T_0\right)\right] \qquad [\mathrm{m^2\,s^{-1}}], \tag{2.95a}$$

$$\nu_a = 1.33 \cdot 10^{-5} \left[1 + 0.007 \left(T_a - T_0\right)\right] \qquad [\mathrm{m^2\,s^{-1}}], \tag{2.95b}$$

where the first term on the right hand side are the reference values at temperature $T_0 = 273.15\,K$. Since we assume canopy air space to be a perfect gas, thermal dilatation is $\varepsilon_a = {}^1/_{T_a}$ (Dufour and van Mieghem, 1975).

For forced convection the flow of air through the object at different temperature causes the heat exchange, therefore Nusselt number is written as a function of the Reynolds number Re, a dimensionless index that relates inertial and viscous forces. Like in the free convection case, we use the same empirical functions as Monteith and Unsworth and the same shapes as the free convection case:

$$\mathrm{Nu}^{\mathrm{Forced}}_{\lambda_m} = \max\left[\underbrace{0.60\,\mathrm{Re}^{0.5}_{\lambda_m}}_{\text{Laminar flow}}, \underbrace{0.032\,\mathrm{Re}^{0.8}_{\lambda_m}}_{\text{Turbulent flow}}\right], \tag{2.96a}$$

$$\mathrm{Nu}^{\mathrm{Forced}}_{\omega_m} = \max\left[\underbrace{0.32 + 0.51\,\mathrm{Re}^{0.52}_{\omega_m}}_{\text{Laminar flow}}, \underbrace{0.24\,\mathrm{Re}^{0.60}_{\omega_m}}_{\text{Turbulent flow}}\right], \tag{2.96b}$$

$$\mathrm{Re}_{?_m} = \frac{u_{\pi_m} \beta_{?_m}}{\eta_a}, \tag{2.96c}$$

where u_{π_m} is the wind speed experienced by the cohort m. The wind profile within the canopy air space is determined in two steps. Above the tallest cohort, we assume that the wind can be determined from the similarity theory; from Eqn. (2.77c) we define $\zeta_f = \zeta\left(z_{a_f}\right)$, and use wind profile function from the similarity theory (Eqn. 2.81) to determine the wind speed at the top of the vegetated layer $u_{a_F} = u(\zeta_F)$. Within the canopy, we estimate the wind speed reduction using

the wind profile as a function of cumulative drag(Albini, 1981; Massman, 1997); the wind speed experienced by the cohort is the average wind between the layers where the bottom ($\hat{z}_{\pi_m}$) and top (z_{π_m}) of the crown are located:

$$u_{a_f} = u_{a_F} \exp\left(-\frac{\Xi_F - \Xi_f}{\xi_{\text{sfc}}}\right) \tag{2.97a}$$

$$u_{\pi_m} = \max\left[0.25\,\text{m}\,\text{s}^{-1}, \frac{u_{a_F}}{z_{a_{f_m}} - z_{a_{\hat{f}_m}}} \sum_{f'=\hat{f}_m}^{f_m} \left(u_{a_{f'}} \Delta z_{a_{f'}}\right)\right], \tag{2.97b}$$

where $\hat{f}_m$ and f_m are the layers corresponding to the bottom and top of the cohort. The minimum wind speed of $0.25\,\text{m}\,\text{s}^{-1}$ is imposed to avoid conductance to become unrealistically low and to account for some mixing due to gusts when the mean wind is very weak. Once the heat conductance is determined, we use the same vapor to heat ratio as Leuning et al. (1995) to calculate the water vapor conductance $g_{W?_m} = 1.075\, g_{H?_m}$.

Temporary surface water and soil

Sensible heat and water fluxes between the temporary surface water and soil and the canopy air space are calculated similarly to leaves and branches. Surface conductance g_{sfc} is assumed to be the same for both heat and water, and also the same for soil and temporary surface water:

$$\dot{Q}_{s_J,a} = f_{\text{tsw}}\, g_{\text{sfc}}\, \rho_a\, q_{p_a} (T_{s_J} - T_a)\,, \tag{2.98a}$$

$$\dot{W}_{s_J,a} = f_{\text{tsw}}\, g_{\text{sfc}}\, \rho_a\, (w_{s_J} - w_a)\,, \tag{2.98b}$$

$$\dot{Q}_{g_K,a} = (1 - f_{\text{tsw}})\, g_{\text{sfc}}\, \rho_a\, q_{p_a} (T_{s_J} - T_a)\,, \tag{2.98c}$$

$$\dot{W}_{s_J,a} = (1 - f_{\text{tsw}})\, g_{\text{sfc}}\, \rho_a\, (w_{g_K} - w_a)\,. \tag{2.98d}$$

Specific humidity for temporary surface water is computed exactly as leaves and branches, $w_{s_J} = w^{\equiv}(T_{s_J}, p_a)$ (Eqn. 2.90 and Eqn. 2.91). For soils the specific humidity also accounts for the soil moisture and the sign of the flux, using a method similar to Avissar and Mahrer (1988):

$$w_{g_K} = \begin{cases} s_g\, r_g\, w^{\equiv}(T_{g_K}, p_a) + (1 - s_g)\, w_a & \text{, if } w^{\equiv}(T_{g_K}, p_a) > w_a \\ w^{\equiv}(T_{g_K}, p_a) & \text{, if } w^{\equiv}(T_{g_K}, p_a) \leq w_a \end{cases}, \tag{2.99}$$

where r_g is the soil pore relative humidity derived from the Kelvin equation (Philip, 1957), and s_g is the soil wetness function, which takes a similar functional form as the relative humidity term from Noilhan and Planton (1989) and the β term from Lee and Pielke (1992):

$$r_g = \exp\left(\frac{\mathcal{M}_w g_{\oplus} \Psi_{g_K}}{\mathcal{R}^{\star} T_{g_K}}\right), \tag{2.100a}$$

$$s_g = \frac{1}{2}\left\{1.0 - \cos\left[\pi \frac{\min(\vartheta_k, \vartheta_{\mathrm{Fc}}) - \vartheta_{\mathrm{Re}}}{\vartheta_{\mathrm{Fc}} - \vartheta_{\mathrm{Re}}}\right]\right\}. \tag{2.100b}$$

The total resistance between the surface and the canopy air space is a combination of the resistance if the surface was bare (which is assumed to be the same as γ_a from Eqn. 2.85) , plus the resistance due to the vegetation. In terms of conductance:

$$\frac{1}{g_{\mathrm{Sfc}}} = \frac{1}{g_a} + \frac{1}{g_{\mathrm{Veg}}}. \tag{2.101}$$

The vegetation conductance g_{Veg} definition is based on the Simple Biosphere Model (SiB-2, Sellers et al., 1996). Let the conductance be the total contribution of diffusivity from ground to the top of vegetated layer:

$$\frac{1}{g_{\mathrm{Veg}}} = \int_{z_{0\varnothing}}^{z_{\pi_1}} \frac{1}{K_{\Theta}(z)}\, \mathrm{d}z \approx \sum_{f=1}^{F} \frac{\mathrm{Pr}}{K_{U_f}} \Delta z_{a_f}; \tag{2.102}$$

if we assume that $K_{U_f} \overset{\text{def}}{=} \iota_U\, u_x$ (Sellers et al., 1986), and that within the vegetated layer the winds are determined through Eqn. (2.97a), Eqn. (2.102) becomes

$$\frac{1}{g_{\mathrm{Veg}}} = \sum_{f=1}^{F} \left[\frac{\mathrm{Pr}}{\iota_U\, u_{a_f}} \exp\left(\frac{\Xi_F - \Xi_f}{\xi_{\mathrm{Sfc}}}\right)\right]. \tag{2.103}$$

If we assume that ι_U is constant and the wind profile is continuous, and combine Eqn. (2.73), Eqn. (2.75a), Eqn. (2.78a), and Eqn. (2.79) at $\zeta = \zeta_F$, ι_U can be estimated as:

$$\iota_U = \frac{\kappa u^\star \left(z_{\pi_1} - z_d\right)}{u_{a_F}} \frac{1}{1 - \zeta_F \dfrac{\partial \Psi_U}{\partial \zeta}(\zeta_F)}. \tag{2.104}$$

Enthalpy flux due to evaporation and condensation

Dew and frost are made of water that was in the canopy air space and has been transferred to the surface and condensed; likewise, water that evaporates and ice that sublimates from the surfaces immediately become part of the canopy air space. In terms of energy transfer, two processes occur, the phase change and the mass exchange, and both must be accounted for the enthalpy flux. Phase change depends on the latent heat of vaporization ($l_{\ell v}$) and sublimation (l_{iv}), which are linear functions of temperature, based on Eqn. (2.6):

$$l_{\ell v}(T) = l_{\ell v 3} + \left(q_{pv} - q_\ell\right)\left(T - T_3\right), \tag{2.105a}$$
$$l_{iv}(T) = l_{iv3} + \left(q_{pv} - q_i\right)\left(T - T_3\right). \tag{2.105b}$$

The temperature for phase change must be the surface temperature because this is where the phase change occurs. In the most generic case, if a surface y at temperature T_y and a liquid water fraction ℓ_y, the total enthalpy flux between the surface and canopy air space $\dot{H}_{y,a}$ associated with the water flux $W_{y,a}$ is:

$$\dot{H}_{y,a} = \dot{W}_{y,a} \left\{ \underbrace{\left[\left(1-\ell_y\right) q_i T_y + \ell_y q_\ell \left(T_y - T_{sc\ell}\right)\right]}_{\text{Energy flux due to mass exchange}} + \underbrace{\left[\left(1-\ell_y\right) l_{iv}(T_y) + \ell_y\, l_{\ell v}(T_y)\right]}_{\text{Enthalpy flux due to phase change}} \right\}. \tag{2.106}$$

By using the definitions from Eqn. (2.7c), Eqn. (2.106) can be further simplified to:

$$\dot{H}_{y,a} = \dot{W}_{y,a}\left[q_{pv}\left(T_y - T_{scv}\right)\right] = \dot{W}_{y,a} \underbrace{h\left(T_y, w_y = 1\right)}_{\text{Eqn. (2.7))}}, \tag{2.107}$$

which is consistent with the exchange of pure water vapor and enthalpy between the thermodynamic systems. Equation (2.107) is used to determine $\dot{H}_{g_K,a}$, $\dot{H}_{s_J,a}$, and $\dot{H}_{\pi_m,a}, m \in \{1,2,\ldots,M\}$.

2.4.6 Leaf physiology

In ED-2.2 (and previous versions, c.f. Moorcroft et al., 2001; Medvigy et al., 2009), leaf physiology is represented by a model based on (Farquhar et al., 1980; Ball et al., 1987; Collatz et al., 1991) for C_3, and Collatz et al. (1992) for C_4. Although the concept is the same as in previous versions of ED, the solver algorithm has changed and therefore we present it here.

Let $\dot{A}_m[\,\mathrm{mol_C\,m_{leaf}^{-2}\,s^{-1}}]$ be the net leaf-level CO_2 uptake rate controlled exclusively by the leaf environment, and let $\dot{S}_m[\,\mathrm{mol_{H_2O}\,m_{leaf}^{-2}\,s^{-1}}]$ be the corresponding water loss through transpiration. From Farquhar et al. (1980), the net CO_2 assimilation rate $\dot{A}_m$ is determined as:

$$\dot{A}_m = \underbrace{\dot{V}_{C_m}}_{\text{Carboxylation}} - \underbrace{\frac{1}{2}\dot{V}_{O_m}}_{\substack{\text{Oxygenation}\\ \text{(Photorespiration)}}} - \underbrace{\dot{D}_m}_{\text{Dark respiration}} . \tag{2.108}$$

Dark respiration comprises all leaf respiration terms that are not dependent on photosynthesis, and it is mostly due to mitochondrial respiration. Oxygenation releases $0.5\,\mathrm{mol_{CO_2}}$ for each $\mathrm{mol_{O_2}}$, hence the $-\frac{1}{2}$ term, and it is related to carboxylation by means of the CO_2 compensation point $\Gamma^\star_m$ (Lambers et al., 2008):

$$\dot{V}_{O_m} = \frac{2\,\Gamma^\star_m}{c_{\chi_m}}\dot{V}_{C_m} \tag{2.109}$$

where c_{χ_m} is the CO_2 mixing ratio at the leaf intercellular space[6]. The CO_2 compensation point is determined after Collatz et al. (1991, 1992):

$$\Gamma^\star_m = \begin{cases} \dfrac{{O_2}^\oplus}{2\,\tau} & \text{, if cohort } m \text{ is a } C_3 \text{ plant} \\ 0 & \text{, if cohort } m \text{ is a } C_4 \text{ plant} \end{cases}, \tag{2.110}$$

where ${O_2}^\oplus$ is the reference O_2 mixing ratio, and τ represents the ratio between the rates of carboxylase to oxygenase and is a function of temperature.

Because C_4 plants have a mechanism to considerably enhance intracellular CO_2, photorespiration is nearly inexistent in C_4 plants (Lambers et al., 2008), hence the assumption that $\Gamma^\star_m$ is

[6]Using CO_2 at the intercellular space should be regarded as an approximation, since the photochemical reactions occur at the chloroplast (Sharkey et al., 2007; Lambers et al., 2008).

zero. Indeed, for C_4, photosynthesis is ultimately limited by the maximum capacity of RuBisCO (Ribulose-1,5-Biphosphate Carboxylase Oxygenase) to perform carboxylation ($\dot{V}_{C_m} = \dot{V}_{C_m}^{\max}$), provided that the leaf cells have unlimited CO_2 and enough photosynthetically active radiation. For C_3, this rate is unattainable because even when light is sufficient and neither CO_2 nor O_2 are limiting on their own, carboxylation and oxygenation are mutually inhibitive reactions (Lambers et al., 2008). Therefore, the maximum rate is often referred as the RuBP-saturated rate $\dot{V}_{C_m} = \dot{V}_{C,1}$, and is expressed by a modified Michaelis-Menten kinetics equation:

$$\dot{V}_{C_m,1} = \begin{cases} \dot{V}_{C_m}^{\max} \dfrac{c_{\chi_m}}{c_{\chi_m} + \mathcal{K}_{ME_m}} & \text{, if cohort } m \text{ is a } C_3 \text{ plant} \\ \dot{V}_{C_m}^{\max} & \text{, if cohort } m \text{ is a } C_4 \text{ plant} \end{cases}, \tag{2.111}$$

where $\mathcal{K}_{ME_m} = \mathcal{K}_{C_m}\left(1 + {O_2}^{\oplus}/\mathcal{K}_{O_m}\right)$ is the effective Michaelis constant, and $\mathcal{K}_{C_m}$ and $\mathcal{K}_{O_m}$ are the Michaelis constants for carboxylation and oxygenation, respectively.

At low CO_2 concentrations C_3 photosynthesis is also limited by the RuBisCO activity; for C_4 plants, carboxylation at very low CO_2 concentration is also reduced due to a lower activity of the PEP carboxylase, which in turn reduces the CO_2 concentration in the bundle sheath below saturation (von Caemmerer, 2000). Collatz et al. (1992) pointed out that uptake increases linearly with increasing CO_2, until it reaches the saturation imposed by $\dot{V}_{C_m}^{\max}$. The original expression for CO_2-limited carboxylation ($\dot{V}_{C_m,2}$) for C_4 plants by Collatz et al. (1992) has been modified later (e.g. Foley et al., 1996) to explicitly include $\dot{V}_{C_m}^{\max}$; this is the same expression used in ED-2.2:

$$\dot{V}_{C_m,2} = \begin{cases} \dot{V}_{C_m,1} & \text{, if cohort } m \text{ is a } C_3 \text{ plant} \\ k_{PEP_m}\, c_{\chi_m}\, \dot{V}_{C_m}^{\max} & \text{, if cohort } m \text{ is a } C_4 \text{ plant} \end{cases}, \tag{2.112}$$

where $k_{PEP_m} \overset{\text{def}}{=} 4000\,\text{mol}_{\text{Air}}\,\text{mol}_{CO_2}{-}1$ is the same value used by CLM-4 (Oleson et al., 2010).

From the total photosynthetically active irradiance absorbed by the cohort $\dot{Q}_{1,a,\pi_m}$ (Eqn. 2.58b), we define the photon flux that is absorbed by the leaf ($\dot{q}_m[\,\text{mol}\,\text{m}_{\text{leaf}}^{-2}\,\text{s}^{-1}]$):

$$\dot{q}_m = \frac{1}{j}\,\frac{p_m}{\tilde{\Pi}_m}\,\dot{Q}_{1,a,\pi_m}, \tag{2.113}$$

where j is the average photon specific energy in the PAR band, assumed to be $2.17 \cdot 10^5\,\text{J}\,\text{mol}^{-2}$.

Even though a high fraction ε'_m of the absorbed irradiance is used to transport electrons needed by the light reactions of photosynthesis (Lambers et al., 2008), only a fraction of the irradiance absorbed by the leaf is absorbed by the chlorophyll; in addition, the number electrons needed by each carboxylation and oxygenation reaction poses an additional restriction to the total carboxylation rate. The product of these three factors is combined into a single scaling factor for total absorbed PAR, the quantum yield (ε_m), which is a PFT-dependent property in ED-2.2. The maximum carboxylation rate under light limitation $\dot{V}_{\mathrm{C}_m,3}$ is:

$$\dot{V}_{\mathrm{C}_m,3} = \varepsilon_m \dot{q}_m \frac{1}{1+\dfrac{\dot{V}_{\mathrm{O}_m}}{\dot{V}_{\mathrm{C}_m}}} = \begin{cases} \varepsilon_m \dot{q}_m \dfrac{c_{\chi_m}}{c_{\chi_m}+2\Gamma^\star_m} & \text{, if cohort } m \text{ is a } \mathrm{C}_3 \text{ plant} \\ \varepsilon_m \dot{q}_m & \text{, if cohort } m \text{ is a } \mathrm{C}_4 \text{ plant} \end{cases}. \tag{2.114}$$

As von Caemmerer (2000) points out, carboxylation may also be limited by the export rate of starch and sucrose that is synthesised by triose phospate, especially when CO_2 concentration is high combined with high irradiance, or when temperature or O_2 concentration are low. This limitation, however, is currently not included in ED-2.2.

Given the low storage capacity of leaf boundary layer air, we assume that the the flux entering and exiting the boundary layer have the same magnitude, thus a single flux value is sought. As shown in Fig. 2.7, fluxes of water and carbon between the leaf intercellular space and the canopy air space must overcome both the stomatal resistance and the boundary layer resistance, whereas sensible heat flux and water flux from leaf surface water must overcome the boundary layer resistance only. Let $c_{\beta_m}[\,\mathrm{mol_C\,mol_{Air}^{-1}}]$ and $w_{\beta_m}[\,\mathrm{mol_{H_2O}\,mol_{Air}^{-1}}]$ be the CO_2 mixing ratio and the specific humidity of the leaf boundary layer air space[7], respectively, and let the specific humidity at the leaf intercellular space to be at saturation at the leaf temperature $w_{\chi_m} \stackrel{\mathrm{def}}{=} w^{\equiv}(T_{\pi_m}, p_a)$. The potential fluxes of CO_2 and water can be written as:

[7] As shown in Fig. 2.7, this is different than the leaf specific humidity of intercepted water. For hypostomatous plants, evaporation and condensation at the leaf surface occurs on the opposite side where stomata are located.

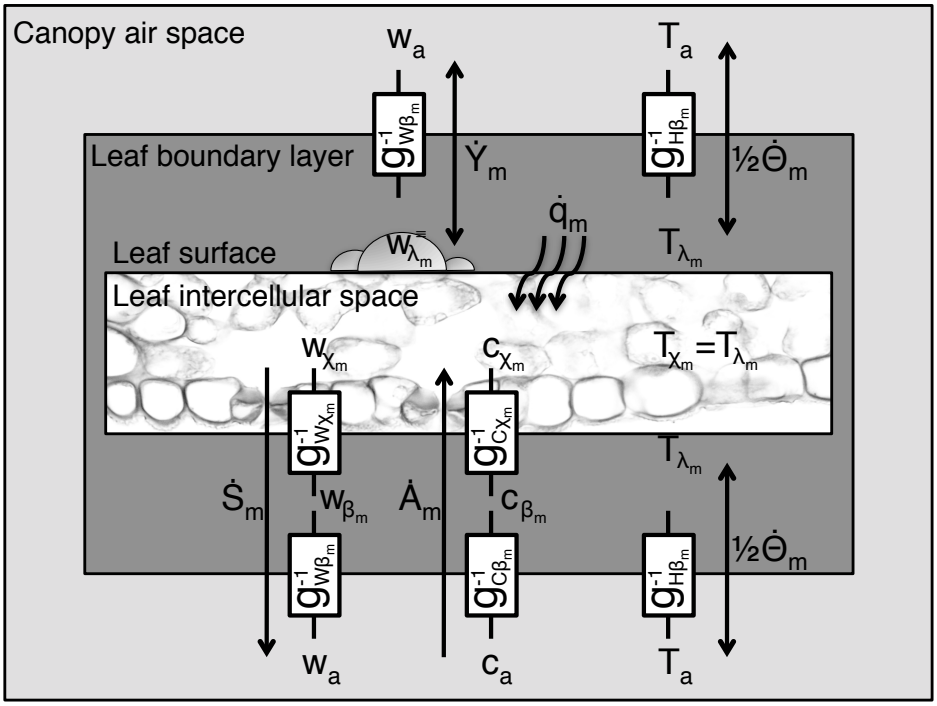

Figure 2.7: Schematic of the leaf fluxes for a hypostomatous plant during the photo period. Conductance are represented by the resistance between the different environments (g^{-1}). For comparison, the leaf-level sensible heat $\dot{\Theta}_m$ and water vapor fluxes $\dot{Y}_m$ between the leaf surface and the canopy air space are also shown.

$$\dot{A}_m = \underbrace{\frac{\rho_a g_{C\beta_m}}{\mathcal{M}_d}}_{\hat{g}_{C\beta_m}} \left(c_a - c_{\beta_m}\right) \quad = \underbrace{\frac{\rho_a g_{C\chi_m}}{\mathcal{M}_d}}_{\hat{g}_{C\chi_m}} \left(c_{\beta_m} - c_{\chi_m}\right), \quad = \frac{\hat{g}_{C\beta_m}\hat{g}_{C\chi_m}}{\hat{g}_{C\beta_m} + \hat{g}_{C\chi_m}} \left(c_a - c_{\chi_m}\right) \quad , \tag{2.115a}$$

$$\dot{S}_m = \underbrace{\frac{\rho_a g_{W\beta_m}}{\mathcal{M}_d}}_{\hat{g}_{W\beta_m}} \left(w_{\beta_m} - w_a\right) = \underbrace{\frac{\rho_a g_{W\chi_m}}{\mathcal{M}_d}}_{\hat{g}_{W\chi_m}} \left(w_{\chi_m} - w_{\beta_m}\right), = \frac{\hat{g}_{W\beta_m}\hat{g}_{W\chi_m}}{\hat{g}_{W\beta_m} + \hat{g}_{W\chi_m}} \left(w_{\chi_m} - w_a\right). \tag{2.115b}$$

where $g_{C\chi_m}[\mathrm{m\,s^{-1}}]$ and $g_{W\chi_m}[\mathrm{m\,s^{-1}}]$ are the stomatal conductance for CO_2 and water, respectively. Stomatal conductance is controlled by plants and is a result of a trade-off between the amount of carbon that leaves can uptake and the amount of water that plants may lose. Leuning (1995) proposed a semi-empirical stomatal conductance expression for water based on these trade-offs:

$$\hat{g}_{W\chi_m} = \begin{cases} \hat{g}^{\varnothing}_{W\chi_m} + \dfrac{m_m \dot{A}_m}{\left(c_{\beta_m} - \Gamma^{\star}_m\right)\left(1 + \dfrac{w_{\chi_m} - w_{\beta_m}}{\text{Đ}_m}\right)} & \text{, if } \dot{A}_m > 0 \\ \hat{g}^{\varnothing}_{W\chi_m} & \text{, if } \dot{A}_m \leq 0 \end{cases}, \tag{2.116}$$

where $\hat{g}^{\varnothing}_{W\chi_m}$ is the residual conductance when stomata are closed, m_m is a slope parameter, and Đ_m is an empirical coefficient to control conductance under severe leaf-level water deficit; all of them being PFT-dependent parameters. From Cowan and Troughton (1971), stomatal conductance of CO_2 is estimated by the ratio between CO_2 and water diffusivity in the air ($\gamma_\chi \approx 1.60$), whereas the boundary layer conductance follows the $\gamma_\beta \approx \gamma_\chi^{\frac{2}{3}}$ ratio because of convection in addition to diffusivity in the leaf boundary layer:

$$\hat{g}_{W\chi_m} = \gamma_\chi \, \hat{g}_{C\chi_m} \tag{2.117a}$$

$$\hat{g}_{W\beta_m} = \gamma_\beta \, \hat{g}_{C\beta_m}. \tag{2.117b}$$

The temperature dependency of the solubility ratio τ and the Michaelis constants for carboxylation are expressed either as an Arrhenius or a Q_{10} function:

$$\mathcal{T}(T,x) = x_{15} \times \begin{cases} \exp\left[\mathcal{A}_x \left(\dfrac{1}{T_{15}} - \dfrac{1}{T}\right)\right] & \text{Arrhenius function} \\ q_x^{\left(\frac{T - T_{15}}{10}\right)} & \text{Q}_{10} \text{ function} \end{cases} \tag{2.118}$$

where x_{15} is the value of variable x at temperature $T_{15} = 288.15$ K, and $\mathcal{A}_x$ and q_x are the parameters which describe temperature dependence. In ED-2.2 the user may choose which formulation to use and import the needed parameters. $\dot{V}^{\max}_{C_m}$ and $\dot{D}_m$ are also functions of temperature, although they include an additional scaling function to account for the fast decline of both productivity and respiration at low and high temperatures (Sellers et al., 1996; Moorcroft et al., 2001):

$$\mathcal{T}'(T,x) = \frac{\mathcal{T}(T,x)}{\left[1 + \mathrm{e}^{-\eth_x\left(T - T_x^{\text{Cold}}\right)}\right]\left[1 + \mathrm{e}^{+\eth_x\left(T - T_x^{\text{Hot}}\right)}\right]}, \tag{2.119}$$

where $\eth$, T^{Cold} and T^{Hot} for $\dot{V}^{\max}_{C_m}$ and $\dot{D}_m$ are PFT-dependent parameters.

While w_{χ_m}, $\dot{V}_{\mathrm{C}_m}^{\max}$, $\dot{D}_m$, τ_m, $\mathcal{K}_{\mathrm{O}_m}$, $\mathcal{K}_{\mathrm{C}_m}$, $\Gamma_m^\star$, and $\mathcal{K}_{\mathrm{ME}_m}$ are functions of only leaf temperature and canopy airspace pressure, nine variables are unknown for each limitation case as well as for the case when the stomata are closed: $\dot{S}_m$, $\dot{A}_m$, c_{χ_m}, $\hat{g}_{W\chi_m}$, $\dot{V}_{\mathrm{C}_m}$, $\dot{V}_{\mathrm{O}_m}$, $\hat{g}_{C\chi_m}$, c_{β_m}, and w_{β_m}. Both the temperature-dependence functions and the solution for the system of equations are presented in App. A. Once all cases are determined, the solution is determined similarly by either a law of minimum (Collatz et al., 1991, 1992; Moorcroft et al., 2001); or when one of the limiting cases does not yield any viable solution, we assume that photosynthesis cannot occur and that stomata are closed; this happens when available light or c_{χ_m} are near or below their compensation point:

$$\dot{A}_m = \begin{cases} \min\limits_{l=1}^{3} \dot{A}_{l,m} & \text{, if } \dot{A}_{l,m} \in \mathbb{R} \quad \forall \quad l \in \{1,2,3\} \\ \dot{A}_{0,m} & \text{, otherwise} \end{cases}, \tag{2.120a}$$

$$\dot{S}_m = \dot{S}_{l^\star,m}, \tag{2.120b}$$

where $l^\star$ is the limiting case chosen in Eqn. (2.120a). The result from Eqn. (2.120a) implicitly ignores soil moisture limitation on photosynthesis, since Leuning (1995) semi-empirical model for stomatal conductance was developed from seedlings that were well watered. Soil moisture limitation is incorporated as a scaling function o_{g,π_m} based on Moorcroft et al. (2001), although it has been re-defined in terms of soil matric potential because it is more directly related to the resistance to bring water from the ground to the leaves:

$$o_{g,\pi_m} = \frac{1}{1+\dfrac{\text{Demand}}{\text{Supply}}} = \frac{1}{1+\dfrac{\mathcal{M}_{\mathrm{W}}\,\Lambda_m\,\dot{S}_m}{G_{\rho_m}\,n_m\,C_{\rho_m}\,W^\star_{g,k_{\rho_m}}}}, \tag{2.121a}$$

$$W^\star_{g,k} = \sum_{k'=k}^{K} \left[\rho_\ell \left(\vartheta_{\mathrm{Fc}} - \vartheta_{\mathrm{Wp}}\right) \Psi^\star_{k'}\, \Delta z_{g_{k'}}\right] \tag{2.121b}$$

$$\Psi^\star_k = \ell_{g_k}\, \frac{\max\left\{\min\left[\Psi_k + \frac{1}{2}\left(z_{g_k} + z_{g_{k+1}}\right), \Psi_{\mathrm{Fc}}\right], \Psi_{\mathrm{Wp}}\right\} - \Psi_{\mathrm{Wp}}}{\Psi_{\mathrm{Fc}} - \Psi_{\mathrm{Wp}}} \tag{2.121c}$$

where $G_{\rho_m}[\,\mathrm{m^2\,kg^{-1}_{C_{root}}\,s^{-1}}]$ is a scaling parameter related to fine root conductance, $C_{\rho_m}[\,\mathrm{kg_{C_{root}}\,m^{-2}}]$ is the fine root biomass, $W^\star_{g,k}[\,\mathrm{kg_W\,m^{-2}}]$ is the available water for photosynthesis, $\Psi^\star_m$ is a factor

that represents the reduction of available water due to force needed to extract the water. Because there is always some residual stomatal conductance cannot be zero, the scaling factor interpolates between the fully closed case and the solution without soil moisture limitation, yielding to the actual fluxes of CO_2 ($\dot{C}_{\chi_m,a}[\,\mathrm{mol_C\,m^{-2}\,s^{-1}}]$) and water ($\dot{W}_{\chi_m,a}[\,\mathrm{kg_W\,m^{-2}\,s^{-1}}]$):

$$\dot{C}_{\chi_m,a} = -\#_m\,\Lambda_m\,\left[(1-o_{g,\pi_m})\,\dot{A}_{0,m} + o_{g,\pi_m}\dot{A}_{l^\star,m}\right], \tag{2.122a}$$
$$\dot{W}_{\chi_m,a} = \#_m\,\mathcal{M}_w\,\Lambda_m\,\left[(1-o_{g,\pi_m})\,\dot{S}_{0,m} + o_{g,\pi_m}\dot{S}_{l^\star,m}\right], \tag{2.122b}$$

where $\#_m$ is 1 if the PFT is hypostomatous or 2 if the PFT is amphistomatous or needleleaf. Similarly, the individual gross primary productivity ($\mathrm{GPP}_m[\,\mathrm{kg_C\,plant^{-1}\,s^{-1}}]$) and leaf respiration[8] ($\dot{R}_{\lambda_m}[\,\mathrm{kg_C\,plant^{-1}\,s^{-1}}]$) are defined by:

$$\mathrm{GPP}_m = \frac{\mathcal{M}_\mathrm{C}\,\#_m\,\Lambda_m}{n_m}\cdot\left[(1-o_{g,\pi_m})\,\dot{A}_{0,m} + o_{g,\pi_m}\dot{A}_{l^\star,m} + \dot{D}_m\right] \tag{2.123a}$$
$$\dot{R}_{\lambda_m} = \frac{\mathcal{M}_\mathrm{C}\,\#_m\,\Lambda_m}{n_m}\cdot\dot{D}_m \tag{2.123b}$$

The amount of water lost through transpiration at any given time is assumed to exactly match the amount of soil water brought to the leaf intercellular space through the plant vascular system. Plants may extract water from all layers they have access, and the amount of water extracted from each layer is proportional to the available water in the layer relative to the total available water:

$$\sum_{k'=k_{\rho_m}}^{K}\left(\dot{W}_{g_{k'},\chi_m}\right) \stackrel{\mathrm{def}}{=} \dot{W}_{\chi_m,a}, \tag{2.124a}$$
$$\dot{W}_{g_k,\chi_m} = \dot{W}_{\chi_m,a}\,\frac{W^\star_{g,k} - W^\star_{g,k+1}}{W^\star_{g,k_{\rho_m}}}, \tag{2.124b}$$

where $W^\star_{g,K+1} \stackrel{\mathrm{def}}{=} 0$. Although the net water flux due to transpiration at the leaf is assumed to be zero, the net energy flux is not zero because the water enters the leaf as liquid water at the soil temperature, reaches thermal equilibrium with leaves, and is lost to the canopy air space as

[8] Excluding photo-respiration.

water vapor at the leaf temperature. Therefore, the internal energy flux between the soil layers and the cohort is calculated similarly to Eqn. (2.40), whereas the enthalpy flux between the leaf intercellular space and the canopy air space is solved similarly to Eqn. (2.107):

$$\dot{E}_{g_k,\chi_m} = \dot{W}_{g_k,\chi_m}\, q_\ell \left(T_{g_k} - T_{sc\ell}\right), \tag{2.125a}$$

$$\dot{H}_{\chi_m,a} = \dot{W}_{\chi_m,a}\, q_{pv} \left(T_{\pi_m} - T_{scv}\right). \tag{2.125b}$$

2.4.7 Non-leaf autotrophic respiration

Respiration from fine roots is defined using a phenomenological function of temperature that has the same functional form of leaf respiration (Moorcroft et al., 2001). Because roots are allowed in multiple layers, and in ED-2.2 roots have a uniform distribution of mass throughout the profile, the total respiration (individual-based $\dot{R}_{\rho_m}[\,\mathrm{kg_C\,plant^{-1}\,s^{-1}}]$ or flux-based $\dot{C}_{\rho_m,a}[\,\mathrm{mol_C\,m^{-2}\,s^{-1}}]$) is the integral of the contribution from each soil layer, weighted by the layer thickness:

$$\dot{R}_{\rho_m} = \frac{1}{z_{g_{K+1}} - z_{g_{k_{\rho m}}}}\, C_{\rho_m} \sum_{k=k_{\rho_m}}^{K} \left[\mathcal{T}'\left(T_{g_k}, \mathcal{B}_{\rho_m}\right) \Delta z_{g_k}\right], \tag{2.126a}$$

$$\dot{C}_{\rho_m,a} = \frac{n_m\, \dot{R}_{\rho_m}}{\mathcal{M}_\mathrm{C}} \tag{2.126b}$$

where $\mathcal{B}_{\rho_m}[\,\mathrm{s^{-1}}]$ is the PFT-dependent decay rate due to root respiration, and $\mathcal{T}'$ is the same temperature-dependent function from Eqn. (2.119).

Total storage respiration is a combination of two terms: a constant, long-term turnover rate of the accumulated storage pool (individual-based $\dot{R}_{\tau_m}$ $[\,\mathrm{kg_C\,plant^{-1}\,s^{-1}}]$ or flux-based $\dot{C}_{\tau_m,a}$ $[\,\mathrm{mol_C\,m^{-2}\,s^{-1}}]$), and one term related to the losses due to using the assimilated carbon for growth and maintenance of the living tissues (individual-based $\dot{R}_{\Delta_m}$ $[\,\mathrm{kg_C\,plant^{-1}\,s^{-1}}]$ or flux-based $\dot{C}_{\Delta_m,a}$ $[\,\mathrm{mol_C\,m^{-2}\,s^{-1}}]$, Amthor, 1984). The latter is a strong function of the plant metabolic rate, which has strong daily variability hence it is a function of the daily carbon balance:

$$\dot{C}_{\tau_m,a} = \frac{n_m}{\mathcal{M}_\mathrm{C}} \underbrace{C_{\tau_m}\,\mathcal{B}_{\tau_m}}_{\stackrel{\text{def}}{=}\dot{R}_{\tau_m}}, \tag{2.127a}$$

$$\dot{C}_{\Delta_m,a} = \frac{n_m}{\mathcal{M}_\mathrm{C}} \underbrace{C_{\mathrm{B}_m}\,\mathcal{B}_{\Delta_m}}_{\stackrel{\text{def}}{=}\dot{R}_{\Delta_m}}, \tag{2.127b}$$

$$C_{\mathrm{B}_m} = \int_{t-\Delta t_\mathrm{live}}^{t} \left(\mathrm{GPP}_m - \dot{R}_{\lambda_m} - \dot{R}_{\rho_m} - \dot{R}_{\Delta_m} - \dot{L}_{\pi_m,z}\right) \mathrm{d}t, \tag{2.127c}$$

$$\dot{L}_{\pi_m,z} = \underbrace{f_{\lambda_m} C_{\lambda_m}}_{\substack{\text{Leaf}\\ \text{maintenance}}} + \underbrace{f_{\rho_m} C_{\rho_m}}_{\substack{\text{Root}\\ \text{maintenance}}} + \dot{C}^{\downarrow}_{\lambda_m}, \tag{2.127d}$$

where $(\mathcal{B}_{\tau_m}, \mathcal{B}_{\Delta_m})[\,\mathrm{s}^{-1}]$ are the PFT-dependent decay rate associated with storage turnover and consumption for growth; $C_{\mathrm{B}_m}[\,\mathrm{kg_C\,plant^{-1}}]$ is the total accumulated carbon from the previous day; $\dot{L}_{\pi_m,z}[\,\mathrm{kg_C\,plant^{-1}\,s^{-1}}]$ is the litter flux to the soil carbon; $(f_{\lambda_m}, f_{\rho_m})[\,\mathrm{s}^{-1}]$ are the leaf and root turnover rates; $(C_{\lambda_m}; C_{\rho_m})[\,\mathrm{kg_C\,plant^{-1}}]$ are the individual leaf and root biomass; and $\dot{C}^{\downarrow}_{\lambda_m}[\,\mathrm{s}^{-1}]$ is the leaf shedding due to phenology. The latter term is always zero for evergreen cohorts; for cold-deciduous cohorts, it is determined either from a prognostic model (Botta et al., 2000; Albani et al., 2006) or prescribed from MODIS-based estimates or from ground observations (Medvigy et al., 2009); drought deciduous phenology is described in App. F.

2.4.8 Heterotrophic respiration

Heterotrophic respiration comes from the decomposition of carbon from the three soil/litter carbon pools. For each carbon pool $i \in (1,2,3)$, we determine the maximum carbon loss based on the characteristic decay rate $\dot{R}_z = \left(3.49\cdot10^{-7}; 1.43\cdot10^{-7}; 6.34\cdot10^{-9}\right)[\,\mathrm{s}^{-1}]$, which roughly corresponds to the typical half-life for metabolic litter and microbes; structural litter; and slow soil organic matter determined from Bolker et al. (1998), respectively:

$$\dot{C}_{zi,a} = \dot{R}_{z_i} \frac{C_i}{\mathcal{M}_\mathrm{C}} F(\overline{T}_{g20}, \overline{\hat{\vartheta}}_{20}), \tag{2.128}$$

where $\overline{T}_{g20}$ and $\overline{\hat{\vartheta}}_{20}$ are the average temperature and relative soil moisture of the top $0.2m$ of soil,

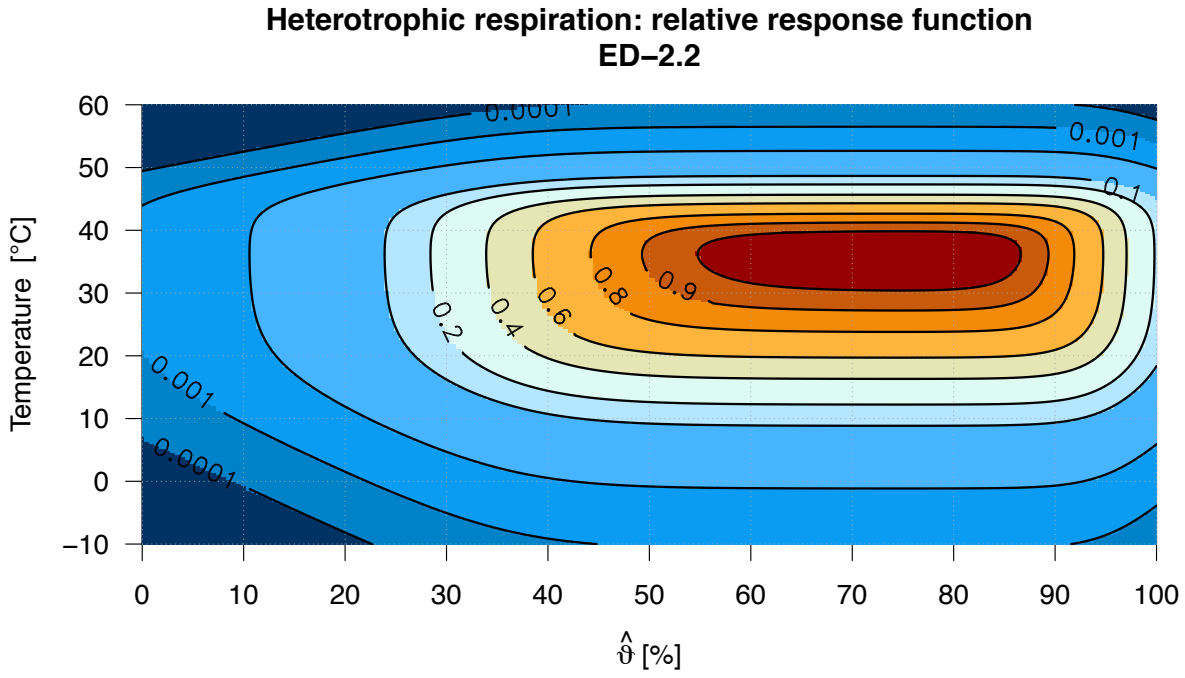

Figure 2.8: Decomposition rate reduction factor ($F(T,\hat{\vartheta})$) as a function of temperature and soil moisture.

the relative soil moisture for each layer being defined as:

$$\hat{\vartheta}_k = \frac{\vartheta_k - \vartheta_{\mathrm{Re}}}{\vartheta_{\mathrm{Po}} - \vartheta_{\mathrm{Re}}}; \tag{2.129}$$

and $F(T,\hat{\vartheta})$ is a function similar to Eqn. (2.119) that reduces the decomposition rate due to temperature or soil moisture under extreme conditions:

$$F(T,\hat{\vartheta}) = \frac{1}{\left[1+\mathrm{e}^{-0.24(T-291.15)}\right]\left[1+\mathrm{e}^{+0.60(T-318.15)}\right]} \times \frac{1}{\left[1+\mathrm{e}^{-0.18\left(\hat{\vartheta}-0.36\right)}\right]\left[1+\mathrm{e}^{+0.36\left(\hat{\vartheta}-0.96\right)}\right]}. \tag{2.130}$$

The combined effect of moisture and temperature limiting the decomposition rates is shown in Fig. 2.8.

Chapter 3

Evaluation of ED-2.2 at multiple time scales for South America

3.1 Introduction

Increase in CO_2 concentration and associated changes in climate are likely to have profound changes in plant community structure, dynamics and ecosystem ability to store carbon, and despite major advances in model representation of dynamic vegetations within the Earth System (Levis, 2010), there is still great uncertainty on how tropical ecosystems may respond to such changes. For example, while various synthesis studies of future climate for the tropics using dynamic global vegetation models (DGVMs) predict that CO_2 fertilization may be the dominant effect in large areas of the tropics and subtropics (Rammig et al., 2010; Cox et al., 2013; Huntingford et al., 2013), recent results from long-term measurements of above-ground net primary productivity at La Selva (Costa Rica) did not detect such dominant effect of CO_2 fertilization (Clark et al., 2013). In addition, several dynamic vegetation models show reasonable equilibrium conditions within forests, but results in these models tend to present sharper transitions in ecological measurements than similar observed values (e.g. see Fig. 3 of Good et al., 2011). Most DGVMs have thorough and mechanistic representation of biophysical and biogeochemical cycles, which increases realism

by mechanistically representing such processes; however, they tend to describe ecosystems based on very simple characteristics, often from average properties of the ecosystem as a whole, which precludes a proper representation of the heterogeneous environment in which individuals live. In reality, the dynamics of an ecosystem is the emerging property that integrates the contribution of a system of individuals with different strategies and ability to access resources needed for their growth, survival, and reproduction (Moorcroft, 2003, 2006; Evans, 2012).

In addition to the impact of individual contribution to long term dynamics, life cycles of individuals, disturbance history, and anthropogenic land use change often create a heterogeneous environment, and the response of such heterogeneous landscape to relatively similar forcings can vary substantially. For example, during the LITFASS-2003 experiment in a 400 km^2 area at a heterogenous rural landscape near Berlin, Beyrich et al. (2006) found large variations of sensible and latent heat flux between different landscapes that included forests, croplands and lakes, but even croplands with similar characteristics showed significant differences. Also, during the EBEX-2000 experiment in California, Oncley et al. (2007) found significant variations in the average sensible and latent heat fluxes over a irrigated cotton field area. In this sense, the Ecosystem Demography Model structure is advantageous because it has a mechanistic representation of the different micro-environments and the distribution of individuals living in it (Moorcroft et al., 2001, Sec. 2.2.1). Since the inception of the second generation of the ED model, there has been a significant development of the biophysical and biogeochemical modules (Medvigy, 2006; Knox, 2012, and Chap. 2), and earlier versions of the model have been optimized for reproducing the biophysics for forest ecosystems at mid-latitudes (Medvigy et al., 2009) and one region in the Amazon (Kim et al., 2012). However, to this point no detailed regional evaluation of both short-term biophysical and physiology modules has been made for the tropics, covering a variety of regions with significantly different characteristics.

Therefore, the aim of this chapter is to evaluate the ability of ED-2.2 to describe both the short-term biophysical and physiology at tropical South America, and whether this improvement in the short-term processes leads to realistic long-term dynamics. In addition, I re-evaluate how differ-

ent levels of complexity of size, age, and functional diversity may affect the equilibrium (potential) vegetation and its trajectories towards equilibrium under the current version of the model. The evaluation presented here is deliberately extensive and cover several different process, using different data sources or published values for references: as pointed out by Vanclay and Skovsgaard (1997), extensive evaluations are important to provide as much information on what are the main strengths and shortcomings of the current model, so new users can decide whether the model is suitable for their applications and needs. In addition to its informative value, extensive evaluation of results provides valuable information to guide future developments, particularly in process-based models, where results are outcomes of various interacting processes. Furthermore, the evaluation intended to use as much biophysical data from multiple sites at both short and long term scales. Short-term comparisons at multiple sites are important because the magnitude of different processes may vary substantially amongst sites, whereas long-term evaluations are necessary to assess whether the accumulated inaccuracies of the model processes could cause large errors in the development of plant communities under a wide range of biomes observed in the tropics, as exemplified by the distribution of above-ground biomass in South America.

Unlike Medvigy et al. (2009) and Kim et al. (2012), I have not carried out any formal optimization at this point. As pointed out by Medlyn et al. (2005), in models that have too many parameters as it is the case of ED-2.2, optimizing some parameters can compensate for other nearly collinear parameters, resulting either in the model low sensitivity. In addition, in case of a process-based model with too many parameters, a full optimization of all parameters simultaneously is not viable, and choosing a subset of parameters brings the risk of drifting away parameters that directly affect a process to compensate parameters that only indirectly affect a process but were not included in the partial optimization, but nevertheless were far from optimal. One practical example would be to tune the photosynthetic capacity and stomatal conductance to improve the model accuracy of gross primary productivity, when in reality a detailed analysis would point that the issue is that the model underestimates absorption of photosynthetically active radiation by leaves. Therefore it is necessary to first carry out a thorough assessment of which processes and parameters present the

main differences between model and observations, and how discrepancies observed in different processes may be intertwined, and thus identify which processes and parameters must be included in any optimization.

In Sec. 3.2, I describe the simulation design for the model evaluation at short and long term dynamics, in addition to the overview of the selected sites. In Sec. 3.3, I present the main results of the multiple site comparison with site level measurements of eddy covariance fluxes, radiation, and additional site level measurements and published values from previous studies. In Sec. 3.4 I present the results from long-term simulations at multiple sites covering three different biomes in South America using both the default ED-2.2 configuration and simulations without size, age, or functional diversity structures (and combinations). In Sec. 3.5 I discuss the main results from this suite of simulations, and in Sec. 3.6 I summarize the main concluding remarks.

3.2 Material and methods

3.2.1 Biophysical and biogeochemical cycles

To assess the ability to represent the biophysical and biogeochemical cycles, I carried out a series of simulations with ED-2.2 for six sites in tropical South America where both eddy flux towers and tree inventories were available (Fig. 1.2 and Tab. 3.1). Five of these sites are part of the Brazil Flux Network[1] (Restrepo-Coupe et al., 2013), plus the Guyaflux tower at Paracou, French Guiana (Bonal et al., 2008, GYF). All sites are closed canopy tropical rainforests, with the exception of Pé-de-Gigante (PDG), which is a woody savannah (Cerrado), and all sites are assumed to be old-growth primary vegetation, with the exception of Santarém km 83 (S83), which has been logged in 2001 as part of a reduced-impact logging study (c.f. Miller et al., 2011, and references therein). Although limited in number, these sites cover a variety of climates, soil conditions and

[1]Some sites from the Brazil Flux Network were excluded from the analysis: Fazenda Nossa Senhora (FNS) and Santarém km 77 (S77) were excluded because they were pastures and croplands; Caxiuanã (CAX) was rejected due to excessive number of gaps in most variables needed to drive ED-2.2; Bananal Island (BAN) was not included because no individual-level tree inventory from the region was available, although it was included in the long-term experiments (Sec. 3.2.2).

plant community, and all sites have high temporal resolution of meteorological variables needed to drive the model and multiple eddy flux and outgoing radiation measurements which can be directly compared with the model predictions, and all had tree inventories either at the same site as the tower or at the same region. All data sets had been previously aggregated to 30 or 60 min averages and for the comparisons presented in this chapter they have been standardized to 60 min. All hourly averaged data underwent multiple-stage quality control; in addition, variables used as input for for ED-2.2 were gap filled. Both the quality control and gap filling methods are described in App. D.

Initial demographic conditions were determined from the closest tree inventory available. None of the sites had information on stand age, therefore I split the data into equally spaced patches with roughly $20\,\mathrm{m} \times 20\,\mathrm{m}$, adjusted to conform with the original shape of the plots. For sites where the taxonomic species were known, plant functional types were assigned according to wood density (c.f. Appendix E); otherwise taxonomic information was estimated from common names and look-up tables from previous forestry reports near each site. None of the sites had measurements of trees as small as the minimum recruitment size in ED-2.2, thus I carried out a preliminary near bare ground simulation with dynamic vegetation turned on until equilibrium, and appended the average cohort distribution between the minimum recruitment size of ED-2.2 and the minimum size measured at the inventory. Likewise, soil carbon pools were initialized from the equilibrium simulation.

Initial conditions for the thermodynamic variables were the following: canopy air space was at the same potential temperature and with the same specific humidity and CO_2 mixing ratio as the air aloft; leaves and branches were to be at the same temperature as the canopy air space and with no intercepted water; temporary surface water was assumed absent; and soil was in thermal equilibrium with canopy air space and soil moisture was assumed at field capacity at all layers. These simulations were carried out for a total of five years to equilibrate soil moisture, followed by one full cycle of the eddy flux tower. The meteorological driver for the five-year spin-up period came from recycling the meteorological driver, and the spin-up period was discarded for all analysis

Table 3.1: Overview of the sites; site names in bold were used for all simulations, site names in italic were used only for the short-term dynamics, and those in regular typeface were only used for long-term simulations. Mean precipitation and dry season length (period in which a 30-day running average of rainfall is $< 100\,\mathrm{mm\,mo^{-1}}$) are 1972–2011 means for the closest rain gauge available; data in parentheses are based on the tower only. Letters in the reference column are: (E) time-dependent environmental data; (S) soil texture, depth and boundary condition; and (B) tree inventory used for initial conditions.

Site	Code	Coordinates (Long;Lat.)	Period	Rainfall $\mathrm{mm\,yr^{-1}}$	Dry season mo	Soil properties				References
						Sand	Clay	Depth m	B.C.[a]	
Guyaflux tower (Paracou)	**GYF**	(-52.91;5.28)	2004–2012	3578 (3176)	2.1 (2.4)	0.56	0.34	8.0	FD	Bonal et al. (2008, E,S) Epron et al. (2006, S) Phillips et al. (2010, B)
Tapajós Natl. Forest (Santarém km 67)	**S67**	(-54.96;-2.86)	2001–2011	1912 (1815)	4.9 (5.0)	0.39[b]	0.59[b]	8.0	FD	Hutyra et al. (2007, E) Ivanov et al. (2012, S)[b] Pyle et al. (2008, B)
TNF (logged) (Santarém km 83)	*S83*	(-54.97;-3.02)	2000–2003	1914 (1934)	4.9 (5.5)	0.39	0.59	8.0	FD	Miller et al. (2011, E) Nepstad et al. (2002, S) Miller et al. (2004, B)
Vassununga State Park (Pé-de-Gigante)	**PDG**	(-47.65;-21.62)	2001–2003	1472 (1284)	6.0 (6.8)	0.85	0.03	6.0	FD	da Rocha et al. (2002, E) Ruggiero et al. (2006, S) (Silva and Batalha, 2009, B)[c]
Jaru Biol. Reserve (Rebio Jaru)	**RJA**	(-61.93;-10.08)	1999–2002	2240 (2263)	4.0 (3.5)	0.80	0.10	3.0[g]	LD	von Randow et al. (2004, E,S)[d] Saatchi (2006, B)[e]
Cuieiras Biol. Reserve (Manaus K34)	**M34**	(-60.21;-2.61)	1999–2006	2293 (2549)	3.3 (3.8)	0.20	0.68	8.0	FD	Araújo et al. (2002, E) Tomasella et al. (2008a, S) Chambers et al. (2001, B)[c,e]
Embrapa Semi-Árido (Petrolina)	PNZ	(-40.37;-9.17)	2004–2012[k]	506 (458)	10.2 (10.6)	0.82	0.05	3.0	LD	de Oliveira et al. (2006, E)[f] SONDA/INPE (2013, E)[f] Nascimento et al. (2003, S)
Cantão State Park (Bananal Island)	BAN	(-50.16;-9.82)	2004–2006	1790 (1688)	4.9 (4.7)	0.24	0.37	3.0	LD	Borma et al. (2009, E)
Águas Emendadas (Brasília)	BSB	(-47.71;-15.60)	2006–2012	1478 (1411)	5.8 (6.0)	0.13[b]	0.53[b]	8.0	FD	SONDA/INPE (2013, E) Garcia-Montiel et al. (2008, S)[b]
Natal	NAT	(-35.21;-5.84)	2009–2012	1601 (1563)	6.2 (5.4)	0.32[g]	0.34[g]	6.0[g]	FD	SONDA/INPE (2013, E) Rossato (2001, S)[g] de Negreiros et al. (2009, S)[g]

[a] The B.C. column stands for soil bottom boundary conditions used in ED-2.2, which can be either RD (reduced drainage) or FD (free drainage).

[b] Equations used in ED-2.2 were fit for soils with less than 60% clay, but soils in S67 and BSB have been reported to contain nearly 90 % and 80 % clay, respectively. For S67, I used the same soils as S83, and for BSB I used the closest ED-2.2 default soil class with less than 60% clay and similar sand content.

[c] Tree inventory is not near the tower: PDG data are from Itirapina and M34 data are from Ducke Reservation, about 70 km southwest and 50 km southeast of the towers, respectively.

[d] Soil depth at was assumed to be $4.0\,m$, but it is reported to vary substantially in the site (von Randow et al., 2004).

[e] Tree inventory did not contain scientific names.

[f] 2004 data are from the eddy flux tower, and 2005-2011 data are from the SONDA network, located 1.5 km south of the tower.

[g] Soil characteristics from gridded dataset. Soil depth is the ED-2.2 default.

presented here. Finally, since the goal of these simulations was to test how ED-2.2 represents the short-term cycles of energy, water, and carbon dioxide as close to the field conditions as possible, all simulations were carried out with the demography dynamics turned off. The main settings for these simulations are shown in Tab. 3.2.

Comparison between model and high frequency observations

To ensure that model and observations at or near eddy covariance flux towers could be directly compared, and that the observed signal was strongly related to actual environment conditions, I aggregated the model results to polygon level hourly averages, and I only used the model output to hours when the variable of interest was an actual observation, and that the 24-hour period preceding any given time had less than 24 gap filled values amongst all seven driver variables. The only exception to this rule were the estimates of productivity and ecosystem respiration from the eddy flux towers, since neither are truly measured. Instead, I compared all times in which the net ecosystem productivity ($\mathrm{NEP}_\sharp[\,\mathrm{kg_C\,m^{-2}\,yr^{-1}}]$) could be determined from tower observations[2] (c.f. App. D.1.1).

In addition to eddy covariance fluxes and radiation, air temperature and humidity profiles within the canopy from the S67 tower (Hutyra, 2007) were also used for comparisons. Because canopy air space is not solved in multiple layers in ED-2.2, observations were aggregated to obtain volume averaged values. For comparisons of soil moisture (all sites except PDG) and temperature (only GYF and S83), I interpolated modelled hourly averages to the same levels as observations.

Daily and fortnightly averages were also used to evaluate longer periods of time. To reduce potential biases in aggregated data, daily means were considered valid only when at least two thirds of the hours were observed. In addition, most sites show a strong diurnal variation of sampling size for ecological data, since nighttime tends to be less turbulent than daytime; therefore I used

[2]While model estimates were also discarded when $u^\star{}_\sharp < u^\star_{\mathrm{min}}$, they were used regardless of the $u^\star$ predicted by the model. As shown in Sec. 2.3.3, ED-2.2 does not account for lateral fluxes in the canopy air space, nor does it have a storage pool of CO_2 in the soil or in the air above canopy and below the tower; therefore in the model Eqn. (2.22) is always equivalent to the sum of eddy covariance and change canopy air space storage

Table 3.2: Summary of parameters and configurations used for the short-term simulations using ED-2.2. Radiation-dependent parameters are given in the format $(x_{\mathrm{PAR}};x_{\mathrm{NIR}};x_{\mathrm{TIR}})$ corresponding to values for photosynthetically active, near infra-red and thermal infrared, respectively. Likewise, PFT-dependent parameters are given in the format $(x_{C4G};x_{C3G};x_{ETR};x_{MTR};x_{LTR})$ corresponding to the values for C_4 and C_3 grasses and early-, mid-, and late-successional cohorts, respectively. Symbols for parameters are consistent with Chap. 2.

Process		**Method**	
Integration scheme		4th order Runge-Kutta	
Temperature-dependent function (photosynthesis)		Q_{10} function	
Leaf phenology		Evergreen/Drought deciduous[a]	
Parameter	**Symbol**	**Value**	**Units**
Biophysics time step	$\Delta t_{\mathrm{biophys}}$	240	s
Cohort water holding capacity	$w_{\max}$	0.11	$\mathrm{kg_W\,m^{-2}_{leaf+wood}}$
Residual stomatal conductance	$\hat{g}^{\varnothing}_{W\chi_m}$	10000[b]	$\mu\mathrm{mol\,m^{-2}\,s^{-1}}$
Leaf-level water stress parameter	$\mathit{Đ}_m$	0.016	$\mathrm{mol_{H_2O}\,mol^{-1}_{Air}}$
Oxygenase/carboxylase ratio at 15°C	tau_{15}	4561[c]	—
Power base for oxygenase/carboxylase ratio	q_τ	0.57[c]	—
Power base for $\dot{V}_C^{\max}$ and $\dot{D}_{15}$	$q_{\dot{V}_C}$; $q_{\dot{V}_C}$	2.4[c]	—
Band-dependent radiation parameters	**Symbol**	**Value**	**Units**
Dry soil reflectance	$\varsigma^{\mathrm{Re}}_{b,g}$	(0.20; 0.31;0.02)	—
Wet soil reflectance	$\varsigma^{\mathrm{Po}}_{b,g}$	(0.10; 0.20;0.02)	—
Leaf transmittance	$\varsigma_{T_{b,\lambda}}$	(0.05; 0.20;0.00)	—
Leaf reflectance (grasses)	$\varsigma_{R_{b,\lambda}}$	(0.10; 0.40;0.04)	—
Leaf reflectance (trees)	$\varsigma_{R_{b,\lambda}}$	(0.10; 0.40;0.05)	—
Wood transmittance	$\varsigma_{T_{b,\omega}}$	(0.05; 0.20;0.00)	—
Wood reflectance (trees)	$\varsigma_{T_{b,\omega}}$	(0.05; 0.20;0.10)	—
PFT**-dependent parameter**	**Symbol**	**Value**	**Units**
Leaf orientation factor	χ_{ν_m}	(0.0; 0.0; 0.1; 0.1; 0.1)	—
Leaf clumping factor	p_m	(1.0; 1.0; 0.8; 0.8; 0.8)	—
Leaf characteristic size	β_λ	(0.05; 0.05; 0.10; 0.10; 0.10)	m
Max. carboxylation rate at 15°C	$\dot{V}^{\max}_{C_{15}}$	(12.5; 20.83; 18.75; 12.50; 6.25)	$\mu\mathrm{mol_C\,m^{-2}_{leaf}\,s^{-1}}$
Dark respiration rate at 15°C	$\dot{D}_{15}$	(0.438; 0.302; 0.272; 0.181; 0.091)	$\mu\mathrm{mol_C\,m^{-2}_{leaf}\,s^{-1}}$
Quantum yield	ε_m	(0.055; 0.080; 0.080; 0.080; 0.080)	—
Slope parameter for stomatal conductance	m_m	(5.2; 9.0; 9.0; 9.0; 9.0)	—
Fine root conductance parameter	G_{ρ_m}	(900; 900; 600; 600; 600)	$\mathrm{m^2\,kg^{-1}_{C_{root}}\,yr^{-1}}$

[a] Forest sites were ran with evergreen phenology, whilst PDG, PNZ, BSB, NAT, and BAN were ran as drought deciduous.
[b] From Medvigy et al. (2009).
[c] From Collatz et al. (1991).

the following formulation for fortnightly means of any variable X:

$$\overline{X}_{f,y} = \begin{cases} \dfrac{1}{8}\displaystyle\sum_{h=1}^{8}\left(\frac{\displaystyle\sum_{n=1}^{N} X_n\, w_n}{\displaystyle\sum_{n=1}^{N} w_n}\right) & \text{if } \displaystyle\sum_{n=1}^{N} w_n > 0 \\ \varnothing & \text{otherwise} \end{cases}, \tag{3.1a}$$

$$O_{X_n} = \begin{cases} 1 & \text{if observed } X_n \text{ is a valid measurement} \\ 0 & \text{otherwise} \end{cases}, \tag{3.1b}$$

$$w_n = O_{X_n}\ \delta_{h_n h}\ \delta_{f_n f}\ \delta_{y_n y}, \tag{3.1c}$$

where y_n is the year, f_n the fortnight period (26 periods per year), and h_n is the time of day for measurement n ($h = 1$ for hourly averages ending at 00, 01, and 02 UTC; $h = 2$ for averages ending at 03, 04, and 05 UTC and so forth); $\delta_{y_n y}$ is the Kronecker delta function for time dimension $y \in \{h, f, y\}$; and $\varnothing$ means missing value (or not available). The mean annual cycle is obtained by averaging all valid $\overline{X}_{f,y}$ for each fortnightly period f, and the whenever presented, the 95 % confidence interval is estimated from bootstrapping the time series in a hierarchical way, by resampling with replacement each time of day within each fortnightly period within each year, then resampling years with replacement.

Finally, to make the evaluation across sites, variables, and times of day more directly comparable, I defined dimensionless forms of mean bias ($\hat{\mu}_R(X)$), residual standard deviation ($\hat{\sigma}_R(X)$), and root mean square error ($\hat{\varepsilon}(X)$) for any subset of valid data $i = \{1, 2, \ldots, I\}$:

$$\hat{\mu}_R(X) = \frac{1}{\sigma_\sharp} \cdot \frac{\displaystyle\sum_{i=1}^{I}\left(X_{M_i} - X_{\sharp_i}\right)}{I}, \tag{3.2a}$$

$$\hat{\sigma}_R(X) = \frac{1}{\sigma_\sharp} \cdot \sqrt{\frac{\displaystyle\sum_{i=1}^{I}\left(X_{M_i} - X_{\sharp_i} - \hat{\mu}_R(X)\right)^2}{I-1}} \equiv \sqrt{1 - R^2}, \tag{3.2b}$$

$$\hat{\varepsilon}(X) = \frac{1}{\sigma_\sharp} \cdot \sqrt{\frac{\sum_{i=1}^{I} \left(X_{M_i} - X_{\sharp_i}\right)^2}{I}} \equiv \sqrt{\hat{\mu}_R^2(X) + \frac{I-1}{I}\hat{\sigma}_R^2(X)} \equiv \sqrt{1-\mathrm{ME}^2}, \quad (3.2c)$$

where $X_{\sharp_i}$ and X_{M_i} are the observed and modelled values of X at time i, and $\sigma_\sharp$ is the standard deviation of observations, and R^2 is the non-adjusted coefficient of determination for the 1:1 line. The root mean square error is sometimes represented in a functional form akin to R^2, referred as the modelling efficiency (ME) by some authors (e.g. Mayer and Butler, 1993; Medlyn et al., 2005). Importantly, bias is not scaled by the mean value but by the standard deviation of the observations, therefore dimensionless bias do not correspond to the bias relative to the mean magnitude of the variable, but relative to the observed variability. This approach highlights the predictive power of the model for variables with low coefficient of variation (e.g. outgoing shortwave radiation), and avoids scaling problems when the mean magnitude is close to zero (e.g. net ecosystem productivity).

Comparison of in-canopy radiation

Since ED-2.2 is an individual-based model, obtaining a realistic light profile is particularly important, because it directly affects the ability of each cohort to perform photosynthesis and maintaining a positive carbon balance thence surviving. None of the focus sites had long-term measurements of light profile during the simulated period, which precluded a detailed evaluation of the model. Notwithstanding, Cabral et al. (1996) measured canopy profiles of downward photosynthetically active radiation at both Rebio Jaru (RJA) and at the Adolpho Ducke Forest Reserve near Manaus — hereafter Reserva Ducke (MDK), as part of the Anglo-BRazilian Amazonian Climate Observation Study (ABRACOS, Gash et al., 1996). Both data sets are available from the Oak Ridge National Laboratory Data Archive Center (Tomasella et al., 2008b). At RJA, data were collected during two measurements campaigns in August–September 1992 and April–June 1993 and measurements were taken at $(2.3; 6.1; 11.6; 15.7; 21.3; 35.0)$ metre above ground; at MDK, the measurement campaign occurred in August–September 1991 and sensors were installed at

$(5.0; 10.0; 15.0; 20.0; 25.0; 35.0)$ metre above ground; in both cases 2 to 3 sensors were installed in each level either East or West of the tower, and both sites used the same quantum radiation sensors of model SKP 215, skye Instruments Ltd, Powys, UK (Tomasella et al., 2008b).

Following Mercado et al. (2007), I only used data from the sensors east of the towers in the morning, and west of the towers in the afternoon, to reduce effects of tower on measurements; in addition, I only used model results from the same days of year as the measurements to avoid seasonal biases. Moreover, the diurnal cycle of any point measurement within the canopy is strongly influenced by local heterogeneities, and results at sub-daily scales can be dramatically affected by the Sun's azimuth and zenith angles (e.g. sun flecks when the sensor is aligned with an opening in the canopy). ED-2.2 does not solve azimuthal heterogeneity, therefore, I limit the comparison to either the average daily radiation relative to the top of the canopy, and the average of the relative radiation of overcast hours. To estimate whether a measurement was obtained under overcast conditions but with sufficient light, I applied the Weiss and Norman (1985) model to the measurements above canopy (35 m), and selected the times when the Sun was at least 10° above the horizon and the estimated direct radiation was zero.

The observed light profile is a result of the optical properties, which are more closely related to the accumulated tree area index (TAI) atop and beneath the sensors than height. Because neither site reported the TAI profile near the sensors during the intensive measurements, I used information reported in the literature near or at the sites to construct a rough estimate of these profiles based on observations and derived independently of ED-2.2 assumptions on tree allometry. For MDK, I used the leaf area density (LAD) profile reported by McWilliam et al. (1993) using destructive sampling from a plot about half way between Reserva Ducke and the eddy covariance tower site (M34); to my knowledge no measurement of wood area index exists near MDK, therefore, I applied a constant WAI:TAI ratio of 0.11 for the entire canopy, which was the ratio obtained via destructive sampling at La Selva, Costa Rica, as reported by Olivas et al. (2013). For RJA, I used the estimated profile of LAI-2000 reported by Simon et al. (2005), which is based on LICOR measurements taken at multiple levels at the eddy covariance tower site. Since LAI-2000 methods do not distinguish

between leaves and wood (Olivas et al., 2013), I did not apply any further correction.

3.2.2 Long-term dynamics

To evaluate the model ability to predict the plant community dynamics at equilibrium, I simulated potential vegetation starting from near bare ground conditions and carrying the simulations out for 511 years (1500–2011) with constant CO_2 mixing ratio above canopy (378 $\mu mol_C\, mol_{Air}^{-1}$), in order to give enough time for both the plant community and soils to reach dynamic equilibrium. All sites listed in Tab. 3.1 were used, with the exception of S83, which is similar to S67.

Using high frequency meteorological data implies a better characterization of sub-daily variability, which has been previously shown to be fundamental to predict more realistic productivity (Medvigy et al., 2010). While the data collection of several sites has been found to be representative of the long term climatology (Rosolem et al., 2008), the time series of the measurement is generally too short to capture extreme events, which may cause significant impacts on ecosystem functioning (Reichstein et al., 2013). For example, the annual rainfall range during the measurement period misses the most extreme events over a 40-year period for nearly all sites (Fig. 3.1), and even the sites with longer time series may also show a significantly narrower distribution (e.g. GYF and S67). Therefore, I developed a simple weather generator based on the high frequency measurements and the long-term rainfall from rain gauges near the towers. Although daily rainfall has some correlation with other variables, this correlation is inconsistent across sites and varies throughout the year. For instance, in incoming shortwave radiation becomes negatively correlated with rainfall at higher rainfall values in January for both GYF and S67 (Fig. 3.2a) in January (wet season at both places), whereas this pattern becomes weaker in September (dry season) and the variability of radiation is lower in GYF (Fig. 3.2b). Instead of fitting parametric models to predict all variables, I produced 40-year long time series for all sites by resampling days from the eddy flux tower period, using the day with the most similar rain for each month. For example, on March 24, 1972 the rain gauge near GYF reported 27.0 mm of rain. Then I searched the day with the closest amount of rainfall among all days in March with eddy flux measurements (March 23, 2006,

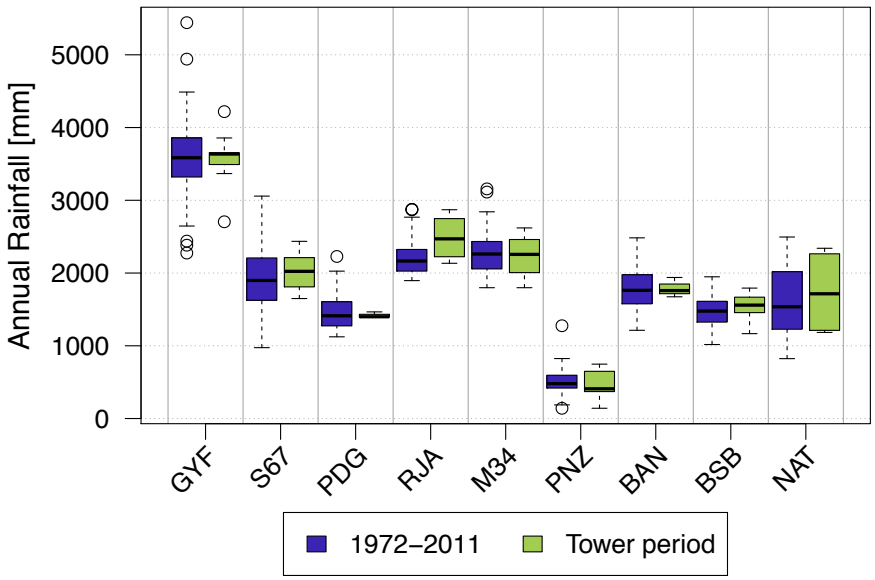

Figure 3.1: Box-and-whisker plot of annual rainfall between 1972 and 2011 using data from conventional weather stations (purple boxes, see main text for detailed description), and using only the period with high frequency meteorological data (green boxes).

when it rained 26.6 mm), and copied all variables from March 23, 2006 to March 24, 1972, scaling the rainfall so the total matches the reported value for March 24, 1972. In case multiple days are equally close to the observation, I randomly picked one of these days. The meteorological drivers were recycled 13 times without shuffling, and the first cycle was trimmed so the years in the last cycle would coincide with the simulation years.

To evaluate the equilibrium state of the potential vegetation, I assumed that the last 40 years of simulation (1972–2011) correspond to near-equilibrium conditions, and compared the average of the equilibrium period with available measurements and estimates from *in situ* measurements and/or remote sensing estimates of basal area, fine litter, combined soil carbon and coarse woody debris, above-ground biomass (AGB), and leaf area index (LAI). For basal area, I calculated total basal area directly from field measurements for those sites with available tree inventory, otherwise, I used estimates from published data sets. Since tree inventories exclude small individuals, I removed all simulated cohorts that fell below the minimum measured size. Fine litter, soil carbon and coarse woody debris were compared to values from previously published values. For

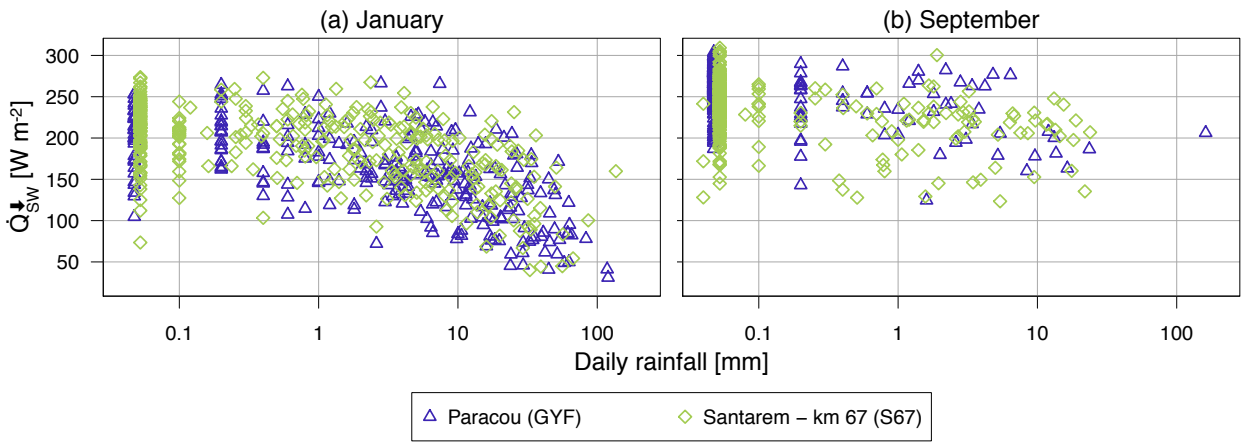

Figure 3.2: Example of scatter plot of daily means for the entire period with measurements, showing incoming shortwave radiation as a function of daily rainfall for GYF (purple) and S67 (green) in (a) January and (b) September; non-precipitating days are represented by the values near 0.05 mm day^{-1}.

those sites with field measurements, I estimated AGB using the allometric equation from Baker et al. (2004) that had been built on top of Chave et al. (2001), since this is the same equation used by ED-2.2. In case data from inventory was not available, I used estimates from site-level measurements published if they existed. In addition, I also compared the model results with multi-sensor carbon stock estimates developed by Baccini et al. (2012). The original data were reprojected to a regular longitude-latitude of $1/240^{\circ}$ resolution, and mean values for each site were estimated from pixels within 25 km from the tower[3] that were classified as forests for GYF, S67, RJA, and M34, or any natural vegetation for the other sites. The land classification was the land use class as of 2012 from the International Geosphere Biosphere Programme (IGBP), available at the MODIS-MCD12Q1 product (NASA/LP-DAAC, 2012). The land classification was also re-projected to the regular longitude-latitude grid of $1/240^{\circ}$ resolution using the MODIS Reprojection Tool (NASA/LP-DAAC and USGS/EROS, 2011) using the nearest neighbor algorithm. Finally, in-situ LAI estimates were obtained from bibliographic review, in addition to the MCD15A2 product (NASA/LP-DAAC, 2007), which was likewise reprojected to the $1/240^{\circ}$ resolution, and subsetted

[3]Given the coastal location of GYF and NAT, the centroid for these sites was moved 10 km south and west, respectively, to ensure enough points were sampled. Likewise, RJA centroid was shifted 10 km northeast due to its proximity to a large, heavily deforested area to the south and west of the tower.

at the same points used for above-ground biomass. All data available from 2002 to 2012 were used to determine average values for each month for each grid point, later aggregated to obtain the time average for each point. For both AGB and LAI, the expected value from remote sensing was obtained by taking the mean of all grid points, and confidence interval was estimated from 1000 simple bootstrapping samples.

In addition to the default long term simulations, which also used configurations shown in Tab. 3.2, I tested the effect of incorporating size, age, and strategy (PFT) to the long term dynamics and the variability and structure of the biophysical and biogeochemical properties within each site, as summarized in Tab. 3.3. Initial near bare ground conditions depend on the choice of the maximum number of cohorts per patch (N_p^{aim}). In case size structure is allowed ($N_p^{\text{aim}} > 1$), each PFT was initialized with a single cohort at minimum height (0.5 m) and population of 0.1 plant m^{-2}, and all cohorts are place in a single patch of age 0. In case no size structure is simulated, cohorts are assumed to be at maximum height, and the initial population was corrected to produce initial leaf area index of 0.1 $\text{m}^2_{\text{leaf}}\,\text{m}^{-2}$.

3.3 Results from short-term simulations

In this section I present a detailed comparison between model predictions and tower measurements and estimates, which is summarized in Fig. 3.3. From the skill diagram[4], one can observe that results are generally close to the average observations ($|\hat{\mu}_R| < 1$) and within predictive range ($R^2 > 0$). The one exception for all sites is the total ecosystem respiration, which shows large biases and large variance of residuals, yielding to low correlation with observations, as shown in the Taylor's diagram (Fig. 3.3b). Also from the Taylor's diagram (Fig. 3.3b), we observe that except for outgoing longwave radiation and sensible heat flux, the variability of the model results is lower than the observed variability. Nonetheless, except for ecosystem respiration, the correlation between

[4]In the skill diagram, the abscissa corresponds to the dimensionless bias ($\hat{\mu}_R$, Eqn. 3.2a) and the ordinate corresponds to the coefficient of determination or modelling efficiency (R^2, Eqn. 3.2b); concentric hemicircles are the relative root mean square error ($\hat{\varepsilon}$, Eqn. 3.2c); and the distance to the target point ($\hat{\mu}_R = 0; R^2 = 1$) is inversely proportional to the model ability to predict the variable of interest.

Table 3.3: Summary of different structure configurations used in the long-term variability simulations. The target number of cohorts per patch (N_p^{aim}) and number of patches per site (P^{aim}) are the strict maximum only when they are set to one, otherwise they are a target number: the actual number depends on how the observed heterogeneity and can be smaller or larger than the number shown here. Likewise, the plant functional type column contains all types at the beginning of the simulation.

Simulation	N_p^{aim}	P^{aim}	**Plant functional types**[a]
$Z_{01}A_{01}D_{02}$	1	1	C4G, MTR
$Z_{01}A_{01}D_{05}$	1	1	C3G, C4G, ETR, MTR, LTR
$Z_{80}A_{01}D_{02}$	80	1	C4G, MTR
$Z_{80}A_{01}D_{05}$	80	1	C3G, C4G, ETR, MTR, LTR
$Z_{80}A_{30}D_{02}$	80	30	C4G, MTR
$Z_{80}A_{30}D_{05}$[b]	80	30	C3G, C4G, ETR, MTR, LTR

[a] C3G: C_3 grass; C4G: C_4 grass; ETR: early-successional tropical broadleaf tree; MTR: mid-successional tropical broadleaf tree; LTR: late-successional tropical broadleaf tree.

[b] This simulation is the default ED-2.2 configuration for tropical forests.

model predictions and tower estimates for ecosystem respiration is generally high (c.f. Fig. 3.3b).

3.3.1 Radiation model

All sites measured either total outgoing shortwave radiation ($\dot{Q}^{\uparrow}_{\text{SW}}$) or both $\dot{Q}^{\uparrow}_{\text{SW}}$ and outgoing photosynthetically active radiation ($Q^{\uparrow}_{\text{PAR}}$), and model results for both variables are generally close to observations as shown in Fig. 3.4. The only exception was RJA, where observed $\dot{Q}^{\uparrow}_{\text{SW}}$ increased towards the end of the dry season, a feature not captured by the model. One possible reason for such discrepancy is that the model did not reach the low moisture threshold at the site, and as a result the plant community remained evergreen. RJA is often described as semi-deciduous forest (e.g. Andreae et al., 2002; da Rocha et al., 2009a), and a dry season increase in albedo had been previously reported at the same site during the ABRACOS campaigns in the early 1990s (Culf et al., 1996). In contrast, such decrease is not detectable by MODIS in undisturbed forests, which instead detects a slight increase in leaf area index during the later dry season (Fig. 3.5).

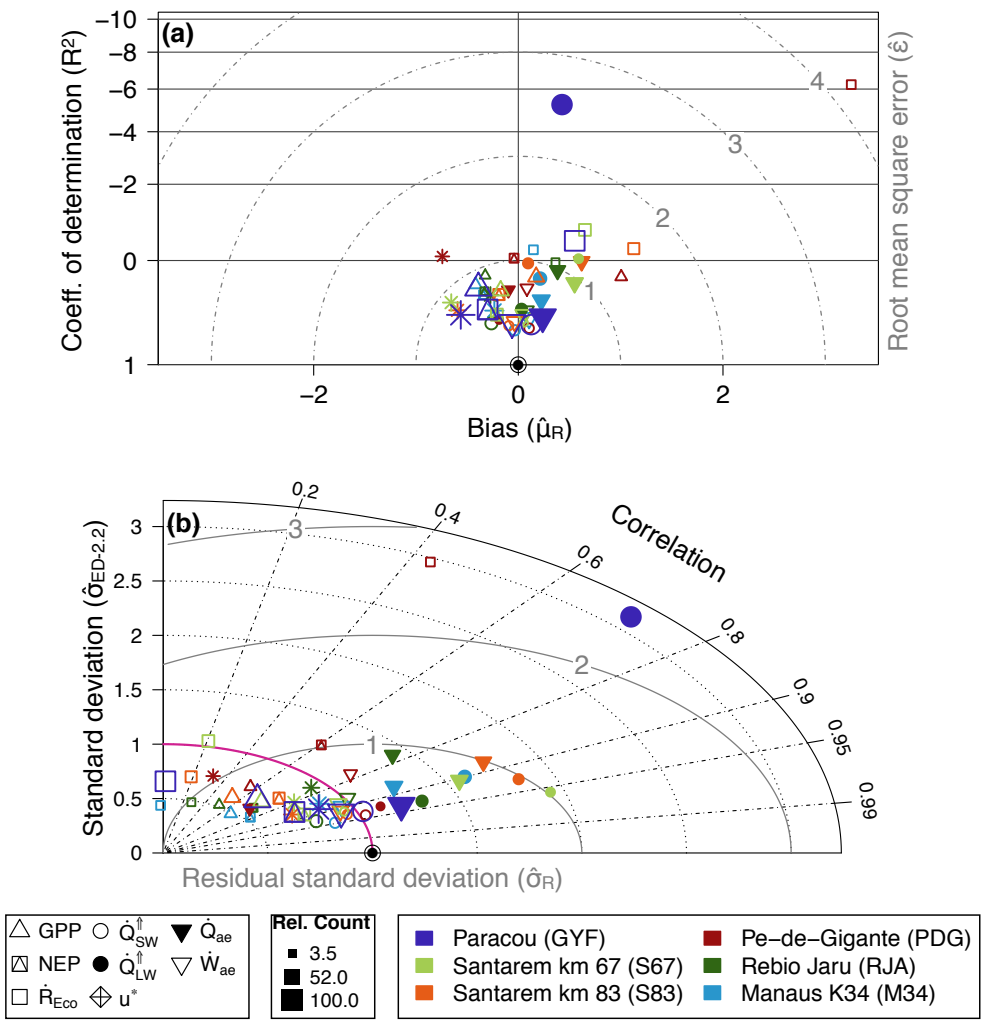

Figure 3.3: Summary of model predictions against tower measurements and estimates for all variables that were measured at all sites: GPP – gross primary productivity; NEP – net ecosystem productivity; $\dot{R}_{\mathrm{Eco}}$ – ecosystem respiration; $\dot{Q}^{\uparrow}_{\mathrm{SW}}$ – outgoing shortwave radiation; $\dot{Q}^{\uparrow}_{\mathrm{LW}}$ – outgoing longwave radiation; $u^{\star}$ – friction velocity; $\dot{Q}_{a,e}$ – sensible heat flux between canopy air space and air aloft; $\dot{W}_{a,e}$ – water vapor flux between canopy air space and air aloft. (a) Skill diagram using all observations and corresponding model predictions (See footnote 4). Point sizes are scaled by the number of observations relative to Paracou, which had the maximum number of valid measurements for all variables. (b) Taylor's (Taylor, 2001) diagram for the same observation. Note that the original Taylor's definition of root mean square error is equivalent to the standard deviation of the residuals, scaled by the standard deviation of observations ($\hat{\sigma}_R$).

In addition, the vertical profiles of daily averages of relative $Q^{\downarrow}_{\mathrm{PAR}}$ are relatively close to the simulations, especially considering the large uncertainties on the observed TAI profile and that the simulated years are not the same as the observations (Fig. 3.6). The subset of times without

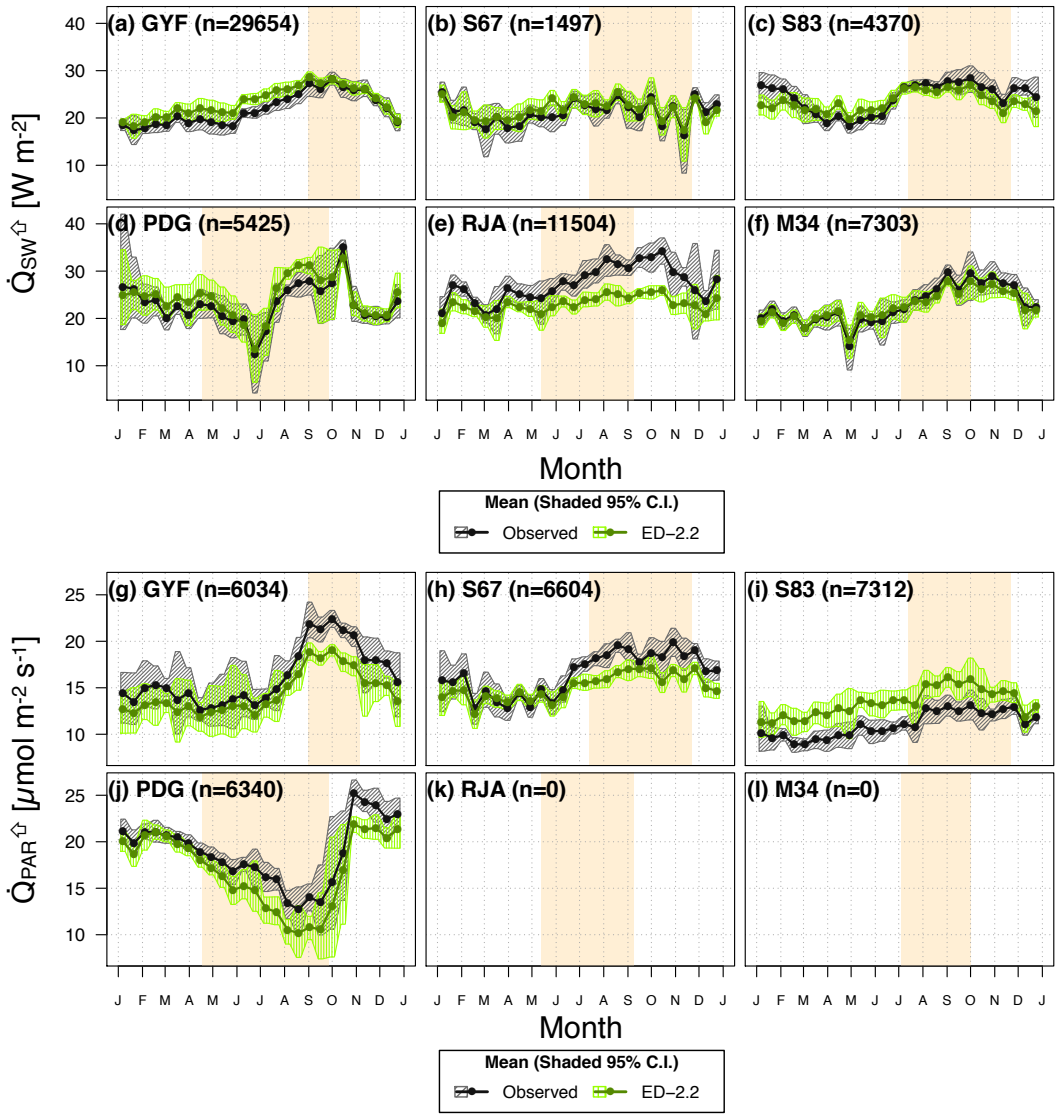

Figure 3.4: Mean annual cycle from fortnightly means of (a-f) outgoing shortwave radiation ($\dot{Q}^{\uparrow}_{\mathrm{SW}}$) and (g-l) outgoing photosynthetically active radiation ($Q^{\uparrow}_{\mathrm{PAR}}$) for all sites; bands are the 95% confidence interval of means. Numbers in parentheses are the total number of valid hours used to generate the plots. No direct measurements of $Q^{\uparrow}_{\mathrm{PAR}}$ were available for RJA and M34. Light yellow background corresponds to the site climatological dry season.

incoming direct radiation is less dependent on different meteorological conditions, and also less sensitive to horizontal heterogeneities particular to the point of measurement; as a result this subsample shows even better agreement with model predictions, particularly at RJA, where the average profile was measured at the same site as the original observations, albeit at different years. While limited by the observation constrains, this comparison suggests that the model is able to reasonably

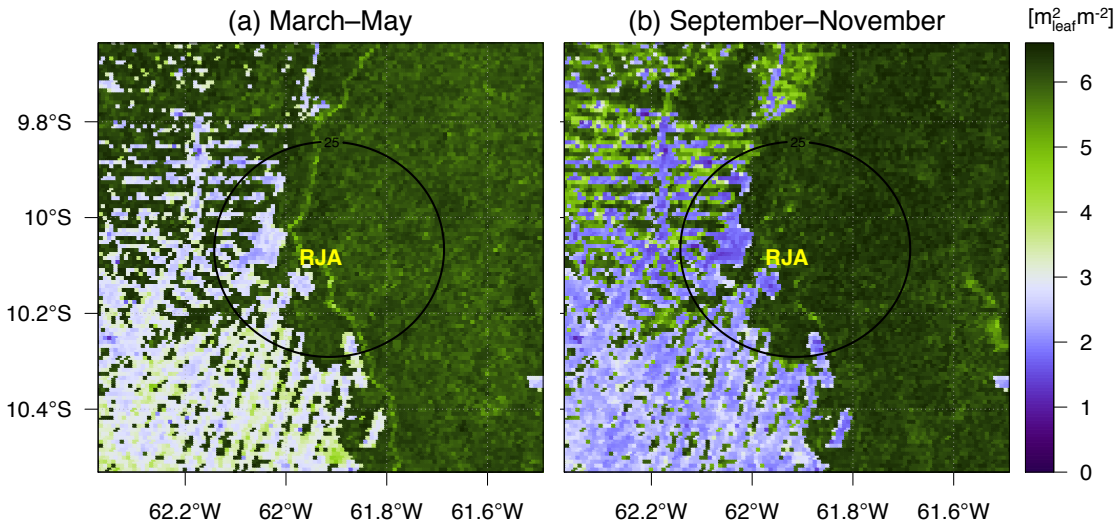

Figure 3.5: Seasonal average of leaf area index near RJA for (a) March-May and (b) September-November, calculated from MODIS MCD15A2 product between 2002 and 2012 (Collection 5, Shabanov et al., 2005; NASA/LP-DAAC, 2007). Averages included only pixels flagged as good quality, cloud state was defined and significant clouds were not present, and when the main method radiation transfer method was used. Low LAI regions in the western part of the domain are deforested areas.

reproduce typical light profiles.

For outgoing long wave radiation, ED-2.2 reasonably reproduces the daily variability for most sites (Fig. 3.7a-f), although the mode of the distribution is positively biased in GYF, S67, and M34 (Fig. 3.7a,b,f). Even though the differences in magnitude were generally small, longwave radiation has very low variability in the tropics, thus the observed deviations are significantly different. Moreover, the model overestimates the amplitude of the diurnal cycle at all sites (Fig. 3.7g-l), even those where the daily mean variability is similar (e.g. S83 Fig. 3.7i), with the main absolute difference occurring mostly during the afternoon hours.

3.3.2 Productivity and respiration

Significant discrepancies in NEP occurred at all sites for at least some part of the year, as it can be observed in Fig. 3.8, and the ability of the model to represent seasonality varied considerably across sites. The seasonal cycle is qualitatively similar in S67, S83, and RJA (Fig. 3.8b,c,e), with

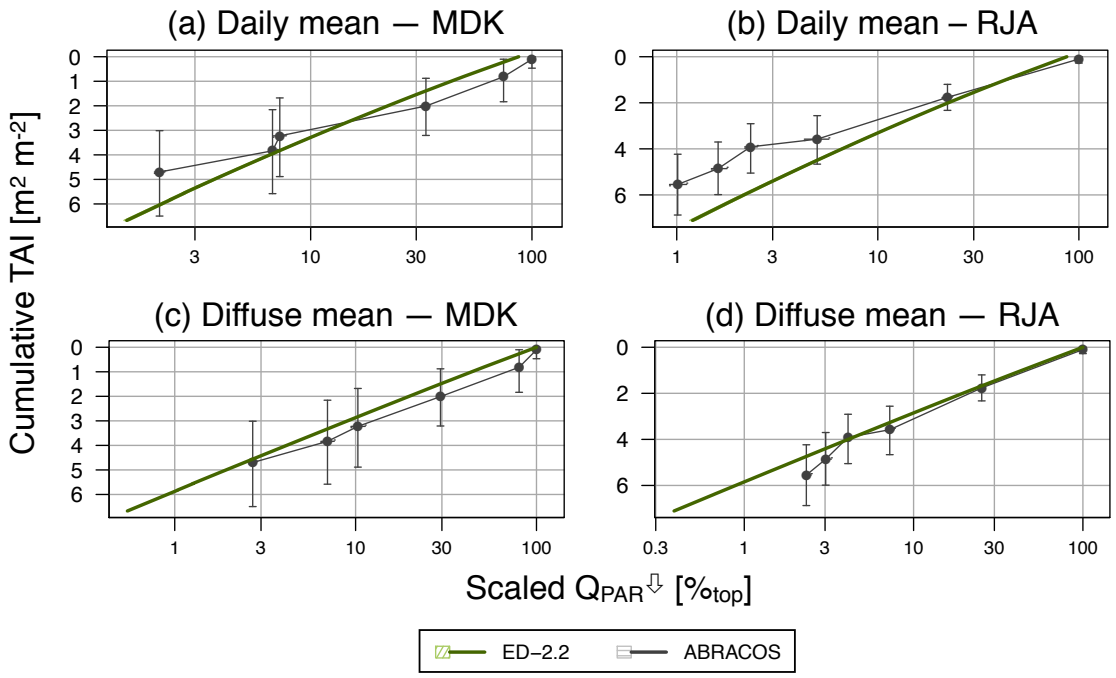

Figure 3.6: Comparison of downward photosynthetically active radiation relative to the top of canopy. (a,b) Average of daily accumulation; (c,d) average of times with diffuse radiation only for (a,c) Reserva Ducke (MDK) and (b,d) Rebio Jaru (RJA). Shaded areas in the model (barely visible) correspond to the 95% confidence interval, using simple bootstrap of the daily and diffuse hour subsamples, respectively. Horizontal whiskers in observed values also correspond to the 95% confidence interval of daily and diffuse subsamples, whereas the vertical whiskers correspond to the interval on leaf area index. In MDK the interval was estimated by bootstrap with replacement of the four profiles measured by McWilliam et al. (1993), whereas in RJA it was estimated using the t-distribution with four degrees of freedom, based on the mean and standard deviation values reported by Simon et al. (2005).

increased productivity during the dry season, although the model predicts a stronger source during the wet season; in M34 (Fig. 3.8f), seasonality is weak in both model and tower estimate, although ED-2.2 is closer to neutral; and in GYF (Fig. 3.8a) and PDG (Fig. 3.8d) the seasonality is reversed. Such differences in the model ability to represent seasonality occur because ED-2.2 invariably predicts negative or low positive productivity during the wet season and increase during the dry season, whereas tower-based estimates NEP do not always show such dependence on seasonal cycles.

To understand what caused the main contributions to the model discrepancy, I also assessed gross primary productivity, and ecosystem respiration and its components. From Fig. 3.9a-f, we

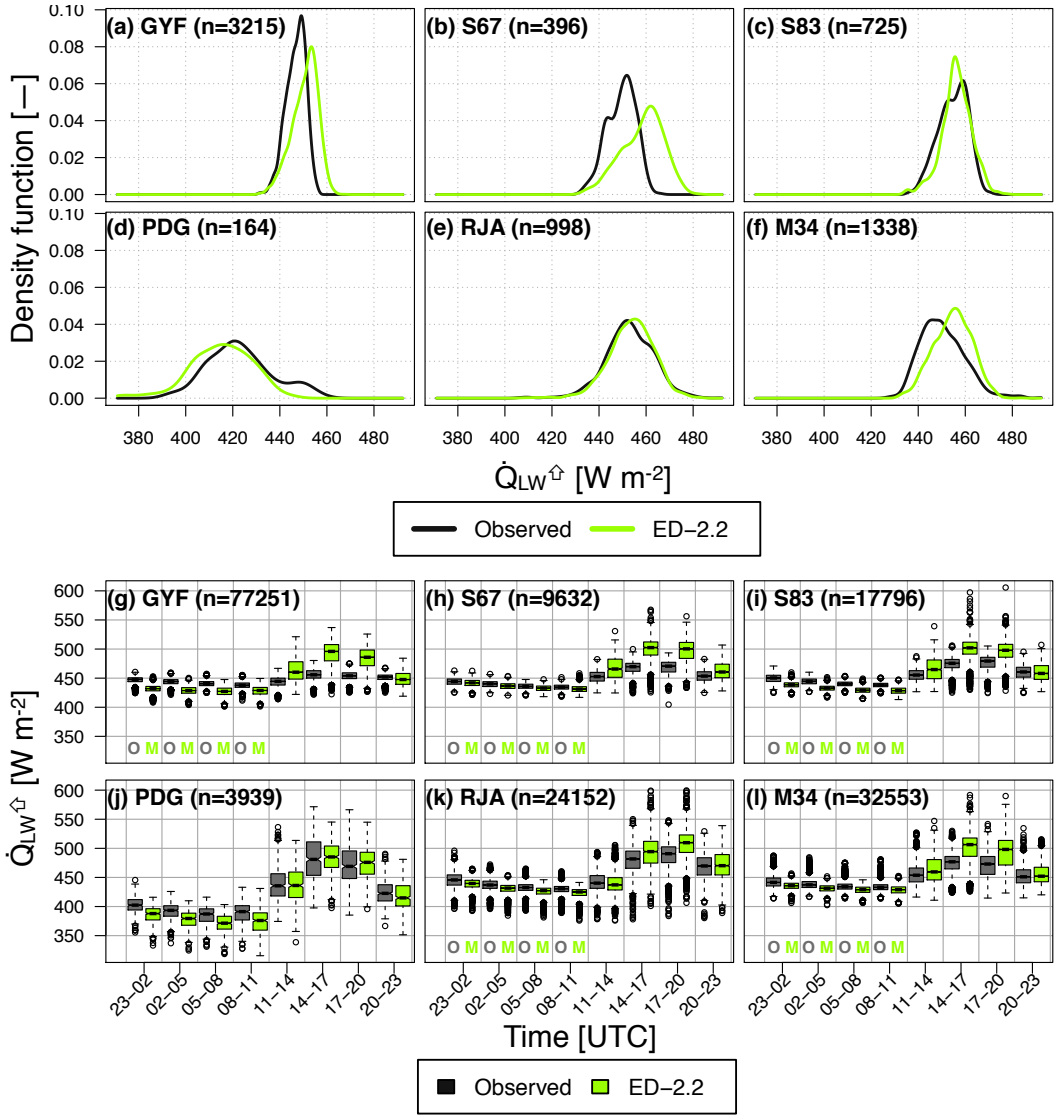

Figure 3.7: (a-f) Density function of daily means of outgoing longwave radiation. (g-l) Box-and-whisker plot of all data by time of the day. In both cases, grey curves and boxes (or boxes above grey "O") are tower observations, whereas green curves and boxes (or boxes above green "M") correspond to ED-2.2 model predictions; numbers in parentheses are the total number of valid days or hours used to generate the distribution.

observe that gross primary productivity is generally underestimated by the model; nonetheless, the model reproduces the weak seasonal cycle at GYF (Fig. 3.9a) and M34 (Fig. 3.9f). In contrast, the model significantly overestimates GPP in PDG, in particular during the dry season PDG (Fig. 3.9d). Also, GPP predicted by the model is within 10% of the observed magnitude at S67 and S83, although the model seasonality does not capture the decrease in productivity during the transition

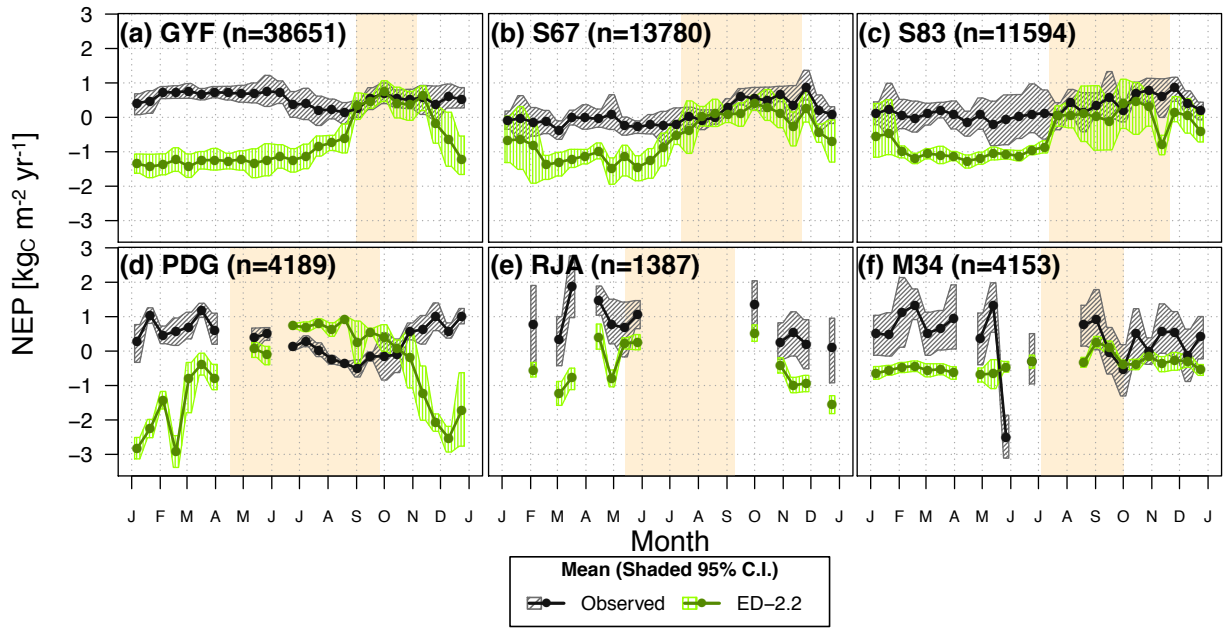

Figure 3.8: Mean annual cycle from fortnightly means of net ecosystem productivity predicted by the model and estimated from tower observations. The $u^{\star}_{\text{min}}$ thresholds for each site are presented in Tab. D.1. The sample size (n) corresponds to the number of valid hours using the published values of $u^{\star}_{\text{min}}$. Confidence intervals were built using hierarchical bootstrap sampling.

from wet to dry season (Fig. 3.9b-c). Despite these issues, the model reasonably represents the response to light in most sites except PDG (Fig. 3.9j); at this site tower-based estimates do not show a clear dependence on light at annual scale because of the strong seasonality in observations that are not captured by the model. Finally, neither tower observations nor the model show significant dependency of GPP on soil moisture for forest sites, and generally the correlation between daily GPP and daily mean air vapour pressure deficit (VPD) was positive and similar to the light response curve, suggesting that the model correctly captures that the forest sites were generally not limited by water during the period (not shown).

Ecosystem respiration from ED-2.2 is more seasonal than the tower estimates for all sites except RJA and M34 (Fig. 3.10a-f), where the amplitude is similar for the few periods with valid tower observations. The largest biases occurred at PDG, where the maximum respiration rates were more than twice the expected values from eddy covariance tower estimates (Fig. 3.10d). In addition, while the model predicts the highest respiration rates during the wet season for all sites

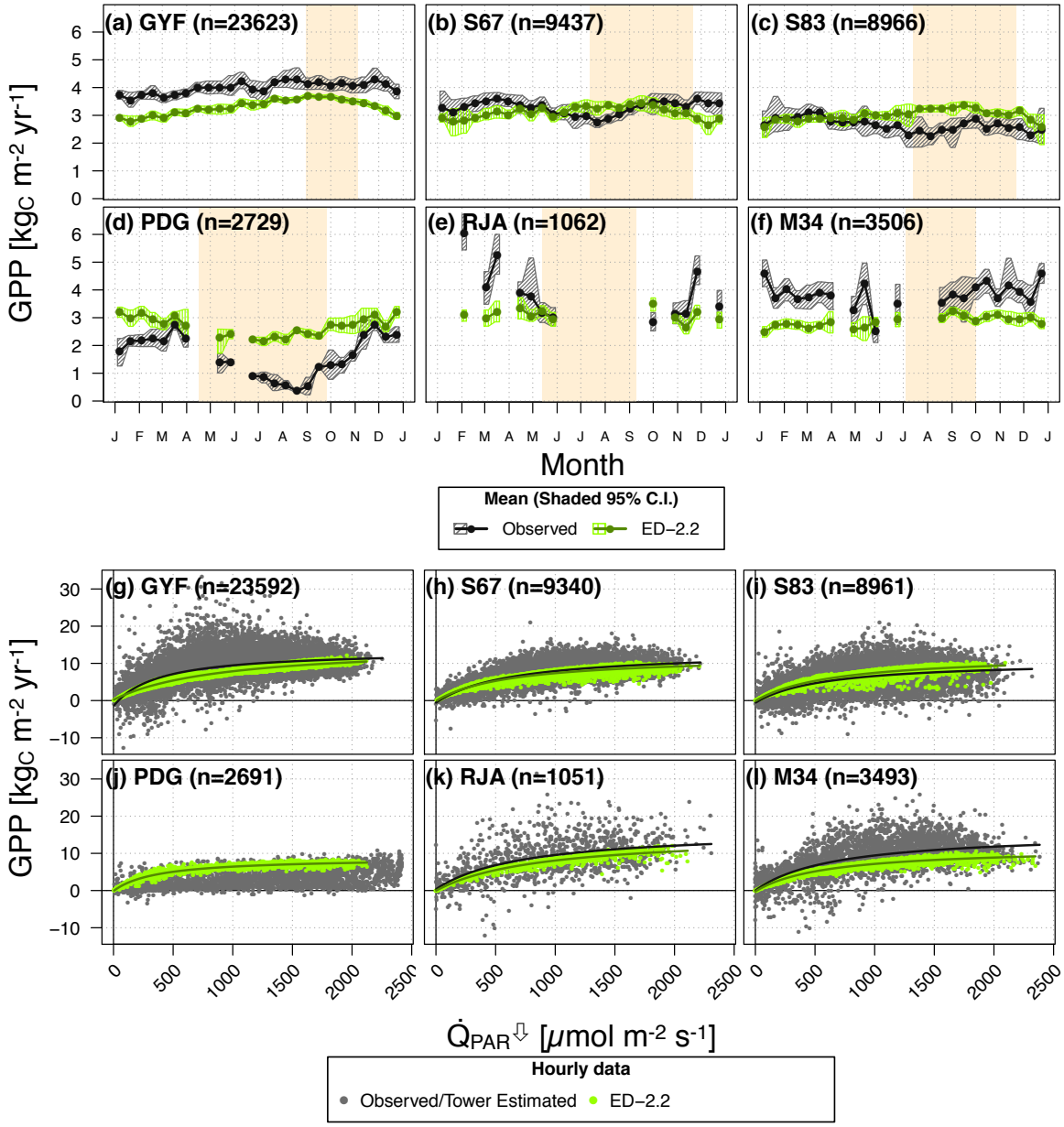

Figure 3.9: (a-f) Similar to Fig. 3.8, but for gross primary productivity. (g-l) Hourly averages of GPP as a function of incoming PAR for both model and tower based estimates; observed GPP was determined using the published $u^{\star}_{\text{min}}$ threshold. For panels (g-l), n is the number of valid hours for both GPP and PAR.

but M34, tower-based estimates do not show a consistent seasonal pattern: respiration reaches the maximum early in the dry season in GYF(Fig. 3.10a), whereas in S67, S83, PDG and RJA (Fig. 3.10b-e) the maximum occurs during the wet season. Due to the weaker nighttime turbu-

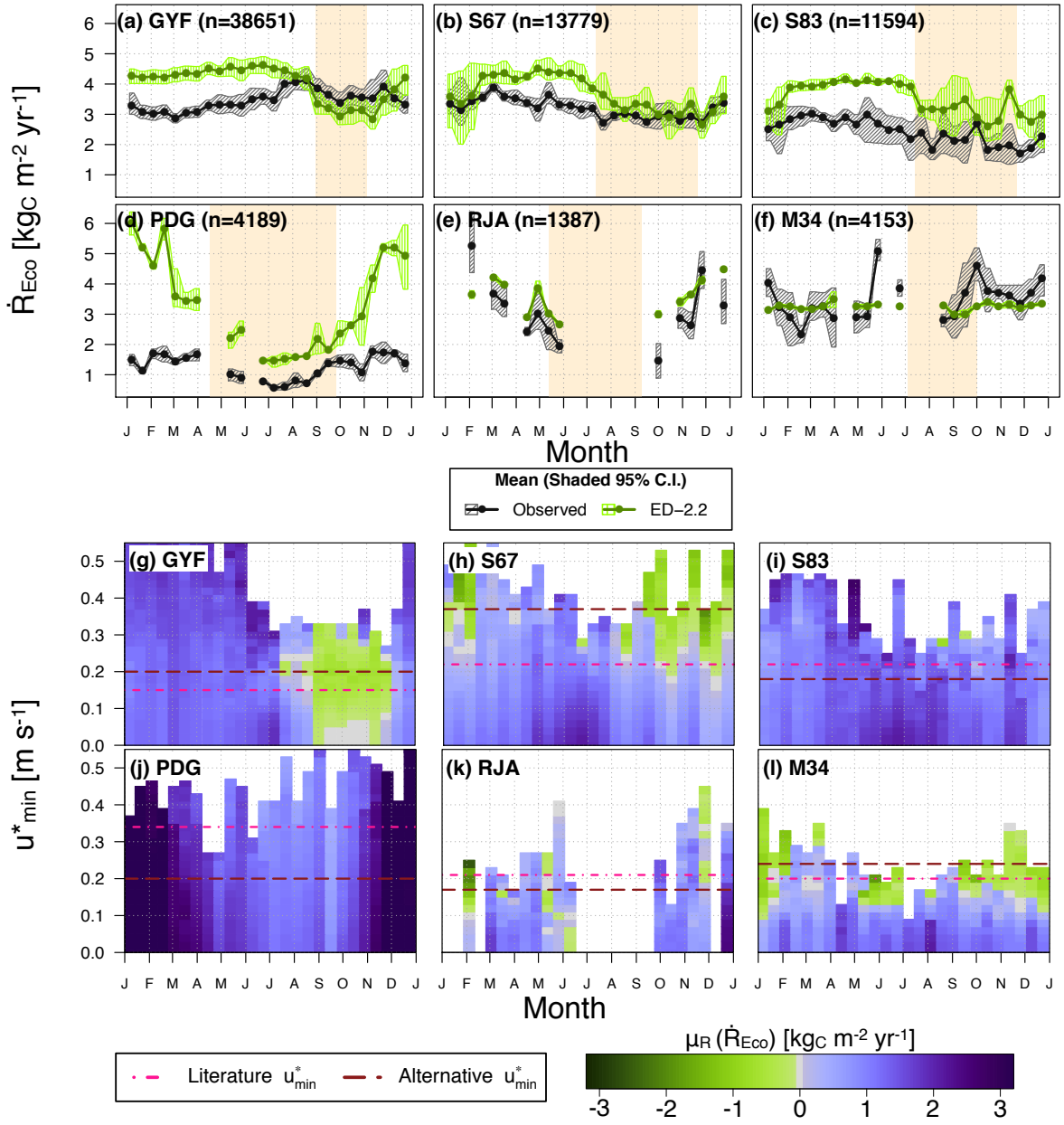

Figure 3.10: (a-f) Similar to Fig. 3.8, but for ecosystem respiration. (g-l) Average bias [$\mu_R(\dot{R}_{\mathrm{Eco}})$] between ecosystem respiration from ED-2.2 and tower estimates, as a function of time of year and different selections of $u^{\star}_{\mathrm{min}}$ ranging from 0 and 0.55 m s^{-1}. Dot-dashed violet lines correspond to the $u^{\star}_{\mathrm{min}}$ from previous studies, whereas dashed brown lines are the values using a standardized algorithm (c.f. App. D.1.1 and Tab. D.1).

lence, tower-derived respiration is particularly sensitive to the choice of $u^{\star}_{\mathrm{min}}$, and even though some methodologies exist to decide the appropriate threshold (e.g. Gu et al., 2005; Reichstein et al., 2005), most often the choice is arbitrary. To account for this uncertainty, I also evaluated the model

bias for a full range of $u^{\star}_{\mathrm{min}}$, between 0 and $0.55\,\mathrm{m\,s^{-1}}$. Changing $u^{\star}_{\mathrm{min}}$ had little influence in bias estimates for GYF (particularly during the wet season – December-July) and PDG(all year), mostly because nighttime turbulence is sufficiently strong so that sufficient data are retained; in contrast, S67 and M34 show significant variation in bias, and the sign of the mean bias changes within the range of plausible thresholds (Fig. 3.10h,l); changes in bias magnitude were also significant in S83, RJA (Fig. 3.10i), although not sufficient to switch the sign of the mean bias. Nevertheless, the seasonality of the model bias is a robust outcome, since it is present at a wide range of $u^{\star}_{\mathrm{min}}$ in all sites at a wide range of $u^{\star}_{\mathrm{min}}$ (Fig. 3.10g-l).

Eddy covariance fluxes cannot be directly used to evaluate each component of the total ecosystem respiration separately, therefore I compared the model results against results from other studies that focussed on measuring or estimating each component of the total respiration. The aim of this comparison is to evaluate the order of magnitude of the global mean, because most of these studies are limited in time and space, and for the components of autotrophic respiration, they are usually carried out at a small number of individuals and extrapolated to the plant community level using simplistic assumptions. Since M34, S67, and GYF had more intensive studies, I limited the comparison to these sites. For M34 and S67, I used the same results from the bottom-up assessment of the carbon cycle compiled by Malhi et al. (2009b,c), whereas for GYF I used results from multiple sources, while aggregating and scaling the reported values following the same methodology as Malhi et al. (2009b) for consistency.

Both the ED-2.2 model averages and the expected values from the bottom-up summary are shown in Tab. 3.4. Assuming that the 95% C.I. for the average of any variable X is roughly $\overline{X} \pm 2\,\mathrm{SE}_{\overline{X}}$, the mean ecosystem respiration predicted by ED-2.2 is within the expected range, albeit only marginally for S67; the expected value is higher in ED-2.2 than the bottom-up estimate for all three sites, and the variability of predicted terms in ED-2.2 amongst sites is smaller than the reference values. For GYF and M34, differences in heterotrophic respiration are the largest and explain most of the difference in the total respiration, whereas in S67 the positive bias in total respiration is due to autotrophic respiration. Within the autotrophic respiration, ED-2.2 consistently

Table 3.4: Comparison of respiration between ED-2.2 and published values for GYF, S67, and M34 ($\overline{X} \pm \mathrm{SE}_{\overline{X}}$ for any variable X). Values in parentheses are the standard error of the mean. For ED-2.2 the standard error was estimated from bootstrapping the annual means. Observed values for S67 and M34 are from Malhi et al. (2009b,c) and references therein. References for direct measurements and scaling to ecosystem for GYF are summarized below, and both scaling and error propagation and weighting were calculated using the same methodology as Malhi et al. (2009b).

Term	Paracou (GYF)		Santarém km 67 (S67)		Manaus K34 (M34)	
	Obs.	**ED-2.2**	**Obs.**	**ED-2.2**	**Obs.**	**ED-2.2**
Leaf	1.4 ± 0.4[b]	0.896 ± 0.004	0.7 ± 0.4	0.937 ± 0.005	1.0 ± 0.4	0.854 ± 0.009
Stem	0.504 ± 0.019[c]	0.94 ± 0.07	0.38 ± 0.10	0.89 ± 0.06	0.42 ± 0.10	0.79 ± 0.06
Root	0.67 ± 0.20[d]	0.542 ± 0.030	0.37 ± 0.08	0.534 ± 0.026	0.56 ± 0.20[i]	0.468 ± 0.029
Autotrophic	2.8 ± 0.5[e]	2.37 ± 0.10	1.5 ± 0.4	2.36 ± 0.09	2.0 ± 0.5	2.12 ± 0.09
Heterotrophic	1.10 ± 0.20[f]	1.66 ± 0.03	1.49 ± 0.14	1.432 ± 0.024	0.96 ± 0.12[i]	1.35 ± 0.03
Soil+CWD[a]	1.84 ± 0.23[g]	2.20 ± 0.05	1.65 ± 0.13	1.97 ± 0.04	1.46 ± 0.17[i]	1.821 ± 0.024
Ecosystem	3.8 ± 0.5[h]	4.03 ± 0.12	3.0 ± 0.4	3.80 ± 0.10	2.9 ± 0.5	3.47 ± 0.07

[a] ED-2.2 does not have a separate coarse woody debris pool, therefore I compare the sum of both.

[b] Leaf-level dark respiration was measured and reported by Stahl (2010). Leaf-level measurements were scaled to ecosystem scale using LAI-2000 measurements also by Stahl. Following Malhi et al. (2009b) and Lloyd et al. (2010) the value was scaled down by 34% to account for diurnal down-regulation of dark respiration.

[c] Individual-level stem respiration was measured and reported by Stahl (2010); Stahl et al. (2011). Values from both *terra firme* and seasonably flooded forest were included. Wet season and dry season values were weighted by the season length in 2008, also reported by Stahl et al. (2011). Although Stahl et al. (2011) had scaled to stand level, I recalculated it to be consistent with Malhi et al. (2009b), by finding the mean stem area index from the forest inventory, following Chambers et al. (2000, 2004). The stem area index was $1.07 \pm 0.03 [\mathrm{m}^2_{\mathrm{stem}}\,\mathrm{m}^{-2}]$.

[d] Taken as the difference between total soil respiration and soil heterotrophic respiration, following Malhi et al. (2009b).

[e] Sum of leaf, stem, and root respiration

[f] Sum of soil heterotrophic and coarse woody debris respiration. Soil heterotrophic respiration was estimated by Bréchet (2009) using trenching method, and coarse woody debris respiration was reported by Rowland et al. (2013).

[g] Soil respiration was reported by Epron et al. (2006) and Bréchet et al. (2011); CWD by Rowland et al. (2013)

[h] Sum of heterotrophic and autotrophic respiration from the bottom-up model. Tower-based estimate for GYF (2004-2012) is $3.48 \pm 0.12\,\mathrm{kg_C\,m^{-2}\,yr^{-1}}$ using the same $u^{\star}_{\mathrm{min}}$ as Bonal et al. (2008).

[i] No direct measurement of soil heterotrophic respiration existed for M34; values reported by Malhi et al. (2009b) are only indirect estimates.

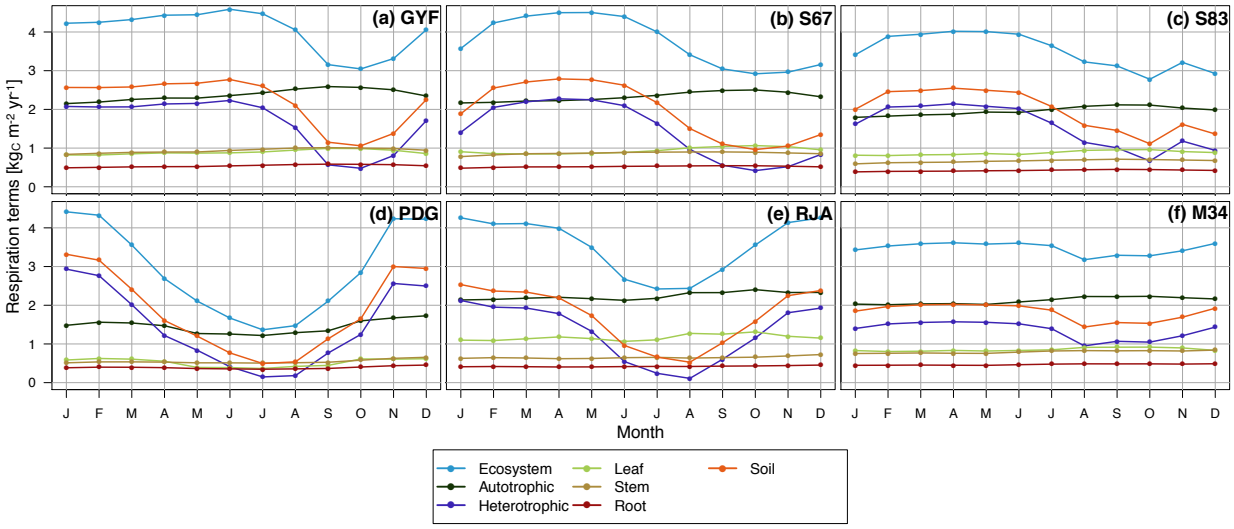

Figure 3.11: Mean annual cycle of respiration components, using all simulated times for all test sites.

predicts higher rates of stem respiration, which is compensated by somewhat lower leaf and root respiration in GYF and M34, so that the total autotrophic respiration is within the range expected from the bottom-up estimate. In S67, the reference leaf and root respiration are relatively low compared to GYF and M34, and as a result, ED-2.2 autotrophic respiration is significantly higher than the estimates. In summary, even though significant discrepancies exist in both autotrophic and heterotrophic respiration, the sign and magnitude of the biases are not consistent across sites, therefore it is not possible to attribute the differences in magnitude of the global averages to a single mechanism.

While the differences in global annual averages come from multiple processes, seasonality of respiration in ED-2.2 is nearly entirely due to heterotrophic respiration for all sites, as shown in Fig. 3.11. The parameterization of decomposition is a strong function of soil moisture near the surface (c.f. Eqn. 2.130 and Fig. 2.8), however ecosystem respiration in ED-2.2 is more strongly related to soil moisture than what is suggested by the observations (Fig. 3.12).

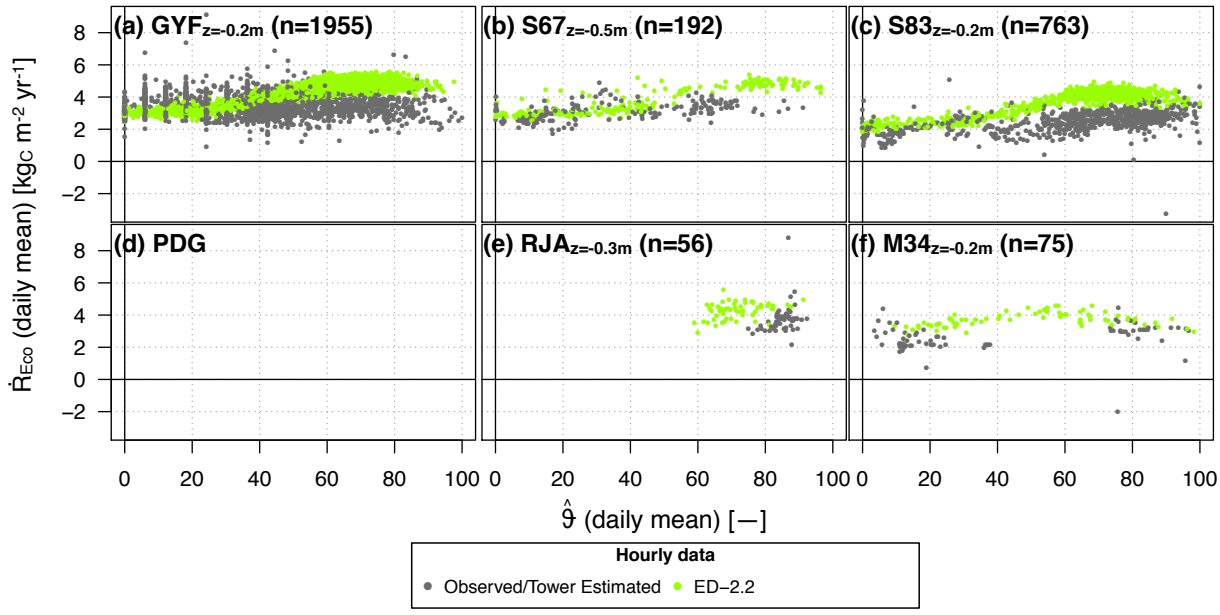

Figure 3.12: Daily mean ecosystem respiration for all sites as a function of daily mean soil moisture near 20 cm, here presented as relative soil moisture ($\hat{\vartheta}$, Eqn. 2.129); in this case n is the number of valid days for both $\dot{R}_{\mathrm{Eco}}$ and $\hat{\vartheta}$.

3.3.3 Water cycle

Both the seasonal and diurnal cycles are well represented in all forest sites, particularly during the dry season. the model correctly represents increased water flux during the dry season in S67 (Fig. 3.13b), S83 (Fig. 3.13c), and M34 (Fig. 3.13f), and that water flux does not increase during the dry season in GYF (Fig. 3.13a) and RJA (Fig. 3.13e), although the model underestimates the fluxes during the first wet season in GYF and overestimates the flux during the early wet season in RJA. In PDG (Fig. 3.13d), the model has good agreement during the wet season and early in the dry season, but it overestimates the flux during the later part of the dry season. The overestimation is a consequence of the model not shedding a significant fraction of leaves: the model predicted a reduction of 25 % of LAI during the dry season of 2001, whereas it did not predict any shedding during the dry seasons of 2002 and 2003 (not shown).

From Fig. 3.14, we observe that at all sites, most of the flux leaving the canopy during the dry season is due to transpiration, with relative contribution varying from $70-75\%$ of total flux

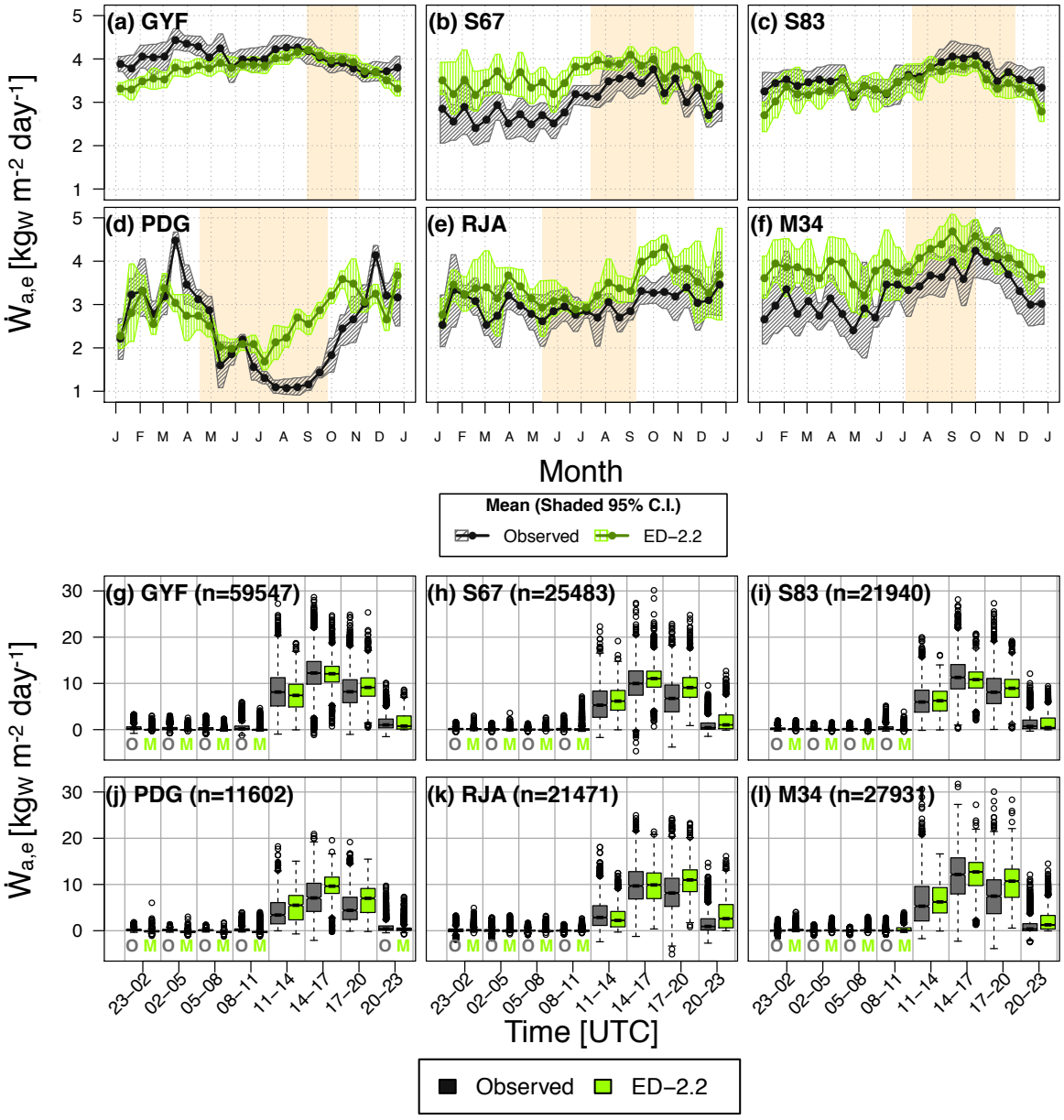

Figure 3.13: (a) Mean annual cycle of water flux at the top of canopy for all sites; bands are the 95% confidence interval of means, and pale yellow background corresponds to the dry season. (b) Box-and-whisker plots of water flux by period of day; grey boxes (or boxes above grey "O") correspond to the observed distribution and green boxes (or boxes above green "M") correspond to model distribution. The number of of valid hours used to generate the distribution is shown in (b), but it is the same for both plots.

at the wettest forest sites (e.g. GYF and M34, Fig. 3.14a,f), to above 90% at PDG (Fig. 3.14d).

Conversely, during the wet season evaporation of intercepted water at the leaf surface contribute

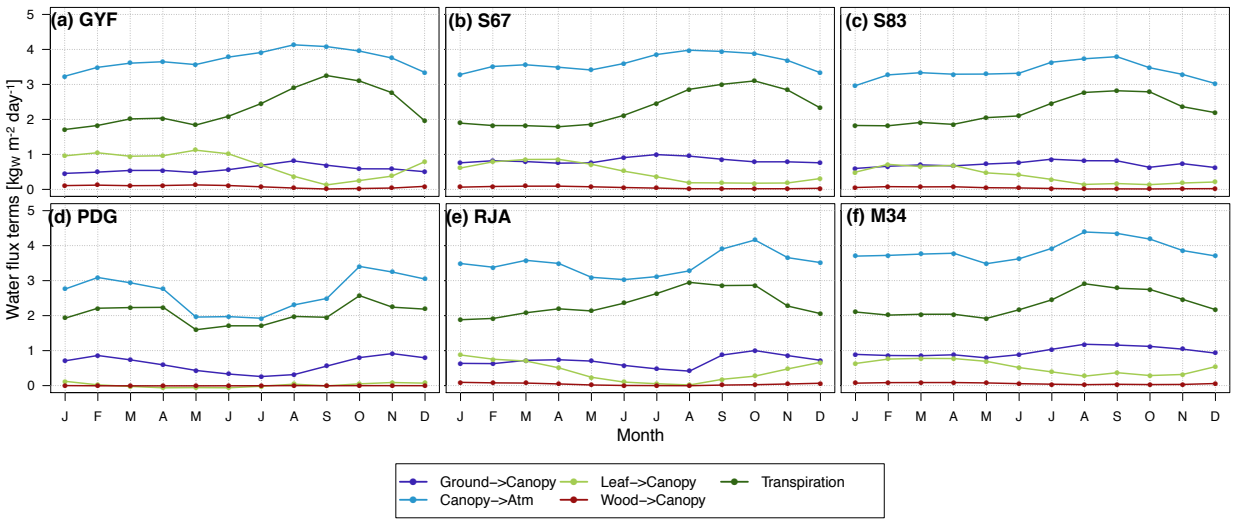

Figure 3.14: Mean annual cycle of components of the water vapour flux, using all simulated times for all test sites.

with as much as $25-30\%$ of the total water flux at the forest sites (e.g. GYF and S67, Fig. 3.14a,b). One exception is PDG (Fig. 3.14d), where leaf evaporation contributes little even during the wet season, and seasonality of soil evaporation is stronger than at forests. Seasonality of transpiration rates show a maximum during the dry season, which is a direct response to light availability for photosynthesis.

To evaluate the canopy air space storage of water, I used the canopy profiles measured at the S67 tower between 2002 and 2006 (Hutyra, 2007; Hutyra et al., 2008). Like the water flux, there is a very good agreement particularly during the dry season, whereas the wet season tends to be somewhat drier than the observations (Fig. 3.15a). Nevertheless, the mean diurnal cycle is generally well captured (Fig. 3.15b).

Since soil moisture has generally less diurnal variability, I used daily averages for comparing with observations. Using the closest level to 50 cm and looking at the general distribution of daily values, we observe a large variation in the results, ranging from very significant overestimations in GYF (Fig. 3.16a) and S67 (Fig. 3.16b), moderate overestimation in S83 (Fig. 3.16c), significant underestimation in RJA(Fig. 3.16e), and good agreement in M34 (Fig. 3.16f). Such discrepancies are strongly related to hydraulic properties of the soil. In ED-2.2, soil moisture cannot be less than

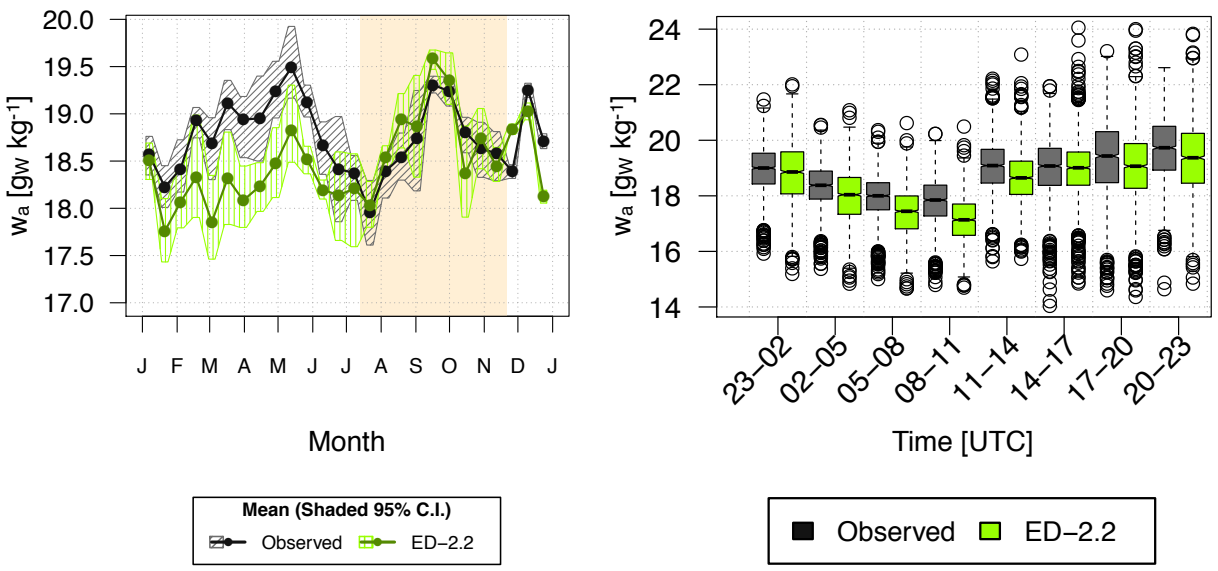

Figure 3.15: (a) Mean annual cycle of average canopy air space specific humidity and (b) box-and-whisker plots of water flux by period of day for Santarém km 67 (S67, $n = 30507$). Notation is the same as in Fig. 3.13.

the residual soil moisture (ϑ_{Re}) and porosity (ϑ_{Po}), and for sites with the largest discrepancies, a large fraction of soil moisture values falls below the model ϑ_{Re} (GYF and S67, Fig. 3.16a-c) or above ϑ_{Po} (RJA, Fig. 3.16e). Although the absolute water content is important for determining the total mass and internal energy of soil layers, most processes in ED-2.2 including photosynthesis and decomposition depend on either soil matric potential (Ψ, Eqn. 2.35a) or the relative soil moisture ($\hat{\vartheta}$, Eqn. 2.129). Soil retention curves were not available for all sites, therefore I did not compare the soil matric potential. To estimate the relative soil moisture from observations, I assumed that the minimum hourly soil moisture for the entire period with measurements was sufficiently close to dry air, and that the maximum hourly measurement was sufficiently close to porosity. The Kolmogorov–Smirnov statistic of daily means decreased in all sites, and the distribution of relative soil moisture is particularly close in S83 (Fig. 3.16i), RJA (Fig. 3.16k) and M34 (Fig. 3.16l), whereas distribution of dry events are underestimated in GYF (Fig. 3.16g) and overestimated in S67 (Fig. 3.16h).

Most sites have measurements only near the surface, and in general the model has moder-

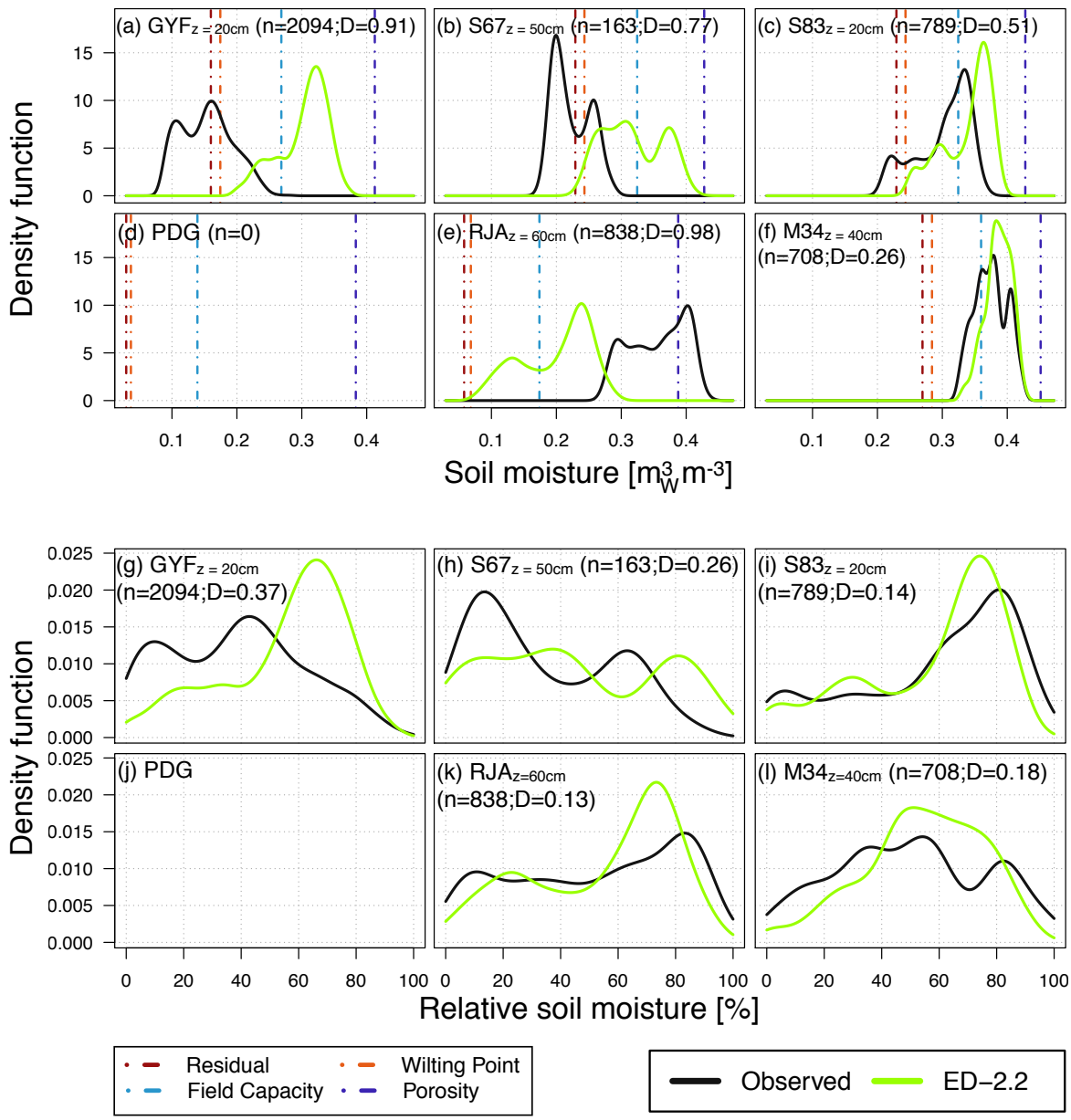

Figure 3.16: Empirical density functions of daily soil moisture for the closest depth to 50 cm that had data: (a-f) volumetric soil moisture; (g-l) relative soil moisture, calculated using Eqn. (2.129) for ED-2.2, and assuming that the minimum and maximum observed moisture were the actual residual soil moisture and porosity. Vertical lines in (a-f) correspond to ED-2.2 values for residual moisture, permanent wilting point, field capacity, and porosity based on sand, clay, and silt fractions. In parentheses are the number of daily averages used to draw the empirical density functions (n), and the Kolmogorov–Smirnov statistic of the daily mean distribution.

ate positive bias at the top 1 m (Fig. 3.17a) and the model variability is less than the observed ((Fig. 3.17)b). Nonetheless, the model is able to explain a significant fraction of the observed

variability, as observed by $R^2 > 0.5$ and high correlation (> 0.6) with observations. Very few observations existed below 1 m: in GYF soil moisture was measured at 2.6 m and has very low bias in relative moisture ((Fig. 3.17)a) and somewhat better agreement in volumetric soil moisture compared to the top layers (not shown); in S67 the model predictions always have higher variability compared to observations ((Fig. 3.17)b), but no clear pattern as function of depth emerges; errors are relatively constant until 5 m but the model has a significant negative bias and negative coefficient of determination at 7 m ((Fig. 3.17)a), which is associated with particularly high interdiurnal variability compared the observations ((Fig. 3.17)b).

3.3.4 Heat and temperature

ED-2.2 overestimated sensible heat flux at all forest sites. This positive bias affects the entire distribution of daily averages, as shown by the Q–Q plot in Fig. 3.18a, with daily average values about 10% higher than observations at GYF, RJA, and M34; biases in S67 and S83 are significantly larger, and daily averages are roughly twice the observations, whereas hourly averages are on average 50% higher (not shown). In PDG, on the other hand, the model shows not only significant deviation from observations but also changes in the sign of bias. At the lower end of the distribution, negative daily averages of sensible heat flux are often close to zero in ED-2.2, whereas observations indicate significantly more negative values, a characteristic also observed in GYF; intermediate values tend to be close to observations but the high end of the distribution is substantially lower for ED-2.2. In Fig. 3.18 we observe a similar pattern for hourly averages: bias is generally positive at all hours at the forest sites, whereas the bias is positive during the night and negative during the day. Despite biases occurring at both day and night, the fraction of variance explained is higher during the day than during the night, except for S83; this result is expected since values have been scaled by the standard deviation, which tends to be lower during the night (not shown).

While sensible heat flux was significantly higher than observations in S67, the fortnightly means of canopy air space temperature are remarkably close to the observations during the wet

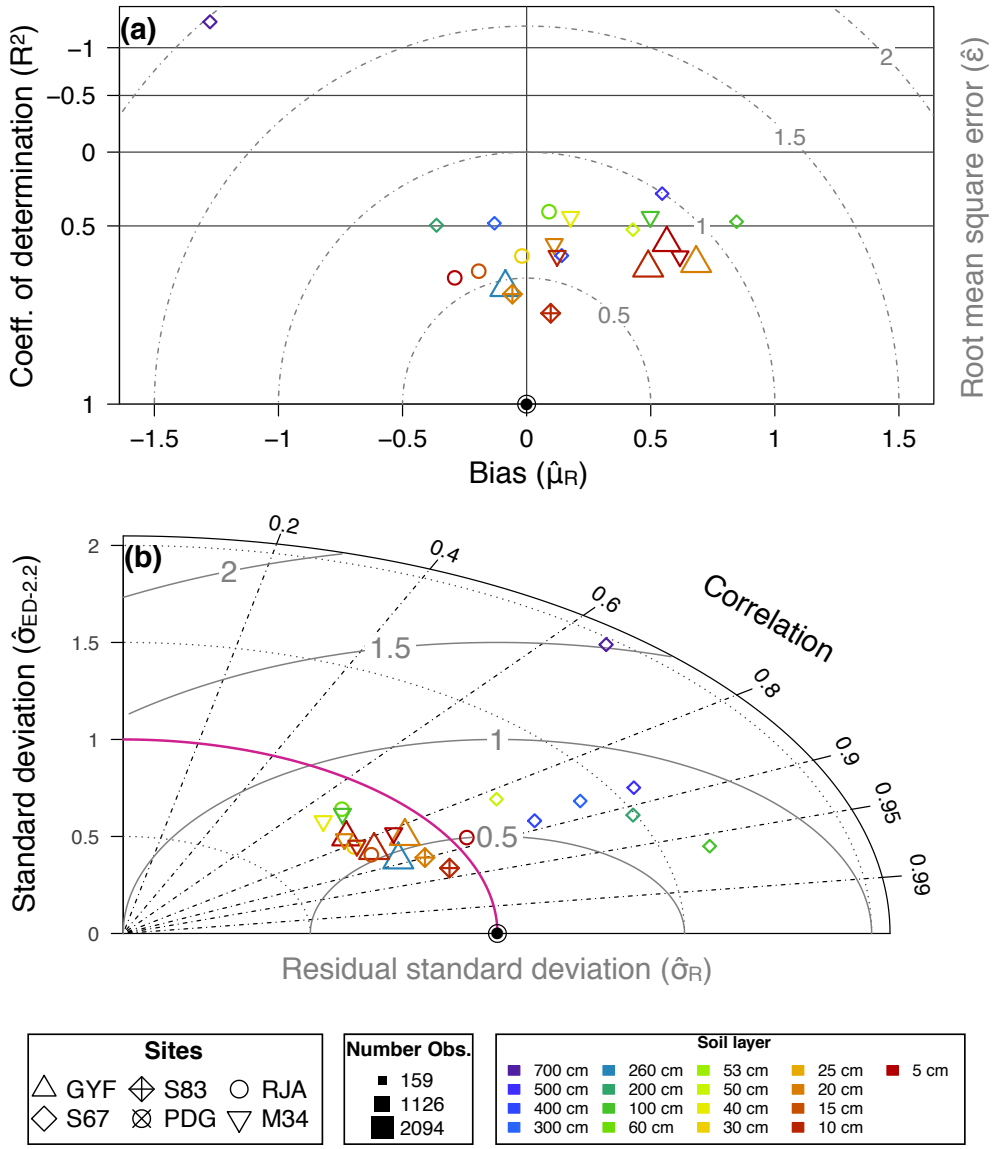

Figure 3.17: (a) Skill and (b) Taylor's diagrams of daily averages of relative soil moisture for all sites (shapes) and soil depths (colors).

season (Fig. 3.19a), although the model tends to overestimate the temperature during the dry season. Likewise, both the median and the range of temperatures for different times of day are close to observations except for afternoon, when the model predicts extreme high temperature events that are not reported in the observations. In addition, the model has relatively low bias ($\hat{\mu}_R(T_a) = 0.14$), high coefficient of determination ($R^2(T_a) = 0.73$) and overall reasonable characterisation of the distribution (Kolmogorov–Smirnov statistic: $D(T_a) = 0.11$).

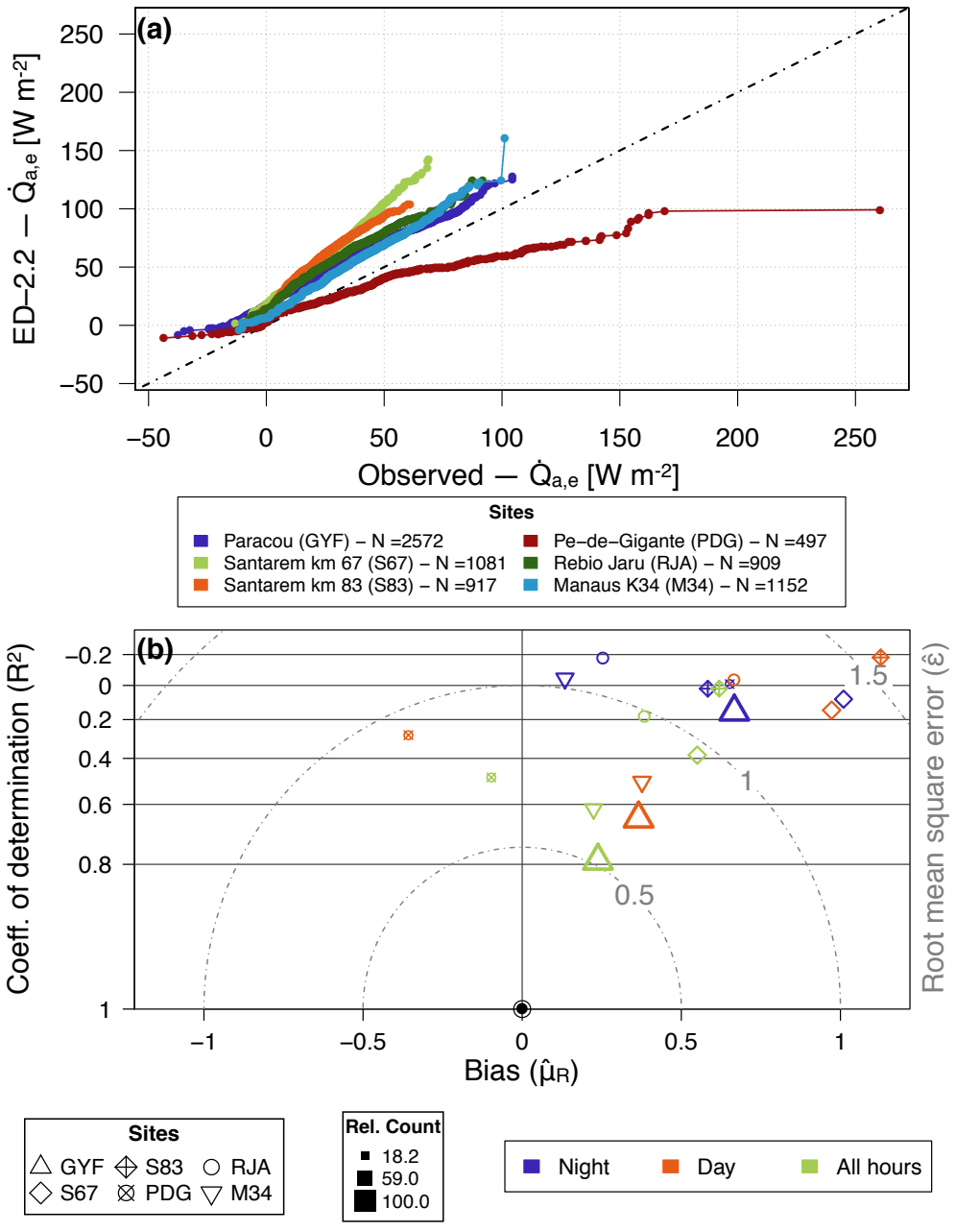

Figure 3.18: (a) Q–Q plot of daily averages of sensible heat flux ($\dot{Q}_{a,e}$) for all sites. Variable N at the legend corresponds to the number of valid days, and dot-dashed line is the 1:1 ratio. (b) Skill plot of hourly averages for all sites; in this plot daytime hours corresponds to all hours when the average Sun height was greater than 6°, whereas nighttime corresponds to when the Sun height was less than $-6°$; all hours also include times when the Sun was near the horizon. The relative count is the number of valid observations for each period relative to the number of observations in GYF, the site with most observations.

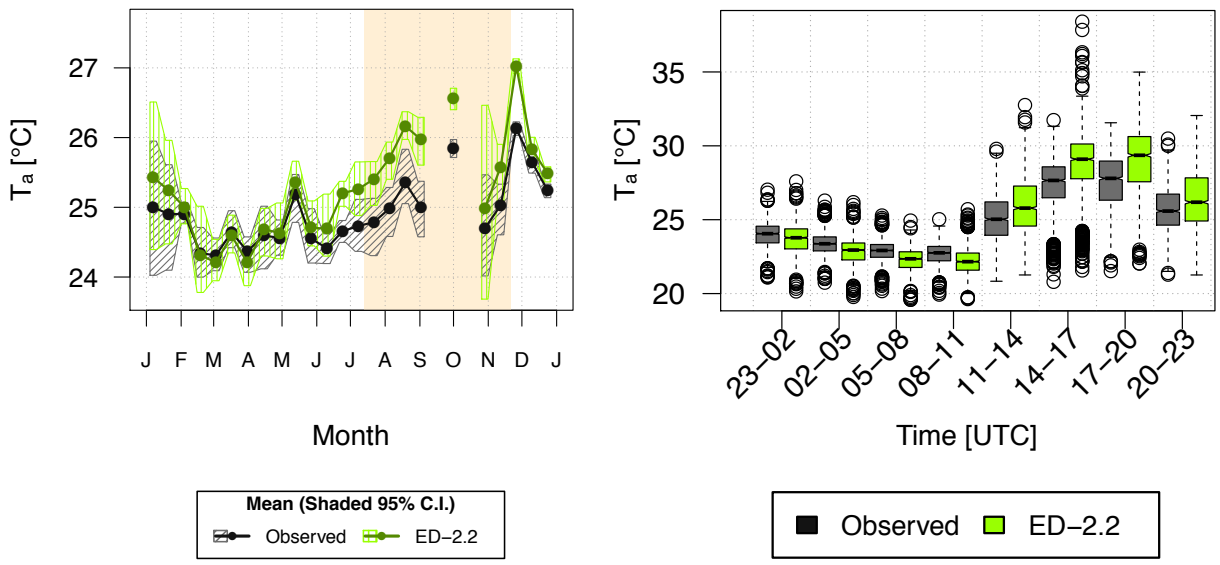

Figure 3.19: Comparison of canopy air space temperature at S67, based on 14,020 hourly averages: (a) mean annual cycle of canopy air space temperature and (b) box-and-whisker plots by the time of the day. The average dry season is shown as the yellow background in (a).

Soil temperature was reported only at GYF and S83, at two levels in each site. Mean soil temperature in GYF has a significant negative bias both near the surface (Fig. 3.20a; $\hat{\mu}_R = -1.6$) and at 53 cm deep (Fig. 3.20b; $\hat{\mu}_R = -2.9$), whereas biases in S83 are generally low (Fig. 3.20c-d; $\hat{\mu}_R \left(T_{s_{10}\,\mathrm{cm}}; T_{s_{40}\,\mathrm{cm}}\right) = (0.44; 0.29)$). In addition, the amplitude of the diurnal cycle is too large near the surface at both sites (Fig. 3.20a,c); at deeper layers, the amplitude of the diurnal cycle is substantially reduced, however the predicted amplitude within each time period is still larger than the observed (Fig. 3.20b,d), the reason being that the model predicts larger seasonal variations of temperature than reported at both sites (not shown).

3.3.5 Momentum

Comparison of friction velocity between ED-2.2 and observations showed consistent patterns across all sites: ED-2.2 predictions were both negatively biased (Fig. 3.21a) and showed lower variability compared to observations (Fig. 3.21b). Moreover, both the negative bias (not shown) and the low variability of hourly averages (Fig. 3.21b) occurred at night and day. Nonetheless, the

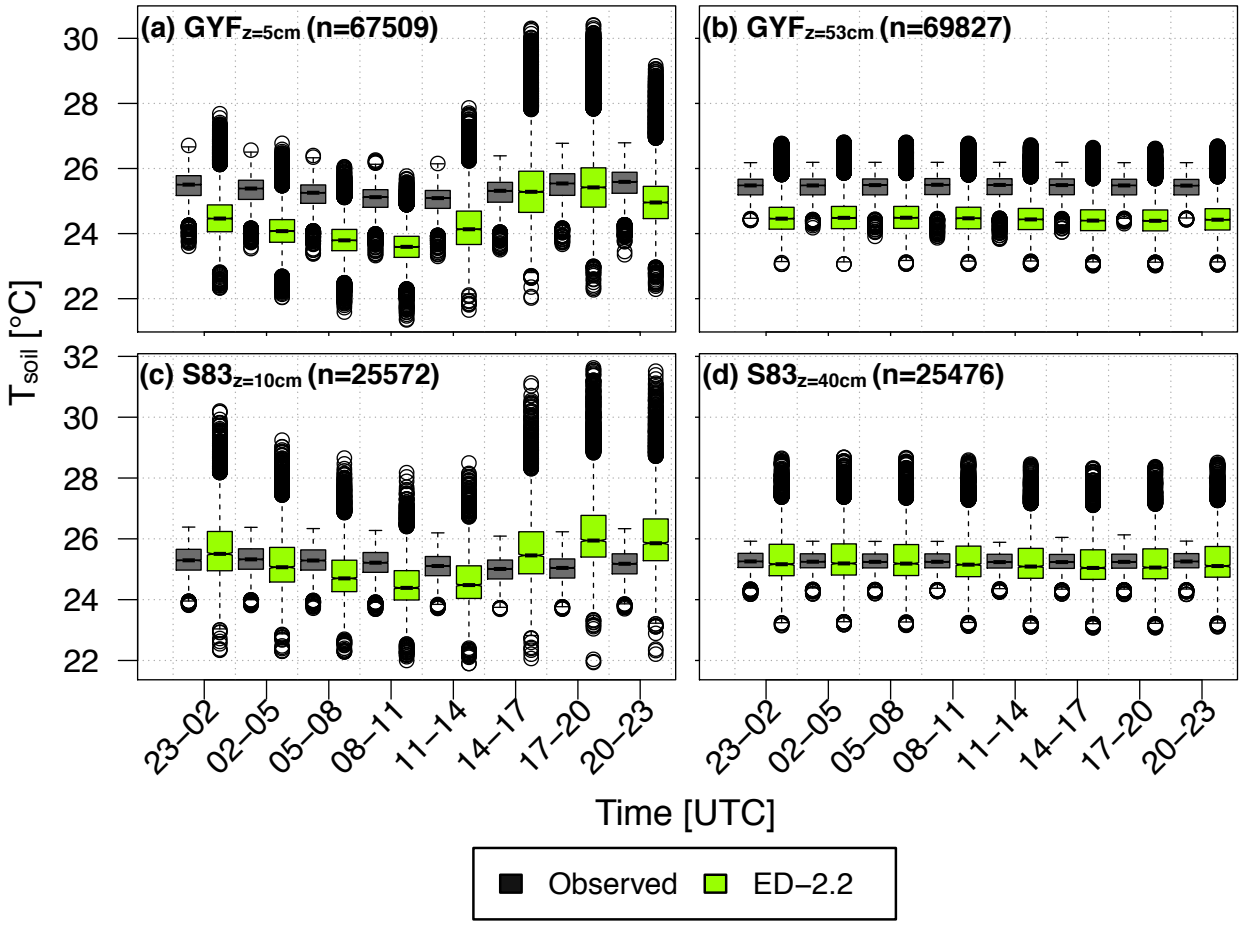

Figure 3.20: Box-and-whisker plot of soil temperature as a function of time of day: GYF at (a) 5 cm and (b) 53 cm deep, and S83 at (c) 10 cm and (d) 40 cm deep. The total number of hours (n) is shown in each panel.

model correlation with observations were relatively high during the day and when all hours were taken into account for all sites except PDG (Fig. 3.21b). Nighttime data, on the other hand, had generally lower correlation for all sites, which is partly due to extremely low variability in some sites. Moreover, the Q–Q plot shows that high turbulence extremes are generally missed by the model, and these differences are particularly large in GYF, the windiest site, but also significant in S67, S83, and PDG.

Momentum flux is seldom compared to observations in model evaluation; however, in ED-2.2 we allow enthalpy, water, and carbon dioxide to be stored in the canopy air space, therefore fluxes and storage in the canopy air space are directly affected by momentum transfer. Momentum flux

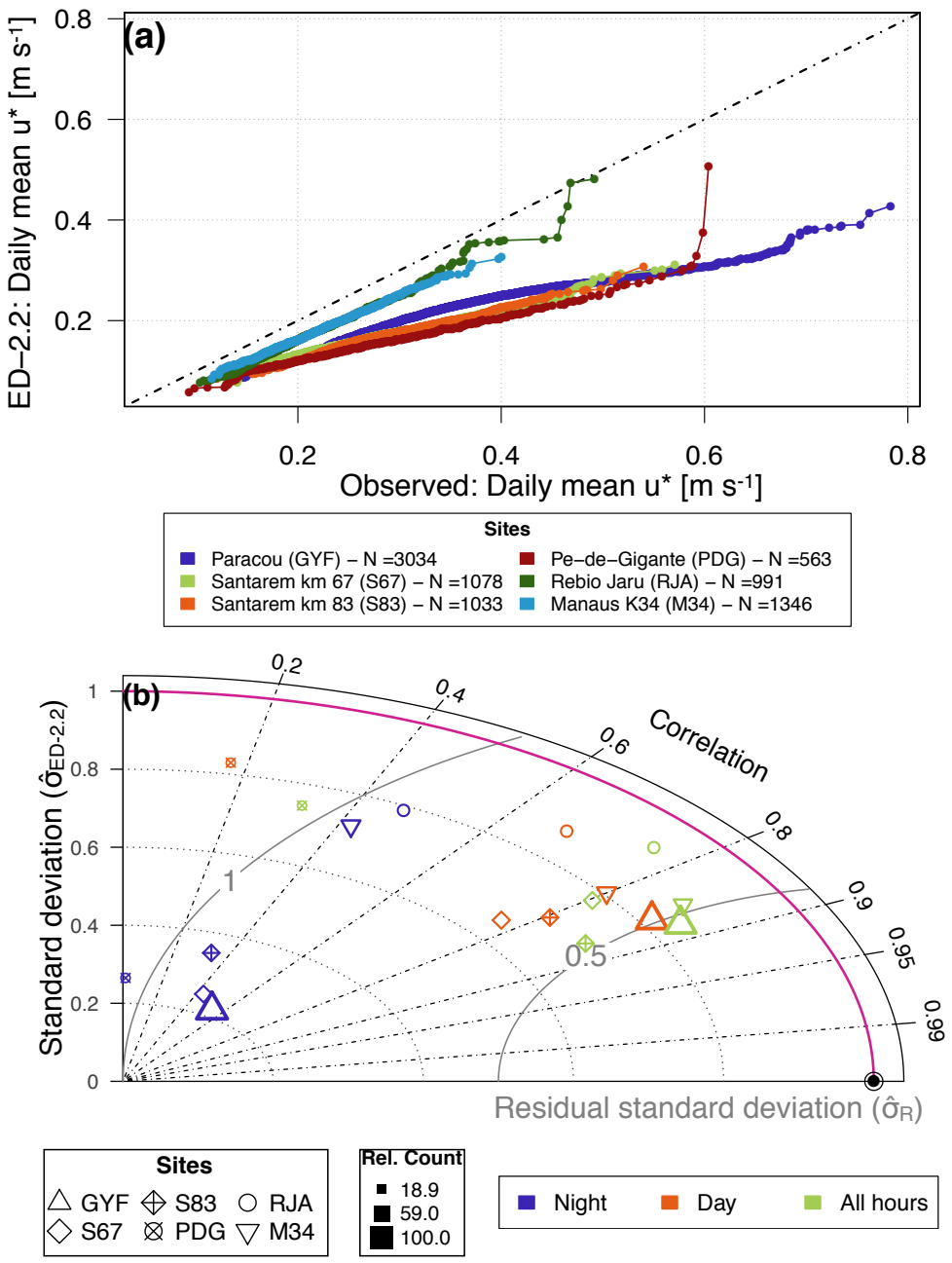

Figure 3.21: (a) Q–Q plot of daily averages of friction velocity ($u^{\star}$). Variable N at the legend corresponds to the number of valid days, and dot-dashed line is the 1:1 ratio. (b) Taylor's diagrams of hourly averages of friction velocity for all sites. See Fig. 3.18 for definition of daytime and nighttime hours.

is particularly during the night, when buoyancy at the top of the canopy is generally negative and forced convection is the only mechanism that allows air to leave the canopy air space. To evaluate

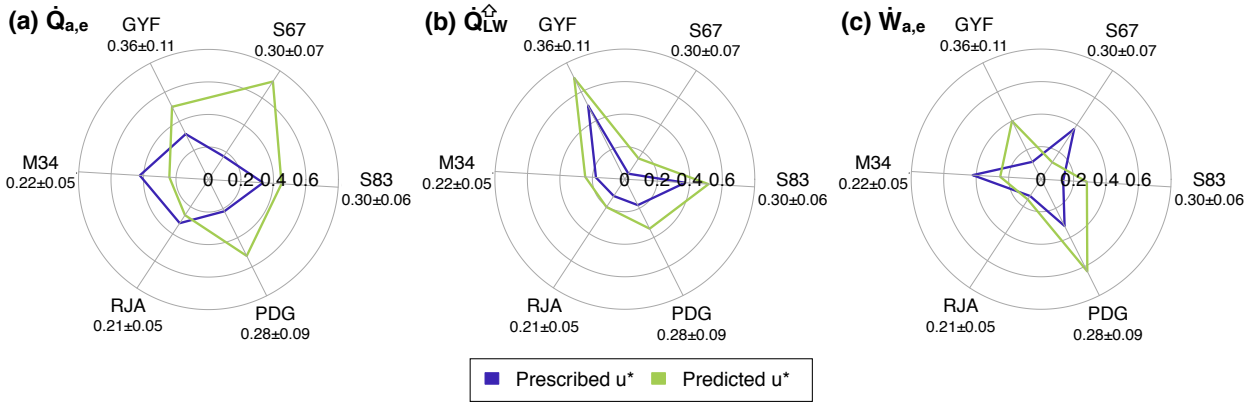

Figure 3.22: Comparison of the Kolmogorov–Smirnov statistic (D) for nighttime hourly averages using the predicted (green lines) and prescribed (purple lines) model: (a) sensible heat flux at the top of the canopy ($\dot{Q}_{a,e}$), (b) outgoing longwave radiation ($\dot{Q}^{\uparrow}_{\mathrm{LW}}$), and (c) water vapour flux at the top of the canopy ($\dot{W}_{a,e}$). Numbers beneath sites in indicate the mean and standard deviation (not standard error) of daily averages of $u^{\star}$.

the impact of properly representing friction velocity, I carried out the a set of simulations with the same configuration as the simulations presented in this section, with the exception of friction velocity, which was prescribed from the observations instead of using the algorithm presented in Sec. 2.4.4. The dimensionless scale ζ was determined from Eqn. (2.81) and other terms were calculated as presented in Sec. 2.4.4.

Imposing prescribed friction velocity had the most impact on nocturnal fluxes, which is expected: most of the mixing between canopy air space and free atmosphere occurs due to mechanical turbulence since the atmospheric profile at the top of the canopy is usually stable at night. The model has significant improvements in representing the distribution of sensible heat flux at the sites where the biases were the largest (GYF, S67, S83, and PDG, Fig. 3.22a); in addition the distribution of nighttime outgoing longwave radiation improved at all sites (Fig. 3.22a,b). The distribution of hourly nocturnal water fluxes improved at most sites, but not at S67 and M34 (Fig. 3.22c). These sites are characterized by very low nocturnal fluxes (0.13 and 0.013 $\mathrm{kg_W\,m^{-2}\,day^{-1}}$, respectively), and mean nocturnal flux predicted by ED-2.2 increased at all sites when the model was driven with prescribed mechanical turbulence, which improved the model prediction at the other sites, but not at S67 and M34 because the flux was indeed very small.

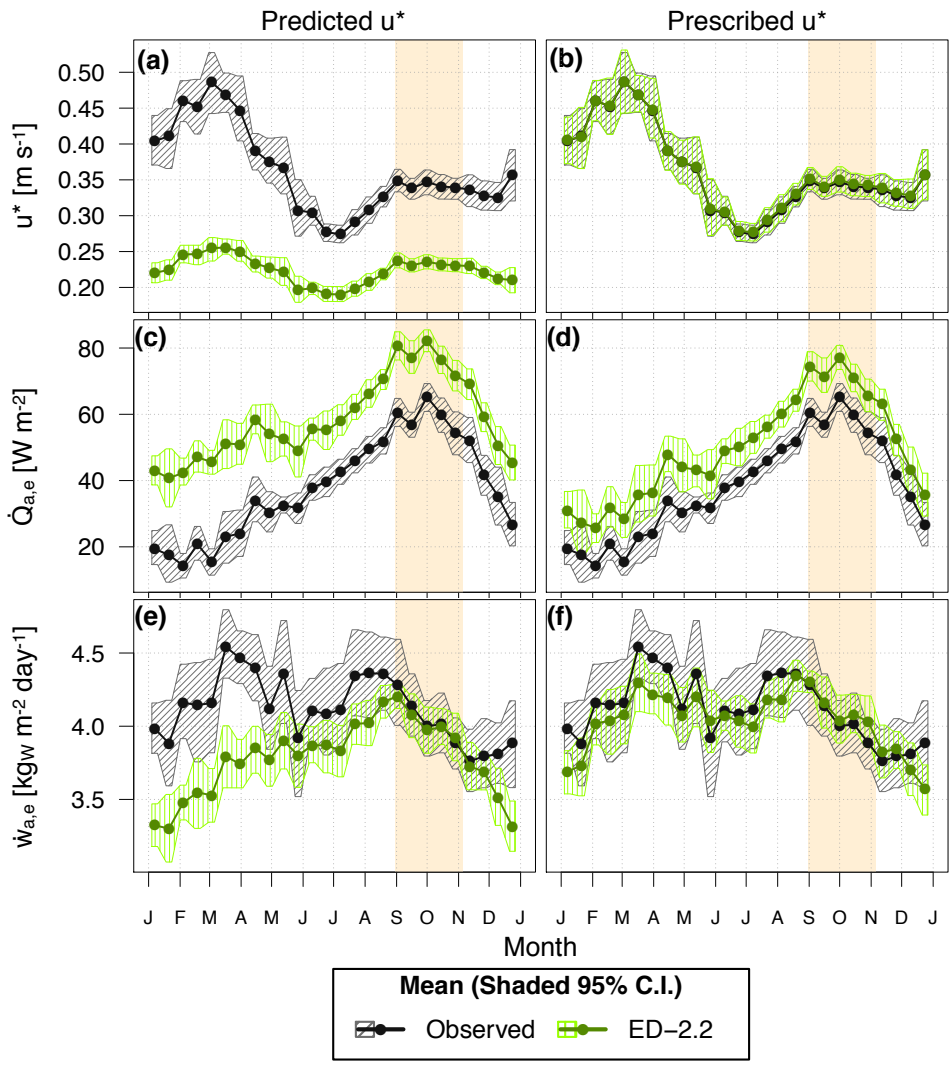

Figure 3.23: Comparison of mean annual cycle from fortnightly means at Paracou (GYF): friction velocity ($u^\star$–a,b), sensible heat flux ($\dot{Q}_{a,e}$–c,d), and water vapor flux ($\dot{W}_{a,e}$–e,f) using (a,c,e) predicted $u^\star$ and (b,d,f) prescribed $u^\star$. Yellow background corresponds to the average dry season.

The impact of prescribing momentum fluxes was negligible during the day, and nocturnal fluxes of both heat and water vapour are generally much lower in magnitude than the diurnal counterparts. For most sites, prescribing momentum made little difference. In GYF, however, forced convection during the night is sufficiently strong due to stronger winds, particularly during the wet season (Fig. 3.23a,b), and the seasonal variation of both sensible heat (Fig. 3.23c,d) and water fluxes (Fig. 3.23e,f) considerably improved when mechanical turbulence was prescribed.

3.4 Results from long-term simulations

3.4.1 Evaluation of default potential vegetation

From Tab. 3.5 we observe that the variation of basal area and above-ground biomass across sites are qualitatively similar for most sites when using the default ED-2.2 configuration (simulation $Z_{80}A_{30}D_{05}$, see Tab. 3.3 for simulation names): GYF, M34, RJA and S67 have higher biomass and basal area, whereas BAN shows substantially lower biomass, but nevertheless higher than BSB and NAT; PNZ shows the least biomass. The simulated dynamics at PDG, however, is significantly different from observations: in ED-2.2, the vegetation equilibrated at high biomass and basal area, akin of forest sites. Compared to remote sensing estimates, the modelled biomass at equilibrium at the forest sites was generally higher, whereas leaf area index was generally lower.

Succession of the plant community at GYF, S67, RJA, M34 and PDG was typical of forests (Fig. 3.24a–e and Fig. 3.25a–e): grasses only occur at the beginning of the simulation, rapidly going extinct once early successional cohorts become dominant. Early successional contribute with most of the biomass and leaf area during the first fifty years, but it is eventually superseded by late successional cohorts, although they maintain a population; mid-successional never became dominant, and went extinct once late-successional cohorts became dominant. Succession at S67 (Fig. 3.24b and Fig. 3.25b) yielded lower biomass and the time series showed higher interannual variability compared to the other sites that developed forests. At BAN, the equilibrium biomass was about half of the biomass at the aforementioned sites, although the succession was somewhat similar, with dominance of early successional at the beginning of the simulation, and eventual dominance of late successional cohorts both at biomass and leaf area index (Fig. 3.24g and Fig. 3.25g); unlike forest sites, mid-successional cohorts were able to maintain a relatively high biomass and leaf area index for most of the simulation. In the semi-arid site (PNZ Fig. 3.24f and Fig. 3.25f), trees went extinct within a few years, and only C_4 maintained some population, also with considerable seasonal and inter-annual variability; since no trees existed for most of the simulation, the total biomass was very low. It also must be noted that PNZ was the only site where grasses

Table 3.5: Comparison of equilibrium conditions of basal area, AGB and LAI (±95%CI) between ED-2.2, remote sensing (R.S.), and site measurements. Confidence intervals for ED-2.2 were obtained using the probability distribution associated with age over the last 40 years of simulation (1972–2011); remote sensing CI. was obtained from spatial distribution of valid grid points within 25 km of the point of interest using block bootstrapping. See notes for site-level CI.

Basal area $[\mathrm{cm^2\,m^{-2}}]$				
Site	**ED-2.2**	**R.S.**	**In situ**	**References for site measurements**
GYF	28.8 ± 0.9	—	31.0 ± 1.7	Bonal et al. (2008)[a]
S67	22.5 ± 0.8	—	27.6 ± 1.7	Pyle et al. (2008)[a]
PDG	31.9 ± 0.9	—	12.5 ± 2.8	Silva and Batalha (2009)[a]
RJA	27.6 ± 0.9	—	32.6 ± 2.9	Saatchi (2006)[a]
M34	26.9 ± 0.9	—	27.3 ± 1.6	Chambers et al. (2001)[a]
PNZ	0.0 ± 0.0	—	19.3 ± 2.6	Calixto Júnior (2009)[b]
BAN	14.3 ± 0.4	—	25.9 ± 3.8	Brito et al. (2008)[b]
BSB	12.7 ± 0.4	—	7.7 ± 1.1	Assunção and Felfili (2004)[b]
NAT	8.9 ± 0.2	—	19.4 ± 3.4	Cestaro (2002)[b]
Above-ground biomass $[\mathrm{kg_C\,m^{-2}}]$				
Site	**ED-2.2**	**R.S.**	**In situ**	**References for site measurements**
GYF	17.8 ± 1.8	11.8 ± 1.1	14.9 ± 1.0	Bonal et al. (2008)[a]
S67	12.6 ± 1.3	12.1 ± 1.4	14.5 ± 1.2	Pyle et al. (2008)[a]
PDG	18.7 ± 1.9	6.7 ± 0.8	4.8 ± 1.2	Silva and Batalha (2009)[a]
RJA	16.5 ± 1.7	10.9 ± 1.2	16.9 ± 2.2	Saatchi (2006)[a]
M34	16.5 ± 1.7	12.5 ± 0.9	13.2 ± 1.2	Chambers et al. (2001)[a]
PNZ	0.0 ± 0.0	1.44 ± 0.11	—	—
BAN	7.2 ± 0.6	6.9 ± 0.7	—	—
BSB	4.14 ± 0.32	3.4 ± 0.5	—	—
NAT	2.61 ± 0.17	1.95 ± 0.21	—	—
Leaf area index $[\mathrm{m^2_{leaf}\,m^{-2}}]$				
Site	**ED-2.2**	**R.S.**	**In situ**	**References for site measurements**
GYF	3.87 ± 0.07	4.7 ± 0.6	6.15 ± 0.30	Stahl et al. (2011)
S67	3.68 ± 0.07	5.1 ± 0.5	5.3 ± 1.3	Domingues et al. (2005) Stark et al. (2012)[c]
PDG	4.40 ± 0.08	2.5 ± 0.8	2.19 ± 0.16	Bitencourt et al. (2007)[d]
RJA	3.98 ± 0.07	5.5 ± 0.5	4.9 ± 0.4	Simon et al. (2005)[e]
M34	3.83 ± 0.07	5.42 ± 0.14	5.7 ± 0.8	McWilliam et al. (1993)[e]
PNZ	0.66 ± 0.02	0.95 ± 0.11	—	—
BAN	3.06 ± 0.06	3.7 ± 0.9	—	—
BSB	3.26 ± 0.09	1.34 ± 0.18	0.86 ± 0.06	Ferreira et al. (2007)[f]
NAT	2.17 ± 0.06	1.8 ± 0.5	—	—

[a] Basal area and AGB calculated from raw tree inventory data for individuals with DBH ≥ 10 cm. Confidence intervals were determined from 1000 bootstrap samples of the sub-plots with replacement.

[b] Basal area from publications were corrected to include only individuals with DBH ≥ 10 cm. C.I. is found by generating 1000 realizations of individual DBH, estimated from the reported demography by DBH class and assuming uniform distribution within each class.

[c] Estimates from both references were combined, and C.I. was determined using *t* distribution.

[d] Mean value was obtained by averaging results for all permanent plots for wet and dry seasons. C.I. was estimated from the square root of the sum of the squares of standard error for wet and dry seasons, using *t* distribution.

[e] Original references provided standard deviation, C.I. was determined using *t* distribution.

[f] Similar to (d), but mean value was obtained from average the dry season and end of the wet season measurements.

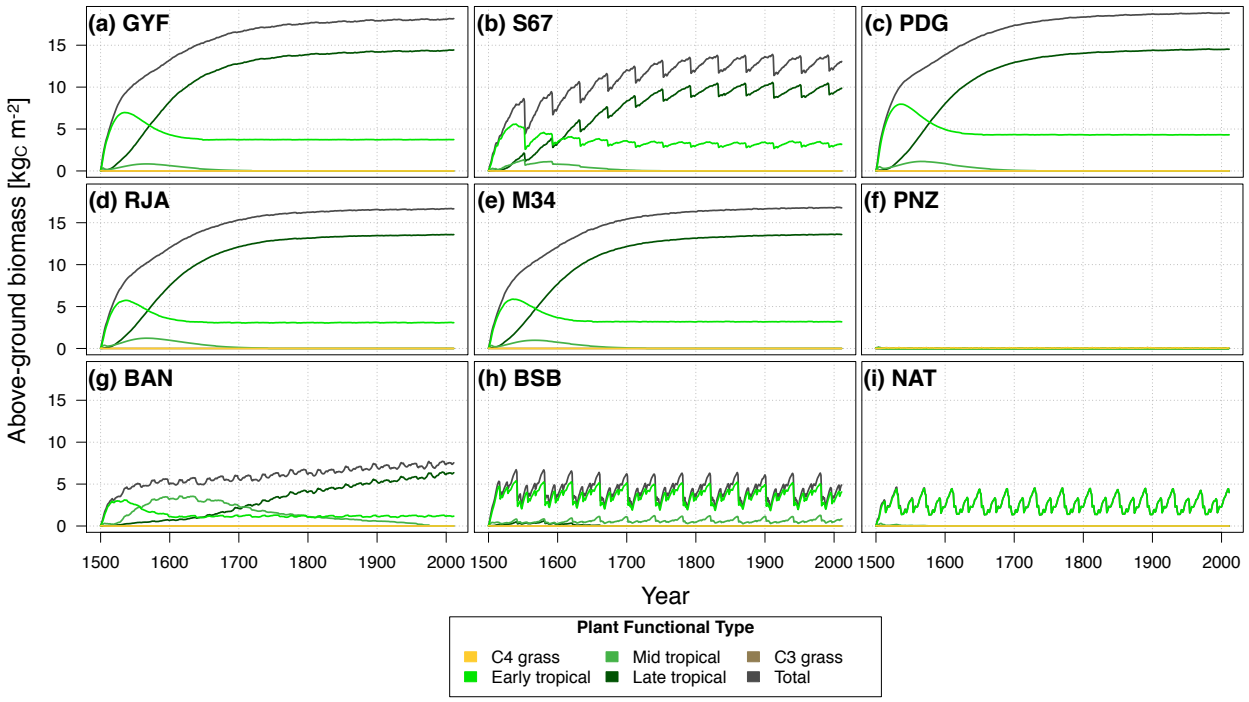

Figure 3.24: Time series of annual means of above-ground biomass for simulation $Z_{80}A_{30}D_{05}$ for all sites. Colours indicate different plant functional types and grey corresponds to the total when more than one plant functional type exists.

did not go extinct. In (Fig. 3.24h-i and Fig. 3.25h-i), we observe that both BSB and NAT showed dynamics that are intermediate between BAN and PNZ: in both cases the biomass was relatively low, but wet season rainfall was often sufficient to maintain some low biomass population of trees, mostly (BSB) or entirely (NAT) comprised of early successional cohorts.

Most of the time series trajectory of biomass, and to a lesser extent leaf area index, can be attributed to the disturbance and mortality regime. At the sites with the highest equilibrium biomass (GYF, PDG, RJA, M34) fires did not occur throughout the simulation, and peaks in density-dependent, carbon-starvation related mortality occurred only sporadically (Fig. 3.26a,c,d,e). Amongst the forest sites, S67 was the only location where mortality due to fire disturbances occurred (Fig. 3.26b), although they were very infrequent; in addition, S67 had higher mortality rates due to negative carbon balance. From Fig. 3.26g, we observe that mortality rates due to negative carbon balance were somewhat also moderately high in BAN, and despite that fires did

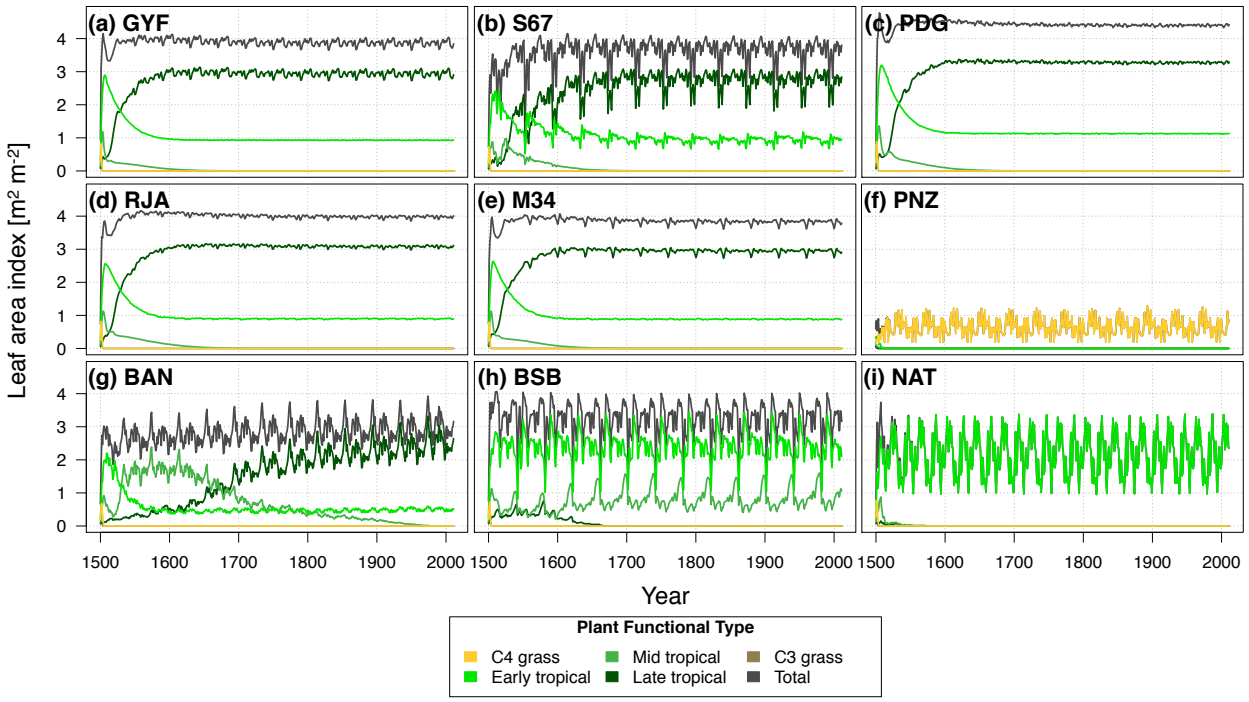

Figure 3.25: Same as Fig. 3.24 but for leaf area index.

not occur, the total mortality was generally higher in BAN than in S67. In BSB and NAT, both fires and high mortality events were significantly more frequent than the aforementioned sites (Fig. 3.26h,i), which resulted in lower biomass and absence of late-successional trees. In PNZ (Fig. 3.26f), droughts are very common occurrence and a combination of extreme fires and very negative carbon balance quickly caused the mortality rates of cohorts with DBH $\geq 10\,\mathrm{cm}$ to approach $100\,\%_{\mathrm{pop}}\,\mathrm{yr}^{-1}$, thus extinguishing all trees.

Like the living biomass, soil carbon dynamics showed high variability amongst sites: in fire-free sites in the Amazon (GYF, RJA, and M34, Fig. 3.27a,d,e), all soil carbon pools reached equilibrium in about 50 yr, and total mass converged to near $10\,\mathrm{kg_C\,m^{-2}}$, roughly equally split between structural and slow soil carbon and a much smaller contribution of the fast pool. In addition, similar values and partition were also found in S67 (Fig. 3.27b), BAN (Fig. 3.27g), and NAT (Fig. 3.27i), despite the differences in forest structure and disturbance dynamics. Although the partition and time to equilibrium was also similar for PDG and BSB (Fig. 3.27c,h), the total soil carbon was considerably higher, being 60 % higher than above-ground biomass in PDG and

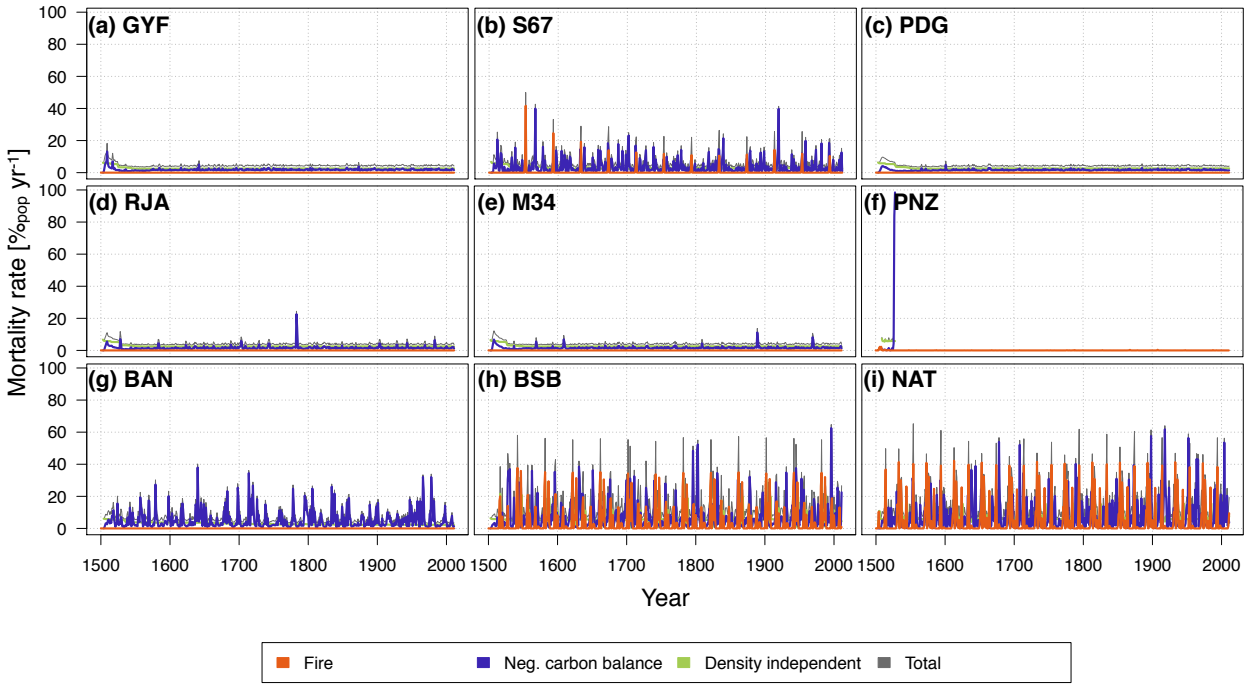

Figure 3.26: Similar as Fig. 3.24 but for mortality rates shown as fraction rates (Sheil and May, 1996), thus the sum of the terms does not correspond exactly to the total mortality. Colours indicate the different types of mortality rates, whereas grey corresponds to the total. Only cohorts with DBH $\geq$ 10 cm were included to mortality, hence the absence of mortality in PNZ. See additional information on how mortality rates are parameterized in ED-2.2 at App. F.3.

near 750 % higher in BSB. On the other hand, the absence of trees in PNZ lead to a low stock of carbon in the soils (Fig. 3.27i), and the three carbon pools contributed to roughly $\frac{1}{3}$ of the total soil carbon towards the end of the simulation.

Finally, to test whether the site-level discrepancies could affect the regional patterns of vegetation at equilibrium, I carried out a regional level simulation for tropical South America. In this simulation I used the same configurations as the default simulation ($Z_{80}A_{30}D_{05}$) for tropical South America, initializing soils with texture obtained from Quesada et al. (2011) for the Amazon, RADAMBRASIL (de Negreiros et al., 2009) for non-Amazonian areas of Brazil, and IGBP (Tempel et al., 1996) for non-Amazonian areas elsewhere, and the meteorological forcing from the Princeton University Global Meteorological Forcing Dataset (PGMF, Sheffield et al., 2006) for 1969 to 2008, which was recycled multiple times to simulate a period equivalent to 1500 through

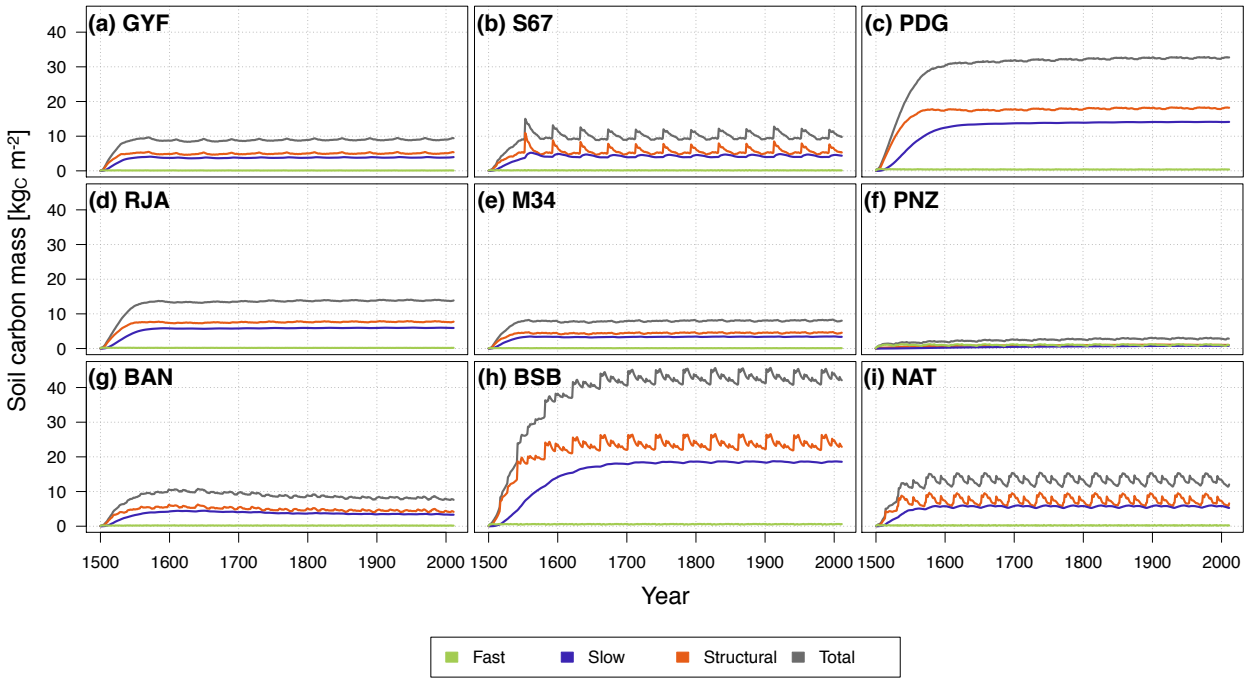

Figure 3.27: Similar to Fig. 3.24 but for soil carbon. Colours indicate the different soil carbon pools, whereas grey corresponds to the total.

2008. As shown in Fig. 3.28, the model tends to produce higher biomass than the estimated value using the high-resolution carbon density model by Baccini et al. (2012). Also, in this simulation I did not include anthropogenic disturbance, and even though I only selected pixels with natural vegetation, deforested areas in Rondônia, Northern Mato Grosso, and Eastern Pará states appear as forests in the simulation. Degraded forests and partially converted lands may have been classified as natural vegetation, since these categories do not exist in MCD12Q1, and this could introduce large biases in the aggregated biomass. In contrast, the model predicted low biomass for a significant area north of S67, which was cause by high incidence of fire disturbance associated with relatively drier climate. Notwithstanding, the model captures the average pre-deforestation extent of the Amazon Forests and the transitions to the Cerrado (Central Brazil woody savannahs) and the Lavrado (open savannahs and grasslands in Northeastern Roraima).

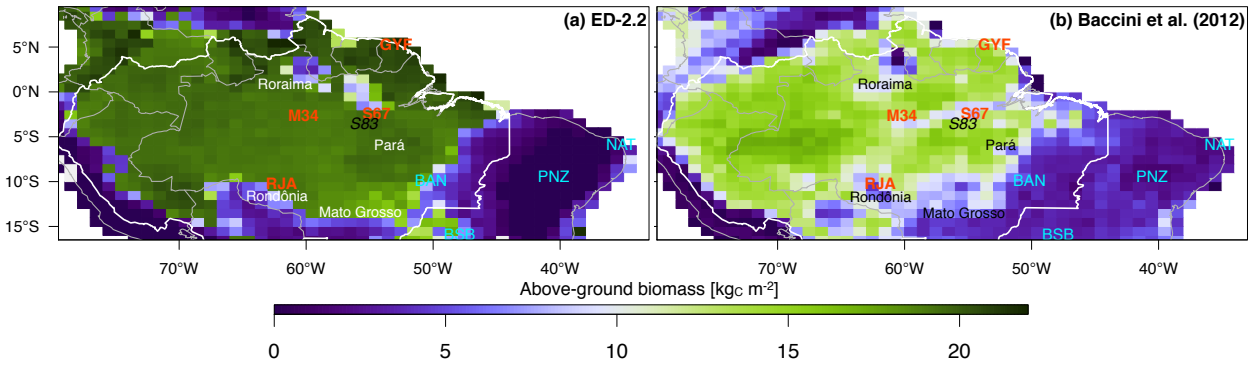

Figure 3.28: Comparison of above-ground biomass (a) at potential vegetation equilibrium (averages for the last 40 years, 1969–2008) using ED-2.2 and (b) estimated by Baccini et al. (2012), aggregated to 1° resolution using only pixels flagged as natural vegetation by the MCD12Q1 product (NASA/LP-DAAC, 2012) using the IGBP classification.

3.4.2 Role of size, age, and strategy heterogeneity in long-term dynamics

In Fig. 3.29, I present a summary of the equilibrium state of long-term simulations using different combinations of vertical structure, horizontal heterogeneity and functional diversity. At GYF and M34, simulations with two PFTs and simulation $Z_{01}A_{01}D_{05}$ equilibrate at similar above-ground biomass, whereas basal area is lower for simulations with size structure but only two PFTs; in addition, all simulations except $Z_{01}A_{01}D_{05}$ equilibrated at significantly lower leaf area index. At the more seasonal sites of RJA, S67 and PDG, the resulting basal area, biomass and leaf area index are significantly lower for simulation $Z_{01}A_{01}D_{02}$, and were likewise low at S67 and PDG even when all PFTs were included ($Z_{01}A_{01}D_{05}$); the remaining simulations reached similar values of basal area, above-ground biomass and leaf area index as GYF and M34. None of the simulations in BSB, NAT, and BAN equilibrated at basal area or biomass similar to forests, but like in S67 and PDG, simulations with no size structure ($Z_{01}A_{01}D_{02/05}$) remained at very low basal area, biomass, and LAI, whereas they reached basal area and biomass of about 30% of the forest sites for the other simulations. Finally, in PNZ, trees went extinct in all simulations, causing biomass and basal area to remain close to zero, and leaf area index significantly lower than other sites.

Even though less seasonal forest simulations equilibrated at comparable biomass and leaf area indices regardless of size, age, and strategy structure, the trajectory through which the simula-

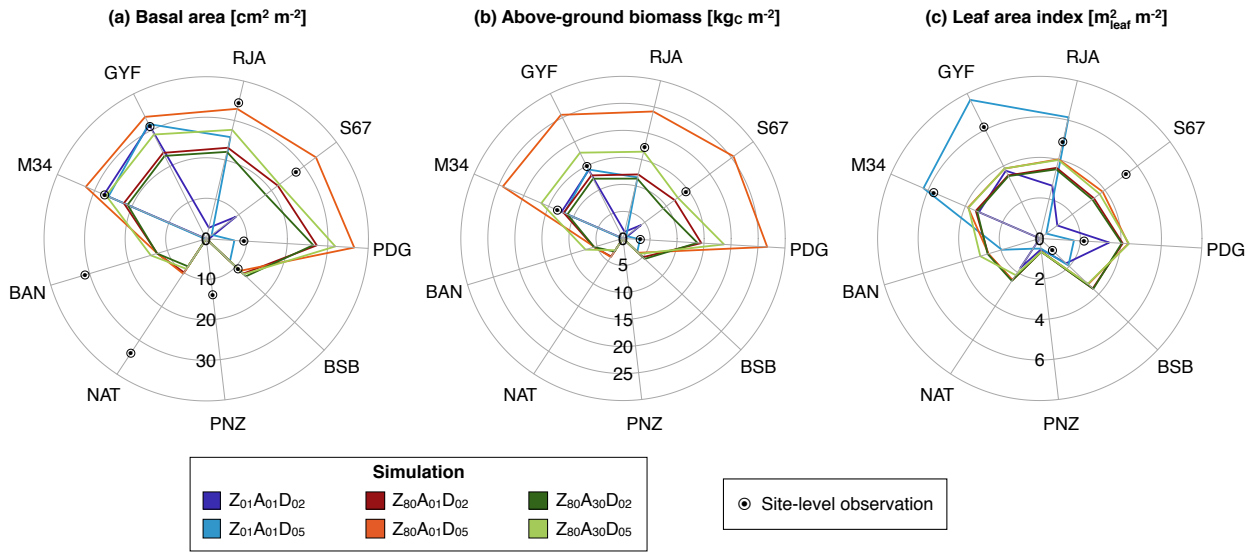

Figure 3.29: Average of (a) basal area, (b) above-ground biomass and (c) leaf area index at equilibrium (1972–2011) for all sites and simulations. Color lines correspond to different simulations, and fisheye mark corresponds to the site level observations.

tions reach equilibrium are very different. To illustrate the differences in forest ecosystems, I focus on Paracou (GYF), where simulated biotic properties at equilibrium were typical of forests and disturbance rates due to extreme events were relatively low. All simulations equilibrated at biomass typical of forests and similar leaf area index, although in the simulations with no size structure, the dominance of tree cohorts did not occur until 150 years for the case where only mid-successional trees existed (Fig. 3.30a,g), or about 40 years when late-successional trees were present (Fig. 3.30d,j), and in both cases the dominant PFT at early stages of the simulation were C_4 grasses. In simulation $Z_{80}A_{01}D_{02}$, grasses go extinct at much shorter time scales due to shading, and mid-successional cohorts reach equilibrium in less than 100 years (Fig. 3.30b,h). Incorporating age structure only ($Z_{80}A_{30}D_{02}$) has no noticeable effect on biomass and leaf area (Fig. 3.30c,i), whereas incorporating life strategy diversity but not allowing microenvironment heterogeneity results in equilibrium with only late-successional cohorts and much higher AGB slightly over 25 $kg_C\,m^{-2}$, but with leaf area index comparable to the other simulations with size structure (Fig. 3.30e,k). When size, age, and life strategy heterogeneity are simultaneously accounted (Fig. 3.30f,l), the forest reaches biomass equilibrium after 250 years; unlike the other sim-

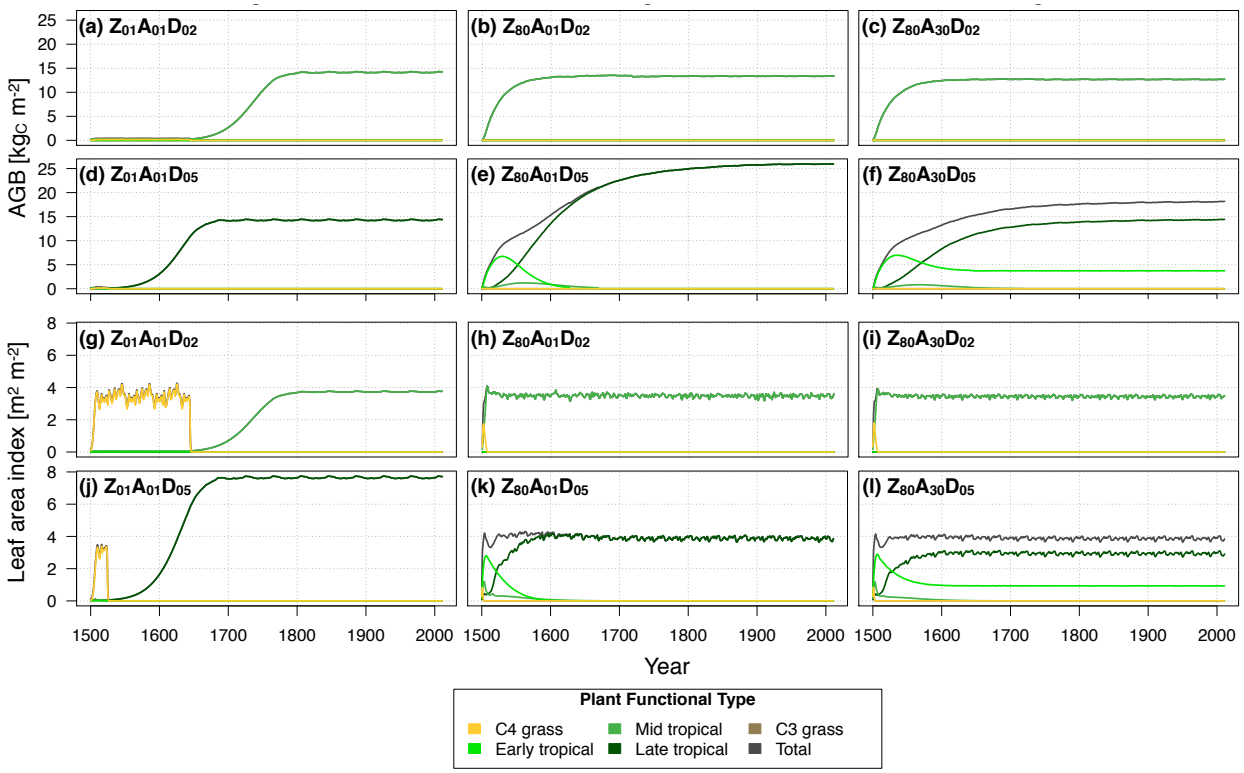

Figure 3.30: Time series of annual means of (a-f) above-ground biomass and (g-l) leaf area index at Paracou (GYF), for the tested combinations of vertical and horizontal heterogeneity, and functional diversity (Tab. 3.3). Colours indicate different plant functional types and grey corresponds to the total when more than one plant functional type exists.

ulations, the equilibrium also allows coexistence between two PFT, early- and late-successional trees.

Using Brasília (BSB) as an example of succession in savannahs (Fig. 3.31), we observe that grasses maintain a relatively high contribution of leaf area index when size and age structure are not included, and outcompete mid-successional trees when these are the only trees allowed ($Z_{01}A_{01}D_{02}$, Fig. 3.31a,g), or they are eventually replaced by late-successional trees if all PFTs are allowed ($Z_{01}A_{01}D_{05}$, Fig. 3.31d,j), although C_4 grasses persist longer compared to forests. Like the forest cases, grasses are quickly suppressed by growing trees when size structure is included ($Z_{80}A_{01}D_{02}$, Fig. 3.31b,h), and incorporating age structure has little impact on the plant community succession if only one tree functional type is allowed, although the inter-annual variability is reduced ($Z_{80}A_{01}D_{02}$, Fig. 3.31c,i). Unlike the forests, late successional trees did not become the

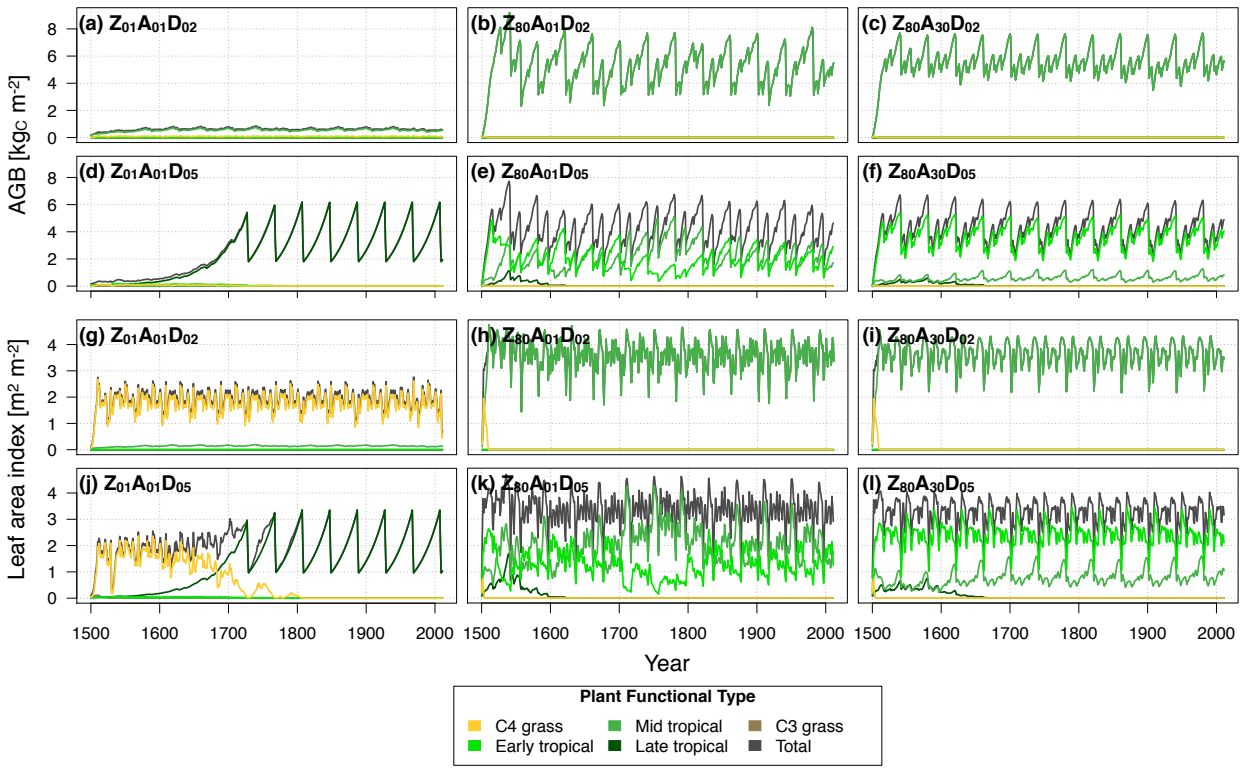

Figure 3.31: Similar to Fig. 3.30, but for Brasília (BSB).

dominant PFT when size structure and multiple PFTs were included ($Z_{80}A_{xx}D_{05}$ (Fig. 3.31e,f,k,l): at equilibrium, early and mid-successional trees coexisted, roughly maintaining half of the biomass and leaf area index when no horizontal heterogeneity was included ($Z_{80}A_{01}D_{05}$ (Fig. 3.31e,k), and with early successional being the most dominant PFT when age structure was incorporated ($Z_{80}A_{30}D_{05}$, Fig. 3.31f,l).

Not only the trajectory towards equilibrium is different, but the variability of the biophysical and biogeochemical properties at equilibrium is strongly influenced by the model structure. To quantify this influence, I determined the probability density function for each month using function `density` in `R` using the monthly means for each patch and each month between 1972 and 2011, and attributed a weighting factor proportional to the fractional area at each time. The probability density function was then determined at 511 evenly spaced blocks covering the entire range of monthly means. Using again GYF as an example of forest with low inter-annual variability

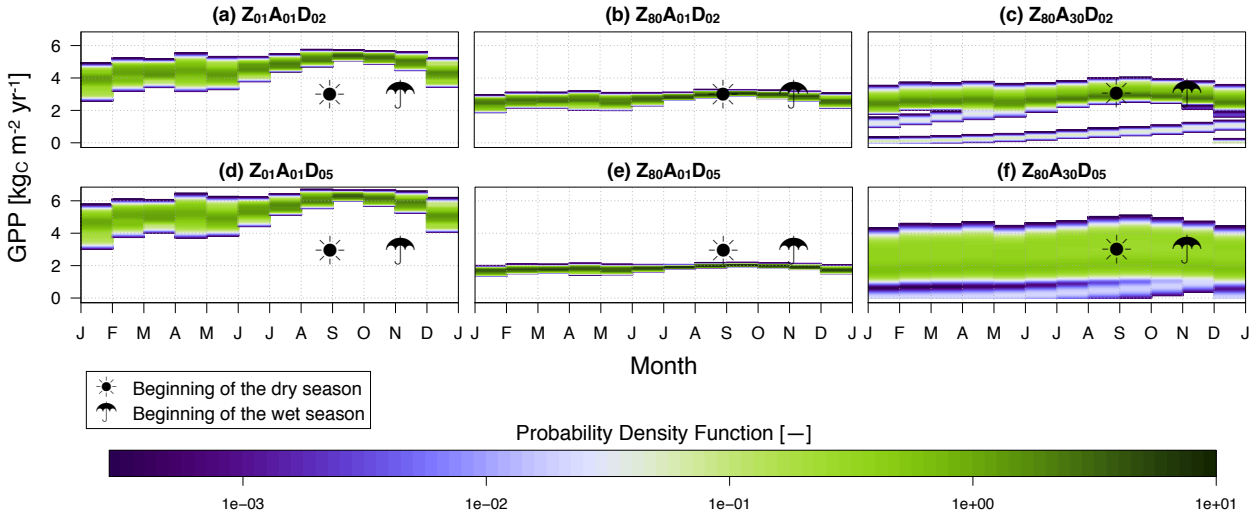

Figure 3.32: Annual cycle of the probability density function for GPP at GYF during the equilibrium period (1972-2011) for all simulation configurations, using $\Delta\text{GPP} = 0.0127\,\text{kg}_\text{C}\,\text{m}^{-2}\,\text{yr}^{-1}$.

of the plant community state at equilibrium and taking the distribution of GPP[5] to illustrate the differences (Fig. 3.32), we observe that the mode for all simulations show similar seasonality, with maximum productivity during the dry season. However, seasonal differences of the mode are more pronounced for simulations ($Z_{01}A_{01}D_{02/05}$ Fig. 3.32a,d), whereas including size structure but not including age structure ($Z_{80}A_{01}D_{02/05}$) reduces the mode magnitude and its seasonal differences, and amplitude of the distribution around the mode for all months (Fig. 3.32b,e). When both the size and age structure are included ($Z_{80}A_{30}D_{02/05}$, Fig. 3.32c,f), the magnitude and seasonality of the mode are similar to simulations $Z_{80}A_{01}D_{02/05}$, however the amplitude of the distribution becomes significantly wider and secondary modes appear, particularly when functional diversity is accounted ($Z_{80}A_{01}D_{05}$). Moreover, simulations $Z_{80}A_{01}D_{02/05}$ also develop secondary modes with values near zero in January (Fig. 3.32c,f), which steadily increase throughout the year: this pattern is due to the model patch dynamics, which applies disturbances to create new patches once a year, always in January. Similar patterns are observed in ecosystem respiration (Fig. 3.33), although the seasonality is reversed, peaking during the wet season.

The large-scale environmental conditions are identical for all simulations, thus the wider dis-

[5]Although only GPP is presented here, most biophysical and biogeochemical variables and fluxes have similar patterns.

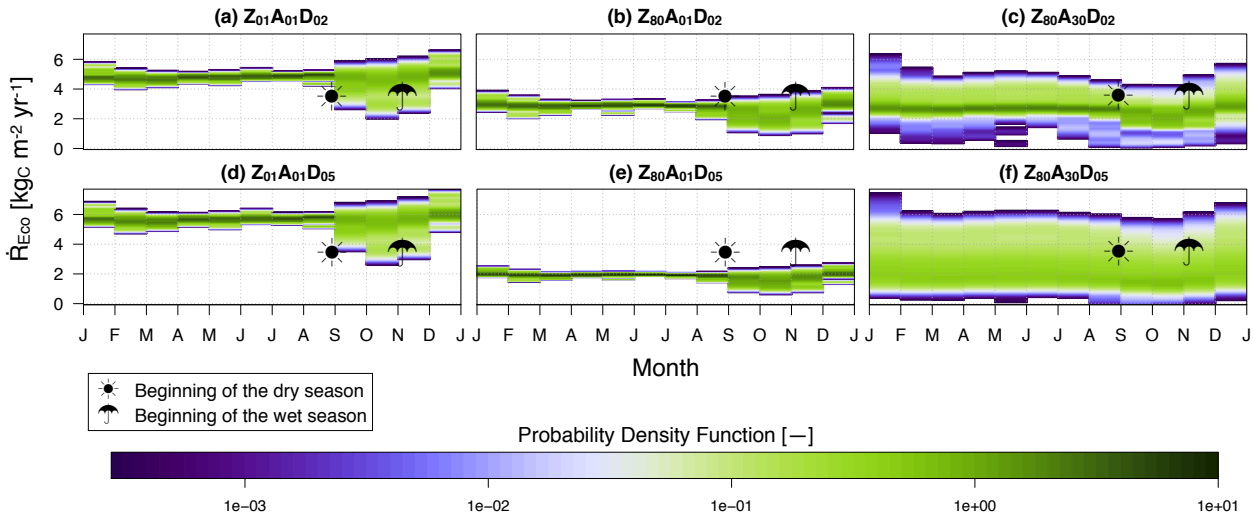

Figure 3.33: Similar to Fig. 3.32, but for ecosystem respiration.

tribution of most variables and fluxes in simulation $Z_{80}A_{30}D_{05}$ are due to increased heterogeneity in the microenvironment, which is mostly due to the distribution of ages since last disturbance. In Fig. 3.34a we observe that biomass dependence on age is similar amongst most sites (except PNZ), with continuous increase in biomass starting immediately after disturbance. In contrast, leaf area index (Fig. 3.34b) tends to reach the maximum value within 3–7 years, followed by a slow decline after 20–30 years, which is due to decline of short-lived early successional trees and emergence of mid- and late-successional trees, which grow more slowly, in addition to their lower specific leaf area (Moorcroft et al., 2001). Total soil and ground carbon reaches the maximum when the disturbance occurs (Fig. 3.34c), as a result of locally high mortality rates. Decomposition eventually reduces these pools, although net losses become more significant only after 5-10 years. As shown in Fig. 3.34d, loss of necromass is the dominant effect within 20 years following a disturbance event. Afterwards, the net productivity at all sites becomes significantly closer to zero, but generally acting as a net carbon sink. Unlike other sites, the grassland dynamics in PNZ shows positive productivity during the first years following disturbance, later becoming nearly carbon neutral. The opposite sign is due to the absence of large necromass inputs after disturbance (Fig. 3.34c), followed by low biomass accumulation that equilibrates quickly (Fig. 3.34a).

In addition to the carbon cycles, the diversity of micro-environments is also reflected in the

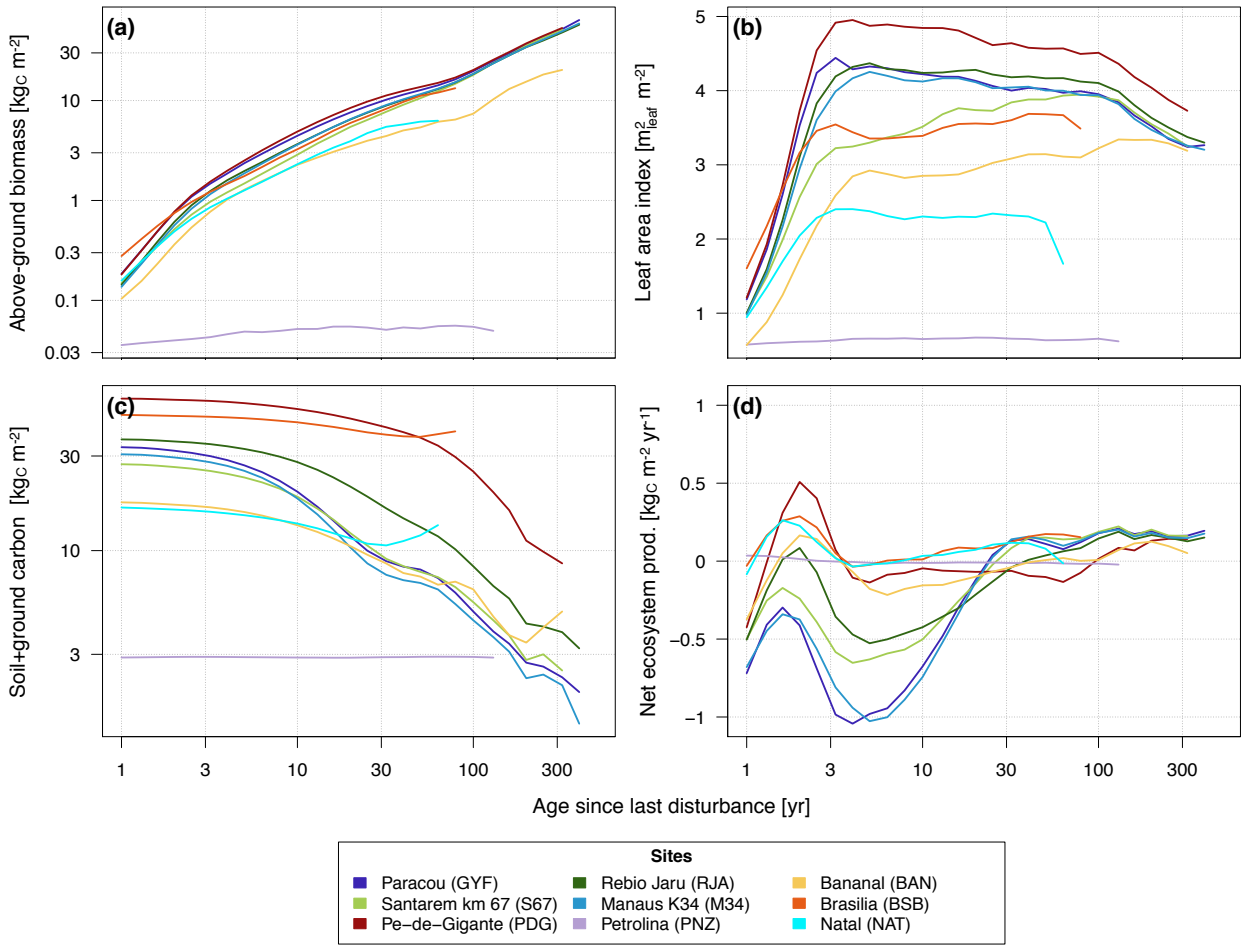

Figure 3.34: (a) Above-ground biomass, (b) leaf area index, (c) total soil and ground carbon (including litter and coarse woody debris), and (d) net ecosystem productivity as a function of age since last disturbance, here presented as averages for the equilibrium period (1972-2011). To determine the averages over the entire period, monthly mean averages for each patch at any given time were interpolated to fixed age points, using function `interp` in `R`, and excluding extrapolated points. The interpolated points were then used to obtain the average for the entire period.

energy and water cycles. In Fig. 3.35 we observe that the Bowen ratio[6] (B) increases towards the end of the dry season at all sites except PDG and PNZ, where negative nocturnal sensible heat fluxes nearly compensates positive diurnal fluxes, and in case of PNZ the total evapotranspiration approaches zero during the dry season, causing singularities at the ratio calculation. Moreover, younger patches usually experience stronger seasonality, and the period during which $B > 1$ is often longer at these patches (e.g. S67, BAN, BSB, Fig. 3.35b,g,h), although high B are predicted

[6]Bowen ratio is defined as the ratio between the monthly mean averages of sensible and latent heat fluxes.

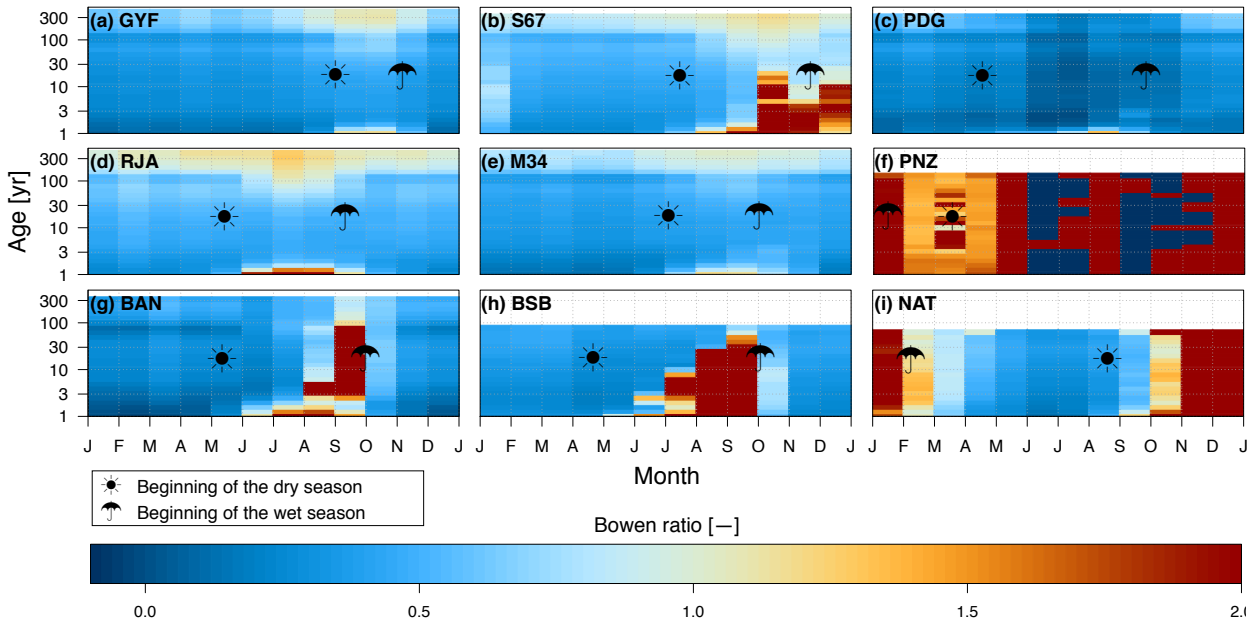

Figure 3.35: Annual cycle of Bowen ratio for simulation $Z_{80}A_{30}D_{05}$ at all sites as a function of age since last disturbance. Values were truncated at -0.1 and 2.0

in very recently disturbed patches even at sites with generally low seasonality (e.g. GYF and M34 Fig. 3.35a,e). Likewise, the relative contribution of different processes contributing to the total fluxes vary as the plant community evolves. For instance, nearly all water flux comes from transpiration during the dry season at all sites except PNZ[7] regardless of the age since last disturbance (Fig. 3.36); conversely, transpiration has little contribution to water flux during the wet season at most recently disturbed patches, when the total leaf area is stil low. Transpiration becomes less prevalent during the wet season for the oldest patches (see GYF and M34 Fig. 3.36a,e), which is also a consequence of the lower photosynthetic activity and leaf area of dominant late-successional trees.

[7] At PNZ, this is also true during the early part of the dry season, but as plants often shed all leaves during the later part of the dry season, thence evaporation from surfaces becomes the most relevant contribution. Nonetheless, the total water flux is generally very small (not shown).

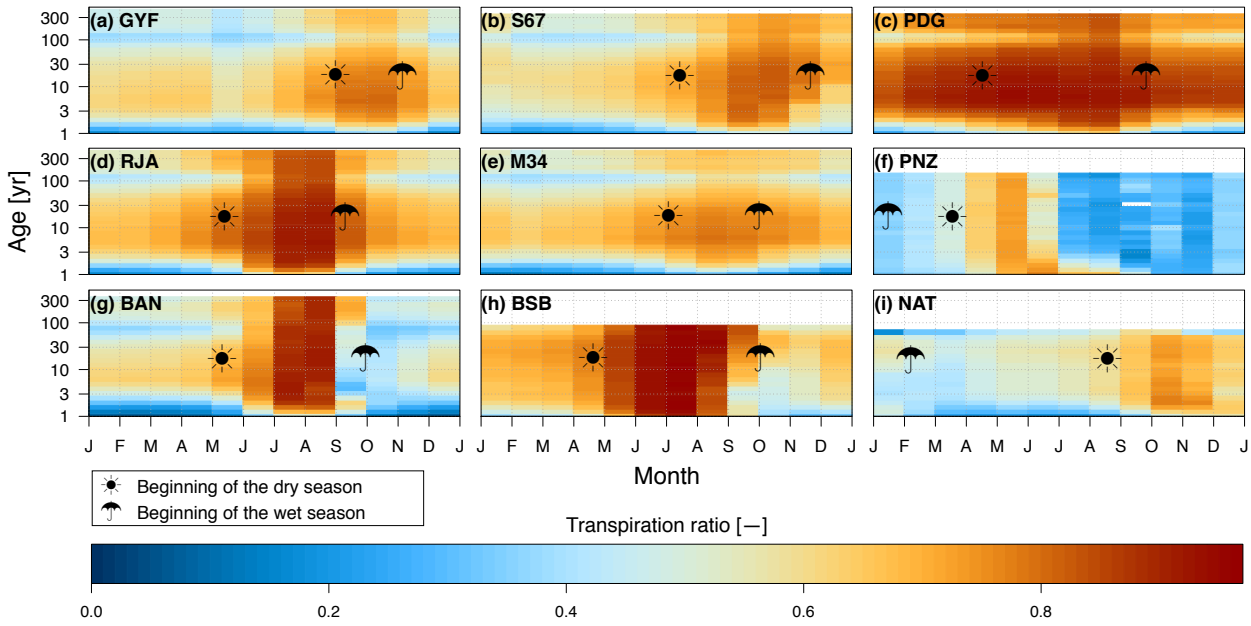

Figure 3.36: Similar to Fig. 3.36, but for the transpiration ratio, defined as the ratio between transpiration and water flux between canopy air space and the free atmosphere ($\dot{W}_{a,e}$).

3.5 Discussion

Simulations presented in Sec. 3.3 showed that given observed forest structure and composition, the model is able to realistically represent the outgoing radiation at the top of the canopy at most sites, and with the limited information available, the model is also able to represent the light environment within the canopy, at least for forests. Some of the more seasonal sites (RJA and PDG) underestimated outgoing radiation, which could be caused by the model limitation in reproducing leaf phenology. Frequent site level measurements of leaf area index are relatively rare in the Amazon: some studies near S67 (Asner et al., 2004; Malhado et al., 2009) and Sinop, a transitional site in Southeastern Amazon (Pinto-Júnior et al., 2011) estimated leaf area index decrease early in the dry season and maximum LAI at the end of the dry season; likewise, litterfall measurements at GYF usually show increase early in the dry season (Bonal et al., 2008; Soudani et al., 2012). Conversely, remote sensing estimates usually suggest increase in leaf area during the dry season (Samanta et al., 2012, see also Fig. 3.5). A phenological cycle akin to observed at S67 has been previously implemented in ED-2.2 (Kim et al., 2012), although when it was attempted in the cur-

rent version, results showed excessive seasonality of albedo and GPP (not shown). Kim et al. did not account for seasonal variations in leaf optical properties, which have been previously shown to vary as leaves age Toomey et al. (2009), and incorporating such features could further improve the model representation of radiation.

Comparisons of GPP between model and tower-based estimates revealed that the model seasonality at forest sites is mostly driven by light, thus the maximum productivity often occurs during the dry season, whereas observations suggest a more complex pattern, with minimum occurring late in the wet season, and modestly increasing productivity during the dry season. In savannahs, the model correctly diminishes productivity during the winter (dry season), albeit the difference between wet and dry seasons is much weaker in the model than observations. GPP is a typical case of emerging property that depends on multiple parameterizations and processes, and the resulting discrepances cannot be entirely attributed to the current photosynthesis scheme. First, the seasonality in forests is similar to the seasonality of LAI, which also decreases during the end of the wet season and increase during the dry season; this seasonality suggests that the observed seasonality of productivity is closely related to leaf phenology. In addition, GPP is also directly scaled by the leaf area index, which is also an emerging property that must be determined from allometric equations. The current allometric equation for leaf biomass in ED-2.2 (App. C), which has been applied to the initial conditions, also carry large uncertainties, as they are based on few commercially relevant Neotropical species (Cole and Ewel, 2006; Calvo-Alvarado et al., 2008). While allometric equations relating individual size and above-ground biomass are abundant for the Amazon (e.g. Chambers et al., 2001; Chave et al., 2005; Feldpausch et al., 2012, amongst others), few studies developed allometric equations for living tissues and leaf area index for Amazonian forests (but see Lescure et al., 1983; Saldarriaga et al., 1988, the latter being the basis for ED-1.0 allometry), and results from such equations vary substantially (Tab. 3.6), which corroborates the large uncertainty regarding the biomass of living tissues. Moreover, sites with significantly lower LAI in ED-2.2 also underestimated productivity (except RJA), whereas in PDG the model predicted both high productivity and high LAI. Despite these uncertainties, the model captured the

Table 3.6: Comparison of maximum leaf area index $\pm 95\% C.I.$ $[\,m^2_{leaf}\,m^{-2}]$ determined from forest inventories using the current ED-2.2 allometry, and estimated from two alternative allometric equations. Reference values are the same as the in situ observations shown in Tab. 3.5. Confidence intervals were obtained by bootstrapping the sub-plots (roughly 20 m × 20 m) for all sites.

Site	**ED-2.2**	**Lescure et al. (1983)**	**Saldarriaga et al. (1988)**	**References**
GYF	5.51 ± 0.14	6.88 ± 0.38	3.78 ± 0.14	6.15 ± 0.30
S67	4.76 ± 0.15	5.80 ± 0.33	3.04 ± 0.13	5.3 ± 1.3
S83	4.71 ± 0.20	6.20 ± 0.54	3.20 ± 0.20	5.3 ± 1.3
PDG	4.18 ± 0.44	1.77 ± 0.40	1.67 ± 0.28	2.19 ± 0.16
RJA	5.84 ± 0.24	6.78 ± 0.49	3.86 ± 0.18	4.9 ± 0.4
M34	4.92 ± 0.16	5.87 ± 0.34	3.40 ± 0.14	5.7 ± 0.8

light response curve at canopy level within reasonable range compared to tower estimates, and also showed low dependence on water stress as the tower estimates did, which suggests that at least part of the discrepancies can be attributed to the scaling from leaf- to community-level, as opposed to problems in the photosynthesis model parameters only.

Ecosystem respiration, on the other hand, showed significant discrepancies that cannot be explained only by uncertainties on processes upon which respiration depends, and the strong covariance of ED-2.2 and soil moisture is not supported by observations at all sites. Moreover, comparisons of relative soil moisture at the shallower soil layers generally agree well with observations, which further suggests that the differences between model and observations are due to the decomposition model being too sensitive to soil moisture. By evaluating the separate components of respiration, I showed that the strong seasonality is entirely due to the heterotrophic respiration, and by comparing the terms with available information on different components of respiration for three intensively studied sites (GYF, S67, and M34), I found that total autotrophic respiration is within range for all sites, albeit only marginally for S67. It must be noted, however, that several terms estimated from observations also carry large uncertainties and assumptions, and often come from very limited sampling due to logistic reasons that could nevertheless introduce important biases. For example, stem respiration is often measured near the surface (e.g Chambers et al., 2004; Stahl, 2010) since this is the most accessible part, and results from such measurements are often scaled

to the ecosystem level. This, however, could significantly underestimate the total stem respiration, since branches may have significantly higher respiration rates (Cavaleri et al., 2006). Furthermore, observed differences of expected values between sites are generally much larger than the differences obtained by the model, and such differences may reflect true differences of plant community functioning between sites, or differences in sampling and techniques (Malhi et al., 2009b).

In general, water cycle was qualitatively well captured by the model. For instance, comparisons of water fluxes and storage at the canopy air space storage between model and observations were encouraging, with results reasonably reproducing both the annual cycle and the seasonality, with results being generally more accurate during the dry season. During the dry season, a substantial fraction of water flux comes from transpiration, whereas during the wet season evaporation of intercepted becomes relatively more important. Discrepancies with eddy flux measurements are the largest during the wet season, which suggests that the main source of error at forests is the evaporation of canopy intercepted water. Such fluxes do not directly depend on plant physiology, but they are nevertheless dependent on how much leaf and wood area exist, once again a function of allometry and leaf phenology, how much water a given surface can hold, and how long do the water remains on top of canopy surfaces after a rainfall event until it completely evaporates. The average ratio between canopy evaporation and total rainfall ranged from $7-11\%$ at forest sites[8], which is at the low end but in the same range of values founds in previous studies ($9-20\%$ Tobón Marin et al., 2000, and references therein). Simulations using prescribed $u^\star$ generally increased the ratio at forests to $8-12\%$, and despite the small change, this increase was sufficient to significantly improve water fluxes at GYF, which is the site with the most turbulent and the site that receives the most rain during the wet season, which suggests that proper characterization of momentum flux can play a significant role in areas with similar climate. The hydrological cycle, on the other hand, showed some important deviations in absolute value, particularly close to the surface, despite that the relative soil moisture showed reasonable seasonality. Large biases in absolute soil moisture were caused by the mismatches in the soil hydraulic properties that ultimately define the residual

[8]The canopy evaporation–rainfall ratio was less than 1% in PDG

moisture and wilting point, field capacity, and porosity, thence the range of possible values of soil moisture. Soil hydraulic properties were derived from texture characteristics previously published for all sites; however, in ED-2.2 these properties were simplified to a single fraction assumed constant at every patch and throughout the profile, whereas in reality soil properties are known to vary significantly within the same area and with depth (e.g. Epron et al., 2006, for the GYF site). Moreover, soils in ED-2.2 are assumed mineral, whereas in reality macropores and soil organic content can substantially affect such properties (Rawls et al., 2003; Saxton and Rawls, 2006).

Energy fluxes were positively biased at all sites except PDG, and bias at the forest sites occurred at both day and night. Similarly, outgoing longwave radiation showed positive bias particularly during the day, and especially at GYF, both of which suggestive that the surface temperatures were overestimated. Unlike the fluxes, canopy air space temperature at S67, one of the sites with the most significant bias in sensible heat flux, usually showed very good agreement with observations, even though it showed slight positive bias during the dry season. Despite the bias and that none of the model parameters have been formally optimized, the model showed good predictive power during the day at most sites. Given the bias in soil temperature at GYF and larger diurnal and seasonal amplitude of soil temperature at both GYF and S83, and the differences in range of soil water holding capacity, one possibility is that the soil in ED-2.2 is storing less energy is storing less energy than in reality. Moreover, in ED-2.2 the only means by which enthalpy can be exchanged with the outside environment are eddy fluxes at the top of the canopy, radiation, rainfall, runoff (surface and sub-surface), and changes in pressure, and enthalpy conservation is checked every time step, to ensure the model conserves total enthalpy (Fig. 3.37). Observations from eddy flux towers, on the other hand, may also contain significant sources and sinks that are not accounted in ED-2.2, such as lateral advection and air drainage, which has been previously shown to be a significant component for CO_2 exchange (e.g. Tóta et al., 2008) and likewise may be also important for the total energy closure. In addition, Mauder et al. (2010) showed that energy budget can approach closure when the local heterogeneity is sampled by a network of nearby towers, whereas the closure cannot be achieve by one single tower even when aggregated for longer periods. Furthermore,

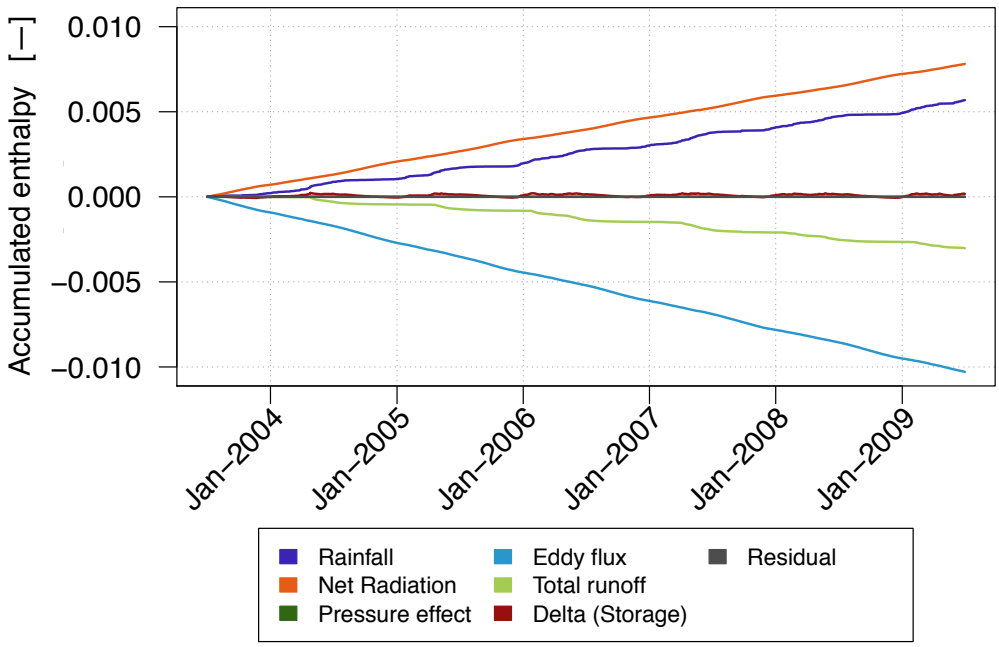

Figure 3.37: Example of enthalpy conservation in ED-2.2, for a simulation at GYF. Terms are presented as values relative to the total stored energy, and sources and sinks are accumulated over time. Pressure effect is the contribution of pressure change to the changes in enthalpy, and their values are very small compared to other terms. Delta (storage) is the total change in storage, whereas residual corresponds to the deviation from the perfect enthalpy closure, mostly due to the linearization of the prognostic equations due to changes in density at the canopy air space.

da Rocha et al. (2009b) previously evaluated the closure of the budget for most sites used in the model evaluation presented here, and found that the energy closure varied from 0.70 to 1.1 (1.0 meaning all perfect closure), value which is in the similar range found by Stoy et al. (2013) from a synthesis analysis using several FLUXNET sites; since the model conserves enthalpy without lateral exchange, and has shown reasonable agreement in radiation and water flux generally agree well with observations in the long term averages, the discrepancies in sensible heat are likely to be influenced by the model energy closure.

Long-term simulations using the biophysical and biogeochemical model described in Chap. 2 captured the typical values of basal area and above-ground biomass of most of the selected sites covering a wide range of rainfall regimes in tropical South America, and also the main patterns of biomass across tropical South America. Both the dynamics and distribution of biomass and basal

area were strongly controlled by fire and drought regimes. Agreement was best at forest sites in the Amazon, which is expected since the model has been first developed for tropical rainforests, and plant functional types have been developed to represent tropical rainforest trees (c.f. Moorcroft et al., 2001), but the model correctly predicted lower biomass at most transitional sites. Leaf area index at equilibrium, on the other hand, was lower than expected from site-level measurements and remote sensing, which further reinforces the need for improving the allocation to living tissues. One exception for the long term was PDG, which, despite similar rainfall seasonality and temperature range as BSB, equilibrated at very high biomass and leaf area index, similar to forests. Although PDG is at a transitional region with savannahs and semi-deciduous forests, woody savannahs were the predominant vegetation prior to widespread land conversion to agriculture and forest plantations (Shida, 2005). Long term tests with different soil textures with much higher clay content had no effect (not shown), and two other mechanisms may have the most contribution to the high biomass: combination of lower temperature and incoming radiation caused respiration and water use to decrease more than productivity, hence reducing water stress; and absence of fires. In addition, the current fire model is extremely simple and only accounts water deficit and total living biomass as ignition; furthermore, the current fire model removes living biomass, but not fine litter and woody debris, and the biomass removed by fire is not included in emissions to the canopy air space. Additional work on improving the fire model in ED-2.2 could also provide more realistic dynamics at fire-prone regions.

Compared to the synthesis carbon accounting by Malhi et al. (2009b), results of combined soil carbon and coarse woody debris at tropical forests in ED-2.2 are significantly lower, although the model captured slightly higher values in S67 compared to M34. In fact, S67 had significantly more coarse woody debris than other sites, which had been attributed to a strong disturbance event shortly before the start of intensive measurements (Rice et al., 2004; Keller et al., 2004a; Pyle et al., 2008); likewise, the higher mass in ED-2.2 was caused by increases due to disturbances, particularly the high mortality event that occurred after the extreme 1992 drought.

Finally, the relevance of incorporating size, age, and functional diversity to represent the dy-

namics of the plant community, which had been partially tested by Moorcroft et al. (2001), was re-assessed in this model evaluation. Here I presented the results of all possible combinations these structures, which allowed determining the contribution of each structure to the long term dynamics towards equilibrium, using a fully developed representation of the biophysical processes. On the one hand, all levels of complexity converged to similar results of integrated quantities such as total above-ground biomass and total leaf area index at equilibrium both for sites with low seasonality of rainfall and interannual variability and for the semi-arid regions, while sites with high interannual variability and/or closer to transitional zones experienced the largest differences. On the other hand, the trajectory towards equilibrium varied significantly, and in general the combination of all three structures yielded the most realistic dynamics in terms of time scales and competition between morphologically distinct functional groups. In particular, excluding size structure caused grasses to persist as the dominant functional group for several decades, since no direct shading of one PFT onto another was represented. Age structure and functional diversity, however, made a significant difference in forests only when both were considered at the same time. Including age structure without allowing functional diversity does not allow an efficient use of resources under different local environments, whereas including functional diversity without allowing a range of landscapes did not allow multiple functional groups to thrive under different micro-environments, and the better adapted functional group (late successional trees) eventually outcompeted all other types. Moreover, results showed the response of ecosystem being strongly dependent on age since last disturbance: like in Moorcroft et al. (2001), results of net carbon balance showed the "slow in, rapid out" effect (Körner, 2003), in which recently disturbed patches act as sources of carbon whereas in older patches the plant community is mostly accumulating carbon. Finally, the model results showed that variability in the micro-environment also affects how the plant community respond to similar environmental forcing. For example, the higher Bowen ratios during the dry season at the most recently disturbed patches, and maintenance of longer periods of high Bowen ratio suggests that even at the same area trees may experience different different responses: a recently disturbed patch experiencing high sensible heat flux during the dry season is likely to

experience more drought stress due to warmer leaves and more vapor pressure deficit at the leaf level. Because of warmer leaves, plants may reduce stomatal conductance, which reduces transpiration and carbon assimilation. With less assimilation, these plants may become more susceptible to drought-related mortality, at the same time that plants in older patches may be experiencing little or no stress. The net result may be localized high mortality events, but less dramatic than if the entire plant community was experienced such stress.

3.6 Conclusions

The model evaluation presented here highlighted the main strengths and areas and processes that could benefit from model developments and formal optimization for short and long-term dynamics in the tropics. While the model generally showed good agreement with observations for radiation and water fluxes, I identified leaf allometry and phenology, which consequently affected productivity, leaf evaporation and the long term dynamics as an important aspect of the model to be improved. Additional data from different areas of the Amazon on leaf mass and elongation as a function of individual size and functional group as opposed to the full ecosystem scale could be particularly important for further constraining the model. Likewise, the decomposition model showed too strong dependence on soil moisture, which is not observed everywhere in the Amazon. In addition, because the model evaluation suggested that discrepancies in the model come from heterotrophic respiration, the model could significantly improve the carbon cycle dynamics through a formal optimization of the parameters controlling the decomposition model, using multiple data sets such as total necromass and its decay rate, litter fall rates, soil respiration, and full accounting of soil carbon, preferably using data covering long periods of time for multiple regions in the Amazon and the forest. Finally, the model generally overestimated sensible heat flux, although this can be partially explained by the model closure, which limits exchange of energy through the canopy air space whereas in reality lateral flow could account for a significant fraction of the energy.

Comparisons of the long-term dynamics showed that ED-2.2 converged to realistic biomass

and basal area at equilibrium at most forests and savannah sites tested and produced a realistic distribution of biomass compared to remote sensing estimates for most of the region. However, ED-2.2 it significantly overestimated the plant community density at the most sub-tropical savannah site, where the model predicted low drought- and fire- related mortality. In general including size and age structures, and plant functional diversity made little difference on the equilibrium values at the least seasonal forests; however, the trajectory towards equilibrium creates a more reasonable time scale for the dynamics towards equilibrium, and allowed significant variability of biophysical environments within the same large scale forcing. While this result shows an additional relevance for including an individual-based structure, little observation exists on how energy and water cycles vary within the micro-environment. Additional measurements with high resolution that explored the landscape heterogeneity could be important to better characterize the energy, water, and carbon cycles in tropical ecosystems.

Chapter 4

Forest vulnerability to drier rainfall regime in the Amazon

4.1 Introduction

Home of a great biodiversity, with as many as 50,000 different species of flowering plants (Hubbell et al., 2008), 16,000 of them being trees and 230 being hyperdominant (ter Steege et al., 2013), the Amazon forest is also the largest contiguous tropical rain forest in the world, storing about $70-110$ Pg_C (Malhi et al., 2006; Saatchi et al., 2007), or about 40 % of the global biomass of tropical forests (Saatchi et al., 2011). The total biomass and the relative carbon balance of the Amazon depends on several complex processes such as photosynthesis; respiration; turnover of living tissues; forest structure and composition, and their demographic changes due to competition, reproduction, mortality; decomposition of dead material; and biomass burning. Ongoing changes in climate, as well as land use changes due to deforestation and logging, affect all aforementioned processes, and despite that many studies have been carried out over the past 20 years (c.f. Davidson et al., 2012), there is still uncertainty on how resilient the forest is to future climate change. Increased frequency and severity of droughts has been of special concern: van der Molen et al. (2011) and references therein illustrate the multiple impacts that droughts impose to

ecosystem functioning: short-term changes in primary productivity to respiration, and changes in structural allocation; carry-over effects of droughts like inability to restore depleted reservoirs such as non-structural carbon and soil moisture, and increased vulnerability to other disturbances and mortality, although the actual response depends on the differential species strategies under drought stress and ability to recover from disturbance.

Under normal conditions, water is thought to be less limiting to the Amazon forest productivity than light (e.g. Nemani et al., 2003) due to high precipitation rates over most of the Amazon region (Fig. 4.1a), even though most of Eastern and Southern Amazon experiences regular dry seasons (Fig. 4.1). Despite this seasonality, forests in Eastern Amazon show either no significant seasonality in gross primary productivity (GPP) between wet and dry season, or moderate increases during the dry season (Hutyra et al., 2007; Bonal et al., 2008; Saleska et al., 2009), and except for the areas near the transition to drier biomes, plants are typically evergreen (Borchert, 1998). The maintenance or increase in GPP during the dry season has been attributed to multiple factors, such as the ability of plants to extract water from deepest soil layers during the dry season (Nepstad et al., 1994; Bruno et al., 2006; Ivanov et al., 2012), increased light availability due to sunnier conditions (Saleska et al., 2009), the replacement of leaves shortly before the onset of the dry season (Rice et al., 2004; Soudani et al., 2012; Kim et al., 2012) followed by increase in leaf area index later in the dry season (Doughty and Goulden, 2008), which may be an adaptation to replace of old, epiphyll-infested leaves with lower photosynthetic capacity when light conditions become more favorable (Doughty and Goulden, 2008; Toomey et al., 2009).

Such adaptations, however, may fail when droughts become more frequent or more severe. Recently, Ponce Campos et al. (2013) compared the above-ground net primary production for a variety of biomes including rain forests in Puerto Rico and Australia and suggested that all biomes showed biome-scale adaptation and resilience to recent droughts, with increased water use efficiency during the driest years. Nevertheless, they also suggested that this resilience may break in case droughts become more frequent and more severe; in fact, Lenton et al. (2008) and Marengo et al. (2011a) (and references therein) pointed out that the Amazon is one the largest areas in the

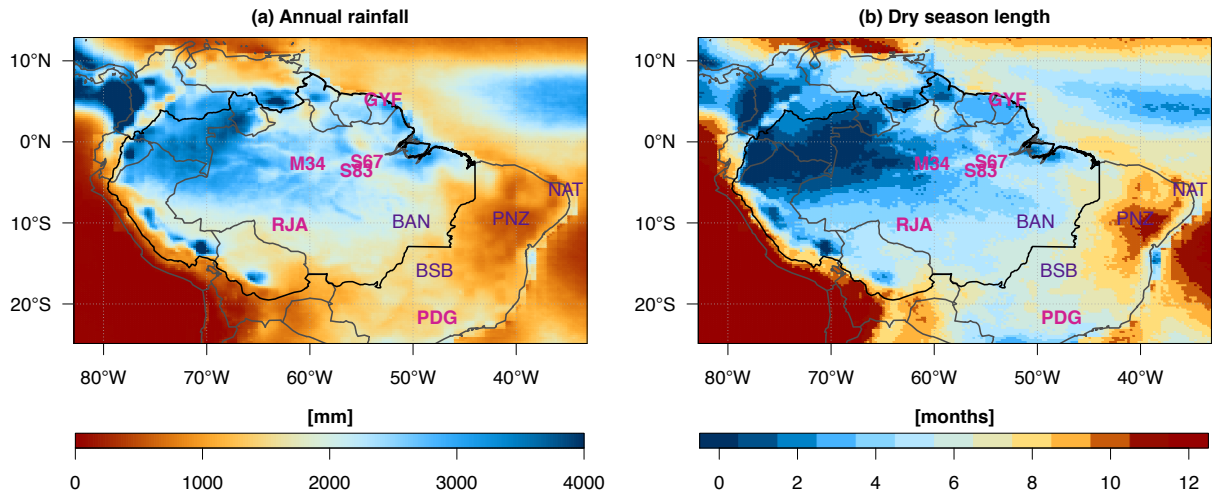

Figure 4.1: (a) Mean precipitation rates and (b) mean dry season length, defined as number of months with rainfall below 100 *mm* in tropical South America between 1998 and 2012, estimated using the Tropical Rainfall Measurement Mission (TRMM), product 3B43, available at Mirador GSFC/NASA (Liu et al., 2012). The Amazon forest area is denoted by the black lines, grey lines are the political boundaries. In this chapter I focus on (GYF and S67), and additional sites used in Chap. 3 are also shown for reference.

world thought to be susceptible to a tipping point that could cause biodiversity loss and significant degradation; within the Amazon, the drier Southern and Eastern regions are thought to be particularly vulnerable (e.g. Senna et al., 2009; Hirota et al., 2011); it has been also suggested that land-use change, which happens more intensively in these areas, may make the shift towards a more savannah-like biome more likely and less reversible (Nepstad et al., 2008). Detecting signs of an oncoming tipping point, and assessing the Amazon resilience or susceptibility to droughts turned into a pressing research question after multiple widespread and severe droughts affected the region over the past two decades, most notably in 1992 (Eastern Amazon, Borchert, 1998; Davidson et al., 2012), 1998 (Eastern Amazon: Williamson et al., 2000), 2005 (Southwestern Amazon, Marengo et al., 2008), and 2010 (Southern and Western Amazon: Lewis et al., 2011; Marengo et al., 2011b). The spatial and temporal impact of such droughts on the ecosystem is still unknown. An initial study by Saleska et al. (2007) using the Moderate Resolution Imaging Spectroradiometer (MODIS) reported anomalously high values of the Enhanced Vegetation Index (EVI), or a green-up, as a response to the 2005 drought, which suggested that forests were resilient to the drought. This result

has been later challenged by Samanta et al. (2010) who attributed the green-up to inclusion of data contaminated by clouds and aerosols, and by a similar analysis carried out for the 2010 drought that found reductions in EVI (Xu et al., 2011); nonetheless Anderson et al. (2010) provided an alternative hypothesis in which higher EVI, albeit less widespread than in Saleska et al.),and lower normalized differential water index (NDWI) during the 2005 drought were not due to a green-up, but instead due to changes in the canopy structure; more recently Saatchi et al. (2013), using microwave backscattering data from the SeaWinds Scatterometer (QScat) also suggested that the 2005 drought caused permanent changes in canopy, and such anomalies persisted at least until the sensor failed late in 2009.

Although decreased photosynthetic activity and growth is observed even in milder droughts (e.g Bonal et al., 2008; Wagner et al., 2012), they are unlikely to produce any long-lasting effect as mortality. Mortality due to droughts encompasses interdependent mechanisms such as reduced non-structural carbon reserves, embolism and cavitation, and inability to maintain defense mechanisms against pathogens (McDowell et al., 2011, and references therein), and higher vulnerability to fires (Aragão et al., 2007). To determine the impact of droughts on Amazon forests, two site-level experiments were established in Eastern Amazon, in which through fall water was diverted from the reaching the soil to simulate a 50 % reduction of rainfall (Nepstad et al., 2007; da Costa et al., 2010), and in both cases the authors reported a significant increase in mortality after three years of treatment, especially among the largest trees. Also, Phillips et al. (2009) used the ground-based observations from the RAINFOR network dataset and found a significant increase in mortality and some reduction in forest productivity after the drought of 2005, particularly in areas with the largest deviation from the typical climatological water deficit; nonetheless a follow-up study (Phillips et al., 2010) suggested that the surveyed plots in the Amazon are generally less susceptible to drought mortality than those in Borneo. One important difference between the results of Phillips et al. (2009) and Nepstad et al. (2007); da Costa et al. (2010) is the time scale: the former found increased mortality after one anomalous dry season, whereas the mortality rates did not increase at the through fall exclusion experiments until three years after the exclusion began. This discrepancy

may be due to the different nature of the droughts and sampling sizes: the through fall exclusion experiments changed the amount of water reaching the ground in 1 ha plots, but they could not alter other environmental properties that are likely to be anomalous during real droughts such water vapor pressure deficit, temperature, and incoming radiation, and all of them could reduce the forest resilience to low precipitation significantly. In addition, Phillips et al. (2009) analysis was done over a real drought and with much larger sample size: while it has the advantage of capturing the drought with all aspects and the spatial variability, it also means that the analysis is based on data collected under uncontrolled conditions that may contain confounding variables such as storm-driven wind throw (Negrón-Juárez et al., 2010), or possible biases towards trees that were in poor health condition in which case droughts only accelerated their fate but contributed little to the long-term demographic dynamics (van der Molen et al., 2011).

While these studies suggest the potential of significant mortality, much uncertainty remains on how the Amazon will response to future climate change. This question is particularly relevant because the variability of the response of land carbon to climate change is largely driven by the maintenance of tropical forests (Friedlingstein et al., 2006). Christensen et al. (2007) acknowledge that numerical predictions of rainfall included in the Fourth Assessment Report of the Intergovernmental Panel on Climate Change (IPCC) have a very high noise to signal ratio for the Amazon region, thus it is still unknown whether droughts will become more likely; nevertheless Christensen et al. (2007) and Malhi et al. (2008) pointed out that the models tend to show rainfall reduction during the dry season in Eastern Amazon, possibly due to more persistent El-Niño-like conditions. Malhi et al. (2009a) used the same models for the A2 scenario (IPCC, 2007), but correcting the current climate precipitation to match the observed rainfall, and found the general trend that the current rain forest areas could approach climates that are more typical of seasonal forests and savannahs, due to increased drought severity and drought frequency. On the other hand, after constraining the model results with observed inter-annual variability, Cox et al. (2013) pointed out that if the CO_2 fertilization effect in forests is as large as predicted by the models, then the risk of a major die-back in the Amazon is lower than previously suggested (Cox et al., 2004; Friedlingstein

et al., 2006); this result also agrees with independent studies not included in the IPCC, in which the effect of CO_2 fertilization had been included (e.g. Lapola et al., 2009; Salazar and Nobre, 2010). However, the magnitude of CO_2 fertilization in tropical forests is still unknown (Nobre and Borma, 2009), and nutrient availability may play an important role limiting growth in the Amazon (Davidson and Martinelli, 2009), even under increased CO_2. In addition, most predictions on the future of the Amazon have been based on dynamic global vegetation models (DGVMs). While such models have dramatically evolved over the past 30 years, and currently represent the most relevant biophysical and biogeochemical processes (Levis, 2010, and references therein), they are largely based on biomes as opposed to individuals (van der Molen et al., 2011), and even though some models include the within-grid abiotic heterogeneity, biotic heterogeneity is seldom properly accounted (Moorcroft, 2003, 2006), with forests often assumed to be one or few homogeneous layers with a single life history strategy. However, previous studies have shown that both functional diversity within biomes and the range of plant sizes are fundamental to understand the observed mortality. For example, Breshears et al. (2008) found that the two dominant species of a woodland in New Mexico had dramatically different survivorship after a warm drought in 2001–2003: mortality rates for piñon pines (*Pinus edulis*) were above 90%, whereas the mortality rate of junipers (*Juniperus monosperma*) remained low. In addition, during the throughfall exclusion experiments in the Amazon, both Nepstad et al. (2007) and da Costa et al. (2010) found significant differences in mortality between genera, and in both cases mortality rates were higher among larger trees, the latter outcome being also observed in dry forests in Ghana (Fauset et al., 2012).

The aim of this study is to understand how the plant community in different locations in Eastern Amazon would respond to changes in the rainfall regime. Recently, Powell et al. (2013) compared a suite of model predictions of the throughfall exclusion experiments in Eastern Amazon using a standardized protocol, and despite the magnitudes not being accurate, the Ecosystem Demography Model (ED-2.2), the only individual-based model included in the study, was the only model that reproduced the timing of the collapse of the canopy biomass at the sites. In this study I test the forest dynamics under drier rainfall regime scenarios and evaluate how the plant community

would respond to increasing to such changes in climate. I focussed primarily on two locations where comprehensive observations of carbon and plant community dynamics are available and that are sufficiently close to conventional meteorological stations with longer records of rainfall to understand the long-term variability of the climate. The drought scenarios were generated based on the long-term time series of rainfall, and were generated by resampling annual rainfall over the past forty years, with increasing probability of selecting drier years, and used the Ecosystem Demography model (ED-2.2) to evaluate how the plant community would respond to increasing drought frequency. Within this framework I explored the resilience of plants to drought as a function of plant size and life strategy, and I extended the results to the entire Amazon to evaluate which regions could be potentially more vulnerable to changes in climate.

4.2 Materials and Methods

4.2.1 Overview of selected sites

The first site (GYF) is the Guyaflux tower site located at the Paracou Field Station (52°55′W; 5°17′N) near Sinnamary, French Guiana. The site is also a closed canopy forest at 35 m with emergent trees reaching 40 m (Bonal et al., 2008), and about half of above-ground biomass (AGB) is comprised by families Fabaceae, Lecythidaceae, and Sapotaceae, whereas Lecythidaceae is the commonest family among the smallest trees. Soils are classified as nutrient-poor acrisols, with some sandy ultisols areas (Bonal et al.). Epron et al. (2006) and Wagner et al. (2011) showed that the site has variable drainage, with a mix of soils with vertical drainage (Alt and USh following the nomenclature of Sabatier et al. (1997) for French Guiana) and soils with barriers to vertical drainage (SLD and DhS) lateral drainage. This site is located in one of the rainiest places in Eastern Amazon (Fig. 4.1), averaging 3050 mm per year. Nevertheless, GYF experiences a 4-month long dry season between August and November (Gourlet-Fleury et al., 2004).

The second site (S67) is located at the Tapajós National Forest (54°58′W; 2°51′S), near Santarém, Brazil and near km 67 of the BR-163 (Santarém-Cuiabá) road mark. The site is a closed

canopy forest at 40 m , with large number of emergent trees reaching 55 m (Saleska et al., 2003). Like in GYF, half of the AGB is comprised by individuals from families Fabaceae, Lecythidaceae, and Sapotaceae, whereas Rubiaceae is the dominant family among the smaller trees. Soils are classified as clay oxisols (Silver et al., 2000), with no impeding layers until at least 12 m below ground (Nepstad et al., 2007), and measurements near the site suggest that the water table is about 100 m deep (Nepstad et al., 2002). This site is located in one the driest regions of Eastern Amazon (Fig. 4.1), receiving approximately 1900 mm of rainfall per year, with a 5-month long dry season extending from mid-July until mid-December (da Rocha et al., 2009a).

At both sites, the forest inventory and eddy flux measurements were designed in an integrated way with forest biometry surveys in the upwind tower footprint (Fig. 4.2a,b). At GYF, ten plots of $0.49-0.50$ ha were randomly assigned ENE of the tower, and within each plot, all individuals with DBH ≥ 10 cm were surveyed in March 2004, 2006, 2008, 2010, and 2013. At S67, four 50 m $\times$ 1000 m transects east of the tower were surveyed in 1999, 2001, 2005, 2008, 2009, 2010, and 2011, usually around July; within each transect, all individuals with DBH ≥ 35 cm were surveyed, and all individuals with DBH ≥ 10 cm were surveyed along the inner 10 m sub-transect around the central transect lines. Neither S67 nor GYF are directly affected by variations in drainage of the major rivers in the Amazon basin: GYF is at the Sinnamary River Basin, which is not part of the Amazon Basin, instead draining directly to the Atlantic Ocean, while S67 is at the top of a plateau that is roughly 100 m higher than the Tapajós river, and thus is not directly affected by variation in the water table. This simplifies the analysis because variations in soil water availability are mostly due to local rainfall variability, and not by indirect effects on water table and drainage due to droughts upstream, an effect widely observed in the Amazon Basin during the 2005 and 2010 droughts (Marengo et al., 2008; Tomasella et al., 2011; Marengo et al., 2011b).

4.2.2 Model overview and settings

Like most DGVMs, ED-2.2 has a complete biophysical and biogeochemical module (Chap. 2), but the model is individual-based, and the plant community dynamics is solved through a system of

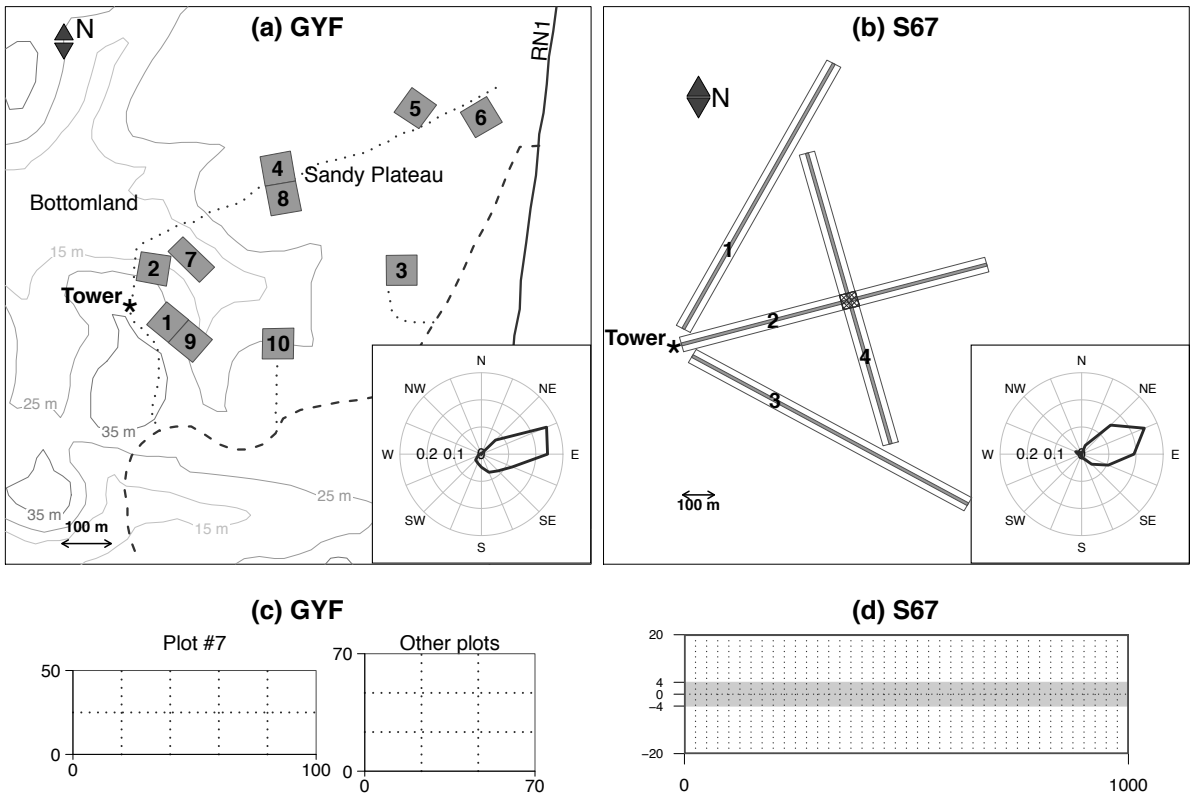

Figure 4.2: Overview of the site configuration for (a) Paracou (GYF) and (b) Santarém km 67 (S67), adapted from Stahl (2010) andStark et al. (2012), respectively. In the main plot the geographic location of plots and transects with respect to the tower are shown (hatched area in S67 has been surveyed but excluded from analysis), and the inset shows the histogram of non gap-filled wind direction for times when the mean wind speed was greater than $1\,\mathrm{m\,s^{-1}}$. Patch sub-division strategy for (c) GYF, for plot 7 and other plots, and (d) for S67. Dotted lines in the plot or transect splitting corresponds to the patch boundaries, and grey area in S67 corresponds to the sub-transect where all trees with DBH $\geq 10\,\mathrm{cm}$ were measured and included.

partial differential equations that represent the change in the distribution of plant sizes of different plant functional types (PFT)[1] nested in a distribution of ages since last disturbance of community patches, or the size-, succession-, and age-structure approach (SSAS, Sec. 2.2.1). Under this approach, individuals are only grouped when they are of similar size and same PFT, and live in an area with similar disturbance history and resulting population structure. Because the method is based on individuals, ecological measurements made at individual scale (such as recruitment

[1] In ED-2.2 the concept of plant functional type is linked to plant traits as opposed to biome characteristics, similar to the plant strategical property (PSP) definition by van der Molen et al. (2011).

and mortality rates) can be directly compared with the model. In addition, the model represents different storage pools such as multiple soil moisture levels, canopy air space with non-negligible storage capacity and full canopy radiative transfer model, which also allows direct comparison with common site-level biophysical measurements as shown in Chap. 3.

The structure and composition of the plant community at the beginning of the simulation is calculated from the first forest inventory available at each site (2004 for GYF, and 1999 for S67). Since neither site had age information, I split the plots into regularly spaced patches in order to capture the horizontal heterogeneity in canopy structure. For GYF, I generated 91 patches using all plots and trees surveyed, as shown in Fig. 4.2c. For S67 plants that were too close to the edges on the Y axis were not consistently surveyed, therefore, I used only the inner 40 m of the transect line, and the inner 8 m of the sub-transect, as shown in Fig. 4.2d, and excluded the area where transects 2 and 4 intersect, yielding to 312 plots. Tree population with $10 \leq \text{DBH} < 35$ cm from the inner sub-transects were scaled to the entire patch area. In ED-2.2, DBH corresponding to the smallest representable individuals (0.5 m-tall) is less than 10 cm. Since neither site had demographic density for these classes, initial conditions for such trees were estimated from the resulting population of the near-bare ground simulation until they reached equilibrium. The average demographic density of small plants was appended to all patches. Plant functional type was attributed to individuals based on the wood density (see App. E for further details). The distributions of basal area by size and plant functional type show some significant differences between the sites: at GYF (Fig. 4.3a), less 1% of the plant community basal area is from trees with DBH > 100 cm, and 70% of the basal area are from trees with DBH < 50 cm, whereas in S67 (Fig. 4.3b), trees with DBH larger than 100 cm constitute 16% of the total basal area, and only 49% of the basal area is comprised of trees with DBH < 50 cm; in addition late successional trees are mostly absent among larger classes. Moreover, the distribution of patch-level basal area also has significant differences (Fig. 4.3c): the mode of the distribution is higher at GYF than at S67, which is a consequence of higher demographic density of mid-sized trees $20 - 70$ cm, whereas the distribution is narrower and the mode occurs at higher values, which may be a result of the smaller sampling size.

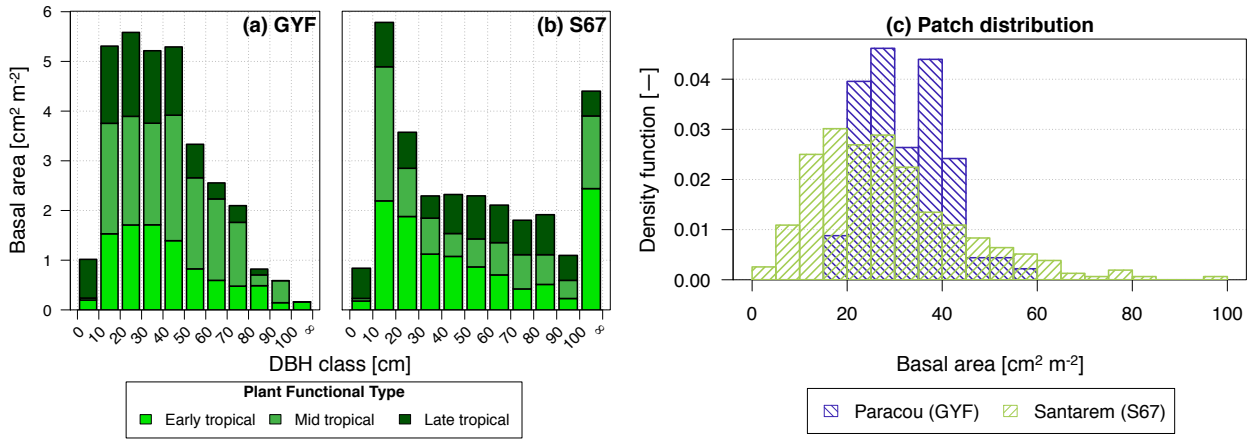

Figure 4.3: Initial distribution of basal area by DBH class and PFT at (a) GYF and (b) S67. (c) Histogram of basal area from the initial patch assignment for GYF and S67.

Available eddy covariance flux and meteorological forcing data at GYF covers the entire period between January 2004 and December 2012, whereas data at S67 covers two periods, from April 2001 to January 2006, and from August 2008 through December 2011[2]. While both sites have longer measurement periods compared to most eddy flux towers associated with the Large Scale Biosphere-Atmosphere experiment in Amazonia (LBA), they are still too short to describe the annual variability in precipitation, therefore I used the same climate generator described in Sec. 3.2.2. Both sites are relatively close to conventional weather stations that are part of the World Meteorological Organization network and report daily rainfall: Belterra (WMO-82246) is 25 km north of S67, and Cayenne-Félix Eboué airport (WMO-81405) is 79 km East of GYF. Both these stations have been operating for at least forty years. In Fig. 4.4a, I show the time series of annual rainfall for these sites, along with other locations near additional eddy flux measurements in the Amazon (RJA and M34) and the Cerrado (woody savannahs, BSB and PDG). In case of S67, annual rainfall often reaches totals that are comparable to woody savannah sites (BSB and PDG). The annual variability near GYF is also significant, however the total amounts of rainfall are generally higher than any other site, even for the driest years. In addition, I explored the variability of rainfall seasonality,

[2]Only meteorological measurements were valid for 2001, and a major interruption in measurements occurred between 2006 and 2008 after the tower was damaged by a falling tree.

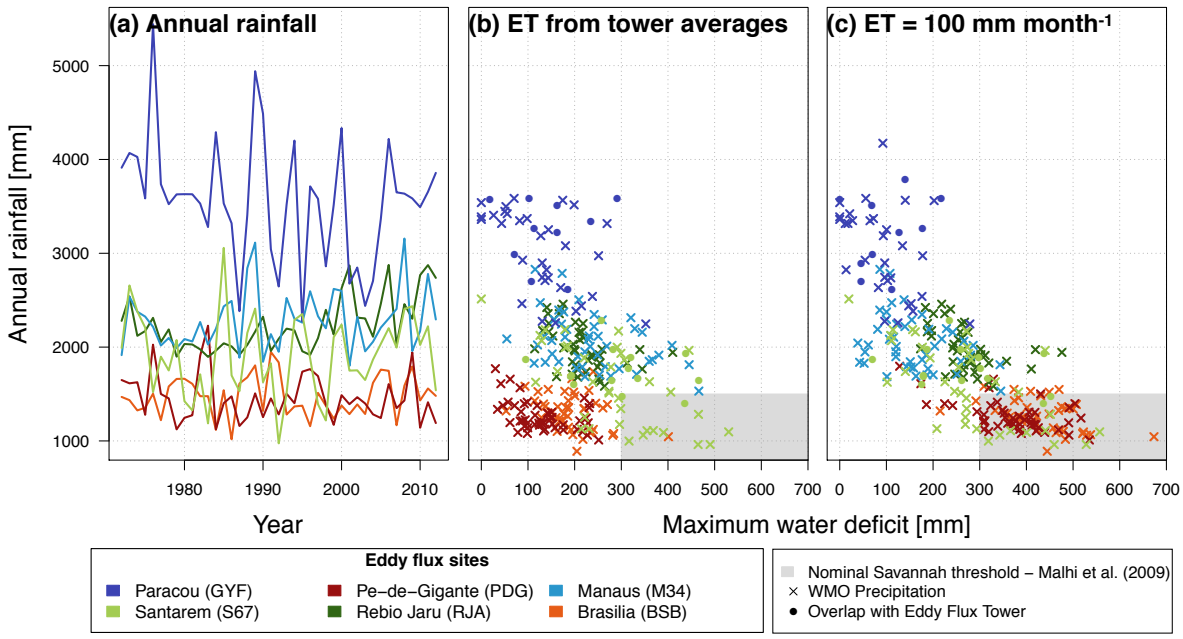

Figure 4.4: (a) Time series of annual precipitation from weather stations near the selected sites for the 1972-2011 period, along with other sites with eddy flux towers in Brazil shown here for reference. Scatter plot of the maximum water deficit and rainfall for the previous 12 months for the same sites using (b) the mean monthly evapotranspiration from eddy flux tower and (c) $100\,\mathrm{mm\,mo^{-1}}$. The grey box corresponds to the savannah region as suggested by Malhi et al. (2009a). Long-term rainfall data near RJA and GYF were obtained from NCDC/NOAA (2013), and data near the other sites were obtained from INMET (2013).

expressed by the maximum water deficit. This variable was defined somewhat similarly to Malhi et al. (2009a), but using all years instead of spatial averages. For each month t since January 1972, I estimated the water deficit ($\mathrm{WD}(t)$) as:

$$\mathrm{WD}(t) = \max\left\{0,\ \mathrm{WD}(t-\Delta t) + \int_{t-\Delta t}^{t} \left[\dot{\varepsilon}(t') + \dot{\tau}(t') - \dot{r}(t')\right] \mathrm{d}t'\right\} \tag{4.1}$$

where Δt is defined as 1 month; and $\dot{r}$, $\dot{\varepsilon}$ and $\dot{\tau}$ are respectively the rainfall, evaporation and transpiration rates obtained from the model output. Rainfall was determined directly from observations, whereas the total evapotranspiration $(\dot{\varepsilon} + \dot{\tau})$ was estimated in two different ways. First I assumed constant values for each month using the monthly mean evapotranspiration estimated from the towers either from literature (Santos et al. (2003, BSB)) or directly from the data for all other sites (Restrepo-Coupe et al., 2013). Alternatively, I used the same assumption as Malhi

et al. (2009a) and fixed the evapotranspiration to be 100 mm mo^{-1}. Evapotranspiration based tower fluxes (Fig. 4.4b) and the fixed evapotranspiration assumption (Fig. 4.4c) lead to significant differences in water deficit the savannah sites: using the typical values of evapotranspiration for each site, the combination of low rainfall and strong water deficit is uncommon in the savannahs (BSB and PDG), which suggests that in the long-term the vegetation in most sites are not too far from equilibrium with the amount of water they typically receive. On the other hand, S67 experienced the combination of low rainfall and strong water deficit has occurred multiple times over the past 40 years, in particular during strong El Niño events such as 1983, 1992–1993, and 1997–1998 (not shown).

4.2.3 Assessment of demographic rates

To evaluate the model response to the current climate conditions, I carried out a series of simulations for both sites using the initial conditions and the meteorological driver described in Sec. 4.2.2 and compared the forest dynamics obtained by the model for the period with available observations of mortality, growth and recruitment. In these simulations, I varied the initial year of simulation, soil texture class, and leaf phenology for both sites. The initial year was varied from 5 to 60 years before the first year with eddy flux tower. For soil texture classes, I restricted to two most representative soil classes in each site: sandy clay loam (SaCL) and clay loam (CL) in GYF, and clayey sand (CSa) and clay (C) in S67. Leaf phenology was assumed to be either evergreen or drought deciduous for the entire plant community, since I did not have information on the phenology of the species.

Modelled cohorts were identified as new recruits if they had reached the minimum recruitment size of the field surveys (i.e. DBH $\geq$ 10 cm) at the same months when the field surveys were carried out. Modelled mortality and growth rates included only cohorts that had been tagged at both the beginning and end of the interval, to ensure that cohorts that would grow into the minimum recruitment size after one actual field survey and died before the following survey occurred would not be included in the mortality and growth rates, as such individuals would never be surveyed in

the field. The method to aggregate mortality and growth rates from cohort to community-wide is presented in App. F.

4.2.4 Climate scenario

To simulate the forest resilience to drier climates, I conducted a series of simulations with the same initial plant community described in Sec. 4.2.2. Since the forest response at the throughfall exclusion experiments suggested that mortality usually takes place after multiple years of drought, and the amount of available water for plants depends on the hydraulic conditions of the soils, I tested the plant community response to drought by varying two key aspects of the abiotic environment: the distribution of dry and wet years, and the soil texture. Unless stated otherwise, all simulations were carried out for 60 years, and the first twenty years, which were driven by the meteorological conditions between 1992 and 2011 for model equilibration, were discarded from the analysis.

To test the changes in climate, I started from the reference 40-year meteorological forcing discussed on Sec. 4.2.2, and fitted a skew normal distribution of annual rainfall R (Azzalini, 2005):

$$p_{\mathrm{SN}}(R|\xi_R,\omega_R,\alpha_R) = \frac{1}{\omega_R\sqrt{2\pi}}\exp\left[-\frac{1}{2}\left(\frac{R-\xi_R}{\omega_R}\right)^2\right]\left\{1+\mathrm{erf}\left[\frac{1}{\sqrt{2}}\frac{\alpha_R\,(R-\xi_R)}{\omega_R}\right]\right\}, \qquad (4.2)$$

where $(\xi_R;\omega_R;\alpha_R)$ are the estimates of the location, scale, and shape parameters from the 40-year time series of observed annual rainfall. From the original distribution, I produced additional rainfall climates by keeping ω_R and α_R the same and shifting the estimate for location parameter by $\Delta\xi_{R_n} = -0.2\cdot n\cdot\omega_R$, $n\in\{0,1,\ldots,8\}$. For each rainfall regime n, I created 16 realizations: each realization was found by randomly generating 40-element vectors corresponding to the time series of annual rainfall, using $p_{\mathrm{SN}}(R|\xi_R+\Delta\xi_{R_n},\omega_R,\alpha_R)$ to describe the probability distribution function, and assigned the observed year with the closest annual rainfall to the random variable, creating the rainfall distributions shown in Fig. 4.5a. Because I forced annual rainfall to be selected from one of the years on record, I effectively reduced the inter-annual variability for the driest scenarios and made the skewness less negative or more positive; however, this should be regarded as a

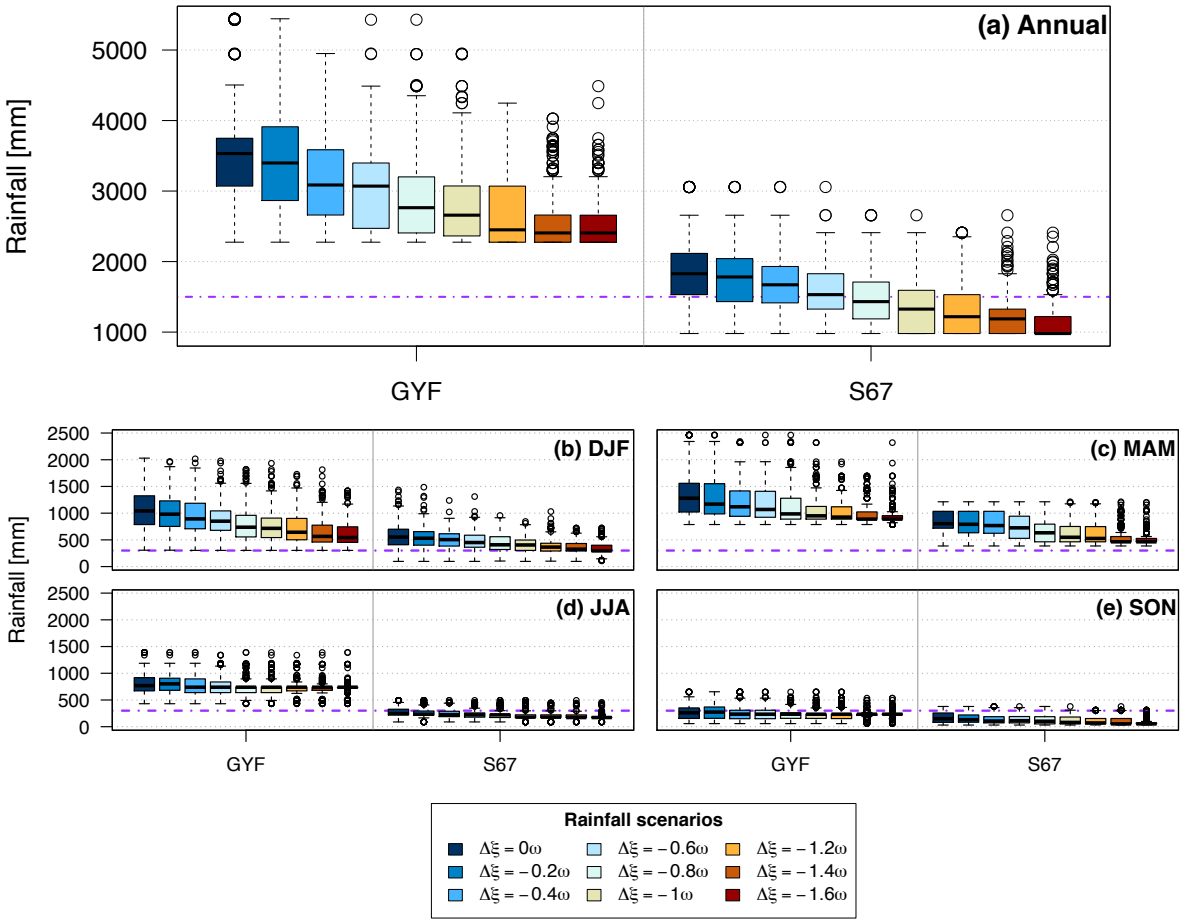

Figure 4.5: Box-and whisker plot showing the rainfall distribution for the two sites as a function of the shift in the location parameter (units are the scale parameter), including all realizations for (a) total annual means, and by season: (b) December–February, (c) March–May, (d) June–August, and (e) September–November. Purple lines corresponds to (a) 1500 mm and (b–e) 300 mm, often used as the lowest rainfall associated with tropical rainforests and typical dry season definition (e.g. Malhi et al., 2009a).

conservative approach, since the probability of annual rainfall that is lower than the driest year on record would increase in a climate that is drier on average.

At both sites, most of the rainfall variability is due to the wet season rainfall (Fig. 4.5b,c), therefore the scenarios effectively reduced mostly wet season rainfall, even though the sampling did not take seasonality into account. The random selection of years assumes that rainfall is not autocorrelated at annual scale, which is a reasonable assumption for both locations: by using a partial autocorrelation function on annual rainfall, I found no statistically significant autocorrela-

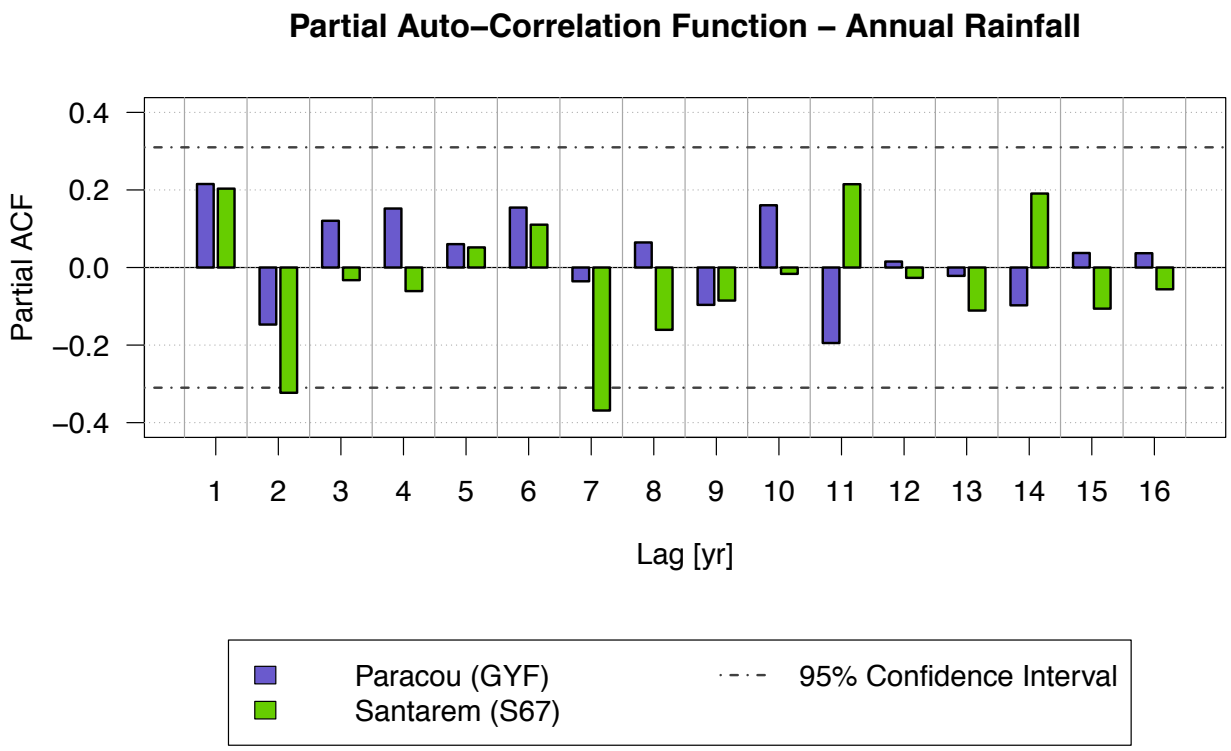

Figure 4.6: Partial Auto-Correlation Function analysis for the gap-filled observed annual rainfall in both sites between 1972 and 2011, using function `pacf` (package `stats`) in `R`. Dashed lines are the 95% confidence interval for the null hypothesis (no auto-correlation).

tion for GYF, whereas S67 showed negative autocorrelations for 2- and 7-year lags that were only marginally significant at 95% confidence interval (Fig. 4.6).

To test the forest response as a function of soil texture, I selected five soil texture types, four of them based on the commonest soil classes found in the Amazon. The commonest classes are based on a combination of three datasets: Quesada et al. (2011) for forest areas within the Amazon, Rossato (2001) for non-forest areas in Brazil[3], and IGBP-DIS (Tempel et al., 1996) for non-forest areas elsewhere. The original datasets were mapped onto the existing soil texture classes in ED-2.2 by Ke Zhang (Quesada et al.; Tempel et al.) and Humberto da Rocha (Rossato), and aggregated to a regular grid of $1^\circ \times 1^\circ$, where the dominant class was selected[4]. The predominant classes are shown in Fig. 4.7, and the three predominant classes are clayey sand (CSa), sandy clay loam (SaCL) and clay loam (CL). In addition, I included loamy sand (LSa) to represent all sandy soils

[3]Both Quesada et al. and Rossato are based on RADAMBRASIL (de Negreiros et al., 2009).
[4]The aggregation was necessary for the analysis presented in Sec. 4.4.3.

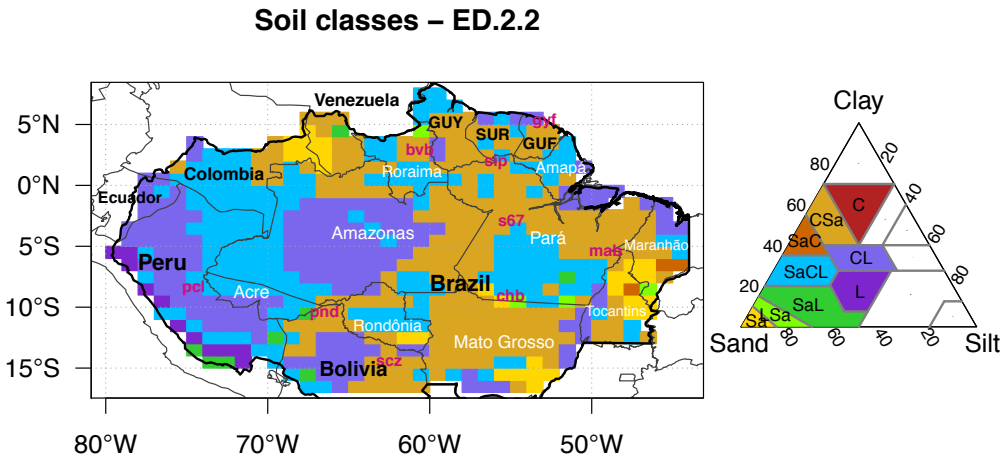

Figure 4.7: Predominant soil texture class in the Amazon region using the composite of soil types (C: clay, Sa: sand, L: loam, Si: silt), here aggregated to 1 deg $\times$ 1 deg blocks. a (GUY: Guyana, SUR: Suriname, GUF: French Guiana), Brazilian States are in white, and the position of Paracou (GYF) and Santarém km 67 (S67) towers are in violet. In addition, I included the position of multiple sites that are discussed in Sec. 4.4.3: Boa Vista (BVB), Pucallpa (PCL), Pando Department (PND), Santa Cruz Department (SCD), Cachimbo Mountains (CHB), Marabá (MAB) and Sipaliwini Savannah (SIP).

(fourth highest count if combined), and clay (C), which is typically found near S67 (Nepstad et al., 2002; Ivanov et al., 2012).

In addition, to test the impact of phenological responses to drought, I simulated the plant community using the two phenology options currently available for tropical trees, namely evergreen and drought deciduous. In ED-2.2 these strategies differ not only on whether or not plants shed their leaves during periods with low water availability, but they also on how they use the storage pool when under stress. When a plant's net carbon uptake is not enough to maintain its tissues (i.e. negative carbon balance), the evergreen trees consume carbon from the storage pool in an attempt to maintain the allometric ratios of its living tissues. If the tree undergoes a long period of negative carbon balance so that it consumes all non-structural carbon, then it will no longer maintain allometry, and mortality rates will quickly increase (the dependence of mortality on carbon balance is explained in App. F). In contrast, in the drought-deciduous physiological scheme, trees stop maintaining their live tissues, and save the stored carbon until soil moisture conditions improve. As a result, drought deciduous trees usually go into negative carbon balance only if the growing

season is too short to store enough carbon, or when the stress season is so long that most of the stored carbon is lost through turnover. In reality, a much broader range of drought strategies exist in the real forest, and these two cases can be interpreted as the extreme cases in water use strategy. Although previous studies have classified different species according to drought tolerance and leaf phenology (e.g. Bonal et al., 2000; Nepstad et al., 2007; da Costa et al., 2010), I could not attribute one or other life strategy to all surveyed individuals, therefore I simulated only the two extreme cases, in which I assumed the entire plant community to be either evergreen or entirely drought deciduous.

4.3 Observed and modelled variability of forest demographic rates

In this section I present a summary of comparisons of community-wide demographic rates for both GYF and S67 for each plant functional type, and additional comparisons by plant functional type and size are available at App. F. It is important to point out that the plant functional type attribution is less accurate in S67 than GYF because new recruits from 2001 onwards were not taxonomically identified in S67, and plant functional type were attributed based only on common name and compared with common name attributed in 1999 (App. E).

In Fig. 4.8 I present the expected mortality rates from both model and observations, where it can be seen that mortality rates are higher than observed at both sites for early (Fig. 4.8a,b,g,h) and mid-successional plants (Fig. 4.8c,d,i,j), although the model did not predict significant differences between evergreen and drought deciduous case. The magnitude of mortality rate of late successional trees generally agrees well with observations at both locations, although the model tends to overestimate the mortality at GYF (Fig. 4.8e,f), but less so at S67 (Fig. 4.8k,l), particularly for the evergreen.

To understand some of the differences, I also included the contribution of density-dependent and density-independent mortality rates to the total predicted mortality (see App. F.3 for how they

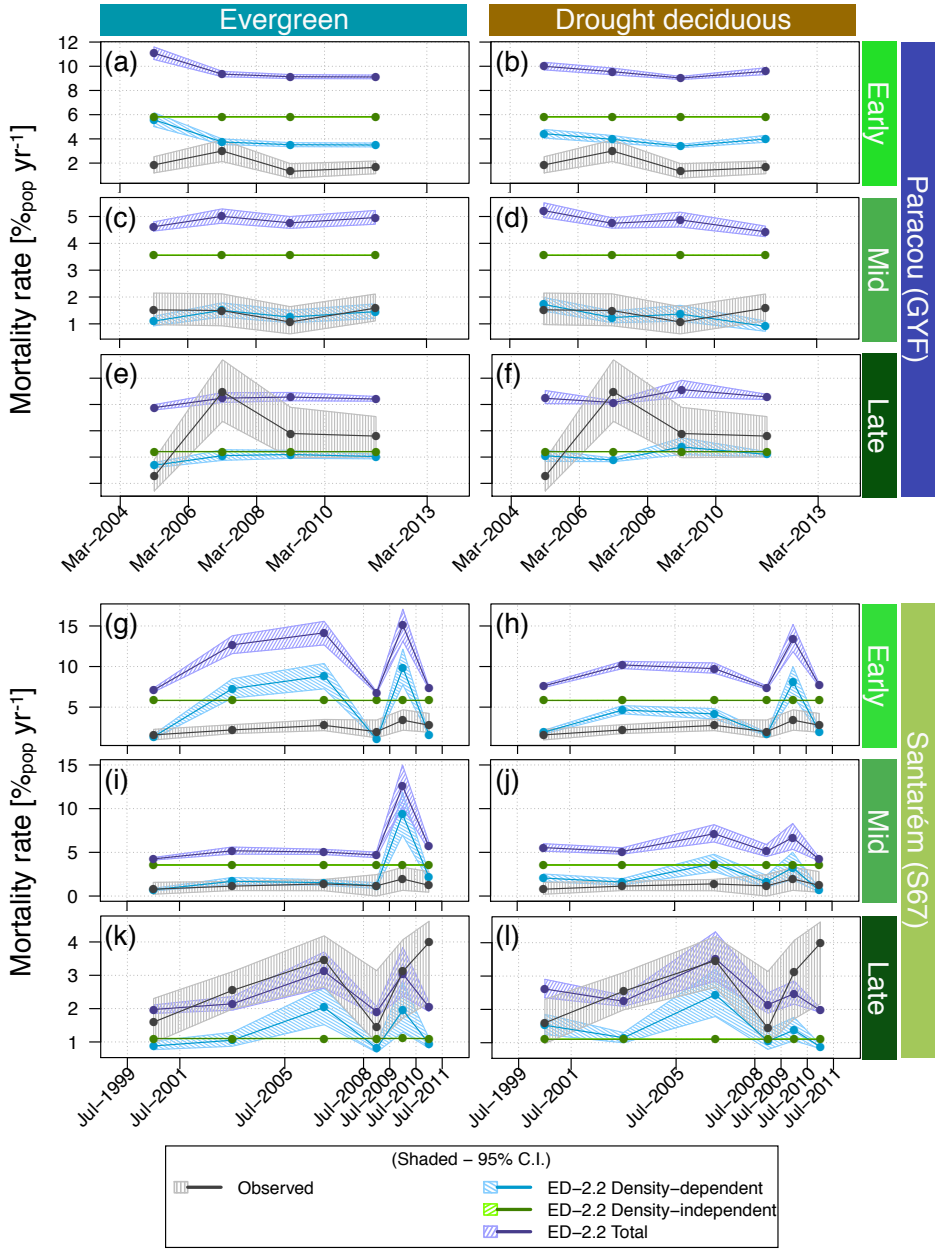

Figure 4.8: Comparison of mortality rates by plant functional type and leaf phenology obtained from the forest inventories and ED-2.2 for GYF and S67. In all cases, the points correspond to value for the interval of the actual surveys, denoted by vertical dotted lines. For ED-2.2 I also show the contribution of density-independent and density-dependent mortality rates (c.f. App. F). For the model output, the mean values are the average of the 10 simulations in which I varied soil type and the initial year, using the same survey intervals as the observations. ED-2.2 confidence intervals were obtaining from bootstrap, resampling the monthly time series using all months within each interval from all simulations 1000 times.

are defined). Following Moorcroft et al. (2001), density-dependent mortality is mortality directly related to carbon balance, which depends on environmental conditions and the ability of each plant to access the resources needed within the plant community and can substantially vary over time, whereas density-independent term is related to the expected life-span of the individuals and the disturbance rate, and are constants for each plant functional type. Both rates are overestimated in ED-2.2 for early and mid-successional cohorts (Fig. 4.8a-d,g-j), and density-dependent rates increased considerably in S67 between 2005 and 2008, which was slightly more pronounced at the evergreen simulations, and more evident amongst early and mid-successional (Fig. 4.8g-j). Mortality rates had different accuracy depending on the size classes, mostly amongst the smaller cohorts (DBH < 20 cm, see App. F.4). At GYF, the results were also overestimated, but like the observations the variability between consecutive surveys was small. Simulations at S67 showed some variations of mortality rates after years in which the dry season was either severe or lasted longer than usual (time series of rainfall not shown): 2004, 2006, and 2009. Early- and mid-successional showed noticeable increase in some of these dry seasons, although the result was not dramatic nor was it consistent across all plant functional types at the same time (Fig. 4.8a-f). In GYF a drier than average period extended throughout the 2008 dry season (Stahl et al., 2011), but no signficant response was observed in any of the plant functional types and phenology (Fig. 4.8a-f). Growth rates tend to be overestimated in ED-2.2, as shown in Fig. 4.9. Also, the positive bias is more pronounced in GYF than in S67 and, like in the mortality case, rates are normally more overestimated for early- and mid-successional (Fig. 4.9), especially for smaller cohorts (App. F.4). Nonetheless, growth rates generally showed low variability between the surveys at GYF for both observations and model. Finally, magnitude of growth rates between sites tend to be more similar in model simulations than in observations, especially for early- (c.f. Fig. 4.9a,b,g,h) and late-successional (c.f. Fig. 4.9e,f,k,l). Like mortality rates, differences in growth rates were generally minor between evergreen and drought deciduous.

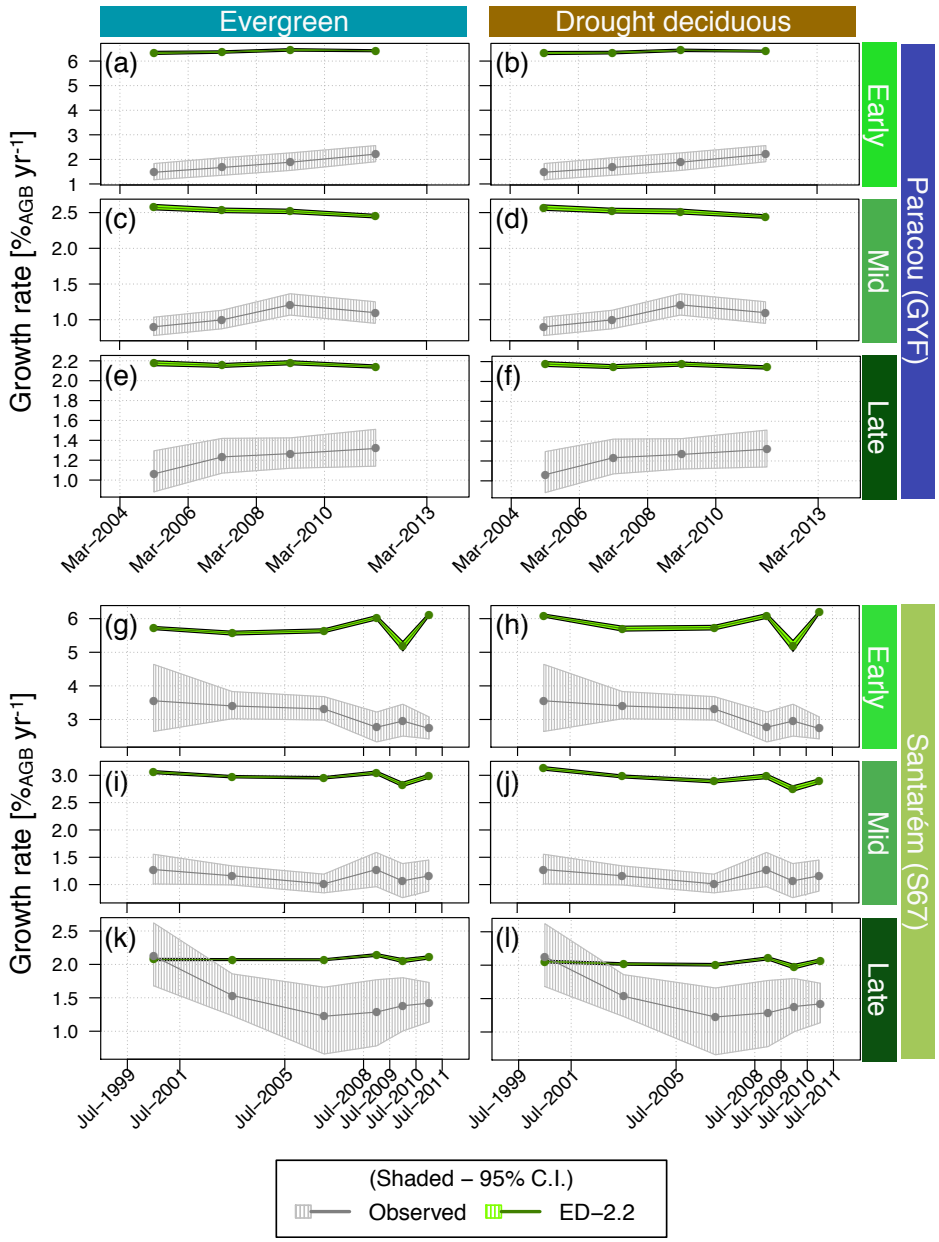

Figure 4.9: Similar to Fig. 4.8, but for relative growth in biomass.

4.4 Results from scenarios

4.4.1 Ecosystem level responses to shifts in climate

The total biomass response to drier climate is very different in GYF and S67, as shown in Fig. 4.10. In GYF even the most dramatic shift in rainfall was insufficient to cause any loss in the total above

ground biomass regardless of the soil texture or the leaf phenology (Fig. 4.10a,b), whereas many simulations in S67 experienced significant decrease in above-ground biomass. The turning point position and magnitude of biomass loss is strongly dependent on leaf phenology and soil texture: simulations using sandy soils generally maintained similar biomass to the control scenario until the location parameter $\Delta\xi$ was shifted between -0.6ω and -0.8ω, whereas soils with high clay content started experiencing significant biomass loss at -0.2ω and -0.4ω; also, drought deciduous generally lost less biomass for same soil texture and shift in rainfall regime (Fig. 4.10c,d).

To understand the different response between the two sites, I also present the corresponding total runoff (surface and sub-surface) simulated at both places for all scenarios Fig. 4.11, we observe that runoff in GYF is near $2000\,\mathrm{mm\,yr^{-1}}$, whereas in S67 the values are considerably lower, of the order of $500\,\mathrm{mm\,yr^{-1}}$. Given that average rainfall is roughly $3500\,\mathrm{mm\,yr^{-1}}$ and $2000\,\mathrm{mm\,yr^{-1}}$ for GYF and S67, respectively. This corresponds to approximately $1500\,\mathrm{mm\,yr^{-1}}$ rainfall that is effectively evaporated and transpired back to the atmosphere. Therefore, when rainfall is greater than $1500\,\mathrm{mm\,yr^{-1}}$, plants will be unlikely to experience water stress. At S67, the $\Delta\xi = -0.6\omega$ scenarios correspond to the case where average annual rainfall for most simulations is approximately 1500 mm, which means that rainfall use efficiency is approaching the maximum for the given plant community, and drier conditions will increase water stress hence approaching the total runoff even closer to zero (Fig. 4.11c,d at driest cases for all sites), whereas in GYF even the driest scenarios still had total runoff above 1000 mm. Drier conditions also increased total incoming radiation: in GYF the 5% increase in incoming radiation during the wet season produced only a minor change in primary productivity, because most most of variation of absorbed photosynthetically active radiation occurred among the largest trees, whose productivity is usually not limited by low light even during the wet season (not shown).

These definitions are more directly linked to the photosynthetic activity, therefore values presented here tend to be higher than those calculated from biomass change (e.g. Ponce Campos et al., 2013) since they include losses that are not directly measured from biomass-based NPP estimates, such as leaf (dark), root, and growth respiration.

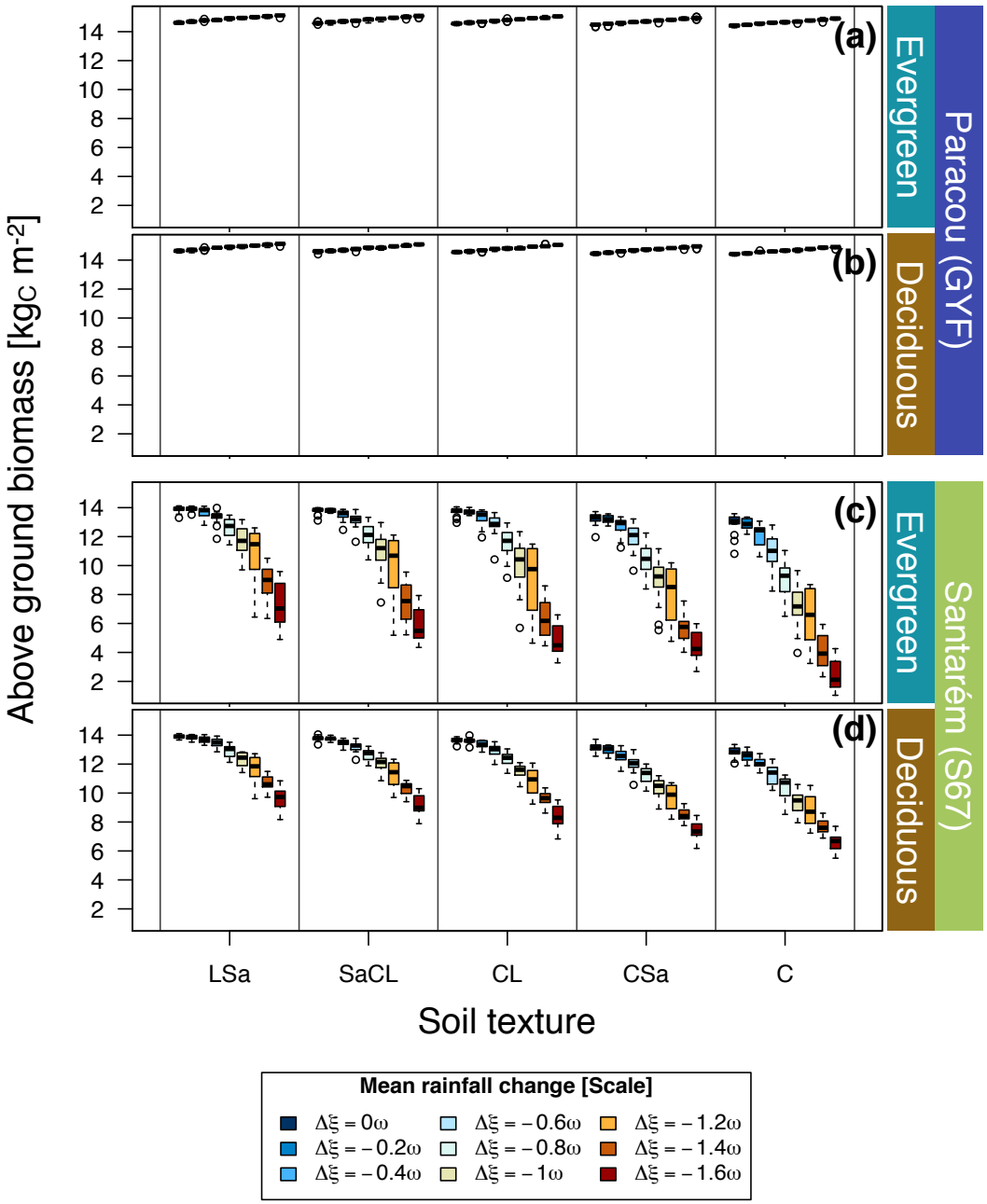

Figure 4.10: Box-and-whisker plot of the mean above-ground biomass $kg_C\,m^{-2}$ across all realizations and soil textures (loamy sand – LSa, sandy clay loam – SaCL, clay loam – CL, clayey sand – CSa, clay – C) for (a,b) Paracou – GYF, and (b,d) Santarém km 67 – S67; and (a,c) evergreen and (b,d) drought deciduous.. Each point of the box corresponds to the simulation mean (one value for each realization).

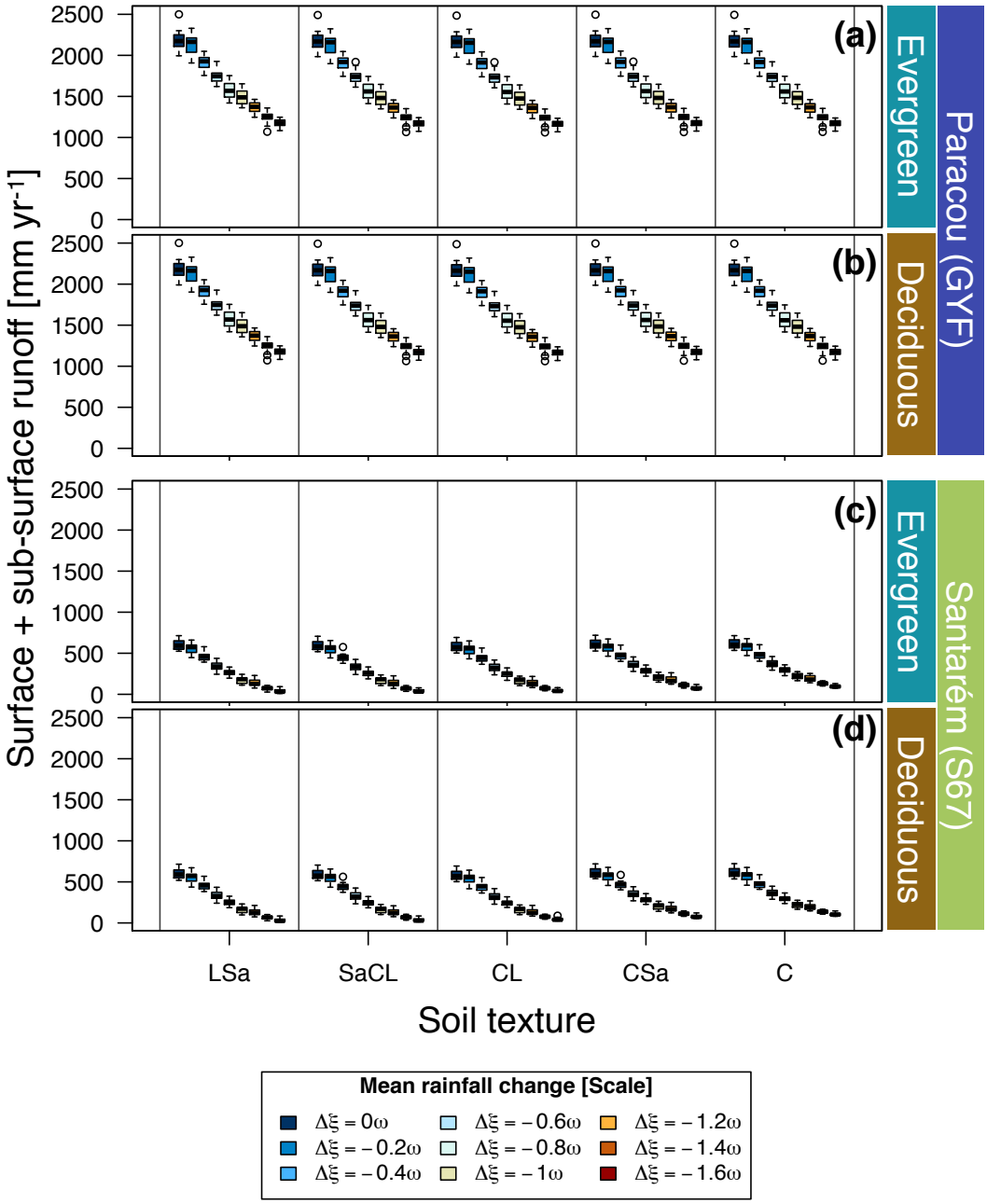

Figure 4.11: Similar to Fig. 4.10, but for total runoff (surface and sub-surface).

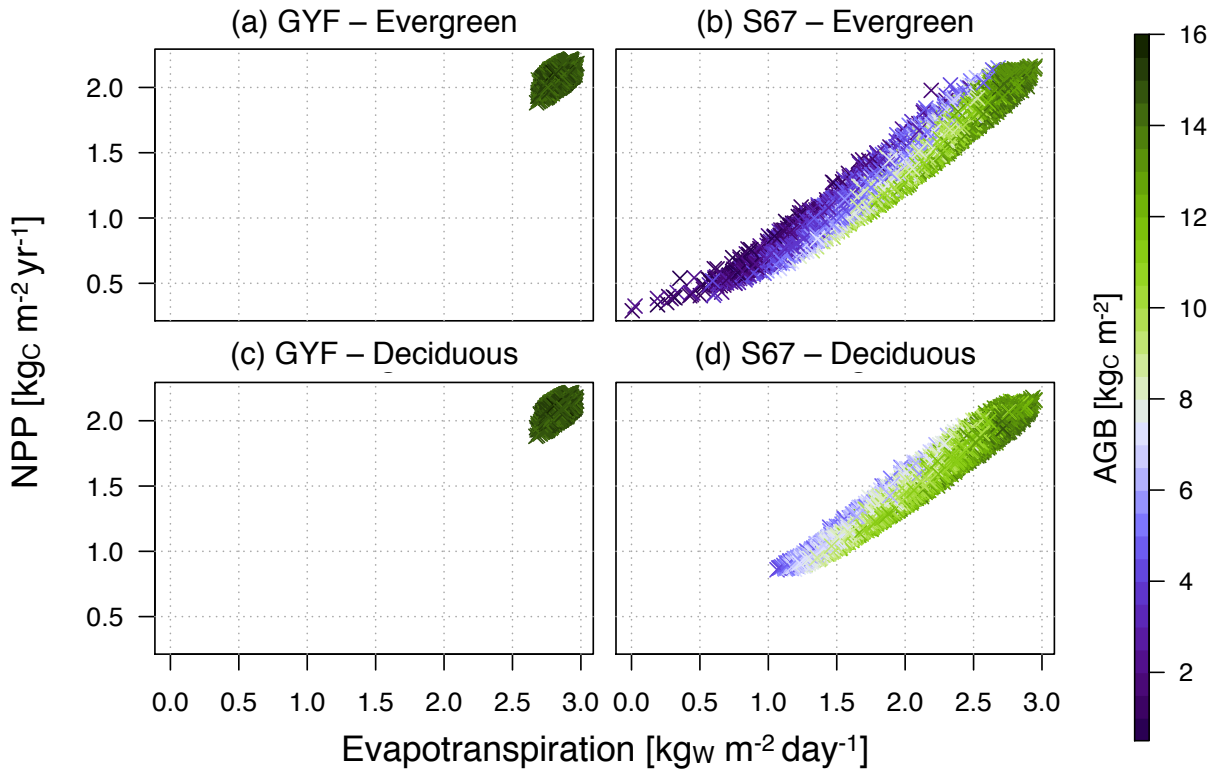

Figure 4.12: Scatter plot of the annual means of total plant community evapotranspiration (abscissa) and above-ground biomass net primary productivity (ordinate) for all realizations and climate scenarios. Colors represent above-ground biomass.

As it can be seen in Fig. 4.12, the net primary productivity is strongly correlated with evapotranspiration for all simulations at both GYF and S67. The linear relation between NPP and evapotranspiration, which is due to the link between transpiration and carbon assimilation associated with stomatal conductance, becomes shallower as biomass increases in S67 (Fig. 4.12b,d)[5]. A similar pattern had been also observed by (e.g. Ponce Campos et al., 2013); however, in their analysis they attributed it to resilience to drought, whereas here pattern of steeper slope at drier conditions holds even when the plant community has lost significant amount of biomass. In ED-2.2, relative increase in the slope for the driest cases is associated with reduction of intercepted water by the canopy, meaning that a larger fraction of water is lost through transpiration despite the lower total evapotranspiration (not shown).

The higher variability of average biomass for the driest cases suggests that drier climates are

[5]This is also true at GYF (Fig. 4.12a,c), although the magnitudes are significantly smallers at the three axes).

more likely to experience the conditions that cause high mortality, but these conditions may or may not occur. Based on the results from the through fall exclusion experiment (Nepstad et al., 2007; da Costa et al., 2010), it is expected that long droughts are more likely to cause major biomass losses, and this is also true in these simulations. Using a similar definition of water deficit (WD) as Eqn. (4.1) (page 151) but using the model evapotranspiration, I defined drought length as the number of consecutive months during which WD $> 10\,\mathrm{mm}$[6]. In Fig. 4.13, one can observe that under this definition of drought length, GYF never experienced droughts that lasted more than one year, and even though the highest water deficit sometimes exceed 300 mm, the nominal threshold used by Malhi et al. (2009a) to define significant rainfall seasonality, these events were too sporadic to cause significant losses of biomass due to negative carbon balance, regardless of the leaf phenology. In contrast, several realizations predicted multiple year droughts in S67, some of them lasting 7–8 years (Fig. 4.13b,d). For the evergreen case, (Fig. 4.13b), the highest mortality rates occurred when droughts were the longest; within the same drought length, higher water deficit was associated with higher mortality rates. Compared to the evergreen case, drought deciduous simulations showed similar patterns, but mortality rates were slightly lower for similar drought duration and maximum drought stress. Finally, the realizations that produced even longer droughts caused the plant community to collapse, with major reduction in transpiration rates making high WD less likely, which is similar to the observed deficits in more seasonal sites (c.f. Fig. 4.4).

To understand the dynamics associated with the high mortality events, I present the time series of biomass and drought length for one realization of the scenario $\Delta\xi_R = -1.0 \cdot \omega_R$ (Fig. 4.14). For the evergreen case (Fig. 4.14a), we observe that short droughts are not sufficient to cause major collapses in the ecosystem; such losses occur only during extremely long droughts as we would expect from Fig. 4.13. Once drought conditions are alleviated, the biomass starts to increase again, until another extreme drought reduces biomass again. In case of drought deciduous phenology (Fig. 4.14b) both biomass losses and recovery from drought are slower, which reflects their drought

[6]Although this definition does not distinguish between drought and dry season, one can still assume that during a drought the length of the hydraulic stress period will be longer than the climatological dry season. In addition, the choice of 10 mm is arbitrary and aimed to reduce brief periods with lower rainfall to be categorized as droughts.

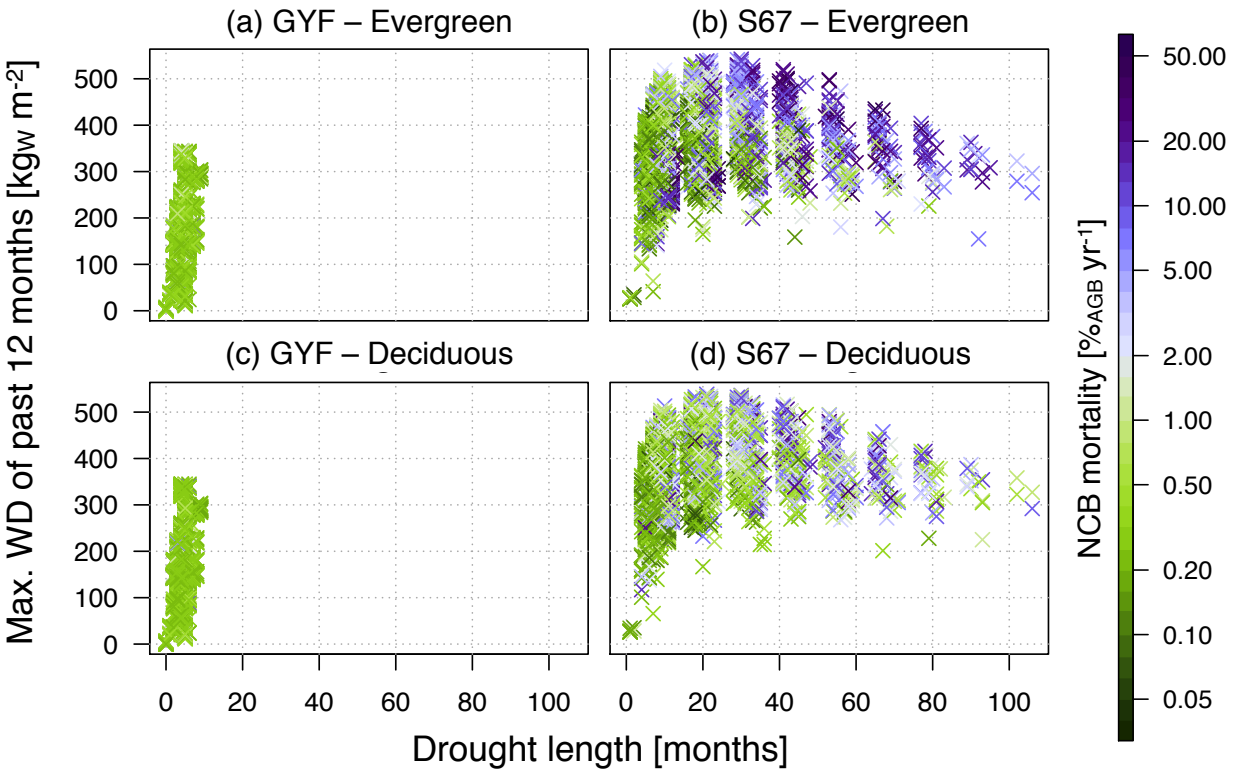

Figure 4.13: Scatter plot of annual maxima of drought length (abscissa) and water deficit (ordinate) for all simulations using clayey sand (CSa). Colors represent the annual and community-wide average of density-dependent mortality rate.

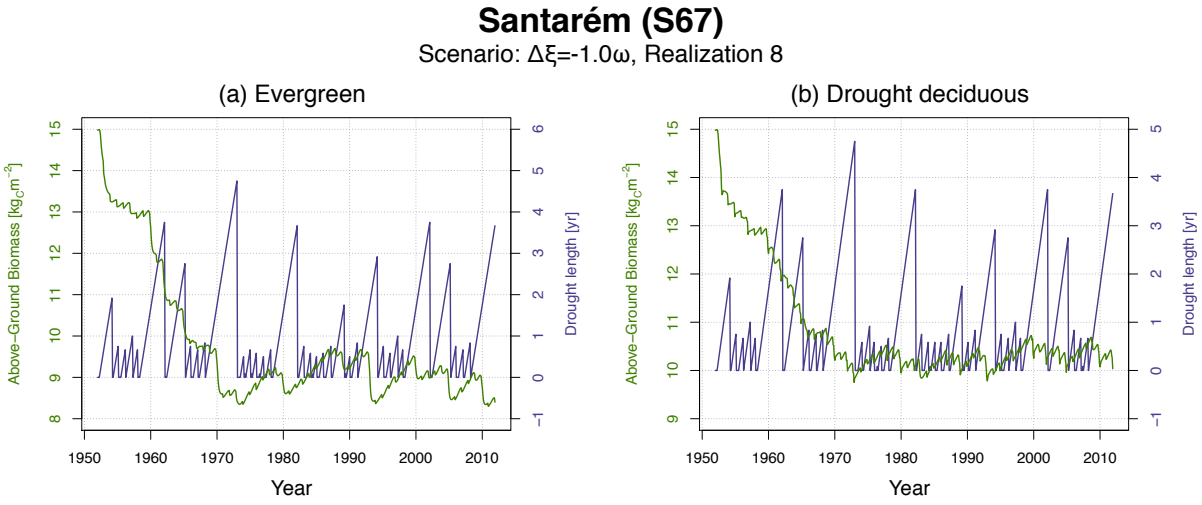

Figure 4.14: Time series of above-ground biomass and drought duration for one sample simulation for Santarém km 67 with clayey sand soils and (a) evergreen and (b) drought deciduous phenology.

tolerance, but also that short droughts may also reduce their growth.

The response to drought length and drought intensity also depended on soil texture. In Fig. 4.15, we observe that drought lengths are much longer for sandy soils, reaching as long as 35 years, whereas the longest cases in clayey soils do not last longer than 6 years. The fact that clayey soils do not experience longer droughts is a result of the ecosystem collapsing and reducing their water demand at much shorter droughts. Since rainfall is the only external source of water, the higher water deficit in sandy soils suggest that they have higher storage capacity of water that is accessible to plants. Although this result appears counter-intuitive, given that sandy soils drain more quickly than clayey soils, this is a consequence of the differences in porosity, and how they relate to the matric potential, as shown in Fig. 4.16. For any soil moisture, hydraulic conductivity tends to be higher for sandier soils; however, clay particles are smaller, and thus soil matric potential reaches the wilting point much more quickly for clayey soils than for sandy soils; in addition, hydraulic conductivity is much lower for sandy soils than for clayey soils at the same matric potential. Soil matric potential is related to the effort that the plant needs to make to extract water from the soil, and the stomatal conductance is directly related to this variable, albeit through a phenomenological scaling factor $o_{sW}, [0-1]$, similar to many other DGVMs (Eqn. 2.121, Sec. 2.4.6).

While the sensitivity to soil texture implies that soil moisture stress is a major contributor to the plant community response, other environmental changes associated with drought will impose additional stress on the ecosystem, which will affect how efficiently the ecosystem will assimilate carbon. Here I introduce two indices to relate carbon assimilation to water usage and efficiency in doing so: the leaf-level water use efficiency (LWUE), and carbon use efficiency (CUE):

$$\mathrm{LWUE}(t) = \frac{\int_{t-\Delta t}^{t} \mathrm{NPP}(t')\,\mathrm{d}t'}{\int_{t-\Delta t}^{t} \dot{\tau}(t')\,\mathrm{d}t'}, \text{ Leaf water use efficiency, } [\,\mathrm{g_C\,kg_W^{-1}}] \tag{4.3}$$

$$\mathrm{CUE}(t) = \frac{\int_{t-\Delta t}^{t} \mathrm{NPP}(t')\,\mathrm{d}t'}{\int_{t-\Delta t}^{t} \mathrm{GPP}(t')\,\mathrm{d}t'}, \text{ Carbon use efficiency, } [\,\mathrm{kg_C\,kg_C^{-1}}] \tag{4.4}$$

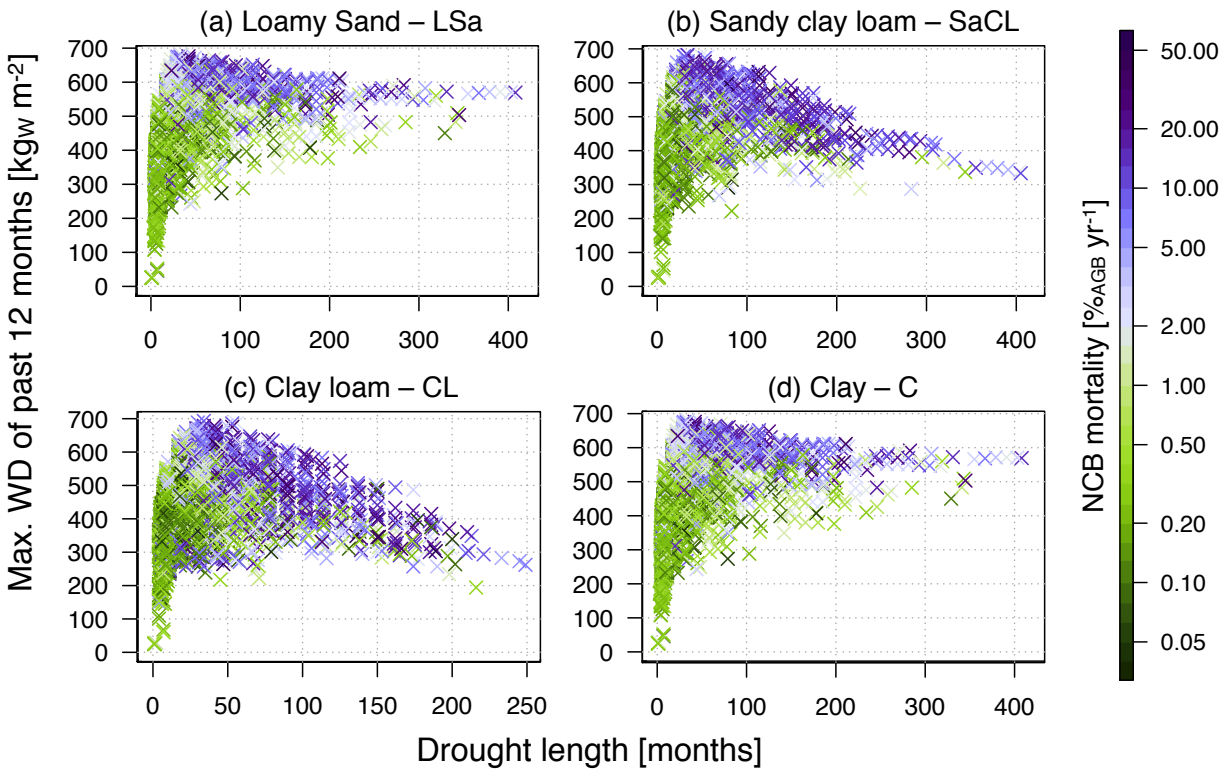

Figure 4.15: Scatter plot of annual maxima of drought length (abscissa) and water deficit (ordinate) for all simulations in S67 with evergreen phenology for the other soil texture classes. Colors represent the annual and community-wide average of density-dependent mortality rate.

where NPP$[\,\mathrm{kg_C\,m^{-2}\,yr^{-1}}]$ is the physiological net primary productivity defined as the gross primary productivity GPP$[\,\mathrm{kg_C\,m^{-2}\,yr^{-1}}]$ minus total plant respiration R_{Plant}; and $\dot{\tau}[\,\mathrm{kg_W\,m^{-2}\,day^{-1}}]$ is the total plant community transpiration rate. The former relates how much carbon is produced per unit of water spent, and the latter how much carbon is produced per unit of carbon that was assimilated. As shown in Fig. 4.17, in GYF, the reductions of LWUE are small and mostly related to LVPD, as observed by the color gradient being nearly paralel to the LVPD axis, and differences between evergreen and drought deciduous are minimal (Fig. 4.17a,c). Conversely, in S67 the average leaf vapor pressure deficit (LVPD) is positively correlated to higher soil matric potential, and both are negatively correlated with LWUE (Fig. 4.17a,c), which suggests that both above-ground and below-ground water stress reduce the efficiency of the ecosystem of using the water that is

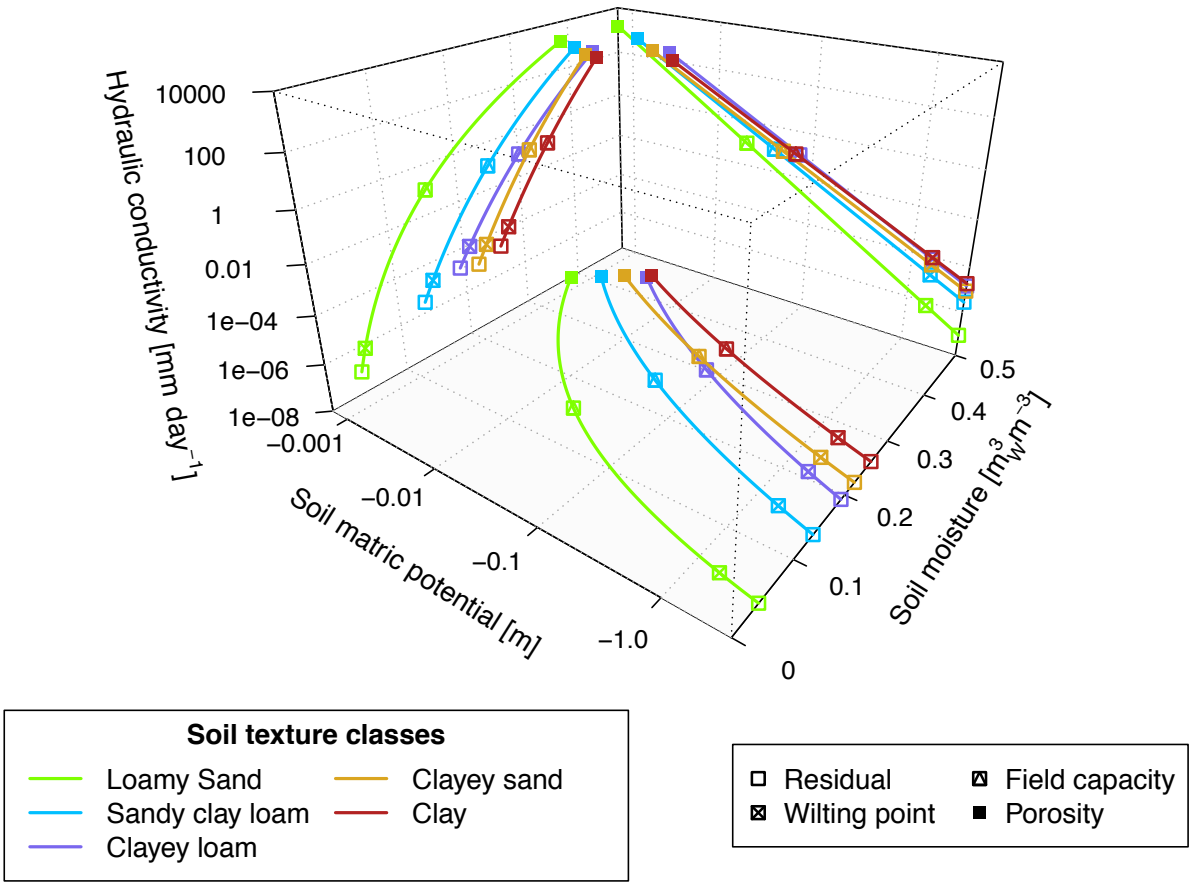

Figure 4.16: Hydraulic conductivity as a function of soil moisture and soil matric potential for the five soils tested (only projections onto the planes are shown for clarity). Note that the negative soil matric potential and hydraulic conductivity axes are logarithmic.

accessed by the ecosystem. Leaf water user efficiency decreased to even lower values for the evergreen case (Fig. 4.17a), a condition that is avoided by the drought deciduous case because the demand for water is diminished due to partial leaf shedding at higher soil matric potential. Finally, in GYF, the decrease in LWUE is due to an increase in transpiration while NPP did not significantly change, whereas in S67 the reduction at the highest LVPD and matric potential is due to NPP decreasing faster than transpiration (not shown).

Similar patterns are also observed for carbon use efficiency (Fig. 4.18). CUE is reduced because GPP decrease is not as fast as NPP (Fig. 4.18), which means that more carbon is being lost through respiration for the same amount of assimilated carbon and loss of water. The higher LVPD is a direct consequence of warmer leaves, which in turn result from increased radiation at the leaf level

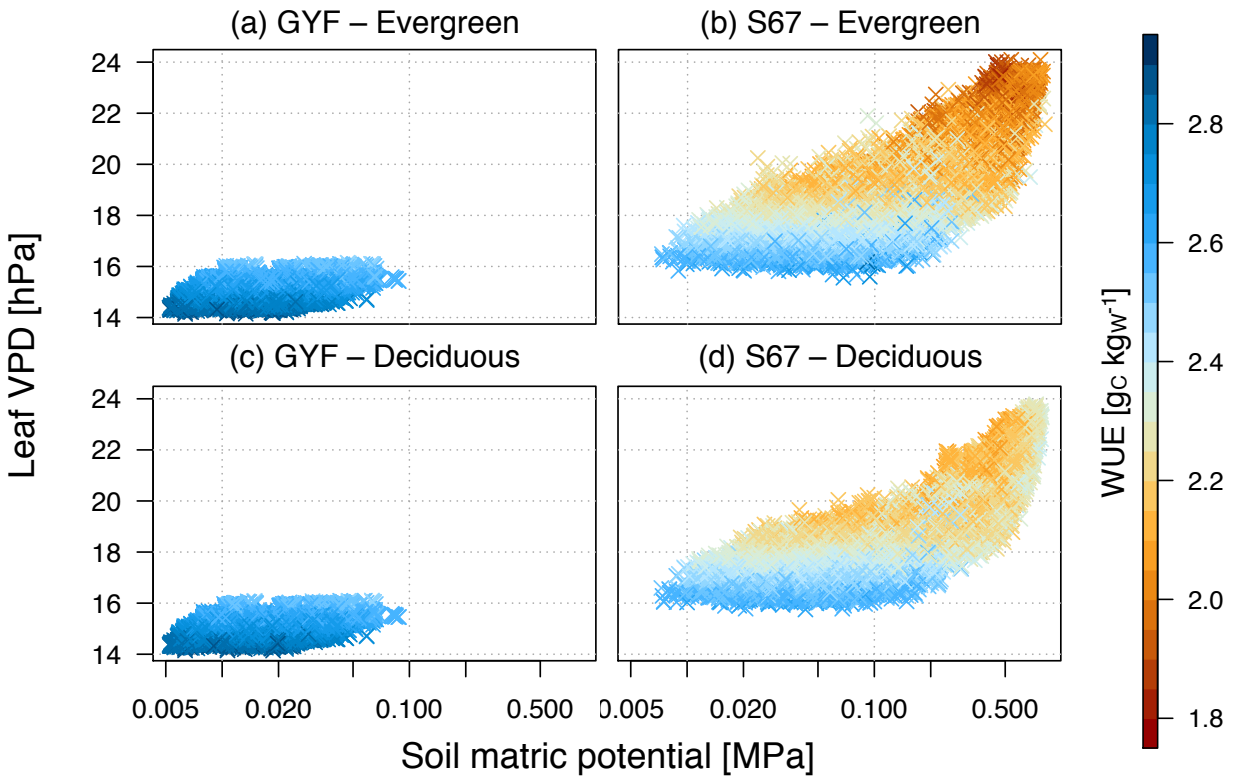

Figure 4.17: Scatter plots of annual and vertical mean of soil matric potential (abscissa) and annual mean of leaf vapor pressure deficit (ordinate) for all simulations and realizations that used clayey sand. Colors represent the leaf water use efficiency (LWUE).

and reduced water interception in the driest scenarios. A similar mechanism has been previously discussed by Medvigy et al. (2010), who showed that representing sub-monthly variability reduces the net productivity in temperate forests by increasing throughfall during rain events but increasing the period in which leaves are unable to cool through evaporation of intercepted water. In addition, increased LVPD may accelerate the establishment of severe drought conditions, since more water will be lost through transpiration, potentially reducing the drought length needed to reach the point predicted by the throughfall exclusion experiments in which mortality increases significantly.

In Fig. 4.19, we observe that for GYF, not only the drier rainfall regime had insignificant effect on total biomass, but also the demographic rates were remarkably similar, and the minor responses to drier climate were due to light regime as opposed to rainfall: both evergreen and drought deciduous showed very minor increases in growth rates (Fig. 4.19c,d) and no increase in

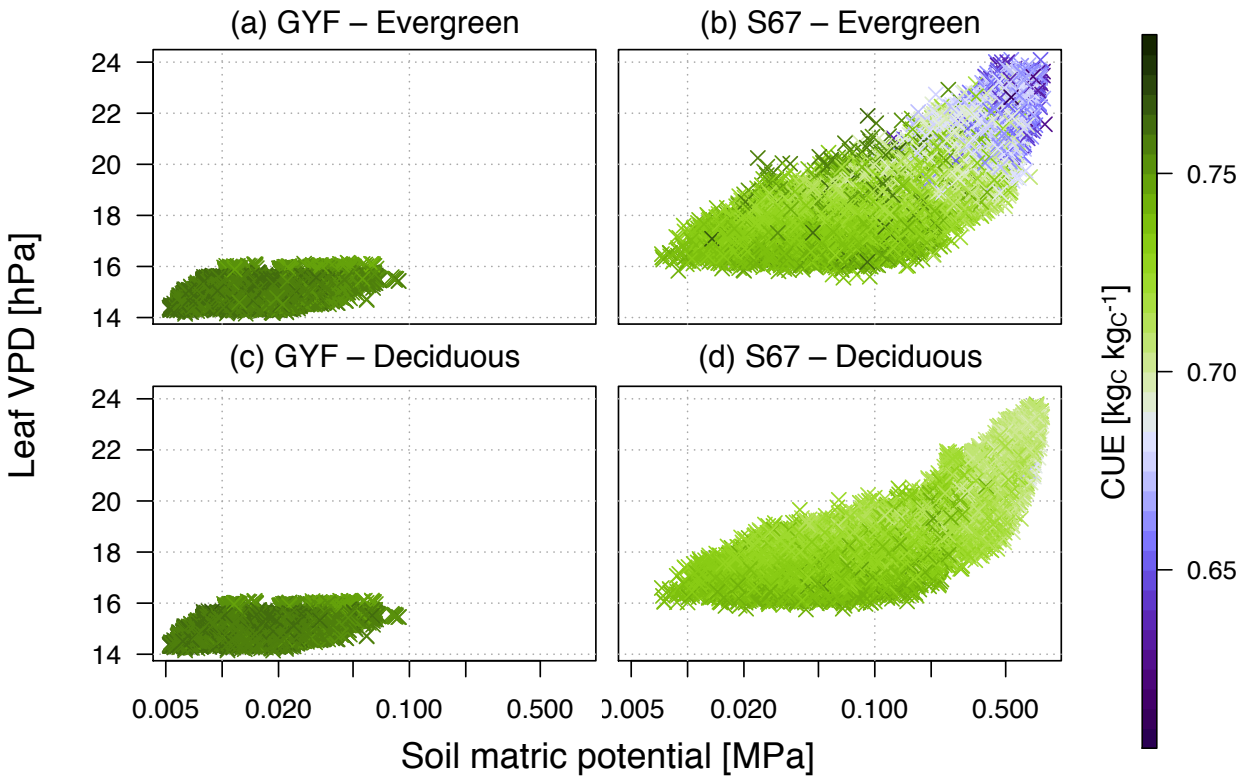

Figure 4.18: Similar to Fig. 4.17, but colors refer to carbon use efficiency (CUE).

mortality rates (Fig. 4.19c,d), and consequently, biomass on average increased more at the drier scenarios (Fig. 4.19a,b).

On the other hand, the demographic changes in S67 (Fig. 4.20) reflect the increased variability of the final AGB, which can be seen in Fig. 4.10, especially for the evergreen case. Unsurprisingly, the net change in plant community was negative at both the evergreen (Fig. 4.10a) and drought deciduous (Fig. 4.10b), and as anticipated by the final biomass, the net change was more negative in the evergreen case. The resulting biomass, however, was not a simple response to higher mortality rate, which, as previous results suggested, increased significantly at both the evergreen and (Fig. 4.10e) the drought deciduous cases (Fig. 4.10f). Moreover, both the evergreen and drought deciduous simulations showed decrease in growth rates (Fig. 4.10c,d), and growth rates were generally lower for the evergreen case, which further reduced the ability to recover. As the example of time series of above-ground biomass suggested (Fig. 4.14), however, the lower growth rates

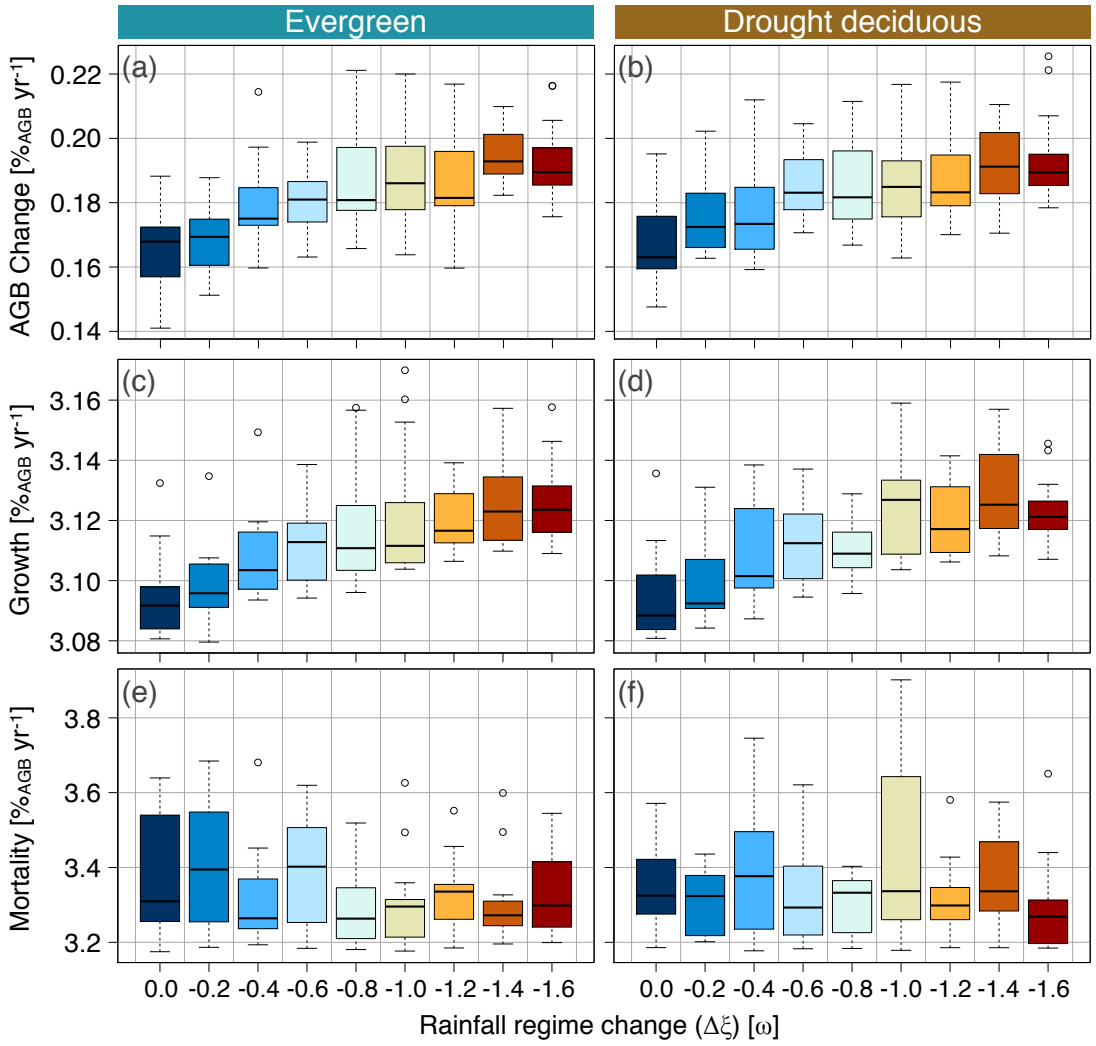

Figure 4.19: Box-and-whisker plot of the average community dynamics for GYF and sandy clay loam soils. Demographic rates were expressed in rate of change in relative above-ground biomass, including only cohorts with DBH $\geq$ 10 cm. Points used to generate the boxes were the simulation mean of each realization within each climate scenario.

occurred not due to a generalized decrease in growth, but to extended periods where the evergreen plants were unable to grow following droughts, since they had lower carbon storage at the end of the drought period (not shown).

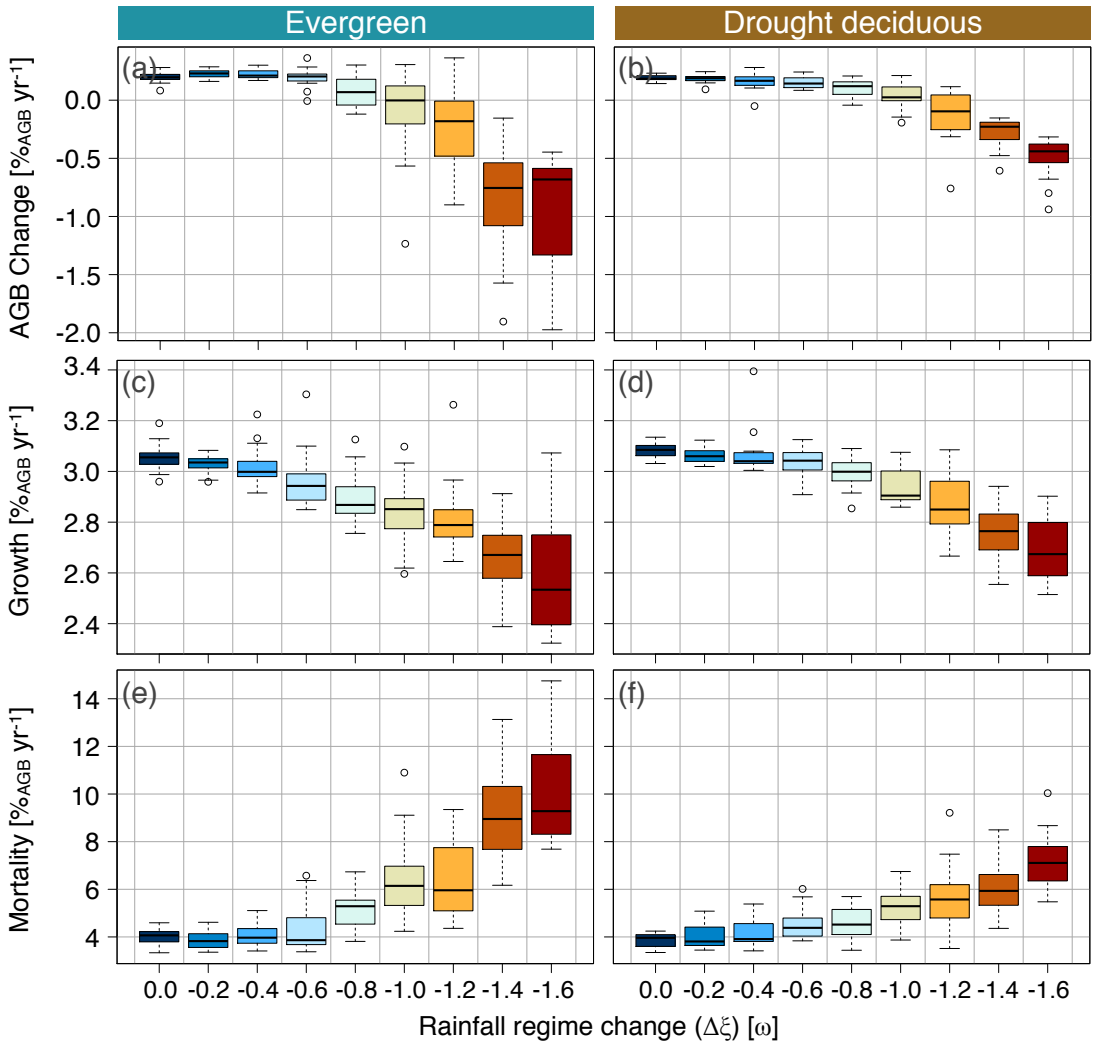

Figure 4.20: Similar to Fig. 4.19, but for S67 and clayey sand soils. Note the change in scale.

4.4.2 Within-community response to the shift in climate

While in the previous section I explored some of the mechanisms that created the response of the entire plant community to the drier climates, these changes were emerging properties of the processes and dynamics within the plant community, which includes a full distribution of plants of different sizes and functional types competing for shared resources, each one with different demands and different access to them. In GYF the structure and composition remained largely the same regardless of the soil texture and shift in rainfall regime (not shown). Therefore, for most of

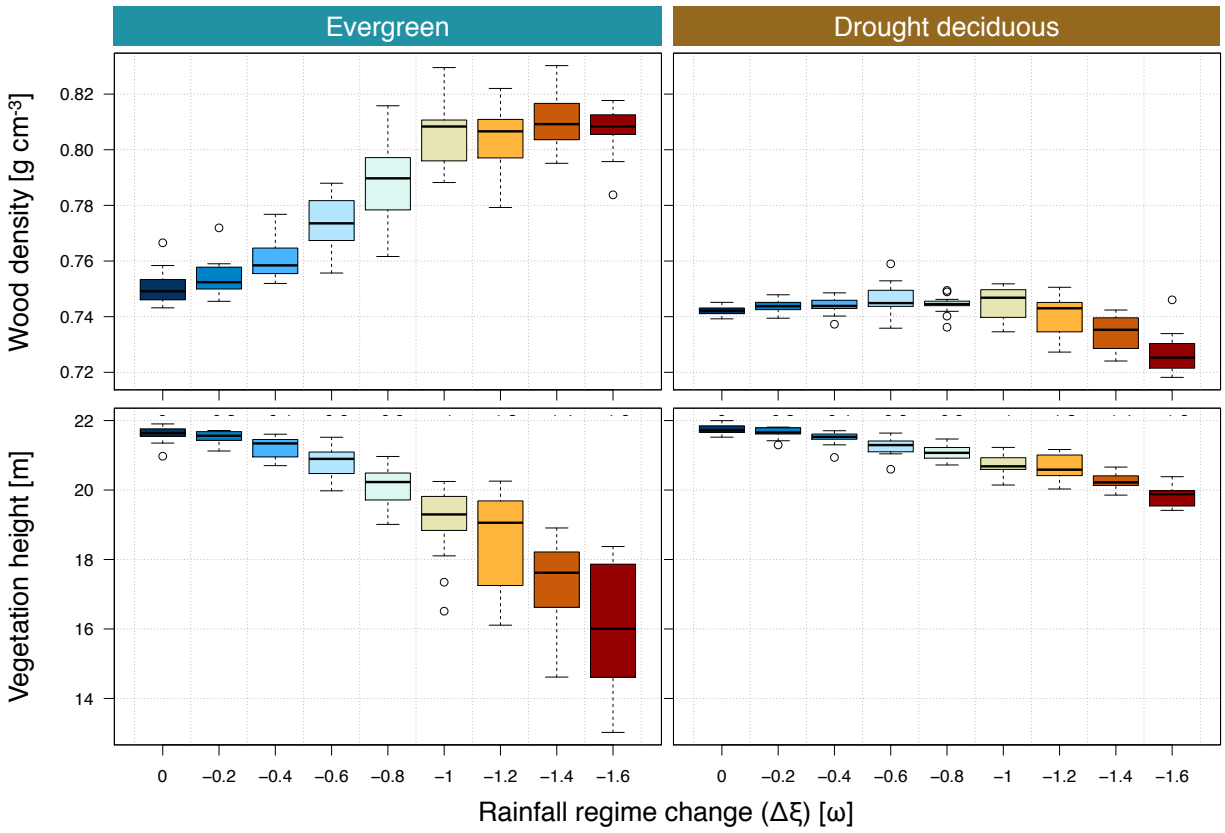

Figure 4.21: Box-and-whisker plot of the basal-area weighted mean community-wide wood density $[\,\mathrm{g\,cm^{-3}}]$ and mean tree height $[\,\mathrm{m}]$ across all realizations within each rainfall regime scenario for clayey sand for (a) evergreen and (b) drought deciduous in Santarém km 67. Each point of the box corresponds to the simulation mean (one value for each realization). Wood density for all simulations at Paracou had wood density near $0.74\,\mathrm{g\,cm^{-3}}$ and mean vegetation height was near $22.5\,\mathrm{m}$ with almost no variability hence not shown.

this section, I focus on S67, where the mean vegetation height decreased for both evergreen and drought deciduous cases, suggesting that taller trees were lost at higher rate (Fig. 4.21). Wood density, however, showed opposite trends, with increase in mean wood density for the evergreen case and slight decrease in drought deciduous case, suggestive that the early successional trees had the most loss in the former case whereas the proportion of late-successional decreased in the latter case.

In Fig. 4.22, I present the shift the forest structure as a response to drier regime. Firstly, the model has a tendency of replacing the observed forest structure by a more late-successional

dominated forests even under the control experiment ($\Delta\xi = 0\omega$), which is a consequence of high density-independent mortality rates of early and mid-successional cohorts, therefore I focus on the differences between the control simulations and the different scenarios. Both the average basal area and leaf area index decreased with drier climates for all classes with DBH $\geq$ 10 cm, and sub-canopy cohorts (35 $\leq$ DBH $<$ 55 cm) experienced the largest relative loss at the driest rainfall regime: 87% loss of basal area and leaf area index in the evergreen case, and about 55% loss of basal area and 60% loss of leaf area index in the drought deciduous case. On the other hand, smaller cohorts (DBH $<$ 10 cm) increased basal area (leaf area index) by 35% (10%) for the evergreen case, although these cohorts also lost about 8% (35%) of basal area (leaf area index) for the drought deciduous case. As suggested by the changes in wood density, the most dramatic shift in the evergreen case occurred amongst early successional trees, which went extinct in all size classes for most realizations with $\Delta\xi_R \leq -1.4\omega_R$. With less early successional cohorts, the basal area for mid-successional increased 165% in basal area for cohorts with DBH $<$ 35 cm. Late successional cohorts were lost in all classes and in both scenarios, and the losses were most significant amongst cohorts with DBH $<$ 35 cm. Early successional cohorts in the understory declined sharply at lower rainfall regime changes in the evergreen case, and much slower in the drought deciduous case.

Cohorts of all size classes with DBH $\geq$ 10 cm eventually experienced increase in density-dependent mortality rates (Fig. 4.23), although significant increase in larger trees occurred only for scenarios drier than $\Delta\xi_R = -0.6 \cdot \omega_R$, when density-dependent mortality rates became comparable or outweighed the modelled density-independent rates. Growth rates steadily decreased for all PFTs and all classes with DBH $\geq$ 35 cm. Higher growth rates and increase in biomass among smaller late- and especially mid-successional cohorts (not shown) in the evergreen case was due to reduced competition with early successional and more light availability following the canopy thinning. One of the main differences between the evergreen and drought deciduous case was that larger trees did not experience as much biomass reduction as in the evergreen case, particularly cohorts with 35 $\leq$ DBH $<$ 55 cm, and as a consequence, the understory growth rates did not increase as much as in the evergreen case (not shown). In addition, the mortality rates was sub-

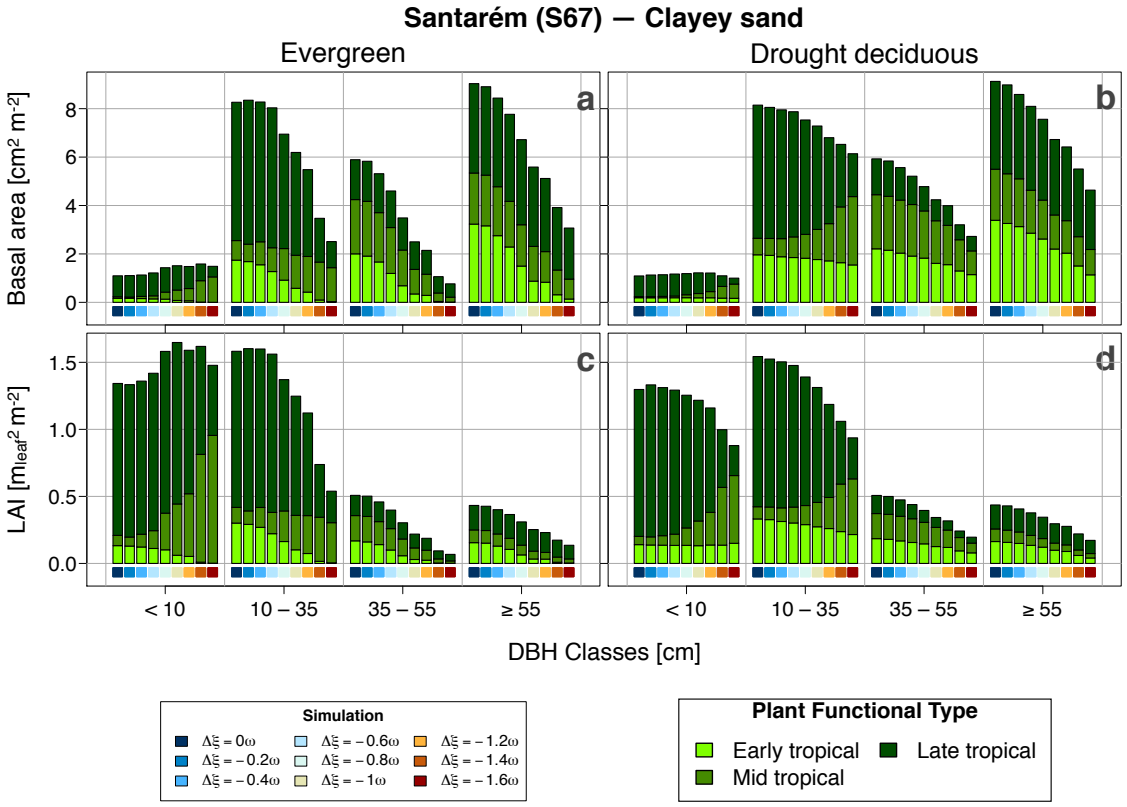

Figure 4.22: Structure of plant community as a function of size and PFT for S67, simulated with clayey sand soil, averaged over the last 40 years of simulations for all 10 realizations within each rainfall scenario. Structure is shown in terms of (a,b) basal area and (c,d) leaf area index for (a,c) evergreen and (b,d) drought deciduous.

stantially lower for early successional cohorts. Other soil types showed similar response, although the changes were generally smaller for high sand content and larger for the clay simulation (not shown).

The shift in the model plant community towards smaller and less early successional trees, especially for the evergreen scenario, reflects a combination of three factors: the prescribed life strategy under drought conditions, the amount of resources needed to maintain a positive carbon balance, and the amount of resources used by plants of different sizes. In ED-2.2, the different leaf phenologies matter only during drought periods: under stress, evergreens will always try to rebuild lost and damaged tissues and go back to allometry, and if their daily carbon uptake is insufficient, they will use any stored non-structural carbon to rebuild the lost tissues; drought

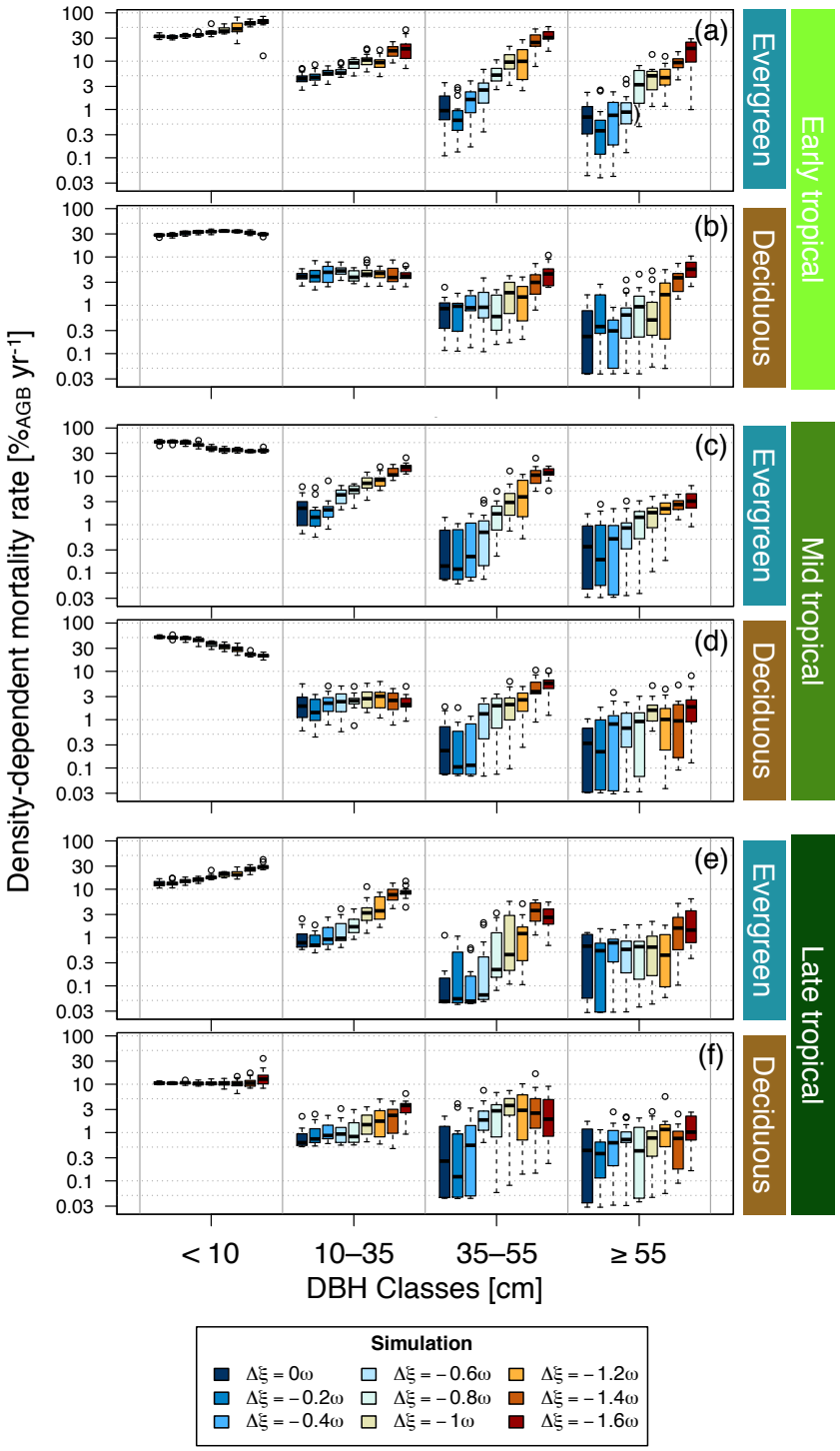

Figure 4.23: Density-dependent mortality rates as a function of plant functional type and DBH class in Santarém km 67 (S67) using clayey sand: (a,b) early successional tropical tree, (c,d) mid-successional, (e,f) late successional; (a,c,e) evergreen, and (b,d,f) drought deciduous. Each point used in the box plot corresponds to one simulation average.

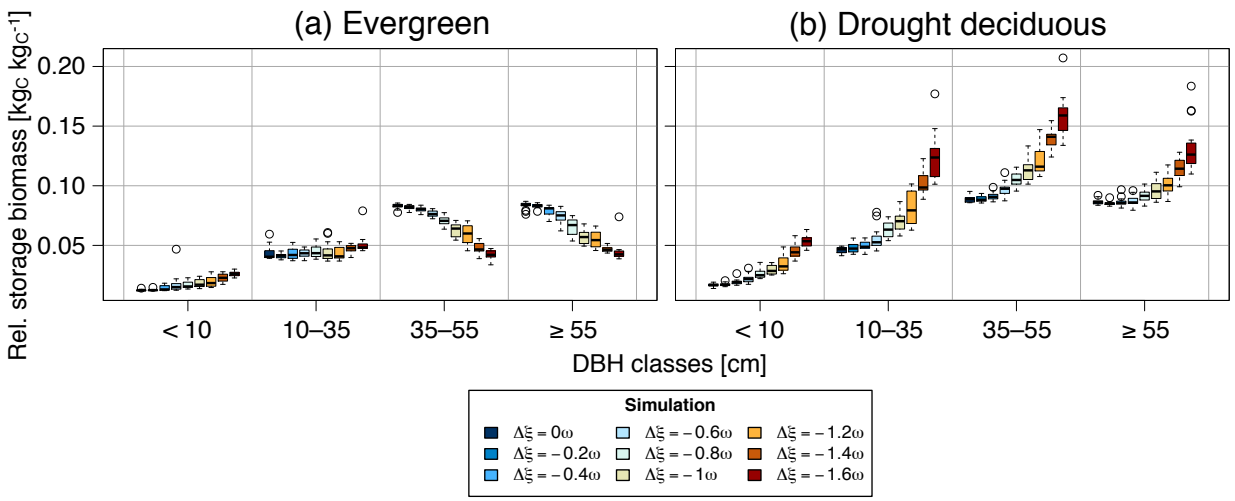

Figure 4.24: Stored carbon distribution by size class for Santarém km 67 (S67) and clayey sand soils, for the (a) evergreen and (b) drought deciduous cases. Stored carbon was normalized by the total biomass of living tissues.

deciduous will only use storage if soil water conditions are good or improving, and during the stress period, if carbon balance is negative, drought deciduous keep the storage carbon and do not attempt to replace damaged or lost tissues. As a result, the variation of storage carbon relative to the total biomass of living tissues is the opposite when drought becomes more frequent, especially for larger trees, as shown in Fig. 4.24. Because drought deciduous store carbon during the drought periods, the average storage biomass increases for all PFTs (not shown), and this strategy reduces carbon loss due to turnover, and avoids very negative carbon balances and mortality, since the density-dependent mortality rates depend on the carbon balance and stored carbon, as shown in App. F.

The forest dynamics, including mortality, depends on several processes that are solved by the model, many of which being highly correlated. To summarize the dynamics of all simulations, I performed a simple principal component analysis on annual means of several variables for each site and leaf phenology, and DBH class, and use the two components that explain the most variance to understand how the different environments correlate with each other. Since the simulations in GYF had negligible response to different rainfall regimes, it represents a forest that is generally not affected by severe water stress. In this case, as shown in Fig. 4.25, mortality rates have very

low impact on the two most explanatory components, mostly because the rates were dominated by the density independent mortality rates which remained nearly constant throughout the simulation for most size classes. The only exception occurred for cohorts with $10 \leq \text{DBH} < 35\,\text{cm}$. The seemingly counter-intuitive positive correlation between wood density and mortality is due to a combination of drift towards late successional and higher negative carbon balance for mid-successional cohorts at this class. More importantly, however, is that all variables associated with water cycle are almost orthogonal to mortality, and radiation is anti-correlated with mortality, consistent with that water is not limiting in GYF even in the driest scenarios ad the forest remained as light-limited. The drought deciduous case is nearly identical to evergreen in GYF thus not presented.

The evergreen parameter space in S67 (evergreen, Fig. 4.26) is dramatically different from GYF. First, mortality rates are usually captured by the most significant components, and for the cohorts with $\text{DBH} < 35\,\text{cm}$, they are nearly orthogonal to wood density, and for all classes, mortality is positively correlated to all drought-related indices and negatively correlated to total rainfall, reflecting that water became a major limiting factor for all classes. Moreover, the leaf water use efficiency became strongly anti-correlated with both soil matric potential and LVPD, which shows that both low water availability and warmer leaves contributed to water stress. The only exception were the understory cohorts, in which improved light conditions counterbalanced some of the increased water stress leading to the poor correlation. It is also noteworthy that the maximum water deficit had the least correlation with mortality for all classes, becoming nearly orthogonal for the largest classes, which suggests that the duration of water limited conditions is more important than the severity of a single dry season. Both growth and recruitment rates were strongly correlated with stomatal conductance, storage biomass and carbon balance for all classes, although their correlation with other environmental variables depended on the position within the canopy. Cohorts with $\text{DBH} < 10\,\text{cm}$ are in the understory under current climate conditions, thus they are somewhat correlated with the amount of absorbed PAR and the water-stress related variables, again a consequence of improved light conditions after the canopy thinned as a consequence of droughts,

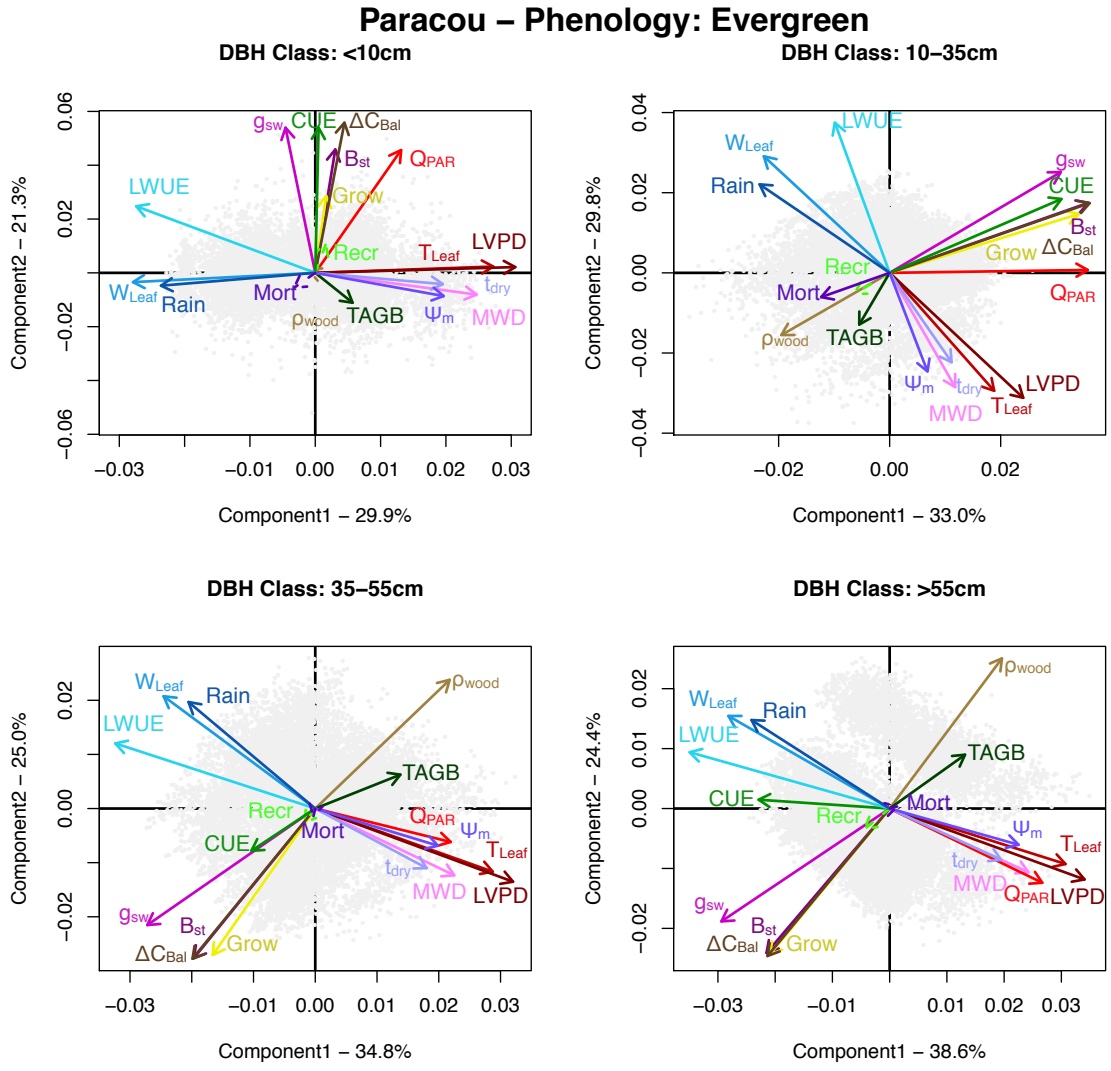

Figure 4.25: Bi-plot of principal component analysis of selected variables using annual means for Paracou (GYF), evergreen case, aggregated by size class for variables that depend on size classes. All realizations of all climate change scenarios for all tested soil texture types were included. The two most explanatory components are shown (percentage explained in the axis annotation); and arrows representing the variables are scaled according to their contribution to each component. Labels are: MWD, maximum water deficit; g_{sw} stomatal conductance; B_{st} storage biomass; Q_{PAR}, leaf absorption of photosynthetically active radiation; T_{Leaf}, leaf temperature; grow, relative grow rates; ρ_{wood}, wood density; ΔC_{Bal}; recr, recruitment rates; CUE, carbon use efficiency; AGB, above-ground biomass; LWUE, leaf water use efficiency; W_{Leaf}, leaf surface water; Rain, rainfall; t_{dry}, drought season length; Ψ_m soil matric potential averaged over the rooting zone; and Mort, mortality rates.

which is also reflected by growth and recruitment rates being nearly anti-parallel to total biomass.

For larger cohorts, both rates become less correlated with light and water stress until they become

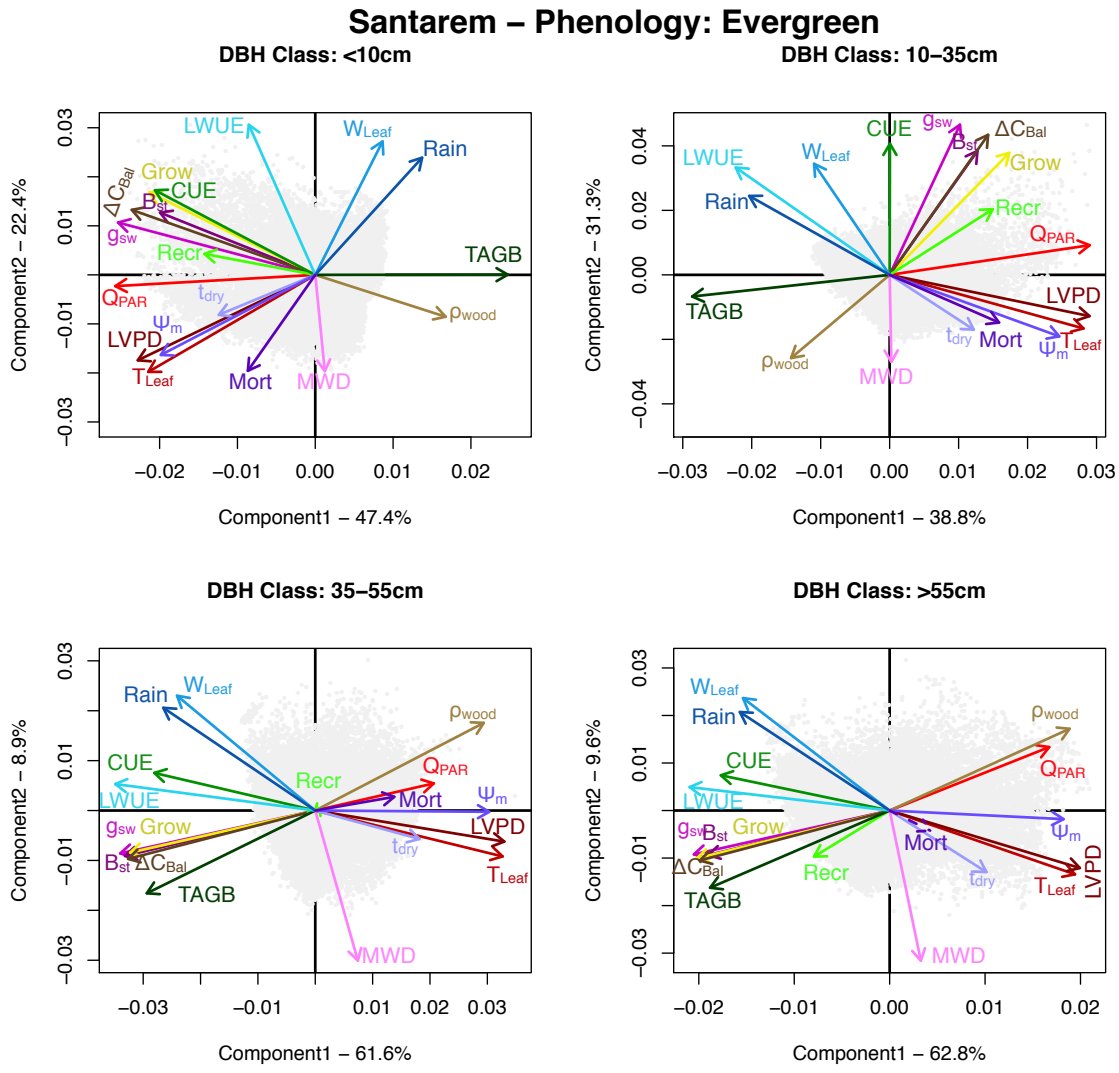

Figure 4.26: Similar to Fig. 4.25, but for Santarém km 67 (S67).

negatively correlated to both for larger trees, with radiation being nearly anti-parallel to these rates while they become parallel to total biomass. Light is not a limiting resource for larger cohorts, thus they do not benefit from more sunlight: instead, more absorbed radiation make the leaves warmer and more demanding for water due to higher LVPD, which forces stomatal closure for longer periods. While lower stomatal conductance reduces transpiration, it also reduces productivity, and transpiration decreases more slowly than GPP because of higher LVPD, which explains why LWUE is anti-correlated to both LVPD and soil matric potential. Likewise, carbon use efficiency decreases because NPP decreases more rapidly than GPP since both dark leaf and fine root

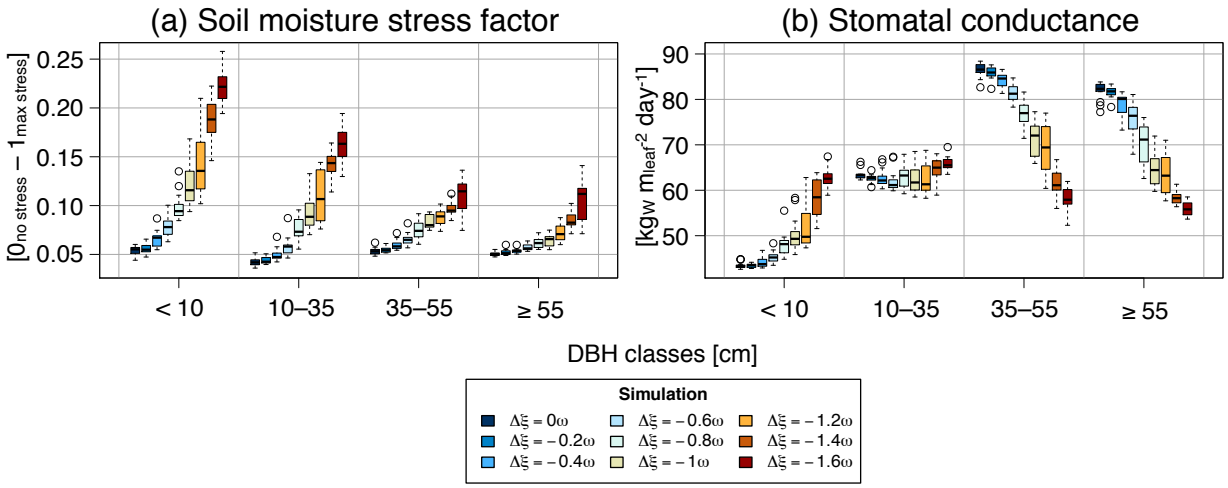

Figure 4.27: Individual averages weighted by leaf area index of (a) soil moisture stress factor on leaf stomatal conductance and (b) leaf stomatal conductance, for Santarém km 67 (S67), evergreen case and clayey sand soils.

respiration rates tend to increase with temperature. In Fig. 4.27 I present the how water stress combined with light availability affect the total conductance across different size classes. On the one hand the scaling factor to stomatal conductance due to soil moisture stress (o_{sW}) decreased for all classes, particularly the smaller classes, which is expected due their shallower roots and reduced rainfall. On the other hand, the actual leaf stomatal conductance varied little and even increased for the smaller cohorts, while it decreased for the larger trees, a somewhat counter-intuitive result due to several factors. The higher conductance of smaller cohorts is mostly a consequence of the plant community changes. The smallest cohorts are mostly in the understory under current conditions, therefore their stomatal conductance is low because photosynthetic activity is light-limited, and once large trees declined, the reduced light limitation more than compensated the increased stress; meanwhile, the remaining larger trees are not limited by light, thus the soil moisture was not counterbalanced.

For the drought deciduous case in S67 (Fig. 4.28), mortality rates were also positively correlated with water stress variables and light, which suggests that the shift in climate was strong enough to increase the stress even for drought tolerant. For larger classes, however, mortality became more orthogonal to water stress, similarly to GYF case, which suggests that a combination

of full access to light and better use of storage during droughts increased the chances of survival. Since the drought deciduous case did not lose as much biomass as in the evergreen, smaller cohorts did not experience as much increase in sunlight and had more competition for water. Unlike the evergreen case, growth and recruitment rates are not nearly parallel for the smallest classes (DBH < 35 cm). For the understorey, growth rates tend to be anti-correlated with absorbed PAR and water stress variables. Because larger trees were still present, smaller cohorts were also limited by light while competing for water with more individuals. Since these cohorts have shallower roots, they are more prone to go under water stress and lose leaves and not maintain fine roots, and being light limited means that they also take longer to uptake enough carbon to rebuild the lost tissues, which compromise their growth rates during droughts. Recruitment, however, is not as affected because they depend on the performance of most cohorts including the large ones.

4.4.3 Estimate of vulnerability

Results presented in Sec. 4.4.2 reflect that the model predicted the largest losses in biomass when severe, multi-year dry season occurred, while the model predicted some biomass increase in biomass between these extreme droughts, even in the driest climate scenarios (e.g. Fig. 4.14). The plant community could eventually return to a similar structure and total biomass after a drought event, and the time to recover previous functioning depending on the drought severity and on the species that were affected the most by the drought event. However, if such droughts become too frequent, then the ecosystem may not be able to return to the original state, especially if recovery from disturbance becomes slower as the plant community approaches a tipping point towards an alternative equilibrium state (c.f. Scheffer et al., 2012; Veraart et al., 2012). Therefore, I calculated the simulation-long relative change in biomass $\delta_{\mathrm{AGB}}[\,\%_{\mathrm{AGB}}\,\mathrm{yr}^{-1}]$, and counted the number of drought events N_{D1} that lasted one year and the corresponding return period $\tau_{D1}[\,\mathrm{yr}]$ as:

$$\delta_{\mathrm{AGB}} = \frac{100}{\Delta t_S} \times \ln\left[\frac{\mathrm{AGB}\,(t = t_0 + \Delta t_S)}{\mathrm{AGB}\,(t = t_0)}\right], \tag{4.5}$$

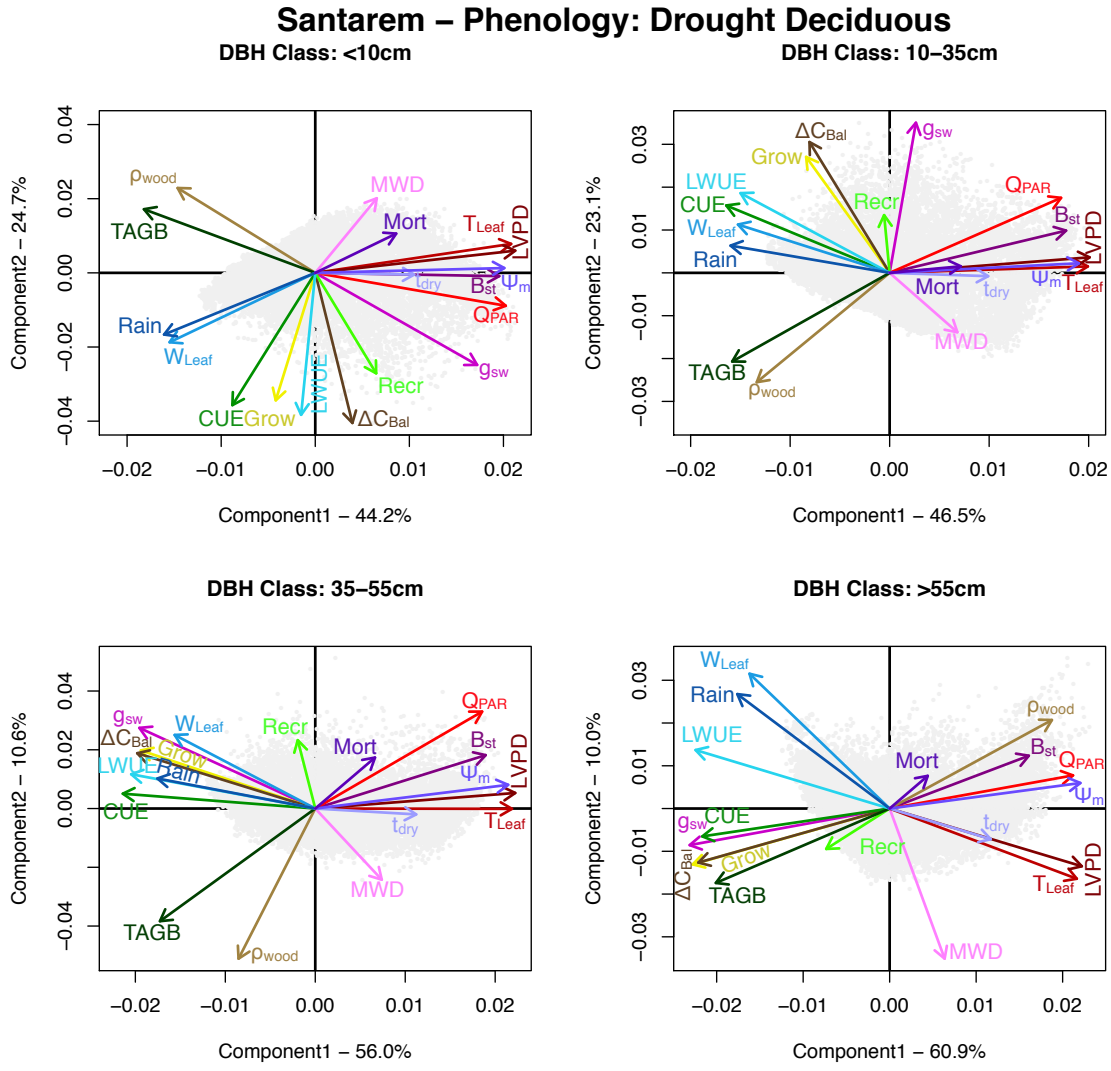

Figure 4.28: Similar to Fig. 4.26, but for drought deciduous case.

$$N_{D1} = \sum_{n=1}^{N} \lfloor t_{D_d} \rfloor \,, \tag{4.6}$$

$$\tau_{D1} = \begin{cases} \dfrac{\Delta t_S}{N_{D1}} & , \text{if } N_{D1} > 0 \\ \dfrac{1}{p_{SN}\left(t_D \geq 1\,\text{yr} | \xi_R, \omega_R, \alpha_R\right)} & , \text{if } N_{D1} = 0 \end{cases} , \tag{4.7}$$

where t_0 is the simulation initial time; Δt_S is the simulation duration; n is the index given for each drought, defined as the continuous period in which the water deficit was $\geq 10\,\text{mm}$; and $p_{SN}(t_D \geq 1\,\text{yr})$ is the probability of occurrence of a drought longer than one year, assuming that annual rainfall variability can be represented by skew normal distribution. The floor operator ($\lfloor\ \rfloor$)

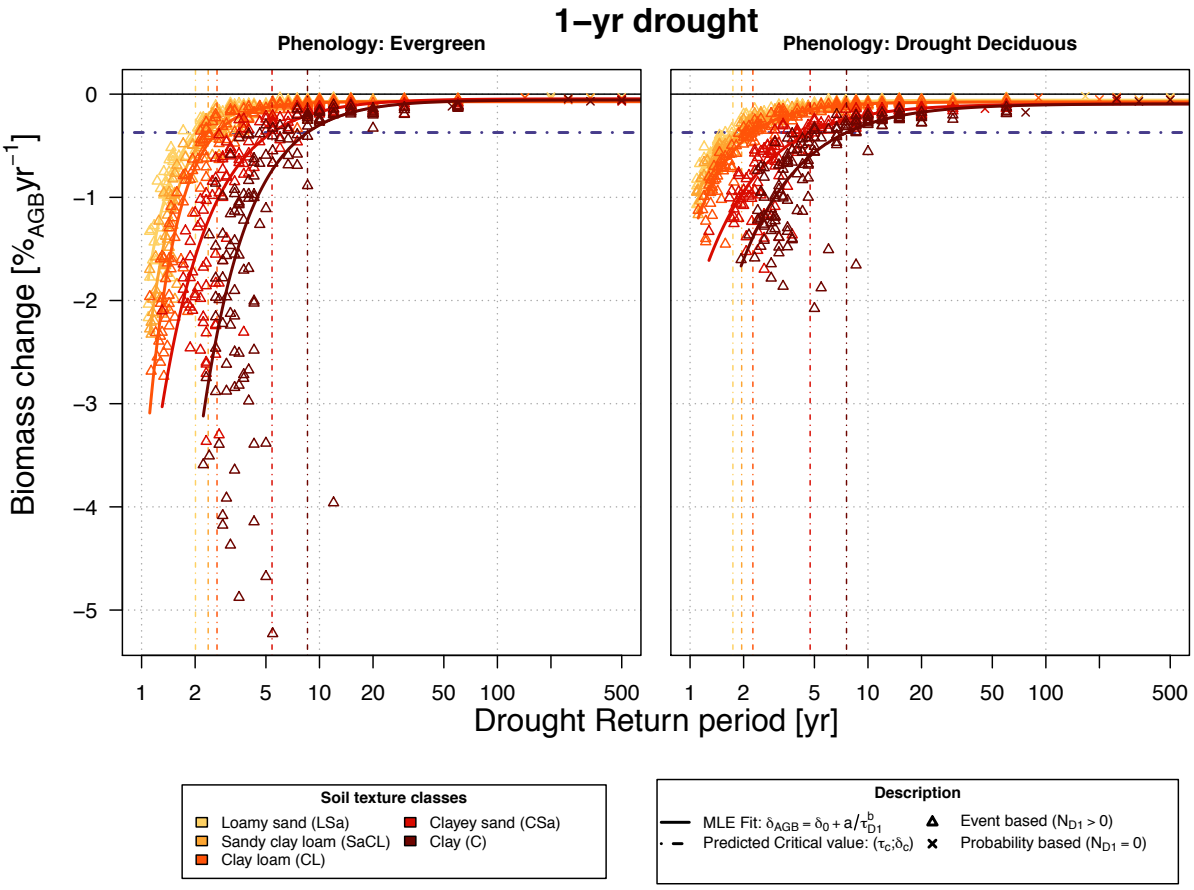

Figure 4.29: Average relative biomass change for all simulations (S67 and GYF) with (a) evergreen and (b) drought deciduous phenology, as function of the mean return period of droughts longer than one year (one point for simulation). Horizontal dashed line corresponds to the critical return period τ_c and vertical dashed line is the critical biomass loss (ΔAGB_c), both defined in the main text and Tab. 4.1.

is applied to N_{D1} so multiple-year droughts are considered multiple consecutive droughts; the probability-based estimation is needed to produce a finite estimate of the return period in case no event happened in the simulation.

From Fig. 4.29, biomass did not change significantly until the return period became short (about 10 years for clay soils and 2 years for loamy sand soils), at which point the long-term biomass loss sharply declined for both evergreen and drought deciduous cases, although the magnitude of the biomass loss in the drought deciduous case was generally lower. To represent the dependence of biomass loss $\Delta\text{AGB}\,[\,\%_{\text{AGB}}\,\text{yr}^{-1}]$ upon return period, I fitted a hyperbolic curve of form

Table 4.1: Coefficients for the hyperbolic fit $(\Delta\text{AGB} - \Delta\text{AGB}_0) \cdot \tau_{D1}^b = a$ for each soil texture and leaf phenology. Standard errors are in parentheses, and coefficients that are statistically significant at the 0.1, 0.05, 0.01, 0.001 levels are flagged as ., $\star$, $\star\star$, and $\star\star\star$, respectively. In addition, the adjusted coefficient of determination (R^2, corrected for the number of degrees of freedom), and the predicted critical return period τ_c are also shown. Soil texture classes are loamy sand (LSa), sandy clay loam (SaCL), clay loam (CL), clayey sand (CSa) and clay (C), and leaf phenologies are evergreen (EGN) and drought deciduous (DRD).

Soil texture	**Phenology**	ΔAGB_0	**a**	**b**	τ_c	$\mathbf{R^2}$
LSa	EGN	-0.069 (0.008)	-2.22 (0.23)***	2.86 (0.28)***	2.009(0.028)	0.90
	DRD	-0.058 (0.005)	-0.94 (0.08)**	1.98 (0.18)***	1.740(0.015)	0.94
SaCL	EGN	-0.068 (0.006)	-2.98 (0.11)***	2.65 (0.13)***	2.37(0.04)	0.90
	DRD	-0.073 (0.005)	-1.07 (0.05)***	1.92 (0.12)***	1.95(0.016)	0.95
CL	EGN	-0.073 (0.008)	-4.0 (0.3)***	2.66 (0.19)***	2.66 (0.08)	0.89
	DRD	-0.076 (0.006)	-1.37 (0.07)***	1.89 (0.11)***	2.26 (0.04)	0.90
CSa	EGN	-0.045 (0.018)	-4.5 (0.8) ***	1.56 (0.16)***	5.4(0.5)	0.64
	DRD	-0.093 (0.017)	-2.08 (0.21)***	1.30 (0.13)***	4.73(0.026)	0.70
C	EGN	-0.06 (0.04)	-11.7 (3.1)***	1.69 (0.22)***	8.6(1.7)	0.38
	DRD	-0.094 (0.020)	-3.6 (0.5)***	1.27 (0.11)***	7.6(0.7)	0.55

$(\Delta\text{AGB} - \Delta\text{AGB}_0)\,\tau_{D1}^b = a$ using a non-linear robust estimator (function `nlrob` in `R`). Using the fitted curve, I defined the critical point $(\tau_c; \Delta\text{AGB}_c)$ where biomass loss is expected to be 20% in 50 years, which is the length of the simulations. Although the definition of the critical point is arbitrary, it roughly represents the point in which biomass is already at rapid decline Fig. 4.29. The fitted coefficients, coefficient of determination and associated critical points are shown in Tab. 4.1. We observe that the fit is generally better for sandy soils than clayey soils; simulations using clayey soils had more variability between different realizations in the same scenario, mainly because they responded more strongly to severe droughts but the final change in biomass also depended on when in the simulation the severe droughts happened.

Based on the relation between return period and biomass loss that emerged from the different scenarios and soil texture types, I conducted a meta-analysis to estimate vulnerability to changes in rainfall climate for different areas in the Amazon. First let vulnerability to be how much the current rainfall regime would need to shift from current climate so that the return period of one-year long droughts would be equal to τ_c. Although changes in climate could completely shift the annual rainfall distribution, I assumed that annual rainfall could be represented by a skew normal distribution, neglected autocorrelation of the time series. Vulnerability was then estimated by

how much each parameter (location, scale, and shape) that describes the current climate would need to change until the return period of annual rainfall events below R_c would become τ_c, hence generating three dimensionless vulnerability indices associated with each parameter:

$$V_\xi = \min\left(0, \frac{\xi_c - \xi_R}{\omega_R}\right) \quad , p_{SN}\left(R \leq R_c | \xi_c, \omega_R, \alpha_R\right) = \frac{1}{\tau_c}, \tag{4.8a}$$

$$V_\omega = \max\left(0, \frac{\omega_c - \omega_R}{\omega_R}\right), p_{SN}\left(R \leq R_c | \xi_R, \omega_c, \alpha_R\right) = \frac{1}{\tau_c}, \tag{4.8b}$$

$$V_\alpha = \min\left(0, \alpha_c - \alpha_R\right) \quad , p_{SN}\left(R \leq R_c | \xi_R, \omega_R, \alpha_c\right) = \frac{1}{\tau_c}, \tag{4.8c}$$

where $(\xi_R; \omega_R; \alpha_R)$ are respectively the location, scale, and shape parameters of the current climate; ξ_c, ω_c, and α_c are the that would make the return period of one-year-long droughts τ_c while keeping the other parameters the same; and R_c is a critical value of annual rainfall below which I would expect droughts to last one year. In all cases, zero means that the current climate already causes the return period to be τ_c or less. To solve Eqn. (4.8) I first must determine the predominant soil texture for different regions to select the appropriate τ_c, the location, scale, and shape parameters for the current climate, and define a critical rainfall R_c based on evapotranspiration.

The predominant soil texture type is derived from the dataset presented in Fig. 4.7. Since not all soils were simulated in the parameter evaluation, I grouped all sandy soils (Sa, LSa, SaL) to loamy sand (LSa) and loamy soils (L, CL) to clay loam (CL).

Location, scale, and shape parameters were determined by fitting the skew normal distribution on annual rainfall from six different gridded data sets: the Princeton University Global Meteorological Forcing Dataset (PGMF, Sheffield et al., 2006); the University of Delaware Dataset, version 3.01 (UDel-3.01, Matsuura and Willmott, 2012); the Global Precipitation Climatology Centre, version 6.0 (GPCC-6.0, Schneider et al., 2014); the National Oceanic and Atmospheric Administration's Precipitation Reconstruction over Land (PREC-L, Chen et al., 2002); the Global Precipitation Climate Project (GPCP-2.2, Huffman et al., 2009); and the NASA Tropical Rainfall Measurement Mission version 7.0 (TRMM/3B43-7.0, Liu et al., 2012). The widely used Climate Research Unit dataset (CRU-3.10.01, Harris et al., 2013) was not included in this analysis be-

cause PGMF precipitation is based upon CRU, thus not independent; I opted for keeping PGMF because it is the driver used to drive ED-2.2 for the region. The data sets were also spatially aggregated from their native resolution to $1^\circ \times 1^\circ$, except GPCP which has resolution of $2.5^\circ \times 2.5^\circ$ and the nearest neighbor was used instead. I also restricted the period for all data sets to 40-year period (1969–2008) to be comparable with the scenario simulations and to reduce errors due to very scarce measurements in the region before 1969, except GPCP and TRMM/3B43, for which I used the entire time series since the complete time series were shorter than the others. The mean, standard deviation, and skewness of the distributions are shown in Fig. 4.30, where it is shown that the average rainfall values and spatial distribution is similar for most data sets, with maximum at Northwestern Amazon and secondary maximum along the coast between French Guiana and Pará. While the inter-annual variability shows some similar patterns, with maximum in Northeastern Peru and minimum in the Southeastern region, the magnitude of the variability is significantly different for regions, with CRU-based PGMF showing a very low variability near CHB, while GPCC shows a very high variability in Northeastern Peru. Skewness shows even higher discrepancies, although there is a weak general pattern of positive skewness in the Southern and Eastern parts of the Amazon, which indicate that extremely wet years are more common than extremely dry years. The stronger disagreement at higher order statistics was also suggested by Costa and Foley (1998) and Negrón-Juárez et al. (2009), who compared multiple datasets and found that while datasets based on rain gauge reasonably agreed for long term average rainfall, they tended to disagree more for interannual and interdecadal variability.

Critical rainfall R_c must be related to evapotranspiration, since the drought duration was defined in terms of water deficit. To determine the climatological evapotranspiration, I used a regional ED-2.2 simulation that covered the Amazon with $1^\circ \times 1^\circ$ resolution, starting from near bare ground conditions and spanning for 508 years, driven by the 3-hourly resolution PGMF dataset for 1969–2008 (Sheffield et al., 2006) as the meteorological forcing. The meteorological forcing was recycled multiple times, and the soils for each grid were the same as in Fig. 4.7. The climatological annual evapotranspiration was assumed to be a simple average of the last 40 years of simulation.

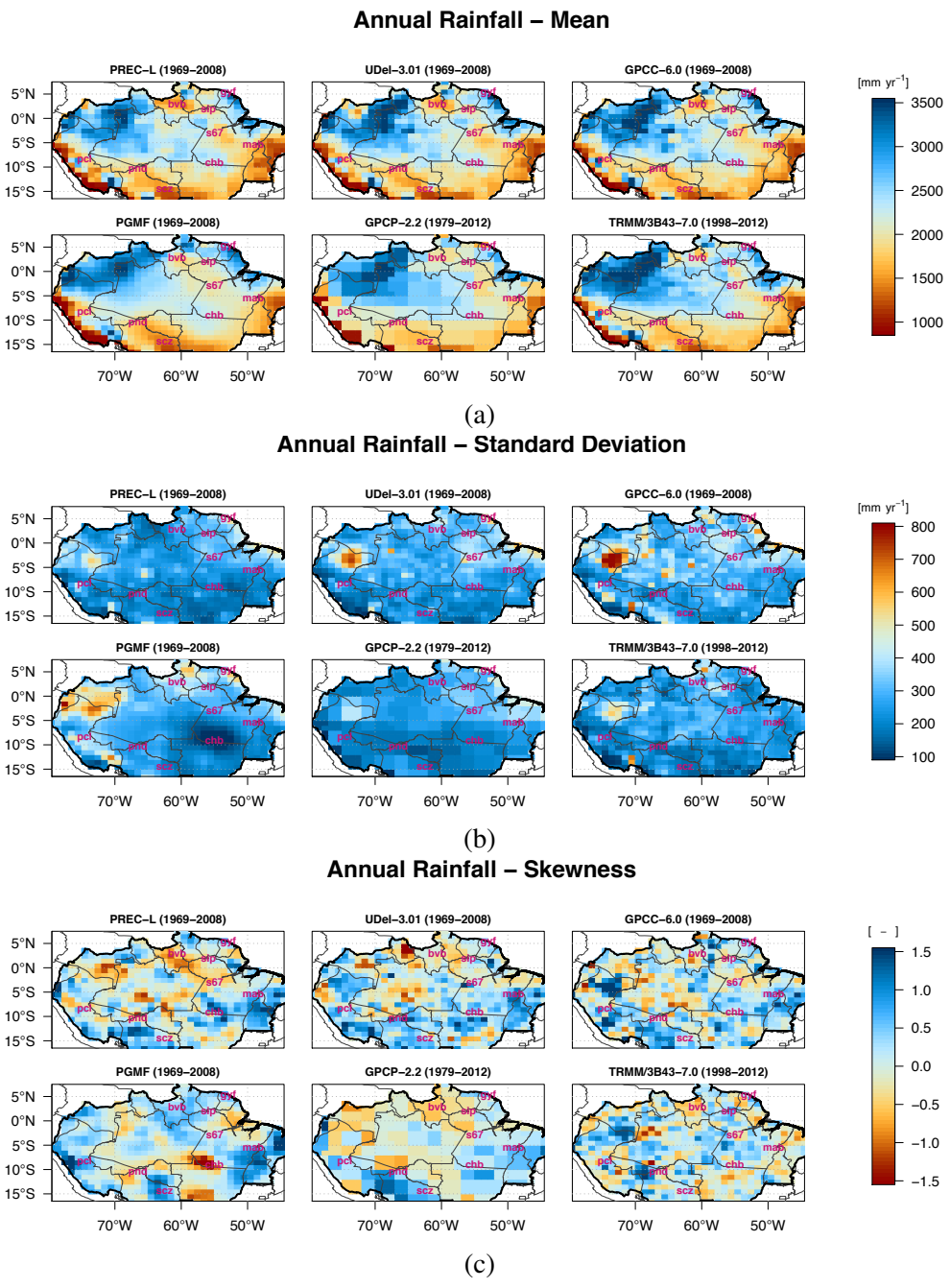

Figure 4.30: (a) Mean, (b) standard deviation, and (c) skewness for the annual rainfall for the six data sets spatially aggregated to 1 deg $\times$ 1 deg. Color levels were truncated at the extreme points for clarity.

The average value is shown in Fig. 4.31a, where it can be observed that rates are generally lower in Western Amazonia due to temperatures moderated by lower radiation, and in areas at higher altitude such as the Andean region and to a lesser extent the Cachimbo Mountain Range between S67,

MAB, and CHB (not shown). In general, evapotranspiration estimated by ED-2.2 falls between previous estimates by Negrón-Juárez et al. (2008) and Jung et al. (2010), although patterns within the region differ from these estimates. In particular, ED-2.2 estimates at the Southern and Eastern parts are higher than in Central Amazonia, which is the opposite found by Negrón-Juárez et al. (2008), and shows higher variability within the forest than estimates by Jung et al. (2010). It must be noted, however, that the model by Negrón-Juárez et al. (2008) does not include dependence on temperature or vapor pressure deficit, which is found to be positively correlated with evapotranspiration at the edge of the domain by Jung et al. (2010). In addition, the low variability within the forest in Jung et al. (2010) model could be due to the very limited number of eddy covariance towers available in tropical regions, which may not limit the sensitivity of environmental controls to evapotranspiration. This is also true for ED-2.2 estimates, which have been evaluated against eddy covariance towers and showed reasonable results for most sites (Sec. 3.3.3), but could not be capture all range of climates in the Amazon region due to data availability.

To establish a relation between R_c, $\dot{\varepsilon}_0 + \dot{\tau}_0$ and drought length, I calculated the ratio between the climatological evapotranspiration and the total rainfall of the previous 12 months at the end of the drought (or the entire length of the drought in case the drought lasted longer than 12 months) for all droughts that occurred over the period of 40 years across the basin, using the water-deficit-based definition. Although there is a significant spread, the results suggest that the ratio approaches 1 for droughts longer than 12 months (Fig. 4.31b), therefore, I assumed that R_c corresponded to the climatological evapotranspiration. This approximation has been also used in the past to describe transition between rain forests and drier ecosystems (c.f. Holdridge, 1947; Hutyra et al., 2005).

To account the differences between the data sets, I aggregated the three vulnerability indices using a simple weighted average for each grid point. Ideally, the weights must account for the length of the climatology, and also how well the data sets represent the in situ rainfall variability. Errors were estimated using all rain gauge data available from both INMET (2013) and NCDC/NOAA (2013), using only years with less than 10% missing values, and only stations that had at least 25 valid years. The missing daily rainfall rates for selected stations were filled with random sample

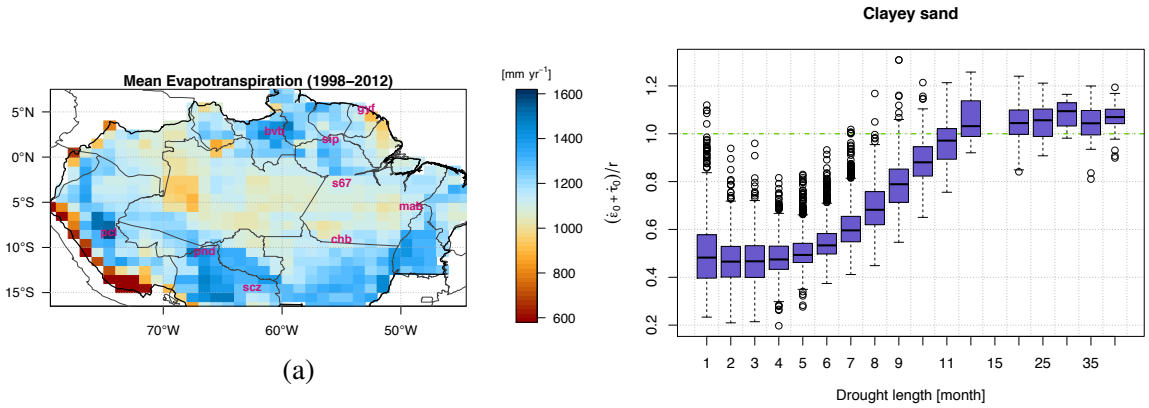

(a)

(b)

Figure 4.31: (a Average of evapotranspiration over the last 40 years of the 508-year potential vegetation simulation (assumed to be R_c), and (b) box plots of the ratio between long-term mean evapotranspiration and rainfall over the previous 12 months or entire drought duration for droughts that lasted longer than 12 months, as a function of drought length for all droughts reported in the Amazon grid points whose predominant soil texture was clayey sand (commonest soil texture in the Amazon). Other soil textures show similar patterns thus omitted.

from reported rainfall from any year and same month as the month of the missing recorded, but I only allowed samples to be drawn from months that had no missing data to reduce biases. Figure 4.32a shows that most observations occur in most heavily inhabited Eastern and Southern parts and along the Amazon River [7].

For each data set d, I determined the mean squared error (MSE) of the estimator as the weighted average of the MSE for each place p, weighted by the number of years with both rain gauge measurements and gridded rainfall ($Y_{p,d}$):

[7] Even though rainfall data existed in Peru, Ecuador, Bolivia, Guyana, and Suriname, none of the stations there met both criteria.

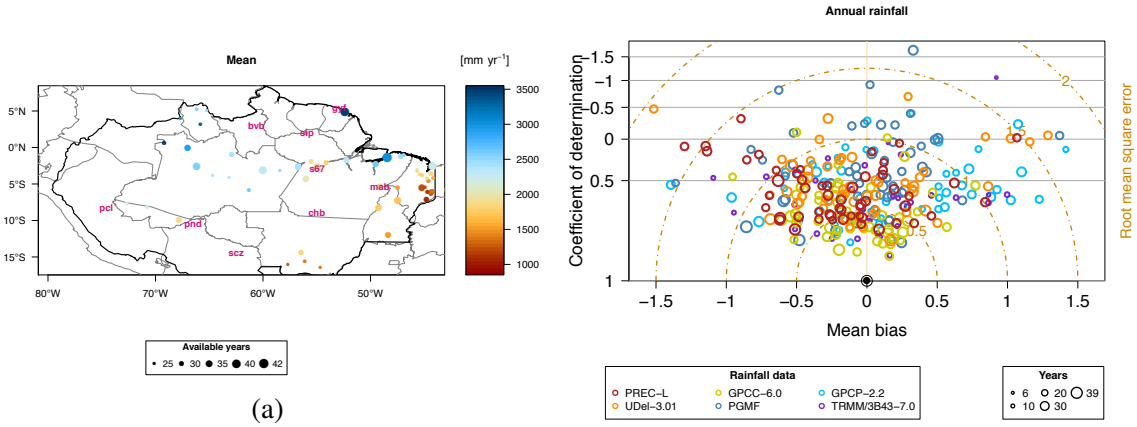

(a) (b)

Figure 4.32: (a) Mean annual rainfall for all sites used to calculate the error calculated from rain gauge data, and (b) skill plot of all gridded data sets compared to all stations, with both bias and root mean squared error normalized by the observed standard deviation. In both figures, the point size is proportional to the number of years used to estimate the statistic, and the numbers are lower in (b) because it corresponds to the number of years with both rain gauge and gridded annual rainfall.

$$\overline{\mathrm{MSE}}_d = \frac{\sum_{p=1}^{P} Y_{p,d} \cdot \underbrace{\left\{ \underbrace{\frac{\sum_{y=1}^{Y_{p,d}} \left(R_{y,p,d} - R^{\star}_{y,p}\right)^2}{Y_{p,d} - 1}}_{\text{Variance of residuals}} + \underbrace{\left[\frac{\sum_{y=1}^{Y_{p,d}} \left(R_{y,p,d} - R^{\star}_{y,p}\right)}{Y_{p,d}} \right]^2}_{\text{Mean bias (squared)}} \right\}}_{\text{MSE of data set } d \text{ at place } p}}{\sum_{p=1}^{P} Y_{p,d}}, \tag{4.9}$$

where $R_{y,p,d}$ and $R^{\star}_{y,p}$ are the annual rainfall at place p and year y the estimated by dataset d and observed, respectively; and P is the number of places. The weight for each data set (W_p) was set to be proportional to the inverse of $\overline{\mathrm{MSE}}_d$, as shown in Tab. 4.2. While biases were generally small, the lower standard deviation of GPCC-6.0 contributed for the higher weight, whereas the short term time series of TRMM-3B43 significantly reduced the weight, even though TRMM-3B43 usually had very good agreement with observations.

In Fig. 4.33, I present the weighted average of the three vulnerability indices for the entire

Table 4.2: The average number of years used to estimate the errors ($\overline{Y}$), and the summary of the errors associated with each gridded data set. Both mean bias ($\overline{\beta}_{\text{res}}$) and mean standard deviation of the residuals ($\overline{\sigma}_{\text{res}}$) are weighted averages across all points using the number of years as weights. W_p is the weighting factor applied to the vulnerability indices.

Data set	$\overline{\mathbf{Y}}$	$\overline{\beta}_{\mathbf{Res}}$ $[\,\mathrm{mm\,yr^{-1}}]$	$\overline{\sigma}_{\mathbf{Res}}$ $[\,\mathrm{mm\,yr^{-1}}]$	$\overline{\mathrm{MSE}}$ $[\,\mathrm{mm^2\,yr^{-2}}]$	$\mathbf{W_p}$
GPCC-6.0	28.3	-36.9	167	1722	0.321
PREC-L	28.3	-78.6	221	3126	0.177
UDel-3.01	28.3	-15.1	240	3348	0.165
PGMF	28.3	-18.6	266	3819	0.145
GPCP-2.2	23.4	33.1	228	4451	0.124
TRMM/3B43-7.0	8.31	-17.7	186	8217	0.067

domain. Most of the regions where all three indices suggest high vulnerability are non-forested regions, such as Northern Bolivia, Tocantins, Eastern Maranhão and the Lavrado savannahs and grasslands near Boa Vista[8]. Within the Amazon, V_ξ is generally less negative thus more vulnerable in four regions: the moist forests in Northern Santa Cruz Department in Bolivia, the Pando Department in Bolivia, a large band from central Roraima and Southern and Eastern Guyana to Santarém km 67, extending to Marabá (hereafter the Boa Vista–Marabá band), and area near and northwest of Pucallpa in Peru. While all four areas have relatively lower annual rainfall, the Boa Vista–Marabá band has higher mean rainfall rates associated with higher inter-annual variability. Unlike the other three areas, both V_ω and V_α show show a much smaller area of strong vulnerability, mostly confined in the regions that are already savannahs, and in many regions no possible solution existed for V_ω and particularly V_α, since the current mean rainfall is sufficiently higher than R_c so that the maximum probability on the negative side of the distribution saturate at lower values than τ_c^{-1}. Surprisingly, this analysis suggest that a large area in Southeastern Amazonia (near and East of the Cachimbo mountains) could be relatively resilient despite being closer to the Cerrado in Central Brazil and not particularly wet. The low vulnerability scores were due to a combination of lower evapotranspiration rates, which is a consequence of lower temperature associated due to somewhat higher altitude ($250 - 400\,\mathrm{m}$), and relatively low inter-annual variability

[8]The area along the Andes in Peru also shows high vulnerability, although this result is mostly due to the coarse resolution used, which tends to average regions with very different altitudes and on both sides of the Andes.

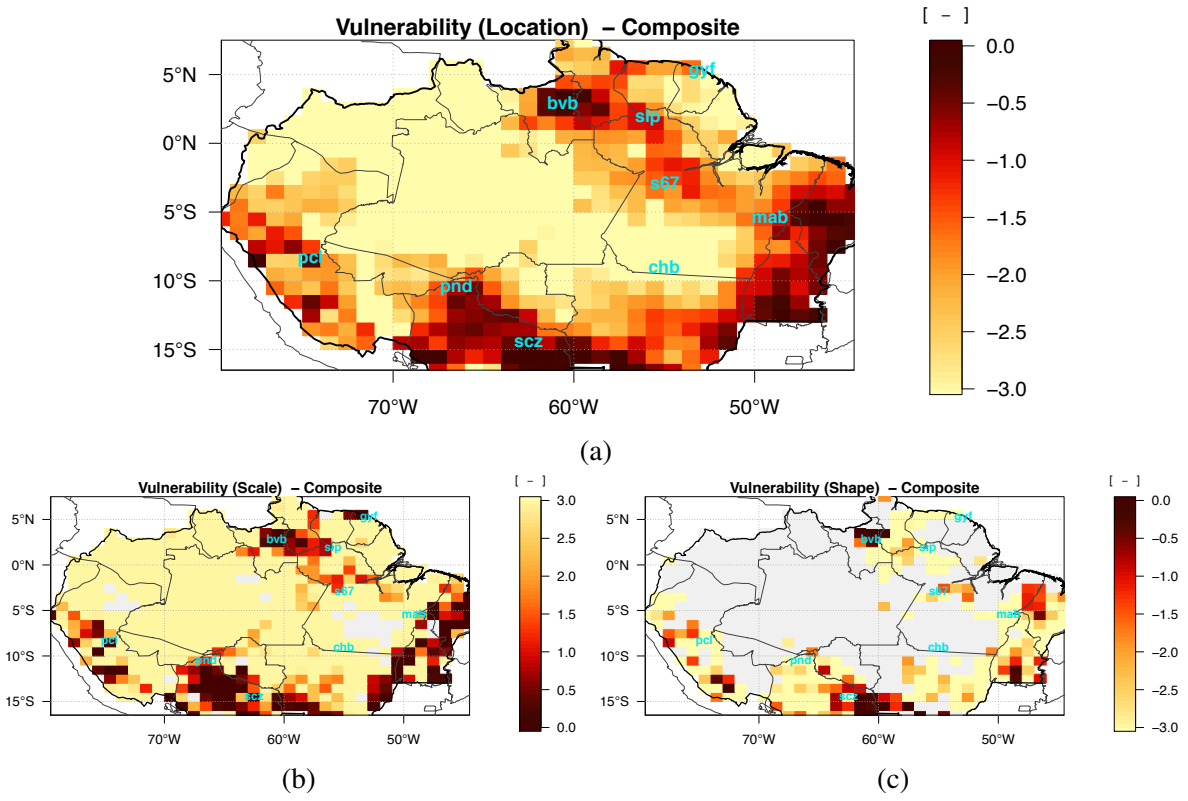

Figure 4.33: Vulnerability indices from weighted average composite of all six data sets: (a) relative change in location (V_ξ), (b) relative change in scale (V_ω), and (c) change in shape (V_α) parameters need to bring the return period of one-year long droughts to τ_c. Color levels were truncated at the extreme points for clarity, and grey areas corresponds to regions where no solution could be found. Darker color represent the most vulnerable regions in all three indices.

(Fig. 4.30b), particularly in the PGMF dataset, and is also observed in CRU-3.10.01 (not shown).

4.5 Discussion

4.5.1 Evaluation of demographic rates

Growth and mortality rates showed discrepancies with observations, and the most significant and consistent pattern was higher growth and higher mortality rates compared to observations, which growth rates being particularly overestimated in GYF, and being the furthest from observations amongst early- and mid-successional trees. In addition, aggregated demographic rates are strongly

dependent on size, thus if the model predicts a size distribution that is different than the observations, both mortality and growth rates could be higher (lower) than observations if the model predicts a larger (smaller) relative contribution of smaller trees to the total population. Moreover, in this comparison I did not attribute possible errors due to PFT attribution based on absence or misidentification of tree species, which could also contribute to the discrepancies between model and observations. For example, if the successional stage of the forest is closer to late successional than what was provided to ED-2.2, the overestimation of mortality and growth rates could be due to the excessive number of early successional trees in the model.

Density-independent mortality is the original parameterization from ED-1.0 (Moorcroft et al., 2001), and described in App. F. While the original formulation is based on the well established observation that low wood density tropical trees have generally higher mortality rates than high wood density ones (e.g. King et al., 2006; Chave et al., 2009; Kraft et al., 2010), the linear coefficient is an estimate based on very limited data at the time, an earlier study by Uhl and Jordan (1984) on secondary forest regrowth that included several canonical short-lived pioneer genera such as *Vismia* and *Cecropia*. While these genera are also present in the study area, many shade-intolerant species are much longer lived, yet are classified as early successional due to lower wood density, and the slope is overestimated compared to more recent studies such as (Kraft et al., 2010, see also App. F). Higher density-independent mortality rates amongst early- and mid-successional caused the composition of large trees in the model to shift to late successional, since the population of early- and mid-successional declined before they could reach larger sizes, which contributed to the even higher rates of early and mid-successional trees.

Finally, the lack of inter-annual variability of mortality in ED-2.2 in GYF can be attributed to occurrence of disturbances in the plots. Treefall disturbance rate is assumed constant in the model and represents the probability of forming a gap within a sufficiently large area that represents the full distribution of ages since last disturbance. On the other hand, demographic rates derived from permanent plots are limited in area, therefore one can expect disturbances to have high inter-annual variability depending on whether disturbance events affect the sampled area or not, particularly

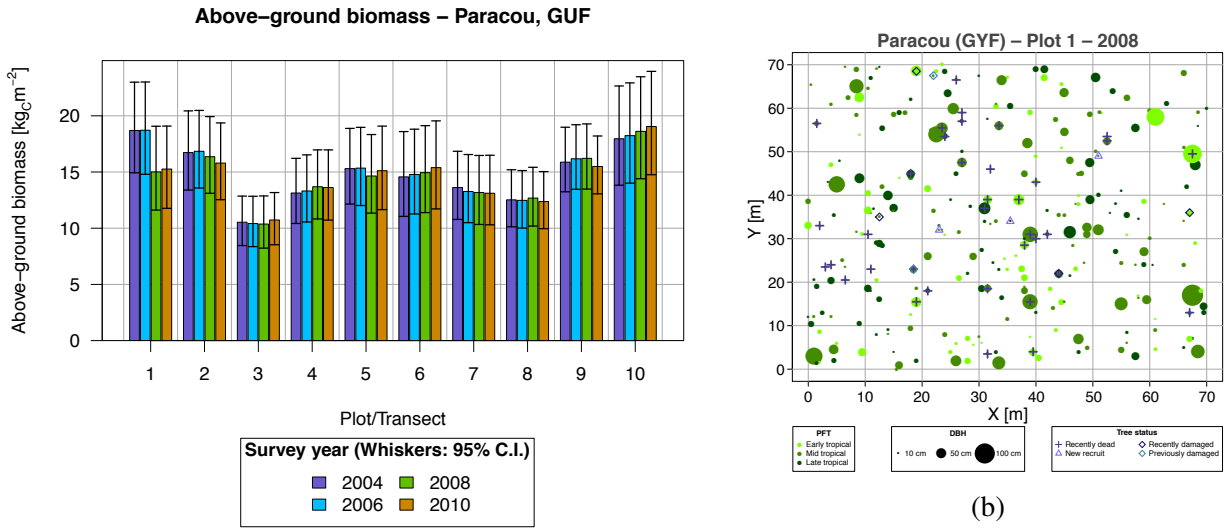

(a) (b)

Figure 4.34: (a) Time series of above-ground biomass for GYF for each plot, with confidence intervals determined from bootstrap; (b) overview of plot 1, which concentrated 31% of individuals that died between 2006 and 2008. Trees that had been reported damaged in the field notes are shown, although damage on dead trees are likely not be reported.

those rarer but larger events (Chambers et al., 2013). This variability is also dependent on the sampling size, being more pronounced on smaller sampled areas such as GYF. In fact, this is the likely reason why the mortality rate increased in GYF between 2006 and 2008: field notes of the 2008 survey included a higher number of trees that had been reported as either damaged and/or fallen, and the largest pulse of mortality came from a single plot (number 1), as shown in Fig. 4.34a, and within this plot, dead trees were concentrated in clusters (Fig. 4.34).

In ED-2.2, the model tends to overestimate growth, particularly for early- and mid-successional trees, a characteristic also found in mortality rate. The higher growth rates of woody tissues have been also reported in the model intercomparison for the throughfall exclusion experiments, and it appears to be a general bias in most models (Powell et al., 2013). Also, the partition of assimilated carbon to the different pools is fixed in ED-2.2, whereas in reality many species may respond to variations in the environmental conditions by allocating more resources to different pools (e.g. roots in case of droughts or low nutrient availability), potentially affecting inter-annual variability

of the above-ground accumulation. Moreover, nutrient cycles and their limitation on productivity and wood production are not yet implemented for tropical environments in ED-2.2, and soil nutrient availability, particularly phosphorous, has been shown to be correlated with wood productivity in the Amazon (e.g., Quesada et al., 2012), and the nutrient-poor soils at GYF (e.g, Baraloto et al., 2005) could also explain some of the consistently lower growth rates for all PFTs compared to S67. In addition, tropical rain forests have numerous morphological types, including lianas which are not represented in ED-2.2 and could play a significant role reducing the tree growth. For example, van der Heijden and Phillips (2009) estimated that growth reduction was 29% lower for trees that were directly competing for light and water with lianas. Finally, higher growth rates may be also due to tree allometry and allocation to living tissues, which may be underestimated, causing growth of structural tissues to be overestimated.

These results suggest that there are important improvements to be done in the model, and that the model overestimation should be taken into account when analyzing the results and these differences. Notwithstanding, the long-term simulation in Chap. 3 show that the model is able to equilibrate at reasonable dynamics and time scale, however, the model tends to cycle between growth, mortality, and recruitment too quickly.

4.5.2 Community response to abiotic changes

The selected sites for the detailed numerical experiment represent the extremes in terms of total rainfall in Eastern Amazon; however both places experience a significant dry season with rainfall remaining below 100 mm for 3–5 months in typical years, and the difference in total rainfall is due to extremely high rainfall rates in GYF during the wet seasons. According to results in ED-2.2, the total rainfall during the wet season in GYF exceeds by a wide margin the maximum amount of water the soil can hold, causing the model to predict that about 58% of the total rainfall is lost through runoff and drainage. The run-off and drainage parameterizations are extremely simple, and the actual loss depends on terrain slope, soil texture, soil depth and bottom boundary conditions, all of which are known to be highly variable in Paracou area (Gourlet-Fleury et al.,

2004; Epron et al., 2006); nevertheless, the total evapotranspiration is well captured by the model at this site (Chap. 3), which suggests that a large fraction of rainfall is in fact lost. As a result, the shift towards drier climate caused little impact on the forest dynamics, since reduced rainfall was compensated by reduced runoff. On the other hand, the total simulated runoff in S67 was much lower at current conditions (28% of total rainfall), and like in GYF it decreased for drier climates, and once runoff approached zero on average (scenarios drier than $\Delta\xi_R = -0.6 \cdot \omega_R$), water became a severely limiting factor.

While the simulations suggest that the forests are more likely to lose biomass once the mean rainfall becomes less than 1500 mm, the biomass loss is not a result of a continuous decline, but instead it occurs in steps that are associated with periods in which water deficit conditions persisted for multiple years as a consequence of wet season being repeatedly shorter and/or drier than average. In the scenarios tested in this study, this condition never occurred in GYF, where even the driest years experienced at the site brought enough wet season rainfall to reset water deficit, whereas in S67, long periods with continuous water deficit occurred in the past according to the model, including a 31-month period between July 1991 and January 1994, and a 20-month period between June 1997 and January 1999 (not shown). Such droughts are likely to have caused major mortality events in S67, and measurements carried out earlier in the 2000s suggest that the forest was indeed recovering from a recent disturbance (Keller et al., 2004a; Rice et al., 2004; Pyle et al., 2008). Even though such drought events may have shifted the forest from equilibrium, the absence of severe droughts in the subsequent years caused the forest to accrue living biomass and remain a functional forest. Under the driest scenarios, the realizations that produced the highest loss of biomass were those in which severely dry years extended for a very long time, and also those in which the return time for droughts longer than 12 months were the shortest. This suggests that while a tipping point after a catastrophic drought may shift the forest in S67 area towards a lower biomass, such transition may also occur if severe but similar to previously experienced droughts became more frequent. Frequent droughts mean that the plant community will not have time to regain the biomass lost due to drought, and subsequent droughts would maintain lower biomass

even if they caused less new biomass loss, in line with the hypothesis presented by Hirota et al. (2011), in which the basin of attraction become shallower close to the transition point. Moreover, productivity and evapotranspiration showed a nearly linear relation for all realizations and years, with some increase in the BWUE for drier scenarios as predicted by Ponce Campos et al. (2013); however, this relation had little variation even when the biomass reduced by as much as 70% in S67, which shows that productivity–evapotranspiration relation is more related to the carrying capacity of the ecosystem than its resilience to changes in climate.

Under drought stress conditions, other abiotic factors such as soil characteristics may also play an important role defining the resilience of forests. In this study I only explored the effect of soil texture for any given soil moisture, and model results suggest that when all other characteristics are equal, forests seem to be more resilient in sandier soils. This result is a direct consequence of sandy soils having very low hydraulic conductivity at much less negative matric potential than clayey soils. In the model water potential is the driver for water stress, thus the plant community responds to drought at much higher water deficits and longer drought periods for sandy soils. This result may appear contrary to observations since regions with white sand soils in the Amazon are associated with lower biomass and lower biodiversity (Anderson, 1981; Saatchi et al., 2011); however, changes in soil texture in ED-2.2 affected only hydraulic properties of the soil, whereas confounding variables associated with soil texture exist and play a significant role in the ecosystem composition and functioning, particularly in terms of nutrient content. Sandy soils are normally very nutrient-poor compared to clayey soils (Laurance et al., 1999; Jiménez et al., 2009), and have higher toxic aluminium concentrations, at least near Manaus (Laurance et al.); also, forests in white sand regions tend to be less productive (Malhi et al., 2004) and have a higher proportion of slow-grower species that invest more in defense mechanisms against herbivory (Fine et al., 2006), and higher allocation to fine roots (Jiménez et al., 2009). Notwithstanding, the model results suggests that other abiotic factors that have little influence under current conditions could become relevant under different climate conditions.

In addition to soil moisture stress, another direct effect of drier climate is the reduction of rain-

fall interception. This effect is also important because evaporation of the intercepted water reduces the leaf temperature, especially during the photoperiod. Warmer leaves mean higher LVPD, which increases the stress in two different ways: when soil moisture is not limiting photosynthesis, this may increase the transpiration rates which can bring the plant community into drought stress more quickly; if plants reduce the stomatal conductance to down-regulate transpiration, this reduces the photosynthetic rates and thence carbon balance. While the model predicted down-regulation and lower LWUE due to higher LVPD in both sites and in all phenology strategies and, this effect was not sufficient to substantially affect the CUE in Paracou, where daytime LVPD was much lower than in Santarém km 67 in all cases, due to a combination of longer wet season and lower daytime temperatures (not shown). In S67 the combination of strong soil moisture and leaf vapor pressure deficits caused the LWUE to decrease by as much as 33%, thus affecting the ecosystem functioning and the ability to maintain the same structure.

4.5.3 Plant community dynamics, and change in structure and function

Not only the total simulated biomass had little to no response in GYF, but also the demographic rates and the proportion of biomass by size and functional type remained largely the same for all simulations, which further supports the strong resilience to variations in climate due to the excessive mean precipitation, and even in the driest cases the wet season rainfall was more than sufficient to recharge the soils. On the other hand, in S67 not only did the biomass decline, but the plant community also responded by shifting the structure and composition; therefore, both mean and interannual variability are needed to explain the different responses (Zimmermann et al., 2009). The impact of drier climate simulated by ED-2.2 has similarities to what was observed in the throughfall exclusion experiments carried out in the Amazon Nepstad et al. (2007); da Costa et al. (2010) and for most pan-tropical sites included in Phillips et al. (2010) analysis, in which losses were more significant amongst large trees. While in the experiments mortality rates were significantly higher for larger trees but comparable to control plots for smaller classes, in ED-2.2 mortality rates increased for all size classes, more similar to the observed mortality in Barro

Colorado Island (Panama) following the 1982-1983 drought (Condit et al., 1995), and predicted biomass loss was more severe amongst larger trees because the recruitment and growth rates increased for smaller classes (DBH < 35 cm, but especially DBH < 10 cm), while remaining similar or decreasing slightly for the largest classes, which was also observed in the throughfall exclusion experiment near Santarém km 67 (Nepstad et al., 2007).

The results also stress the importance to represent the population structure and direct competition for limiting resources such as light and water. In the evergreen case, smaller cohorts grew more because of more light, which was a direct consequence of less larger cohorts, while this effect was significantly reduced in the drought deciduous case because larger cohorts sustained more biomass. Although absorbed PAR increased in the understory, the light levels for drier scenarios were still within the light levels that would keep the plants under light-limiting conditions for most of the day and reduced the overheating effect, whereas taller trees are normally not limited by light, therefore additional light has only a negative effect by increasing temperature thence LVPD and respiration. Despite being a completely different ecosystem, a controlled experiment in Mediterranean oaks suggested the drought impacts would be the strongest under high light (Quero et al., 2006). In case of water, while larger cohorts have higher individual transpiration rates, most of the total transpired water comes from mid-canopy trees, with an additional significant contribution from the understory. Such partition in transpiration also means that a significant fraction of extracted soil moisture is due to the smaller cohorts, even though they have no access to deeper water in ED-2.2 and have relatively low demand as individuals. Since in these simulations I assumed no sub-surface source of water, and that capillarity is a negligible term (Ivanov et al., 2012), rainfall is the only source of soil moisture, and before throughfall water reaches deeper soil, it must go through layers to which all plants have access. If the dry season becomes too long or wet season rainfall is scarce, then most of the water is extracted and transpired before it reaches deeper layers, hence making deeper roots less advantageous, consistently with previous model studies for S67 (Markewitz et al., 2010; Ivanov et al., 2012). Furthermore, larger plants have higher maintenance costs, and as a result, their relative carbon balance becomes negative more quickly, and because in

ED-2.2 carbon balance is directly related to mortality, their mortality rates increase more rapidly than the smaller cohorts. Another outcome of competition and change in the population structure is the change in available resources: less canopy trees result in more available water to the remaining individuals, and more light to normally light-limited smaller trees, hence the increase in their stomatal conductance and productivity of the smallest individuals at drier scenarios.

Although this mechanism is observed on both evergreen and drought deciduous simulations, in the drought deciduous case, available water depletion induces the cohorts to halt growth and reduce the leaf area, and store the net productivity as non-structural carbon until conditions improve, resulting in lower mortality rates for larger trees. On the other hand, smaller trees require less carbon and are in the understory, and there is a trade-off between more water limitation and higher carbon use efficiency. Although the available information precluded us to simulate the direct competition between evergreen and drought deciduous, these results suggest that different strategies may work better depending on where in the canopy the individual is: since smaller individuals require less carbon, keeping the leaves during mild droughts may increase their total uptake and therefore be advantageous, whereas for larger trees the drought deciduous or at least drought-adapted strategy significantly increase their chance of surviving. This hypothesis has some support from observation in water-limited environments: for instance, Killeen et al. (1998) pointed out that in the tropical dry forest they studied in Bolivia, the under storey and lianas have a larger proportion of evergreens, whereas Markesteijn et al. (2007) mentions that nearly all canopy trees in the same site are drought deciduous. Lugo et al. (2002) also mentions that in the dry forests of Puerto Rico the tall trees are the first to shed leaves, and for some period of the year the forest stays leafless at the canopy with leafy understory.

In addition to changes in structure, the plant community composition in S67 was also affected. For drought deciduous cases, the shift in composition was much less pronounced, with late-successional plants in the mid-canopy (DBH class: $10-35$ cm) declining more than the other PFTs and sizes, due to the reduced growth rates under shorter growing seasons. In the evergreen case, storage biomass decreased significantly as a consequence of reduced LWUE and CUE, which

had the most impact on early successional cohorts. These cohorts have the highest relative maintenance cost due to short lifespan of leaves and fine roots (Reich et al., 1997) and drier conditions hindered the maintenance of a viable population once productivity was not enough to maintain the non-structural carbon pools. While the early successional population declined, lower-maintenance mid-successional plants took advantage of the reduced competition and their biomass increased especially at the smallest classes. In addition, in the model early successional trees have higher carboxylation rates (Kim et al., 2012); while this increases photosynthesis when light is not limiting, it also makes these cohorts more shade intolerant and more sensitive to higher temperatures, since leaf respiration in ED-2.2 is assumed to be proportional to carboxylation rates, after Collatz et al. (1991) and Foley et al. (1996).

The large losses of early-successional and their partial replacement by mid-successional in the evergreen case is an excellent example of how incorporating different life strategies within the plant community may increase the predicted impact of changes in climate to the plant community, by shifting the community composition towards life forms that are better adapted to the new environment conditions instead of an irreplaceable collapse. The outcome depends upon the assumed traits for the three plant functional types included in these simulations, which obviously cannot represent the full diversity in life strategy and resource allocation, nor the different trade-offs in resource allocation that are observed in tropical biomes. In fact, observed changes in wood density and successional groups in different tropical wet and dry forests following long-term droughts or drier climate are rather diverse: on the one hand, Feeley et al. (2011) showed a consistent increase in the mean wood density of the forests in Barro Colorado after the 1982-1983 drought, and Chave et al. (2009) and Markesteijn et al. (2011) suggest that both the Caatinga region in Northeastern Brazil and the Chaco in central South America possess a higher number of high wood density species; on the other hand, Enquist and Enquist (2011) pointed out that non-pioneer early successional species have became more abundant while shade-tolerant biomass have declined in a tropical dry forest in Guanacaste, Costa Rica after a 20-year period in which droughts became more frequent, whereas Fauset et al. (2012) analyzed multiple long-term plots in Ghana that also have been

affected by a drying trend and found that both pioneers and shade-tolerant species dominance decreased over time, even though no consistent shift in wood density was observed. It must be noted, however, that these long-term observations had long interval between observations which may include other controls to the plant community dynamics such as herbivory pulses, which affected the mortality of at least one species in Barro Colorado (Condit et al., 1995) and anthropogenic disturbances, which caused two Ghanian plots to show very different dynamics, with increase in pioneer species (Fauset et al., 2012). Moreover, drought adaptation is not a simple matter of leaf phenology and non-structural carbon usage: for example, variations in leaf and stem hydraulic conductivities were not included in the simulations presented here, but are known to be a significant trait related to drought tolerance (e.g Markesteijn et al., 2011); while this study also suggests that leaf and wood traits with respect to drought tolerance are interdependent, as they are currently assumed in ED-2.2 (Moorcroft et al., 2001), Baraloto et al. (2010) analyzed leaf and wood traits for over 600 species in Paracou and found that wood density is nearly orthogonal to leaf traits, which if true elsewhere, may also explain some of the variability and provide an important axis of variation for future PFT assignment.

4.5.4 Evaluating vulnerability to droughts

Although I tested the response on shifts in climate in only two sites, the current plant functional types intend to represent generic successional traits that are not specific to GYF or S67, therefore, I also sought to determine which forest regions in the Amazon could be vulnerable to droughts. This question has been extensively asked in the past (e.g. Hutyra et al., 2005; Senna et al., 2009; Salazar and Nobre, 2010; Hirota et al., 2011; Cox et al., 2013, amongst others), however the present analysis has some important differences. First I used the emerging responses of a structured plant community model to changes in climate, which incorporated the effects of competition for resources, and some hydraulic soil properties by including the effect of soil texture. Second, the vulnerability was assessed in terms of biomass loss as opposed to shifts in biome, which also accounts for changes in structure and composition even if the biome would still be classified as forest. Finally,

I incorporated the effect of inter-annual variability in climate, which is known to play an important role in the response of the plant community and habitat selection (c.f. Zimmermann et al., 2009; Reyer et al., 2013), and quantified vulnerability in terms of how much the climatological rainfall would need to change compared to current climate, with climate defined as the probability distribution of rainfall. Consistently to Reyer et al. (2013) conclusions that extreme events may be more important than the mean climate, the simulations that yielded the largest losses of biomass were those with multiple extreme droughts. Nevertheless, these extremes were not independent of mean rainfall, which has been also pointed out by Zimmermann et al. (2009), since our scenarios shifted the entire distribution, simultaneously lowering the mean rainfall and increasing the probability of extreme droughts.

By using the relationship between the return period and biomass loss, I estimated how much the current distribution of annual rainfall would need to change before extreme droughts became too common by changing the mean climate, the climate variability, and the skewness of extreme events. As expected, regions that are already savannahs (e.g. the Cerrado and Lavrado in Brazil, and Beni Department in Bolivia) had the most vulnerability regardless of the shift. Likewise, forest regions such as Southern Guyana and Santa Cruz and Pando Departments in Bolivia, which are in the vicinity of such savannahs, and some areas in Central Peru near the border of Ucayali and Loreto regions were also considered vulnerable due to their relatively low mean annual rainfall (less than 1700 mm). Especially for the shift in the mean annual rainfall, the very vulnerable area near the Lavrado extended throughout a long band to Marabá, and a region in Central Peru near the border of Ucayali and Loreto Regions also appeared vulnerable. Both regions have a relatively high inter-annual variability of rainfall, so shifts in the mean climate could dramatically increase the probability of droughts. In addition, the Boa Vista–Marabá band, which includes Santarém km 67 area, was considered vulnerable especially with respect to shift in the mean rainfall. Several savannah enclaves exist along the band (Fig. 1 in Barbosa et al., 2007), and the climate along the band is also relatively dry and also present high inter-annual variability, which reduces the relative shift needed to dramatically reduce the return period of extreme droughts. On the other

hand, this analysis predicted that most of the Amazon Forest, particularly along the coast and in the West would require dramatic changes in the mean climate and its variability before reaching a critical point. Surprisingly, even some areas near the transition to Cerrado, such as the Cachimbo Mountain Range in Southern Pará could be significantly more resilient, due to a combination of lower interannual variability in rainfall, lower evapotranspiration due to cooler temperatures (most of the area is between $250 - 400\,\mathrm{m_{ASL}}$), and to a lesser extent, soils with lower clay content. However, few of the aforementioned regions had consistent rain gauge records, at least based on the data sets I used, thus the results depend on whether the interpolation scheme used by the gridded dataset is able to reproduce the actual distribution of annual rainfall.

4.5.5 Limitations and challenges for future studies

Representing the plant community in terms of its size-, succession-, and age-structure is an important difference between ED-2.2 and most dynamic global vegetation models, and the results presented here stress that individual access, demand, and competition for shared and limited resources is fundamental to better understand how the ecosystems may respond to changes in climate. Nevertheless, adding such structures increase the model complexity and also require a much larger number of parameters and sub-models, many of which not directly available from or comparable to observations, and several of them that must be better constrained in the future.

First of all, mortality rates in ED-2.2 tend to be overestimated compared to the available site-level observations (Fig. 4.8). I carried out initial comparisons of mortality with the observed rates by plant functional type in GYF and a pan-tropical analysis by Kraft et al. (2010), and identified that the rates are consistently higher for early- and mid-successional plants (App. F). While mortality rates during extreme droughts would be much higher than the background mortality, higher density mortality rates reduce the recovery of these functional groups following disturbance, and also may explain why ED-2.2 underestimates their demographic density in old-growth patches. On the other hand, mortality rates during drought could be even more dramatic if the population at the time has a higher proportion of more susceptible early- and mid-successional individuals. The

amount of information on wood density available for tropical species has considerably increased since the original formulation of the density-independent mortality in ED-2.2 (Moorcroft et al., 2001), and comprehensive compilations of wood density are now available (c.f., Chave et al., 2009; Zanne et al., 2009), and these databases could be used in conjunction with multiple permanent plots in the Amazon, for example, from the RAINFOR database (Peacock et al., 2007) to constrain the background mortality. Moreover, density-dependent mortality rates are currently parameterized as a simple function of the carbon balance (App. F), whereas in reality drought mortality can arise from multiple inter-dependent mechanisms such as reduced carbon uptake, depleted non-structural carbon reserves, hydraulic failure and desiccation, and reduced defense mechanisms (Allen et al., 2010; McDowell et al., 2011; van der Molen et al., 2011). Understanding and quantifying the contribution of each of these mechanisms across different functional groups from both controlled experiments and observations could also allow the development of mechanism-based models for drought mortality.

In addition, even though it is generally accepted that grouping several species into functional groups is sufficient to describe the main characteristics of ecosystem functioning (Hooper et al., 2002; Reiss et al., 2009), the Amazon forest covers approximately $5,500,000 km^2$ with thousands of species of flowering plants (Hubbell et al., 2008) that are represented in ED-2.2 by only two grasses (C_3 and C_4) and three tree functional types (early-, mid-, and late-successional trees that can be simulated as evergreen or drought deciduous but not simultaneously). Even though ter Steege et al. (2013) recently showed that only 227 species are considered hyperdominant and could explain a large fraction of the processes, three functional types are still obviously insufficient to capture the main axes of succession, resource allocation, phenology, and life forms in the tropical forest. Currently the tropical tree PFTs are represented along a single trait axis which includes wood density, mean tree age, photosynthetic capacity, turnover rate of leaves and fine roots, and specific leaf area (Kim et al., 2012). While previous studies support that wood density is negatively correlated with tropical tree life span and growth rates from both pan-tropical analyses (Kraft et al., 2010) and from the moist forests in Santa Cruz Department in Bolivia(Poorter et al., 2010) and

hydraulic conductance (Poorter et al.), Baraloto et al. (2010) found that leaf traits were nearly orthogonal to above-ground wood traits in French Guiana, and more recently Fortunel et al. (2012) obtained similar results in the Loreto Region in Peru, and that root traits are more closely related to wood than to leaf traits at both places. Expanding the PFT definition along these two axes, leaf and wood+root axes, including stem hydraulic properties, could considerably increase realism of the forest dynamics. The results from different leaf phenology scenarios also suggest that forests could respond very differently depending on whether they are evergreen (deciduous) and naïve (efficient) in their use of non-structural carbon (NSC) stores. While I believe that these correspond to the most extreme cases of a full spectrum of leaf phenologies and NSC usage, little is known about how such traits vary across different species in the Amazon.

One important result that emerged from these simulations is that a large fraction of evapotranspiration and carbon uptake is attributed to cohorts with $DBH \leq 35[\,\mathrm{cm}]$, which if true could significantly reduce the amount of water reaching deeper layers and increase stress of larger trees if wet season rainfall is insufficient. Although this result may be qualitatively true, this depends on how accurate the model represents biomass of leaves and fine roots, as well as the rooting profile from the individual perspective. To my knowledge no community-wide measurements of individual-based transpiration exists for the Amazon, and such experiment could provide valuable data to constrain the model. Moreover, while many studies have developed or updated allometric equations for above-ground biomass for different parts of the Amazon (e.g. Chambers et al., 2001; Baker et al., 2004; Chave et al., 2005), far fewer studies have established relations between DBH or height and biomass of different living tissues (leaf, fine roots, sapwood). Moreover, individual roots are assumed to be evenly distributed throughout the layers and the total rooting depth is a simple function of DBH, and none of them are based on actual observations because of extremely limited data at individual level for the Amazon. In fact, Stahl et al. (2013) recently suggested that the depth of water uptake is not even well correlated with tree size, at least in GYF. If this is the case for more areas in the Amazon, then smaller trees could put even more stress on larger trees during extreme drought events.

Finally, while in this work the focus has been on the plant community response to droughts, changes in temperature and CO_2 in the Amazon are also going to affect the ecosystem functioning, although it is unclear how these environmental conditions are likely to affect the future climate. While numerical modelling studies have suggested that CO_2 fertilization may become the dominant effect (Cox et al., 2013; Huntingford et al., 2013), this has yet to be confirmed. There is an ongoing effort to establish the first free-air CO_2 enrichment (FACE, Ainsworth and Long, 2005, and references therein) experiment in the Amazon (Tollefson, 2013), although as Körner (2009) had pointed out, these experiments also have limitations: they are mostly focussed on net primary productivity and tend to be biased towards undisturbed areas in the forest. In addition, results of most numerical models (ED-2.2 included) are strongly dependent on choice of parameters, and the response to changes in climate also carry large uncertainties in the parameter space (Booth et al., 2012).

4.6 Conclusions

In this modelling study, I sought to define forest vulnerability to drought as how much the rainfall regime would need to change before significant changes in the ecosystem functioning occurred, using a size-, succession-, and age-structured model. In this study, I sought understanding how different parts of the Amazon would respond to similar changes in climate using a size-, succession-, and age-structured model. Results from multiple scenarios suggest that in wetter parts of the Amazon such as French Guiana coast, wet season rainfall in all tested scenarios were more than sufficient to recharge soils even with recurrent short dry seasons, and the plant community did not experience any significant change in composition or dynamics; moreover, mortality and growth rates were not correlated with water-stress variables. On the other hand, in drier areas such as Santarém in Brazil, the plant community started to lose biomass at relatively small shifts in the mean rainfall regime, with scenarios simulating an evergreen, drought intolerant stand on clayey soils decreasing biomass at minor shifts in climate (0.2-0.4 scale parameters), whereas drought

deciduous stands on sandy soils started to lose biomass at shifts of the order of 1 scale parameter. Furthermore, in S67, not only the biomass declined, but the plant community structure changes particularly in the evergreen, drought intolerant case, where larger trees and early successional lost the most biomass, whereas seedlings and smaller trees were somewhat more stable in terms of population, although the turnover rate increased.

Importantly, this study also showed the relevance of incorporating inter-annual variability: particularly for intermediate shifts in climates, the long-term biomass loss depended on how many extreme long drought events occurred throughout the simulation, suggesting that the ecosystem is no longer able to maintain biomass because the recovery time is longer than the mean return time of high mortality events. Using the return period of such droughts, I estimated the vulnerability for the entire Amazon by exploring the relative shift in three basic climate parameters that would be needed before drought became too frequent to maintain biomass. Unsurprisingly, regions near the current savannahs such as the moist forests in Bolivia, Roraima, and near the transition to the Cerrado appeared as the most vulnerable; however, I also identified that some of these regions could extend well into the forest, such as the leeward of the Guiana Shield and the medium Ucayali River in Peru, where a combination of lower rainfall and higher variability could increase the frequency of catastrophic droughts. In fact, both areas have experienced the impact of the severe droughts of 1992 and 1997, and 2005 and 2010.

The modelling study presented here is an encouraging first step to use a size-, succession-, and age-structured model to understand mechanisms that control shifts in species and size distribution in the Amazon should the climate becomes drier. However, many aspects relevant to drought tolerance and vulnerability could be incorporated to improve the predictability to changes in rainfall regime, such as a better representation of the spectrum of traits directly associated with water extraction and water use efficiency, such as root biomass allocation, hydraulic conductance, wider range of usage of non-structural carbon, and inclusion of additional effects associated with droughts such as biomass burning.

Chapter 5

Conclusions

The main goal of this dissertation was to explore the vulnerability of the Amazon forests to drier rainfall regime by estimating how much change in climate would need to occur before the forest experienced significant losses of biomass, and to provide insights on how drier climates could affect the structure and functioning of the plant community. To achieve this goal, I first took part on a collaborative work to develop, improve, and use a state-of-the-art dynamic vegetation model with mechanistic representation of most processes and structured around individuals. This project generated many deliverables have been developed along with new insights on how the forests in the Amazon may respond to changes in climate, both of which to be discussed in Sec. 5.1. In addition, throughout this work I found some limitations on the findings, which could be the starting point for future research, and I discuss these points in Sec. 5.2.

5.1 Key deliverables and findings of this study

The main deliverable of the work presented here are my contributions to the development that became part of the new Ecosystem Demography model (ED-2.2), which is now in the process of becoming released to the public, and freely available for future users and developers. In addition, the model developments have been thoroughly documented both at the code and here at Chap. 2 and appendices, which will enable future model users and developers to identify and understand

how multiple processes work in theory and have been implemented in ED-2.2, which should allow future development to be done more efficiently. Furthermore, I have been directly contributing to the annual Ecosystem Demography workshops, which aims at both training new users and bringing together developers from various universities and institutions.

The evaluation presented in Chap. 3 provides important information of the main strengths and deficiencies of the current model, which can guide future users on the most suitable applications and potential developments. In this model assessment, I compared the model with multiple datasets collected at multiple locations to reduce uncertainties about which processes were causing the source. By conducting this evaluation, I identified the main strengths (e.g. radiation transmission through the canopy and water cycles) and areas that could benefit from future developments (e.g. momentum flux and heterotrophic respiration). In addition, the extensive evaluation raised two important points:

1. Often the cause of discrepancy in any given variable is not caused by the most direct module, but by other models and parameterizations that define the conditions where the process takes place. For example, the relatively low leaf area index in forests associated with little to no seasonality also caused negative biases and low seasonality in gross primary productivity. Without extensive comparisons, one could incorrectly infer that the only cause of discrepancies are the parameters controlling the leaf photosynthesis.

2. Process-based models should be evaluated against as much data as availability permits, to ensure that processes that are not dominant everywhere can be also tested. For example, momentum fluxes were significantly stronger at GYF than any other tested site, and ED-2.2 tends to underestimate this variable. By prescribing the friction velocity, a significant improvement occurred at GYF on associated fluxes (sensible heat and water vapor fluxes), but no significant improvement was observed at other sites.

Moreover, the model evaluation also helped to identify problems with the observed data: for example, the large drift in radiation near Santarém km 67 (S67) were only detected because earlier

model simulations caused exceedingly lower productivity and water fluxes than any other tested sites. Therefore, results presented here certainly give support to a point previously made by Vanclay and Skovsgaard (1997):

> *However, a model should not be rejected simply because it behaves in a counter-intuitive fashion; it may be our preconceptions that are wrong. Thus, discrepancies should cause a critical reappraisal of the model, the data, and of preconceptions.*
>
> (Vanclay and Skovsgaard 1997)

The simulated drought scenarios provided important insights on what conditions are most likely to cause significant impacts on the forest functioning. First, it pointed out that two sites with very different total amount of rainfall, but with significant seasonality, responded very differently to relative shifts in the distribution of annual precipitation, which reinforces the need to distinguish between climate extremes from the statistical point of view and from the ecological point of view (Smith, 2011; Reichstein et al., 2013). At Paracou (GYF), the rainiest site tested, large shifts in the probability did not cause any significant change in the functioning of the plant community. In contrast, significant losses of biomass started to happen at Santarém km 67 (S67) at relatively modest changes in the annual rainfall distribution.

Model results also indicated that both the wet season rainfall and the competition for water between individuals of all sizes and functional groups is important. Wet season rainfall was sufficient to recharge soils in GYF even at the driest cases, whereas iin S67 this was not always the case, hence the eventual loss of biomass. Results at S67 agree at least qualitatively with the root niche separation hypothesis previously proposed by Ivanov et al. (2012), since in ED-2.2 the allometric equations assume that smaller trees have shallower roots than the larger trees. As a result, during normal years, wet season recharges the soil moisture profile, and moisture in deep soil layers provides an important source of water to taller trees during the dry season. Also, as hypothesized by Ivanov et al. (2012), larger trees demand more water due to their position in the canopy (higher light) and the larger local leaf area index. If the rainfall is insufficient during the wet season, the limited water input is shared by large and small trees and fails to recharge deeper layers, in which case having deeper roots does not give any advantage to larger trees. Moreover, while the water

shortage affects both small and larger trees, the model predicted that larger trees were likely to be affected the most. Smaller trees are generally more abundant than larger trees, so even if they demand less water and light as individuals than the larger trees, their higher demographic density partially compensates the individual differences and as a result smaller trees tend to respire a comparable amount of water to larger trees, thus effectively competing for water. Because they are more abundant and require less carbon uptake as individuals, they are also able to recover population quickly, but if droughts become too frequent, they will not have enough time to grow into the larger categories, leading to canopy thinning and lowering the biomass. Likewise, early successional evergreen trees were affected the most under drier conditions: combination of high turnover rate of living tissues with higher respiration rates reduced their survivorship, which was partly compensated by the increase of mid-successional trees. In case of drought deciduous trees, storage was not used to rebuild damaged tissues until conditions improved, which increased their survivorship. While this increased the resilience to droughts, it was not sufficient to maintain the same biomass for the driest scenarios.

Another important result was that the return period of one-year long drought, defined as a continuous period with water deficit, is a good predictor of biomass losses, and I used this relationship to estimate how much shift in climate would need to occur before the return period of such droughts became too short for the ecosystem to recover from previous droughts. Once the return period becomes less than 10 years, biomass rapidly declines, particularly at soils with high clay content. By using this information to determine when significant losses of biomass would occur throughout the Amazon forests, I was able to identify the most vulnerable regions as those areas where the distribution of annual rainfall would need to change the least before reaching low return periods. While results here also showed high vulnerability at the South and Eastern edges of the Amazon forest (Mato Grosso and Maranhão states in Brazil and Santa Cruz department in Bolivia), other regions that are not as close to the Cerrado region also showed high vulnerability, in particular the Pucallpa area in Peru, the Pando department in Bolivia and the leeward of the Guiana Shield north of Santarém, the latter region extending over a large area and central and Northern parts of the

Amazon forests. At these areas the short return period of extreme droughts could be achieved by relatively small changes in the average rainfall or increased inter-annual variability. Conversely, several areas that are relatively close to the southeastern edge of the forest could be more resilient than previously thought, although this depends on how well the different gridded rainfall products perform over this region.

5.2 Suggestions for future work and studies

The need of individual-based, mechanistic dynamic vegetation models has been long advocated (Moorcroft, 2006; Purves and Pacala, 2008; Evans, 2012) and results presented here corroborated the relevance of incorporating the biotic and abiotic heterogeneity within the ecosystem; in addition, ecosystem-level integrated or averaged properties such as eddy covariance data are extremely relevant for constraining and identifying strengths and shortcomings for models and have been used extensively to evaluate different models (e.g. Dietze et al., 2011; von Randow et al., 2013). However, the move to individual-based models will also require more individual-based observations, to ensure that not only the emerging properties but also the processes that build the emerging properties are correct. For example, knowing the total ecosystem water exchange provides important constrains to the model, but equally important is to know how much water is being extracted by plants of different sizes if one wants to understand whether it makes sense that water stress is strongly affecting larger trees because smaller trees are transpiring a substantial amount of soil water.

In addition, estimates of ecosystem-scale above-ground biomass and leaf area index are fundamental to understand the model behaviour over larger areas, but equally important is to know how such properties scale from individual- to community-level. On the one hand, allometric equations relating individual size to total above-ground biomass are very common for the tropics (e.g. Chambers et al., 2001; Chave et al., 2005; Feldpausch et al., 2012), and such estimates usually work well because most of the biomass is stored amongst larger trees. Active tissues, however,

often correspond to a very minor fraction of the total biomass, and obtaining reasonable estimates of total biomass is no guarantee that the model allocation to different tissues bears any resemblance with what actually happens in the forest. Current allometric equations for living tissues are largely unconstrained in ED-2.2: for example leaf allometry is based on very limited information available for Costa Rica (Cole and Ewel, 2006; Calvo-Alvarado et al., 2008), and even though few other allometric equations exist for leaf biomass (Lescure et al., 1983; Saldarriaga et al., 1988), such methods rarely sample saplings, and extrapolating these scant allometric relations to smaller classes often lead to differences of order of magnitudes. Underestimating leaf biomass at the early stage can significantly affect the ability of a functional group to establish a population and survive. Moreover, fine root biomass is assumed the same as leaf biomass at maximum elongation, and sapwood biomass is derived from a pipe model originally developed for a few commercially relevant species in the temperate zone (Moorcroft et al., 2001), and neither biomass of these tissues nor rooting depth have ever been constrained from actual observation.

The goal of this study was to assess how limited water availability due to droughts could affect the plant community dynamics in the Amazon. Droughts, however, also increase the risk of fires, which can dramatically increase mortality, particularly amongst smaller tree classes (Balch et al., 2011), and could increase the forest vulnerability even when the drought is not sufficiently long to cause widespread physiological failure. For example, the 1998 drought caused one of the largest fire events in recent history in the Amazon, with nearly $1,000,000$ ha of forest burnt in the state of Roraima (Elvidge et al., 2001), while the state of Acre experienced a 5-fold increase in fire counts during the 2005 drought (Aragão et al., 2007). Such fires could affect the long-term forest structure and composition, as observed in Roraima (Xaud et al., 2013), and the regeneration dynamics, with reduced seedling diversity and seedling contribution to regeneration after fires, as observed by Balch et al. (2013) after a controlled fire experiment in Southeastern Amazon. Furthermore, the fire risk is also exacerbated for forests close to areas with intensive deforestation, mostly due to fire leakage (Cochrane, 2003; Cochrane and Barber, 2009; Morton et al., 2013). Currently, ED-2.2 has a very simple fire model, which could be developed in the future to incorporate better controls on

fire probability and intensity, type of fire (canopy or understory), and survivorship that is dependent on size and plant functional type, thus providing a more realistic picture of the forest vulnerability to droughts.

In this work I only addressed the impact of changing the rainfall regime; however, increase in both CO_2 and temperature are also likely to affect the forest dynamics, and warming and incrasing atmospheric CO_2 trends have higher confidence than future changes in rainfall (Magrin et al., 2007), and DGVM simulations for the $21st^{c}$entury suggest that positive effect of CO_2 fertilization could largely offset the negative impacts of warmer and drier climate (e.g. Rammig et al., 2010; Huntingford et al., 2013). Most of these predictions, however, have been drawn from big-leaf simulations that normally do not representation of competition between individuals of different sizes and successional types. For example, Körner (2009) has pointed out that the light compensation point could reduce in a CO_2-enriched atmosphere, potentially giving fast-growing trees and lianas greater competitive advantage, which would increase photosynthetic uptake without necessarily increasing biomass due to higher turnover. Moreover, such shift in composition could potentially reduce the drought resilience that would otherwise come with higher CO_2, since lianas and low wood density trees may be more vulnerable to drought (Nepstad et al., 2007; Markesteijn, 2010). In this sense, ED-2.2 has an appropriate framework to simulate the effects across size and succession, although it would still require including the cycles and effects of nutrients, particularly phosphorous, which is generally viewed as the main limiting nutrient for tissue growth in the Amazon (Cleveland et al., 2011; Quesada et al., 2012).

Finally, the site-level observation network in the Amazon has vastly improved for the past fifteen years thanks to initiatives such as the Large-Scale Biosphere Atmosphere Experiment in Amazonia (LBA, Keller et al., 2004b; Davidson et al., 2012, and references therein), and the integration of efforts in the RAINFOR network (Malhi et al., 2002; Peacock et al., 2007), and any person who spent some time in the field in the Amazon knows how hard is to overcome the long distances and logistic constraints involved, which considerably limits access to vast regions. However vast the current coverage in ground-based measurements is in contrast with past, there are still large areas

in the Amazon that have only very limited long-term studies that could provide significant new insight on the forest dynamics. As a simple attempt to identify such regions regions, I used the geographic location of all RAINFOR plots[1] as the input for Maxent (Phillips et al., 2004, 2006), a niche-based model that takes into account environmental conditions and presence-only information of any given species of interest to estimate the probability of occurrence. For environmental conditions I used climatological averages from the Climate Research Unit (Harris et al., 2013), and vegetation classification from IGBP (Tempel et al., 1996); and the resulting probability of finding a RAINFOR plot is shown in Fig. 5.1. Evidently, access significantly constrains the probability of finding a RAINFOR plot: walk around forests near Manaus, the largest city in central Amazon, and chances are that you will find a forest plot. Likewise, areas near Santa Cruz and Pando departments in Bolivia have been extensively surveyed and are well represented according to the model. On the other hand, large areas in Eastern Amazonia and Northern Amazonia, including the southern range of the Guiana Shield (high vulnerability) and the region south of Santarém km 67 are very poorly characterized by the current distribution of measurements. Coincidentally, these regions have been surprisingly characterized as very resilient by the analysis presented in Sec. 4.4.3, therefore they should be regarded as high-priority regions for future measurements since they may represent important parts of the vulnerability range within the Amazon.

[1] Geographic location was obtained from `http://www.rainfor.org/en/map`.

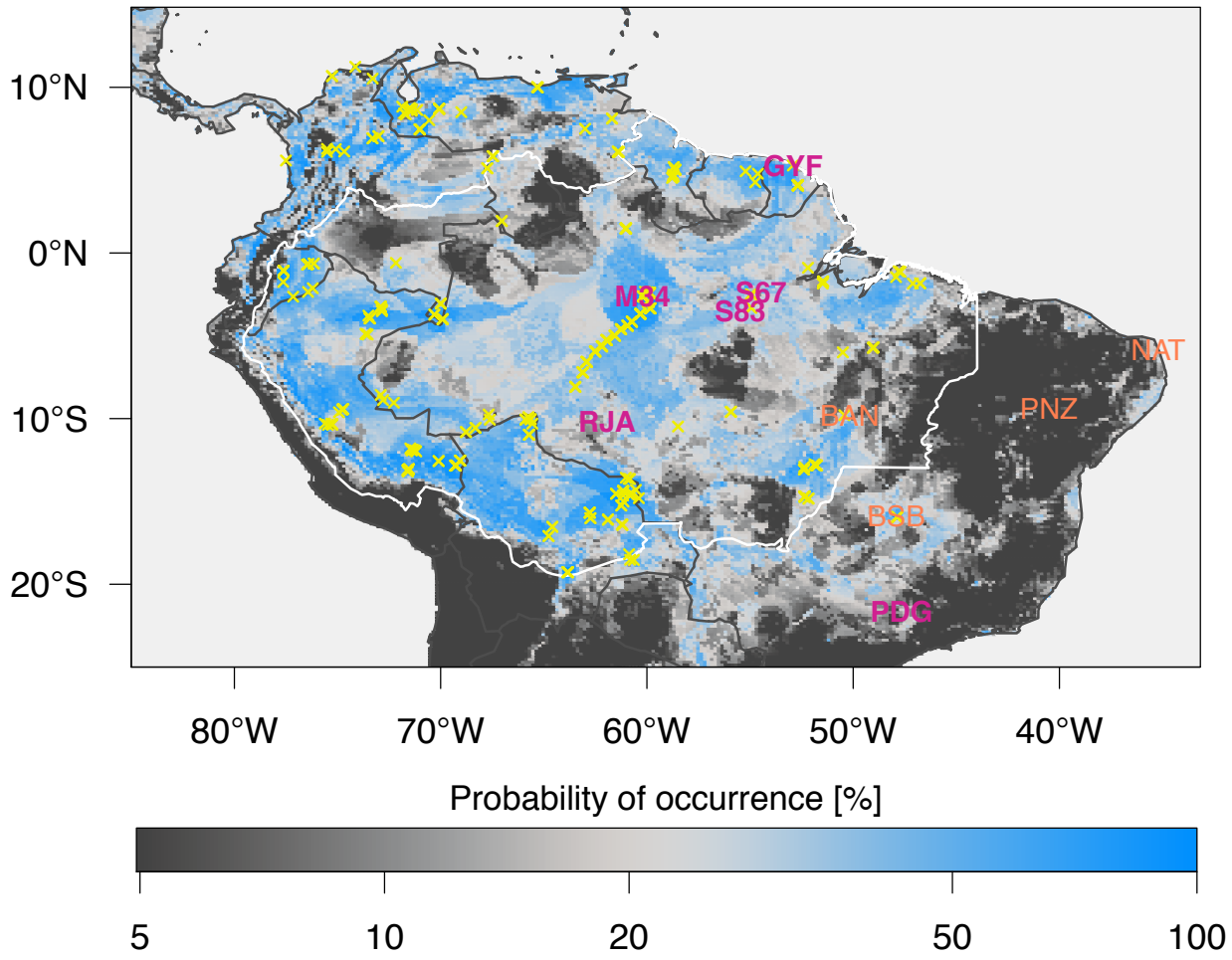

Figure 5.1: Probability of occurrence of a RAINFOR plot predicted by Maxent using climatology estimated from CRU data set for 1961–1990 period and vegetation classification from IGBP (see main text for references). The white contour corresponds to Amazonia (here defined as the Amazon Basin plus the Guiana Shield), and the yellow crosses are the location of all RAINFOR plots.

Appendix A

Algorithm for determining the CO_2 assimilation rates and transpiration

Ultimately we are interested in determining the assimilation rate ($\dot{A}_m$) and transpiration rate $\dot{S}_m$ for any cohort m[1]. By combining multiple equations from Sec. 2.4.6, it is possible to obtain fluxes by leaving only two additional unknowns, the intercellular CO_2 (c_{χ_m}) and stomatal conductance for water ($\hat{g}_{W\chi_m}$). First, I substitute Eqn. (2.109) and either Eqn. (2.111), Eqn. (2.112) or Eqn. (2.114) into Eqn. (2.108) and write a general functional form for $\dot{A}_{l,m}$, similarly to Medvigy (2006), that is a function of only one unknown, c_χ:

$$\dot{A}_{l,m}\left(c_\chi\right) = \frac{\alpha^{\mathrm{A}}_{l,m}\, c_\chi + \alpha^{\mathrm{B}}_{l,m}}{\alpha^{\mathrm{C}}_{l,m}\, c_\chi + \alpha^{\mathrm{D}}_{l,m}} - \dot{D}_m, \tag{A.1}$$

where parameters α depend on the limitation and the photosynthetic pathway, as shown in Tab. A.1.

I then combine Eqn. (2.115a) and Eqn. (2.117) to eliminate $\hat{g}_{C\chi_m}$ and c_{β_m}, and write an alternative equation for $\hat{g}_{W\chi_m}$:

$$\hat{g}_{W\chi_{l,m}} = \frac{\gamma_\chi\, \hat{g}_{W\beta_m}\, \dot{A}_m}{\hat{g}_{W\beta_m}\left(c_a - c_{\chi_m}\right) - \gamma_\beta \dot{A}_m}. \tag{A.2}$$

Finally, I use Eqn. (2.115a) and Eqn. (2.115b) to eliminate c_{β_m} and w_{β_m} from Eqn. (2.116); and

[1] In this chapter, I follow the same notation and symbols as in Sec. 2.4.6.

Table A.1: Coefficients used in equation (A.1) for each limitation and photosynthetic path. The special case in which the stomata are closed is also shown for reference.

Case	C_3 photosynthesis				C_4 photosynthesis			
	$\alpha^{\mathbf{A}}$	$\alpha^{\mathbf{B}}$	$\alpha^{\mathbf{C}}$	$\alpha^{\mathbf{D}}$	$\alpha^{\mathbf{A}}$	$\alpha^{\mathbf{B}}$	$\alpha^{\mathbf{C}}$	$\alpha^{\mathbf{D}}$
Closed stomata ($l=0$)	0	0	0	1	0	0	0	1
RuBP-saturated ($l=1$)	$\dot{V}_{C_m}^{\max}$	$-\dot{V}_{C_m}^{\max}\Gamma_m^\star$	1	$\mathcal{K}_{ME_m}$	0	$\dot{V}_{C_m}^{\max}$	0	1
CO_2-limited ($l=2$)	$\dot{V}_{C_m}^{\max}$	$-\dot{V}_{C_m}^{\max}\Gamma_m^\star$	1	$\mathcal{K}_{ME_m}$	$k_{PEP_m}\dot{V}_{C_m}^{\max}$	0	0	1
Light-limited ($l=3$)	$\varepsilon_m \dot{q}_m$	$-\varepsilon_m \dot{q}_m \Gamma_m^\star$	1	$2\Gamma_m^\star$	0	$\varepsilon m \dot{q}_m$	0	1

eliminate $\hat{g}_{W\chi_{l,m}}$ by replacing the left hand side of Eqn. (2.116) by the alternative Eqn. (A.2), yielding to the following function $F(c_\chi)$ for which we seek the solution $F(c_{\chi_{l,m}})=0$:

$$F(c_\chi) = F_1(c_\chi)\,F_2(c_\chi)\,F_3(c_\chi) - 1 \tag{A.3a}$$

$$F_1(c_\chi) = \frac{\left(\gamma_\chi - \gamma_\beta \dfrac{\hat{g}^{\varnothing}_{W\chi_m}}{\hat{g}_{W\beta_m}}\right)\dot{A}_{l,m}(c_\chi) - \hat{g}^{\varnothing}_{W\chi_m}\left(c_a - c_\chi\right)}{m_m \dot{A}_{l,m}(c_\chi)} \tag{A.3b}$$

$$F_2(c_\chi) = \frac{\hat{g}_{W\beta_m}\left(c_a - \Gamma_m^\star\right) - \gamma_\beta\,\dot{A}_{l,m}(c_\chi)}{\hat{g}_{W\beta_m}\left(c_a - c_\chi\right) - \gamma_\beta\,\dot{A}_{l,m}(c_\chi)} \tag{A.3c}$$

$$F_3(c_\chi) = 1 + \frac{w_a - w_{\chi_m}}{\mathcal{D}_m}\,\frac{\hat{g}_{W\beta_m}\left(c_a - c_\chi\right) - \gamma_\beta \dot{A}_{l,m}(c_\chi)}{\hat{g}_{W\beta_m}\left(c_a - c_\chi\right) + \left(\gamma_\chi - \gamma_\beta\right)\dot{A}_{l,m}(c_\chi)} \tag{A.3d}$$

For the limitation cases in which Eqn. (A.1) does not depend on c_χ, Eqn. (A.3) is reduced to a quadratic equation. For the other cases, Eqn. (A.3) could be written as a fifth-order polynomial, which cannot be solved algebraically. Nevertheless, Eqn. (A.3) is convenient because it highlights the range of plausible solutions, corresponding to the singularities associated with F_1 and F_2[2]. Function F_1 is singular when $\dot{A}_{l,m}=0$; from Eqn. (A.2), this means that $\hat{g}_{W\chi_m}$ must be 0, unless $c_{\chi_m}=c_a$. Function F_2 is singular when $\dot{A}_{l,m}=\hat{g}_{C\beta_m}\left(c_a - c_{\chi_m}\right)$; from Eqn. (A.2), this happens only when $c_{\chi_m}=c_a$ or at $\lim_{\hat{g}_{W\chi_m}\to\infty}$. The singularities for when $c_a \neq c_{\chi_m}$ are obtained by substituting Eqn. (A.1) into Eqn. (2.115a), and by taking the $\lim_{\hat{g}_{W\chi_m}\to 0}\dot{A}_m$ and $\lim_{\hat{g}_{W\chi_m}\to\infty}\dot{A}_m$:

[2]The singularities associated with F_3 requires $c_\chi \geq c_a$ which can be only achieved with negative $\hat{g}_{W\chi_m}$ or $\dot{A}_m < -\dot{D}_m$, and none of them are meaningful.

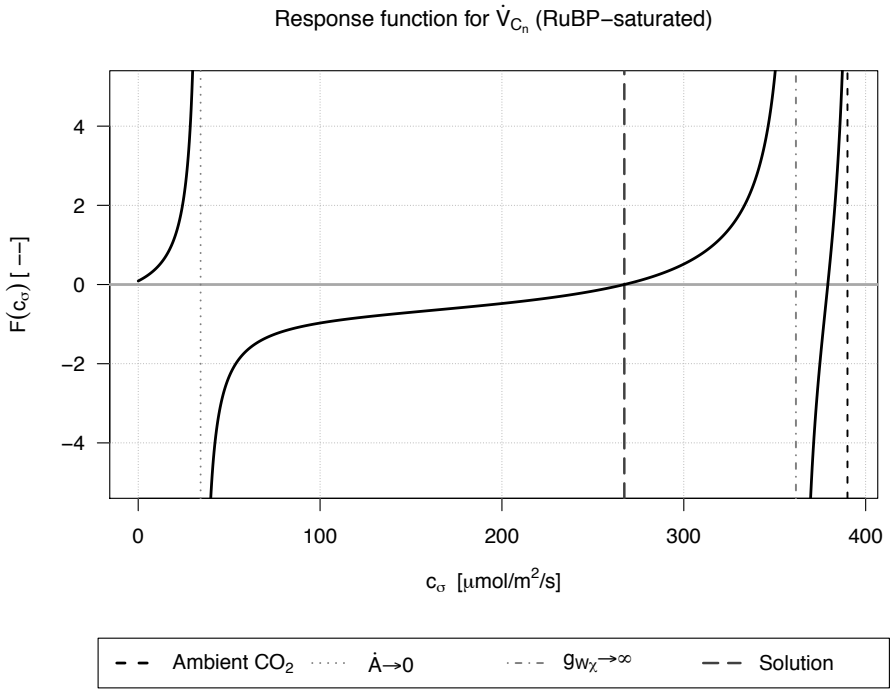

Figure A.1: Example for the function F(c_χ) curve for the RuBP-saturated case for a mid-successional, tropical broadleaf tree when $\dot{Q}_{1,e,m} = 100\,\mathrm{W\,m^{-2}}$, $T_{\lambda_m} = T_a = 301.15\,\mathrm{K}$, $w_a = 0.017\,\mathrm{kg_C\,kg_A^{-1}}$, $u_{\pi_m} = 0.25\,\mathrm{m\,s^{-1}}$, and $c_a = 390\,\mu\mathrm{mol_C\,mol_{Air}^{-1}}$. Vertical lines shows the solution and the singularities within the plausible range.

$$c_{\chi_{\min}} + \frac{\alpha^{\mathrm{D}}_{l,m}\,\dot{D}_m - \alpha^{\mathrm{B}}_{l,m}}{\alpha^{\mathrm{C}}_{l,m}\,\dot{D}_m - \alpha^{\mathrm{A}}_{l,m}} = 0, \quad \text{(A.4a)}$$

$$c^2_{\chi_{\max}} + \frac{\hat{g}_{C\beta_m}\,\alpha^{\mathrm{D}}_{l,m} + \alpha^{\mathrm{B}}_{l,m} - \alpha^{\mathrm{C}}_{l,m}\left(\hat{g}_{C\beta_m}\,c_a + \dot{D}_m\right)}{\hat{g}_{C\beta_m}\,\alpha^{\mathrm{C}}_{l,m}}\,c_{\chi_{\max}} + \frac{\alpha^{\mathrm{B}}_{l,m} - \alpha^{\mathrm{D}}_{l,m}\left(\hat{g}_{C\beta_m}\,c_a + \dot{D}_m\right)}{\hat{g}_{C\beta_m}\,\alpha^{\mathrm{C}}_{l,m}} = 0. \quad \text{(A.4b)}$$

From Eqn. (A.4b) up to two roots are possible, but normally only one is plausible. In case both values are greater than c_a, we use c_a as the upper boundary, since c_a is also a singularity; otherwise we chose the root that is between $c_{\chi_{\min}}$ and c_a. If none of them are in this range, then there is no viable solution for this limitation, and we assume that the stomata must be closed. Once the boundaries are defined, we seek the solution in the $\left]c_{\chi_{\min}}; c_{\chi_{\max}}\right[$, where there is only one possible solution, as illustrated in Fig. A.1.

Appendix B

Soil texture classification and properties in ED-2.2

Most of the soil parameterization in ED-2.2 is derived from LEAF-3 (Walko et al., 2000), and uses the soil classification based on the United States Department of Agriculture (e.g. Cosby et al., 1984). Several soils in the Amazon would fall under the Clay class of the USDA classification, even though their sand, silt, and clay fraction would vary significantly from the average values of this class. To avoid large deviations from observations, I further split the original *Clay* class into four categories, temporarily named as *Clayey sand*, *Clayey silt*, *Clay*, and *Heavy Clay*, as shown in Fig. B.1. In addition, Naomi Levine further modified the code to allow using the actual texture fractions instead of mapping the observed soil onto the look up table. Both systems are still acceptable in ED-2.2, since some data sets do not provide the texture fractions.

Most soil hydraulic parameters are taken from Cosby et al. (1984) and shown here for reference:

$$\vartheta_{\mathrm{Po}} = 0.0505 - 0.0142\ \mathcal{V}_{\mathrm{Sand}} - 0.0037\ \mathcal{V}_{\mathrm{Clay}}, \tag{B.1a}$$

$$\Psi_{\mathrm{Po}} = -0.01 \cdot 10^{2.17 - 1.58\ \mathcal{V}_{\mathrm{Sand}} - 0.63\ \mathcal{V}_{\mathrm{Clay}}}, \tag{B.1b}$$

$$b = 3.10 - 0.3 \cdot \mathcal{V}_{\mathrm{Sand}} + 15.7 \cdot \mathcal{V}_{\mathrm{Clay}}, \tag{B.1c}$$

$$G_{\Psi,\mathrm{Po}} = 6.817 \cdot 10^{-6} \cdot 10^{-0.60 + 1.26\ \mathcal{V}_{\mathrm{Sand}} - 0.64\ \mathcal{V}_{\mathrm{Clay}}}, \tag{B.1d}$$

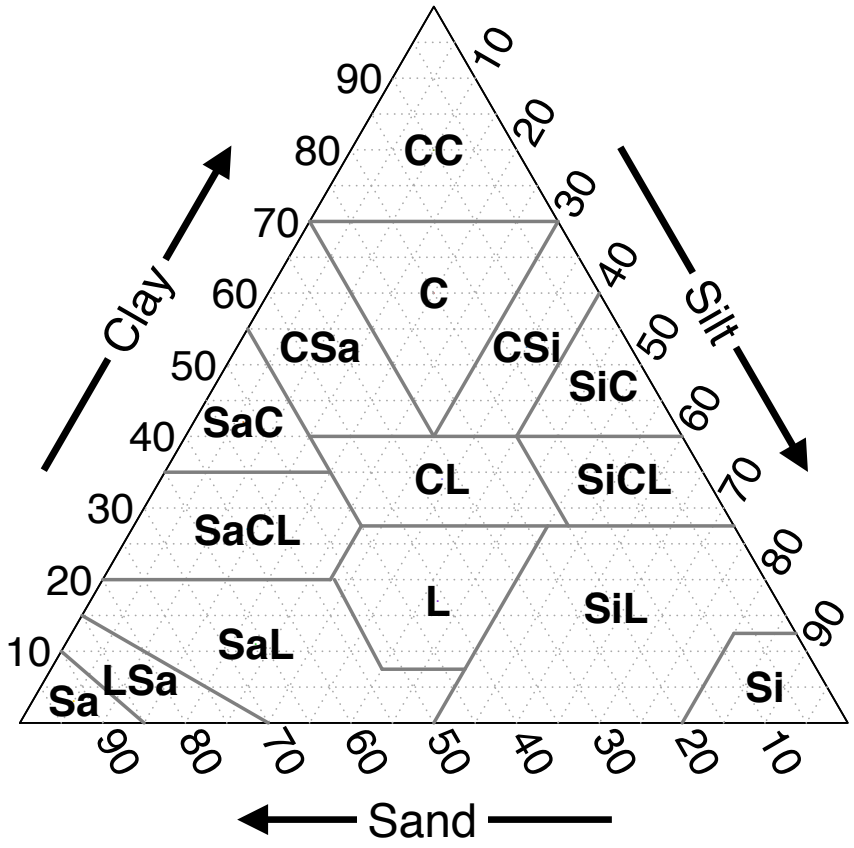

Figure B.1: Barycentric diagram of volumetric fraction of soil particle sizes (sand, silt, and clay) along with the canonical soil texture classes in ED-2.2. Classes are: sand (1, Sa), loamy sand (2, LSa), sandy loam (3, SaL), silty loam (4, SiL), loam (5, L), sandy clay loam (6, SaCL), silty clay loam (7,SiCL), clay loam (8, CL), sandy clay (9, SaC), silty clay (10, SiC), clay (11, C), silt (14, Si), heavy clay (15, CC), clayey sand (16, CSa), and clayey silt (17, CSi). Classes 12 and 13 correspond to peat and bedrock, respectively, and are not represented here.

where $\vartheta_{\mathrm{Po}}[\,\mathrm{m}^3_{\mathrm{W}}\,\mathrm{m}^{-3}]$ is the soil porosity (maximum soil moisture possible), $\Psi_{\mathrm{Po}}\ [\mathrm{m}]$ is the soil matric potential at porosity, β is the slope of the logarithmic water retention curve, and $G_{\Psi,\mathrm{Po}}$ $[\,\mathrm{kg}_{\mathrm{W}}\,\mathrm{m}^{-2}\,\mathrm{s}^{-1}]$ is the soil hydraulic conductivity at bubbling pressure, assumed to occur when $\vartheta = \vartheta_{\mathrm{Po}}$.

Additional reference points are determined using the above equations combined with Eqn. (2.35a) and Eqn. (2.35b). The permanent wilting point ϑ_{Wp} and residual soil moisture ϑ_{Re} are defined as the soil moisture at which the soil matric potential is equivalent to -1.5 and $-3.1\,\mathrm{MPa}$:

$$\vartheta_{\mathrm{Wp}} = \vartheta_{\mathrm{Po}} \cdot \left(-\frac{g_{\oplus} \cdot \Psi_{\mathrm{Po}}}{1.5\rho_{\ell}} \right)^{\frac{1}{\beta}}, \tag{B.2a}$$

$$\vartheta_{\mathrm{Re}} = \vartheta_{\mathrm{Po}} \cdot \left(-\frac{g_{\oplus} \cdot \Psi_{\mathrm{Po}}}{3.1\rho_{\ell}} \right)^{\frac{1}{\beta}}, \tag{B.2b}$$

where $g_{\oplus}$ is the gravity acceleration and ρ_{ℓ} is the density of liquid water. Likewise, the field capacity is defined as the soil moisture at which the soil hydraulic conductivity is $0.1\,\mathrm{mm\,day}^{-1}$:

$$\vartheta_{\mathrm{Fc}} = \vartheta_{\mathrm{Po}} \cdot \left(\frac{1.16 \cdot 10^{-9}}{G_{\Psi,\mathrm{Po}}} \right)^{\frac{1}{2\beta+3}}. \tag{B.3}$$

Appendix C

Allometric equations in ED-2.2

In this appendix, I present the allometric equations for tropical plant functional types (PFT) only; allometric equations for temperate PFTs can be found at Albani et al. (2006) and Medvigy et al. (2009). In ED-2.2, most allometric equations use the diameter at the breast height (DBH[cm]) as the size-dependent explanatory variable. The only time when DBH is the dependent variable is at the structural growth time step, at which point DBH is determined from the structural biomass.

Cohort height (z_π[m]) is taken from Poorter et al. (2006) allometric equation for moist forests in Bolivia, although it a maximum height of 35 m is imposed:

$$z_\pi = \min\left\{35.0, 61.7 \cdot \left[1 - \exp\left(-0.0352 \cdot \mathrm{DBH}^{0.694}\right)\right]\right\}. \tag{C.1}$$

Likewise, the height at the bottom of the crown $\hat{z}_\pi$[m] is determined from Poorter et al. (2006) for trees, whereas it is assumed to be 99 % of the height for grasses. Unlike most allometric equations shown in this chapter, this is a function of tree height:

$$\hat{z}_\pi = \max\left[0.05, z_\pi - (0.99; 0.99; 0.31; 0.31; 0.31) \cdot z_\pi^{(1.0;1.0;1.098;1.098;1.098)}\right], \tag{C.2}$$

where the vector elements corresponds to the PFTs: C_4 grass (C4G), C_3 grass (C3G), early-successional (ETR), mid-successional (MTR), and late-successional trees (LTR)[1]. A minimum value of 5 cm is imposed to avoid singularities.

[1] Throughout this chapter, I will present the PFT-specific parameters as vectors, always in this order.

Maximum leaf biomass ($C_\lambda^\star$ $[\mathrm{kg_C\,m^{-2}}]$), corresponding to the state when leaves are fully flushed, is derived from the allometric equations presented by Cole and Ewel (2006) and Calvo-Alvarado et al. (2008) for several species in Costa Rica. Given that ED-2.2 must cover a wide range of DBH, I generated artificial data points from all species within the range of measurements used to determine the allometric equations for each class, and fitted an exponential fitting, yielding to:

$$C_\lambda^\star = (0.158; 0.158; 0.418; 0.560; 0.701)\,\mathrm{DBH}^{0.975}. \tag{C.3}$$

A comparison with the original allometric equations is presented in Fig. C.1, where we observe that the largest discrepancies in order of magnitude occur at the smallest size classes. Although these classes contribute little to total biomass and leaf area index, obtaining reasonable biomass of living tissues is important because it determines the ability of smaller indviduals to establish and grow to larger classes. Moreover, extremely low values of leaf biomass can cause the model to reduce the Runge-Kutta time step to very small steps and higher risk of numerical instabilities.

Maximum root ($C_\rho^\star$ $[\mathrm{kg_C\,m^{-2}}]$) and maximum sapwood (C_σ $[\mathrm{kg_C\,m^{-2}}]$) biomass are determined from $C_\lambda^\star$ using the same functional form as Moorcroft et al. (2001), whose formulation of sapwood biomass was was based on the pipe model by Shinozaki et al. (1964a,b):

$$C_\rho^\star = q_\rho\, C_\lambda^\star, \tag{C.4}$$

$$C_\sigma^\star = \frac{\mathrm{SLA}}{r_\sigma}\, z_\pi\, C_\lambda^\star, \tag{C.5}$$

$$\tag{C.6}$$

where q_ρ is a tuneable parameter, currently set to 1 for for all tropical PFTs as of ED-2.2; r_σ is a constant currently set to 3900 for all tropical PFTs, $\mathrm{SLA}[\mathrm{m^2\,kg_C^{-1}}]$ is the specific leaf area, determined from Kim et al. (2012) fit of specific leaf area as a function of leaf turnover rate, using the GLOPNET leaf economics dataset (Wright et al., 2004):

$$\mathrm{SLA} = (22.7; 22.7; 16.0; 11.6; 9.66)\,. \tag{C.7}$$

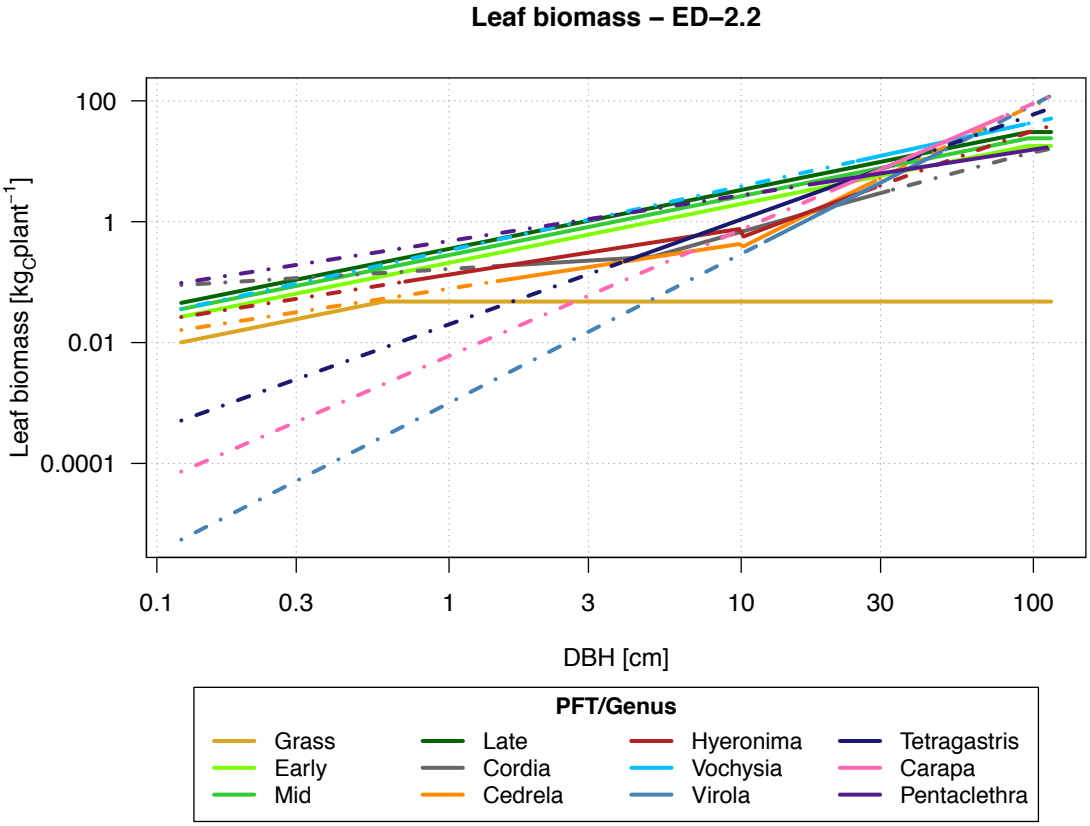

Figure C.1: Result from allometric equations using the genera studied by Cole and Ewel (2006) and Calvo-Alvarado et al. (2008) compared to the current allometry. Green lines are the fitted lines for ED-2.2, and other colours are the fitted lines from the references. Dashed lines corresponds to the region outside the range of measurements.

Total structural biomass (C_δ [$\mathrm{kg_C\,m^{-2}}$]) is based on Baker et al. (2004) equation of above-ground biomass in turn based on the allometric equation by Chave et al. (2001) for French Guiana. This allometric equation was used instead of the allometric equation based on Chambers et al. (2001) because in ED-2.2 the function relating C_δ and DBH must be bijective, which cannot be attained with the polynomial fits of higher order. To correct the coefficients, I calculated the AGB using the original formulation, subtracted the fraction of biomass corresponding to roots, leaves, and 70% of the total sapwood (above-ground fraction), determined the above-ground structural biomass and added 30% corresponding to the below-ground structural biomass. The result of this calculation yielded to:

$$C_\delta = \begin{cases} (0.0627; 0.0627; 0.166; 0.222; 0.282)\ \mathrm{DBH}^{2.432} & \text{, if DBH} \leq \mathrm{DBH}_C \\ (0.0647; 0.0647; 0.172; 0.230; 0.291)\ \mathrm{DBH}^{2.426} & \text{, if DBH} > \mathrm{DBH}_C \end{cases} \tag{C.8}$$

No individual-based allometry was found for rooting depth (z_ρ) for tropical rainforest in the Neotropics ecozone, therefore, the current allometric equation is a simplified exponential function that allows tree depths to reach 5 m:

$$z_\rho = -1.114\ \mathrm{DBH}^{0.422} \tag{C.9}$$

Although the maximum rooting depth is shallow compared to Nepstad et al. (1994) results, it produces a rooting profile similar to other dynamic global vegetation models, and reflects that little variation in soil moisture exists at very deep layers (Christoffersen, 2013).

Leaf area index (Λ [$\mathrm{m^2_{leaf}\,m^{-2}}$]) was determined from leaf biomass and specific leaf area:

$$\Lambda = n\ \mathrm{SLA}\ C_\lambda, \tag{C.10}$$

where n[$\mathrm{plant\,m^{-2}}$] is the demographic density. No allometric equation was found for wood area index (Ω[$\mathrm{m^2_{wood}\,m^{-2}}$]) for evergreen forests. For trees, I used an allometric equation for temperate zone by Hörmann et al. (2003), and assumed it to be zero for grasses. In addition, I imposed maximum area at DBH_C, similarly to C_λ:

$$\Omega = n\ (0.0000; 0.0000; 0.0096; 0.0096; 0.0096)\ \min\left(\mathrm{DBH}, \mathrm{DBH}_C\right)^{2.0947}. \tag{C.11}$$

Crown area index ($X[\,\mathrm{m}^2_{\mathrm{crown}}\,\mathrm{m}^{-2}]$) is based on Poorter et al. (2006), after substituting their allometric equation for height, so it also becomes a function of DBH. Like in the previous cases, crown growth was capped at DBH_C, and local crown area was not allowed to exceed 1.0 or to be less than the local leaf area:

$$X = \min\left\{1.0, \min\left[\Lambda, n\ 1.126\,\mathrm{DBH}^{1.052}\right]\right\}. \tag{C.12}$$

Finally, cohort volume ($\mathcal{V}_\pi[\,\mathrm{cm}^3]$) is a simplified version of the model by Picard et al. (2012), without intercept:

$$\mathcal{V}_\pi = 0.03146\ \underbrace{\frac{\pi}{4}\mathrm{DBH}^2}_{\text{Basal area}}\ z_\pi. \tag{C.13}$$

From Eqn. (C.13), we estimate the typical size of branch wood $\beta_\omega[\,\mathrm{m}]$ to be:

$$\beta_\omega = 10^{-2}\ \sqrt[3]{\mathcal{V}_\pi}. \tag{C.14}$$

Appendix D

Quality control and gap filling of meteorological and eddy flux data

In this appendix I describe the quality assurance and quality control steps applied to all eddy flux tower data used in this analysis, and the gap-filling techniques that were used to generate the meteorological drivers needed by ED-2.2. The work presented in this appendix has been done in collaboration with Matthew N. Hayek.

D.1 Outlier removal and drift correction

With the exception of rainfall, all variables were checked for outliers, in which data points were rejected when the estimated probability of obtaining the observation was too low, using the following iterative approach:

1. For any variable x, we used the package `sn` in `R` (Azzalini, 2011), to obtain a set of location (ξ_h), scale (ω_h), and shape (α_h) parameters of a skew normal distribution, one set for each hour h of the day. We opted for skew normal distribution because most variables present significant skewness at least in some hours of the day (e.g. Fig. D.1), and many valid points in the long tail would be rejected if we had used normal distribution.

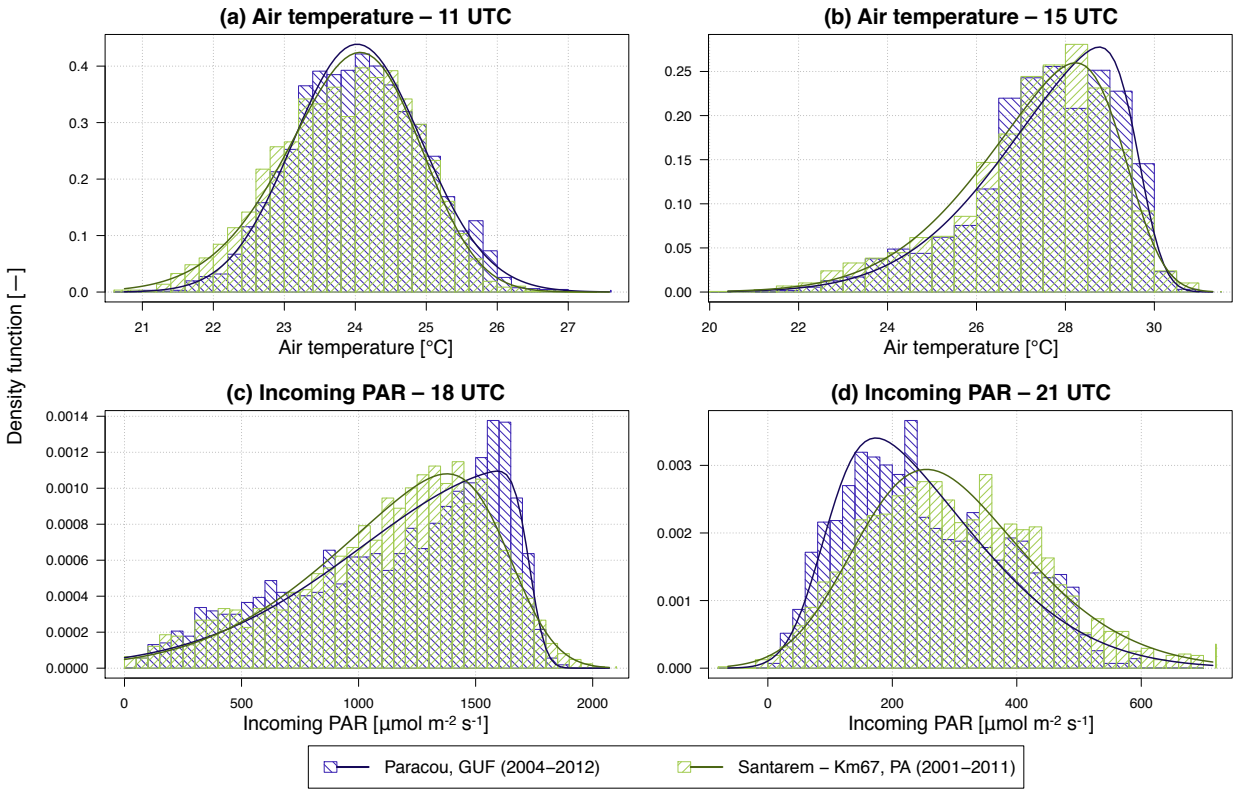

Figure D.1: Example of histograms and fitted skew normal distributions for S67 and GYF air temperature at (a) 11 UTC and (b) 15 UTC; incoming photosynthetically active radiation at (c) 18 UTC and (d) 21 UTC. Lines are the fitted skew normal distribution.

2. Normalize the time series:

   - Find the cumulative distribution function of each observation $P(x_i, h_i)$for every point in the time series:

$$P_i = \mathrm{P}(x_i, h_i) = \tfrac{1}{2}\left[1 + \mathrm{erf}\left(\frac{\tilde{x}_i}{\sqrt{2}}\right)\right] - 2\,\mathrm{T}(\tilde{x}_i, \alpha_h) \tag{D.1a}$$

$$\tilde{x}_i = \frac{x_i - \xi_h}{\omega_h} \tag{D.1b}$$

$$\mathrm{erf}(y) = \frac{2}{\pi}\int_{-\infty}^{y} \exp\left(-\frac{t^2}{2}\right) \mathrm{d}t \tag{D.1c}$$

$$\mathrm{T}(y, a) = \frac{1}{2\pi}\int_{0}^{a} \frac{\exp\left[-\frac{1}{2}y^2\left(1+t^2\right)\right]}{1+t^2}\,\mathrm{d}t \tag{D.1d}$$

where erf is the error function and T is the Owen's T function. Equation (D.1a) is

solved using function `psn` of package `sn` in `R`.

- Find the equivalent quantile function of a normal distribution, i.e. $(\xi;\omega;\alpha) = (0;1;0)$:

$$z_i = \mathrm{Z}(P_i) = \sqrt{2}\,\mathrm{erf}^{-1}(2P_i - 1) \tag{D.2}$$

Eqn. (D.2) is solved using command `qnorm` in `R`, with mean set to 0.0 and standard deviation set to 1.0.

3. Count the total number of valid observations N_x, and determine the minimum and maximum value of quantile function that we accept.

$$z_{\min} = \min\left[-3, \mathrm{Z}\left(\frac{2}{N_x}\right)\right] \tag{D.3a}$$

$$z_{\max} = \max\left[+3, \mathrm{Z}\left(1 - \frac{2}{N_x}\right)\right] \tag{D.3b}$$

where -3 and 3 are imposed in case the time series is too short.

4. Keep only the points for which $z_{\min} \leq z_i \leq z_{\max}$. If no points were excluded, leave the routine, otherwise, go back to step 1. The iteration was necessary because extreme outliers can significantly shift the shape of the distribution so when they are present other less extreme outliers could be erroneously accepted.

Data were also checked for bogus drifts. We only corrected drifts that were present in the eddy flux tower time series but not in nearby stations, to avoid removing true trends. Once detected, the drifts were corrected differently depending on whether they were "Sun" variables — shortwave radiation or photosynthetically active radiation (PAR) — or not. For Sun variables, we determined the trend by defining the relative radiation, which is the the observed radiation divided by the maximum radiation at the observation time[1]. We selected only the points that were greater than the 95 % quantile when the sun was at least half of the maximum sun height during the winter

[1]The maximum radiation was estimated using the Weiss and Norman (1985) model.

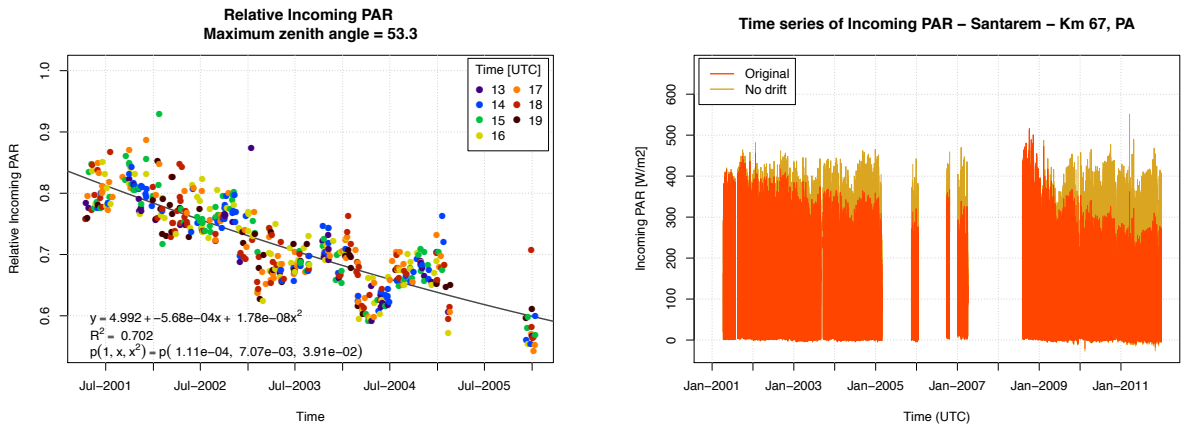

(a) (b)

Figure D.2: (a) Time series of the relative incoming photosynthetically active radiation above the 95 % quantile used for detrending in Santarém km 67 between 2001 and 2006. (b) Time series of incoming photosynthetically active radiation in Santarém km 67, before and after the detrending and rescaling between periods.

solstice. Although arbitrary, these values were chosen to include sufficient number of data points during sunny days for all months. We then fitted either a linear or a quadratic function and scaled the radiation back using the ratio between the fitted value and the fitted value at the beginning of the time series. For the other variables, we used a similar approach except that we retained all observations. Examples of the time series before and after the drift correction are shown in Fig. D.2.

D.1.1 NEE estimation and removal of NEE under weak turbulence conditions $u^{\star}_{\mathrm{min}}$

Tower-derived net ecosystem exchange ($\mathrm{NEE}_{\sharp}[\,\mathrm{mol_C\,m^{-2}\,s^{-1}}]$) was estimated by the commonly used combination of eddy flux and canopy storage (c.f. Baldocchi et al., 1988; Wofsy et al., 1993):

$$\mathrm{NEE}_{\sharp} = \frac{\rho_{\sharp}}{\mathcal{M}_d} \cdot \left\{ \underbrace{\frac{1}{\Delta t}\int_t^{t+\Delta t} u_z'\left(z_{\sharp}\right) c_{\sharp}'\left(z_{\sharp}\right)\,\mathrm{d}t'}_{\mathrm{CO_2\ eddy\ flux}\ (\dot{C}_{a,e})} + \underbrace{\frac{1}{\Delta t}\int_t^{t+\Delta t}\left[\frac{\partial}{\partial t'}\left(\int_0^{z_{\sharp}} c\left(z'\right)\mathrm{d}z'\right)\mathrm{d}t'\right]}_{\mathrm{CO_2\ Storage}\ (\Delta C_a)} \right\}, \qquad \text{(D.4)}$$

where $\rho\sharp$ is the air density, $\mathcal{M}_d$ is the dry air molar mass, $z_{\sharp}$ is the height of the eddy flux measurement, u_z is the vertical velocity, and c is the CO_2 mixing ratio. The apostrophe denotes the anomalies around the mean between t and Δt, thus $u_z' c_{\sharp}'$ represents the eddy covariance between vertical velocity and mixing ratio.

Tower-based ecosystem respiration ($\dot{R}_{\mathrm{Eco}_{\sharp}}[\,\mathrm{mol_C\,m^{-2}\,s^{-1}}]$) was assumed to be the same as $\mathrm{NEE}_{\sharp}$ at night; daytime respiration was interpolated using a running average of the 50 closest nocturnal hours that had valid observations, and diurnal estimate of gross primary productivity ($\mathrm{GPP}_{\sharp}[\,\mathrm{mol_C\,m^{-2}\,s^{-1}}]$) was estimated as:

$$\mathrm{GPP}_{\sharp} = \dot{R}_{\mathrm{Eco}_{\sharp}} - \mathrm{NEE}_{\sharp}. \qquad \text{(D.5)}$$

Both GPP and $\dot{R}_{\mathrm{Eco}}$ were discarded whenever CO_2 eddy covariance flux, change in CO_2 storage[2], or $u^{\star}$ was missing. In addition, Eqn. (D.4) fails to capture the actual $\mathrm{NEE}_{\sharp}$ at very low turbulence (e.g. Goulden et al., 1996; Kruijt et al., 2004), therefore all the ecosystem flux estimates were discarded whenever the average observed friction velocity ${u^{\star}}_{\sharp} < u^{\star}_{\mathrm{min}}$, where $u^{\star}_{\mathrm{min}}$ is a site-dependent threshold.

This threshold has been previously determined for all sites, however, techniques used to determine the threshold varied amongst sites, and the choice is often arbitrary. To assess the robustness of the estimates, and to provide a standardized choice of $u^{\star}_{\mathrm{min}}$, I defined an alternative threshold. In this approach, the aim is to retain as much information as possible while ensuring that NEE is no longer dependent on $u^{\star}$, and that most of the signal is from the eddy covariance flux and not the storage. The latter requirement is imposed because carbon storage is measured at only one location and most of the measurements occur beneath the canopy top, thus local effects may play

[2]The only exception is PDG, where storage was not measured. In this case, storage was assumed to be negligible.

a significant role, whereas the eddy covariance flux is representative of a larger area.

The algorithm consists of the following steps:

1. Subset the data so only nocturnal $u^\star$, $\dot{C}_{a,e}$, ΔC_a, $\mathrm{NEE}_\sharp$ are used.

2. Split data into classes of $u^\star$ with width of $0.01\,\mathrm{m\,s^{-1}}$. If any class has less than 10 observations (normally very low and very high turbulence), merge it with the closest class with more than 10 observations. Let N be the total number of classes after merging.

3. Find the lowest class n_0 in which $\dot{C}_{a,e}$ is significantly greater than ΔC_a at 95 % confidence level, using an one-sided t-test.

4. Set $n = n_0$ as the first guess, and repeat the following steps until a solution is found:

   (a) Check whether the subset is homoscedastic using a median-based Levene's test. If the null hypothesis is rejected at 95 % confidence level, warn the user (this never occurred with the data sets used).

   (b) Select the NEE data from classes n–$\min(N, n+4)$, and apply an F-test on the mean between the selected classes.

   (c) Group the NEE and corresponding $u^\star$ data, and fit a linear model.

   (d) If the p-value of both the F-test and the slope coefficient are greater than 50%, assume that NEE does not depend on turbulence, and define $u^\star_{\mathrm{min}}$ as the lower bound of class n. Otherwise, set n to $n+1$ and repeat step 4.

Both the class width, minimum number of observations by class, and the confidence levels can be adjusted for different data sets, but they should not cover a very large range of $u^\star$ at a time, while defining a very safe margin to not reject the null hypothesis.

Tab. D.1 shows the $u^\star_{\mathrm{min}}$ thresholds for all sites using this algorithm, along with values previously reported in the literature. As shown in Fig. D.3, the algorithm is able to detect the point where the average NEE has low dependence on $u^\star$. The difference between threshold was at least 18 % for

Table D.1: Site-specific $u^{\star}_{\mathrm{min}}[\,\mathrm{m\,s^{-1}}]$ determined from the algorithm described in this section — $u^{\star}_{\mathrm{min}}$(Alg.), and from previous references for the site — $u^{\star}_{\mathrm{min}}$(Ref.).

Site	Code	$u^{\star}_{\mathrm{min}}$(Alg.)	$u^{\star}_{\mathrm{min}}$(Ref.)	Reference
Paracou	GYF	0.20	0.15	Bonal et al. (2008)
Santarém km 67	S67	0.37	0.22	Hutyra et al. (2007)
Santarém km 83	S83	0.18	0.22	Miller et al. (2011)
Pé-de-Gigante	PDG	0.20	0.34	Restrepo-Coupe et al. (2013)
Rebio Jaru	RJA	0.17	0.21	Restrepo-Coupe et al. (2013)
Manaus K34	M34	0.24	0.20	Araújo et al. (2002)

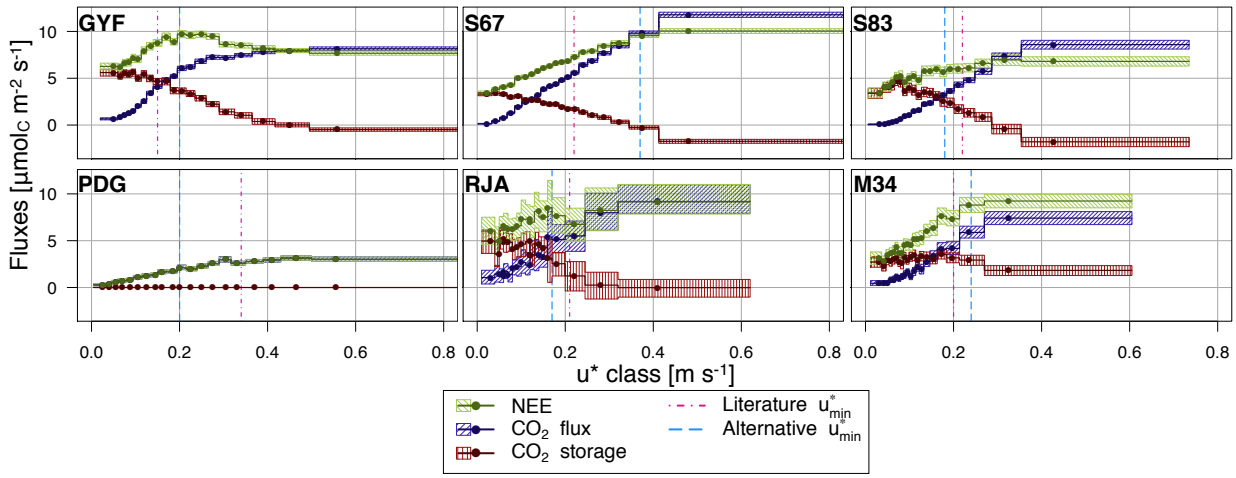

Figure D.3: Average nighttime NEE as a function of $u^{\star}$, along with the corresponding contributions from eddy covariance flux and change in CO_2 storage at the canopy air space for Paracou (GYF), Santarém km 67 (S67), Santarém km 83, Pé-de-Gigante (PDG), Rebio Jaru (RJA), and Manaus K34 (M34). Dashed violet lines are the $u^{\star}_{\mathrm{min}}$ values obtained from literature (Tab. D.1), whereas dashed blue is the $u^{\star}_{\mathrm{min}}$ described in this section.

all sites, and ranged from a 41 % decrease at PDG to 68 % increase in S67. Although the shift has little impact on NEE because daytime values are generally higher in magnitude and less likely to be discarded, the choice of $u^{\star}$ may affect the partition between respiration and GPP.

D.1.2 Gap-filling of time series

Multiple approaches were used to fill missing values in the time series, depending on the variable and the availability of data from other stations in the region.

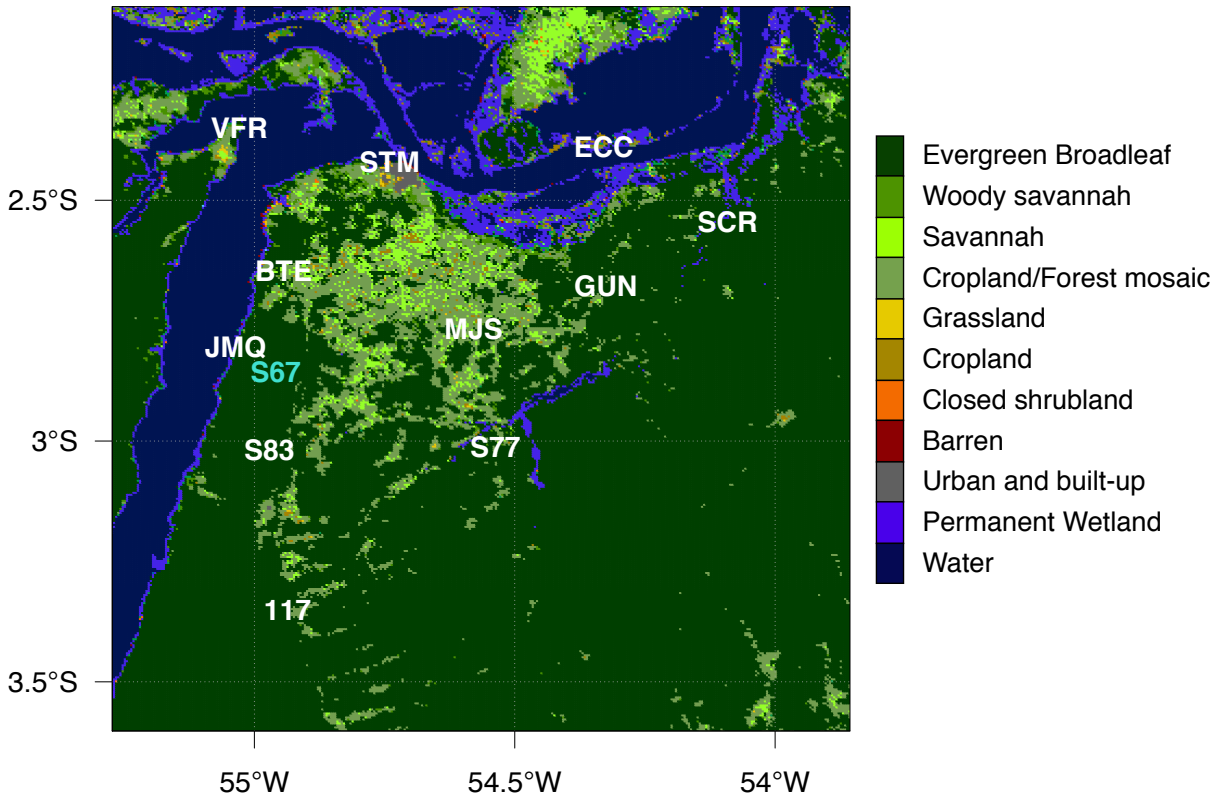

Figure D.4: Location of sites used for objective analysis near the S67 site. Sites and periods used for the objective analysis are: BTE – Belterra (2001-2010); ECC – Cacoal Grande, Embrapa (2002-2006); SCR – Curuá-Una, Sudam (2002-2005); GUN – Guaraná (2001-2005); JMQ – Jamaraquá (2001-2010); MJS – Mojuí dos Campos (2001-2010); STM – Santarém, UFOPA (2006-2010); S77 – BR-163, Km 77 (2001-2005); S83 – BR-163, Km 83 (2001-2004); 117 – BR-163, Km 117 (2001-2006); VFR – Vila Franca (2002-2010). Land classification (IGBP NASA/LP-DAAC, 2012) shown for reference.

Simplified objective analysis

This method was applied only to S67. For the objective analysis, we used the data from the mesoscale meteorological network near S67 (Fitzjarrald et al., 2009), in addition to two eddy flux towers that were also operating in the region, one in a cropland/pasture near the km 77 mark of the BR-163 (Santarém-Cuiabá) road (Fitzjarrald and Sakai, 2010), and a managed forest near km 83 of the same road (Miller et al., 2009). The location of the sites relative to S67 is shown in Fig. D.4. The objective analysis used in this work is based on the first iteration of the method described in Koch et al. (1983) and was applied to all variables needed by ED-2.2. Rainfall was a special case

that will be explained later, but the other variables were solved in a similar method:

1. Call the site of interest S67 site number 0. For each variable x_i, determine the statistics of skewed normal distribution for each hour of the day h (location ξ_{0h}, scale ω_{0h}, and shape α_{0h}), in the same way that is shown in Sec. D.1.

2. For all the other sites $s = 1, 2, \ldots, S$, determine the statistics of skewed normal distribution for each hour ($\xi_{sh}; \omega_{sh}; \alpha_{sh}$), and normalise the time series to obtain $z_{si} = z(t_i | x_{si}, h_i, \xi_{sh}, \omega_{sh}, \alpha_{sh})$, also using the methodology described in Sec. D.1. We normalised the variables to avoid introducing biases: although we are using only sites that are less than 110 km from S67, the other sites are located either in different land use areas or at different altitude.

3. Determine the quantile function at S67 z_{0i} using the first step of the objective analysis:

$$z_{0i} = \frac{\sum_{s=1}^{S} \exp\left(-\frac{d_{0s}^2}{\kappa_0}\right) z_{si}}{\sum_{s=1}^{S} \exp\left(-\frac{d_{0s}^2}{\kappa_0}\right)} \tag{D.6}$$

   where d_{0s} is the distance between S67 and site s, and κ_0 is a parameter to control the decay rate of the influence that depends on the mean and is calculated using the same approach described by Koch et al. (1983), that takes into account the spacing between observations:

$$\kappa_0 = -\left(\frac{2\Delta n}{\pi}\right) \ln D_0 \tag{D.7a}$$

$$D_0 = \frac{1}{\mathrm{e}^1 \left(1 + D_0^{\gamma-1} - D_0^{\gamma}\right)} \tag{D.7b}$$

   where Δn is the average distance between the observation points, and γ is a parameter (set to 0.2 as in Koch et al. (1983)). D_0 is found using a standard root finding function (`uniroot` in `R`).

4. Once z_{0i} is found, we revert back to observation using the statistics obtained in step 1:

(a) Find the cumulative distribution function P using the inverse of Eqn. (D.2), by invoking function `pnorm` in `R` with mean set to zero and standard deviation set to one

(b) Use the inverse of Eqn. (D.1a) to scale back to the original distribution, by invoking function `qsn` of package `sn` in `R`, with parameters $(\xi_{0h}; \omega_{0h}; \alpha_{0h})$.

Rainfall R_i is not properly represented by this skewed normal distribution, so we estimated it by splitting rainfall into two components: one is a simple binary flag that is 0 when rainfall is zero, and 1 when there is rainfall. We applied step 3 to obtain a fraction that roughly represents the probability p_i of observing rain at S67 given the other observations. The probability increases as more sites report rain, and also higher when the sites that are the closest to S67 report rain. We then used function `runif` in `R` to generate random numbers b_i with uniform distribution, and if the random number was less than p_i then we assumed rainfall occurred at S67, otherwise we assumed zero rainfall. For the points that we assumed rainfall had occurred, we applied step 3 to the untransformed, absolute rainfall rates, using only the sites that reported rain, to estimate the rainfall at S67.

Figure D.5 shows the gap-filling done by the simplified objective analysis for two different gap lengths. The main advantages of this method are the ability to capture the variability on the regional climate and that it has little sensitivity to the length of gaps, as long as there are sufficient information from nearby observations.

Harmonic analysis

The harmonic analysis is loosely based on the method described by Kondrashov and Ghil (2006), in the sense we use the signal available from the defined part of the time series and apply an iterative approach to add information to the missing points until convergence. The approach presented here, however, is based on fast Fourier transforms (FFT) because they are numerically more efficient, which makes a significant run time difference for times series with tens of thousands of points.

The method presented here is useful to fill gaps that are not to long, and this method should be used only if no parametric model can be easily found. In addition, this approach works better when

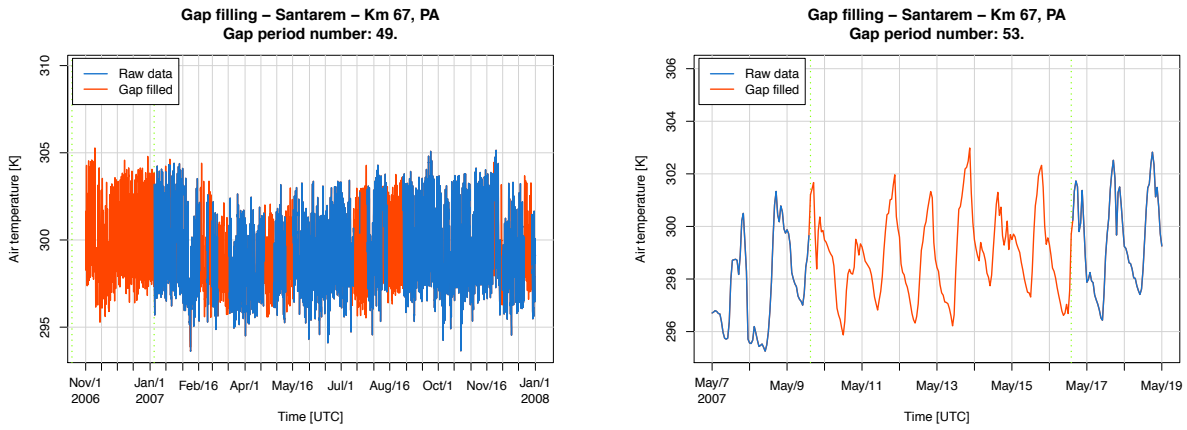

(a) (b)

Figure D.5: Examples of gap filling of atmospheric temperature using objective analysis in S67 between November 2006 and January 2008. (a) overview of the entire period, including a long gap between November 2006 and January 2007; (b) zoom on a short gap in May 2007.

the time series has strong frequencies associated with the variation (such as diurnal cycle, annual cycle, synoptic patterns), and that the time series has a relatively small fraction of missing data. We applied this method for most variables needed by ED-2.2 plus net radiation, but we did not use the method to fill remaining gaps in incoming longwave radiation and rainfall, whose gap filling method will be presented in the next sections. Because we could not apply objective analysis to most sites, this was the main gap filling option.

Let $\mathbf{x} = (x_1; x_2; \ldots; x_N)$ be a time series with N points equally spaced in time, although some of the points x_i points are missing values (hereafter missing values will be represented by $\varnothing$). Also, for simplicity, to fill in these points, we apply the following algorithm:

1. Remove the mean of the time series $\bar{x}$, and detrend it in case the trend is significant. We refer to this time series as $\tilde{\mathbf{x}}$.

2. Make the time series twice as long:

$$\begin{aligned} \mathbf{z}^{(\mathbf{a})} &= \left(z_1^{(a)}, z_2^{(a)}, \ldots, z_E^{(a)}\right) \\ &= \left(\tilde{x}_{\lfloor N/2 \rfloor+1}; \tilde{x}_{\lfloor N/2 \rfloor+2}; \ldots; \tilde{x}_N; \tilde{x}_1; \tilde{x}_2, \ldots, \tilde{x}_N; \tilde{x}_1; \tilde{x}_2; \ldots; \tilde{x}_{\lfloor N/2 \rfloor}\right) \end{aligned} \tag{D.8}$$

where $E = 2N$, and $\lfloor x_i \rfloor$ is the floor operator, and $z_i^{(a)}$ is the normalised value based on actual observation. The reason we double the size of the time series is because we are only using full years or a sequence of full years, and the harmonic analysis tends to perform poorly when large sequences of missing values are too close to the beginning or the end of the time series.

3. Determine the Nyquist frequency ν of the extended time series:

$$\nu = 1 + \left\lceil \frac{E-1}{2} \right\rceil \tag{D.9}$$

where $\lceil x \rceil$ is the ceiling operator.

4. Set the first guess for the time series:

$$z_i^{(0)} = \begin{cases} z_i^{(a)} & \text{, if } z_i^{(a)} \neq \varnothing \\ 0 & \text{, if } z_i^{(a)} = \varnothing \end{cases} \tag{D.10}$$

5. Find the FFT of time series $\mathbf{z}^{(\mathbf{0})}$:

$$\mathbf{f}^{(0)} = \mathcal{F}\left(\mathbf{z}^{(\mathbf{0})}\right) = \sum_{n=1}^{E} z_n^{(0)} \mathrm{e}^{-\mathrm{i}2\pi \frac{m-1}{E} n}, \ \forall m \in \mathbb{M} \tag{D.11}$$

where $\mathbb{M} = \{1, 2, \ldots, \nu\}$. Equation (D.11) is solved using function `fft` in `R`.

6. Rank the frequencies by their magnitude $p(f_m^{(0)})$, from highest ($o = 1$) to lowest ($o = \nu$); and find the relative cumulative contribution of each mode to the total spectrum ($P(f_m^{(0)})$):

$$p(f_m^{(0)}) = \left(f_m^{(0)}\right)^2, \ \forall m \in \mathbb{M} \tag{D.12a}$$

$$P(f_m^{(0)}) = \frac{\sum_{j=1}^{o_m} \left(f_{o=j}^{(0)}\right)^2}{\sum_{j=1}^{\nu} \left(f_j^{(0)}\right)^2}, \ \forall m \in \mathbb{M} \tag{D.12b}$$

7. Determine the maximum power to be used for gap filling. Because the time series contains both real oscillation patterns and noise, results tend to be better when the weakest powers are not used. From trial and error, we have chosen to retain only the J most powerful modes, such that $P(f_J^{(0)}) \preccurlyeq 0.80$, which attempts to conceal that we want to capture most of the signal, but exclude weaker powers that only add noise.

8. Set $j = 0$ and enter the outer loop:

   (a) Update j: $j \mapsto j+1$.

   (b) Set $k = 0$, and define a working guess $\hat{\mathbf{z}} = \mathbf{z}^{(j-1)}$

   (c) Enter the inner loop:

      i. Update k: $k \mapsto k+1$.

      ii. Find the FFT of the working guess $\mathbf{f} = \mathcal{F}(\hat{\mathbf{z}})$

      iii. Keep only the j^{th} highest ranked terms of $\mathbf{f}$ (we use the rank obtained by the first guess in step 6):

$$\mathbf{f}^\star : f_m^\star = \begin{cases} f_m & \text{if } o_m \leq j \\ 0+0\text{i} & \text{if } o_m > j \end{cases}, \ \forall m \in \mathbb{M} \tag{D.13}$$

      iv. Find a new guess for the time series $\hat{\mathbf{z}} = \mathcal{F}^{-1}(\mathbf{f}^\star)$.

      v. Estimate the coefficient of determination R_k^2:

$$R_k^2 = 1 - \frac{N_v - 1}{N_v - j - 1} \left[\frac{\sum\limits_{\substack{i=1 \\ z_i^{(0)} \neq \varnothing}}^{E} \left(\hat{z}_i - z_i^{(0)} \right)^2}{\sum\limits_{\substack{i=1 \\ z_i^{(0)} \neq \varnothing}}^{E} \left(\overline{z^{(0)}} - z_i^{(0)} \right)^2} \right] \tag{D.14}$$

      vi. Determine the gain of this step:

$$g_k = \begin{cases} 2\dfrac{R_k^2 - R_{k-1}^2}{R_k^2 + R_{k-1}^2} & \text{, if } k > 1 \\ +\infty & \text{, if } k = 1 \end{cases} \tag{D.15}$$

vii. If $g_k > g_0$, go back to step 8(c)i; otherwise go to step 8d. We used $g_0 = 0.001$, and it is usually achieved in 2 or 3 iterations. Notice that the convergence criterion does not have absolute values: this is to make sure we stop iterating if the method is making R_k^2 worse (which may happen if we add weak powers that are not real signals).

(d) Update guess using the latest working guess:

$$z_i^{(j)} = \begin{cases} z_i^{(a)} & \text{, if } z_i^{(a)} \neq \varnothing \\ \hat{z}_i & \text{, if } z_i^{(a)} = \varnothing \end{cases}, \forall\, i \in \mathbb{E} \tag{D.16}$$

where $\mathbb{E} = \{1, 2, \ldots, E\}$

(e) If $j < J$, go back to step to step 8a; otherwise go to step 9.

9. Crop the time series $\mathbf{z}^{(J)}$ back to the original size, and add the trend back. The new time series $\mathbf{x}^{\star}$ becomes the gap filled time series.

Figure D.6 shows the gap-filling done by the harmonic analysis for two different gap lengths. We observe that even though it captures significant information on variability, the magnitude becomes dampened when the gaps are longer.

Gap filling for incoming longwave radiation

On average, incoming longwave radiation is the most important source of radiant energy reaching the ground in the tropics. Although the energy is not used by photosynthesis, and that net longwave radiation is relatively small because the outgoing radiation due to ground emission has similar magnitude, it still plays an important role on the energy budget and the leaf temperature, which ultimately affects the photosynthesis rates (Monteith and Unsworth, 2008). Nevertheless, many eddy flux towers have very limited or no record of this variable, and several previous studies describe models used to estimative this component of the energy budget (cf. Monteith and Unsworth, 2008; Sedlar and Hock, 2009; Marthews et al., 2012).

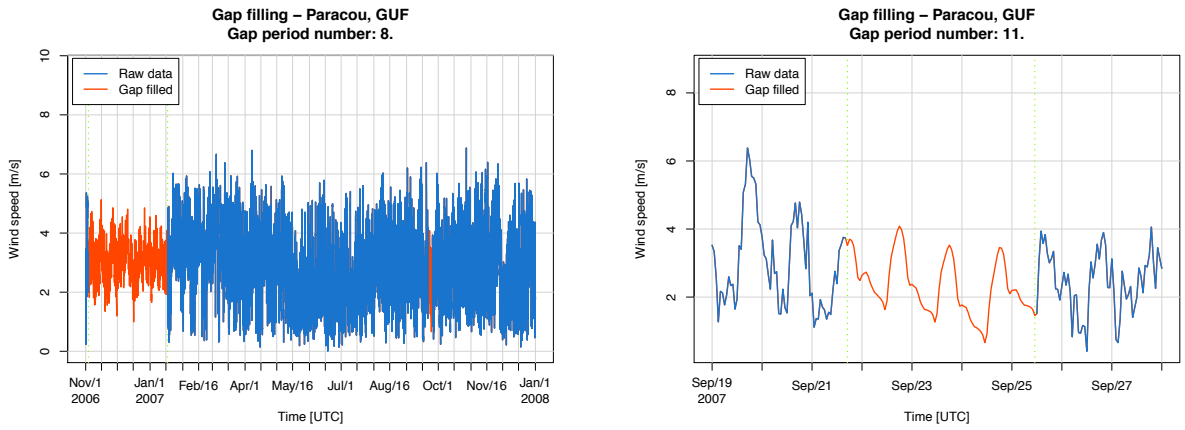

(a) (b)

Figure D.6: Examples of gap filling of wind speed using harmonic analysis in GYF between November 2006 and January 2008. (a) overview of the entire period, including a long gap between November 2006 and January 2007; (b) zoom on a short gap in September 2007.

We applied two approaches to fill the time series. The first method was applied only during the night when both net radiation and air temperature ($T_a[\,\mathrm{K}]$) were available. Because incoming and reflected shortwave radiation are both zero at night, we define the radiation budget as:

$$\begin{aligned} \dot{Q}^{\downarrow}_{\mathrm{LW}} &= \dot{Q}_{\mathrm{Net}} + \dot{Q}^{\uparrow}_{\mathrm{LW}} \\ \dot{Q}^{\downarrow}_{\mathrm{LW}} &= \dot{Q}_{\mathrm{Net}} + \varepsilon_{\mathrm{sfc}}\sigma T^4_{\mathrm{sfc}} \end{aligned}, \tag{D.17}$$

where $\dot{Q}^{\uparrow}_{\mathrm{LW}}$ is the outgoing longwave radiation, $\sigma = 5.67\,10^{-8}\,\mathrm{W\,m^{-2}\,K^{-4}}$ is the Stefan-Boltzmann constant, $T_{\mathrm{sfc}}[\,\mathrm{K}]$ is the temperature of the emitting object (a mix of ground and vegetation), and $\varepsilon_{\mathrm{sfc}}$ is the emissivity of the object. T_{sfc} is not directly measured, therefore, we use the air temperature instead and correct the emissivity to obtain:

$$\dot{Q}^{\downarrow}_{\mathrm{LW}} = \dot{Q}_{\mathrm{Net}} - \varepsilon_{\mathrm{g}}\sigma T^4_a \tag{D.18}$$

Because the sensors may have different calibrations and perceive different contributions from the canopy, we also include a bias term to obtain the following linear model:

$$\dot{Q}^{\downarrow}_{\mathrm{LW}} = \beta_0 + \beta_1\dot{Q}_{\mathrm{Net}} + \beta_2\sigma T^4_a \tag{D.19}$$

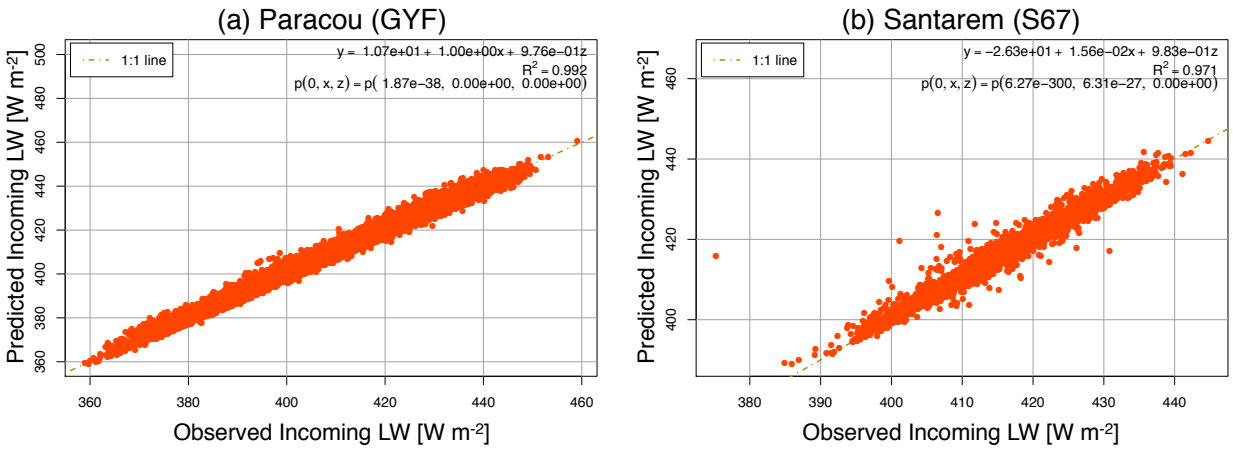

Figure D.7: Model evaluation of nighttime incoming long wave radiation as a function of net radiation and temperature for (a) GYF and (b) S67. The fit is shown at the top, where $x = \dot{Q}_{\mathrm{Net}}$ and $z = \sigma T_a^4$.

Figure D.7 shows the predictions obtained by fitting Eqn. (D.19) for GYF and S67. While the fitted models were very good predictors both in S67 and in GYF, the contribution of net radiation varied significantly between sites. In GYF, the coefficient was very close to 1.0 as expected, and both variables are strongly correlated; In S67, however, the variables were not well correlated and as a result the net radiation coefficient was substantially lower. In both cases β_2 was close to 0.98, which is typical for canopy emissivity in the thermal infrared (Monteith and Unsworth, 2008; Wang and Leuning, 1998).

The remainder data were filled using a parametric model. Marthews et al. (2012) tested several different models for Caxiuanã (CAX), a tropical rainforest site in Eastern Amazon. We started by using several different combinations of the models they tested for CAX; although the root mean square error was of the same order of magnitude reported at CAX, the coefficient of determination was always extremely low and often negative, even for the methods reported as the best approximation. At first I optimized the parameters the models presented by Marthews et al. (2012) using maximum likelihood for the least squares. The optimization, however, lead to physically unrealistic coefficients for most of the methods, therefore I also developed and optimized the alternative model shown below. The empirical equations were written in such way that none of the physically

meaningful parameters could go outside the physically reasonable range.

The starting point of the alternative parametric model is the same as Monteith and Unsworth (2008). For partly cloudy skies with a single cloud layer, the incoming radiation $\dot{Q}^{\downarrow}_{\mathrm{LW}}$ can be approximated by:

$$\dot{Q}^{\downarrow}_{\mathrm{LW}} = \underbrace{(1-C)\varepsilon_a \sigma T_a^4}_{\text{Clear sky}} + \underbrace{C\left[\varepsilon_a \sigma T_a^4 + (1-\varepsilon_a)\,\sigma T_c^4\right]}_{\text{Overcast sky}}, \tag{D.20}$$

where C is the fraction of cloudy sky, $T_a[\mathrm{K}]$ is the air temperature, ε_a is the apparent emissivity of cloudless sky, and $T_c[\mathrm{K}]$ is the cloud temperature.

First, I present the model for cloudless sky. Water vapor has high emissivity/absorptance in the longwave spectrum, therefore most methods presented in Marthews et al. (2012) relate emissivity to some water-related quantity. Ideally I would use precipitable water P_w, because it is the integral of water mixing ratio over the entire atmospheric column. This quantity, however, cannot be determined from ground observations only at the sought frequency: instead I use the same approximation derived by Prata (1996), and also used by Monteith and Unsworth (2008) and Marthews et al. (2012):

$$P_w \approx 4.65\frac{e_a}{T_a}, \tag{D.21}$$

where $e_a[\mathrm{Pa}]$ is the partial pressure of water vapour at the tower, determined using the equations by Murphy and Koop (2005). ε_a is then defined as a function of the precipitable water P_w in the atmospheric column:

$$\varepsilon_a = q_1 + (1-q_1)\,\mathrm{logit}^{-1}\left[q_2\,(P_w + q_3)\right] \tag{D.22a}$$

$$\mathrm{logit}^{-1}(x) = \frac{1}{1-\exp(-x)} \tag{D.22b}$$

where q_1, q_2, q_3 are coefficients to be fitted, and logit^{-1} is the logistic function. Equation (D.22a) has the advantage that clear-sky emissivity is always bounded between q_1 and 1, where q_1 intends to represent the emissivity of an absolutely dry atmosphere.

Cloud fraction is estimated based on the incoming shortwave radiation and how it relates to the theoretical maximum:

$$C = 1 - \text{logit}^{-1}\left[q_4\left(\kappa + q_5\right)\right], \tag{D.23a}$$

$$\kappa = \frac{\dot{Q}_{\text{SW}}^{\downarrow}}{Q_{\text{SW}}^{\odot}\cos Z^{\odot}}, \tag{D.23b}$$

where q_4 and q_5 are coefficients to be fitted, $\dot{Q}_{\text{SW}}^{\downarrow}[\,\text{W}\,\text{m}^{-2}]$ is the incoming shortwave radiation a the surface, $Q_{\text{SW}}^{\odot} \approx 1360\,\text{W}\,\text{m}^{-2}$ is the solar constant, and $Z^{\odot}$ is the Sun's zenith angle. This equation also ensures that the cloud fraction is always bounded between 0 and 1. Because κ cannot be determined during the night and cannot be easily modelled with the available variables, we linearly interpolated κ from the previous afternoon to the following morning.

Like Marthews et al. (2012), we estimated cloud temperature from the lifting condensation level temperature ($T_{\text{LCL}}[\,\text{K}]$). T_{LCL} tends to overestimate the actual cloud temperature, especially when clouds are high and not convective in origin. Marthews et al. (2012) pointed out that this overestimation is partially compensated by the fact that high clouds may be much colder than the layers close to the surface and therefore contribute less than lower layers, and T_c should ultimately represent the temperature of the emitting object. However, T_{LCL} was rarely far from the ground even when the cloud fraction was low, so we included a simple correction term to lower the temperature based on relative humidity:

$$T_c = \left[q_6 + (1 - q_6)\,\text{RH}\right] T_{\text{LCL}} \tag{D.24}$$

where q_6 is a coefficient to be fitted and RH is the relative humidity (fraction).

In Tab. D.2 I present the fitted coefficients for the method presented in this appendix for all sites that had incoming longwave measurements. In addition, Tab. D.3 and Tab. D.4 summarize the errors for this method and some of the methods tested by Marthews et al. (2012), and for GYF and S67 we also show the coefficient of determination before the optimization for reference.

While the optimization improved the coefficient of determination most methods and site, one can

Table D.2: Optimized coefficients for all sites with available incoming longwave radiation measurements for at least part of the period.

Site	q_1	q_2	q_3	q_4	q_5	q_6
GYF	0.718	0.0246	-45.9	9.36	-0.493	0.328
S67	0.937	-0.3078	-32.3	20.4	0.613	-1.60
M34	0.833	0.00927	-54.2	4.55	-0.558	-0.413
S83	0.779	0.0426	-36.6	11.2	-0.314	-1.12
PNZ	0.631	0.0676	-31.9	3.90	-0.323	-0.829
RJA	0.743	0.0254	-16.6	7.95	-0.165	0.526
PDG	0.746	3.58	-49.4	8.65	2.51	3.41
BSB	0.668	0.0457	-51.3	4.64	-0.542	0.775

observe that in some sites such as GYF, none of the optimized fits have high R^2 even after the optimization. Notwithstanding, the fit presented in this appendix yielded a slightly better fit than the other models that included partially cloudy skies for all sites except PDG, while having much less parameters than Flerchinger et al. (2009), which had produced the best daytime estimate in Caxiuanã according to Marthews et al. (2012) study. The poor fitting for most sites also reflects that incoming longwave radiation cannot be accurately estimated from other near-surface measurements. Since incoming longwave radiation is an important component of the energy balance hence a required variable to drive most biophysical models, ED-2.2 included, it should be regarded as a fundamental quantity when designing future tower measurements, as also pointed out by Stöckli (2007).

D.1.3 Summary of gap-filling for the meteorological drivers

Table D.5 summarizes the fraction of gap filling applied to the eddy flux towers for each variable needed to drive ED-2.2, where it can be seen that different sites have a considerable variation in how much actual data are available. When the model output is compared to observations, it is important to acknowledge that meteorological drivers with high percentage of gap filled data are less likely to represent the true environment perceived by the ecosystem, and a larger fraction of

Table D.3: Number of parameters (M) Root mean square error (σ) and coefficient of determination (R^2) of different models described and used by Marthews et al. (2012) with their original parameters as well as the optimized parameters for GYF and S67. I used the same notation as Marthews et al. (2012) to identify the methods we tested. The optimized values for the model presented in this section is also shown.

Model			**Paracou (GYF)**				**Santarém, km 67 (S67)**			
			Original		*Optimized*		*Original*		*Optimized*	
Reference	**Code**	M	R^2	σ	R^2	σ	R^2	σ	R^2	σ
Idso and Jackson (1969)	CIJ	2	-7.11	53.81	0.06	18.31	-9.45	64.46	0.06	19.34
Idso (1981)	CID	3	-0.25	21.15	-0.06	19.42	-1.76	33.16	-0.73	26.20
Dilley and O'Brien (1998)[a]	CDO	3	-2.90	37.31	0.06	18.28	-4.12	45.16	0.83	8.27
Monteith and Unsworth (2008)	CMU	2	-7.70	55.74	0.01	18.76	-9.48	64.58	0.83	8.33
Monteith and Unsworth (2008)	AMU	5	0.01	18.79	∅[c]	∅[c]	-2.11	35.17	∅[c]	∅[c]
Stöckli (2007)	ALM	4	-3.90	41.82	0.25	16.39	-4.84	48.20	-0.63	25.44
Flerchinger et al. (2009)[b]	ADK	12	-0.31	21.61	0.23	16.62	-0.45	24.07	0.72	10.55
The model presented in this appendix	AZZ	6	—	—	0.35	15.30	—	—	0.75	10.03

[a] Like in Marthews et al. (2012), I only tested their model B.
[b] Like in Marthews et al. (2012), I only tested their combination of Dilley and O'Brien (1998) for clear sky and the Kimball et al. (1982) model for cloudy sky.
[c] All optimization attempts failed for Monteith and Unsworth (2008).

Table D.4: Number of parameters (M), root mean square error (σ) and coefficient of determination (R^2) for additional sites using the same models presented in D.3 after undergoing optimization using least squares. All optimization attempts failed for the partly cloudy parameterization by Monteith and Unsworth (2008) (AMU) thus it is omitted.

Model		**M34**		**S83**		**PNZ**		**RJA**		**PDG**		**BSB**	
Code	M	R^2	σ	R^2	σ	R^2	σ	R^2	σ	R^2	σ	R^2	σ
CIJ	2	-0.22	23.42	-0.09	19.42	0.14	23.82	0.05	23.45	-0.08	31.33	0.60	20.60
CID	3	-0.96	29.64	-0.86	25.38	-1.69	42.13	-0.80	32.21	-0.25	33.61	-0.32	37.47
CDO	3	0.12	19.93	0.15	17.15	0.47	18.63	0.36	19.17	0.21	26.79	0.69	18.07
CMU	2	0.10	20.08	0.13	17.39	0.11	24.16	0.34	19.52	0.17	27.46	0.12	30.51
ALM	4	-0.28	23.98	-0.69	24.17	-0.21	28.25	-0.83	32.55	-0.25	33.61	0.52	22.70
ADK	12	0.09	20.25	0.15	17.19	0.49	18.25	0.34	19.47	-0.08	31.26	-0.14	34.86
AZZ	6	0.17	19.31	0.32	15.35	0.58	16.70	0.44	18.02	0.08	28.87	0.77	15.61

discrepancies between modelled and observed fluxes may be attributable to errors in the input data.

Table D.5: Percentage of data by gap-filling procedure for all meteorological variables needed to drive ED-2.2 by each variable and site during the period with intensive measurements. *Measured* is the fraction of hourly data that was measured and not rejected, and presented as the mean for the entire period, along with fraction the most complete and least complete years for reference ($\times n$ means n occurrences of minimum or maximum); other columns are the fraction of each gap-filling technique for the entire period: redundant observation in the same site (RDNT); objective analysis (OBJA); harmonic analysis (HARM); linear model with non-redundant observation (LINE); and other methods (OTHR), namely such as rainfall sampling, Weiss and Norman (1985) shortwave radiation model, and the longwave radiation model described in this appendix. Variables are incoming shortwave radiation ($\dot{Q}^{\downarrow}_{\mathrm{SW}}$), incoming photosynthetically active radiation ($Q^{\downarrow}_{\mathrm{PAR}}$), incoming thermal infrared radiation ($\dot{Q}^{\downarrow}_{\mathrm{LW}}$), ambient pressure above canopy (p_e), ambient temperature above canopy (T_e), ambient humidity above canopy (w_e), horizontal wind speed above canopy (u_e), and rainfall ($\dot{W}_{\infty,e}$).

Variable	Site	Measured			RDNT	OBJA	HARM	LINE	OTHR
		Mean	Min (Year)	Max (Year)					
$\dot{Q}^{\downarrow}_{\mathrm{SW}}$	GYF	99.4	100.0 (2012)	98.4 (2007)	0.3	—	—	0.2	—
	S67	19.3	64.7 (2005)	— ($\times$7)	45.5	32.6	2.6	—	—
	S83	77.8	89.5 (2001)	46.3 (2000)	1.2	—	—	20.9	—
	PDG	94.6	96.5 (2003)	92.2 (2002)	1.0	—	—	4.4	—
	RJA	81.6	94.4 (2001)	64.9 (1999)	1.8	—	—	16.6	—
	M34	79.5	97.6 (2004)	54.7 (1999)	—	—	—	20.5	—
	PNZ	82.3	99.3 (2011)	53.5 (2006)	—	—	—	17.7	—
	BAN	74.7	77.4 (2005)	73.3 (2004)	19.6	—	—	5.7	—
	CAX	61.5	76.0 (2002)	52.1 (2003)	2.3	—	—	36.2	—
$Q^{\downarrow}_{\mathrm{PAR}}$	GYF	64.9	100.0 (2004)	— ($\times$3)	—	—	—	—	35.1
	S67	60.0	89.1 (2003)	11.6 (2006)	—	39.7	0.3	—	—
	S83	76.0	88.8 (2001)	45.5 (2000)	—	—	—	—	24.0
	PDG	68.8	70.6 (2003)	67.4 (2001)	—	—	—	—	31.2
	RJA	73.1	90.0 (2001)	59.8 (1999)	—	—	—	—	26.9
	M34	—	—	—	—	—	—	—	100.0
	PNZ	75.0	99.3 (2011)	37.5 (2004)	—	—	—	—	25.0
	BAN	80.3	85.7 (2005)	77.6 (2006)	—	—	—	—	19.7
	CAX	63.0	80.9 (2002)	52.4 (2003)	—	—	—	—	37.0
$\dot{Q}^{\downarrow}_{\mathrm{LW}}$	GYF	98.0	100.0 ($\times$3)	85.4 (2012)	0.9	—	—	—	1.2
	S67	18.1	71.8 (2004)	— ($\times$7)	17.6	16.7	—	—	47.6
	S83	53.6	90.8 (2002)	— (2000)	11.7	—	—	—	34.7
	PDG	15.0	45.0 (2003)	— ($\times$2)	39.1	—	—	—	45.9
	RJA	83.4	98.6 (2001)	68.4 (1999)	1.0	—	—	—	15.7
	M34	59.1	88.1 (2004)	— (2002)	4.0	—	—	—	36.9
	PNZ	69.6	100.0 (2004)	— ($\times$2)	—	—	—	—	30.4
	BAN	—	—	—	—	—	—	—	100.0
	CAX	64.2	82.7 (2002)	53.3 (2003)	—	—	—	—	35.8

Table D.5: Continued.

Variable	Site	Measured			RDNT	OBJA	HARM	LINE	OTHR
		Mean	Min (Year)	Max (Year)					
p_e	GYF	99.8	100.0 (×6)	99.0 (2007)	—	—	0.2	—	—
	S67	52.0	100.0 (2009)	— (×2)	—	46.5	1.5	—	—
	S83	75.0	86.1 (2002)	45.6 (2000)	—	—	25.0	—	—
	PDG	97.1	98.8 (2001)	94.1 (2002)	—	—	2.9	—	—
	RJA	84.1	94.3 (2000)	68.5 (1999)	—	—	15.9	—	—
	M34	68.3	88.2 (2004)	49.3 (2003)	—	—	31.7	—	—
	PNZ	84.0	100.0 (2004)	54.8 (2006)	—	—	16.0	—	—
	BAN	86.7	92.9 (2004)	76.5 (2006)	—	—	13.3	—	—
	CAX	50.8	86.2 (2002)	— (×2)	—	—	49.2	—	—
T_e	GYF	99.9	100.0 (×2)	99.2 (2010)	—	—	0.1	—	—
	S67	72.5	95.5 (2003)	11.4 (2006)	1.0	26.4	0.1	—	—
	S83	81.7	93.9 (2003)	47.0 (2000)	—	—	18.3	—	—
	PDG	98.9	99.1 (2001)	98.6 (2003)	0.7	—	0.4	—	—
	RJA	82.7	99.2 (2001)	69.6 (1999)	0.1	—	17.2	—	—
	M34	60.4	97.9 (2004)	— (2001)	15.4	—	24.1	—	—
	PNZ	84.2	100.0 (2004)	55.3 (2006)	—	—	15.8	—	—
	BAN	97.7	100.0 (2005)	93.7 (2006)	—	—	2.2	—	—
	CAX	49.4	64.7 (2000)	27.4 (2001)	11.2	—	39.4	—	—
u_e	GYF	97.6	100.0 (×2)	83.9 (2006)	—	—	2.4	—	—
	S67	67.8	91.3 (2003)	10.7 (2006)	—	27.2	5.0	—	—
	S83	78.4	90.8 (2002)	46.7 (2000)	—	—	21.6	—	—
	PDG	99.1	99.7 (2002)	98.6 (2003)	0.5	—	0.4	—	—
	RJA	71.8	92.4 (2001)	45.1 (1999)	10.8	—	17.3	—	—
	M34	63.0	86.6 (2003)	39.8 (1999)	6.5	—	30.4	—	—
	PNZ	84.3	100.0 (2004)	55.4 (2006)	—	—	15.7	—	—
	BAN	86.7	92.8 (2004)	76.5 (2006)	11.1	—	2.2	—	—
	CAX	33.6	42.5 (2000)	26.7 (2003)	36.9	—	29.5	—	—
$\dot{W}_{\infty,e}$	GYF	99.9	100.0 (×7)	99.6 (2009)	—	—	—	—	0.1
	S67				—	98.5	—	—	1.5
	S83	79.5	91.8 (2001)	46.8 (2000)	—	—	—	—	20.5
	PDG	100.0	100.0 (×2)	99.9 (2001)	—	—	—	—	—
	RJA	87.0	99.9 (2001)	68.4 (1999)	—	—	—	—	13.0
	M34	69.5	98.1 (2004)	5.6 (2001)	—	—	—	—	30.5
	PNZ	83.2	100.0 (2004)	52.7 (2006)	—	—	—	—	16.8
	BAN	97.7	100.0 (2005)	93.7 (2006)	—	—	—	—	2.3
	CAX	42.8	52.5 (2002)	28.7 (1999)	—	—	—	—	57.2

Appendix E

Plant functional type assignment and estimation of demographic rates from forest inventories

This appendix summarizes the calculation of mortality and growth from the biomass inventories carried out at Paracou (GYF) and Santarém km 67 (S67). Part of the data processing for S67 was done in collaboration with Luciana Alves and Scott Stark.

At GYF, trees were initially surveyed in March 2004, with subsequent measurements in 2006, 2008, 2010, and 2013, always in March. At S67, the initial survey occurred in July 1999, and subsequent surveys were conducted in 2001, 2003, 2005, 2006, 2007, 2008, 2009, 2010, and 2011, always some time between June and September. At S67, some of the surveys were excluded from the final analysis because of the large number of trees that could not be found due to missing or incorrect information on tree location (2003 and 2006) or because growth rates had suspicious shifts across all size classes, suggesting that the DBH measurements were taken at the wrong reference height (2007). Nevertheless, all information from these surveys were used to correct the mortality and growth rates whenever they could be used to reduce uncertainties in the retained surveys.

E.1 Wood density and plant functional type assignment

At GYF most individuals, including new recruits, were identified to the species level, or the closest taxonomic level, whereas at S67 this identification occurred only in the first survey in 1999, with new recruits assigned only common names. Lianas were not originally measured in S67, but they have been included since 2006; likewise, palm trees were generally skipped although a few spurious individuals have been included. To avoid biases in recruitment and mortality, all individuals that have been identified as lianas or palms in S67 were excluded from the analysis. On the other hand, both palms and lianas have been consistently surveyed at GYF and thus were not excluded.

To attribute wood density (ω) to every individual, I used the database from Chave et al. (2009) and Zanne et al. (2009), with additional information for liana wood density from Putz and Holbrook (1991). If the species was known and included in the database, I used the mean value for the species. In case the genus was known but not the species, or when no wood density information was available for the species but other species from the same genus were available, I used the average value of the known species in the same genus. For all other individuals, I assigned wood density by randomly sampling from the other individuals with known species or genus and from the same family if the family was known, or from the entire plant community in case family was not known. I opted for randomly sampling instead of using the community average to reduce bias towards the mid-successional plant functional type, and without making any assumption on the distribution of wood densities within the plant community. A summary of the species identification level for both sites is available at Tab. E.1.

E.2 Mortality rates from observations

Mortality rates at any survey were determined based on the fraction rate as described by Sheil and May (1996), but extended to be also applicable for other quantities such as above-ground biomass:

Table E.1: Level of identification of individuals for both sites at the first forest inventory, based on the information available from the original data. Wood density is the basal area weighted average wood density of all individuals in each case. *Common* means that only local common name were known, and species and genus were attributed based on individuals with known species and same common name.

Known species	**Wood density sampling**	**Paracou (GYF)**		**Santarém km 67 (S67)**	
		Count ([%])	ω [$\mathrm{g\,cm^{-3}}$]	Count ([%])	ω [$\mathrm{g\,cm^{-3}}$]
Yes	Species	2198 (77.2)	0.72	1673 (71.7)	0.67
Yes	Genus	547 (19.1)	0.62	504 (21.8)	0.76
Yes	Family	15 (0.5)	0.79	0 (0.0)	—
Common	Species	0 (0.0)	—	90 (3.9)	0.66
Common	Genus	0 (0.0)	—	62 (2.7)	0.65
No	Community	87 (3.0)	0.66	3 (0.1)	0.78
Total		2847 (100.0)	0.70	2332 (100.0)	0.68

$$\dot{m}_t = 1 - \left(\frac{S_t}{N_{t-1}}\right)^{\frac{1}{y_t - y_{t-1}}}, \tag{E.1a}$$

$$N_{t-1} = \sum_{i=1}^{I} \left(X_{i,t-1} \cdot \ell_{i,t-1}\right), \tag{E.1b}$$

$$S_t = \sum_{i=1}^{I} \left(X_{i,t-1} \cdot \ell_{i,t-1} \cdot \ell_{i,t}\right), \tag{E.1c}$$

$$\ell_{i,t} = \begin{cases} 1 & \text{if tree was alive at survey } t \\ 0 & \text{if tree was dead or had not been recruited yet at survey } t \end{cases} \tag{E.1d}$$

where $t \in \{2,3,\ldots,T\}$ is the survey index, $X_{i,t}$ is the property of interest per unit area of individual i at survey t; y_t is the time the survey was taken (accurate to the monthly scale); and I is the total number of individuals. Equation (E.1) would suffice if living trees had been measured at every survey, and if all trees had been reported dead at the first survey after the tree died. Because the fraction of missing trees and death report varied from year to year, particularly at S67 (Tab. E.2), I incorporated the error due to incomplete information by estimating two probabilities for each individual i: $p_\ell(i,t) \stackrel{\text{def}}{=} p(\ell_{i,t-1} = 1)$ and $p_s(i,t) \equiv p(\ell_{i,t} = 1 | \ell_{i,t-1} = 1)$. The functional form of p_ℓ and p_s are derived from the least informative assumption, in which the probabilities of each outcome given the information available are the same:

Table E.2: Summary of total number of individuals for each combination of t_ℓ (rows) and t_d (columns) for both Paracou (GYF) and Santarém km 67 (S67). Italic values correspond to the cases in which more than one possible outcome exists. Combinations of t_ℓ and t_d that never happened were omitted, whereas cases denoted by — correspond to cases post the last survey and are represented by the rightmost column instead.

Site	$\mathbf{y_{t_\ell}}$	$\mathbf{t_d = t_{\ell+1}}$	$\mathbf{t_d = t_{\ell+2}}$	$\mathbf{t_d = t_{\ell+3}}$	$\mathbf{t_d = T+1}$
GYF	**2004**	69	0	0	0
	2006	117	0	—	*8*
	2008	71	—	—	0
	2010	116	—	—	9
	2013	—	—	—	2658
S67	**1999**	62	*2*	0	*1*
	2001	185	*12*	0	*17*
	2005	150	*5*	*1*	*31*
	2008	20	*3*	0	*7*
	2009	52	0	—	2
	2010	42	—	—	25
	2011	—	—	—	2347

$$p_\ell(i,t) = \begin{cases} 1 & \text{, if } t \leq t_\ell + 1 \\ 1 - \dfrac{t - t_\ell - 1}{t_d - t_\ell} & \text{, if } t_\ell + 1 < t \leq t_d \\ 0 & \text{, if } t > t_d \end{cases}, \tag{E.2a}$$

$$p_s(i,t) = \begin{cases} 1 & \text{, if } t \leq t_\ell \\ 1 - \dfrac{1}{t_d - t + 1} & \text{, if } t_\ell < t \leq t_d \\ 0 & \text{, if } t > t_d \end{cases}, \tag{E.2b}$$

where t_ℓ is the index of the last survey when the individual was reported alive in the field notes, and t_d is the index of the first survey in which the individual was reported dead in the field notes. In case the individual was never reported dead, we assume $t_d = T+1$ ($y_{T+1} \stackrel{\text{def}}{=} \infty$), which corresponds to the tree dying at some unknown time after the last survey. In addition, I defined two auxiliary probabilities:

$$p_a(i,t) \stackrel{\text{def}}{=} p(\ell_{i,t} = 1) \qquad = p_\ell(i,t) \cdot p_s(i,t), \tag{E.3a}$$

$$p_d(i,t) \stackrel{\text{def}}{=} p\ell_{i,t} = 0 | \ell_{i,t-1} = 1 = p_\ell(i,t) \cdot (1 - p_s(i,t)), \tag{E.3b}$$

Table E.3: Probabilities calculated for a hypothetical collection of 5 surveys ($T = 5$). In this case, we consider four individuals that were alive at survey $t = 1$. Individual 1 was alive during the entire period (regardless whether it was measured at every survey); individual 2 was reported dead at survey $t = 2$; individual 3 was not reported again until survey $t = 4$, when it was found dead, and individual 4 was never reported again.

	Individual 1 ($t_\ell = 5; t_d = 6$)				**Individual 2** ($t_\ell = 1; t_d = 2$)				**Individual 3** ($t_\ell = 1; t_d = 4$)				**Individual 4** ($t_\ell = 1; t_d = 6$)			
t	$\mathbf{p}_\ell$	$\mathbf{p_s}$	$\mathbf{p_a}$	$\mathbf{p_d}$	$\mathbf{p}_\ell$	$\mathbf{p_s}$	$\mathbf{p_a}$	$\mathbf{p_d}$	$\mathbf{p}_\ell$	$\mathbf{p_s}$	$\mathbf{p_a}$	$\mathbf{p_d}$	$\mathbf{p}_\ell$	$\mathbf{p_s}$	$\mathbf{p_a}$	$\mathbf{p_d}$
1	1	1	1	0	1	1	1	0	1	1	1	0	1	1	1	0
2	1	1	1	0	1	0	0	1	1	$\frac{2}{3}$	$\frac{2}{3}$	$\frac{1}{3}$	1	$\frac{4}{5}$	$\frac{4}{5}$	$\frac{1}{5}$
3	1	1	1	0	0	0	0	0	$\frac{2}{3}$	$\frac{1}{2}$	$\frac{1}{3}$	$\frac{1}{3}$	$\frac{4}{5}$	$\frac{3}{4}$	$\frac{3}{5}$	$\frac{1}{5}$
4	1	1	1	0	0	0	0	0	$\frac{1}{3}$	0	0	$\frac{1}{3}$	$\frac{3}{5}$	$\frac{2}{3}$	$\frac{2}{5}$	$\frac{1}{5}$
5	1	1	1	0	0	0	0	0	0	0	0	0	$\frac{2}{5}$	$\frac{1}{2}$	$\frac{1}{5}$	$\frac{1}{5}$
Post-survey	1	0	0	1	0	0	0	0	0	0	0	0	$\frac{1}{5}$	0	0	$\frac{1}{5}$

which correspond to the probability that the individual was alive at survey t and the probability that the individual died between survey $t-1$ and t, respectively. One example of these probabilities for four typical cases is shown at Tab. E.3: in all cases the sum of p_d is always 1, and that p_a will always decrease towards zero, which is consistent with the fact that all trees will eventually die, even if it happens after the last survey. Also, the non-zero terms of p_d are always numerically the same, which is consistent with the least informative assumption. Both p_ℓ and p_s were calculated for all individuals for all surveys, and mortality rates and confidence intervals were calculated using functions `boot` and `boot.ci` from package `boot` in `R`. For each of the 100,000 realizations for each time interval, $\ell_{i,t-1}$ and $\ell_{i,t}$ of the selected individuals were calculated using function `rbinom` in `R` using $p_\ell(i,t)$ and $p_s(i,t)$. The individual-based mortality rates are shown in Fig. E.1. Since the number of missing trees was generally higher in S67, the 95% confidence intervals tended to be larger for the entire community compared to GYF. On the other hand, fewer large trees were surveyed in GYF and fewer large trees were missing in S67, resulting in broader confidence intervals for GYF.

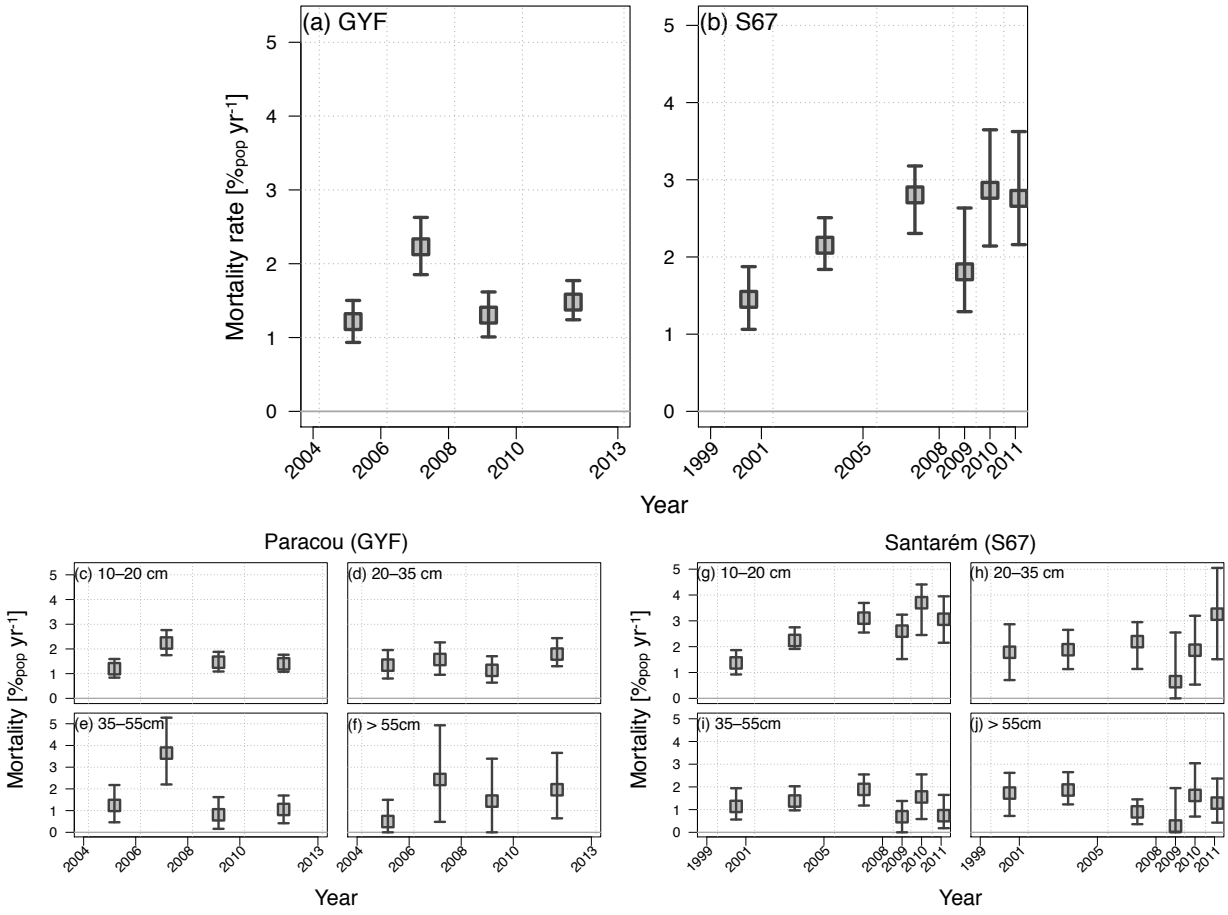

Figure E.1: Population-based mortality rates calculated (a,b) for the entire community surveyed and (c-j) for different DBH classes in (c-f) Paracou (GYF) and (g-j) Santarém km 67 (S67).

E.3 Growth rates from observations

First, I defined growth rate $\dot{g}_{i,t}$ of each individual i between surveys y_{t-1} and y_t, for any individual that was recruited and alive at both surveys, and let $X_{i,t-1}$ and $X_{i,t}$ be the magnitude of the property of interest of this individual at both surveys, such as DBH, above-ground biomass (AGB), or basal area (BA):

$$\dot{g}_{i,t} = \frac{\ln\left(X_{i,t}\right) - \ln\left(X_{i,t-1}\right)}{y_t - y_{t-1}} \tag{E.4}$$

In case $X_{i,t}$ is a variable that can be aggregated to the stand level (AGB or BA), it is also possible to define the average growth rate $\overline{\dot{g}}_t$ of the entire plant community comprised of I individuals:

$$X_{\Sigma,t} = \sum_{i=1}^{I} \left(X_{i,t} \cdot \ell_{i,t-1} \cdot \ell_{i,t} \right), \tag{E.5a}$$

$$X_{0\Sigma,t} = \sum_{i=1}^{I} \left(X_{i-1,t} \cdot \ell_{i,t-1} \cdot \ell_{i,t} \right), \tag{E.5b}$$

$$\overline{\dot{g}}_t = \frac{\ln\left(X_{\Sigma,t}\right) - \ln\left(X_{0\Sigma,t}\right)}{y_t - y_{t-1}}, \tag{E.5c}$$

where $X_{0\Sigma,t}$ and $X_{\Sigma,t}$ are the ecosystem level property aggregated from all individuals included in both surveys, and $\ell_{i,t}$ is the same as defined in Eqn. (E.1d). Average growth rate can be determined from individual growth rate, and here I derive the relation in a way that can be also used by ED-2.2. First, I substitute Eqn. (E.4) into Eqn. (E.5b):

$$X_{0\Sigma,t} = \sum_{i=1}^{I} \left\{ \exp\left[-\dot{g}_{i,t} \left(y_t - y_{t-1} \right) \right] \cdot X_{i,t} \right\}, \tag{E.6}$$

and then substitute Eqn. (E.6) and Eqn. (E.5a) into Eqn. (E.5c) to obtain:

$$\overline{\dot{g}}_t = -\frac{1}{y_t - y_{t-1}} \ln \left(\frac{\sum_{i=1}^{I} \left\{ \exp\left[-\dot{g}_{i,t} \left(y_t - y_{t-1} \right) \right] \cdot X_{i,t} \cdot \ell_{i,t-1} \cdot \ell_{i,t} \right\}}{\sum_{i=1}^{I} \left(X_{i,t} \cdot \ell_{i,t-1} \cdot \ell_{i,t} \right)} \right) \tag{E.7}$$

In Fig. E.2, I present the growth rates calculated for all surveys in GYF and S67, using the equations above. Considering the plant community as a whole, growth rates at GYF (Fig. E.2a) are generally lower than at S67 (Fig. E.2b), although the rates show opposite trends. The reduction in growth rates at S67 may be a return to typical growth rates: for example Rice et al. (2004); Keller et al. (2004a) attributed the large coarse woody debris pool at the region to a previous disturbance, which could also cause higher growth rates earlier in the measurements. In GYF, the increase in growth rates are dependent on the plots, with highest increases observed in plots 1 and 6, which were also the plots that observed the highest mortality rate between 2006 and 2008 (not shown), suggesting that the growth rates may be responding to disturbance as well. When comparing the growth rates by size class, one can observe that the largest differences in magnitude

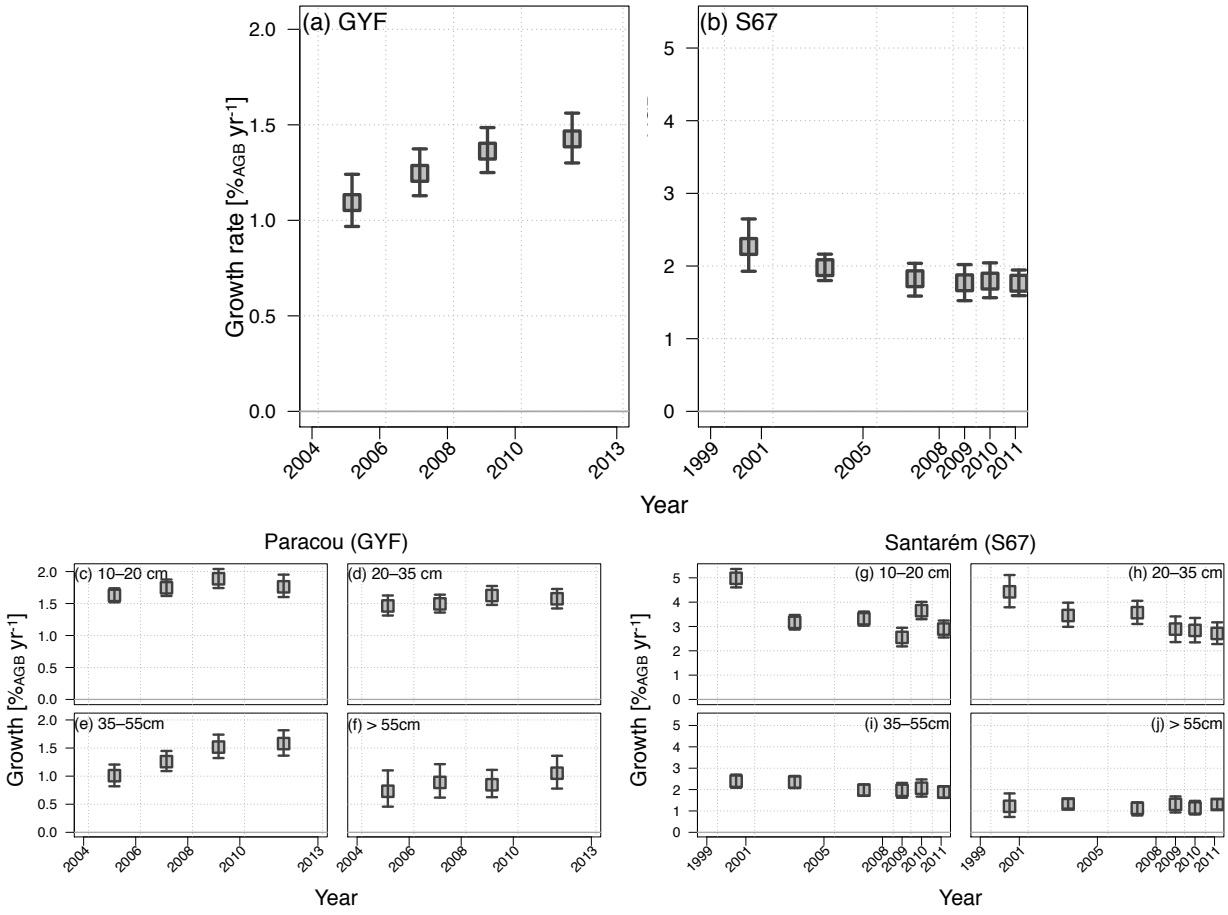

Figure E.2: AGB-based mortality rates calculated (a,b) for the entire community surveyed and (c-j) for different DBH classes in (c-f) Paracou (GYF) and (g-j) Santarém km 67 (S67) using Eqn. (E.7). Note the different scales between GYF and S67.

between GYF and S67 occur amongst the smaller classes, which could be also due the response to a large disturbance and higher proportion of fast growing trees. In fact, the basal-area weighted average of wood density is lower for S67 than GYF at all classes except the largest trees, which is also the class with the least differences (not shown).

Appendix F

Phenology and demographic rates from ED-2.2 model

F.1 Tropical leaf phenology

The current version of ED-2.2 allows the user to solve tropical trees using either evergreen, drought deciduous, or light-controlled phenology; tropical light controlled has been previously described by Kim et al. (2012) thus not discussed here. The drought deciduous and evergreen leaf phenology schemes are a further development of the original schemes by Moorcroft et al. (2001) and Hurtt et al. (2002), respectively, and the development presented here has been done in collaboration between myself, Naomi Levine and Yeonjoo Kim.

First, let $C_\lambda^\star[\,\mathrm{kg_C\,plant^{-1}}]$ be the maximum leaf biomass for any cohort m, as defined in App. C, and let x_λ and $x_\lambda^\star$ be the actual and maximum elongation factor for leaves (cohort subscripts omitted for clarity):

$$x_\lambda = \frac{C_\lambda}{C_\lambda^\star} \tag{F.1a}$$

$$x^\star_\lambda = \begin{cases} 1 & \text{, if evergreen or } \overline{W}^\star_\pi \geq 1 \\ \overline{W}^\star_\pi & \text{, if } 0.05 \leq \overline{W}^\star_\pi < 1 \\ 0 & \text{, if } \overline{W}^\star_\pi < 0.05 \end{cases}, \tag{F.1b}$$

$$\overline{W}^\star_\pi = \frac{1}{\Delta z_{g_{k_\rho}} \cdot \Delta t_{\mathrm{RA}}} \int_{t-\Delta t_{\mathrm{RA}}}^{t} \left(\sum_{k'=k_\rho}^{K} \left\{ \frac{\max\left[0, \Psi_k(t') + \frac{1}{2}\left(z_{g_k} + z_{g_{k+1}}\right) - \Psi_{\mathrm{Wp}}\right]}{\Psi_{\mathrm{Ld}} - \Psi_{\mathrm{Wp}}} \Delta z_{g_k} \right\} \right) \mathrm{d}t', \tag{F.1c}$$

where $\overline{W}^\star_\pi$ is an available water index averaged over $\Delta t_{\mathrm{RA}} \stackrel{\mathrm{def}}{=} 10\,\mathrm{days}$, k_ρ is the deepest soil layer to which roots have access, $\Psi_k(t')$ is the soil matric potential at layer k, $z_{g_k} \leq 0$ is the depth of layer k; Ψ_{Wp} is the soil matric potential at the wilting point, and Ψ_{Ld} is a tuneable threshold based on soil matric potential, below which cohorts may shed leaves. The default value is Ψ_{Ld} is $-1.2\,\mathrm{MPa}$, which is close to the wilting point ($\Psi_{\mathrm{Wp}} \stackrel{\mathrm{def}}{=} -1.5\,\mathrm{MPa}$).

Active leaf shedding ($\dot{C}^\downarrow_\lambda [\,\mathrm{kg_C\,plant^{-1}\,s^{-1}}]$) occurs whenever soil is drier than the threshold and drought conditions are deteriorating:

$$\dot{C}^\downarrow_\lambda = \max\left[0, \frac{\left(x_\lambda - x^\star_\lambda\right) C^\star_\lambda}{\Delta t_{\mathrm{live}}}\right]. \tag{F.2}$$

Leaf flushing occurs whenever soil moisture conditions improve, and total leaf flush will depend on carbon availability as it will be shown in Sec. F.2. To avoid flushing when conditions are nearly steady, conditions are assumed to be improving when the maximum elongation factor $x^\star_\lambda \geq \max\left(x_\lambda + 0.05, 1.0\right)$, or if $x^\star_\lambda \geq x_\lambda$ and plant was already flushing leaves. Because $x^\star_\lambda \stackrel{\mathrm{def}}{=} 1$ for evergreen cohorts, these individuals will always flush new leaves to recover losses from turnover, unless their storage pool is zero and the net primary productivity is negative.

F.2 Growth rates

Individual-based growth depends on the total change in all living and structural tissues, and non-structural carbon. The rate of change is calculated similarly to Medvigy et al. (2009) and Kim et al. (2012):

$$\frac{\mathrm{d}C_\lambda}{\mathrm{d}t} = \dot{C}_\lambda^{\uparrow} - \dot{C}_\lambda^{\downarrow} - f_\lambda\, C_\lambda \tag{F.3a}$$

$$\frac{\mathrm{d}C_\rho}{\mathrm{d}t} = \dot{C}_\rho^{\uparrow} - f_\rho\, C_\rho \tag{F.3b}$$

$$\frac{\mathrm{d}C_\sigma}{\mathrm{d}t} = \dot{C}_\sigma^{\uparrow} - f_\sigma\, C_\sigma \tag{F.3c}$$

$$\frac{\mathrm{d}C_\tau}{\mathrm{d}t} = \Delta C_\pi + f_{\mathrm{LD}}\dot{C}_\lambda^{\downarrow} - \dot{C}_\lambda^{\uparrow} - \dot{C}_\rho^{\uparrow} - \dot{C}_\sigma^{\uparrow} - f_\tau\, C_\tau \tag{F.3d}$$

where $(C_\lambda; C_\rho; C_\sigma; C_\tau)$ $[\mathrm{kg_C\,plant^{-1}}]$ are the leaf, root, sapwood, and storage biomass; $(\dot{C}_\lambda^{\uparrow}; \dot{C}_\rho^{\uparrow}; \dot{C}_\sigma^{\uparrow})$ $[\mathrm{kg_C\,plant^{-1}\,s^{-1}}]$ is the allocation rates to leaves, root, and sapwood, respectively, $(f_\lambda; f_\rho; f_\sigma; f_\tau)$ $[\mathrm{s^{-1}}]$ are the turnover rates of leaves, roots, sapwood, and storage, respectively; ΔC_π $[\mathrm{kg_C\,plant^{-1}\,s^{-1}}]$ is the individual-level daily net primary productivity (c.f. Eqn. 2.23); and f_{LD} is the fraction of carbon retained from active leaf drop as storage, currently assumed to be 0.5.

The allocation to living tissues is proportional to the amount needed by each pool, and dependent on whether the plant carbon balance and environmental conditions are favourable for growing. First, let $(\Delta C_\lambda^\star; \Delta C_\rho^\star; \Delta C_\sigma^\star)$ $[\mathrm{kg_C\,plant^{-1}}]$ be the biomass needed to bring the plant living tissues on allometry:

$$\Delta C_\lambda^\star = \max\left[0, x_\lambda^\star\, C_\lambda^\star - C_\lambda\, \left(1 - f_\lambda \Delta t_{\mathrm{live}}\right)\right], \tag{F.4a}$$

$$\Delta C_\rho^\star = \max\left[0, C_\rho^\star - C_\rho\, \left(1 - f_\rho \Delta t_{\mathrm{live}}\right)\right], \tag{F.4b}$$

$$\Delta C_\sigma^\star = \max\left[0, C_\sigma^\star - C_\sigma\, \left(1 - f_\sigma \Delta t_{\mathrm{live}}\right)\right], \tag{F.4c}$$

$$\Delta C_\alpha^\star = \Delta C_\lambda^\star + \Delta C_\rho^\star + \Delta C_\sigma^\star, \tag{F.4d}$$

where Δt_{live} is the phenology time step (c.f. Tab. 2.1). In addition, let $\mathcal{U}_{\mathrm{Grow}}$ be variable that controls whether the plant should grow living tissues or not:

$$\mathcal{U}_{\mathrm{Grow}} = \begin{cases} 0 & \text{, if } \Delta C_\alpha^\star = 0,\ \dot{C}_\lambda^{\downarrow} > 0, \text{ or } C_\tau\left(1 - f_\tau \Delta t_{\mathrm{live}}\right) < -\Delta C_\pi \\ \dfrac{1}{\Delta C_\alpha^\star} & \text{, otherwise} \end{cases}. \tag{F.5}$$

Growth rates of the individual tissues are then defined as:

$$\dot{C}_{\lambda}^{\uparrow} = \mathcal{U}_{\text{Grow}}\,\Delta C_{\lambda}^{\star}\,\min\left[\Delta C_{\alpha}^{\star}, C_{\tau}\,(1-f_{\tau})+\Delta C_{\pi}\right], \tag{F.6a}$$

$$\dot{C}_{\rho}^{\uparrow} = \mathcal{U}_{\text{Grow}}\,\Delta C_{\rho}^{\star}\,\min\left[\Delta C_{\alpha}^{\star}, C_{\tau}\,(1-f_{\tau})+\Delta C_{\pi}\right], \tag{F.6b}$$

$$\dot{C}_{\sigma}^{\uparrow} = \mathcal{U}_{\text{Grow}}\,\Delta C_{\sigma}^{\star}\,\min\left[\Delta C_{\alpha}^{\star}, C_{\tau}\,(1-f_{\tau})+\Delta C_{\pi}\right]. \tag{F.6c}$$

Growth of structural tissues is calculated at the monthly time step (Δt_{cohort}, Tab. 2.1), after the biomass of the living tissues have been updated.

$$\frac{\mathrm{d}C_{\delta}}{\mathrm{d}t} = \begin{cases} \left(1-f_{\text{Repro}}-f_{\text{Store}}\right)\,\dfrac{C_{\tau}}{\Delta t_{\text{cohort}}} & \text{, if } \Delta C_{\alpha}^{\star}=0 \text{ and } x_{\lambda}=1 \\ 0 & \text{, otherwise} \end{cases}, \tag{F.7}$$

where

$$f_{\text{Repro}} = \begin{cases} 0.0 & \text{, if PFT is a tree and height is less than 5 m.} \\ 1.0 & \text{, if PFT is a grass at maximum attainable height. ,} \\ 0.3 & \text{, otherwise.} \end{cases} \tag{F.8}$$

$$f_{\text{Store}} = 0.0 \tag{F.9}$$

where f_{Repro} and f_{Store} are the fractions of carbon storage that are devoted to reproduction and kept as storage, respectively. The values shown in Eqn. (F.8) and Eqn. (F.9) are the default fraction for all PFTs as of ED-2.2, but they are tuneable parameters.

F.3 Mortality rates

In ED-2.2 the change of demographic density is determined from the differential equation described in ED-1.0 (c.f. Moorcroft et al., 2001). Following Sheil and May (1996) notation, ED-2.2 mortality rates $\dot{\mu}_n$ correspond to the exponential mortality rate, but throughout this manuscript the native rates are converted to fraction rates for presentation purposes, since fraction rates are bounded. The conversion between exponential and fraction also comes from Sheil and May (1996) and is does not depend on time:

$$\dot{m}_x = 1 - \mathrm{e}^{-\dot{\mu}_x}, \tag{F.10}$$

where $\dot{\mu}_x$ can be any type of mortality. Following Moorcroft et al. (2001), individual-based mortality rate of any cohort m in a patch i in ED-2.2 is the sum of four terms:

$$\dot{\mu}_n = \underbrace{\dot{\mu}_{\mathrm{DI}_{m,i}}}_{\substack{\text{Ageing}\\ \text{(Density independent)}}} + \underbrace{\dot{\mu}_{\mathrm{DD}_{m,i}}}_{\substack{\text{Carbon starvation}\\ \text{(Density dependent)}}} + \underbrace{\dot{\mu}_{\mathrm{CD}_i}}_{\text{Cold/Frost}} + \underbrace{\dot{\mu}_{\mathrm{FR}}}_{\text{Fire}}. \tag{F.11}$$

As in Moorcroft et al. (2001), density-independent mortality is the component attributable to ageing of the cohort, and it depends both on the typical tree fall disturbance rate λ_{TF} and the cohort wood density ρ_m:

$$\dot{\mu}_{\mathrm{DI}_{m,i}} = \lambda_{\mathrm{TF}} \cdot \left[1 + 10.714 \cdot \left(1 - \frac{\rho_{m,i}}{\rho_{\mathrm{LTR}}}\right)\right], \tag{F.12}$$

where $(\rho_{\mathrm{ETR}}; \rho_{\mathrm{MTR}}; \rho_{\mathrm{LTR}}) \equiv (0.53; 0.71; 0.90)\ \mathrm{g\,cm^{-3}}$ are the wood densities for early-, mid-, and late-successional, tropical broadleaf trees, respectively. In the simulations shown in this work $\lambda_{\mathrm{TF}} = 0.0111\ \mathrm{yr^{-1}}$. Even though the original formulation is based on typical values found in the literature (c.f. Moorcroft et al., 2001), more recent studies suggest that the density independent is overestimating mortality. In Fig. F.1 we observe that the density-independent mortality rate has similar magnitude as the prediction for most tropical sites, including GYF, which was calculated using the same methodology as Kraft et al. (2010) except that I used genus instead of taxonomic species[1]. Mortality rates, however, are overestimated for early and mid-successional trees. Although this introduces a bias in the mortality, the predicted values in ED-2.2 are still relatively low during the extreme drought conditions simulated in this work.

Mortality due to cold or frost is also determined through a phenomenological parameterization, being a linear function of the daily mean temperature of the canopy air space of patch i ($\overline{T}_{a,i,d}[\mathrm{K}]$), after Albani et al. (2006):

[1] Since new recruits were not identified taxonomically in S67, we did not perform this analysis for that site.

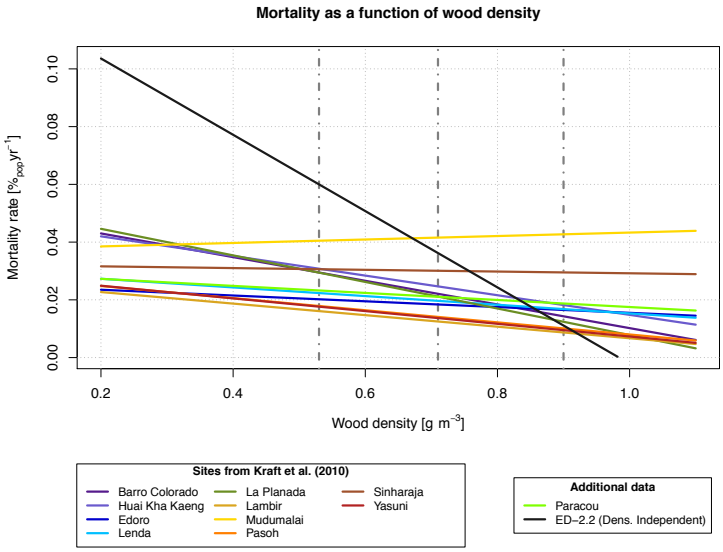

Figure F.1: Comparison between the density independent mortality as a function of wood density in ED-2.2 and the fit obtained by different sites obtained by Kraft et al. (2010). A similar approach was used to determine the dependence on mortality on wood density at GYF, and the fit is also shown.

$$\dot{\mu}_{\mathrm{CD}_i} = \frac{1}{D_{\mathrm{month}}} \sum_{d=1}^{D_{\mathrm{month}}} \left\{ 3.0 \cdot \max\left[0, \min\left(1, 1 - \frac{\overline{T}_{a,i,d} - T_{F_m}}{5}\right)\right]\right\}, \tag{F.13}$$

where T_{F_m} is a temperature threshold set to 275.65 K for all tropical plants, and D_{month} is the number of days in the month.

Mortality due to fire in ED-2.2 follows the original implementation by Moorcroft et al. (2001), and assumes that while fire depends on local scale dryness, once it ignites, it can spread throughout the entire landscape, thus it must take multiple patches into account. First, let $\dot{\lambda}_{\mathrm{FR}}[\,\mathrm{s}^{-1}]$ be the disturbance rate associated to fires, defined as in Moorcroft et al. (2001):

$$\dot{\lambda}_{\mathrm{FR}} = \kappa_{\mathrm{FR}} \sum_{i=1}^{I} \sum_{m=1}^{M_i} \left(n_{m,i}\, C_{\mathrm{Fuel}_{m,i}}\, \mathcal{Y}_i\, \alpha_i\right), \tag{F.14}$$

where I is the number of patches, M_I is the number of cohorts at patch i, $n_{m,i}[\,\mathrm{plant\,m}^{-2}]$ is the local demographic density $C_{\mathrm{Fuel}_m}[\,\mathrm{kg_C\,plant}^{-1}]$ is the amount of fuel associated with cohort $(m;i)$, $\mathcal{Y}_i$ is the binary ignition function, α_i is the relative area of patch i, and $\kappa_{\mathrm{FR}} = 0.5\,\mathrm{yr}^{-1}$ is a (tuneable)

parameter controlling intensity. The fuel is the total above-ground biomass:

$$C_{\mathrm{Fuel}_{m,i}} = C_{\lambda_{m,i}} + f_{\mathrm{AG}_{m,i}} \left(C_{\sigma_{m,i}} + C_{\delta_{m,i}} \right), \tag{F.15}$$

where $C_{\lambda_{m,i}}$, $C_{\sigma_{m,i}}$ and $C_{\delta_{m,i}}$ $[\,\mathrm{kg_C\,plant^{-1}}]$ are the biomass of leaves, sapwood and structural tissues, respectively, and $f_{\mathrm{AG}_{m,i}}$ is the fraction of the tissue that is above ground.

The ignition switch is defined in terms of the dryness of the environment. The original formulation by Moorcroft et al. (2001) used soil moisture to estimate dryness; while soil moisture has the advantage of capturing long term trends, the relative moisture is strongly dependent on the soil texture, which causes fires to occur preferably at sandy sites (or clayey sites if it were replaced by matric potential). To reduce the dependence on soil moisture, an optional threshold has been defined:

$$\mathcal{Y}_i = \begin{cases} 1 & \text{, if } \dfrac{\displaystyle\int_{t-\Delta t}^{t} \mathrm{WD}_i(t)\,\mathrm{d}t}{\displaystyle\int_{t-\Delta t}^{t} \dot{W}_{\infty,e}(t)\,\mathrm{d}t} > \mathcal{Y}_0 \\ 0 & \text{, otherwise} \end{cases}, \tag{F.16}$$

where $\mathrm{WD}_i[\,\mathrm{kg_W\,m^{-2}\,s^{-1}}]$ is the water deficit (rainfall minus evapotranspiration) at patch i, and $\dot{W}_{\infty,e}(t)[\,\mathrm{kg_W\,m^{-2}\,s^{-1}}]$ is the rainfall rate, both integrated over the period of one year. $\mathcal{Y}_0$ is a adjustable parameter, currently set to 0.45.

Once the fire disturbance rate is determined, mortality rate can be determined from the definition of disturbance rate (c.f. Moorcroft et al., 2001):

$$\dot{\mu}_{\mathrm{FR}_{m,i}} = \ln \left[\frac{1}{\sigma_{\mathrm{FR}} + (1 - \sigma_{\mathrm{FR}})\ \mathrm{e}^{-\dot{\lambda}_{\mathrm{FR}}}} \right], \tag{F.17}$$

where σ_{FR} is the fire survivorship, currently assumed to be zero for all PFTs.

Density-dependent mortality rate is called so because the ability of each plant to fix carbon is strongly influenced by the competition for resources with the other individuals next to it. Following Moorcroft et al. (2001), the original density-dependent mortality rate in ED-2.2 represents the effect of competition for light in a forest on survivorship, and is defined as:

$$\dot{\mu}_{\mathrm{DD}_{n,p}}(t) = \frac{\dot{\mu}_{\mathrm{DD}}^{\max}}{1+\exp\left(\alpha \cdot \overline{c}_{\star_{n,p}}(t)\right)}, \tag{F.18}$$

$$\dot{\mu}_{\mathrm{DD}}^{\max} = \lim_{\overline{c}_{\star} \to -\infty} \dot{\mu}_{\mathrm{DD}}(t) \tag{F.19}$$

$$\overline{c}_{\star_{n,p}}(t) = \frac{c_{\star_{n,p}}(t) + 11 \cdot \overline{c}_{\star_{n,p}}(t-\Delta t)}{12}, \tag{F.20}$$

where $\dot{\mu}_{\mathrm{DD}_{n,p}}(t)$ is the density-dependent mortality rate at time t, $\dot{\mu}_{\mathrm{DD}}^{\max}$ and α are PFT-dependent parameters, and $\overline{c}_{\star}$ is the running average of the relative carbon balance at monthly time step Δt, with typical memory time of one year. The relative carbon balance at time t ($c_{\star_{n,p}}(t)$) was originally defined in terms of light availability, but the same principle can be applied to any limiting resource (r):

$$c_{\star_r}(t) = \frac{C_{\mathrm{B}}^{\mathrm{actual}}(t)}{C_{\mathrm{B}_r}^{\max}(t)}, \tag{F.21}$$

where $C_{\mathrm{B}}^{\mathrm{actual}}$ is the actual accumulated carbon balance over the course of the previous month, and $C_{\mathrm{B}_r}^{\max}$ is the potential accumulated carbon balance if resource r did not limit carbon uptake. In case of light, $C_{\mathrm{B}_r}^{\max}$ corresponds to the carbon balance the cohort would attain if it were not shaded by any other cohort, and in case of water, it corresponds to the carbon balance if soil moisture were always at porosity. The current implementation includes only light and moisture, although the idea can be extended to any limiting resource. Since the relative carbon balance decreases when the resource is not available, stress is inversely proportional to the relative carbon balance, hence the net relative carbon balance $c_{\star}$, or the sum of the stress due to all R limitations can be written as:

$$\begin{aligned} \frac{1}{c_{\star} - c_{\star_{\mathrm{ES}}}} &= \sum_{r=1}^{R} \left[\frac{\kappa_r}{c_{\star_r} - c_{\star_{\mathrm{ES}}}} \right], \\ \sum_{r=1}^{R} \kappa_r &= 1, \end{aligned} \tag{F.22}$$

where κ_r are phenomenological parameters which scale the relative importance of each resource, and $c_{\star_{\mathrm{ES}}}$ correspond to the minimum carbon balance possible, below which mortality rate ap-

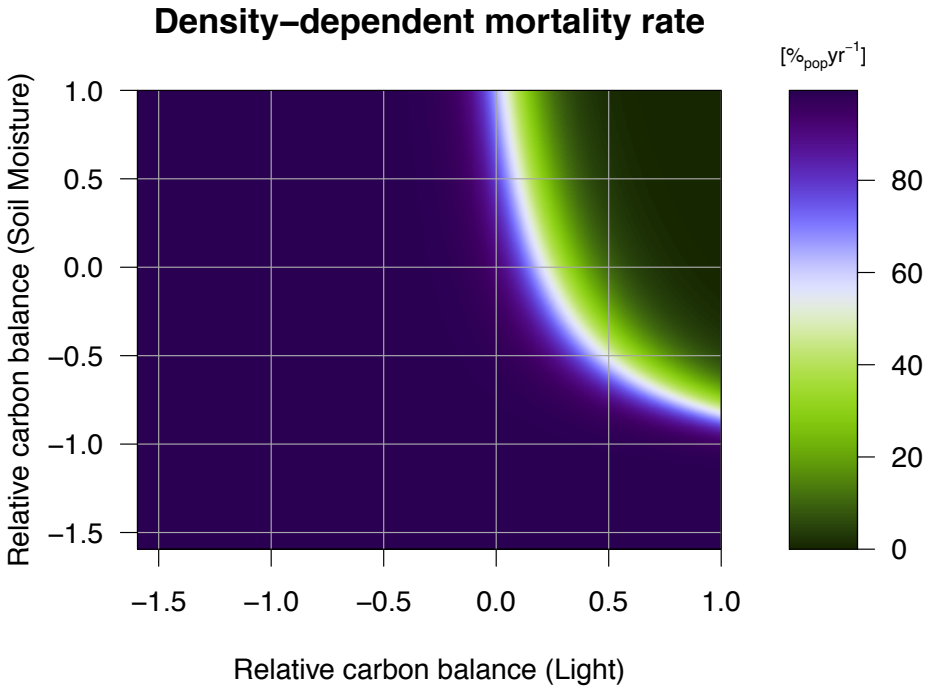

Figure F.2: Density-dependent mortality rate as a function of relative carbon balance associated with light and moisture. Mortality is presented in the exponential form, for $\kappa_{(\text{light})} = 0.8$ and $\kappa_{(\text{water})} = 0.2$.

proaches $\dot{\mu}_{\text{DD}}^{\max}$. From Eqn. (F.19), $c_{\star_{\text{ES}}}$ should be $-\infty$, however due to floating point truncation, the denominator of Eqn. (F.18) becomes 1 when the exponential term is less than the machine precision $\varepsilon = 2^{-23}$, therefore we fix $c_{\star_{\text{ES}}}$ to:

$$c_{\star_{\text{ES}}} \overset{\text{def}}{=} \frac{\ln(\varepsilon)}{\alpha}. \tag{F.23}$$

The functional form of the density dependent mortality rate as a function of relative carbon balance under light and moisture conditions is shown in Fig. F.2. One can observe that the multiple limitations act to accelerate mortality rates, and that mortality rates approach 100 % once any of the resources become very limiting. In addition, because a higher weight was given to light, the mortality rates increase faster for this resource.

Because similar cohorts may be fused and cohorts may be split if their total leaf area is greater

than 1 $m^2_{leaf} m^{-2}$, we must determine the previous demographic density of each cohort by integrating the exponential decay backwards in time. The plot-level exponential mortality rate in terms of demographic variable x ($\overline{\mu}_x$) is determined by:

$$\overline{\mu}_X|_{t-\Delta t}^{t} = \frac{1}{\Delta t} \cdot \ln \left[\frac{\sum_{p=1}^{P} \sum_{n=1}^{N_p} x_{n,p}(t) \cdot e^{\dot{\mu}_{n,p}|_{t-\Delta t}^{t} \Delta t} \cdot \alpha_p(t)}{\sum_{p=1}^{P} \sum_{n}^{N_p} x_{n,p}(t) \cdot \alpha_p(t)} \right], \tag{F.24}$$

where $x_{n,p}$ is the demographic variable (e.g. demographic density, above-ground biomass or basal area), and α_p is the relative area of the patch.

F.4 Mortality and growth rates by PFT and size class

In this section I compare the mortality and growth rates by the model with the observed rates for each plant functional type and size class at both sites. In general, one can observe from Fig. F.3 through Fig. F.8 that both mortality and growth rates tend to be more overestimated for early successional trees and for smaller classes.

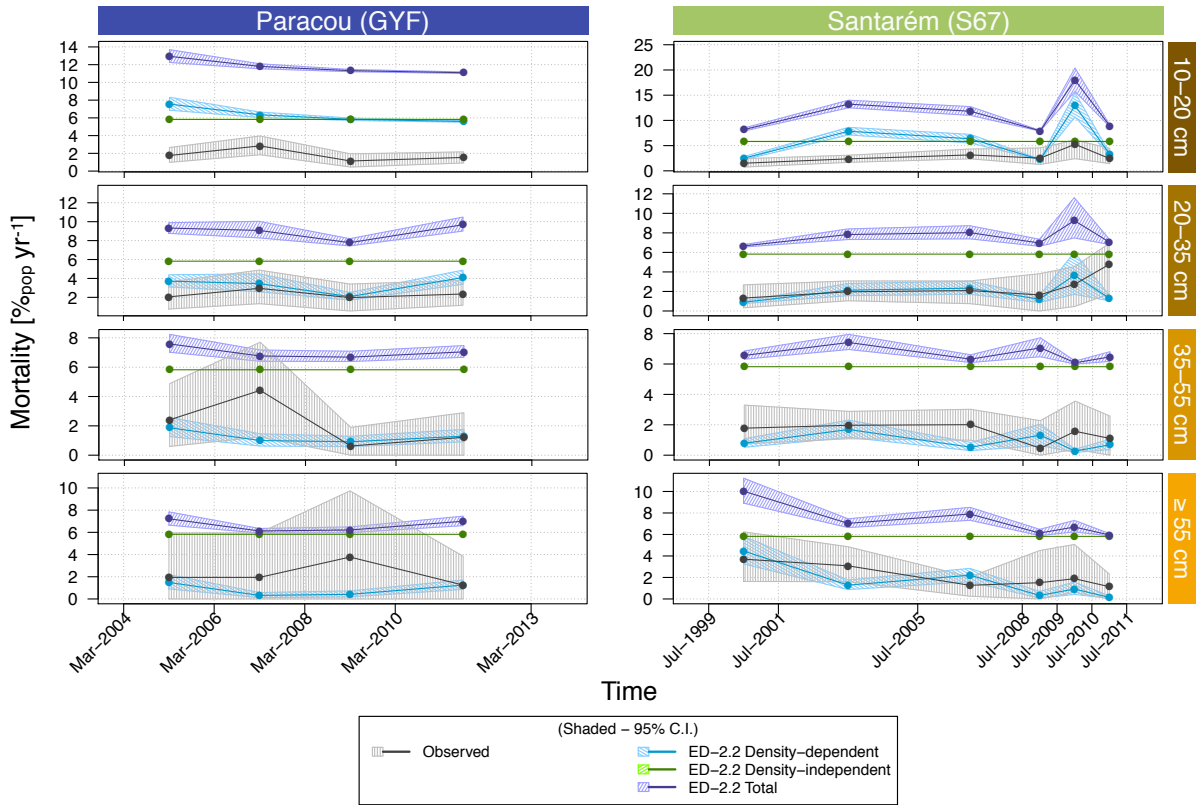

Figure F.3: Comparison between mortality rates from ED-2.2 and observations for early successional cohorts for (a) GYF and (b) S67, for drought deciduous simulations. Evergreen simulations had similar patterns and thus are not shown.

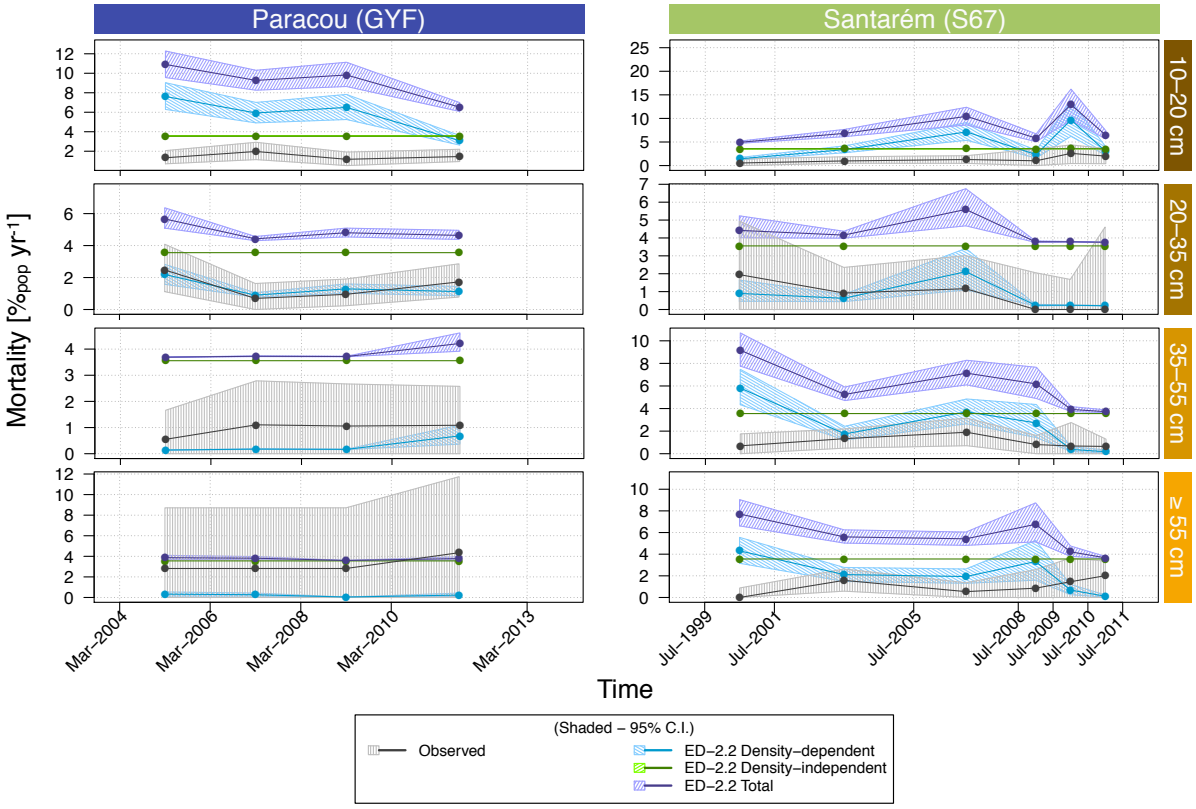

Figure F.4: Similar to Fig. F.3 but for mid-successional cohorts.

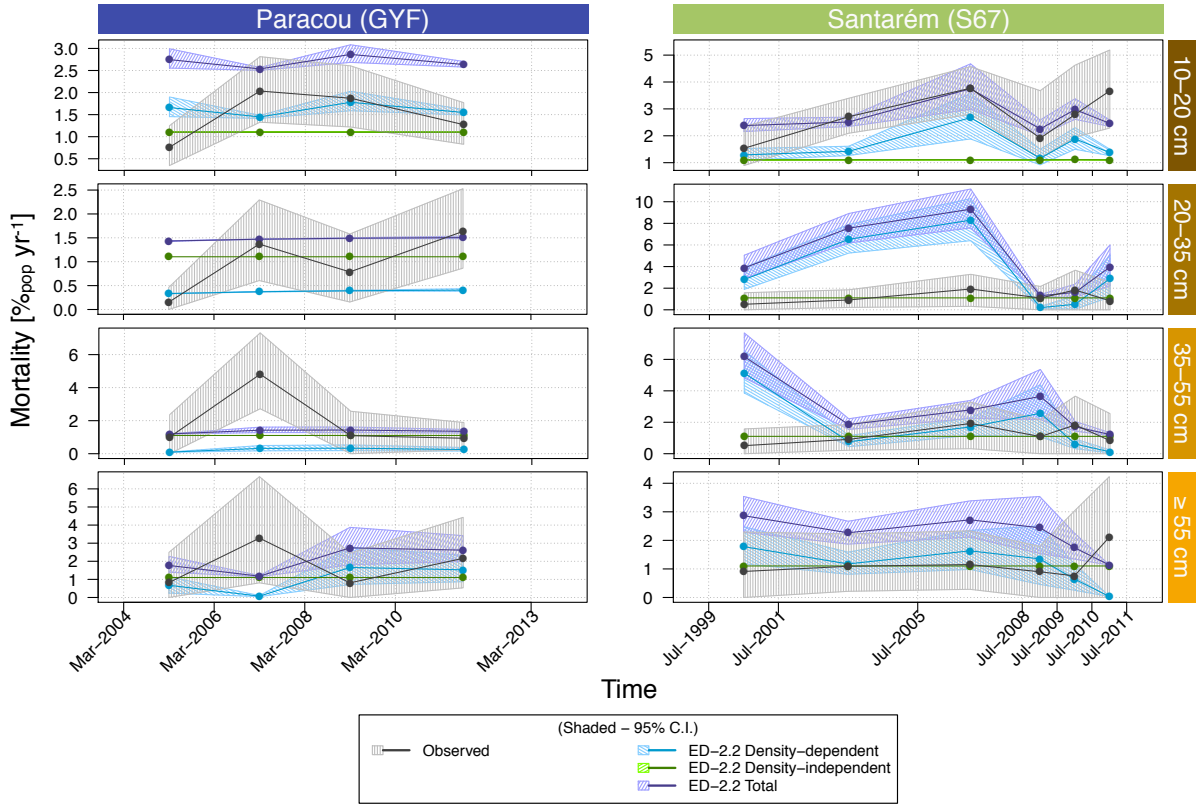

Figure F.5: Similar to Fig. F.3 but for late-successional cohorts.

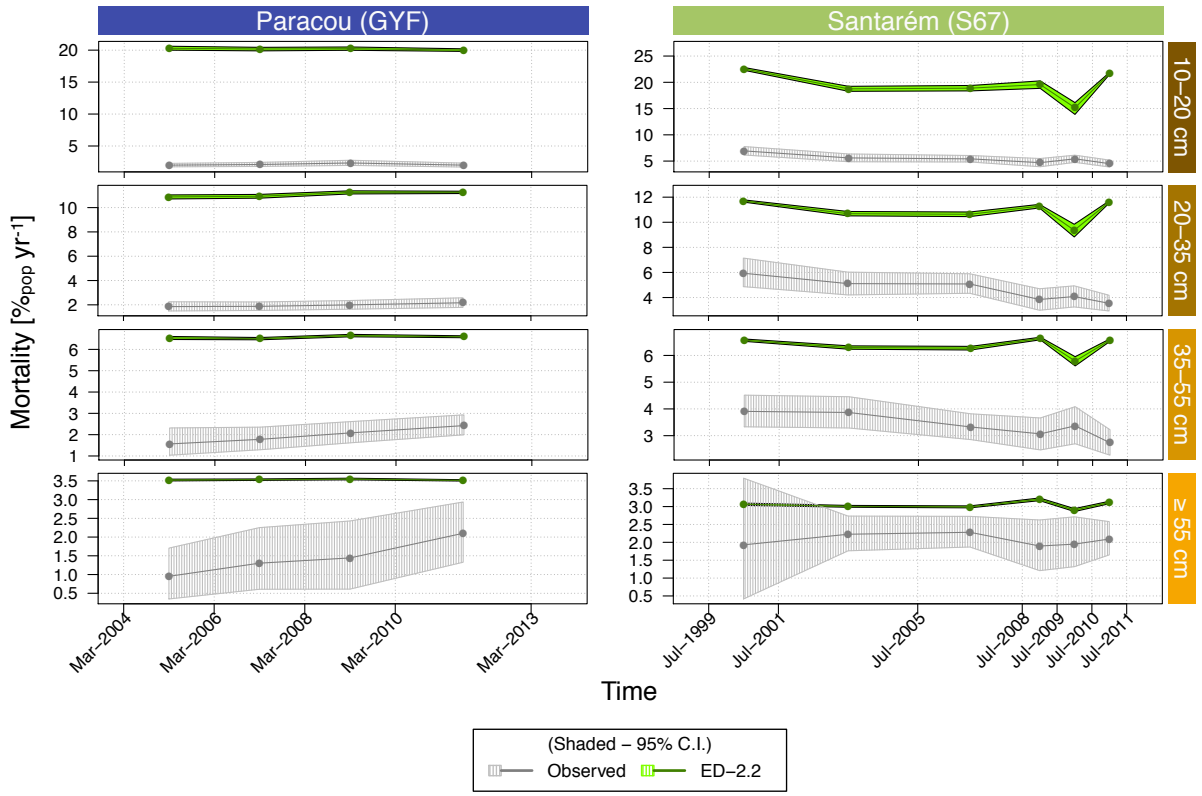

Figure F.6: Comparison between relative above-ground biomass growth rates from ED-2.2 and observations for early successional cohorts for (a) GYF and (b) S67, for drought deciduous simulations. Evergreen simulations had similar patterns and thus is not shown.

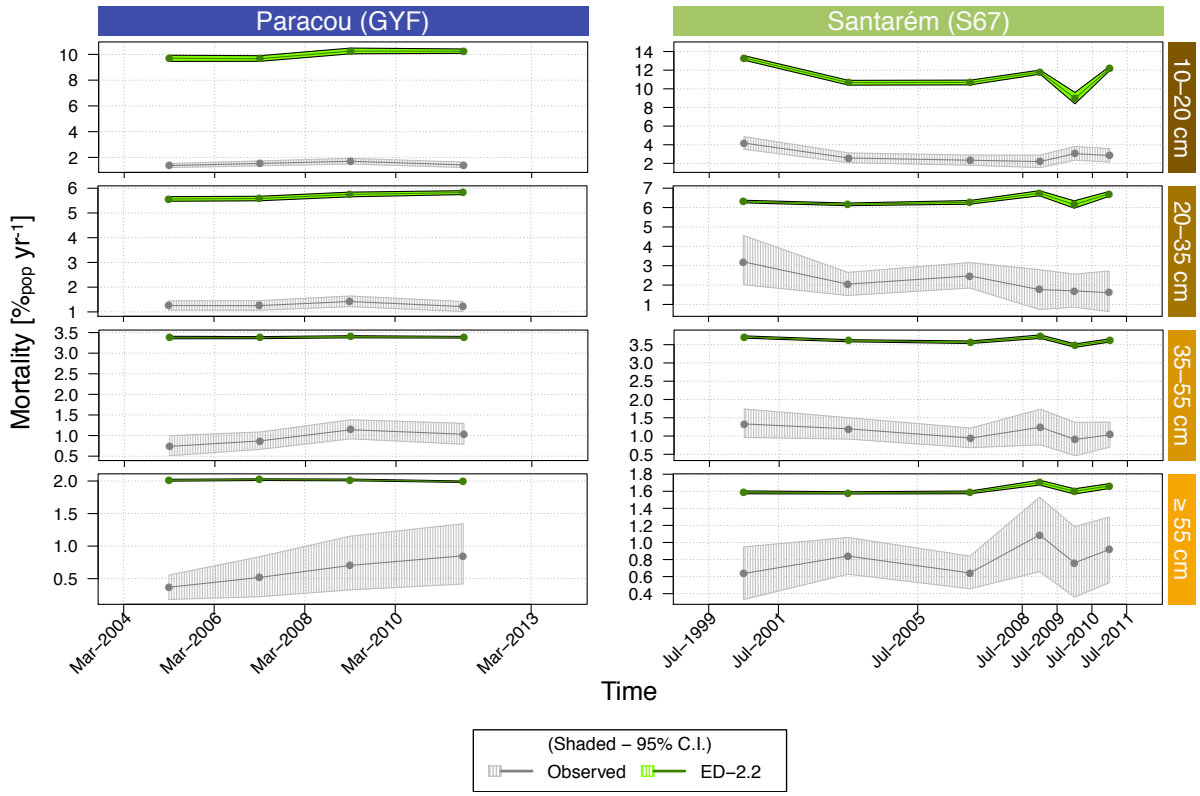

Figure F.7: Similar to Fig. F.7 but for mid-successional cohorts.

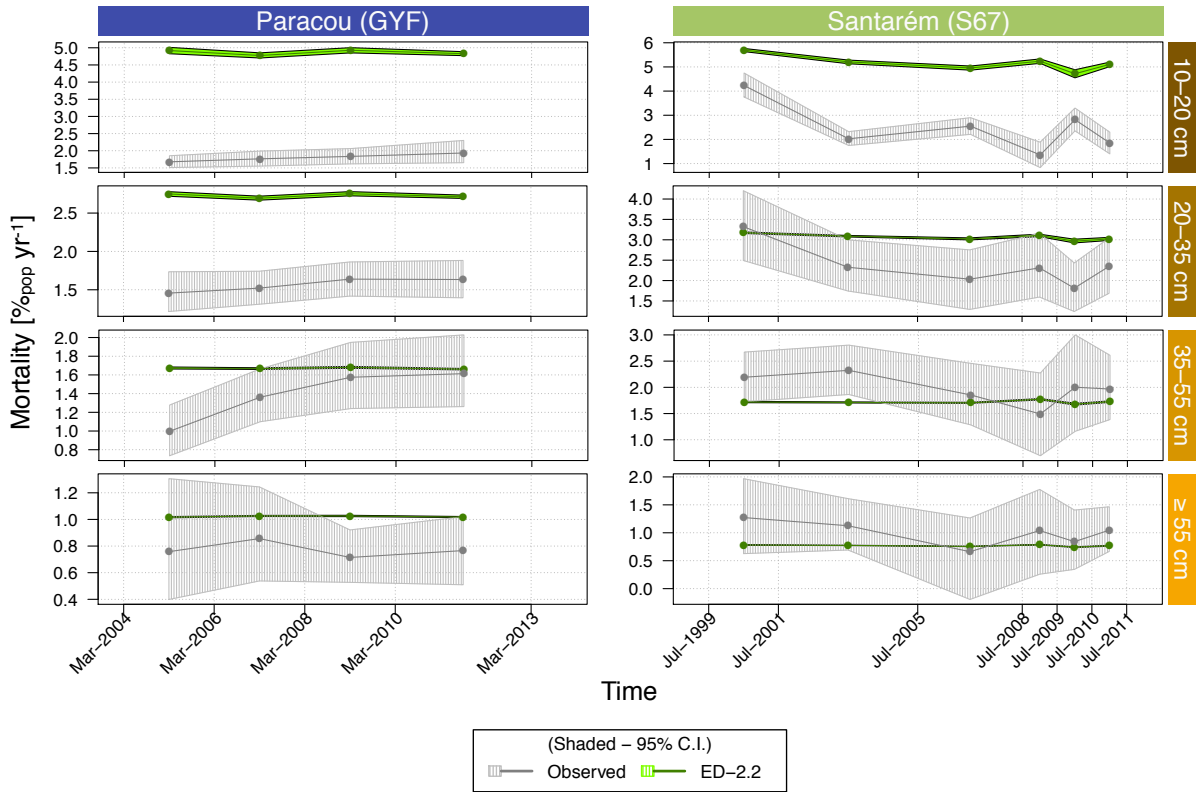

Figure F.8: Similar to Fig. F.7 but for late-successional cohorts.

Bibliography

Ainsworth, E. A. and Long, S. P.: What have we learned from 15 years of free-air CO_2 enrichment (FACE)? A meta-analytic review of the responses of photosynthesis, canopy properties and plant production to rising CO_2, New Phytol., 165, 351–372, doi:10.1111/j.1469-8137.2004.01224.x, 2005.

Albani, M., Medvigy, D., Hurtt, G. C., and Moorcroft, P. R.: The contributions of land-use change, CO2 fertilization, and climate variability to the Eastern US carbon sink, Glob. Change Biol., 12, 2370–2390, doi:10.1111/j.1365-2486.2006.01254.x, 2006.

Albini, F. A.: A Phenomenological Model for Wind Speed and Shear Stress Profiles in Vegetation Cover Layers, J. Appl. Meteor., 20, 1325–1335, doi:10.1175/1520-0450(1981)020<1325:APMFWS>2.0.CO;2, 1981.

Allen, C. D., Macalady, A. K., Chenchouni, H., Bachelet, D., McDowell, N., Vennetier, M., Kitzberger, T., Rigling, A., Breshears, D. D., Hogg, E. T., Gonzalez, P., Fensham, R., Zhang, Z., Castro, J., Demidova, N., Lim, J.-H., Allard, G., Running, S. W., Semerci, A., and Cobb, N.: A global overview of drought and heat-induced tree mortality reveals emerging climate change risks for forests, Forest Ecol. Manag., 259, 660–684, doi:10.1016/j.foreco.2009.09.001, 2010.

Amthor, J. S.: The role of maintenance respiration in plant growth, Plant Cell Environ., 7, 561–569, doi:10.1111/1365-3040.ep11591833, 1984.

Anderson, A. B.: White-Sand Vegetation of Brazilian Amazonia, Biotropica, 13, 199–210, doi:10.2307/2388125, 1981.

Anderson, L. O., Malhi, Y., Aragão, L. E. O. C., Ladle, R., Arai, E., Barbier, N., and Phillips, O.: Remote sensing detection of droughts in Amazonian forest canopies, New Phytol., 187, 733–750, doi:10.1111/j.1469-8137.2010.03355.x, 2010.

Andreae, M. O., Artaxo, P., Brandão, C., Carswell, F. E., Ciccioli, P., da Costa, A. L., Culf, A. D., Esteves, J. L., Gash, J. H. C., Grace, J., Kabat, P., Lelieveld, J., Malhi, Y., Manzi, A. O., Meixner, F. X., Nobre, A. D., Nobre, C., Ruivo, M. d. L. P., Silva-Dias, M. A., Stefani, P., Valentini, R., von Jouanne, J., and Waterloo, M. J.: Biogeochemical cycling of carbon, water, energy, trace gases, and aerosols in Amazonia: The LBA-EUSTACH experiments, J. Geophys. Res.-Atmos., 107, LBA 33–1–LBA 33–25, doi:10.1029/2001JD000524, 2002.

Antonarakis, A. S., Saatchi, S. S., Chazdon, R. L., and Moorcroft, P. R.: Using Lidar and Radar measurements to constrain predictions of forest ecosystem structure and function, Ecol. Appl., 21, 1120–1137, doi:10.1890/10-0274.1, 2011.

Aragão, L. E. O. C., Malhi, Y., Roman-Cuesta, R. M., Saatchi, S., Anderson, L. O., and Shimabukuro, Y. E.: Spatial patterns and fire response of recent Amazonian droughts, Geophys. Res. Lett., 34, L07 701, doi:10.1029/2006GL028946, 2007.

Araújo, A., Nobre, A., Kruijt, B., Elbers, J., Dallarosa, R., Stefani, P., von Randow, C., Manzi, A., Culf, A., Gash, J., Valentini, R., and Kabat, P.: Comparative measurements of carbon dioxide fluxes from two nearby towers in a central Amazonian rainforest: The Manaus LBA site, J. Geophys. Res.-Atmos., 107, 8090, doi:10.1029/2001JD000676, 2002.

Asner, G. P., Nepstad, D., Cardinot, G., and Ray, D.: Drought stress and carbon uptake in an Amazon forest measured with spaceborne imaging spectroscopy, Proc. Natl. Acad. Sci. U. S. A., 101, 6039–6044, doi:10.1073/pnas.0400168101, 2004.

Assunção, S. F. and Felfili, J. M.: Phytosociology of a cerrado sensu stricto fragment at the Paranoá Environmental Protection Area, Brasília, DF, Brazil, Acta Bot. Bras., 18, 903–909, doi:10.1590/S0102-33062004000400021, in Portuguese, 2004.

Avissar, R. and Mahrer, Y.: Mapping Frost-Sensitive Areas with a Three-Dimensional Local-Scale Numerical Model. Part I. Physical and Numerical Aspects, J. Appl. Meteor., 27, 400–413, doi:10.1175/1520-0450(1988)027<0400:MFSAWA>2.0.CO;2, 1988.

Azzalini, A.: The Skew-normal Distribution and Related Multivariate Families, Scand. J. Stat., 32, 159–188, doi:10.1111/j.1467-9469.2005.00426.x, 2005.

Azzalini, A.: R package `sn`: The skew-normal and skew-*t* distributions (version 0.4-17), URL `http://cran.r-project.org/web/packages/sn/index.html`, 2011.

Baccini, A., Goetz, S. J., Walker, W. S., Laporte, N. T., Sun, M., Sulla-Menashe, D., Hackler, J., Beck, P. S. A., Dubayah, R., Friedl, M. A., Samanta, S., and Houghton, R. A.: Estimated carbon dioxide emissions from tropical deforestation improved by carbon-density maps, Nature Clim. Change, 2, 182–185, 2012.

Baker, T. R., Phillips, O. L., Malhi, Y., Almeida, S., Arroyo, L., Di Fiore, A., Erwin, T., Killeen, T. J., Laurance, S. G., Laurance, W. F., Lewis, S. L., Lloyd, J., Monteagudo, A., Neill, D. A., Patiño, S., Pitman, N. C. A., M. Silva, J. N., and Vásquez Martínez, R.: Variation in wood density determines spatial patterns in Amazonian forest biomass, Glob. Change Biol., 10, 545–562, doi:10.1111/j.1365-2486.2004.00751.x, 2004.

Balch, J. K., Nepstad, D. C., Curran, L. M., Brando, P. M., Portela, O., Guilherme, P., Reuning-Scherer, J. D., and de Carvalho Jr., O.: Size, species, and fire behavior predict tree and liana mortality from experimental burns in the Brazilian Amazon, Forest Ecol. Manag., 261, 68 –77, doi:10.1016/j.foreco.2010.09.029, 2011.

Balch, J. K., Massad, T. J., Brando, P. M., Nepstad, D. C., and Curran, L. M.: Effects of high-frequency understorey fires on woody plant regeneration in southeastern Amazonian forests, Philos. Trans. R. Soc. B-Biol. Sci., 368, 20120 157, doi:10.1098/rstb.2012.0157, 2013.

Baldocchi, D. D., Hincks, B. B., and Meyers, T. P.: Measuring Biosphere-Atmosphere Exchanges of Biologically Related Gases with Micrometeorological Methods, Ecology, 69, 1331–1340, doi:10.2307/1941631, 1988.

Ball, J. T., Woodrow, I. E., and Berry, J. A.: A model predicting stomatal conductance and its contribution to the control of photosynthesis under different environmental conditions, in: Progress in photosynthesis research, edited by Biggins, J., vol. 4, pp. 221–224, Martinus Nijhoff Publishers, Dordrecht, 1987.

Baraloto, C., Goldberg, D. E., and Bonal, D.: Performance trade-offs among tropical tree seedlings in contrasting microhabitats, Ecology, 86, 2461–2472, doi:10.1890/04-1956, 2005.

Baraloto, C., Timothy Paine, C. E., Poorter, L., Beauchene, J., Bonal, D., Domenach, A.-M., Hérault, B., Patiño, S., Roggy, J.-C., and Chave, J.: Decoupled leaf and stem economics in rain forest trees, Ecol. Lett., 13, 1338–1347, doi:10.1111/j.1461-0248.2010.01517.x, 2010.

Barbosa, R. I., Campos, C., Pinto, F., and Fearnside, P. M.: The "Lavrados" of Roraima: biodiversity and conservation of Brazil's Amazonian savannas, Func. Ecosyst. Commun., 1, 29–41, 2007.

Beljaars, A. C. M. and Holtslag, A. A. M.: Flux Parameterization over Land Surfaces for Atmospheric Models, J. Appl. Meteor., 30, 327–341, doi:10.1175/1520-0450(1991)030<0327:FPOLSF>2.0.CO;2, 1991.

Best, M. J., Pryor, M., Clark, D. B., Rooney, G. G., Essery, R. L. H., Ménard, C. B., Edwards, J. M., Hendry, M. A., Porson, A., Gedney, N., Mercado, L. M., Sitch, S., Blyth, E., Boucher, O., Cox, P. M., Grimmond, C. S. B., and Harding, R. J.: The Joint UK Land Environment Simulator (JULES), model description – Part 1: Energy and water fluxes, Geosci. Model Dev., 4, 677–699, doi:10.5194/gmd-4-677-2011, 2011.

Beyrich, F., Leps, J.-P., Mauder, M., Bange, J., Foken, T., Huneke, S., Lohse, H., Lüdi, A., Meijninger, W., Mironov, D., Weisensee, U., and Zittel, P.: Area-averaged surface fluxes over the LITFASS region based on eddy-covariance measurements, Boundary-Layer Meteorol., 121, 33–65, doi:10.1007/s10546-006-9052-x, 2006.

Bitencourt, M. D., de Mesquita, Jr., H. N., Kuntschik, G., da Rocha, H. R., and Furley, P. A.: Cerrado vegetation study using optical and radar remote sensing: two Brazilian case studies, Can. J. Remote Sens., 33, 468–480, doi:10.5589/m07-054, 2007.

Blyth, E., Clark, D. B., Ellis, R., Huntingford, C., Los, S., Pryor, M., Best, M., and Sitch, S.: A comprehensive set of benchmark tests for a land surface model of simultaneous fluxes of water and carbon at both the global and seasonal scale, Geosci. Model Dev., 4, 255–269, doi:10.5194/gmd-4-255-2011, 2011.

Bolker, B. M., Pacala, S. W., and Parton, W. J.: Linear analysis of soil decomposition: insights from the CENTURY model, Ecol. Appl., 8, 425–439, doi:10.1890/1051-0761(1998)008[0425:LAOSDI]2.0.CO;2, 1998.

Bonal, D., Sabatier, D., Montpied, P., Tremeaux, D., and Guehl, J.-M.: Interspecific variability of δ^{13}C among trees in rainforests of French Guiana: functional groups and canopy integration, Oecologia, 124, 454–468, doi:10.1007/PL00008871, 2000.

Bonal, D., Bosc, A., Ponton, S., Goret, J.-Y., Burban, B., Gross, P., Bonnefond, J.-M., Elbers, J., Longdoz, B., Epron, D., Guehl, J.-M., and Granier, A.: Impact of severe dry season on net ecosystem exchange in the Neotropical rainforest of French Guiana, Glob. Change Biol., 14, 1917–1933, doi:10.1111/j.1365-2486.2008.01610.x, 2008.

Bonan, G. B.: Land-atmosphere CO2 exchange simulated by a land surface process model coupled to an atmospheric general circulation model, J. Geophys. Res.-Atmos., 100, 2817–2831, doi:10.1029/94JD02961, 1995.

Bonan, G. B.: Ecological Climatology, Cambridge Univ. Press, Cambridge, UK, 2nd edn., 2008.

Booth, B. B. B., Jones, C. D., Collins, M., Totterdell, I. J., Cox, P. M., Sitch, S., Huntingford, C., Betts, R. A., Harris, G. R., and Lloyd, J.: High sensitivity of future global warming to land carbon cycle processes, Environ. Res. Lett., 7, 024 002, doi:10.1088/1748-9326/7/2/024002, 2012.

Borchert, R.: Responses of Tropical Trees to Rainfall Seasonality and its Long-Term Changes, Climatic Change, 39, 381–393, doi:10.1023/A:1005383020063, 1998.

Borma, L. S., da Rocha, H. R., Cabral, O. M., von Randow, C., Collicchio, E., Kurzatkowski, D., Brugger, P. J., Freitas, H., Tannus, R., Oliveira, L., Renno, C. D., and Artaxo, P.: Atmosphere and hydrological controls of the evapotranspiration over a floodplain forest in the Bananal Island region, Amazonia, J. Geophys. Res.-Biogeosci., 114, G01 003, doi:10.1029/2007JG000641, 2009.

Botta, A., Viovy, N., Ciais, P., Friedlingstein, P., and Monfray, P.: A global prognostic scheme of leaf onset using satellite data, Glob. Change Biol., 6, 709–725, doi:10.1046/j.1365-2486.2000.00362.x, 2000.

Bréchet, L.: Contribution à l'étude de la variabilité spatiale des composantes du bilan de carbone d'un sol de forêt tropicale humide (Paracou, Guyane française), Ph.d. thesis, Université Henri Poincaré de Nancy, Nancy, Lorraine, France, URL `http://www.theses.fr/2009NAN10105`, in French, 2009.

Bréchet, L., Ponton, S., Alméras, T., Bonal, D., and Epron, D.: Does spatial distribution of tree size account for spatial variation in soil respiration in a tropical forest?., Plant Soil, 347, 293–303, doi:10.1007/s11104-011-0848-1, 2011.

Breshears, D. D., Myers, O. B., Meyer, C. W., Barnes, F. J., Zou, C. B., Allen, C. D., McDowell, N. G., and Pockman, W. T.: Tree die-off in response to global change-type drought: mortality insights from a decade of plant water potential measurements, Front. Ecol. Environ., 7, 185–189, doi:10.1890/080016, 2008.

Brito, E. R., Martins, S. V., de Oliveira-Filho, A. T., Silva, E., and da Silva, A. F.: Phytosociological structure of a natural fragment of floodplain forest in area of Campo Sujo, municipal district of Lagoa da Confusão, Tocantins, Brazil., Acta Amazonica, 38, 379–386, doi:10.1590/S0044-59672008000300002, in Portuguese, 2008.

Brooks, R. H. and Corey, A. T.: Hydraulic properties of porous media, Hydrology Papers 3, Colorado State University, Fort Collins, U.S.A., 1964.

Bruno, R. D., da Rocha, H. R., de Freitas, H. C., Goulden, M. L., and Miller, S. D.: Soil moisture dynamics in an eastern Amazonian tropical forest, Hydrol. Process., 20, 2477–2489, doi:10.1002/hyp.6211, 2006.

Bugmann, H.: A Review of Forest Gap Models, Climatic Change, 51, 259–305, doi:10.1023/A:1012525626267, 2001.

Businger, J. A., Wyngaard, J. C., Izumi, Y., and Bradley, E. F.: Flux-Profile Relationships in the Atmospheric Surface Layer, J. Atmos. Sci., 28, 181–189, doi:10.1175/1520-0469(1971)028<0181:FPRITA>2.0.CO;2, 1971.

Cabral, O. M. R., McWilliam, A.-L. C., and Roberts, J. M.: In-canopy microclimate of Amazonian forest and estimates of transpiration, in: Amazon deforestation and climate, edited by Gash, J. H. C., Nobre, C. A., Roberts, J. M., and Victoria, R. L., chap. 12, pp. 207–219, John Wiley & Sons, Inc., Chichester, West Sussex, United Kingdom, 1996.

Calixto Júnior, J. T.: Análise estrutural de duas fitofisionomias de caatinga em diferentes estados de conservaćão no semiárido pernambucano, Msc. thesis, Federal University of Campina Grande, Patos, PB, Brazil, in Portuguese, 2009.

Calvo-Alvarado, J. C., McDowell, N. G., and Waring, R. H.: Allometric relationships predicting foliar biomass and leaf area:sapwood area ratio from tree height in five Costa Rican rain forest species, Tree Physiol., 28, 1601–1608, doi:10.1093/treephys/28.11.1601, 2008.

Camillo, P. and Schmugge, T. J.: A computer program for the simulation of heat and moisture flow in soils, Technical Memorandum TM-82121, NASA, Greenbelt, United States, 1981.

Cardinale, B. J., Wright, J. P., Cadotte, M. W., Carroll, I. T., Hector, A., Srivastava, D. S., Loreau, M., and Weis, J. J.: Impacts of plant diversity on biomass production increase through time because of species complementarity, Proc. Natl. Acad. Sci. U. S. A., 104, 18 123–18 128, doi:10.1073/pnas.0709069104, 2007.

Carnicer, J., Coll, M., Ninyerola, M., Pons, X., Sánchez, G., and Peñuelas, J.: Widespread crown condition decline, food web disruption, and amplified tree mortality with increased climate change-type drought, Proc. Natl. Acad. Sci. U. S. A., 108, 1474–1478, doi:10.1073/pnas.1010070108, 2011.

Cavaleri, M. A., Oberbauer, S. F., and Ryan, M. G.: Wood CO_2 efflux in a primary tropical rain forest, Glob. Change Biol., 12, 2442–2458, doi:10.1111/j.1365-2486.2006.01269.x, 2006.

Cestaro, L. A.: Fragmentos de florestas Atlânticas no Rio Grande do Norte: relações estruturais, florísticas e fitogeográficas, Ph.d. thesis, Universidade Federal de São Carlos, São Carlos, SP, Brazil, URL http://www.bdtd.ufscar.br, in Portuguese, 2002.

Chambers, J. Q., Higuchi, N., Schimel, J. P., Ferreira, L. V., and Melack, J. M.: Decomposition and carbon cycling of dead trees in tropical forests of the central Amazon, Oecologia, 122, 380–388, doi:10.1007/s004420050044, 2000.

Chambers, J. Q., dos Santos, J., Ribeiro, R. J., and Higuchi, N.: Tree damage, allometric relationships, and above-ground net primary production in central Amazon forest, Forest Ecol. Manag., 152, 73–84, doi:10.1016/S0378-1127(00)00591-0, 2001.

Chambers, J. Q., Tribuzy, E. S., Toledo, L. C., Crispim, B. F., Higuchi, N., Santos, J. d., Araújo, A. C., Kruijt, B., Nobre, A. D., and Trumbore, S. E.: Respiration from a tropical forest ecosystem: partitioning of sources and low carbon use efficiency, Ecol. Appl., 14, S72–S88, doi:10.1890/01-6012, 2004.

Chambers, J. Q., Robertson, A. L., Carneiro, V. M. C., Lima, A. J. N., Smith, M.-L., Plourde, L. C., and Higuchi, N.: Hyperspectral remote detection of niche partitioning among canopy trees driven by blowdown gap disturbances in the Central Amazon, Oecologia, 160, 107–117, doi:10.1007/s00442-008-1274-9, URL http://dx.doi.org/10.1007/s00442-008-1274-9, 2009.

Chambers, J. Q., Negron-Juarez, R. I., Marra, D. M., Di Vittorio, A., Tews, J., Roberts, D., Ribeiro, G. H. P. M., Trumbore, S. E., and Higuchi, N.: The steady-state mosaic of disturbance and succession across an old-growth Central Amazon forest landscape, Proceedings of the National Academy of Sciences, 110, 3949–3954, doi:10.1073/pnas.1202894110, 2013.

Charney, J., Stone, P. H., and Quirk, W. J.: Drought in the Sahara: A Biogeophysical Feedback Mechanism, Science, 187, 434–435, doi:10.1126/science.187.4175.434, 1975.

Chave, J., Riéra, B., and Dubois, M.-A.: Estimation of biomass in a neotropical forest of French Guiana: spatial and temporal variability, J. Trop. Ecol., 17, 79–96, doi:10.1017/S0266467401001055, 2001.

Chave, J., Andalo, C., Brown, S., Cairns, M., Chambers, J., Eamus, D., Fölster, H., Fromard, F., Higuchi, N., Kira, T., Lescure, J.-P., Nelson, B., Ogawa, H., Puig, H., Riéra, B., and Yamakura, T.: Tree allometry and improved estimation of carbon stocks and balance in tropical forests, Oecologia, 145, 87–99, doi:10.1007/s00442-005-0100-x, 2005.

Chave, J., Coomes, D., Jansen, S., Lewis, S. L., Swenson, N. G., and Zanne, A. E.: Towards a worldwide wood economics spectrum, Ecol. Lett., 12, 351–366, doi:10.1111/j.1461-0248.2009.01285.x, 2009.

Chen, J. and Black, T.: Foliage area and architecture of plant canopies from sunfleck size distributions, Agric. For. Meteorol., 60, 249–266, doi:10.1016/0168-1923(92)90040-B, 1992.

Chen, M., Xie, P., Janowiak, J. E., and Arkin, P. A.: Global Land Precipitation: A 50-yr Monthly Analysis Based on Gauge Observations, J. Hydrometeor., 3, 249–266, doi:10.1175/1525-7541(2002)003<0249:GLPAYM>2.0.CO;2, 2002.

Christensen, J. H., Hewitson, B., Busuioc, A., Chen, A., Gao, X., Held, I., Jones, R., Kolli, R., Kwon, W.-T., Laprise, R., na Rueda, V. M., Mearns, L., Menéndez, C., Räisänen, J., Rinke, A., Sarr, A., and Whetton, P.: Regional climate projections, in: Climate change 2007: the physical science basis. Contribution of working group I to the fourth assessment report of the Intergovernmental Panel on Climate Change, edited by Solomon, S., Qin, D., Manning, M., Chen, Z., Marquis, M., Averyt, K. B., Tignor, M., and Miller, H. L., chap. 11, pp. 847–940, Cambridge Univ. Press, Cambridge, UK and New York, NY, USA, 2007.

Christoffersen, B. O.: The ecohydrological mechanisms of resilience and vulnerability of Amazonian tropical forests to water stress, Ph.d. dissertation, University of Arizona, Tucson, AZ, USA, URL http://hdl.handle.net/10150/293566, 2013.

Ciais, P., Gasser, T., Paris, J. D., Caldeira, K., Raupach, M. R., Canadell, J. G., Patwardhan, A., Friedlingstein, P., Piao, S. L., and Gitz, V.: Attributing the increase in atmospheric CO_2 to emitters and absorbers, Nature Clim. Change, 3, 926–930, URL http://dx.doi.org/10.1038/nclimate1942, 2013.

Clark, D. A., Clark, D. B., and Oberbauer, S. F.: Field-quantified responses of tropical rainforest aboveground productivity to increasing CO_2 and climatic stress, 1997–2009, J. Geophys. Res.-Biogeosci., 118, 783–794, doi:10.1002/jgrg.20067, 2013.

Clark, D. B., Mercado, L. M., Sitch, S., Jones, C. D., Gedney, N., Best, M. J., Pryor, M., Rooney, G. G., Essery, R. L. H., Blyth, E., Boucher, O., Harding, R. J., Huntingford, C., and Cox, P. M.: The Joint UK Land Environment Simulator (JULES), model description – Part 2: Carbon fluxes and vegetation dynamics, Geosci. Model Dev., 4, 701–722, doi:10.5194/gmd-4-701-2011, 2011.

Cleveland, C. C., Townsend, A. R., Taylor, P., Alvarez-Clare, S., Bustamante, M. M. C., Chuyong, G., Dobrowski, S. Z., Grierson, P., Harms, K. E., Houlton, B. Z., Marklein, A., Parton, W., Porder, S., Reed, S. C., Sierra, C. A., Silver, W. L., Tanner, E. V. J., and Wieder, W. R.: Relationships among net primary productivity, nutrients and climate in tropical rain forest: a pan-tropical analysis, Ecology Letters, 14, 1313–1317, doi:10.1111/j.1461-0248.2011.01711.x, 2011.

Cochrane, M. A.: Fire science for rainforests, Nature, 421, 913–919, doi:10.1038/nature01437, 2003.

Cochrane, M. A. and Barber, C. P.: Climate change, human land use and future fires in the Amazon, Glob. Change Biol., 15, 601–612, doi:10.1111/j.1365-2486.2008.01786.x, 2009.

Cole, T. G. and Ewel, J. J.: Allometric equations for four valuable tropical tree species, Forest Ecol. Manag., 229, 351–360, doi:10.1016/j.foreco.2006.04.017, 2006.

Collatz, G., Ribas-Carbo, M., and Berry, J.: Coupled Photosynthesis-Stomatal Conductance Model for Leaves of C_4 Plants, Aust. J. Plant Physiol., 19, 519–538, doi:10.1071/PP9920519, 1992.

Collatz, G. J., Ball, J., Grivet, C., and Berry, J. A.: Physiological and environmental regulation of stomatal conductance, photosynthesis and transpiration: a model that includes a laminar boundary layer, Agric. For. Meteorol., 54, 107 – 136, doi:10.1016/0168-1923(91)90002-8, 1991.

Condit, R., Hubbell, Stephen P., S., and Foster, R. B.: Mortality rates of 205 neotropical tree and shrub species and the impact of a severe drought, Ecological Monographs, 65, 419–439, doi:10.2307/2963497, 1995.

Cosby, B. J., Hornberger, G. M., Clapp, R. B., and Ginn, T. R.: A Statistical Exploration of the Relationships of Soil Moisture Characteristics to the Physical Properties of Soils, Water Resour. Res., 20, 682–690, doi:10.1029/WR020i006p00682, URL http://dx.doi.org/10.1029/WR020i006p00682, 1984.

Costa, M. H. and Foley, J. A.: A comparison of precipitation datasets for the Amazon basin, Geophys. Res. Lett., 25, 155–158, doi:10.1029/97GL03502, 1998.

Cowan, I. and Troughton, J.: The relative role of stomata in transpiration and assimilation, Planta, 97, 325–336, doi:10.1007/BF00390212, 1971.

Cox, P. M., Betts, R. A., Collins, M., Harris, P. P., Huntingford, C., and Jones, C. D.: Amazonian forest dieback under climate-carbon cycle projections for the 21st century, Theor. Appl. Climatol., 78, 137–156, doi:10.1007/s00704-004-0049-4, 2004.

Cox, P. M., Pearson, D., Booth, B. B., Friedlingstein, P., Huntingford, C., Jones, C. D., and Luke, C. M.: Sensitivity of tropical carbon to climate change constrained by carbon dioxide variability, Nature, 494, 341–344, doi:10.1038/nature11882, 2013.

Culf, A. D., Esteves, J. L., Marques Filho, A. O., and da Rocha, H. R.: Radiation, temperature and humidity over forest and pasture in Amazonia, in: Amazonian deforestation and climate, edited by Gash, J. H. C., Nobre, C. A., Roberts, J. M., and Victoria, R. L., chap. 10, pp. 175–192, John Wiley & Sons, Inc., Chichester, West Sussex, United Kingdom, 1996.

da Costa, A. C. L., Galbraith, D., Almeida, S., Portela, B. T. T., da Costa, M., de Athaydes Silva Junior, J. a., Braga, A. P., de Gonçalves, P. H. L., de Oliveira, A. A., Fisher, R., Phillips, O. L., Metcalfe, D. B., Levy, P., and Meir, P.: Effect of 7 yr of experimental drought on vegetation dynamics and biomass storage of an eastern Amazonian rainforest, New Phytol., 187, 579–591, doi:10.1111/j.1469-8137.2010.03309.x, 2010.

da Rocha, H. R., Freitas, H. C., Rosolem, R., Negron-Juarez, R. I. N., Tannus, R. N., Ligo, M. A., Cabral, O. M., and Silva Dias, M. A. a. F.: Measurements of CO2 exchange over a woodland savanna (Cerrado Sensu stricto) in southeast Brasil., Biota Neotropica, 2, URL http://www.biotaneotropica.org.br/v2n1/en/abstract?article+BN01702012002, 2002.

da Rocha, H. R., Manzi, A. O., Cabral, O. M., Miller, S. D., Goulden, M. L., Saleska, S. R., Coupe, N. R., Wofsy, S. C., Borma, L. S., Artaxo, P., Vourlitis, G., Nogueira, J. S., Cardoso, F. L., Nobre, A. D., Kruijt, B., Freitas, H. C., von Randow, C., Aguiar, R. G., and Maia, J. F.: Patterns of water and heat flux across a biome gradient from tropical forest to savanna in Brazil, J. Geophys. Res.-Biogeosci., 114, G00B12, doi:10.1029/2007JG000640, 2009a.

da Rocha, H. R., Manzi, A. O., and Shuttleworth, W. J.: Evapotranspiration, in: Amazonia and Global Change, edited by Keller, M., Bustamante, M., Gash, J., and Silva Dias, P. L., vol. 186 of *Geophysical Monograph*, chap. 16, pp. 261–272, American Geophysical Union, Washington, DC, USA, doi:10.1029/2008GM000817, 2009b.

Davidson, E. A. and Martinelli, L. A.: Nutrient limitations to secondary forest regrowth, in: Amazonia and global change, edited by Keller, M., Bustamante, M., Gash, J., and Silva Dias, P. L., vol. 186 of *Geophysical Monograph*, chap. 19, pp. 299–309, American Geophysical Union, doi:10.1029/2008GM000718, 2009.

Davidson, E. A., de Araújo, A. C., Artaxo, P., Balch, J. K., Brown, I. F., Bustamante, M. M. C., Coe, M. T., DeFries, R. S., Keller, M., Longo, M., Munger, J. W., Schroeder, W., Soares-Filho, B. S., Souza, Jr., C. M., and Wofsy, S. C.: The Amazon basin in transition, Nature, 481, 321–328, doi:10.1038/nature10717, 2012.

De Frenne, P., Rodríguez-Sánchez, F., Coomes, D. A., Baeten, L., Verstraeten, G., Vellend, M., Bernhardt-Römermann, M., Brown, C. D., Brunet, J., Cornelis, J., Decocq, G. M., Dierschke, H., Eriksson, O., Gilliam, F. S., Hédl, R., Heinken, T., Hermy, M., Hommel, P., Jenkins, M. A., Kelly, D. L., Kirby, K. J., Mitchell, F. J. G., Naaf, T., Newman, M., Peterken, G., Petřík, P., Schultz, J., Sonnier, G., Van Calster, H., Waller, D. M., Walther, G.-R., White, P. S., Woods, K. D., Wulf, M., Graae, B. J., and Verheyen, K.: Microclimate moderates plant responses to macroclimate warming, Proc. Natl. Acad. Sci. U. S. A., 110, 18 561–18 565, doi:10.1073/pnas.1311190110, 2013.

de Negreiros, G. H., Alencar, A. C., Schlesinger, P., Nepstad, D. C., and Lefebvre, P. A.: Pre-LBA RADAMBRASIL project data., doi:10.3334/ORNLDAAC/941, URL `http://daac.orln.gov`, 2009.

de Oliveira, M. B. L., Santos, A. J. B., Manzi, A. O., dos Santos Alvalá, R. C., de Fátima Correia, M., and de Moura, M. S. B.: Energy exchange and carbon fluxes between caatinga vegetation and the atmosphere in Northeastern Brazil, Rev. Brasil. Meteorol., 21, 378–386, in Portuguese, 2006.

Deardorff, J. W.: Efficient prediction of ground surface temperature and moisture, with inclusion of a layer of vegetation, Journal of Geophysical Research: Oceans, 83, 1889–1903, doi:10.1029/JC083iC04p01889, 1978.

Desai, A. R., Moorcroft, P. R., Bolstad, P. V., and Davis, K. J.: Regional carbon fluxes from an observationally constrained dynamic ecosystem model: Impacts of disturbance, CO_2 fertilization, and heterogeneous land cover, J. Geophys. Res.-Biogeosci., 112, G01 017, doi:10.1029/2006JG000264, URL `http://dx.doi.org/10.1029/2006JG000264`, 2007.

Dickinson, R., Henderson-Sellers, A., Kennedy, P., and Wilson, M.: Biosphere-atmosphere Transfer Scheme (BATS) for the NCAR Community Climate Model, Technical Note NCAR/TN-275+STR, NCAR, Boulder, CO, doi:10.5065/D6668B58, 1986.

Dietze, M. C., Vargas, R., Richardson, A. D., Stoy, P. C., Barr, A. G., Anderson, R. S., Arain, M. A., Baker, I. T., Black, T. A., Chen, J. M., Ciais, P., Flanagan, L. B., Gough, C. M., Grant, R. F., Hollinger, D., Izaurralde, R. C., Kucharik, C. J., Lafleur, P., Liu, S., Lokupitiya, E., Luo, Y., Munger, J. W., Peng, C., Poulter, B., Price, D. T., Ricciuto, D. M., Riley, W. J., Sahoo, A. K., Schaefer, K., Suyker, A. E., Tian, H., Tonitto, C., Verbeeck, H., Verma, S. B., Wang, W., and Weng, E.: Characterizing the performance of ecosystem models across time scales: A spectral analysis of the North American Carbon Program site-level synthesis, J. Geophys. Res.-Biogeosci., 116, G04 029, doi:10.1029/2011JG001661, 2011.

Dilley, A. C. and O'Brien, D. M.: Estimating downward clear sky long-wave irradiance at the surface from screen temperature and precipitable water, Quart. J. Royal Meteorol. Soc., 124, 1391–1401, doi:10.1002/qj.49712454903, 1998.

Domingues, T. F., Berry, J. A., Martinelli, L. A., Ometto, J. P. H. B., and Ehleringer, J. R.: Parameterization of Canopy Structure and Leaf-Level Gas Exchange for an Eastern Amazonian Tropical Rain Forest (Tapajós National Forest, Pará, Brazil), Earth Interact., 9, 1–23, doi:10.1175/EI149.1, 2005.

Doughty, C. E. and Goulden, M. L.: Seasonal patterns of tropical forest leaf area index and CO_2 exchange, J. Geophys. Res.-Biogeosci., 113, G00B06, doi:10.1029/2007JG000590, 2008.

Dufour, L. and van Mieghem, J.: Thermodynamique de l'Atmosphère, Institut Royal Météorologique de Belgique, Gembloux, Belgium, 2 edn., in French, 1975.

Elvidge, C., Hobson, V., Baugh, K., Dietz, J., Shimabukuro, Y., Krug, T., Novo, E., and Echavarria, F.: DMSP-OLS estimation of tropical forest area impacted by surface fires in Roraima, Brazil: 1995 versus 1998, Int. J. Remote Sens., 22, 2661–2673, doi:10.1080/01431160120888, 2001.

Enquist, B. J. and Enquist, C. A. F.: Long-term change within a Neotropical forest: assessing differential functional and floristic responses to disturbance and drought, Glob. Change Biol., 17, 1408–1424, doi:10.1111/j.1365-2486.2010.02326.x, 2011.

Epron, D., Bosc, A., Bonal, D., and Freycon, V.: Spatial variation of soil respiration across a topographic gradient in a tropical rain forest in French Guiana, J. Trop. Ecol., 22, 565–574, doi:10.1017/S0266467406003415, 2006.

Evans, M. R.: Modelling ecological systems in a changing world, Philos. Trans. R. Soc. B-Biol. Sci., 367, 181–190, doi:10.1098/rstb.2011.0172, 2012.

Farquhar, G., Caemmerer, S., and Berry, J.: A biochemical model of photosynthetic CO2 assimilation in leaves of C3 species, Planta, 149, 78–90, doi:10.1007/BF00386231, 1980.

Fauset, S., Baker, T. R., Lewis, S. L., Feldpausch, T. R., Affum-Baffoe, K., Foli, E. G., Hamer, K. C., and Swaine, M. D.: Drought-induced shifts in the floristic and functional composition of tropical forests in Ghana, Ecol. Lett., 15, 1120–1129, doi:10.1111/j.1461-0248.2012.01834.x, 2012.

Feeley, K. J., Davies, S. J., Perez, R., Hubbell, S. P., and Foster, R. B.: Directional changes in the species composition of a tropical forest, Ecology, 92, 871–882, doi:10.1890/10-0724.1, 2011.

Feldpausch, T. R., Lloyd, J., Lewis, S. L., Brienen, R. J. W., Gloor, M., Monteagudo Mendoza, A., Lopez-Gonzalez, G., Banin, L., Abu Salim, K., Affum-Baffoe, K., Alexiades, M., Almeida, S., Amaral, I., Andrade, A., Aragão, L. E. O. C., Araujo Murakami, A., Arets, E. J. M. M., Arroyo, L., Aymard C., G. A., Baker, T. R., Bánki, O. S., Berry, N. J., Cardozo, N., Chave, J., Comiskey, J. A., Alvarez, E., de Oliveira, A., Di Fiore, A., Djagbletey, G., Domingues, T. F., Erwin, T. L., Fearnside, P. M., França, M. B., Freitas, M. A., Higuchi, N., Honorio, E., Iida, Y., Jiménez, E., Kassim, A. R., Killeen, T. J., Laurance, W. F., Lovett, J. C., Malhi, Y., Marimon, B. S., Marimon-Junior, B. H., Lenza, E., Marshall, A. R., Mendoza, C., Metcalfe, D. J., Mitchard, E. T. A., Neill, D. A., Nelson, B. W., Nilus, R., Nogueira, E. M., Parada, A., Peh, K. S.-H., Pena Cruz, A., Peñuela, M. C., Pitman, N. C. A., Prieto, A., Quesada, C. A., Ramírez, F., Ramírez-Angulo, H., Reitsma, J. M., Rudas, A., Saiz, G., Salomão, R. P., Schwarz, M., Silva, N., Silva-Espejo, J. E., Silveira, M., Sonké, B., Stropp, J., Taedoumg, H. E., Tan, S., ter Steege, H., Terborgh, J., Torello-Raventos, M., van der Heijden, G. M. F., Vásquez, R., Vilanova, E., Vos, V. A., White, L., Willcock, S., Woell, H., and Phillips, O. L.: Tree height integrated into pantropical forest biomass estimates, Biogeosciences, 9, 3381–3403, doi:10.5194/bg-9-3381-2012, 2012.

Ferreira, J. N., Bustamante, M., Garcia-Montiel, D. C., Caylor, K. K., and Davidson, E. A.: Spatial variation in vegetation structure coupled to plant available water determined by two-dimensional soil resistivity profiling in a Brazilian savanna, Oecologia, 153, 417–430, doi:10.1007/s00442-007-0747-6, 2007.

Fine, P. V. A., Miller, Z. J., Mesones, I., Irazuzta, S., Appel, H. M., Stevens, M. H. H., Sääksjärvi, I., Schultz, J. C., and Coley, P. D.: The growth-defense trade-off and habitat specialization by plants in Amazonian forests, Ecology, 87, S150–S162, doi:10.1890/0012-9658(2006)87[150:TGTAHS]2.0.CO;2, 2006.

Fisher, R., McDowell, N., Purves, D., Moorcroft, P., Sitch, S., Cox, P., Huntingford, C., Meir, P., and Ian Woodward, F.: Assessing uncertainties in a second-generation dynamic vegetation model caused by ecological scale limitations, New Phytol., 187, 666–681, doi:10.1111/j.1469-8137.2010.03340.x, 2010.

Fitzjarrald, D. R. and Sakai, R. K.: LBA-ECO CD-03 Flux-Meteorological Data, km 77 Pasture Site, Para, Brazil: 2000-2005. Data set., doi:10.3334/ORNLDAAC/962, URL `http://daac.ornl.gov`, oak Ridge National Laboratory Distributed Active Archive Center, Oak Ridge, Tennessee, U.S.A., 2010.

Fitzjarrald, D. R., Sakai, R. K., and de Moraes, O. L. L.: LBA-ECO CD-03 Mesoscale Meteorological Data, Santarem Region, Para, Brazil: 1998-2006. Data set., doi:10.3334/ORNLDAAC/944, URL `http://daac.ornl.gov`, oak Ridge National Laboratory Distributed Active Archive Center, Oak Ridge, Tennessee, U.S.A., 2009.

Flerchinger, G. N., Xaio, W., Marks, D., Sauer, T. J., and Yu, Q.: Comparison of algorithms for incoming atmospheric long-wave radiation, Water Resources Research, 45, doi:10.1029/2008WR007394, 2009.

Foken, T.: 50 Years of the Monin–Obukhov Similarity Theory, Boundary-Layer Meteorol., 119, 431–447, doi:10.1007/s10546-006-9048-6, 2006.

Foley, J. A., Prentice, I. C., Ramankutty, N., Levis, S., Pollard, D., Sitch, S., and Haxeltine, A.: An integrated biosphere model of land surface processes, terrestrial carbon balance, and vegetation dynamics, Global Biogeochem. Cycles, 10, 603–628, doi:10.1029/96GB02692, 1996.

Forest Products Laboratory: Wood handbook - wood as an engineering material, General Technical Report FPL-GTR-190, U.S. Department of Agriculture, Madison, WI, URL http://www.fpl.fs.fed.us/products/publications/specific_pub.php?posting$_$id=18102$&$header$_$id$=$p, 2010.

Fortunel, C., Fine, P. V. A., and Baraloto, C.: Leaf, stem and root tissue strategies across 758 Neotropical tree species, Funct. Ecol., 26, 1153–1161, doi:10.1111/j.1365-2435.2012.02020.x, 2012.

Friedlingstein, P., Cox, P., Betts, R., Bopp, L., von Bloh, W., Brovkin, V., Cadule, P., Doney, S., Eby, M., Fung, I., Bala, G., John, J., Jones, C., Joos, F., Kato, T., Kawamiya, M., Knorr, W., Lindsay, K., Matthews, H. D., Raddatz, T., Rayner, P., Reick, C., Roeckner, E., Schnitzler, K. G., Schnur, R., Strassmann, K., Weaver, A. J., Yoshikawa, C., and Zeng, N.: Climate–Carbon Cycle Feedback Analysis: Results from the C^4MIP Model Intercomparison, J. Clim., 19, 3337–3353, doi:10.1175/JCLI3800.1, 2006.

Fu, R., Yin, L., Li, W., Arias, P. A., Dickinson, R. E., Huang, L., Chakraborty, S., Fernandes, K., Liebmann, B., Fisher, R., and Myneni, R. B.: Increased dry-season length over southern Amazonia in recent decades and its implication for future climate projection, Proc. Natl. Acad. Sci. U. S. A., 110, 18 110–18 115, doi:10.1073/pnas.1302584110, 2013.

Garcia-Montiel, D. C., Coe, M. T., Cruz, M. P., Ferreira, J. N., da Silva, E. M., and Davidson, E. A.: Estimating Seasonal Changes in Volumetric Soil Water Content at Landscape Scales in a Savanna Ecosystem Using Two-Dimensional Resistivity Profiling, Earth Interact., 12, 1–25, doi:10.1175/2007EI238.1, 2008.

Gash, J. H. C., Nobre, C. A., Roberts, J. M., and Victoria, R. L.: An overview of ABRACOS, in: Amazon deforestation and climate, edited by Gash, J. H. C., Nobre, C. A., Roberts, J. M., and Victoria, R. L., chap. 1, pp. 1–14, John Wiley & Sons, Inc., Chichester, West Sussex, United Kingdom, 1996.

Good, P., Jones, C., Lowe, J., Betts, R., Booth, B., and Huntingford, C.: Quantifying Environmental Drivers of Future Tropical Forest Extent, J. Clim., 24, 1337–1349, doi:10.1175/2010JCLI3865.1, 2011.

Goudriaan, J.: Crop meteorology: a simulation study, Ph.D. thesis, Wageningen University and Research Centre, Wageningen, Netherlands, 1977.

Goulden, M. L., Munger, J. W., Fan, S.-M., Daube, B. C., and Wofsy, S. C.: Measurements of carbon sequestration by long-term eddy covariance: methods and a critical evaluation of accuracy, Glob. Change Biol., 2, 169–182, doi:10.1111/j.1365-2486.1996.tb00070.x, 1996.

Gourlet-Fleury, S., Ferry, B., Molino, J.-F., Petronelli, P., and Schmitt, L.: Experimental Plots: Key Features, in: Ecology and Management of a Neotropical Rainforest: Lessons Drawn from

Paracou, a Long-term Experimental Research Site in French Guiana, edited by Gourlet-Fleury, S., Marc Guehl, J., and Laroussinie, O., chap. I–1, pp. 3–60, Elsevier, Paris, 2004.

Gu, L., Falge, E. M., Boden, T., Baldocchi, D. D., Black, T., Saleska, S. R., Suni, T., Verma, S. B., Vesala, T., Wofsy, S. C., and Xu, L.: Objective threshold determination for nighttime eddy flux filtering, Agric. For. Meteorol., 128, 179–197, doi:10.1016/j.agrformet.2004.11.006, 2005.

Gu, L., Meyers, T., Pallardy, S. G., Hanson, P. J., Yang, B., Heuer, M., Hosman, K. P., Liu, Q., Riggs, J. S., Sluss, D., and Wullschleger, S. D.: Influences of biomass heat and biochemical energy storages on the land surface fluxes and radiative temperature, J. Geophys. Res., 112, D02 107, doi:10.1029/2006JD007425, 2007.

Harris, I., Jones, P. D., Osborn, T. J., and Lister, D. H.: Updated high-resolution grids of monthly climatic observations – the CRU TS3.10 dataset, Intl. J. Climatol., doi:10.1002/joc.3711, 2013.

Haxeltine, A. and Prentice, I. C.: BIOME3: An equilibrium terrestrial biosphere model based on ecophysiological constraints, resource availability, and competition among plant functional types, Global Biogeochem. Cycles, 10, 693–709, doi:10.1029/96GB02344, 1996.

Hirota, M., Holmgren, M., Van Nes, E. H., and Scheffer, M.: Global Resilience of Tropical Forest and Savanna to Critical Transitions, Science, 334, 232–235, doi:10.1126/science.1210657, 2011.

Holdridge, L. R.: Determination of World Plant Formations from Simple Climatic Data, Science, 105, 367–368, doi:10.1126/science.105.2727.367, 1947.

Hooper, D. U., Solan, M., Symstad, A., Diaz, S., Gessner, M. O., Buchmann, N., Degrange, V., Grime, P., Hulot, F., Mermillod-Bolondin, F., Roy, J., Spehn, E., and van Peer, L.: Species diversity, functional diversity, and ecosystem functioning, in: Biodiversity and ecosystem functioning: synthesis and perspectives, edited by Loreau, M., Naeem, S., and Inchausti, P., chap. 17, pp. 195–208, Oxford University Press, Oxford, U.K., 2002.

Hörmann, G., Irrgan, S., Jochheim, H., Lukes, M., Meesenburg, H., Müller, J., Scheler, B., Scherzer, J., Schüler, G., Schultze, B., Strohbach, B., Suckow, F., Wegehenkel, M., and Wessolek, G.: Wasserhaushalt von Waldökosystemen: methodenleitfaden zur bestimmung der wasserhaushaltskomponenten auf level II-Flächen, Technical note, Bundesministerium für Verbraucherschutz, Ernährung und Landwirtschaft (BMVEL), Bonn, Germany, URL `http://www.wasklim.de/download/Methodenband.pdf`, in German, 2003.

Hubbell, S. P., He, F., Condit, R., Borda-de Água, L., Kellner, J., and ter Steege, H.: How many tree species and how many of them are there in the Amazon will go extinct?, Proc. Natl. Acad. Sci. U. S. A., 105, 11 498–11 504, doi:10.1073/pnas.0801915105, 2008.

Huffman, G. J., Adler, R. F., Bolvin, D. T., and Gu, G.: Improving the global precipitation record: GPCP Version 2.1, Geophys. Res. Lett., 36, L17 808, doi:10.1029/2009GL040000, 2009.

Hughes, J. K., Valdes, P. J., and Betts, R. A.: Dynamical properties of the TRIFFID dynamic global vegetation model, Technical Note HCTN, No. 56, U.K. Met Office Hadley Centre, Exeter, U. K., 2004.

Huntingford, C., Zelazowski, P., Galbraith, D., Mercado, L. M., Sitch, S., Fisher, R., Lomas, M., Walker, A. P., Jones, C. D., Booth, B. B. B., Malhi, Y., Hemming, D., Kay, G., Good, P., Lewis, S. L., Phillips, O. L., Atkin, O. K., Lloyd, J., Gloor, E., Zaragoza-Castells, J., Meir, P., Betts, R., Harris, P. P., Nobre, C., Marengo, J., and Cox, P. M.: Simulated resilience of tropical rainforests to CO2-induced climate change, Nature Geosci., 6, 268–273, doi:10.1038/ngeo1741, 2013.

Hurtt, G. C., Pacala, S. W., Moorcroft, P. R., Caspersen, J., Shevliakova, E., Houghton, R. A., and Moore, B.: Projecting the future of the U.S. carbon sink, Proc. Natl. Acad. Sci. U. S. A., 99, 1389–1394, doi:10.1073/pnas.012249999, 2002.

Hutyra, L. R.: Carbon and water exchange in Amazonian rainforests, Ph.d. dissertation, Harvard University, Cambridge, MA, 2007.

Hutyra, L. R., Munger, J. W., Nobre, C. A., Saleska, S. R., Vieira, S. A., and Wofsy, S. C.: Climatic variability and vegetation vulnerability in Amazônia, Geophys. Res. Lett., 32, L24 712, doi:10.1029/2005GL024981, 2005.

Hutyra, L. R., Munger, J. W., Saleska, S. R., Gottlieb, E., Daube, B. C., Dunn, A. L., Amaral, D. F., de Camargo, P. B., and Wofsy, S. C.: Seasonal controls on the exchange of carbon and water in an Amazonian rain forest, J. Geophys. Res.-Biogeosci., 112, G03 008, doi:10.1029/2006JG000365, 2007.

Hutyra, L. R., Munger, J. W., Gottlieb, E. W., Daube, B. C., Camargo, P. B., and Wofsy, S. C.: LBA-ECO CD-10 H_2O profiles at km 67 tower site, Tapajós National Forest, doi:10.3334/ORNLDAAC/861, URL `http://daac.ornl.gov`, oak Ridge National Laboratory Distributed Active Archive Center, Oak Ridge, Tennessee, U.S.A., 2008.

Idso, S.: A set of equations for full spectrum and 8- to 14-μm and 10.5- to 12.5-μm thermal radiation from cloudless skies, Water Resources Research, 17, 295–304, doi:10.1029/WR017i002p00295, 1981.

Idso, S. and Jackson, R.: Thermal radiation from atmosphere, Journal of Geophysical Research, 74, 5397–5403, doi:10.1029/JC074i023p05397, 1969.

INMET: Historical data from the Brazilian National Institute of Meteorology weather station network (BDMEP/INMET), URL `http://www.inmet.gov.br/portal/index.php?r=bdmep/bdmep`, in Portuguese, 2013.

IPCC: Summary for policymakers, in: Climate change 2007: the physical science basis. Contribution of working group I to the fourth assessment report of the Intergovernmental Panel on Climate Change, edited by Solomon, S., Qin, D., Manning, M., Chen, Z., Marquis, M., Averyt, K. B., and Miller, H. L., pp. 1–18, Cambridge Univ. Press, Cambridge, UK and New York, NY, USA, 2007.

IPCC: Summary for policymakers, in: Climate change 2013: the physical science basis. Contribution of working group I to the fifth assessment report of the Intergovernmental Panel on Climate Change, edited by Stocker, T. F., Qin, D., Plattner, G.-K., Tignor, M., Allen, S. K., Boschung, J., Nauels, A., Xia, Y., Bex, V., and Midgley, P. M., pp. 1–33, Cambridge Univ. Press, Cambridge, UK and New York, NY, USA, 2013.

Ise, T. and Moorcroft, P. R.: Simulating boreal forest dynamics from perspectives of ecophysiology, resource availability, and climate change, Ecol. Res., 25, 501–511, doi:10.1007/s11284-009-0680-8, 2010.

Ivanov, V. Y., Hutyra, L. R., Wofsy, S. C., Munger, J. W., Saleska, S. R., de Oliveira, R. C., and de Camargo, P. B.: Root niche separation can explain avoidance of seasonal drought stress and vulnerability of overstory trees to extended drought in a mature Amazonian forest, Water Resour. Res., 48, W12 507, doi:10.1029/2012WR011972, 2012.

Jiménez, E. M., Moreno, F. H., Peñuela, M. C., Patiño, S., and Lloyd, J.: Fine root dynamics for forests on contrasting soils in the Colombian Amazon, Biogeosciences, 6, 2809–2827, doi:10.5194/bg-6-2809-2009, 2009.

Jin, J., Gao, X., Sorooshian, S., Yang, Z.-L., Bales, R., Dickinson, R. E., Sun, S.-F., and Wu, G.-X.: One-dimensional snow water and energy balance model for vegetated surfaces, Hydrological Processes, 13, 2467–2482, doi:10.1002/(SICI)1099-1085(199910)13:14/15<2467::AID-HYP861>3.0.CO;2-J, 1999.

Jones, C., Lowe, J., Liddicoat, S., and Betts, R.: Committed terrestrial ecosystem changes due to climate change, Nature Geosci., 2, 484–487, doi:10.1038/ngeo555, 2009.

Jones, C., Robertson, E., Arora, V., Friedlingstein, P., Shevliakova, E., Bopp, L., Brovkin, V., Hajima, T., Kato, E., Kawamiya, M., Liddicoat, S., Lindsay, K., Reick, C. H., Roelandt, C., Segschneider, J., and Tjiputra, J.: Twenty-First-Century Compatible CO_2 Emissions and Airborne Fraction Simulated by CMIP5 Earth System Models under Four Representative Concentration Pathways, J. Clim., 26, 4398–4413, doi:10.1175/JCLI-D-12-00554.1, 2013.

Jucker, T. and Coomes, D. A.: Comment on "Plant Species Richness and Ecosystem Multifunctionality in Global Drylands", Science, 337, 155, doi:10.1126/science.1220473, 2012.

Jung, M., Reichstein, M., Ciais, P., Seneviratne, S. I., Sheffield, J., Goulden, M. L., Bonan, G., Cescatti, A., Chen, J., de Jeu, R., Dolman, A. J., Eugster, W., Gerten, D., Gianelle, D., Gobron, N., Heinke, J., Kimball, J., Law, B. E., Montagnani, L., Mu, Q., Mueller, B., Oleson, K., Papale, D., Richardson, A. D., Roupsard, O., Running, S., Tomelleri, E., Viovy, N., Weber, U., Williams, C., Wood, E., Zaehle, S., and Zhang, K.: Recent decline in the global land evapotranspiration trend due to limited moisture supply, Nature, 467, 951–954, doi:10.1038/nature09396, 2010.

Keller, M., Palace, M., Asner, G. P., Pereira, R., and Silva, J. N. M.: Coarse woody debris in undisturbed and logged forests in the Eastern Brazilian Amazon, Glob. Change Biol., 10, 784–795, doi:10.1111/j.1529-8817.2003.00770.x, 2004a.

Keller, M., Silva Dias, M. A. F., Nepstad, D. C., and Andreae, M. O.: The Large-Scale Biosphere Atmosphere Experiment in Amazonia: analyzing regional land use effects, in: Ecosystems and land use changes, edited by DeFries, R. S., Asner, G. P., and Houghton, R. A., vol. 153 of *Geophysical Monograph*, chap. 23, pp. 321–336, American Geophysical Union, Washington, DC, USA, 2004b.

Killeen, T. J., Jardim, A., Mamani, F., and Rojas, N.: Diversity, composition and structure of a tropical semideciduous forest in the Chiquitanía region of Santa Cruz, Bolivia, J. Trop. Ecol., 14, 803–827, doi:10.1017/S0266467498000583, 1998.

Kim, Y., Knox, R. G., Longo, M., Medvigy, D., Hutyra, L. R., Pyle, E. H., Wofsy, S. C., Bras, R. L., and Moorcroft, P. R.: Seasonal carbon dynamics and water fluxes in an Amazon rainforest, Glob. Change Biol., 18, 1322–1334, doi:10.1111/j.1365-2486.2011.02629.x, 2012.

Kimball, B., Idso, S., and Aase, J.: A model of thermal-radiation from partly cloudy and overcast skies, Water Resources Research, 18, 931–936, doi:10.1029/WR018i004p00931, 1982.

King, D. A., Davies, S. J., Tan, S., and Noor, N. S. M.: The role of wood density and stem support costs in the growth and mortality of tropical trees, J. Ecol, 94, 670–680, doi:10.1111/j.1365-2745.2006.01112.x, 2006.

Knox, R. G.: Land conversion in Amazonia and Northern South America; influences on regional hydrology and ecosystem response, Ph.d. dissertation, Massachusetts Institute of Technology, Cambridge, MA, 2012.

Knox, R. G., Longo, M., Swann, A. L. S., Zhang, K., Levine, N. M., Moorcroft, P. R., and Bras, R. L.: Effects of land-conversion in a biosphere–atmosphere model of Northern South America – Part 1: regional differences in hydrometeorology, Hydrol. Earth Syst. Sci. Discuss., 10, 15 295–15 335, doi:10.5194/hessd-10-15295-2013, 2013a.

Knox, R. G., Longo, M., Swann, A. L. S., Zhang, K., Levine, N. M., Moorcroft, P. R., and Bras, R. L.: Effects of land-conversion in a biosphere–atmosphere model of Northern South America – Part 2: case studies on the mechanisms of differential hydrometeorology, Hydrol. Earth Syst. Sci. Discuss., 10, 15 337–15 373, doi:10.5194/hessd-10-15337-2013, 2013b.

Koch, S., des Jardins, M., and Kocin, P.: An interactive barnes objective map analysis scheme for use with satellite and conventional data, J. Clim. Appl. Meteor., 22, 1487–1503, doi:10.1175/1520-0450(1983)022<1487:AIBOMA>2.0.CO;2, 1983.

Kondrashov, D. and Ghil, M.: Spatio-temporal filling of missing points in geophysical data sets, Nonlinear Proc. Geoph., 13, 151–159, doi:10.5194/npg-13-151-2006, 2006.

Körner, C.: Slow in, Rapid out–Carbon Flux Studies and Kyoto Targets, Science, 300, 1242–1243, doi:10.1126/science.1084460, 2003.

Körner, C.: Responses of Humid Tropical Trees to Rising CO2, Annu. Rev. Ecol. Evol. Syst., 40, 61–79, doi:10.1146/annurev.ecolsys.110308.120217, 2009.

Kraft, N. J. B., Metz, M. R., Condit, R. S., and Chave, J.: The relationship between wood density and mortality in a global tropical forest data set, New Phytol., 188, 1124–1136, doi:10.1111/j.1469-8137.2010.03444.x, 2010.

Kruijt, B., Elbers, J. A., von Randow, C., Araújo, A. C., Oliveira, P. J., Culf, A., Manzi, A. O., Nobre, A. D., Kabat, P., and Moors, E. J.: The Robustness of Eddy Correlation Fluxes for Amazon Rain Forest Conditions, Ecological Applications, 14, S101–S113, doi:10.2307/4493633, URL http://www.jstor.org/stable/4493633, 2004.

Lambers, H., Chapin III, F. S., and Pons, T. L.: Plant physiological ecology, Springer, New York, U.S.A., 2nd edn., doi:10.1007/978-0-387-78341-3, 2008.

Lapola, D. M., Oyama, M. D., and Nobre, C. A.: Exploring the range of climate biome projections for tropical South America: The role of CO_2 fertilization and seasonality, Global Biogeochem. Cycles, 23, GB3003, doi:10.1029/2008GB003357, 2009.

Laurance, W. F., Fearnside, P. M., Laurance, S. G., Delamonica, P., Lovejoy, T. E., de Merona, J. M. R., Chambers, J. Q., and Gascon, C.: Relationship between soils and Amazon forest biomass: a landscape-scale study, Forest Ecol. Manag., 118, 127–138, doi:10.1016/S0378-1127(98)00494-0, 1999.

Lee, T. J. and Pielke, R. A.: Estimating the Soil Surface Specific Humidity, J. Appl. Meteor., 31, 480–484, 1992.

Lenton, T. M., Held, H., Kriegler, E., Hall, J. W., Lucht, W., Rahmstorf, S., and Schellnhuber, H. J.: Tipping elements in the Earth's climate system, Proc. Natl. Acad. Sci. U. S. A., 105, 1786–1793, doi:10.1073/pnas.0705414105, 2008.

Lescure, J.-P., Puig, H., Riera, B., Leclerc, D., Beekman, A., and Beneteau, A.: La phytomasse épigée d'une forêt dense en Guyane Française, Acta Oecol.-Oec. Gen., 4, 237–251, URL `http://www.documentation.ird.fr/hor/fdi:010005089`, in French, 1983.

Leuning, R.: A critical appraisal of a combined stomatal-photosynthesis model for C3 plants, Plant Cell Environ., 18, 339–355, doi:10.1111/j.1365-3040.1995.tb00370.x, 1995.

Leuning, R., Kelliher, F. M., de Pury, D. G. G., and Schulze, E.-D.: Leaf nitrogen, photosynthesis, conductance and transpiration: scaling from leaves to canopies, Plant Cell Environ., 18, 1183–1200, doi:10.1111/j.1365-3040.1995.tb00628.x, 1995.

Levis, S.: Modeling vegetation and land use in models of the Earth System, WIREs Clim. Change, 1, 840–856, doi:10.1002/wcc.83, 2010.

Levis, S., Bonan, G., Vertenstein, M., and Oleson, K.: The Community Land Model's Dynamic Global Vegetation Model (CLM-DGVM): Technical description and user's guide, Technical Note NCAR/TN-459+IA, NCAR, Boulder, CO, doi:10.5065/D6P26W36, 2004.

Lewis, S. L., Brando, P. M., Phillips, O. L., van der Heijden, G. M. F., and Nepstad, D.: The 2010 Amazon drought, Science, 331, 554, doi:10.1126/science.1200807, 2011.

Liou, K. N.: An introduction to atmospheric radiation, vol. 84 of *International Geophysics Series*, Academic Press, 2nd edn., 2002.

Liu, Z., Ostrenga, D., Teng, W., and Kempler, S.: Tropical Rainfall Measuring Mission (TRMM) Precipitation Data and Services for Research and Applications, Bulletin of the American Meteorological Society, 93, 1317–1325, doi:10.1175/BAMS-D-11-00152.1, 2012.

Lloyd, J., Patiño, S., Paiva, R. Q., Nardoto, G. B., Quesada, C. A., Santos, A. J. B., Baker, T. R., Brand, W. A., Hilke, I., Gielmann, H., Raessler, M., Luizão, F. J., Martinelli, L. A., and Mercado, L. M.: Optimisation of photosynthetic carbon gain and within-canopy gradients of associated foliar traits for Amazon forest trees, Biogeosciences, 7, 1833–1859, doi:10.5194/bg-7-1833-2010, 2010.

Longo, K. M., Freitas, S. R., Pirre, M., Marécal, V., Rodrigues, L. F., Panetta, J., Alonso, M. F., Rosário, N. E., Moreira, D. S., Gácita, M. S., Arteta, J., Fonseca, R., Stockler, R., Katsurayama, D. M., Fazenda, A., and Bela, M.: The Chemistry CATT-BRAMS model (CCATT-BRAMS 4.5): a regional atmospheric model system for integrated air quality and weather forecasting and research, Geosci. Model Dev., 6, 1389–1405, doi:10.5194/gmd-6-1389-2013, URL `http://www.geosci-model-dev.net/6/1389/2013/`, 2013.

Lugo, A. E., Scatena, F. N., Silver, W. L., Colón, S. M., and Murphy, P. G.: Resilience of tropical wet and dry forests in Puerto Rico, in: Resilience and the behavior of large-scale systems, edited by Gunderson, L. H. and Pritchard Jr., L., vol. 60 of *Scientific Comittee on Problems of the Environment*, chap. 8, pp. 195–225, Island Press, Washington, DC, USA, 2002.

Magrin, G., Gay García, C., Cruz Choque, D., Giménez, J. C., Moreno, A. R., Nagy, G. J., Nobre, C., and Villamizar, A.: Latin America, in: Climate Change 2007: Impacts, Adaptation and Vulnerability. Contribution of Working Group II to the Fourth Assessment Report of the Intergovernmental Panel on Climate Change, edited by Parry, M. L., Canziani, O. F., Palutikof, J. P., van der Linden, P. J., and Hanson, C. E., chap. 13, pp. 581–615, Cambridge Univ. Press, Cambridge, UK, 2007.

Malhado, A. C., Costa, M. H., de Lima, F. Z., Portilho, K. C., and Figueiredo, D. N.: Seasonal leaf dynamics in an Amazonian tropical forest, Forest Ecol. Manag., 258, 1161–1165, doi:10.1016/j.foreco.2009.06.002, 2009.

Malhi, Y., Phillips, O., Lloyd, J., Baker, T., Wright, J., Almeida, S., Arroyo, L., Frederiksen, T., Grace, J., Higuchi, N., Killeen, T., Laurance, W., Leaño, C., Lewis, S., Meir, P., Monteagudo, A., Neill, D., Núñez Vargas, P., Panfil, S., Patiño, S., Pitman, N., Quesada, C., Rudas-Ll., A., Salomão, R., Saleska, S., Silva, N., Silveira, M., Sombroek, W., Valencia, R., Vásquez Martínez, R., Vieira, I., and Vinceti, B.: An international network to monitor the structure, composition and dynamics of Amazonian forests (RAINFOR), J. Veg. Sci., 13, 439–450, doi:10.1111/j.1654-1103.2002.tb02068.x, 2002.

Malhi, Y., Baker, T. R., Phillips, O. L., Almeida, S., Alvarez, E., Arroyo, L., Chave, J., Czimczik, C. I., di Fiore, A., Higuchi, N., Killeen, T. J., Laurance, S. G., Laurance, W. F., Lewis, S. L., Montoya, L. M. M., Monteagudo, A., Neill, D. A., Vargas, P. N., Patiño, S., Pitman, N. C., Quesada, C. A., Salomão, R., Silva, J. N. M., Lezama, A. T., Martínez, R. V., Terborgh, J., Vinceti, B., and Lloyd, J.: The above-ground coarse wood productivity of 104 Neotropical forest plots, Glob. Change Biol., 10, 563–591, doi:10.1111/j.1529-8817.2003.00778.x, 2004.

Malhi, Y., Wood, D., Baker, T., Wright, J., Phillips, O., Cochrane, T., Meir, P., Chave, J., Almeida, S., Arroyo, L., Higuchi, N., Killeen, T., Laurance, S., Laurance, W., Lewis, S., Monteagudo,

A., Neill, D., Vargas, P., Pitman, N., Quesada, C., Salomao, R., Silva, J., Lezama, A., Terborgh, J., Martinez, R., and Vinceti, B.: The regional variation of aboveground live biomass in old-growth Amazonian forests, Glob. Change Biol., 12, 1107–1138, doi:10.1111/j.1365-2486.2006.01120.x, 2006.

Malhi, Y., Roberts, J. T., Betts, R. A., Killeen, T. J., Li, W., and Nobre, C. A.: Climate Change, Deforestation, and the Fate of the Amazon, Science, 319, 169–172, doi:10.1126/science.1146961, 2008.

Malhi, Y., Aragão, L. E. O. C., Galbraith, D., Huntingford, C., Fisher, R., Zelazowski, P., Sitch, S., McSweeney, C., and Meir, P.: Exploring the likelihood and mechanism of a climate-change-induced dieback of the Amazon rainforest, Proc. Natl. Acad. Sci. U. S. A., 106, 20 610–20 615, doi:10.1073/pnas.0804619106, 2009a.

Malhi, Y., Aragão, L. E. O. C., Metcalfe, D. B., Paiva, R., Quesada, C. A., Almeida, S., Anderson, L. O., Brando, P., Chambers, J. Q., da Costa, A. L., Hutyra, L. R., Oliveira, P., Patino, S., Pyle, E. H., Robertson, A. L., and Teixeira, L. M.: Comprehensive assessment of carbon productivity, allocation and storage in three Amazonian forests, Glob. Change Biol., 15, 1255–1274, doi:10.1111/j.1365-2486.2008.01780.x, 2009b.

Malhi, Y., Saatchi, S. S., Girardin, C., and Aragão, L. E. O. C.: The production, storage, and flow of carbon in Amazonian forests, in: Amazonia and Global Change, edited by Keller, M., Bustamante, M., Gash, J., and Silva Dias, P. L., vol. 186 of *Geophysical Monograph*, chap. 22, pp. 355–372, American Geophysical Union, Washington, DC, USA, doi:10.1029/2008GM000733, 2009c.

Marengo, J., Nobre, C., Sampaio, G., Salazar, L., and Borma, L.: Climate change in the Amazon Basin: Tipping points, changes in extremes, and impacts on natural and human systems, in: Tropical Rainforest Responses to Climatic Change, edited by Bush, M., Flenley, J., and Gosling, W., Springer Praxis Books, chap. 9, pp. 259–283, Springer Berlin Heidelberg, doi:10.1007/978-3-642-05383-2_9, 2011a.

Marengo, J. A., Nobre, C. A., Tomasella, J., Oyama, M. D., De Oliveira, G. S., De Oliveira, R., Camargo, H., Alves, L. M., and Brown, I. F.: The drought of Amazonia in 2005, J. Clim., 21, 495–516, doi:10.1175/2007JCLI1600.1, 2008.

Marengo, J. A., Tomasella, J., Alves, L. M., Soares, W. R., and Rodriguez, D. A.: The drought of 2010 in the context of historical droughts in the Amazon region, Geophys. Res. Lett., 38, L12 703, doi:10.1029/2011GL047436, 2011b.

Markesteijn, L.: Drought tolerance of tropical tree species: functional traits, trade-offs and species distributions, Ph.d. thesis, Wageningen University, Wageningen, Netherlands, 2010.

Markesteijn, L., Poorter, L., and Bongers, F.: Light-dependent leaf trait variation in 43 tropical dry forest tree species, Am. J. Bot., 94, 515–525, doi:10.3732/ajb.94.4.515, 2007.

Markesteijn, L., Poorter, L., Bongers, F., Paz, H., and Sack, L.: Hydraulics and life history of tropical dry forest tree species: coordination of species' drought and shade tolerance, New Phytol., 191, 480–495, doi:10.1111/j.1469-8137.2011.03708.x, 2011.

Markewitz, D., Devine, S., Davidson, E. A., Brando, P., and Nepstad, D. C.: Soil moisture depletion under simulated drought in the Amazon: impacts on deep root uptake, New Phytol., 187, 592–607, doi:10.1111/j.1469-8137.2010.03391.x, 2010.

Marthews, T. R., Malhi, Y., and Iwata, H.: Calculating downward longwave radiation under clear and cloudy conditions over a tropical lowland forest site: an evaluation of model schemes for hourly data, Theoretical and Applied Climatology, 107, 461–477, doi:10.1007/s00704-011-0486-9, 2012.

Massman, W. J.: An analytical one-dimensional model of momentum transfer by vegetation of arbitrary structure, Boundary-Layer Meteorology, 83, 407–421, doi:10.1023/A:1000234813011, 1997.

Matsuura, K. and Willmott, C. J.: Terrestrial precipitation: 1900–2010 gridded monthly time series. Version 3.01, URL `http://climate.geog.udel.edu/~climate/`, 2012.

Mauder, M., Desjardins, R., Pattey, E., and Worth, D.: An Attempt to Close the Daytime Surface Energy Balance Using Spatially-Averaged Flux Measurements, Boundary-Layer Meteorol., 136, 175–191, doi:10.1007/s10546-010-9497-9, 2010.

Mayer, D. and Butler, D.: Statistical validation, Ecol. Model., 68, 21–32, doi:http://dx.doi.org/10.1016/0304-3800(93)90105-2, 1993.

McDowell, N. G., Beerling, D. J., Breshears, D. D., Fisher, R. A., Raffa, K. F., and Stitt, M.: The interdependence of mechanisms underlying climate-driven vegetation mortality, Trends Ecol. Evol., 26, 523–532, doi:10.1016/j.tree.2011.06.003, 2011.

McWilliam, A.-L. C., Roberts, J. M., Cabral, O. M. R., Leitão, M. V. B. R., da Costa, A. C. L., Maitelli, G. T., and Zamparoni, C. A. G. P.: Leaf Area Index and Above-Ground Biomass of terra firme Rain Forest and Adjacent Clearings in Amazonia, Funct. Ecol., 7, 310–317, doi:10.2307/2390210, 1993.

Medlyn, B. E., Robinson, A. P., Clement, R., and McMurtrie, R. E.: On the validation of models of forest CO_2 exchange using eddy covariance data: some perils and pitfalls, Tree Physiol., 25, 839–857, doi:10.1093/treephys/25.7.839, 2005.

Medvigy, D. and Moorcroft, P. R.: Predicting ecosystem dynamics at regional scales: an evaluation of a terrestrial biosphere model for the forests of northeastern North America, Philosophical Transactions of the Royal Society B: Biological Sciences, 367, 222–235, doi:10.1098/rstb.2011.0253, 2012.

Medvigy, D., Wofsy, S. C., Munger, J. W., and Moorcroft, P. R.: Responses of terrestrial ecosystems and carbon budgets to current and future environmental variability, Proceedings of the National Academy of Sciences, 107, 8275–8280, doi:10.1073/pnas.0912032107, 2010.

Medvigy, D. M.: The state of the regional carbon cycle: results from a constrained coupled ecosystem-atmosphere model, Ph.d. dissertation, Harvard University, Cambridge, MA, 2006.

Medvigy, D. M., Wofsy, S. C., Munger, J. W., Hollinger, D. Y., and Moorcroft, P. R.: Mechanistic scaling of ecosystem function and dynamics in space and time: Ecosystem Demography model version 2, J. Geophys. Res.-Biogeosci., 114, G01 002, doi:10.1029/2008JG000812, 2009.

Mercado, L. M., Huntingford, C., Gash, J. H. C., Cox, P. M., and Jogireddy, V.: Improving the representation of radiation interception and photosynthesis for climate model applications, Tellus B, 59, 553–565, doi:10.1111/j.1600-0889.2007.00256.x, 2007.

Merry, F., Soares-Filho, B., Nepstad, D., Amacher, G., and Rodrigues, H.: Balancing Conservation and Economic Sustainability: The Future of the Amazon Timber Industry, Environ. Manage., 44, 395–407, doi:10.1007/s00267-009-9337-1, 2009.

Miller, S. D., Goulden, M. L., Menton, M. C., da Rocha, H. R., de Freitas, H. C., Figueira, A. M. e. S., and Dias de Sousa, C. A.: Biometric and micrometeorological measurements of tropical forest carbon balance, Ecol. Appl., 14, 114–126, doi:10.1890/02-6005, 2004.

Miller, S. D., Goulden, M., and da Rocha, H. R.: LBA-ECO CD-04 Meteorological and Flux Data, km 83 Tower Site, Tapajos National Forest. Data set., doi:10.3334/ORNLDAAC/946, URL `http://daac.ornl.gov`, oak Ridge National Laboratory Distributed Active Archive Center, Oak Ridge, Tennessee, U.S.A., 2009.

Miller, S. D., Goulden, M. L., Hutyra, L. R., Keller, M., Saleska, S. R., Wofsy, S. C., Silva Figueira, A. M., da Rocha, H. R., and de Camargo, P. B.: Reduced impact logging minimally alters tropical rainforest carbon and energy exchange, Proc. Natl. Acad. Sci. U. S. A., 108, 19 431–19 435, doi:10.1073/pnas.1105068108, 2011.

Monin, A. S. and Obukhov, A. M.: Osnovnye zakonomernosti turbulentnogo pere- meshivanija v prizemnom sloe atmosfery (Basic Laws of Turbulent Mixing in the Atmo- sphere Near the Ground), Trudy geofiz. inst. AN SSSR, 24, 163–187, URL `http://mcnaughty.com/keith/papers/Monin_and_Obukhov_1954.pdf`, original in Russian. Translation available at the URL, 1954.

Monteith, J. L. and Unsworth, M. H.: Principles of Environmental Physics, Academic Press, London, 3rd edition edn., 418 pp., 2008.

Moorcroft, P. R.: Recent advances in ecosystem-atmosphere interactions: an ecological perspective, Proc. R. Soc. Lond. B, 270, 1215–1227, doi:10.1098/rspb.2002.2251, 2003.

Moorcroft, P. R.: How close are we to a predictive science of the biosphere?, Trends Ecol. Evol., 21, 400–407, doi:10.1016/j.tree.2006.04.009, 2006.

Moorcroft, P. R., Hurtt, G. C., and Pacala, S. W.: A method for scaling vegetation dynamics: The Ecosystem Demography model (ED), Ecol. Monogr., 71, 557–586, doi:10.1890/0012-9615(2001)071[0557:AMFSVD]2.0.CO;2, 2001.

Morton, D. C., Le Page, Y., DeFries, R. S., Collatz, G. J., and Hurtt, G. C.: Understorey fire frequency and the fate of burned forests in southern Amazonia, Philos. Trans. R. Soc. B-Biol. Sci., 368, 20120 163, doi:10.1098/rstb.2012.0163, 2013.

Murphy, D. M. and Koop, T.: Review of the vapour pressures of ice and supercooled water for atmospheric applications, Quart. J. Royal Meteorol. Soc., 131, 1539–1565, doi:10.1256/qj.04.94, 2005.

Naeem, S. and Li, S.: Biodiversity enhances ecosystem reliability, Nature, 390, 507–509, doi:10.1038/37348, 1997.

NASA/LP-DAAC: MODIS leaf area index – fracion of photosynthetically active radiation 8-day L4 global 1 km, version 005, URL https://lpdaac.usgs.gov/products/modis_products_table/mcd15a2, uSGS/Earth Resources Observation and Science (EROS) Center, Sioux Falls, SD, United States, 2007.

NASA/LP-DAAC: MODIS land cover type yearly L3 global 500 m SIN Grid (MCD12Q1), version 051, URL https://lpdaac.usgs.gov/products/modis_products_table/mcd12q1, uSGS/Earth Resources Observation and Science (EROS) Center, Sioux Falls, SD, United States, 2012.

NASA/LP-DAAC and USGS/EROS: MODIS reprojection tool user's manual, NASA Land Processes DAAC and USGS Earth Resources Observation and Science (EROS), Sioux Falls, SD, United States, URL https://lpdaac.usgs.gov/tools/modis_reprojection_tool, 2011.

Nascimento, C. E. S., Rodal, M. J. N., and Cavalcanti, A. C.: Phytosociology of the remaining xerophytic woodland associated to an environmental gradient at the banks of the São Francisco River - Petrolina, Pernambuco, Brazil, Revista Brasileira de Botânica, 26, 271–287, 2003.

NCDC/NOAA: Climate Data Online, URL http://www.ncdc.noaa.gov/cdo-web/, 2013.

Negrón-Juárez, R. I., Goulden, M. L., Myneni, R. B., Fu, R., Bernardes, S., and Gao, H.: An empirical approach to retrieving monthly evapotranspiration over Amazonia, Int. J. Remote Sens., 29, 7045–7063, doi:10.1080/01431160802226026, 2008.

Negrón-Juárez, R. I., Li, W., Fu, R., Fernandes, K., and de Oliveira Cardoso, A.: Comparison of Precipitation Datasets over the Tropical South American and African Continents, J. Hydrometeor., 10, 289–299, doi:10.1175/2008JHM1023.1, 2009.

Negrón-Juárez, R. I., Chambers, J. Q., Guimarães, G., Zeng, H., Raupp, C. F. M., Marra, D. M., Ribeiro, G. H. P. M., Saatchi, S. S., Nelson, B. W., and Higuchi, N.: Widespread Amazon forest tree mortality from a single cross-basin squall line event, Geophys. Res. Lett., 37, L16 701, doi:10.1029/2010GL043733, 2010.

Neilson, R. P.: A Model for Predicting Continental-Scale Vegetation Distribution and Water Balance, Ecol. Appl., 5, 362–385, doi:10.2307/1942028, 1995.

Nemani, R. R., Keeling, C. D., Hashimoto, H., Jolly, W. M., Piper, S. C., Tucker, C. J., Myneni, R. B., and Running, S. W.: Climate-Driven Increases in Global Terrestrial Net Primary Production from 1982 to 1999, Science, 300, 1560–1563, doi:10.1126/science.1082750, 2003.

Nepstad, D. C., de Carvalho, C. R., Davidson, E. A., Jipp, P. H., Lefebvre, P. A., Negreiros, G. H., da Silva, E. D., Stone, T. A., Trumbore, S. E., and Vieira, S.: The role of deep roots in the hydrological and carbon cycles of Amazonian forests and pastures, Nature, 372, 666–669, doi:10.1038/372666a0, 1994.

Nepstad, D. C., Moutinho, P., Dias-Filho, M. B., Davidson, E., Cardinot, G., Markewitz, D., Figueiredo, R., Vianna, N., Chambers, J., Ray, D., Guerreiros, J. B., Lefebvre, P., Sternberg, L., Moreira, M., Barros, L., Ishida, F. Y., Tohlver, I., Belk, E., Kalif, K., and Schwalbe, K.: The effects of partial throughfall exclusion on canopy processes, aboveground production, and biogeochemistry of an Amazon forest, J. Geophys. Res.-Atmos., 107, 8085, doi:10.1029/2001JD000360, 2002.

Nepstad, D. C., Tohver, I. M., Ray, D., Moutinho, P., and Cardinot, G.: Mortality of large trees and lianas following experimental drought in an Amazon forest, Ecology, 88, 2259–2269, doi:10.1890/06-1046.1, 2007.

Nepstad, D. C., Stickler, C. M., Filho, B. S., and Merry, F.: Interactions among Amazon land use, forests and climate: prospects for a near-term forest tipping point, Philos. Trans. R. Soc. B-Biol. Sci., 363, 1737–1746, doi:10.1098/rstb.2007.0036, 2008.

Niu, G.-Y. and Yang, Z.-L.: An observation-based formulation of snow cover fraction and its evaluation over large North American river basins, J. Geophys. Res.-Atmos., 112, D21 101, doi:10.1029/2007JD008674, 2007.

Nobre, C. A. and Borma, L. S.: 'Tipping points' for the Amazon forest, Curr. Opin. Environ. Sustainability, 1, 28–36, doi:10.1016/j.cosust.2009.07.003, 2009.

Noilhan, J. and Planton, S.: A Simple Parameterization of Land Surface Processes for Meteorological Models, Mon. Wea. Rev., 117, 536–549, doi:10.1175/1520-0493(1989)117<0536:ASPOLS>2.0.CO;2, 1989.

Oleson, K. W., Lawrence, D. M., Bonan, G. B., Flanner, M. G., Kluzek, E., Lawrence, P. J., Levis, S., Swenson, S. C., Thornton, P. E., Dai, A., Decker, M., Dickinson, R., Feddema, J., Heald, C. L., Hoffman, F., Lamarque, J.-F., Mahowald, N., Niu, G.-Y., Qian, T., Randerson, J., Running, S., Sakaguchi, K., Slater, A., Stöckli, R., Wang, A., Yang, Z.-L., Zeng, X., and Zeng, X.: Technical description of version 4.0 of the Community Land Model (CLM), Technical Report NCAR/TN-478+STR, NCAR, Boulder, CO, doi:10.5065/D6FB50WZ, 257pp., 2010.

Olivas, P. C., Oberbauer, S. F., Clark, D. B., Clark, D. A., Ryan, M. G., O'Brien, J. J., and nez, H. O.: Comparison of direct and indirect methods for assessing leaf area index across a tropical rain forest landscape, Agric. For. Meteorol., 177, 110–116, doi:10.1016/j.agrformet.2013.04.010, 2013.

Oncley, S. P., Foken, T., Vogt, R., Kohsiek, W., DeBruin, H. A. R., Bernhofer, C., Christen, A., Gorsel, E., Grantz, D., Feigenwinter, C., Lehner, I., Liebethal, C., Liu, H., Mauder, M., Pitacco, A., Ribeiro, L., and Weidinger, T.: The Energy Balance Experiment EBEX-2000. Part I: overview and energy balance, Boundary-Layer Meteorology, 123, 1–28, doi:10.1007/s10546-007-9161-1, 2007.

Panofsky, H. A.: Determination of stress from wind and temperature measurements, Quart. J. Royal Meteorol. Soc., 89, 85–94, doi:10.1002/qj.49708937906, 1963.

Parlange, M., Cahill, A., Nielsen, D., Hopmans, J., and Wendroth, O.: Review of heat and water movement in field soils, Soil Till. Res., 47, 5–10, doi:10.1016/S0167-1987(98)00066-X, 1998.

Peacock, J., Baker, T., Lewis, S., Lopez-Gonzalez, G., and Phillips, O.: The RAINFOR database: monitoring forest biomass and dynamics, J. Veg. Sci., 18, 535–542, doi:10.1111/j.1654-1103.2007.tb02568.x, 2007.

Philip, J. R.: Evaporation, and moisture and heat fields in the soil, J. Meteor., 14, 354–366, doi:10.1175/1520-0469(1957)014<0354:EAMAHF>2.0.CO;2, 1957.

Phillips, O. L., Aragao, L. E. O. C., Lewis, S. L., Fisher, J. B., Lloyd, J., Lopez-Gonzalez, G., Malhi, Y., Monteagudo, A., Peacock, J., Quesada, C. A., van der Heijden, G., Almeida, S., Amaral, I., Arroyo, L., Aymard, G., Baker, T. R., Banki, O., Blanc, L., Bonal, D., Brando, P., Chave, J., Alves de Oliveira, A. C., Cardozo, N. D., Czimczik, C. I., Feldpausch, T. R., Freitas, M. A., Gloor, E., Higuchi, N., Jimenez, E., Lloyd, G., Meir, P., Mendoza, C., Morel, A., Neill, D. A., Nepstad, D., Patino, S., Cristina Penuela, M., Prieto, A., Ramirez, F., Schwarz, M., Silva, J., Silveira, M., Thomas, A. S., ter Steege, H., Stropp, J., Vasquez, R., Zelazowski, P., Alvarez Davila, E., Andelman, S., Andrade, A., Chao, K.-J., Erwin, T., Di Fiore, A., Honorio C, E., Keeling, H., Killeen, T. J., Laurance, W. F., Pena Cruz, A., Pitman, N. C. A., Nunez Vargas, P., Ramirez-Angulo, H., Rudas, A., Salamao, R., Silva, N., Terborgh, J., and Torres-Lezama, A.: Drought Sensitivity of the Amazon Rainforest, Science, 323, 1344–1347, doi:10.1126/science.1164033, 2009.

Phillips, O. L., van der Heijden, G., Lewis, S. L., López-González, G., Aragão, L. E. O. C., Lloyd, J., Malhi, Y., Monteagudo, A., Almeida, S., Alvarez Dávila, E., Amaral, I., Andelman, S., Andrade, A., Arroyo, L., Aymard, G., Baker, T. R., Blanc, L., Bonal, D., Alves de Oliveira, A. C., Chao, K.-J., Dávila Cardozo, N., da Costa, L., Feldpausch, T. R., Fisher, J. B., Fyllas, N. M., Freitas, M. A., Galbraith, D., Gloor, E., Higuchi, N., Honorio, E., Jiménez, E., Keeling, H., Killeen, T. J., Lovett, J. C., Meir, P., Mendoza, C., Morel, A., Núñez Vargas, P., Patiño, S., Peh, K. S.-H., Peña Cruz, A., Prieto, A., Quesada, C. A., Ramírez, F., Ramírez, H., Rudas, A., Salamão, R., Schwarz, M., Silva, J., Silveira, M., Slik, J. W. F., Sonké, B., Thomas, A. S., Stropp, J., Taplin, J. R. D., Vásquez, R., and Vilanova, E.: Drought-mortality relationships for tropical forests, New Phytol., 187, 631–646, doi:10.1111/j.1469-8137.2010.03359.x, 2010.

Phillips, S. J., Dudík, M., and Schapire, R. E.: A maximum entropy approach to species distribution modeling, in: Proceedings of the 21st International Conference on Machine Learning (ICML-04), edited by Greiner, R. and Schuurmans, D., pp. 43–48, ACM Press, New York, NY, U.S.A., 2004.

Phillips, S. J., Anderson, R. P., and Schapire, R. E.: Maximum entropy modeling of species geographic distributions, Ecol. Model., 190, 231–259, doi:10.1016/j.ecolmodel.2005.03.026, 2006.

Picard, N., Saint André, L., and Henry, M.: Manual for building tree volume and biomass allometric equations: from field measurement to prediction, Food and Agricultural Organisation of the United Nations, Rome, and Centre de Coopération Internationale en

Recherche Agronomique pour le Développement, Montpellier, URL http://www.fao.org/docrep/018/i3058e/i3058e.pdf, 2012.

Pinto-Júnior, O. B., Sanches, L., Almeida Lobo, F., Brandão, A. A., and Souza Nogueira, J.: Leaf area index of a tropical semi-deciduous forest of the southern Amazon Basin, Int. J. Biometeorol., 55, 109–118, doi:10.1007/s00484-010-0317-1, 2011.

Ponce Campos, G. E., Moran, M. S., Huete, A., Zhang, Y., Bresloff, C., Huxman, T. E., Eamus, D., Bosch, D. D., Buda, A. R., Gunter, S. A., Scalley, T. H., Kitchen, S. G., McClaran, M. P., McNab, W. H., Montoya, D. S., Morgan, J. A., Peters, D. P. C., Sadler, E. J., Seyfried, M. S., and Starks, P. J.: Ecosystem resilience despite large-scale altered hydroclimatic conditions, Nature, 494, 349–352, doi:10.1038/nature11836, 2013.

Poorter, L., Bongers, L., and Bongers, F.: Architecture of 54 moist-forest tree species: traits, trade-offs, and functional groups, Ecology, 87, 1289–1301, doi:10.1890/0012-9658(2006)87[1289:AOMTST]2.0.CO;2, 2006.

Poorter, L., McDonald, I., Alarcon, A., Fichtler, E., Licona, J.-C., Pena-Claros, M., Sterck, F., Villegas, Z., and Sass-Klaassen, U.: The importance of wood traits and hydraulic conductance for the performance and life history strategies of 42 rainforest tree species, New Phytol., 185, 481–492, doi:10.1111/j.1469-8137.2009.03092.x, 2010.

Powell, T. L., Galbraith, D. R., Christoffersen, B. O., Harper, A., Imbuzeiro, H. M. A., Rowland, L., Almeida, S., Brando, P. M., da Costa, A. C. L., Costa, M. H., Levine, N. M., Malhi, Y., Saleska, S. R., Sotta, E., Williams, M., Meir, P., and Moorcroft, P. R.: Confronting model predictions of carbon fluxes with measurements of Amazon forests subjected to experimental drought, New Phytol., 200, 350–365, doi:10.1111/nph.12390, 2013.

Prata, A. J.: A new long-wave formula for estimating downward clear-sky radiation at the surface, Quarterly Journal of the Royal Meteorological Society, 122, 1127–1151, doi:10.1002/qj.49712253306, URL http://dx.doi.org/10.1002/qj.49712253306, 1996.

Prentice, I. C., Cramer, W., Harrison, S. P., Leemans, R., Monserud, R. A., and Solomon, A. M.: A Global Biome Model Based on Plant Physiology and Dominance, Soil Properties and Climate, J. Biogeogr., 19, 117–134, doi:10.2307/2845499, 1992.

Purves, D. and Pacala, S.: Predictive Models of Forest Dynamics, Science, 320, 1452–1453, doi:10.1126/science.1155359, 2008.

Putz, F. E. and Holbrook, N. M.: Biomechanical studies of vines, in: The biology of vines, edited by Putz, F. E. and Mooney, H. A., chap. 3, pp. 73–97, Cambridge Univ. Press, Cambridge, UK, 1991.

Pyle, E. H., Santoni, G. W., Nascimento, H. E. M., Hutyra, L. R., Vieira, S., Curran, D. J., van Haren, J., Saleska, S. R., Chow, V. Y., Carmago, P. B., Laurance, W. F., and Wofsy, S. C.: Dynamics of carbon, biomass, and structure in two Amazonian forests, J. Geophys. Res.-Biogeosci., 113, G00B08, doi:10.1029/2007JG000592, 2008.

Quero, J. L. L., Villar, R., Marañón, T., and Zamora, R.: Interactions of drought and shade effects on seedlings of four Quercus species: physiological and structural leaf responses, New Phytol., 170, 819–834, doi:10.1111/j.1469-8137.2006.01713.x, 2006.

Quesada, C. A., Lloyd, J., Anderson, L. O., Fyllas, N. M., Schwarz, M., and Czimczik, C. I.: Soils of Amazonia with particular reference to the RAINFOR sites, Biogeosciences, 8, 1415–1440, doi:10.5194/bg-8-1415-2011, 2011.

Quesada, C. A., Phillips, O. L., Schwarz, M., Czimczik, C. I., Baker, T. R., Patiño, S., Fyllas, N. M., Hodnett, M. G., Herrera, R., Almeida, S., Alvarez Dávila, E., Arneth, A., Arroyo, L., Chao, K. J., Dezzeo, N., Erwin, T., di Fiore, A., Higuchi, N., Honorio Coronado, E., Jimenez, E. M., Killeen, T., Lezama, A. T., Lloyd, G., López-González, G., Luizão, F. J., Malhi, Y., Monteagudo, A., Neill, D. A., Núñez Vargas, P., Paiva, R., Peacock, J., Peñuela, M. C., Peña Cruz, A., Pitman, N., Priante Filho, N., Prieto, A., Ramírez, H., Rudas, A., Salomão, R., Santos, A. J. B., Schmerler, J., Silva, N., Silveira, M., Vásquez, R., Vieira, I., Terborgh, J., and Lloyd, J.: Basin-wide variations in Amazon forest structure and function are mediated by both soils and climate, Biogeosciences, 9, 2203–2246, doi:10.5194/bg-9-2203-2012, URL http://www.biogeosciences.net/9/2203/2012/, 2012.

Raich, J. W., Rastetter, E. B., Melillo, J. M., Kicklighter, D. W., Steudler, P. A., Peterson, B. J., Grace, A. L., Moore, B., and Vorosmarty, C. J.: Potential Net Primary Productivity in South America: Application of a Global Model, Ecol. Appl., 1, 399–429, doi:10.2307/1941899, 1991.

Rammig, A., Jupp, T., Thonicke, K., Tietjen, B., Heinke, J., Ostberg, S., Lucht, W., Cramer, W., and Cox, P.: Estimating the risk of Amazonian forest dieback, New Phytol., 187, 694–706, doi:10.1111/j.1469-8137.2010.03318.x, 2010.

Raupach, M. R.: Simplified expressions for vegetation roughness length and zero-plane displacement as functions of canopy height and area index, Boundary-Layer Meteorol., 71, 211–216, doi:10.1007/BF00709229, 1994.

Raupach, M. R.: Corrigenda, Boundary-Layer Meteorol., 76, 303–304, doi:10.1007/BF00709356, 1995.

Rawls, W. J., Pachepsky, Y. A., Ritchie, J. C., Sobecki, T. M., and Bloodworth, H.: Effect of soil organic carbon on soil water retention, Geoderma, 116, 61–76, doi:http://dx.doi.org/10.1016/S0016-7061(03)00094-6, 2003.

Reich, P. B., Walters, M. B., and Ellsworth, D. S.: From tropics to tundra: Global convergence in plant functioning, Proc. Natl. Acad. Sci. U. S. A., 94, 13 730–13 734, doi:10.1073/pnas.94.25.13730, 1997.

Reichstein, M., Falge, E., Baldocchi, D., Papale, D., Aubinet, M., Berbigier, P., Bernhofer, C., Buchmann, N., Gilmanov, T., Granier, A., Grünwald, T., Havránková, K., Ilvesniemi, H., Janous, D., Knohl, A., Laurila, T., Lohila, A., Loustau, D., Matteucci, G., Meyers, T., Miglietta, F., Ourcival, J.-M., Pumpanen, J., Rambal, S., Rotenberg, E., Sanz, M., Tenhunen, J., Seufert, G., Vaccari, F., Vesala, T., Yakir, D., and Valentini, R.: On the separation of net ecosystem

exchange into assimilation and ecosystem respiration: review and improved algorithm, Glob. Change Biol., 11, 1424–1439, doi:10.1111/j.1365-2486.2005.001002.x, 2005.

Reichstein, M., Bahn, M., Ciais, P., Frank, D., Mahecha, M. D., Seneviratne, S. I., Zscheischler, J., Beer, C., Buchmann, N., Frank, D. C., Papale, D., Rammig, A., Smith, P., Thonicke, K., van der Velde, M., Vicca, S., Walz, A., and Wattenbach, M.: Climate extremes and the carbon cycle, Nature, 500, 287–295, doi:10.1038/nature12350, 2013.

Reiss, J., Bridle, J. R., Montoya, J., and Woodward, G.: Emerging horizons in biodiversity and ecosystem functioning research, Trends Ecol. Evol., 24, 505–514, doi:10.1016/j.tree.2009.03.018, 2009.

Restrepo-Coupe, N., Da Rocha, H. R., Christoffersen, B., de Araújo, A. C., Borma, L. S., Cabral, O. M., de Camargo, P. B., da Costa, A. C. L., Fitzjarrald, D. R., Goulden, M. L., Hutyra, L. R., Kruijt, B., Maia, J. M. F., Malhi, Y., Manzi, A. O., Miller, S. D., Nobre, A. D., von Randow, C., de Sá, Leonardo D. Sakai, R. K., Tota, J., Wofsy, S. C., Zanchi, F. B., and Saleska, S. R.: What drives the seasonality of productivity across the Amazon basin? A cross-site analysis of eddy flux tower measurements from the Brasil flux network, Agric. For. Meteorol., 182–183, 128–144, doi:10.1016/j.agrformet.2013.04.031, 2013.

Reyer, C. P., Leuzinger, S., Rammig, A., Wolf, A., Bartholomeus, R. P., Bonfante, A., de Lorenzi, F., Dury, M., Gloning, P., Abou Jaoudé, R., Klein, T., Kuster, T. M., Martins, M., Niedrist, G., Riccardi, M., Wohlfahrt, G., de Angelis, P., de Dato, G., François, L., Menzel, A., and Pereira, M.: A plant's perspective of extremes: terrestrial plant responses to changing climatic variability, Glob. Change Biol., 19, 75–89, doi:10.1111/gcb.12023, 2013.

Rice, A., Pyle, E., Saleska, S., Hutyra, L., Palace, M., Keller, M., de Camargo, P., Portilho, K., Marques, D., and Wofsy, S.: Carbon balance and vegetation dynamics in an old-growth Amazonian forest, Ecol. Appl., 14, S55–S71, doi:10.1890/02-6006, 2004.

Rosolem, R., Shuttleworth, W. J., and de Gonçalves, L. G. G.: Is the data collection period of the Large-scale Biosphere-Atmosphere experiment in Amazonia representative of long-term climatology?, J. Geophys. Res.-Biogeosci., 113, G00B09, doi:10.1029/2007JG000628, 2008.

Rossato, L.: Estimativa da capacidade de armazenamento de água no solo do Brasil, Msc. thesis, Instituto Nacional de Pesquisas Espaciais (INPE), São José dos Campos, Brazil, in Portuguese, 2001.

Rowland, L., Stahl, C., Bonal, D., Siebicke, L., Williams, M., and Meir, P.: The Response of Tropical Rainforest Dead Wood Respiration to Seasonal Drought, Ecosystems, 16, 1294–1309, doi:10.1007/s10021-013-9684-x, 2013.

Ruggiero, P. G. C., Pivello, V. R., Sparovek, G., Teramoto, E., and Pires-Neto, A. G.: The relationship among soil, vegetation and topography in a cerrado area (Vassununga State Park, SP): how well is it expressed in maps?, Acta Botanica Brasilica, 20, 383–394, doi:http://dx.doi.org/10.1590/S0102-33062006000200013, 2006.

Saatchi, S., Asefi-Najafabady, S., Malhi, Y., Aragão, L. E. O. C., Anderson, L. O., Myneni, R. B., and Nemani, R.: Persistent effects of a severe drought on Amazonian forest canopy, Proc. Natl. Acad. Sci. U. S. A., 110, 565–570, doi:10.1073/pnas.1204651110, 2013.

Saatchi, S. S.: Spatial Variation of Forest Structure and Aboveground Biomass in the Southwestern Brazilian Amazon, URL `http://www-radar.jpl.nasa.gov/carbon/ab/jr.htm`, 2006.

Saatchi, S. S., Houghton, R. A., Alvala, R. C. D. S., Soares, J. V., and Yu, Y.: Distribution of aboveground live biomass in the Amazon basin, Glob. Change Biol., 13, 816–837, doi:10.1111/j.1365-2486.2007.01323.x, 2007.

Saatchi, S. S., Harris, N. L., Brown, S., Lefsky, M., Mitchard, E. T. A., Salas, W., Zutta, B. R., Buermann, W., Lewis, S. L., Hagen, S., Petrova, S., White, L., Silman, M., and Morel, A.: Benchmark map of forest carbon stocks in tropical regions across three continents, Proc. Natl. Acad. Sci. U. S. A., 108, 9899–9904, doi:10.1073/pnas.1019576108, 2011.

Sabatier, D., Grimaldi, M., Prevost, M., Guillaume, J., Godron, M., Dosso, M., and Curmi, P.: The influence of soil cover organization on the floristic and structural heterogeneity of a Guianan rain forest, PLANT ECOLOGY, 131, 81–108, doi:10.1023/A:1009775025850, 1997.

Salazar, L. F. and Nobre, C. A.: Climate change and thresholds of biome shifts in Amazonia, Geophys. Res. Lett., 37, L17 706, doi:10.1029/2010GL043538, 2010.

Saldarriaga, J. G., West, D. C., Tharp, M. L., and Uhl, C.: Long-Term Chronosequence of Forest Succession in the Upper Rio Negro of Colombia and Venezuela, J. Ecol., 76, 938—958, doi:10.2307/2260625, 1988.

Saleska, S., Miller, S., Matross, D., Goulden, M., Wofsy, S., da Rocha, H., de Camargo, P., Crill, P., Daube, B., de Freitas, H., Hutyra, L., Keller, M., Kirchhoff, V., Menton, M., Munger, J., Pyle, E., Rice, A., and Silva, H.: Carbon in Amazon forests: Unexpected seasonal fluxes and disturbance-induced losses, Science, 302, 1554–1557, doi:10.1126/science.1091165, 2003.

Saleska, S. R., Didan, K., Huete, A. R., and da Rocha, H. R.: Amazon Forests Green-Up During 2005 Drought, Science, 318, 612, doi:10.1126/science.1146663, 2007.

Saleska, S. R., da Rocha, H. R., Kruijt, B., and Nobre, A.: Ecosystem Carbon Fluxes and Amazonian Forest Metabolism, in: Amazonia and Global Change, edited by Keller, M., Bustamante, M., Gash, J., and Silva Dias, P. L., vol. 186 of *Geophysical Monograph*, chap. 24, pp. 389–407, American Geophysical Union, doi:10.1029/2008GM000739, 2009.

Samanta, A., Ganguly, S., Hashimoto, H., Devadiga, S., Vermote, E., Knyazikhin, Y., Nemani, R. R., and Myneni, R. B.: Amazon forests did not green-up during the 2005 drought, Geophys. Res. Lett., 37, L05 401, doi:10.1029/2009GL042154, 2010.

Samanta, A., Knyazikhin, Y., Xu, L., Dickinson, R. E., Fu, R., Costa, M. H., Saatchi, S. S., Nemani, R. R., and Myneni, R. B.: Seasonal changes in leaf area of Amazon forests from leaf flushing and abscission, J. Geophys. Res.-Biogeosci., 117, G01 015, doi:10.1029/2011JG001818, 2012.

Santos, A. J. B., Silva, G. T. D. A., Miranda, H. S., Miranda, A. C., and Lloyd, J.: Effects of fire on surface carbon, energy and water vapour fluxes over campo sujo savanna in central Brazil, Funct. Ecol., 17, 711–719, doi:10.1111/j.1365-2435.2003.00790.x, 2003.

Saxton, K. E. and Rawls, W. J.: Soil Water Characteristic Estimates by Texture and Organic Matter for Hydrologic Solutions, Soil Sci. Soc. Am. J., 70, 1569–1578, doi:10.2136/sssaj2005.0117, 2006.

Scheffer, M., Carpenter, S. R., Lenton, T. M., Bascompte, J., Brock, W., Dakos, V., van de Koppel, J., van de Leemput, I. A., Levin, S. A., van Nes, E. H., Pascual, M., and Vandermeer, J.: Anticipating Critical Transitions, Science, 338, 344–348, doi:10.1126/science.1225244, 2012.

Schneider, U., Becker, A., Finger, P., Meyer-Christoffer, A., Ziese, M., and Rudolf, B.: GPCC's new land surface precipitation climatology based on quality-controlled in situ data and its role in quantifying the global water cycle, Theor. Appl. Climatol., 115, 15–40, doi:10.1007/s00704-013-0860-x, 2014.

Schnitzer, S. A. and Bongers, F.: Increasing liana abundance and biomass in tropical forests: emerging patterns and putative mechanisms, Ecol. Lett., 14, 397–406, doi:10.1111/j.1461-0248.2011.01590.x, 2011.

Sedlar, J. and Hock, R.: Testing longwave radiation parameterizations under clear and overcast skies at Storglaciären, Sweden, The Cryosphere, 3, 75–84, doi:10.5194/tc-3-75-2009, 2009.

Sellers, P. J.: Canopy reflectance, photosynthesis and transpiration, Int. J. Remote Sens., 6, 1335–1372, doi:10.1080/01431168508948283, 1985.

Sellers, P. J., Mintz, Y., Sud, Y. C., and Dalcher, A.: A Simple Biosphere Model (SIB) for Use within General Circulation Models, J. Atmos. Sci., 43, 505–531, doi:10.1175/1520-0469(1986)043<0505:ASBMFU>2.0.CO;2, 1986.

Sellers, P. J., Randall, D. A., Collatz, G. J., Berry, J. A., Field, C. B., Dazlich, D. A., Zhang, C., Collelo, G. D., and Bounoua, L.: A Revised Land Surface Parameterization (SiB2) for Atmospheric GCMS. Part I: Model Formulation, J. Clim., 9, 676–705, doi:10.1175/1520-0442(1996)009<0676:ARLSPF>2.0.CO;2, 1996.

Senna, M. C. A., Costa, M. H., and Pires, G. F.: Vegetation-atmosphere-soil nutrient feedbacks in the Amazon for different deforestation scenarios, J. Geophys. Res.-Atmos., 114, D04 104, doi:10.1029/2008JD010401, 2009.

Shabanov, N., Huang, D., Yang, W., Tan, B., Knyazikhin, Y., Myneni, R., Ahl, D., Gower, S., Huete, A., Aragão, L., and Shimabukuro, Y.: Analysis and optimization of the MODIS leaf area index algorithm retrievals over broadleaf forests, IEEE T. Geosci. Remote Sens., 43, 1855—1865, doi:10.1109/TGRS.2005.852477, 2005.

Sharkey, T. D., Bernacchi, C. J., Farquhar, G. D., and Singsaas, E. L.: Fitting photosynthetic carbon dioxide response curves for C3 leaves, Plant Cell Environ., 30, 1035–1040, doi:10.1111/j.1365-3040.2007.01710.x, 2007.

Shaw, R. H. and Pereira, A.: Aerodynamic roughness of a plant canopy: A numerical experiment, Agric. For. Meteorol., 26, 51–65, doi:10.1016/0002-1571(82)90057-7, 1982.

Sheffield, J., Goteti, G., and Wood, E. F.: Development of a 50-Year High-Resolution Global Dataset of Meteorological Forcings for Land Surface Modeling, J. Clim., 19, 3088–3111, doi:10.1175/JCLI3790.1, 2006.

Sheil, D. and May, R. M.: Mortality and recruitment rate evaluations in heterogeneous tropical forests, J. Ecol, 84, 91–100, doi:10.2307/2261703, 1996.

Shida, C. N.: Caracterização física do cerrado Pé-de-Gigante e uso das terras na região, in: O cerrado Pé-de-Gigante: ecologia e conservação – Parque Estadual de Vassununga, edited by Pivello, V. R. and Varanda, E. M., chap. 2, pp. 29–42, Secretaria do Meio Ambiente do Estado de São Paulo, São Paulo, SP, Brazil, in Portuguese, 2005.

Shinozaki, K., Yoda, K., Hozumi, K., and Kira, T.: A quantitative analysis of plant form – the pipe model theory. I. Basic analyses, Jpn. J. Ecol., 14, 97–105, 1964a.

Shinozaki, K., Yoda, K., Hozumi, K., and Kira, T.: A quantitative analysis of plant form – the pipe model theory. II. Further evidence of the theory and its application in forest ecology, Jpn. J. Ecol., 14, 133–139, 1964b.

Silva, I. A. and Batalha, M. A.: Co-occurrence of tree species at fine spatial scale in a woodland cerrado, southeastern Brazil, Plant Ecology, 200, 277–286, doi:10.1007/s11258-008-9452-8, 2009.

Silver, W. L., Neff, J., McGroddy, M., Veldkamp, E., Keller, M., and Cosme, R.: Effects of Soil Texture on Belowground Carbon and Nutrient Storage in a Lowland Amazonian Forest Ecosystem, Ecosystems, 3, 193–209, doi:10.1007/s100210000019, 2000.

Simon, E., Lehmann, B., Ammann, C., Ganzeveld, L., Rummel, U., Meixner, F., Nobre, A., Araújo, A., and Kesselmeier, J.: Lagrangian dispersion of ^{222}Rn, H_2O and CO_2 within Amazonian rain forest, Agric. For. Meteorol., 132, 286–304, doi:10.1016/j.agrformet.2005.08.004, 2005.

Sitch, S., Smith, B., Prentice, I. C., Arneth, A., Bondeau, A., Cramer, W., Kaplan, J. O., Levis, S., Lucht, W., Sykes, M. T., Thonicke, K., and Venevsky, S.: Evaluation of ecosystem dynamics, plant geography and terrestrial carbon cycling in the LPJ dynamic global vegetation model, Global Change Biology, 9, 161–185, doi:10.1046/j.1365-2486.2003.00569.x, 2003.

Sitch, S., Huntingford, C., Gedney, N., Levy, P. E., Lomas, M., Piao, S. L., Betts, R., Ciais, P., Cox, P., Friedlingstein, P., Jones, C. D., Prentice, I. C., and Woodward, F. I.: Evaluation of the terrestrial carbon cycle, future plant geography and climate-carbon cycle feedbacks using five Dynamic Global Vegetation Models (DGVMs), Glob. Change Biol., 14, 2015–2039, doi:10.1111/j.1365-2486.2008.01626.x, 2008.

Smith, M. D.: An ecological perspective on extreme climatic events: a synthetic definition and framework to guide future research, J. Ecol., 99, 656–663, doi:10.1111/j.1365-2745.2011.01798.x, 2011.

Soares-Filho, B. S., Nepstad, D. C., Curran, L. M., Cerqueira, G. C., Garcia, R. A., Ramos, C. A., Voll, E., McDonald, A., Lefebvre, P., and Schlesinger, P.: Modelling conservation in the Amazon basin., Nature, 440, 520 – 523, doi:doi:10.1038/nature04389, 2006.

SONDA/INPE: National Organisation System for Environmental Data, URL http://sonda.ccst.inpe.br/, 2013.

Soudani, K., Hmimina, G., Delpierre, N., Pontailler, J.-Y., Aubinet, M., Bonal, D., Caquet, B., de Grandcourt, A., Burban, B., Flechard, C., Guyon, D., Granier, A., Gross, P., Heinesh, B., Longdoz, B., Loustau, D., Moureaux, C., Ourcival, J.-M., Rambal, S., Saint André, L., and Dufrêne, E.: Ground-based Network of NDVI measurements for tracking temporal dynamics of canopy structure and vegetation phenology in different biomes, Remote Sens. Environ., 123, 234–245, doi:10.1016/j.rse.2012.03.012, 2012.

Stahl, C.: Variations saisonnières des flux de CO_2 et H_2O au niveau des feuilles et des troncs des arbres de la canopée en forêt tropicale humide guyanaise, Ph.d. thesis, Université Henri Poincaré de Nancy, Nancy, Lorraine, France, URL http://www.theses.fr/2010NAN10049, in French, 2010.

Stahl, C., Burban, B., Goret, J.-Y., and Bonal, D.: Seasonal variations in stem CO_2 efflux in the Neotropical rainforest of French Guiana, Ann. For. Sci., 68, 771–782, doi:10.1007/s13595-011-0074-2, URL http://dx.doi.org/10.1007/s13595-011-0074-2, 2011.

Stahl, C., Hérault, B., Rossi, V., Burban, B., Bréchet, C., and Bonal, D.: Depth of soil water uptake by tropical rainforest trees during dry periods: does tree dimension matter?, Oecologia, pp. 1–11, doi:10.1007/s00442-013-2724-6, 2013.

Stark, S. C., Leitold, V., Wu, J. L., Hunter, M. O., de Castilho, C. V., Costa, F. R. C., McMahon, S. M., Parker, G. G., Shimabukuro, M. T., Lefsky, M. A., Keller, M., Alves, L. F., Schietti, J., Shimabukuro, Y. E., Brandão, D. O., Woodcock, T. K., Higuchi, N., de Camargo, P. B., de Oliveira, R. C., and Saleska, S. R.: Amazon forest carbon dynamics predicted by profiles of canopy leaf area and light environment, Ecol. Lett., 15, 1406–1414, doi:10.1111/j.1461-0248.2012.01864.x, 2012.

Stöckli, R.: LBA-MIP driver data gap filling algorithms, URL http://www.climatemodeling.org/lba-mip/LBAmipDriverDataFillingMethods.pdf, 2007.

Stoy, P. C., Mauder, M., Foken, T., Marcolla, B., Boegh, E., Ibrom, A., Arain, M. A., Arneth, A., Aurela, M., Bernhofer, C., Cescatti, A., Dellwik, E., Duce, P., Gianelle, D., van Gorsel, E., Kiely, G., Knohl, A., Margolis, H., McCaughey, H., Merbold, L., Montagnani, L., Papale, D., Reichstein, M., Saunders, M., Serrano-Ortiz, P., Sottocornola, M., Spano, D., Vaccari, F., and Varlagin, A.: A data-driven analysis of energy balance closure across FLUXNET research sites: The role of landscape scale heterogeneity, Agric. For. Meteorol., 171—172, 137–152, doi:http://dx.doi.org/10.1016/j.agrformet.2012.11.004, 2013.

Stull, R. B.: An introduction to boundary layer meteorology, Kluwer Academic Publishers, 666 pp., 1988.

Taylor, K. E.: Summarizing multiple aspects of model performance in a single diagram, J. Geophys. Res.-Atmos., 106, 7183–7192, doi:10.1029/2000JD900719, 2001.

Tempel, P., Batjes, N. H., and van Engelen, V. W. P.: IGBP-DIS soil data set for pedotransfer function development, Working paper and prepint 96/05, International Soil Reference and Information Centre (ISRIC), Wageningen, Netherlands, URL http://gcmd.nasa.gov/r/d/%5BGCMD%5DISRIC_IGBP-DIS-PTFset, 1996.

ter Steege, H., Pitman, N. C. A., Sabatier, D., Baraloto, C., Salomão, R. P., Guevara, J. E., Phillips, O. L., Castilho, C. V., Magnusson, W. E., Molino, J.-F., Monteagudo, A., Núñez Vargas, P., Montero, J. C., Feldpausch, T. R., Coronado, E. N. H., Killeen, T. J., Mostacedo, B., Vasquez, R., Assis, R. L., Terborgh, J., Wittmann, F., Andrade, A., Laurance, W. F., Laurance, S. G. W., Marimon, B. S., Marimon, B.-H., Guimarães Vieira, I. C., Amaral, I. L. a., Brienen, R., Castellanos, H., Cárdenas López, D., Duivenvoorden, J. F., Mogollón, H. F., Matos, F. D. d. A., Dávila, N., García-Villacorta, R., Stevenson Diaz, P. R., Costa, F., Emilio, T., Levis, C., Schietti, J., Souza, P., Alonso, A., Dallmeier, F., Montoya, A. J. D., Fernandez Piedade, M. T., Araujo-Murakami, A., Arroyo, L., Gribel, R., Fine, P. V. A., Peres, C. A., Toledo, M., Aymard C., G. A., Baker, T. R., Cerón, C., Engel, J., Henkel, T. W., Maas, P., Petronelli, P., Stropp, J., Zartman, C. E., Daly, D., Neill, D., Silveira, M., Paredes, M. R., Chave, J., Lima Filho, D. d. A., Jørgensen, P. M., Fuentes, A., Schöngart, J., Cornejo Valverde, F., Di Fiore, A., Jimenez, E. M., Peñuela Mora, M. C., Phillips, J. F., Rivas, G., van Andel, T. R., von Hildebrand, P., Hoffman, B., Zent, E. L., Malhi, Y., Prieto, A., Rudas, A., Ruschell, A. R., Silva, N., Vos, V., Zent, S., Oliveira, A. A., Schutz, A. C., Gonzales, T., Trindade Nascimento, M., Ramirez-Angulo, H., Sierra, R., Tirado, M., Umaña Medina, M. N., van der Heijden, G., Vela, C. I. A., Vilanova Torre, E., Vriesendorp, C., Wang, O., Young, K. R., Baider, C., Balslev, H., Ferreira, C., Mesones, I., Torres-Lezama, A., Urrego Giraldo, L. E., Zagt, R., Alexiades, M. N., Hernandez, L., Huamantupa-Chuquimaco, I., Milliken, W., Palacios Cuenca, W., Pauletto, D., Valderrama Sandoval, E., Valenzuela Gamarra, L., Dexter, K. G., Feeley, K., Lopez-Gonzalez, G., and Silman, M. R.: Hyperdominance in the Amazonian Tree Flora, Science, 342, doi:10.1126/science.1243092, 2013.

Tilman, D. and Downing, John, A.: Biodiversity and stability in grasslands, Nature, 367, 363–365, doi:10.1038/367363a0, 1994.

Tobón Marin, C., Bouten, W., and Sevink, J.: Gross rainfall and its partitioning into throughfall, stemflow and evaporation of intercepted water in four forest ecosystems in western Amazonia, J. Hydrol., 237, 40–57, doi:10.1016/S0022-1694(00)00301-2, 2000.

Tollefson, J.: Experiment aims to steep rainforest in carbon dioxide, doi:10.1038/496405a, 2013.

Tomasella, J., Hodnett, M. G., Cuartas, L. A., Nobre, A. D., Waterloo, M. J., and Oliveira, S. M.: The water balance of an Amazonian micro-catchment: the effect of interannual variability of rainfall on hydrological behaviour, Hydrol. Process., 22, 2133–2147, doi:10.1002/hyp.6813, 2008a.

Tomasella, J., Nobre, C. A., Gash, J. H. C., Shuttleworth, W. J., Roberts, J. M., Cabral, O. M., and Fisch, G. F.: Pre-LBA Anglo-BRazilian Amazonian Climate Observation Study (ABRACOS)

Data, Data set, Oak Ridge National Laboratory Distributed Active Archive Center, Oak Ridge, Tennessee, U.S.A., doi:10.3334/ORNLDAAC/899, 2008b.

Tomasella, J., Borma, L. S., Marengo, J. A., Rodriguez, D. A., Cuartas, L. A., Nobre, C. A., and Prado, M. C. R.: The droughts of 1996-1997 and 2004-2005 in Amazonia: hydrological response in the river main-stem, Hydrol. Process., 25, 1228–1242, doi:10.1002/hyp.7889, 2011.

Toomey, M., Roberts, D., and Nelson, B.: The influence of epiphylls on remote sensing of humid forests, Remote Sens. Environ., 113, 1787–1798, doi:10.1016/j.rse.2009.04.002, 2009.

Tóta, J., Fitzjarrald, D. R., Staebler, R. M., Sakai, R. K., Moraes, O. M. M., Acevedo, O. C., Wofsy, S. C., and Manzi, A. O.: Amazon rain forest subcanopy flow and the carbon budget: Santarém LBA-ECO site, J. Geophys. Res.-Biogeosci., 113, G00B02, doi:10.1029/2007JG000597, 2008.

Uhl, C. and Jordan, C. F.: Succession and Nutrient Dynamics Following Forest Cutting and Burning in Amazonia, Ecology, 65, 1476–1490, doi:10.2307/1939128, 1984.

van der Heijden, G. M. F. and Phillips, O. L.: Liana infestation impacts tree growth in a lowland tropical moist forest, Biogeosciences, 6, 2217–2226, doi:10.5194/bg-6-2217-2009, URL http://www.biogeosciences.net/6/2217/2009/, 2009.

van der Molen, M., Dolman, A., Ciais, P., Eglin, T., Gobron, N., Law, B., Meir, P., Peters, W., Phillips, O., Reichstein, M., Chen, T., Dekker, S., DoubkovÃ!', M., Friedl, M., Jung, M., van den Hurk, B., de Jeu, R., Kruijt, B., Ohta, T., Rebel, K., Plummer, S., Seneviratne, S., Sitch, S., Teuling, A., van der Werf, G., and Wang, G.: Drought and ecosystem carbon cycling, Agric. For. Meteorol., 151, 765–773, doi:10.1016/j.agrformet.2011.01.018, 2011.

Vanclay, J. and Skovsgaard, J.: Evaluating forest growth models, Ecol. Model., 98, 1–12, doi:10.1016/S0304-3800(96)01932-1, 1997.

Veraart, A. J., Faassen, E. J., Dakos, V., van Nes, E. H., Lurling, M., and Scheffer, M.: Recovery rates reflect distance to a tipping point in a living system, Nature, 481, 357–359, doi:10.1038/nature10723, 2012.

Verseghy, D. L.: Class—A Canadian land surface scheme for GCMS. I. Soil model, Intl. J. Climatol., 11, 111–133, doi:10.1002/joc.3370110202, 1991.

von Caemmerer, S.: Biochemical models of leaf photosynthesis, no. 2 in Techniques in Plant Sciences, CSIRO Publishing, Collingwood, VIC, Australia, 2000.

von Randow, C., Manzi, A. O., Kruijt, B., de Oliveira, P. J., Zanchi, F. B., Silva, R. L., Hodnett, M. G., Gash, J. H. C., Elbers, J. A., Waterloo, M. J., Cardoso, F. L., and Kabat, P.: Comparative measurements and seasonal variations in energy and carbon exchange over forest and pasture in South West Amazonia, Theor. Appl. Climatol., 78, 5–26, doi:10.1007/s00704-004-0041-z, 2004.

von Randow, C., Zeri, M., Restrepo-Coupe, N., Muza, M. N., de Gonçalves, L. G. G., Costa, M. H., de Araújo, A. C., Manzi, A. O., da Rocha, H. R., Saleska, S. R., Arain, M. A., Baker, I. T., Cestaro, B. P., Christoffersen, B., Ciais, P., Fisher, J. B., Galbraith, D., Guan,

X., van den Hurk, B., Ichii, K., Imbuzeiro, H., Jain, A., Levine, N., Miguez-Macho, G., Poulter, B., Roberti, D. R., Sahoo, A., Schaefer, K., Shi, M., Tian, H., Verbeeck, H., and Yang, Z.-L.: Inter-annual variability of carbon and water fluxes in Amazonian forest, Cerrado and pasture sites, as simulated by terrestrial biosphere models, Agric. For. Meteorol., 182—183, 145–155, doi:10.1016/j.agrformet.2013.05.015, 2013.

Wagner, F., Herault, B., Stahl, C., Bonal, D., and Rossi, V.: Modeling water availability for trees in tropical forests, Agric. For. Meteorol., 151, 1202–1213, doi:10.1016/j.agrformet.2011.04.012, 2011.

Wagner, F., Rossi, V., Stahl, C., Bonal, D., and Hérault, B.: Water Availability Is the Main Climate Driver of Neotropical Tree Growth, PLoS One, 7, e34 074, doi:10.1371/journal.pone.0034074, 2012.

Walko, R. L., Band, L. E., Baron, J., Kittel, T. G. F., Lammers, R., Lee, T. J., Ojima, D., Pielke, R. A., Taylor, C., Tague, C., Tremback, C. J., and Vidale, P. L.: Coupled Atmosphere–Biophysics–Hydrology Models for Environmental Modeling, J. Appl. Meteor., 39, 931–944, doi:10.1175/1520-0450(2000)039<0931:CABHMF>2.0.CO;2, 2000.

Wang, Y.-P. and Leuning, R.: A two-leaf model for canopy conductance, photosynthesis and partitioning of available energy I:: Model description and comparison with a multi-layered model, Agric. For. Meteorol., 91, 89–111, doi:10.1016/S0168-1923(98)00061-6, 1998.

Weiss, A. and Norman, J.: Partitioning Solar-Radiation into direct and diffuse, visible and near-infrared components, Agric. For. Meteorol., 34, 205–213, doi:10.1016/0168-1923(85)90020-6, 1985.

Williamson, G. B., Laurance, W. F., Oliveira, A. A., Delamônica, P., Gascon, C., Lovejoy, T. E., and Pohl, L.: Amazonian Tree Mortality during the 1997 El Niño Drought, Conserv. Biol., 14, 1538–1542, doi:10.1046/j.1523-1739.2000.99298.x, 2000.

Wofsy, S. C., Goulden, M. L., Munger, J. W., Fan, S.-M., Bakwin, P. S., Daube, B. C., Bassow, S. L., and Bazzaz, F. A.: Net Exchange of CO_2 in a Mid-Latitude Forest, Science, 260, 1314–1317, doi:10.1126/science.260.5112.1314, 1993.

Wohlfahrt, G. and Cernusca, A.: Momentum Transfer By A Mountain Meadow Canopy: A Simulation Analysis Based On Massman's (1997) Model, Boundary-Layer Meteorol., 103, 391–407, doi:10.1023/A:1014960912763, 2002.

Wohlfahrt, G., Bianchi, K., and Cernusca, A.: Leaf and stem maximum water storage capacity of herbaceous plants in a mountain meadow, J. Hydrol., 319, 383 – 390, doi:10.1016/j.jhydrol.2005.06.036, 2006.

Wright, I. J., Reich, P. B., Westoby, M., Ackerly, D. D., Baruch, Z., Bongers, F., Cavender-Bares, J., Chapin, T., Cornelissen, J. H. C., Diemer, M., Flexas, J., Garnier, E., Groom, P. K., Gulias, J., Hikosaka, K., Lamont, B. B., Lee, T., Lee, W., Lusk, C., Midgley, J. J., Navas, M.-L., Niinemets, U., Oleksyn, J., Osada, N., Poorter, H., Poot, P., Prior, L., Pyankov, V. I., Roumet, C., Thomas, S. C., Tjoelker, M. G., Veneklaas, E. J., and Villar, R.: The worldwide leaf economics spectrum, Nature, 428, 821–827, doi:10.1038/nature02403, 2004.

Xaud, H. A. M., Martins, F. S. R. V., and dos Santos, J. R.: Tropical forest degradation by mega-fires in the northern Brazilian Amazon, Forest Ecol. Manag., 294, 97–106, doi:10.1016/j.foreco.2012.11.036, 2013.

Xu, L., Samanta, A., Costa, M. H., Ganguly, S., Nemani, R. R., and Myneni, R. B.: Widespread decline in greenness of Amazonian vegetation due to the 2010 drought, Geophys. Res. Lett., 38, L07 402, doi:10.1029/2011GL046824, 2011.

Zanne, A. E., Lopez-Gonzalez, G., Coomes, D. A., Ilic, J., Jansen, S., Lewis, S. L., Miller, R. B., Swenson, N. G., Wiemann, M. C., and Chave, J.: Data from: Towards a worldwide wood economics spectrum, URL `http://dx.doi.org/10.5061/dryad.234`, dryad Digital Repository, 2009.

Zhao, M. and Running, S. W.: Drought-Induced Reduction in Global Terrestrial Net Primary Production from 2000 Through 2009, Science, 329, 940–943, doi:10.1126/science.1192666, 2010.

Zhao, W. and Qualls, R. J.: A multiple-layer canopy scattering model to simulate shortwave radiation distribution within a homogeneous plant canopy, Water Resour. Res., 41, W08 409, doi:10.1029/2005WR004016, 2005.

Zhao, W. and Qualls, R. J.: Modeling of long-wave and net radiation energy distribution within a homogeneous plant canopy via multiple scattering processes, Water Resour. Res., 42, W08 436, doi:10.1029/2005WR004581, 2006.

Zimmermann, N. E., Yoccoz, N. G., Edwards, T. C., Meier, E. S., Thuiller, W., Guisan, A., Schmatz, D. R., and Pearman, P. B.: Climatic extremes improve predictions of spatial patterns of tree species, Proc. Natl. Acad. Sci. U. S. A., 106, 19 723–19 728, doi:10.1073/pnas.0901643106, 2009.